Draft CMB-S4 Preliminary Baseline Design Report

CMB-S4 Collaboration

March 8, 2021

Preface

This document presents the CMB-S4 Preliminary Baseline Design...

Executive Summary

The Preliminary Baseline Design...

Contents

List of Figures

List of Tables

1

Science Case (*Kevin Huffenberger and Joel Meyers*)

1.1 Introduction

The CMB-S4 project, a millimeter-wavelength survey of unprecedented sensitivity and scientific reach, will extract a wealth of new information from the Cosmic Microwave Background (CMB), the radiation afterglow of the Big Bang that delivers to us a snapshot of the primordial plasma as it existed while the Universe was in its infancy. CMB-S4 will drive our knowledge of fundamental physics and astrophysics forward. Over the last fifty years, CMB measurements have provided conclusive evidence that our Universe evolved from a hot and dense early state known as the Big Bang. These measurements have determined the age and the composition of the Universe with percent-level precision. They have provided the strongest evidence that dark matter cannot be made up of the same building blocks as ordinary matter. They have shown that the processes that generated the fluctuations throughout the Universe—fluctuations in density that later evolve into the large-scale structure of the cosmos—occurred before the Universe became filled with hot, dense plasma. Those fluctuations were already present at the beginning of the Big Bang. The origin of these fluctuations is one of the mysteries that CMB-S4 is designed to solve.

CMB measurements provide opportunities to study many aspects of the Universe throughout its history. Current experiments have only begun to make precise measurements of CMB polarization anisotropies, which are generated by the motion of the primordial plasma and encode significant additional information to the temperature anisotropies that we have now measured well. So-called secondary anisotropies, like the weak gravitational lensing by large-scale structure and scattering by free electrons, document more recent times and hold tremendous promise to improve our understanding of astrophysics and cosmology.

Experiments on the ground, on balloons, and in space can all measure the CMB, and each platform has particular strengths. As the next-generation ground-based effort, CMB-S4 will push the scientific frontier by assembling largest-ever set of cyrogenic microwave-sensitive detectors. Using the CMB to transform our understanding of the early Universe and of particle physics, CMB-S4 will fulfill goals set out in the 2010 Astronomy and Astrophysics Decadal Survey and the 2014 report of the Particle Physics Project Prioritization Panel. Namely, it will discover or set stringent constraints on primordial gravitational waves and light relic particles. Addressing another key goal, CMB-S4 will also constrain neutrino properties and provide critical measurements of the evolution of cosmic structure.

By design, CMB-S4 is also an astronomical survey machine. CMB-S4 will image a large fraction of the sky, including much of the Galaxy, with high-fidelity measurements of intensity and linear polarization. Its maps will cover a range of wavelengths, on angular scales ranging from arcminutes to many degrees. It will detect individual galaxy clusters through Compton scattering of CMB photons by the hot gas present in clusters (the Sunyaev-Zeldovich effect), allowing us to study cluster evolution. Large samples of galaxies can be detected by the thermal emission of their dust or by the synchrotron emission from their active galactic nucleus (AGN). The large-area survey will probe large cosmological volumes to detect the rarest and most extreme objects.

CMB-S4 will provide measurements on a wide variety of timescales. Typical CMB experiments survey the same patch of sky repeatedly to build up the signal-to-noise ratio. This leads to sampling on timescales as fast as multiple times per second, with daily revisits and observations extending over several years. CMB-S4's unprecendented depth allows it to see many objects in the mm-wave transient and variable sky, including gammay-ray bursts, tidal disruption events, blazars, and stars. It will also observe the thermal emission from moving Solar System objects, finding asteroids, dwarf planets, and possibly, unknown worlds in our outer Solar System.

In the following sections, we will tour CMB-S4's diverse scientific applications, touching on many ideas in particle physics, cosmology, astrophysics, and astronomy.

1.2 Summary of Science Themes

Scientific Program of CMB-S4:

1. *Primordial gravitational waves and inflation*
2. *The dark Universe*
3. *Mapping matter in the cosmos*
4. *The time-variable millimeter-wave sky*

CMB-S4's scientific program follows four main themes. The first two science themes relate to fundamental physics. The final two themes related to the broader scientific opportunities made possible by a millimeter-wave survey of unprecedented depth and breadth, and we call them our Legacy Survey themes. We summarize the four science themes in the following short sections and present the full science case in the remainder of the chapter. The narrow set of design-driving science goals in the following chapter (Chapter 2) are the most technically challenging and enable the whole science program.

Primordial gravitational waves and inflation. We have a historic opportunity to open up a window to the primordial Universe. Leading models for the origin of the hot Big Bang imply that CMB-S4 may have the sensitivity to detect the signature of gravitational waves in the primordial plasma. This detection would provide the first evidence for the quantization of gravity, reveal new physics at the energy scale of grand unified theories, and probe the symmetries of nature. Conversely, a null result would rule out large classes of theoretical models of the early Universe and put significant constraints on the leading paradigm for early-Universe cosmology, the theory of cosmic inflation.

Cosmic inflation refers to a period of accelerated expansion prior to the hot Big Bang. During this epoch, quantum fluctuations were imprinted on all spatial scales in the cosmos. These fluctuations seeded the density perturbations that developed into all the structure in the Universe today. While we cannot yet claim with high confidence that the Universe underwent cosmic inflation, the simplest models of inflation are exceptionally successful at matching the data we do have. Specifically, the predictions of inflation include a small mean spatial curvature in the geometry of spacetime and initial density perturbations drawn from a nearly Gaussian distribution. The vast majority of inflationary models predict that the variance of fluctuations is slightly larger on large scales than on small scales. Each of these predictions has been verified to high precision by previous CMB measurements.

The observed (weak) scale-dependence of the density perturbations has tantalizing and quantitative implications for the detection of primordial gravitational waves. In the simplest class of inflation models, the amplitude of primordial gravitational waves (r) is comparable to the deviation from scale invariance, as quantified by parameter $n_s - 1$. Beyond that, *all* inflation models that naturally explain the observed $n_s - 1$ value (and have a characteristic energy scale larger than the Planck mass) generate primordial gravitational waves above the 95% confidence upper limit that CMB-S4 can set (see Fig. 7 for example models). A well-motivated sub-class within this set of models is detectable by CMB-S4 at 5σ.

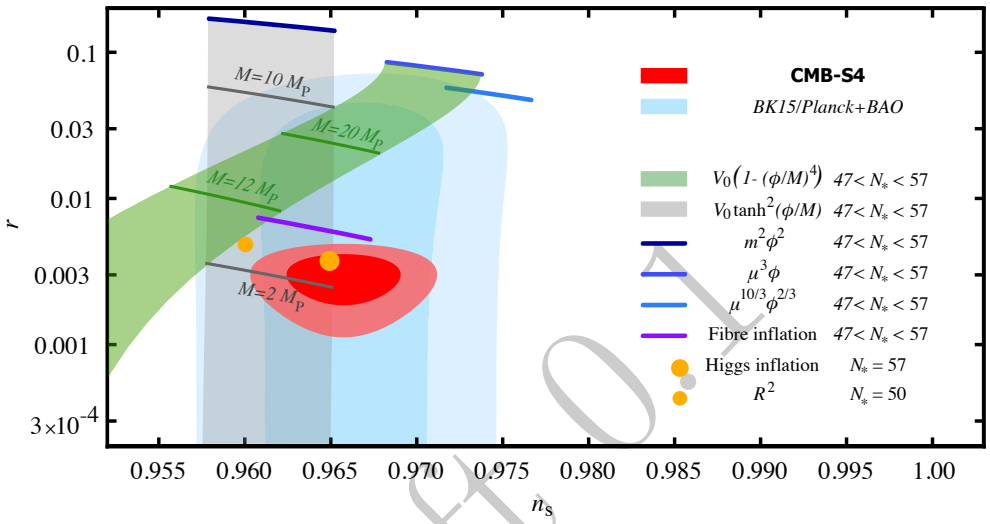

Figure 1: Forecast of CMB-S4 constraints in the n_s–r plane for a fiducial model with $r = 0.003$. Also shown are the current best constraints from a combination of the BICEP2/*Keck Array* experiments and *Planck* [1]. Models that naturally explain the observed departure from scale invariance separate into two viable classes: monomial and plateau. The monomial models ($V(\phi) = \mu^{4-p}\phi^p$) are shown for three values of p as blue lines for $47 < N_* < 57$ (with the spread in N_* reflecting uncertainties in reheating, and smaller N_* predicting lower values of n_s). This class is not completely ruled out by the data, but is disfavored. The plateau models divide into those with plateaus near the scalar field origin, for which we include the quartic hilltop (green band) as an example, and those with plateaus away from the origin, for which we include the *tanh* form (gray band) as an example, as this form arises in a sub-class of α-attractor models [2]. Some particular realizations of physical models in the plateau class are also shown: the Starobinsky model [3] and Higgs inflation [4] (small and large orange filled circles, respectively) and fibre inflation [5] (purple line). The differing choices of N_* for Higgs and Starobinsky reflect differing expectations for reheating efficiency.

Because the Universe has expanded by a tremendous amount since the time when the primordial perturbations were imprinted, CMB observations can probe physics at extraordinarily small length scales, *up to* 10^{10} *times smaller than those probed in terrestrial particle colliders*. The CMB provides a unique window to test new phenomena at these length scales. The observational requirement is also clear: we must measure the polarization to high precision on angular scales from several arcminutes to degrees.

Primordial gravitational waves (tensor perturbations) generate an odd-parity fluctuation pattern in the polarization across the sky, called "B modes" by analogy with electromagnetism. (Scalar density perturbations source only an even parity polarization pattern, called "E modes".) To measure primordial B modes, we must observe at multiple frequencies to remove Galactic foreground contamination and also measure small angular scales to remove the (non-primordial) B modes that are generated by the conversion of E modes

through gravitational lensing. The CMB-S4 design has sufficient sensitivity to detect or tightly constrain the degree-scale B modes generated by gravitational waves in many models, and to measure the amount of gravitational waves (tensor perturbations), detecting or setting an upper limit on the tensor-to-scalar ratio r. With an order of magnitude more detectors than precursor instruments, and exquisite control of systematic errors, we will improve upon limits from previous observations by a factor of 5, allowing us to either detect primordial gravitational waves or rule out a broad class of models with a super-Planckian characteristic energy scale.

Complementary to the search for gravitational waves, CMB-S4 will provide exquisite measurements of primordial *density* fluctuations via E modes. The polarization sensitivity will surpass current measurements of E-mode polarization, which are far from being sample-variance-limited. Because the astrophysical foregrounds are lower in amplitude for polarization than temperature, we will improve measurements across the angular scales already observed in temperature, and push to yet smaller angular scales. These polarization measurements will significantly extend and enhance searches for non-power-law features in the primordial power spectrum, small variations in the equation of state, and small departures from Gaussianity. The CMB is the most robust observable to search for primoridal non-Gaussianities to date and CMB-S4 will provide the tightest constraints on the most compelling signatures, improving the constraints from the *Planck* satellite. Primordial non-Gaussianities can also be produced in models with undetectably small gravitational wave production and provide an independent handle on the early Universe. Non-Gaussianity can also be measured via cross correlation of the CMB-S4 mass map with galaxy surveys, a measurement that has the potential to rule out a large class of inflationary models.

The dark Universe. In the standard cosmological model, about ninety five percent of the mass–energy density of the Universe is in dark matter and dark energy, while only five percent is in well-understood, "normal," baryonic matter. With CMB-S4 we can address numerous questions about these dark ingredients, such as: How is the dark matter distributed on large scales? Does the dark matter have non-gravitational interactions with baryons? And are there additional unseen components beyond dark matter and dark energy?

Light relic particles are one well-motivated possibility. These additional components to the dark sector are light particles produced in the early Universe, and are sometimes referred to as "dark radiation." Many extensions of the Standard Model (SM) predict such light relics, including axion-like particles and sterile neutrinos [6, 7, 8, 9]. For large regions of the unexplored parameter space, these light particles are thermalized in the early Universe. To date, CMB observations by the *Planck* satellite can probe light particles that departed from equilibrium ("froze out") as early as the first 50 micro-seconds of the Universe. With CMB-S4 we can push back this frontier by over a factor of 10,000, to the first fractions of a nanosecond.

CMB-S4 will achieve sensitivity to relics that froze out well before the quark-hadron phase transition (the epoch when the Universe cooled sufficiently that quarks became locked into hadrons like neutrons and protons). The contribution of light relics to the energy density leads to observable consequences in the CMB temperature and polarization anisotropy. This is often parameterized with the "effective number of neutrino species," $N_{\rm eff}$. The collective influence of the three already-known light relics (the three families of neutrinos) has already been detected at high significance. Current data are only sensitive enough to detect additional relics that froze out after the quark-hadron transition, and Stage-3 CMB experiments can only push somewhat into that epoch, so CMB-S4's ability to probe times well before that transition is a major advance.

In addition to precise constraints on $N_{\rm eff}$, CMB-S4 will give an *independent* high-precision measurement of the primordial helium abundance, $Y_{\rm p}$. This is particularly useful since $Y_{\rm p}$ is sensitive to $N_{\rm eff}$ a few minutes after reheating, while the CMB power spectrum is affected by $N_{\rm eff}$ prior to recombination, about 370,000

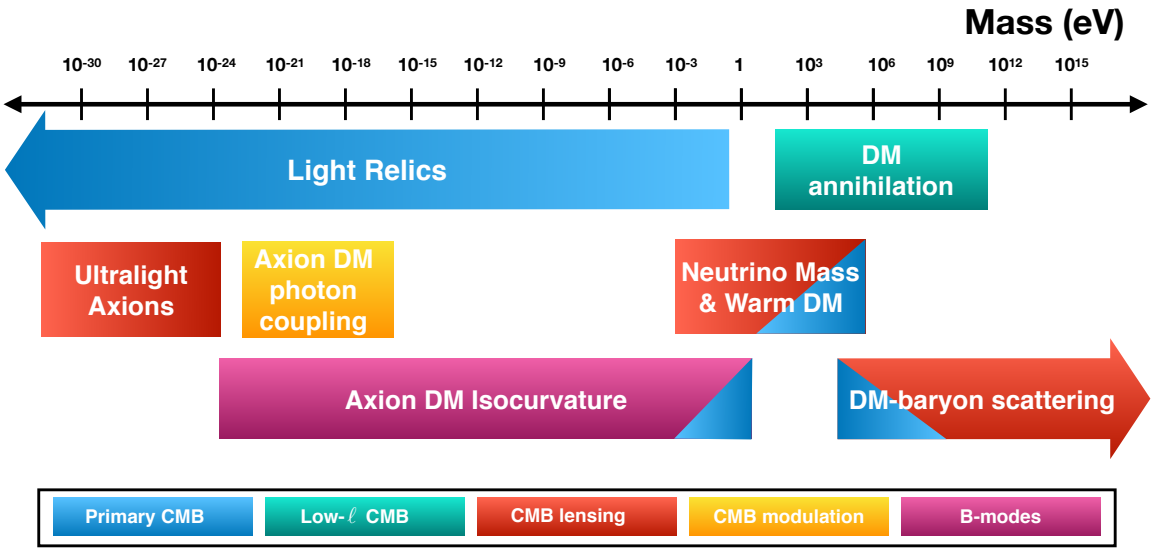

Figure 2: CMB-S4-enabled exploration of light relics, axions, neutrino mass, and dark matter properties. In each case, there is a window in the mass of the relevant particle where the CMB is particularly sensitive. Each such region is shown in a color (or colors) representing the observable(s) that drives the constraint. The primary CMB anisotropies at high-ℓ (blue) are particularly sensitive to light relics, as discussed in Section 1.4.1, and properties of the dark matter discussed in Section 1.4.4. Low-ℓ modes (green) most directly impact constraints on dark matter annihilation. CMB lensing reconstruction (red) is a sensitive probe of matter in the late Universe, particularly effects that suppress clustering power. Axion dark matter can create additional modulations of the CMB polarization angles (yellow) through their coupling to photons. A detection of primordial gravitational waves (pink) would severely constrain the QCD axion because of the implied high scale of inflation.

years later. Measuring the radiation content at these well-separated times provides a window onto any non-trivial evolution in the energy density of radiation in the early Universe. Furthermore, $N_{\rm eff}$ and $Y_{\rm p}$ are sensitive to neutrino physics and physics beyond the Standard Model in related, but different ways, allowing even finer probes of particle physics, especially in the neutrino and dark sectors.

CMB-S4 will also enable a broader exploration of the dark Universe in combination with other probes, often significantly enhancing them by breaking their intrinsic degeneracies. It will improve or detect various possibilities for the dark matter properties beyond the simplest cold-dark-matter scenario, as described in Fig. 2. It will add to dark energy constraints through precision measurements of the primordial power spectrum (where dark energy physics enters through projection effects), through precision measurements of the lensing convergence power spectrum, through the CMB-lensing-derived mass calibration of galaxy clusters, and through CMB lensing tomography in combination with galaxy surveys.

Mapping matter in the cosmos. The amount of dark matter exceeds normal, baryonic matter by a more than a factor of five, and most of the baryonic matter is in the form of hot ionized gas rather than cold gas or stars. CMB-S4 will be able to map out dark and normal matter separately by measuring the fluctuations in the total mass density (using gravitational lensing) and the ionized gas density (using Compton scattering).

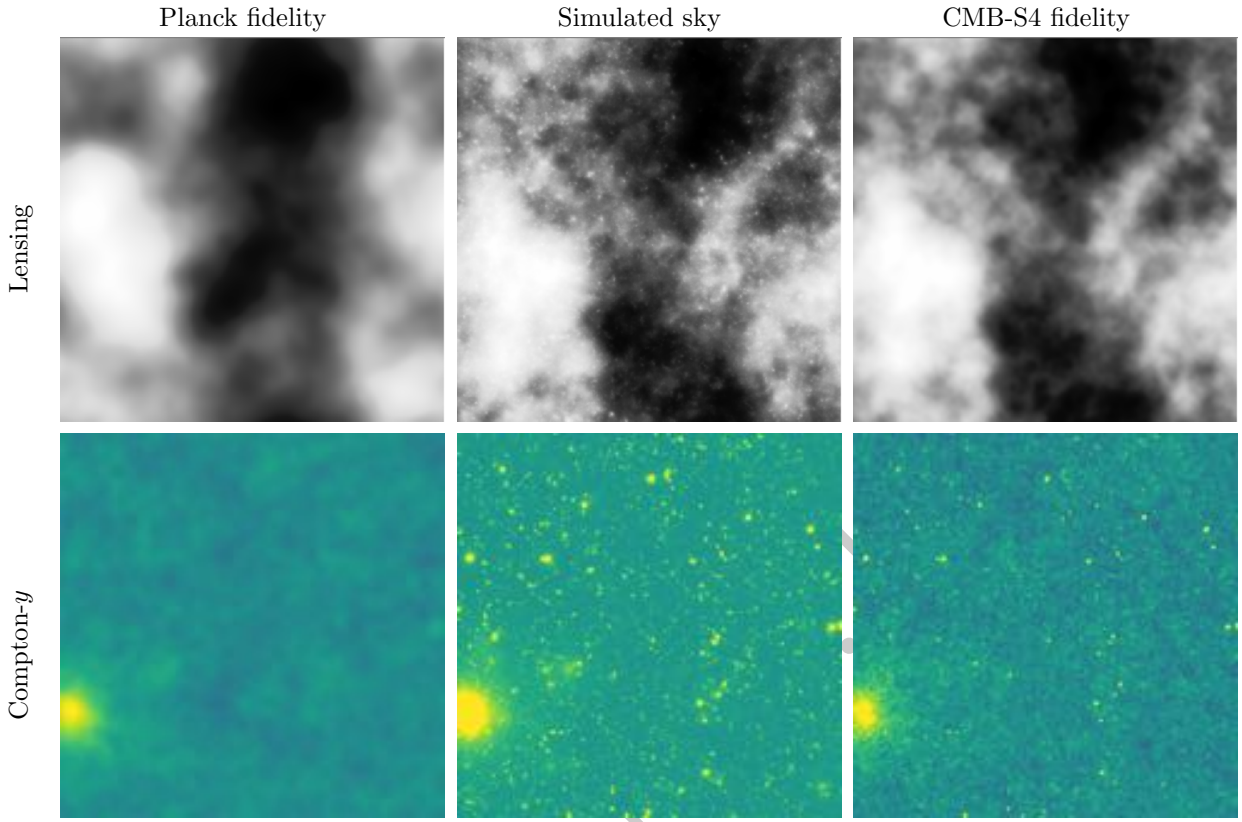

Figure 3: Example lensing-deflection maps (top) and thermal SZ (Compton y-maps, bottom) reconstructed with *Planck* (left) and CMB-S4 data (right). The center panels show a 25 deg^2 patch of the all-sky lensing-deflection field in the WebSky simulations (top) and Compton y (bottom). The left panels show Wiener-filtered maps of the signal after adding (Gaussian) noise and residual foregrounds with levels corresponding to the *Planck* 2018 lensing-deflection map (top) and the *Planck* 2015 "Needlet Internal Linear Combination" tSZ map (bottom). The right panel shows analogous Wiener-filtered maps with noise expected for CMB-S4 (top) and residual foregrounds determined by the CMB-S4 + *Planck* tSZ noise power spectrum in Fig. 20. The significantly higher fidelity of the CMB-S4 reconstruction is evident.

Gravitational lensing of background sources by intervening gravitational potentials leads to detectable distortions in the background images which can be used to reconstruct fluctuations in the mass density. Virtually all of the the density fluctuations within the observable Universe leave an imprint when the CMB is the background source. The map resulting from CMB lensing reconstruction will be wide-area, highly sensitive, and extremely well-calibrated.

On its own, we can use this map to precisely measure the density of large-scale structure at intermediate redshifts, with important applications to dark energy, modified gravity, and studies of neutrino masses. In concert with catalogs of objects, we can use this map to weigh samples (of e.g., galaxies and galaxy clusters) to as high a redshift as such sources can be found. The technique of CMB lensing tomography, enabled by CMB-S4 and galaxy catalogs from—for example—Rubin Observatory/LSST, will allow for the creation of mass maps in broad redshift slices out to redshifts as high as $z \sim 5$, making possible new precision tests

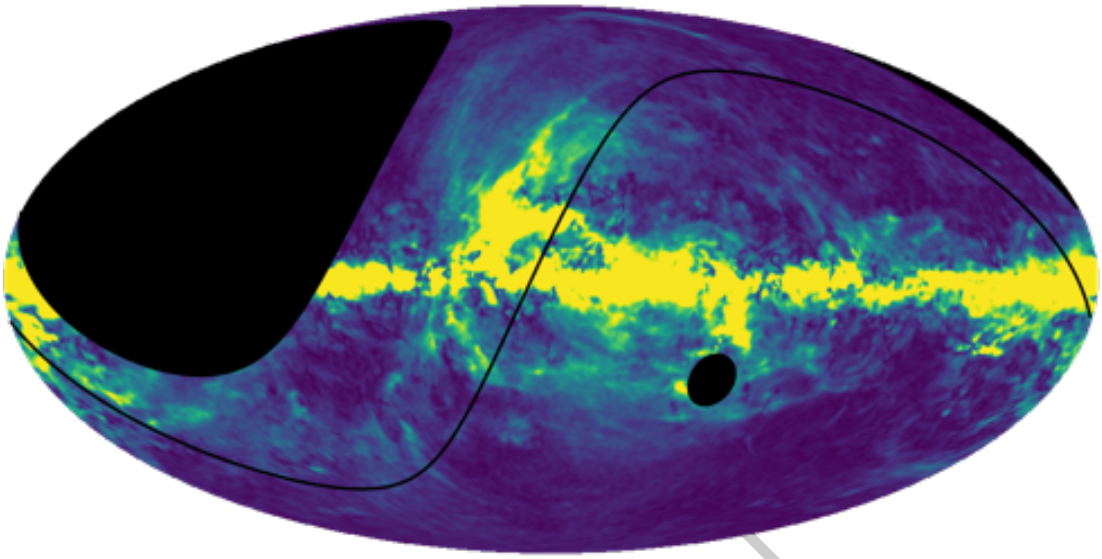

Figure 4: CMB-S4 survey area, in Galactic coordinates, with the ecliptic plane marked as the solid line.

of cosmology. Such results explore the connection between visible baryons and the underlying dark-matter scaffolding. In conjunction with cosmic-shear surveys (e.g., Rubin/LSST) that measure the low-redshift mass distribution, a map of the high-redshift mass distribution can be constructed, gaining new insight into the first galaxies. By calibrating cluster masses at high redshift, the abundance of galaxy clusters can be used as an additional probe of dark energy and neutrino masses.

Low-redshift structure acts to lens both the CMB and the images of intermediate-redshift galaxies. Detailed comparisons provides a valuable cross-check on galaxy shear measurement calibration and enables geometric tests using the longest possible lever arm.

Most of the baryons in the late Universe are believed to be in a diffuse ionized plasma that is difficult to observe. This ionized plasma can leave imprints in the CMB through Compton scattering, the so-called Sunyaev-Zeldovich effects. Two prominent manifestations are a spectral distortion from hot electrons interacting with the relatively cold CMB (thermal SZ or tSZ), and a general redshift or blueshift of the scattered photons due to coherent bulk flows along the line of sight (kinematic SZ or kSZ).

The nature of the scattering makes the tSZ effect independent of redshift, providing a means to detect galaxy clusters out to high redshift. The deep-and-wide field covers a large volume and the ultra-deep field is sensitive lower-mass clusters, making CMB-S4 an effective probe of the crucial regime of $z \gtrsim 2$, when galaxy clusters were both accreting new hot gas vigorously and forming the bulk of their stars. The CMB-S4 cluster catalog will be more than an order of magnitude larger than current catalogs based on tSZ or X-ray measurements, and specifically will contain an order of magnitude more high-redshift clusters at $z > 2$ than will be discovered with Stage 3 CMB experiments. CMB-S4 will also measure the diffuse tSZ signal everywhere on the sky and make a temperature-weighted map of ionized gas which can be used to measure the average thermal pressure profiles around galaxies and groups of galaxies.

CMB-S4 will measure the kSZ effect, which will be combined with data from other surveys to make maps of the projected electron density around samples of objects. Applications of these maps include measuring

ionized gas as a function of radius, directly constraining the impact of feedback from active galactic nuclei and supernovae on the intergalactic medium and constraining theories of modified gravity with the bulk flow amplitude as a function of separation.

Even without overlapping galaxy catalogs, the kSZ signal adds extra small-scale power that is significantly non-Gaussian. Some of this excess power and non-Gaussianity will be coming from the relatively local Universe where the galaxy catalogs overlap, but there should also be a substantial signal coming from the epoch of reionization. By directly probing the ionized gas distribution, these measurements are completely complementary to the measurements of the neutral gas that can be obtained with redshifted Ly-α or redshifted 21-cm studies.

In the course of its survey, CMB-S4 will catalog the emission from galaxies in the mm-wave band, including AGN and dusty star-forming galaxies. The matter in our own Galaxy will also be mapped in intensity and linear polarization over a large fraction of the sky, with extracted images of synchrotron and dust emission with high fidelity on scales ranging from arcminutes to several degrees.

The time-variable millimeter-wave sky. There have been relatively few studies of the variable sky at mm-wavelengths, with few wide-area systematic surveys done to date by CMB experiments [10**?**]. Known contributors to the time-varying sky are transient events, Solar System objects, and variable AGN (especially blazars).

Targeted follow-up observations of gamma-ray bursts, core-collapse supernovae, tidal disruption events, classical novae, X-ray binaries, and stellar flares have found that there are many transient events with measured fluxes that would make them detectable by CMB-S4. A systematic survey of the mm-wave sky with a cadence of a day over a large fraction of the sky would be an excellent complement to other transient surveys, filling a gap between radio and optical searches. Gamma-ray burst afterglows can be detected within a few hours of the burst in many cases, and there is a possibility of capturing mm-wave afterglows that have no corresponding gamma-ray trigger either from the geometry of relativistic beaming and/or from sources being at very high redshift.

Thermal emission from planets, dwarf planets, and asteroids have been measured at these wavelengths, and since such sources have high proper motions, they are easily differentiated from the distant objects in the extrasolar sky. Using the thermal emission rather than reflected light has several complementary aspects: the fall-off with distance is less severe, providing unique information on possible large objects in the distant reaches of the Solar System; the physical information available is also very different, measuring long-wavelength emissivity rather than optical reflectivity; and with long-time baselines for observation it will be possible to build up rotation curves for a large number of objects, enabling detailed comparison with the optical and infrared versions.

CMB-S4 will play an active role in multi-messenger astronomy. Accreting black holes are known to be highly variable. A CMB survey can provide a long baseline with high time sampling in both intensity and linear polarization. This will create a mm-wave archive for multi-messenger astronomy, in particular for future blazars that are discovered to be sources of high-energy neutrinos (such as the blazar TXS 0506+056, thought to be associated with the IceCube event IC170922A). With a large catalog of time-variable blazars, it will be possible to derive detailed variability statistics over several years with nearly daily monitoring for both the detected objects and the sources that are observed to *not* be neutrino sources. Additionally, the natural wide-area nature of the survey will make it straightforward to search for gravitational wave sources that happen to be poorly localized. Although the first binary neutron star merger, GW170817, was not detected at millimeter wavelengths, this was likely due to the low density of the merger environment [11]. There is reason to expect, based on observations of short gamma-ray bursts, that at least some mergers can

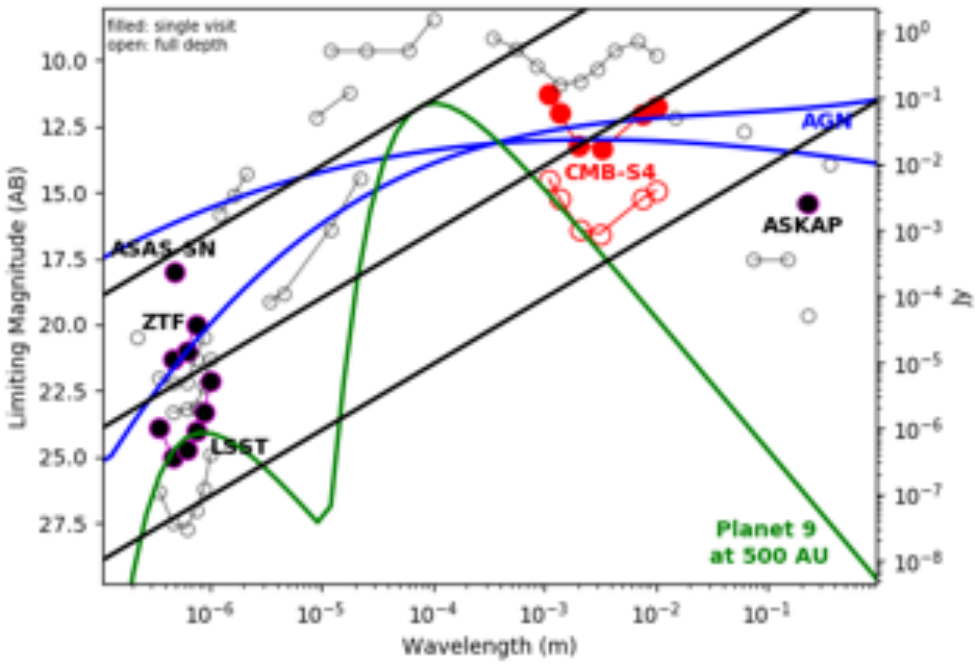

Figure 5: Filled circles show 5σ limiting magnitudes for transient surveys (ASAS-SN, Zwicky Transient Facility, Large Synoptic Sky Survey, Australia SKA Pathfinder, all in black, CMB-S4 weekly flux limit in red) over a large fraction of the sky. Diagonal lines indicate constant νS_ν, lines separated by factors of 100: green shows a Neptune-mass planet at 500 AU, and blue lines show SEDs corresponding to a quasar or blazar, normalized to be representative in flux of the population measurable in daily CMB-S4 maps. Open circles show the coadded 5σ depth for past and near-future surveys that cover large fractions of the sky, with CMB-S4 again shown in red. The ultra-deep CMB-S4 survey (not shown) is a factor of 2-6 deeper than the deep and wide survey, depending on the wavelength.

occur in denser environments, which will make them fainter in the optical, but *enhance* their mm emission [12].

1.3 Primordial gravitational waves and inflation

The first science theme that we examine in detail addresses the physical processes in the very early Universe that generate structure in the Universe.

CMB-S4 has the potential to detect a pristine relic from the primordial Universe: primordial gravitational waves that, at the time of recombination, imprint a polarization pattern of the cosmic microwave background. This discovery would unravel the mechanism responsible for the generation of primordial perturbations.

Cosmologists widely regard inflation, a period of nearly exponential expansion, as the most compelling paradigm for the very early Universe. Many of the predictions of the simplest models of inflation have been verified. As predicted, we have detected a small departure from scale invariance of the density perturbations. The sign and size of that departure implies that constraints on the gravitational wave amplitudes by CMB-S4 will provide key information about the early Universe. For the foreseeable future, precise measurements of CMB polarization are our only way to detect primordial gravitational waves. Even an upper limit from CMB-S4 would provide invaluable insights into the first moment of our Universe.

Because gravitational waves are fluctuations in the spacetime metric rather than the density, such a detection would open a new window into the early Cosmos and transform our understanding of fundamental physics.

In addition, CMB-S4 will provide unprecedented constraints on primordial fluctuations in general. Inflation produces nearly Gaussian fluctuations, but many models make a definite prediction for a small amount of non-Gaussianity. Discovery of that non-Gaussianity would present a true breakthrough, on par with a detection of primordial gravitational waves. *Planck* [13, 14] showed that the non-Gaussianity of the primordial fluctuations is indeed small; however, impressive as these constraints are, they do not yet reach the theoretically motivated thresholds that CMB-S4 can achieve. CMB-S4 will have multiple ways to measure non-Gaussianity, particularly in conjunction with large-scale structure measurements, opening an important range of parameter space.

1.3.1 Primordial gravitational waves

Stars and galaxies form through gravitational collapse, but the primordial density perturbations that seed them were generated in the very early Universe. The detailed mechanism remains unknown, but the mechanisms in many models that produce density perturbations also produce gravitational waves. By measuring or constraining the amplitude of primordial gravitational waves, CMB-S4 will provide invaluable information about the origin of all structure in our Universe.

Our quantitative discussion begins with the line element for a Friedmann-Lemaître-Robertson-Walker (FLRW) universe, which when perturbed in the ADM (Arnowitt-Deser-Misner) formalism [15] is given by

$$\begin{aligned} ds^2 &= -N^2 dt^2 + h_{ij}(dx^i + N^i dt)(dx^j + N^j dt)\,, \\ h_{ij} &= a^2(t)[e^{2\mathcal{R}}\delta_{ij} + \gamma_{ij}]\,. \end{aligned} \tag{1.1}$$

We pay particular attention to the scalar fluctuations $\mathcal{R}$ and tensor fluctuations γ_{ij}, since the Hamiltonian and momentum constraints determine the lapse N and the shift N^i in terms of those dynamical degrees of freedom. (In general h_{ij} may also contain vector perturbations, but these rapidly decay and can be neglected unless they are actively sourced, e.g., by cosmic strings.)

We work with the Fourier transforms of the fluctuations. This is possible because the equations of motion are invariant under translations, and the fluctuations are small enough to be treated perturbatively. They are

$$\mathcal{R}(t,\mathbf{x}) = \int \frac{d^3k}{(2\pi)^3}\mathcal{R}(t,\mathbf{k})e^{i\mathbf{k}\cdot\mathbf{x}} + \text{h.c.} \qquad \text{and} \qquad \gamma_{ij}(t,\mathbf{x}) = \sum_\lambda \int \frac{d^3k}{(2\pi)^3}\gamma_\lambda(t,\mathbf{k})e_{ij}(\mathbf{k},\lambda)e^{i\mathbf{k}\cdot\mathbf{x}} + \text{h.c.}\,, \quad (1.2)$$

where $e_{ij}(\mathbf{k},\lambda)$ is the transverse-traceless polarization tensor for the graviton, λ labels the polarization states of the gravitational waves, and 'h.c.' stands for the Hermitian conjugate.

In a universe that is dominated by matter or radiation the expansion rate $H = \dot{a}/a$ decays more rapidly than the momentum k/a redshifts. So at early times the modes are 'outside the horizon,' $k \ll aH$, and are time-independent. As modes 'enter the horizon,' $k \gg aH$, the modes oscillate.

The statistical properties of the scalar and tensor fluctuations, $\mathcal{R}$ and γ_λ, at times when the modes are outside the horizon, provide the link between late-time observations and the primordial era. For a universe that is statistically homogeneous and isotropic, and in which the primordial fluctuations are adiabatic and Gaussian, the information about the statistical properties is contained entirely in the 2-point correlation functions

$$\begin{aligned}\langle \mathcal{R}(\mathbf{k})\mathcal{R}(\mathbf{k}')\rangle &= (2\pi)^3\delta^3(\mathbf{k}+\mathbf{k}')\frac{2\pi^2}{k^3}\Delta^2_{\mathcal{R}}(k),\\ \langle \gamma_\lambda(\mathbf{k})\gamma_{\lambda'}(\mathbf{k}')\rangle &= (2\pi)^3\delta_{\lambda\lambda'}\delta^3(\mathbf{k}+\mathbf{k}')\frac{2\pi^2}{k^3}\frac{1}{2}\Delta^2_{\gamma}(k),\end{aligned} \quad (1.3)$$

where the factor of $1/2$ in the last line accounts for the fact that the measured power includes contributions from each of the two graviton polarizations.

All current observations are consistent with $\Delta^2_\gamma(k) = 0$ and angular power spectra given by

$$C_{XX,\ell} = \int \frac{dk}{k}\Delta^2_{\mathcal{R}}(k)\left|\int_0^{\tau_0} d\tau S_X(k,\tau)u_{X,\ell}(k(\tau_0-\tau))\right|^2, \quad (1.4)$$

where $S_X(k,\tau)$ with $X = T, E$ are source functions that encode the evolution of the modes, and $u_{X,\ell}$ are functions that encode the geometry of the Universe. In a spatially flat universe $u_{T,\ell}$ is, for example, a spherical Bessel function, $u_{T,\ell} = j_\ell$. The spectrum of primordial perturbations is nearly scale-invariant, i.e.,

$$\Delta^2_{\mathcal{R}}(k) = A_{\rm s}\left(\frac{k}{k_*}\right)^{n_{\rm s}-1+\frac{1}{2}\frac{dn_{\rm s}}{d\ln k}\big|_{k=k_*}\ln(k/k_*)+\ldots} \qquad \text{with} \qquad n_{\rm s}\approx 1 \qquad \text{and} \qquad \left.\frac{dn_{\rm s}}{d\ln k}\right|_{k=k_*} \approx 0\,. \quad (1.5)$$

If primordial gravitational waves are present, they also contribute to the angular power spectra of temperature and polarization anisotropies. Given that the scalar perturbations are nearly scale invariant, we may expect the same for the tensor perturbations and hence parameterize their power spectrum as

$$\Delta^2_{\gamma}(k) = A_{\rm r}\left(\frac{k}{k_*}\right)^{n_{\rm t}+\frac{1}{2}\frac{dn_{\rm r}}{d\ln k}\big|_{k=k_*}\ln(k/k_*)+\ldots} \qquad \text{with} \qquad n_{\rm t}\approx 0 \qquad \text{and} \qquad \left.\frac{dn_{\rm t}}{d\ln k}\right|_{k=k_*} \approx 0\,. \quad (1.6)$$

We can then define the tensor-to-scalar ratio as $r = A_{\rm t}/A_{\rm s}$. At linear order in perturbation theory only the tensor perturbations generate B-mode polarization, and a search for primordial gravitational waves can be cast as a search for B-mode polarization in the cosmic microwave background radiation. Angular power

spectra for anisotropies in the CMB temperature and polarization are shown in Fig. 6. B-mode anisotropies created by gravitational waves are shown for two representative values of the tensor-to-scalar ratio and are significantly fainter than both temperature and E-mode anisotropies, highlighting the experimental precision necessary to detect them.

Primordial gravitational waves are not the only source of degree-scale B modes, since weak gravitational lensing of the cosmic microwave background by large-scale structure converts E- to B-mode polarization. This lensing contribution dominates over the primordial signal for $r \lesssim 0.01$. CMB-S4 will rely on precision measurements of E and B modes on smaller angular scales to remove 90% of this lensing contribution.

In addition, as we will discuss, emission from thermal dust and relativistic electrons in our galaxy lead to B-mode polarization in the microwave sky, and instrumental effects convert temperature or E-mode polarization to B-mode polarization. Both must be controlled to unprecedented levels.

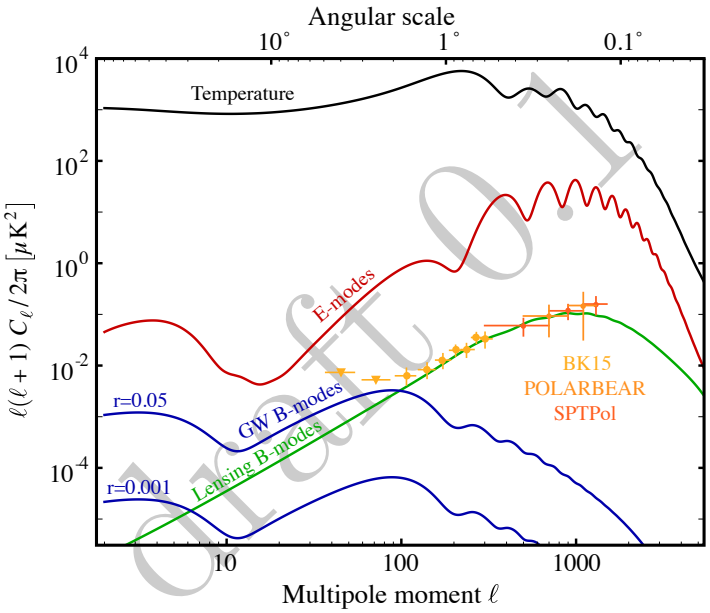

Figure 6: Theoretical predictions for the temperature (black), E-mode (red), and tensor B-mode (blue) power spectra. Primordial B-mode spectra are shown for two representative values of the tensor-to-scalar ratio: $r = 0.001$ and $r = 0.05$. The contribution to tensor B modes from scattering during the recombination epoch peaks at $\ell \approx 80$ and from reionization at $\ell < 10$. Also shown are expected values for the contribution to B modes from gravitationally lensed E modes (green). Current measurements of the B-mode spectrum are shown for BICEP2/*Keck Array* (light orange), POLARBEAR (orange), and SPTPol (dark orange). The lensing contribution to the B-mode spectrum can be partially removed by measuring the E-mode polarization and exploiting the non-Gaussian statistics of the lensing.

Implications for inflation Inflation, a period of accelerated expansion of the early Universe, is the leading paradigm for explaining the origin of the primordial density perturbations that grew into the CMB anisotropies and eventually into the stars and galaxies we see around us. Accelerated expansion requires matter with an energy density that dilutes relatively slowly as the Universe expands. In inflationary models,

such an energy density is usually obtained via the introduction of a new field ϕ, called the inflaton. In the simplest scenarios its Lagrangian density is given by

$$\mathcal{L} = -\frac{1}{2} g^{\mu\nu} \partial_\mu \phi \partial_\nu \phi - V(\phi)\,, \tag{1.7}$$

where $V(\phi)$ is the potential energy density.

The overall evolution of the Universe is well-described by a FLRW line element

$$ds^2 = -dt^2 + a^2(t) \left[\frac{dr^2}{1-kr^2} + r^2 d\Omega^2 \right], \tag{1.8}$$

where $k = 0$ for a flat spatial geometry, $k = \pm 1$ allows for spatial curvature, and the time evolution is specified by the scale factor, $a(t)$. The Hubble parameter, $H = \dot{a}/a$, gives the rate of expansion of the Universe.

A period of inflation will drive the spatial curvature close to zero, in good agreement with current observations. As a consequence, we will assume spatial flatness and set $k = 0$ for most considerations; however, we discuss constraints on curvature obtainable with CMB-S4 in Sect. 1.3.2.2.

In addition to a flat universe, the simplest models of inflation predict that the primordial density perturbations are adiabatic, very nearly Gaussian, and nearly scale-invariant, in agreement with existing observations.

In single-field slow-roll inflation, the gauge-invariant combination of metric and scalar-field fluctuations that is conserved outside the horizon has the power spectrum

$$\Delta^2_{\mathcal{R}}(k) = \frac{1}{2\epsilon M_{\rm P}^2} \left(\frac{H}{2\pi} \right)^2 \Bigg|_{k=aH}, \tag{1.9}$$

where $\epsilon = -\dot{H}/H^2$ is the first slow-roll parameter, and $M_{\rm P} = 1/\sqrt{8\pi G}$ is the reduced Planck mass.

In addition to producing primordial density perturbations, the rapid expansion of spacetime creates primordial gravitational waves that imprint a characteristic polarization pattern onto the CMB. Their power spectrum is given by

$$\Delta^2_{\gamma}(k) = \frac{8}{M_{\rm P}^2} \left(\frac{H}{2\pi} \right)^2 \Bigg|_{k=aH}, \tag{1.10}$$

and is a measure of the expansion rate of the Universe during inflation. Together with the Friedmann equation a detection of primordial gravitational waves would then allow us to infer the inflationary energy scale.[1]

CMB-S4 will be able to detect primordial gravitational waves for $r > 0.003$, and a detection would point to inflationary physics near the energy scale associated with grand unified theories. As a consequence, a detection would provide additional evidence in favor of the idea of the unification of forces, and would probe energy scales far beyond the reach of the Large Hadron Collider (LHC) or any conceivable collider experiment. Selected models within reach of CMB-S4 are shown in Fig. 7 together with current limits and constraints expected for CMB-S4.

The knowledge of the energy scale of inflation would have broad implications for many other aspects of fundamental physics, including ubiquitous ingredients of string theory like axions and moduli, fields that control the shapes and sizes of the compact dimensions.

[1] In some models of inflation the relation between the tensor-to-scalar ratio and the energy scale of inflation are broken because there are additional sources of gravitational wave production [16]. However, the signal in these models is highly non-Gaussian and would not be mistaken for quantum fluctuations.

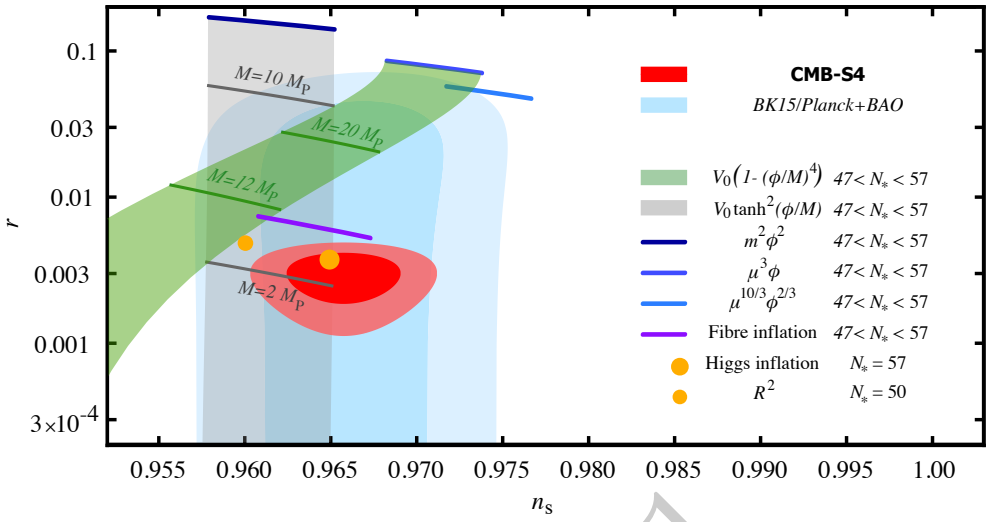

Figure 7: Forecast of CMB-S4 constraints in the n_s–r plane for a fiducial model with $r = 0.003$. For comparison, we also show the current best constraints from a combination of the BICEP2/*Keck Array* experiments, *Planck* [1], and BAO data. These are compared to several theoretical models. Chaotic inflation with $V(\phi) = \mu^{4-p}\phi^p$ for $p = 2/3, 1, 2$ are shown as blue lines for $47 < N_* < 57$ (with smaller N_* predicting lower values of n_s). The Starobinsky model and Higgs inflation are shown as small and large orange filled circles, respectively. The green band shows the predictions for a quartic hilltop model for which the potential throughout the inflationary period is described by $V(\phi) \approx V_0(1 - (\phi/M)^4)$ before developing a minimum. The gray band shows the prediction of a sub-class of α-attractor models [2], and the purple line shows fibre inflation [5].

Because the polarization pattern is due to quantum fluctuations in the metric of spacetime generated during inflation, a detection would also provide evidence that gravity is quantized. Moreover, because many of the models that predict a signal that is strong enough to be detected with CMB-S4 are based on symmetry principles and inflation occurs at high energy and large inflaton field range, a detection would also provide some insights into the nature of quantum gravity.

In the absence of a detection, the upper limit of $r < 0.001$ at 95% CL achievable by CMB-S4 is nearly two orders of magnitude stronger than current limits and about a factor of 5 stronger than projected limits for Stage-3 experiments. As explained in more detail in Ref. [17], such an upper limit would exclude large classes of inflationary models. In summary, there are only two classes of model that naturally explain the observed value of n_s and are consistent with current data. The first class consists of monomial models with potentials that during inflation are well approximated by $V(\phi) = \mu^{4-p}\phi^p$. Representatives in this class are shown in Fig. 7, and the entire class of models is shown in Fig. 8. The second class consists of models in which the potential $V(\phi)$ approaches a plateau, either polynomially or exponentially. The potential for models in this class has a characteristic scale over which the potential varies [17].[2] The sensitivity of CMB-S4 is chosen to exclude all models in this class with a characteristic scale that exceeds the Planck scale. The Planck scale constitutes an important threshold because the scale of gravitational interactions and the characteristic scale may share a common origin and be linked to each other, such as in the Starobinsky model [3], in Higgs inflation [4], or more general models involving non-minimally coupled scalar fields. As a consequence, even

[2]This characteristic scale was introduced in Ref. [17] and should not be confused with the field range or the energy scale of inflation. For a discussion see Refs. [17] and [18].

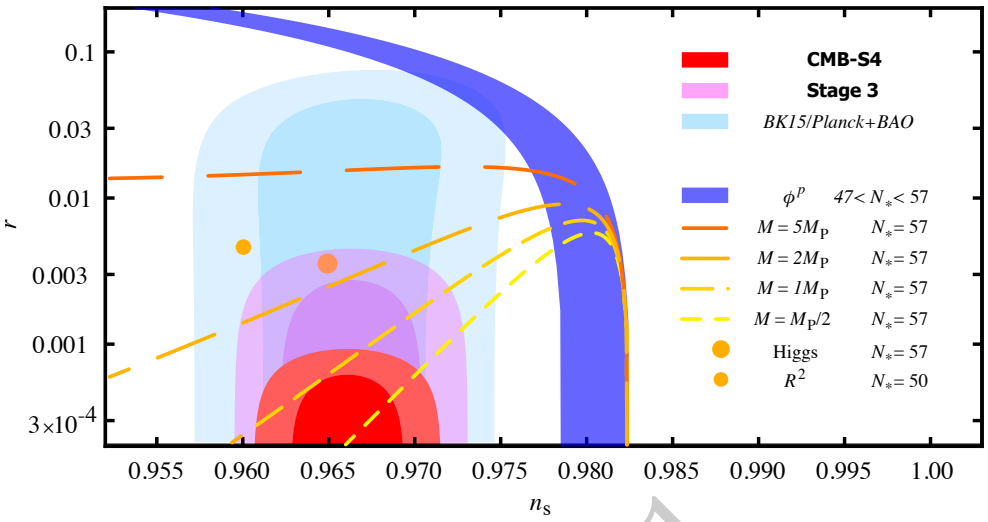

Figure 8: Forecast of CMB-S4 constraints in the n_s–r plane for a fiducial model with $r = 0$. Also shown are the current best constraints from a combination of the BICEP2/*Keck Array* experiments and *Planck* [1]. The Starobinsky model and Higgs inflation are shown as small and large orange filled circles. The lines show the classes of model that naturally explain the observed value of n_s. The corresponding potentials all either polynomially or exponentially approach a plateau. The scale in field space over which the potential approaches the plateau is referred to as the "characteristic scale" (see Ref. [17] for more details). We show different values, $M = M_P/2$, $M = M_P$, $M = 2\,M_P$, and $M = 5\,M_P$. Longer dashes correspond to larger values of the scale M. The Planck scale plays an important role because the gravitational scale and the characteristic scale share a common origin. The number of e-folds N_* chosen for the figure corresponds to nearly instantaneous reheating, which leads to the smallest values for r for a given model. Other reheating scenarios predict larger values of r and are easier to detect or exclude.

in the absence of a detection CMB-S4 would significantly advance our understanding of inflation, and would dramatically affect how we think about the theory. The classes of model that naturally predict the observed value of n_s, together with current constraints and constraints expected for CMB-S4, are shown in Fig. 8.

1.3.2 Primordial density perturbations

CMB-S4 can also seek to characterize the primordial Universe by searching for well-motivated signatures in the scalar fluctuations, in the primordial power spectrum, and non-Gaussianities.

We will begin with discussions of the overall shape of the primordial power spectrum, and generalize to investigate the possibility of measuring features in the primordial power spectrum.

Currently, constraints on non-Gaussianity rely on measurements of the CMB bispectrum, and CMB-S4 will improve on these measurements. Below, we will summarize some well-motivated bispectrum shapes [19, 20]. In addition, the precise measurement of B-mode polarization opens up another possible window to explore the physics of the early Universe. Non-Gaussianities that measure interactions between tensors and scalars, can, for the first time, be constrained with sensitivity that has the potential to exceed that of

scalar non-Gaussianities [21]. Although the presence of these couplings is predicted to be small [22, 23] in the simplest inflation models, such a detection would present evidence of exciting new physics [24, 25]. In addition, theoretical consistency conditions between scalar and tensor non-Gaussianities provide a compelling observational target [26, 27, 28].

In addition to the bispectrum, fluctuations in the galaxy density are also a powerful probe of primordial non-Gaussianity, since the galaxy power spectrum will be biased on large scales in the presence of primordial local non-Gaussianity. Recently, two independent techniques have been proposed to use CMB data to precisely measure the scale-dependence of this galaxy bias on large scales. Precise measurements require "cosmic variance cancellation," which uses multiple tracers of the same field, to remove cosmic variance on this bias. We will present results of forecasts on the local type of non-Gaussianity using CMB-S4 data combined with data from the LSST.

1.3.2.1 Primordial Power Spectrum

Currently, our best constraints on the shape of the primordial power spectrum on large scales come from measurements of the CMB temperature anisotropies by the *Planck* satellite. The current value of the slope of the primordial curvature power spectrum is $n_{\rm s} = 0.965 \pm 0.004$ [29]. The forecasted uncertainty on the slope for a model of ΛCDM + running of the tilt using CMB-S4 noise, including the CMB temperature and polarization fields, is $\sigma_{n_{\rm s}} = 0.002$, reducing the error from *Planck* by a factor of 2. Slow-roll models of inflation predict a running of the tilt of order $(n_{\rm s}-1)^2 \sim 10^{-3}$. With CMB-S4, the forecasted uncertainty on the running is $\sigma_{n_{\rm run}} = 0.0029$ (see Eq. 1.5), which combined with large-scale structure constraints could be tightened even further. For comparison, we find $\sigma_{n_{\rm s}} = 0.0027$ and $\sigma_{n_{\rm run}} = 0.0038$ for Simons Observatory.

Features in the CMB temperature power spectrum [30, 31, 32, 29] have been claimed and interpreted as possible evidence for new physics during inflation. Evidence of a feature would provide us with yet another unique signature that can be used to understand the physics of the early Universe [33]. Specific forms of such features are typically handled on a case-by-case basis. However, for model-independent analyses, it is desirable to have a simple and accurate prescription that relates CMB observables to the shape of the inflationary potential. Various approaches exist in the literature for reconstructing this primordial power spectrum (see e.g., [34, 35, 36, 37, 38, 39, 40, 41])

In a series of papers [42, 43, 44, 45, 46], a formalism (known as "generalized slow roll") has been developed to test the hypotheses of slow-roll and single-field inflation in a general and model-independent way. In this formalism, there is a single source function G' that is responsible for the observable features and it is simply related to the local slope and curvature of the inflationary potential in the same way the tilt is for the case of standard slow roll:

$$G' \approx 3\left(\frac{V'}{V}\right)^2 - 2\frac{V''}{V}, \tag{1.11}$$

where primes denote derivatives with respect to the inflation field. This framework can be used to map constraints from the CMB onto constraints on the shape of the inflationary potential, without assuming any specific model of inflation.

Here we adopt the generalized slow-roll approximation to accommodate order unity variations in the power spectrum from slow-roll predictions. Under this formalism the primordial power spectrum $\Delta^2_{\mathcal{R}}(k)$ can be written in terms of a single unknown source function G', and the rest are known functions. We perform a Fisher matrix analysis varying the six standard ΛCDM cosmological parameters ($A_{\rm s}$, $n_{\rm s}$, τ, θ, $\Omega_{\rm c}$, $\Omega_{\rm b}$) and 40 coefficients that parametrize the source function.

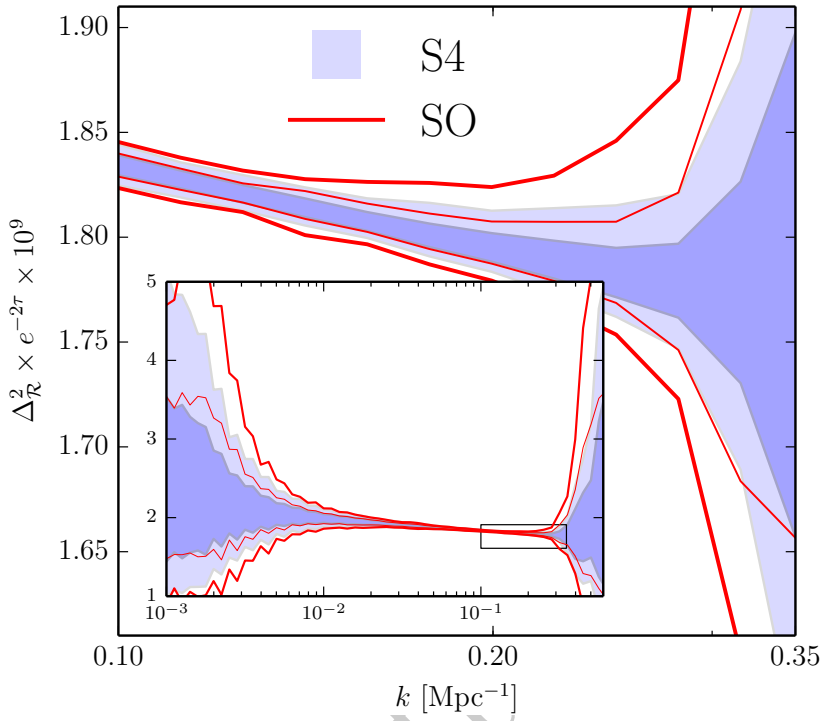

Figure 9: Reconstructed primordial power spectrum with CMB-S4 noise curve including atmospheric noise co-added with Planck noise, noise from point sources, and lensing reconstruction. We parameterize our source function $\delta G'$ in the range $0.5 < s/\mathrm{Mpc} < 4870$ with a total of 40 parameters, equispaced in logarithmic scale. Also shown are the constraints coming from the Simons Observatory baseline, for the same fraction of the sky observed by CMB-S4 (as discussed in Ref. [47]).

The ordinary slow-roll approximation corresponds to $G'(\ln s) = 1 - n_\mathrm{s}$, and results in a power-law curvature power spectrum. We restrict our parameterization of fluctuations, $\delta G'$ (around the constant $G' = 1 - n_\mathrm{s}$) to $0.5 < s/\mathrm{Mpc} < 4870$. We sample $\delta G'$ for a total of 40 parameters, equispaced on a logarithmic scale. We then construct a smooth function using the natural spline of these points. In Figure 9 we show the forecasted reconstructed initial curvature power spectrum for CMB-S4.

1.3.2.2 Spatial Curvature

The theory of inflation predicts an almost flat universe with curvature $|\Omega_K| \sim 10^{-4}$ (from contributions from large-scale modes). If departures from this value were measured at a significant level, this would give us information about the physics of inflation. For instance, it could indicate that the inflaton field was not slowly rolling when the largest scales exited the horizon.

Combining CMB-S4, *Planck* TT on the part of the sky that is not observed by CMB-S4, and *Planck*'s low-ℓ ($\ell < 30$) measurement of TT over the full sky (along with a *Planck* prior on τ of $\sigma(\tau) = 0.007$), the constraints on the curvature reach $\sigma(\Omega_K) = 2.4 \times 10^{-3}$, which is a factor of 2.5 better than current

constraints from the CMB, namely $\sigma(\Omega_K) = 6.5 \times 10^{-3}$ using CMB temperature, polarization, and lensing data from the *Planck* satellite. This constraint could be sharpened even further by combining CMB and baryon acoustic oscillation (BAO) data.

1.3.2.3 Isocurvature

Measurements of CMB temperature and polarization power spectra indicate that the primordial initial conditions are primarily adiabatic; that is, if we define

$$S_{ij} \equiv \frac{\delta n_i}{n_i} - \frac{\delta n_j}{n_j} \,, \tag{1.12}$$

then the adiabatic condition is that $S_{ij} = 0$. Here the species labels i, j can denote baryons, cold dark matter (CDM), photons (γ), or neutrinos. Number densities are denoted by n_i. Adiabatic perturbations are produced if the initial perturbations in all species are seeded by the inflaton. Otherwise, the initial conditions are a mixture of adiabatic and isocurvature perturbations, for which $S_{i\gamma} \neq 0$. These initial conditions determine the acoustic peak structure and large-scale amplitude of CMB anisotropies [48, 49, 50, 51, 52, 53], which can thus probe additional fields present during inflation. Present data still allow subdominant CDM density isocurvature (CDI), baryon density isocurvature (BDI), or neutrino density isocurvature (NDI) initial conditions (described in Refs. [54, 55, 56, 57, 32, 29]) at the roughly 1% level, depending on precise assumptions made about the spectral shape and multi-mode admixtures of isocurvature. CMB-S4 could shed light on inflationary physics by detecting isocurvature fluctuations. As specific examples of the physics that can be measured with CMB-S4, we consider two well-studied scenarios: the curvaton; and compensated isocurvature perturbations (CIPs). Axion-type isocurvature is discussed in Section 1.4.4.5.

The curvaton scenario is a model in which a sub-dominant field σ acquires vacuum fluctuations during inflation, sources ζ (the total gauge-invariant curvature perturbation), and then decays [58, 59, 60, 61, 62]. Curvaton candidates include sneutrinos, among others [63, 64, 65, 66, 67, 68, 69, 70]. Depending on whether a species i (or its set of quantum numbers) is produced by, before, or after curvaton decay, perturbations in i are offset from ζ, with distinct density perturbation ζ_i in the species i on surfaces of constant curvature. Here $i \in \{\nu, \mathrm{b}, \mathrm{c}\}$. The resulting isocurvature perturbations [61, 62, 71] have entropy fluctuation given by

$$S_{i\gamma} = \begin{cases} -3\zeta - 3(\zeta_\gamma - \zeta), & \text{if } i \text{ is produced before } \sigma \text{ decay,} \\ 3\left(\frac{1}{r_\mathrm{D}} - 1\right)\zeta - 3(\zeta_\gamma - \zeta), & \text{if } i \text{ is produced by } \sigma \text{ decay,} \\ -3(\zeta_\gamma - \zeta), & \text{if } i \text{ is produced after } \sigma \text{ decay.} \end{cases} \tag{1.13}$$

The parameter r_D is the fractional energy density in the curvaton when it decays.

The mixture of isocurvature modes is determined by whether or not baryon number, lepton number, and CDM are produced before, by, or after curvaton decay. Curvaton-type isocurvature is distinct from axion isocurvature, because it is correlated (or anti-correlated) with ζ. If lepton number is produced by curvaton decay, the lepton chemical potential ξ_lep sets the size of NDI modes [62, 72, 73]:

$$S_{\nu\gamma} = -\frac{135}{7}\left(\frac{\xi_\mathrm{lep}}{\pi}\right)^2 \zeta_\gamma. \tag{1.14}$$

There are 27 distinct curvaton scenarios, since baryon number, lepton number, and CDM could each be produced before, by, or after curvaton decay. Viable models are those in which one of baryon number or CDM is produced by curvaton decay, and those in which *both* baryon number and CDM are produced after curvaton decay. For curvaton-decay scenarios, we use the notation $(b_{y_\mathrm{b}}, c_{y_\mathrm{c}}, L_{y_\mathrm{L}})$, where the subscripts run

over $y_i \in \{\text{before}, \text{by}, \text{after}\}$ and L denotes lepton number. For example, $(b_{\text{before}}, c_{\text{by}}, L_{\text{by}})$ is a model in which baryon number is produced before curvaton decay, CDM by curvaton decay, and lepton number by curvaton decay. Current isocurvature limits favor values of $r_{\text{D}} \approx 1$, except for models in which baryon number is produced by curvaton decay and CDM before (or vice versa), which favor central values of $r_{\text{D}} \approx 0.16$ ($r_{\text{D}} \approx 0.84$).

The current limits [74] on r_{D} are shown in Table 1-1, along with a forecast of CMB-S4's sensitivity to r_{D} via isocurvature modes. There is dramatic improvement in constraints on the $(b_{\text{by}}, c_{\text{before}}, L_{\text{by}})$ and $(b_{\text{before}}, c_{\text{by}}, L_{\text{by}})$ scenarios because of the accompanying NDI perturbations. One unusual case is $(b_{\text{after}}, c_{\text{after}}, L_{y_{\text{L}}})$, where isocurvature just constrains the combination [74] $\chi_{\text{D}} \equiv [1+\xi^2_{\text{lep}}/(\pi^2)\,(1/r_D - 1)]^{-1}$, while the independent constraint on ξ^2_{lep} is driven by the CMB limit on total relativistic energy density (N_{eff}).

Isocurvature scenario	*Planck*	CMB-S4
	$\Delta r_D/r_D^{\text{adi}}$	$\Delta r_D/r_D^{\text{adi}}$
$(b_{\text{by}}, c_{\text{before}}, L_{y_{\text{L}}})$	0.03	0.005
$(b_{\text{before}}, c_{\text{by}}, L_{y_{\text{L}}})$	0.01	0.004
$(b_{\text{by}}, c_{\text{after}}, L_{y_{\text{L}}})$	0.04	0.01
$(b_{\text{after}}, c_{\text{by}}, L_{y_{\text{L}}})$	0.008	0.002
$(b_{\text{by}}, c_{\text{by}}, L_{y_{\text{L}}})$	0.007	0.002
	$\Delta\chi_{\text{D}}/\chi^{\text{adi}}$	$\Delta\chi_{\text{D}}/\chi^{\text{adi}}$
$(b_{\text{after}}, c_{\text{after}}, L_{y_{\text{L}}})$	0.003	0.0004
	$\Delta\xi^2_{\text{lep}}$	$\Delta\xi^2_{\text{lep}}$
$(b_{\text{by}}, c_{\text{before}}, L_{\text{by}})$	0.02	0.002
$(b_{\text{before}}, c_{\text{by}}, L_{\text{by}})$	0.4	0.04
$(b_{\text{by}}, c_{\text{after}}, L_{\text{by}})$	0.3	0.04
$(b_{\text{after}}, c_{\text{by}}, L_{\text{by}})$	0.3	0.04
$(b_{\text{by}}, c_{\text{by}}, L_{\text{by}})$	0.3	0.04
$(b_{\text{after}}, c_{\text{after}}, L_{\text{by}})$	0.3	0.04

Table 1-1: Isocurvature constraints on r_{D} and ξ^2_{lep}, both at 95% CL using *Planck* TT+BAO+LowP data [74] in viable curvaton decay-scenarios, and Fisher forecasts for CMB-S4 sensitivity.

If baryon number is produced before curvaton decay, while CDM is produced by curvaton decay, CMB 3-pt correlations (see Sec. 1.3.2.4) are excited, with $f^{\text{local}}_{\text{NL}} \approx 5$, also within the reach of CMB-S4. As a result, CMB-S4 provides a useful set of consistency checks if certain curvaton signatures are observed [74].

If baryon number is produced by curvaton decay, but CDM is produced before (or vice versa), a relatively large compensated isocurvature perturbation S_{bc} (CIP) is produced between the baryons and CDM. Curvaton-generated CIPs are proportional to ζ, $S_{\text{bc}} = A\zeta$, where $A \approx 17$ in the $(b_{\text{by}}, c_{\text{before}}, L_{y_{\text{L}}})$ scenario and $A \approx -3$ for $(b_{\text{by}}, c_{\text{before}}, L_{y_{\text{L}}})$. CIPs would induce non-Gaussianities in the CMB [75, 76, 77, 78]. At CMB-S4 sensitivity [78], the threshold for a 95% CL detection is $A \approx 10$, and so a CIP test of the $(b_{\text{by}}, c_{\text{before}}, L_{y_{\text{L}}})$ scenario is within reach of CMB-S4, a substantial improvement over *Planck* sensitivity. For uncorrelated CIPs, we find that the sensitivity of CMB-S4 to a scale-invariant (SI) angular power spectrum of uncorrelated CIPs is $\Delta_{\text{cl}} = 0.003$ at the 95% CL with current parameters [78], assuming *Planck* cosmology [32]. Here

$\Delta_{\rm cl}$ is the rms CIP amplitude on cluster scales. This is a significant improvement over the upper limit of $\Delta_{\rm cl} \leq 0.077$ from the *Wilkinson Microwave Anisotropy Probe* (*WMAP*) [77], or the *Planck* upper limit $\Delta_{\rm cl} \leq 0.064$ obtained in Ref. [79].

1.3.2.4 Primordial non-Gaussianity: the bispectrum

Unlike the scalar and tensor power spectra, higher-order correlations of the scalar modes are directly sensitive to the dynamics and field content responsible for inflation (and its alternatives) [80]. While non-Gaussian correlations are small in conventional single-field slow-roll inflation, there exist many other possibilities for the nature of inflation that give strikingly different predictions when we move beyond the power spectrum. The constraints on non-Gaussianity from the *WMAP* [81, 82] and *Planck* [13, 14] satellites currently place the most stringent limits on a wide range of mechanisms for inflation; however, these measurements are not sufficiently sensitive to suggest that a particular mechanism is favored by the data.

The space of non-Gaussian signals from inflation can broadly be grouped into two conceptual categories that generate distinguishable features in the correlation functions. These are signals that: (1) indicate non-trivial self-interactions of the effective inflaton fluctuation; or (2) indicate interactions with degrees of freedom other than the inflaton. For the first category, self-interactions that respect the time-translation invariance during inflation lead to qualitatively different predictions from self-interactions that violate it. For the second category the signatures qualitatively depend on the mass of the additional degrees of freedom (fields). Additional light degrees of freedom can fluctuate significantly and may have large self-interactions. Heavy degrees of freedom do not fluctuate appreciably, but may come into existence by quantum fluctuations and decay into inflaton quanta, generating non-Gaussian correlations [83, 84, 27, 85]. Alternatively, they may become excited by the dynamics of the inflaton and their backreaction on the inflationary dynamics may lead to non-Gaussian correlations [86, 87, 88, 89].

Constraints on non-Gaussianity are often expressed in terms of the correlator of three scalar modes, described by the bispectrum $B_{\mathcal{R}}(\mathbf{k}_1, \mathbf{k}_2, \mathbf{k}_3)$, defined through

$$\langle \mathcal{R}(\mathbf{k}_1)\mathcal{R}(\mathbf{k}_2)\mathcal{R}(\mathbf{k}_3)\rangle = (2\pi)^3 \delta(\mathbf{k}_1 + \mathbf{k}_2 + \mathbf{k}_3) B_{\mathcal{R}}(\mathbf{k}_1, \mathbf{k}_2, \mathbf{k}_3)\,. \tag{1.15}$$

The structure of particle interactions relevant for inflation provides both a general organizing principle for this functional space and several specific well-motivated forms of the bispectrum. We now briefly review the classification of scalar non-Gaussianity from inflation and comment on non-Gaussian signatures that are especially relevant for large-field inflation.

Our convention for extracting a normalization of the amplitude, $f_{\rm NL}$, follows Refs. [19] and [13], i.e.,

$$B_{\mathcal{R}}(k_1, k_2, k_3) = \frac{3}{5}(4\pi^4) 2A_{\rm s}^2 f_{\rm NL} F(k_1, k_2, k_3), \tag{1.16}$$

where F is referred to as the shape of the bispectrum, which in a scale invariant universe $\propto k^{-6}$. Different physical effects during inflation lead to different shapes for the bispectrum.

All bispectra that come from fluctuations of the field that drives inflation ("single-clock" scenarios) most strongly couple Fourier modes k of similar amplitude. The "squeezed limit" of these bispectra (the coupling of modes $k_1 \ll k_2 \sim k_3$) is very restricted. A large fraction of the parameter space for scenarios involving interactions during inflation that respect the underlying shift symmetry (i.e., are approximately scale-invariant) are well captured by the equilateral [19] and orthogonal shapes [81] shapes. This includes scenarios in which inflaton fluctuations have non-trivial self-interactions [90, 91, 92, 93, 94, 81] or couplings between the inflaton and other (potentially massive) degrees of freedom [95, 96, 97, 98, 99, 87, 83]. Single-field slow-roll inflation necessarily produces $f_{\rm NL}^{\rm equil} < 1$ [100] and therefore any detection of $f_{\rm NL}^{\rm equil} \geq 1$ would rule out

this large class of models. A detection would imply that inflation is a strongly coupled phenomenon and/or involved more than one field [101, 102, 103]. In single-field inflation, the amplitude of the non-Gaussianity typically suggests a new energy scale, M, such that $f_{\rm NL}^{\rm equil} \propto A_{\rm s}^{-1/2}\,(H/M)^2$ [94, 104]; at this energy scale self-interactions become strongly coupled and current limits on non-Gaussianity [14] translate into $M > \mathcal{O}(10)H$. In the presence of additional hidden sectors, the amplitude of non-Gaussanity scales with the strength of the coupling between the inflaton and these additional fields, usually suppressed by an energy scale Λ. Current limits give $\Lambda > (10{-}10^5)H$ [105, 106], with the variation depending mostly on the dimension of the operator coupling the two sectors. For $r > 0.01$, these constraints require some of the interactions to be weaker than gravitational. CMB-S4 would further tighten existing constraints on a wide variety of interactions of the inflaton with itself and any other fields that are excited during inflation.

When light degrees of freedom other than the inflaton contribute to the observed scalar fluctuations, coupling between modes of very different wavelengths is allowed. Historically, the most well-studied signature of this type comes from the "local" shape, which couples short wavelength modes $k_2 \sim k_3$ to a long wavelength mode k_1 ($\ll k_2, k_3$). A significant detection of this shape would rule out all models of single-clock inflation [107]. In addition, such a signal would open the door to significant cosmic variance on all scales, from coupling of fluctuations within our observed volume to any super-Hubble modes [108, 109, 110]. Indeed, there would be room for a significant shift between the observed amplitude of scalar fluctuations (and so the observed r) and the mean value of fluctuations on much larger scales [111]. Any scenario that predicts local non-Gaussianity, together with fluctuations on scales much larger than our observed volume, predicts a probability distribution for our observed $f_{\rm NL}^{\rm local}$, but many well-motivated scenarios also predict a small mean value; these include the simplest modulated reheating scenario [112] and ekpyrotic cosmology [113], both of which predict mean values of $f_{\rm NL}^{\rm local} \approx 5$.

Currently the strongest constraints on the local shape come from the *Planck* 2015 temperature and polarization analysis that finds $f_{\rm NL}^{\rm local} = 0.8 \pm 5.0$ [14]. CMB-S4 will improve these limits by a factor 2 for local and orthogonal shapes.[3] Note that these forecasts assume that CMB-S4 can be combined with large-scale measurements from *Planck*, the impact of secondaries [114] can be reduced, and temperature and polarization can be sufficiently delensed to remove large contributions to the variance [115]. Even under these assumptions, the constraints are insufficient to reach the most compelling theoretical threshold around $|f_{\rm NL}^{\rm local}| \lesssim 1$ [102]. Nonetheless, the landscape of inflationary models is large and a detection would instantly present a monumental discovery similar to that of gravitaional waves. CMB-S4 could, for example, provide hints for the mean level of non-Gaussianity expected from modulated reheating scenario or ekpyrotic cosmology at roughly the $2\,\sigma$ level. The simplest curvaton scenario, which predicts $f_{\rm NL} = -5/4$ [61], will be out of reach using just the bispectrum measured by CMB-S4, but we will show in the next subsection that combining CMB-S4 with LSST data is likely to reach this significant threshold.

Table 1-2 shows the forecasted constraints on the local, equilateral, and orthogonal shapes from CMB-S4 using bispectrum measurements. In fact we expect that CMB-S4 would likely provide the strongest constraints on equilateral and orthogonal templates that will be available for the foreseeable future. Since limits on non-Gaussianity provide a unique and fundamental insight into the nature of inflation, this increased sensitivity would provide a non-trivial improvement in our understanding of the Universe.

Perhaps of special interest for CMB-S4 are non-Gaussian signatures that would be expected in models of large-field inflation, which could lead to non-trivial features in the bispectrum. For example, in models in which the inflaton is an axion, there is an approximate discrete shift symmetry [116, 117, 118] that naturally lead to periodic features in the bispectrum. Often these models predict counterparts in the power spectrum where the associated features are expected to be detected first [119], but this need not be the case [120]. An

[3] Note that constraints on orthogonal and local non-Gaussianities in the CMB scale almost as expected, i.e., as the square root of the number of observed modes. Unfortunately, some information is lost in projection, which particularly affects equilateral non-Gaussianity, scaling more like the fourth root of the number of modes.

attempt has been made [14] to look for resonant and local features in the bispectrum; however, at present, these models have not yet been constrained systematically.

Correlators including at least one B mode will benefit significantly from the improved sensitivity of CMB-S4. In particular, the three point correlation $\langle \mathcal{R}(\mathbf{k}_1)\mathcal{R}(\mathbf{k}_2)\gamma_\lambda(\mathbf{k}_3)\rangle$ can be constrained using $\langle BTT\rangle$, $\langle BTE\rangle$ and $\langle BEE\rangle$.

The details of the tensor-scalar-scalar correlator are contained in the bispectrum $B_{\mathcal{R}\mathcal{R}\gamma_\lambda}(\mathbf{k}_1, \mathbf{k}_2, \mathbf{k}_3)$, defined by pulling out the appropriate polarization structure associated with the tensor mode:

$$\langle \mathcal{R}(\mathbf{k}_1)\mathcal{R}(\mathbf{k}_2)\gamma_\lambda(\mathbf{k}_3)\rangle = (2\pi)^3\delta(\mathbf{k}_1+\mathbf{k}_2+\mathbf{k}_3)B_{\mathcal{R}\mathcal{R}\gamma_\lambda}(k_1,k_2,k_3)e_{ij}(\mathbf{k}_3,\lambda)\hat{k}_1^i\hat{k}_2^j, \tag{1.17}$$

where $e_{ij}(\mathbf{k},\lambda)$ is the transverse-traceless polarization tensor (see Eq. 1.2). The amplitude and momentum dependence of the bispectrum $B_{\mathcal{R}\mathcal{R}\gamma_\lambda}$ can be parametrized by [21]

$$B_{\mathcal{R}\mathcal{R}\gamma_\lambda}(k_1,k_2,k_3) = 16\pi^4 A_{\rm s}^2\sqrt{r}f_{\rm NL}^{\mathcal{R}\mathcal{R}\gamma}F(k_1,k_2,k_3). \tag{1.18}$$

In the bottom half of Table 1-2 we show the results of forecasts for $\sqrt{r}\tilde{f}_{\rm NL}$ using local-, equilateral-, and orthogonal-like templates. A detection of this correlation would be an immediate indication of some deviation from the simple inflationary paradigm [23, 121]. There are known possibilities that would generate a scalar-scalar-tensor bispectrum with larger amplitude and/or different shape: different symmetry patterns (e.g., solid inflation [122] or gauge-flation [123, 124]); gravitational waves not produced as vacuum fluctuations; or multiple tensors (e.g., bigravity [23]). Any non-zero tensor amplitude could also be sourced by a higher-order massive spin field that couples to two scalars and one graviton (see for example Ref. [26] for a discussion of such signatures).

1.3.2.5 Primordial non-Gaussianity: large-scale structure

CMB-S4 can also contribute to the measurement of local primordial non-Gaussianities in an indirect way, by complementing a galaxy survey to exploit so-called sample-variance cancellation. By combing CMB-S4 data with measurements of large-scale structure, for example with LSST [127], impressive constraints could be achieved on $f_{\rm NL}^{\rm local}$. We briefly review this method and forecast constraints on the local parameter.

On linear scales, galaxy bias relates the amplitude of matter perturbations $\delta_{\rm m}$ and galaxy perturbations $\delta_{\rm g}$. Local non-Gaussianities lead to a scale-dependent correction to the galaxy bias $b_{\rm g}$ on large scales, proportional to $f_{\rm NL}^{\rm local}/k^2$ [128]. If one can obtain a measurement of both the biased galaxy field and the unbiased matter field, one can cancel out the stochastic nature of the modes to measure $b_{\rm g} = \delta_{\rm g}/\delta_{\rm m}$ without sample variance [129]. Of course the measurement of both modes will in practice be noisy and limit the effect of sample-variance cancellation.

Two different methods have recently been proposed for how to use high-resolution CMB maps to measure the matter field $\delta_{\rm m}$ in conjunction with a large-scale galaxy survey for sample-variance cancellation: the reconstructed CMB lensing potential [130]; and the kSZ reconstruction [131]. Interestingly these two techniques trace different modes, since lensing probes transverse modes and kSZ velocities probe radial modes of the underlying matter distribution. We now discuss each technique in more detail.

Kinematic Sunyaev-Zeldovich effect The large-scale radial velocity field can be reconstructed by a process called kSZ tomography [132, 133]. This is possible because the kSZ temperature is proportional to the line-of-sight integral over the product of electron density $\rho_{\rm e}$ and radial velocity $v_{\rm r}$. If one uses galaxies

Shape: $\langle\mathcal{RRR}\rangle$ $\langle TTT\rangle$,$\langle TTE\rangle$,$\langle TEE\rangle$,$\langle EEE\rangle$	Current	CMB-S4 goal	Conservative	CV-limited
$\sigma(f_{\rm NL}^{\rm local})$	5	1.9 (5.3)	2.1	0.8 (7.1)
$\sigma(f_{\rm NL}^{\rm equil})$	43	22.1 (-0.4)	23.5	11.8 (-1.9)
$\sigma(f_{\rm NL}^{\rm ortho})$	21	9.0 (-5.0)	10.6	4.4 (-6.3)
Shape: $\langle\mathcal{RR}\gamma\rangle$ $\langle BTT\rangle$,$\langle BTE\rangle$,$\langle BEE\rangle$	Current	CMB-S4 goal	Conservative	CV-limited
$\sigma(\sqrt{r}\tilde{f}_{\rm NL}^{\rm local})$	28	0.79	1.2	0.052
$\sigma(\sqrt{r}\tilde{f}_{\rm NL}^{\rm equil})$	...	16	24	1.7
$\sigma(\sqrt{r}\tilde{f}_{\rm NL}^{\rm ortho})$	...	4.4	7.4	0.41

Table 1-2: Forecasted constraints on non-Gaussianity. $\langle\mathcal{RRR}\rangle$: Current constraints are from *Planck* . Forecasted constraints for CMB-S4 goal use *Planck* noise at low ℓ and bispectra are computed using the *Planck* 2018 cosmology [125]. Forecasts do not include foregrounds or lensing contributions to the covariance, but the signal bias from lensing is given in brackets ($T+E$, see Ref. [126]); some secondaries are expected (see Ref. [114]), in particular in the local and orthogonal shapes constrained using temperature data alone. We quote constraints without using $\langle TTT\rangle$ in the conservative column for reference, where $\sigma_{f_{\rm NL}} = ((\sigma^{\rm All}_{f_{\rm NL}})^{-2} - (\sigma^{T}_{f_{\rm NL}})^{-2})^{-1/2}$. Some of these can be cleaned using e.g., ILC techniques, while others would require simulations. Deprojection of tSZ was performed in Ref. [47], which suggested minimal impact, so we do not expect the constraints to be impacted as much as removing $\langle TTT\rangle$ entirely, but further study is required, especially for contributions that cannot be removed using multi-frequency information such as kSZ. For polarization, apart from the reionization-lensing bispectrum, leakage of secondaries is currently less well studied. Constraints can be combined over 35% of the sky with Planck sensitivity, improving constraints by $\mathcal{O}(10\%)$. One can compare the results to the cosmic variance limited constrains with $\ell_{\rm max} = 5000$ in the last column. $\langle\mathcal{RR}\gamma\rangle$: Current constraint are derived from temperature only and shape considered is not exactly $f_{\rm NL}^{\rm local}$. There are currently no constraints on equilateral and orthogonal non-Gaussianities $\langle\gamma\mathcal{RR}\rangle$. Forecasts add the small-aperture telescopes over 3% of the sky. We assume 13% residual lensed B-mode power. Preliminary studies show that foregrounds could leak into $\langle BTE\rangle$ and $\langle BEE\rangle$, and we show how projected constraints are affected when these combinations are *not* included in the conservative column. Lensing contributions are expected to be present in these observables as well, but neither they nor foregrounds are included in these forecasts.

as tracers for the electron distribution, one can construct a quadratic estimator that combines small-scale CMB temperature fluctuations and the small-scale galaxy distribution, to estimate the large-scale velocity field. The noise in this kSZ velocity reconstruction is independent of the scale of the perturbation. In linear theory the velocity field is related to the matter density field by a factor faH/k, where f is the growth rate, resulting in a density reconstruction noise proportional to k^2 that can be much smaller than galaxy shot noise (which is independent of k) on large scales.

The kSZ-derived matter density can then be cross-correlated with a galaxy tracer of the same large-scale density field [131], as a function of scale, to determine the scale dependence of the clustering bias. Since the same modes are being measured in each survey, there is no sample variance in this comparison, greatly improving the precision on large scales.

We forecast $\sigma(f_{\rm NL}^{\rm local}) = 0.57$ for the combination of CMB-S4 kSZ and LSST, using the forecasting pipeline of Ref. [131], which can be compared to $\sigma(f_{\rm NL}^{\rm local}) = 1.45$ from LSST alone (assuming no internal sample-variance

cancellation within the LSST data). For comparison, for Simons Observatory plus LSST the sensitivity is forecasted to be $\sigma(f_{\rm NL}^{\rm local}) = 1.0$ [134].

CMB Lensing An alternative method to measure $f_{\rm NL}^{\rm local}$ using sample-variance cancellation is to cross-correlate the CMB-S4 CMB lensing measurement with galaxy surveys such as LSST [135, 130]. Since the CMB lensing convergence field is determined by all the structure between the CMB last-scattering surface and the observer, we need to include galaxies at high redshift, $z > 3$, to obtain a large cross-correlation coefficient between CMB lensing and galaxies, which is required for sample-variance cancellation to work efficiently. In addition to the LSST galaxies at $z \leq 3$ specified in the last section, we therefore include additional LSST galaxies at $z = 3$–7, based on extrapolating [130] recent Hyper Suprime-Cam observations [136, 137] of dropout galaxies [138] in that redshift range (not including these high-redshift galaxies would degrade the forecasted $f_{\rm NL}^{\rm local}$ precision reported below by about a factor of 2). We split the LSST galaxies into six tomographic redshift bins at $z = 0$–0.5, 0.5–1, 1–2, 2–3, 3–4, and 4–7, and estimate the ability of CMB-S4 to measure local non-Gaussianity.

The result of this forecast depends strongly on the minimum multipole $\ell_{\rm min}$ of both the LSST galaxy density field and the CMB lensing convergence, since the signal scales as $1/k^2$. For $\ell_{\rm min} = 2, 8, 15, 20$, and 40 we obtain $\sigma(f_{\rm NL}^{\rm local}) = 0.72, 0.99, 1.3, 1.5$, and 2.2, respectively, assuming $f_{\rm sky} = 0.3$ overlap with LSST. Similarly to the kSZ forecast above, this method therefore allows us to probe the $\sigma(f_{\rm NL}^{\rm local}) \approx 1$ regime. With the Simons Observatory, the same forecast yields $\sigma(f_{\rm NL}^{\rm local}) = 1.2, 1.3, 1.5, 1.7$, and 2.6, which is 60% larger than CMB-S4 for $\ell_{\rm min} = 2$ and about 15% larger for $\ell_{\rm min} \geq 15$.

1.4 The dark Universe

The second science theme relates to the fundamental physics of invisible components of the Universe.

CMB-S4 will probe the fundamental physics of components that are difficult or impossible for us to observe directly. It will test for the presence of light, relativistic relic particles, beyond our Standard Model of particle physics, that were thermally produced in the early Universe. To date, CMB observations by the *Planck* satellite can probe light particles that departed from equilibrium ("froze out") as early as the first $\simeq 50$ micro-seconds of the Universe. With CMB-S4 we can push this frontier back by over a factor of 10,000, to the first fractions of a nanosecond.

CMB-S4 will be sensitive to relics that froze out well before the quark-hadron phase transition (the epoch when the Universe cooled sufficiently that quarks became locked into hadrons like neutrons and protons). The contribution of light relics to the energy density leads to observable consequences in the CMB temperature and polarization anisotropy. This is often parameterized with the "effective number of neutrino species," $N_{\rm eff}$. The collective influence of the three already-known light relics (the three families of neutrinos) has already been detected at high significance. Current data are only sensitive enough to detect additional relics that froze out after the quark-hadron transition, and Stage-3 CMB experiments can only push somewhat into that epoch, so CMB-S4's ability to probe times well before the transition is a major advance.

CMB-S4 can measure the summed mass of the neutrino species. Together with terrestrial experiments this may shed light on the mechanism responsible for neutrino mass, one of the biggest mysteries of the Standard Model. The total mass unambiguously determines the absolute mass scale of neutrinos, and if the sum is $\lesssim$ 0.1eV, CMB-S4 can furthermore disfavor the inverted mass hierarchy. Together with neutrino-less double beta-decay experiments, CMB-S4 may provide evidence to help determine if neutrinos are Dirac or Majorana particles, or point to unknown physics in the neutrino sector. The main neutrino observables are CMB lensing, lensing cross-correlation, and the abundances of galaxy clusters.

Current cosmological observations already require the existence of dark energy and dark matter, but these have not been observed in the laboratory. CMB-S4 can target the various predictions that dark-energy models make for the clustering and growth of matter fluctuations at late times, examining the secondary anisotropies from gravitational lensing and interactions with the gas in galaxies and galaxy clusters. Constraints on cosmic birefringence could probe the microphysics of the dark energy.

CMB-S4 can test dark-matter models and constrain parts of the parameter space that are inaccessible to laboratory experiments. In particular, CMB observations directly probe the physics of dark matter throughout cosmic history, and do not rely on assumptions about the local dark-matter phase-space distribution within the Milky Way. CMB-S4 can place constraints on a variety of scenarios, including dark matter that interacts with baryons or with dark radiation, or consists of ultra-light axion-like particles.

1.4.1 Light relics

A natural and important question is whether the elementary particles of the Standard Model are the complete list of particles. Unknown relativistic species in the hot Big Bang will change the radiation density of the Universe and leave a measurable imprint on the CMB which would be determined with high precision by CMB-S4. Variations in the radiation density also change the Universe at late times, by altering the amplitude of clustering, the scale and phase of the baryon acoustic oscillations (BAOs), and abundances of light elements produced during Big Bang nucleosynthesis. Precision measurements of the radiation content of the Universe

with the CMB is both a window into the dark sector and a necessary tool for calibrating measurements of the lower-redshift Universe.

The possibility of additional radiation is also compelling, in the contexts of both particle physics and cosmology [7, 139, 8]. New light particles may arise in the form of axions and sterile neutrinos, or can appear as a byproduct of new symmteries that would explain the small mass of the Higgs boson [140, 141, 142, 143, 144, 145, 146, 6, 147, 148, 149, 150, 7, 151, 152, 139, 153, 8, 154, 155, 156, 157]. Furthermore, light particles can thermalize in the early Universe for wide ranges of unexplored parameter space, leading to an observable level of additional radiation. Light particles may form the dark matter (e.g., axions) or part of a dark sector, they can mediate forces in the dark and visible sectors, or they can result from the decay of new heavier particles. These possibilities may also play a role in explaining the discrepancies observed in the Hubble constant H_0 measurements [158, 159, 160, 161, 162], the amplitude of fluctuations σ_8 [163, 164, 165, 166], and clustering on small scales [167, 125].

CMB-S4 will provide a transformative measurement for the radiation density, particularly for particles that would have thermalized in the early Universe. Any such particle adds at least a percent-level contribution to the radiation energy density; the precise amount, per degree of freedom, is determined entirely by its decoupling temperature. CMB-S4 will be orders of magnitude more sensitive to decoupling temperatures than current experiments, and can reach targets that are not reachable by other means.

Cosmic neutrino background. The cosmic neutrino background is one of the remarkable predictions of the hot Big Bang scenario. In the very early Universe, neutrinos were kept in thermal equilibrium with the Standard Model plasma. As the Universe cooled, neutrinos decoupled from the plasma. A short time later, the relative number density and temperature in photons increased, primarily due to the transfer of entropy to photons from annihilating electron-positron pairs. The background of cosmic neutrinos persists today, with a temperature and number density similar to that of the CMB photons. Their energy density ρ_ν is most commonly expressed in terms of the effective number of neutrino species,

$$N_{\rm eff} = \frac{8}{7}\left(\frac{11}{4}\right)^{4/3}\frac{\rho_\nu}{\rho_\gamma}\,, \tag{1.19}$$

where ρ_γ is the energy density in photons. This definition is chosen so that $N_{\rm eff} = 3$ in the SM if neutrinos had decoupled instantaneously prior to electron-positron annihilation. The neutrino density ρ_ν receives a number of corrections from this simple picture of decoupling, and the best available calculations give $N_{\rm eff}^{\rm SM} = 3.045$ in the SM [168, 169, 170].

Cosmology is sensitive to the gravitational effects of neutrinos, both through their mean energy density [171, 172, 173, 174] and their fluctuations, which propagate at the speed of light in the early Universe due to the free-streaming nature of neutrinos [174, 175, 176]. A radiation fluid whose fluctuations do not exceed the sound speed of the plasma [177, 178] could arise from large neutrino self-interactions [179, 180, 181, 182, 183], neutrino-dark sector interactions [184, 185], or dark radiation self-coupling [186, 187, 188]. Such a radiation fluid can be observationally distinguished from free-streaming radiation, and can serve as both a foil for the cosmic neutrino background and a test of new physics in the neutrino and dark sectors [175, 189, 190].

Neutrinos are messengers from a few seconds after the Big Bang and provide a new window into our cosmological history. While these relics have been detected in cosmological data, higher precision measurements would advance the use of neutrinos as a cosmological probe. Furthermore, the robust measurement of the neutrino abundance from the CMB is crucial for inferring cosmic parameters, including the expansion history using BAOs [191], the neutrino masses [192], and H_0 [162].

Other light relics. *A measurement of the value of $N_{\rm eff}$ provides vastly more information than just the energy density in cosmic neutrinos.* The parameter $N_{\rm eff}$ is a probe of any particles that have the same gravitational influence as relativistic neutrinos, which is true of all kinds of (free-streaming) radiation. Furthermore, this radiation could have been created at much earlier times when the energy densities were even higher than in the cores of stars or supernovae, shedding light on the physics at new extremes of temperature and density, and on our early cosmic history.

New light particles that were thermally produced in the early Universe contribute to the neutrino density ρ_ν and increase $N_{\rm eff}$ above the amount from neutrinos alone. The presence of any additional species can therefore be characterized by $\Delta N_{\rm eff} \equiv N_{\rm eff} - N_{\rm eff}^{\rm SM}$. Since all such thermalized particles behave in the same way from a cosmological point of view, this parametrization captures a vast range of new physics, e.g., axions, sterile neutrinos, dark sectors, and beyond [148, 193, 153, 17].

Constraints on $N_{\rm eff}$ are broadly useful and, most importantly, allow the exploration of new and interesting territory in a variety of well-motivated models. This can be seen with a simple example: dark-matter-baryon scattering. For low-mass (sub-GeV) dark matter, current data allow for relatively large scattering cross-sections [194]. If they scatter through a Yukawa potential, which is a force mediated by a scalar particle, this force is consistent with fifth-force experiments and stellar cooling if the mediator has a mass around 200 keV. However, the particle that mediates the force necessarily[4] contributes $\Delta N_{\rm eff} \geq 0.09$ when it comes into thermal equilibrium with the Standard Model [195]. Excluding this value would require that the strength of the interactions is small enough to prevent the particle from reaching equilibrium at any point in the history of the Universe, which, consequently, limits the scattering cross-section, as shown in the left panel of Fig. 10. This measurement is sensitive to 10–15 orders of magnitude in cross-section that are not probed by direct constraints from cosmology and astrophysics, and is five orders of magnitude stronger than meson decay searches. We see that *cosmological measurements of $\Delta N_{\rm eff}$ are an extremely sensitive probe of dark-sector physics that are complementary to more direct tests, both in the laboratory and with astrophysical observations* [195, 196].

More generally, the contribution to $N_{\rm eff}$ from any thermalized new particle is easy to predict because its energy density in equilibrium is fixed by the temperature and the number of internal states (e.g., spin configurations). Under mild assumptions (see e.g., Ref. [200] for a detailed discussion), the contribution to $\Delta N_{\rm eff}$ is determined by two numbers, the last temperature at which it was in equilibrium, $T_{\rm F}$, and the effective number of spin degrees of freedom, $g_{\rm s}$, according to

$$\Delta N_{\rm eff} = g_{\rm s} \left(\frac{43/4}{g_\star(T_{\rm F})} \right)^{4/3} . \tag{1.20}$$

The function $g_\star(T_{\rm F})$ is the number of effective degrees of freedom (defined as the number of independent states with an additional factor of 7/8 for fermions) of the SM particle content at the temperature $T_{\rm F}$. This function appears in the formula for $\Delta N_{\rm eff}$ because it determines how much the photons are heated relative to a new light particle due to the annihilation of the heavy SM particles as the Universe cooled (see the right panel of Fig. 10). CMB-S4 is expected to reach a precision of $\sigma(N_{\rm eff}) = 0.03$, which would extend our reach in $T_{\rm F}$ by several orders of magnitude for a particle with spin $s > 0$ and be the first measurement sensitive to a real scalar ($s = 0$) that decouples prior to the QCD phase transition.

To understand the impact of such a measurement, recall that equilibrium at temperature T arises when the production rate Γ is much larger than the expansion rate $H(T)$. At high temperatures, production is usually fixed by dimensional analysis, $\Gamma \propto \lambda^2 T^{2n+1}$, where λ is the coupling to the Standard Model with units of [Energy]$^{-n}$. The particle is therefore in equilibrium if $\lambda^2 \gg M_{\rm P}^{-1} T^{-2n+1}$. There are two important features of this formula: (i) the appearance of the Planck scale $M_{\rm P}$ implies that we are sensitive to very weak

[4] The mediator with a mass of 200 keV is too heavy to contribute to $N_{\rm eff}$, but it must decay to sub-eV mass particles, which will increase $N_{\rm eff}$, in order to avoid more stringent constraints.

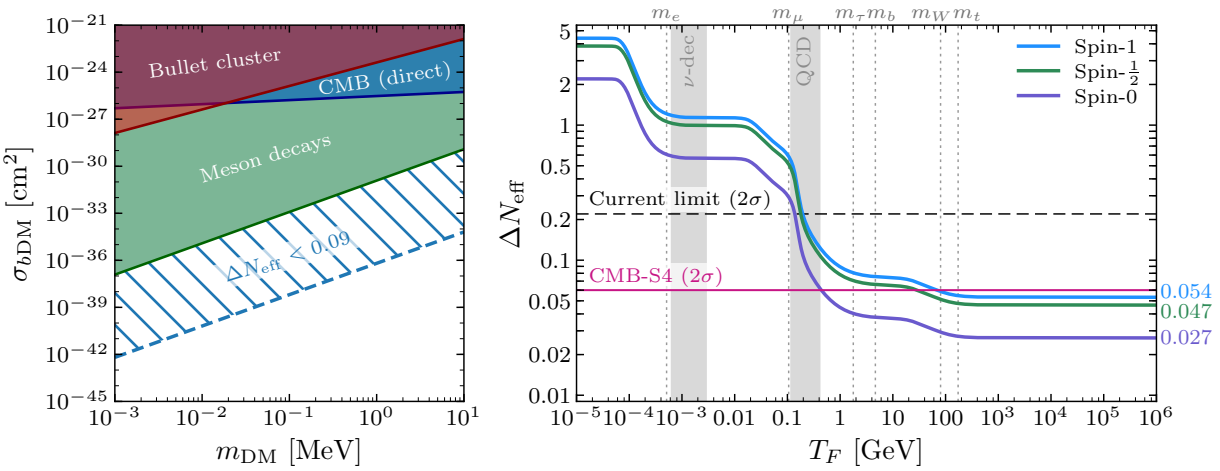

Figure 10: *Left:* Limits on the dark-matter-baryon cross-section $\sigma_{b\rm DM}$ for a Yukawa potential. Future cosmological constraints will restrict $\Delta N_{\rm eff} < 0.09$ and, therefore, exclude cross-sections large enough to thermalize the (200 keV-mass) particle mediating the force [195]. This limit is compared to the direct bound on baryon-dark-matter scattering from the CMB [197] and to the constraints on dark forces from the Bullet Cluster [198]. The strongest current constraint is from the absence of meson decays to the mediator [199]. *Right:* Contributions of a single massless particle, which decoupled from the SM at temperature T_F, to the effective number of relativistic species, $N_{\rm eff} = N_{\rm eff}^{\rm SM} + \Delta N_{\rm eff}$, with the SM expectation $N_{\rm eff}^{\rm SM} = 3.045$ from neutrinos. The dashed line shows the 2σ limit from a combination of current CMB, BAO, and Big Bang nucleosynthesis (BBN) observations [125]. The purple line shows the projected sensitivity of CMB-S4 and illustrates its power to constrain light thermal relics. The displayed values on the right are the observational thresholds for particles with different spins and arbitrarily large decoupling temperatures.

couplings ($M_{\rm P}^{-2} = 8\pi G_N$); and (ii) for $n \geq 1$ it scales like an inverse power of T. As a result, sensitivity to increasingly large $T_{\rm F}$ implies that we are probing increasingly weak couplings (lower production rates) in proportion to the improvement in $T_{\rm F}$ (not $\Delta N_{\rm eff}$). These two features explain why future measurements of $\Delta N_{\rm eff}$ can be orders of magnitude more sensitive than terrestrial and astrophysical probes of the same physics [153, 17].

The impact of the current measurement of $N_{\rm eff}$ and the projected sensitivity of CMB-S4 is illustrated in Fig. 10. Anticipated improvement in measurements of $N_{\rm eff}$ translate into orders of magnitude in sensitivity to the temperature $T_{\rm F}$. This temperature sets the reach in probing fundamental physics. Even in the absence of a detection, future cosmological probes would place constraints that can be orders of magnitude stronger than current probes of the same physics, including for axion-like particles [153] and dark sectors [201, 156, 195, 157]. It is also worth noting that these contributions to $N_{\rm eff}$ asymptote to specific values of $\Delta N_{\rm eff} = 0.027$, 0.047, and 0.054 for a massless (real) spin-0 scalar, spin-1/2 (Weyl) fermion, and spin-1 vector boson, respectively (see Fig. 10).

Even without new light particles, $N_{\rm eff}$ is a *probe of new physics that changes our thermal history, including processes that result in a stochastic background of gravitational waves* [202, 203, 204]. Violent phase transitions and other nonlinear dynamics in the primordial Universe could produce such a background, peaked at frequencies much larger than those accessible to B-mode polarization measurements of the CMB or, in many cases, direct detection experiments such as LIGO and LISA [205, 206, 207, 208, 209]. For particularly violent sources, the energy density in gravitational waves can be large enough to make a measurable contribution to $N_{\rm eff}$ [209, 210, 211].

In addition to precise constraints on $N_{\rm eff}$, cosmological probes will provide an *independent high-precision measurement of the primordial helium abundance* $Y_{\rm p}$, due to the impact of helium on the free electron density prior to recombination. This is particularly useful since $Y_{\rm p}$ is sensitive to $N_{\rm eff}$ a few minutes after the Big Bang, while the CMB and matter power spectra are affected by $N_{\rm eff}$ prior to recombination, about 370 000 years later. Measuring the radiation content at these well-separated times provides a window onto any nontrivial evolution in the energy density of radiation in the early Universe [212, 213, 214, 215]. Furthermore, $N_{\rm eff}$ and $Y_{\rm p}$ are sensitive to neutrinos and physics beyond the Standard Model in related, but different ways, which allows for even finer probes of new physics, especially in the neutrino and dark sectors.

1.4.1.1 Observational signatures

The effect of the radiation density on the damping tail drives the constraint on $N_{\rm eff}$ in the CMB in $\Lambda{\rm CDM}+N_{\rm eff}$ models. The largest effect is from the impact on the mean free path of photons, which introduces an exponential suppression of short wavelength modes [216]. In a more detailed analysis, the effect on the damping tail is subdominant to the change to the scale of matter-radiation equality and the location of the first acoustic peak [173], both of which are precisely measured. As a result, the effect of neutrinos on the damping tail is more accurately represented by holding the first acoustic peak fixed. This changes the sign of the effect on the damping, but the intuition for the origin of the effect remains the same. At the noise level and resolution of CMB-S4, this effect is predominately measured through the TE spectrum at $\ell > 2500$.

In addition to the effect on the expansion rate, perturbations in neutrinos (and dark radiation) affect the photon-baryon fluid through their gravitational influence. The contributions from neutrino fluctuations are well described by a correction to the amplitude and the phase of the acoustic peaks in both temperature and polarization [174]. The phase shift is a particularly compelling signature, since it is not degenerate with other cosmological parameters [174, 175]. This effect is the result of the free-streaming nature of neutrinos, which allows propagation speeds of effectively the speed of light (while the neutrinos are relativistic). Any free-streaming light relics will also contribute to the amplitude and phase shift of the acoustic peaks. Furthermore, light relics that do not freely stream can in principle be disinguished from those that do by measuring their differing impacts on the damping tail and phase shift [175, 190].

Planck has provided a strong constraint on $N_{\rm eff} = 2.92^{+0.18}_{-0.19}$ using temperature and polarization data [125]. Recently, the phase shift from neutrinos has also been established directly in the *Planck* temperature data [217]. This provides the most direct evidence for the presence of free-streaming radiation in the early Universe, consistent with the cosmic neutrino background.

1.4.1.2 Target

One of the features that makes $N_{\rm eff}$ a compelling theoretical target is the degree to which broad classes of models fall into two basic levels of $\Delta N_{\rm eff}$. As illustrated in the left panel of Fig. 11, any species that was in thermal equilibrium with the Standard Model degrees of freedom produces a characteristic correction to $N_{\rm eff}$ that depends only on its spin and its freeze-out temperature. For freeze-out after the QCD phase transition, one finds $\Delta N_{\rm eff} \gtrsim 0.3$. Freeze-out before the QCD phase transition instead produces $0.07 > \Delta N_{\rm eff} > 0.027$ per effective degree of freedom. The first case has been tested by the data from the *Planck* satellite. The second category, which is sensitive to freeze-out temperatures ranging from hundreds of MeV to the reheating temperature, falls into the level of sensitivity attainable by CMB-S4.

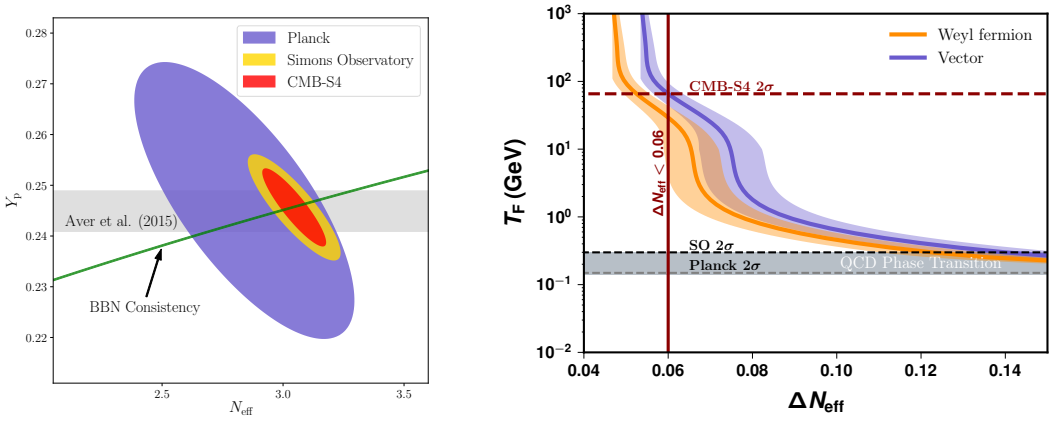

Figure 11: *Left:* Constraints in the Y_p–N_{eff} plane from current and future cosmological surveys, compared to the predictions of standard BBN and current astrophysical measurements of Y_p [218]. *Right:* Inferred reach in T_F for a given sensitivity to N_{eff}. The vertical limits on T_F assume we are using a vector ($g = 2$) to relate 2σ N_{eff} limits to T_F. We see that at CMB-S4 sensitivity, constraints have a reach two orders of magnitude higher in T_F than either *Planck* or the Simons Observatory. Bands show error estimates based on Ref. [219].

The right panel of Fig. 11 shows how a measurement at CMB-S4 sensitivity will dramatically improve our knowledge of physics at higher temperatures (i.e., at earlier times, weaker coupling). CMB-S4 at design sensitivity would place an upper limit of $\Delta N_{eff} < 0.060$ at 2σ, which translates into $T_F = 70\,(30)$ GeV for a light vector (Weyl fermion). This dramatic improvement in sensitivity to T_F over existing limits from *Planck* $T_F = 0.1\ (0.1)$ GeV, and projected constraints from Simons Observatory, $T_F = 0.3\ (0.3)$ GeV, is a direct result of the particle content of the Standard Model, which changes dramatically from quarks and gluons to baryons and mesons around the QCD phase transition (0.1–1 GeV) and thus significantly dilutes the energy densities of particles that decoupled at higher temperatures. Reaching $\Delta N_{eff} < 0.06$–0.07 leads to dramatic improvements in the sensitivity to particles with spin. At this level of sensitivity, the zoo of particles present around the QCD phase transition is insufficient to dilute the energy below experimental sensitivity, and we see a very sharp corresponding rise in the T_F curves. Instead we are limited only by the dilution due to a few heavy particles and thus it is easier to make significant gains.

1.4.2 Neutrino mass

The 2015 Nobel Prize in Physics recognized the discovery of neutrino oscillations, which demonstrated that neutrinos have mass. However, the overall scale of the neutrino masses and some mixing parameters of the full set that determine neutrino oscillations are still not measured. Cosmology offers a unique view of neutrinos; they were produced in large numbers in the high temperatures of the early Universe and left a distinctive imprint in the cosmic microwave background and on the large-scale structure of the Universe. Therefore, CMB-S4 and the DESI and LSST surveys together will have the power to detect properties of neutrinos that complement those probed by large terrestrial experiments such as the Deep Underground Neutrino Experiment (DUNE), and those searching for beta-decay and neutrinoless double-beta decay.

Neutrino flavor oscillations—oscillations between electron, muon, and tau neutrinos—are described by a model where the three neutrino flavor states are a linear combination of three mass states. The matrix that

relates the two is the Pontecorvo-Maki-Nakagawa-Sakata (PMNS) matrix. The PMNS matrix depends upon six real parameters: three mixing angles, θ_{12}, θ_{23}, θ_{13}; and three CP-violating phases, δ, α_1, α_2.

Experiments have measured the three mixing angles of $U_{\rm PMNS}$ and the two mass-squared splittings, $\Delta m^2_{21} = 7.54 \times 10^{-5}\,{\rm eV}^2$ and $|\Delta m^2_{13}| \approx 2.4 \times 10^{-3}\,{\rm eV}^2$ [220]. Despite this, fundamental questions about neutrino mass and mixing remain: (i) the absolute mass scale; (ii) the relative ordering, or *hierarchy* of the masses; (iii) whether neutrinos are Dirac or Majorana particles; and (iv) and whether neutrinos violate charge and parity (measuring δ_{CP}). CMB-S4 will measure the sum of the neutrino masses,

$$M_\nu \equiv \sum m_\nu \tag{1.21}$$

with sufficient sensitivity to be relevant to these open issues. The value of M_ν unambiguously determines the absolute mass scale of neutrinos, and if M_ν is determined to be $\lesssim 0.1\,{\rm eV}$, CMB-S4 can furthermore rule out the inverted mass hierarchy at increasing statistical significance depending on $\sigma(M_\nu)$. There are also circumstances in which the combination of CMB-S4 constraints and neutrinoless double-beta decay measurements can point to neutrinos being Dirac particles. Finally, the observables available to CMB-S4 to probe neutrinos can also provide information about new physics in the neutrino sector: the existence of new sterile neutrino states, neutrino interactions and decays, or a nonstandard thermal history for the Universe.

In the standard cosmology, neutrinos were in thermal equilibrium with photons, electrons, and positrons until the temperature of the Universe dropped below $T \sim 1\,{\rm MeV}$. At this time the weak interaction rate became smaller than the expansion rate of the Universe and neutrinos decoupled. Assuming the standard thermal history, the neutrino temperature can be related to the CMB temperature, and we can predict a relic abundance of $n_\nu \approx 56\,{\rm cm}^{-3}$ for each neutrino and antineutrino state. The CMB-inferred total radiation density in the early Universe is in excellent agreement with a contribution from neutrinos with sub-eV mass and this expected relic abundance. As discussed in 1.4.1, CMB-S4 constraints on the radiation density will put stringent tests on the thermal history of neutrinos.

The neutrino mass-square splittings give lower limits on the masses of two neutrino states of $\geq \sqrt{\Delta m^2_{21}} \approx 0.01\,{\rm eV}$ and $\geq \sqrt{|\Delta m^2_{13}|} \approx 0.05\,{\rm eV}$. These lower limits, in combination with the temperature T_ν, imply that the energy of at least two species of relic neutrinos is today dominated by their rest mass, rather than their momentum. In combination with the inferred relic abundance, this predicts a neutrino contribution to the energy budget of $\Omega_\nu h^2 \gtrsim 0.0006$. This Ω_ν contributes to the matter budget of the Universe at late times.

Since neutrinos were relativistic for much of the history of the Universe and still have relatively large kinetic energy today, their gravitational clustering is qualitatively different from that of cold dark-matter particles or baryons. On large scales, neutrino clustering is identical to that of CDM and baryons. On smaller scales, where the neutrino velocity is important, neutrinos free stream out of gravitational potentials, leaving the CDM and baryons behind; since the free-streaming neutrinos' energy still contributes to the expansion, this causes a suppression to the growth of structure on small scales. The scale separating these two regimes is the neutrino free-streaming scale, defined by [221, 222] $k_{\rm fs}(a) \equiv \sqrt{\frac{3}{2}} aH(a)/v_\nu(a) \approx 0.04\,a^2\sqrt{\Omega_{\rm m}a^{-3} + \Omega_\Lambda}\,(m_\nu/0.05\,{\rm eV})\,h/{\rm Mpc}$ in comoving coordinates. For a fixed CDM and baryon density, massive neutrinos thus induce a suppression in the matter power spectrum given by [221, 223, 224, 225]

$$\frac{P_{\rm mm}(k \gg k_{\rm fs}|\Omega_\nu)}{P_{\rm mm}(k \gg k_{\rm fs}|\Omega_\nu = 0)} \approx 1 - 6\Omega_\nu/\Omega_{\rm m}. \tag{1.22}$$

Cosmological data sets are primarily sensitive to the net suppression, and therefore the neutrino energy density Ω_ν. Since the neutrino number density is separately constrained and is the same for each mass eigenstate, these measurements of Ω_ν determine M_ν.

A central goal of the CMB-S4 experiment is to achieve a robust detection of the neutrino mass for the minimum mass sum implied by oscillation data, $M_\nu = 58\,\mathrm{meV}$ (or $\Omega_\nu h^2 = 0.0006$). In the next section, we will discuss methods through which CMB-S4 can directly constrain the neutrino mass.

1.4.2.1 CMB-S4 observables for M_ν

The main effect of massive neutrinos on large-scale structure is to suppress the matter power spectrum on scales smaller than the neutrino free streaming scale. By measuring the magnitude of this suppression, we can therefore determine the neutrino mass from cosmology.

Typically, this suppression is measured by comparing the amplitude of structure below the free-streaming scale to the nearly unsupressed amplitude of structure seen in the CMB; however, a constraint on the optical-depth parameter τ is required to determine the primordial amplitude from the CMB, and the precision of this optical-depth constraint can therefore be a limiting factor. Beyond the typically limiting optical-depth degeneracy, another degeneracy arises with the matter density (on which structure growth also depends), though this is more easily overcome by combining CMB data with baryon acoustic oscillation measurements.

CMB Lensing: One of the cleanest methods to probe the matter power spectrum, and hence the neutrino mass, is CMB lensing. Along their path to our telescopes, the photons of the CMB are gravitationally deflected by the entire mass distribution through which they pass, remapping the unlensed temperature and polarization as $X(\hat{\mathbf{n}}) = X^{\mathrm{un}}(\hat{\mathbf{n}} + \nabla\phi(\hat{\mathbf{n}}))$ where the CMB $X = T, E, B$ and the lensing potential ϕ is a direct gravitational probe of the projected mass distribution. The lensing potential power spectrum is related to the projected matter power spectrum by $C_\ell^{\phi\phi} = \int_0^{\eta^*} d\eta\, W^2(\eta) P(k = \ell/\eta)$, where W is a geometric projection kernel that depends mainly on distance ratios and η^* is the distance to the CMB last scattering surface. CMB lensing is a relatively clean probe because it arises from linear or mildly non-linear scales that are minimally affected by baryonic feedback and because the source redshift is perfectly known. While non-Gaussianity introduced by extragalactic and Galactic foregrounds must be taken into consideration, such systematics are typically small to begin with and can be further mitigated by improved lensing estimators and multifrequency cleaning.

Lensing cross-correlations: A related probe that can also give insight into the neutrino mass is the measurement of cross-correlations of CMB-S4 lensing with upcoming galaxy surveys such as LSST or Euclid. Since a lensing-galaxy correlation $C_\ell^{\phi\mathrm{g}}$ is proportional to bP_{mm}, where b is galaxy bias, an unknown astrophysical parameter. The galaxy power spectrum scales as $C_\ell^{\mathrm{gg}} \propto b^2 P_{\mathrm{mm}}$, the combination of these two probes provides (to some extent) an independent measure of the amplitude of structure, and hence of the neutrino mass. While the optical-depth degeneracy remains, it is somewhat reduced by the galaxy shape constraint in C_ℓ^{gg}, as well as the sensitivity to low-redshift growth. Furthermore, since the cross-correlations can be broken up into tomographic redshift bins, cross-correlation measurements can help break degeneracies between dark-energy parameters and neutrino masses. While some systematic errors are nulled in cross-correlation, extragalactic foregrounds remain in temperature; in addition, the measurement of galaxy clustering can come with considerable challenges such as photometric redshift uncertainty.

Galaxy Clusters: Via the thermal Sunyaev-Zeldovich effect, CMB-S4 will be able to find tens of thousands of galaxy clusters out to high redshifts. The masses of these galaxy clusters can be obtained via an SZ-mass scaling relation calibrated by both weak lensing (e.g., with LSST) and CMB lensing (internally). This will allow a determination of the mass function, which is a sensitive probe of the amplitude of structure on small scales, and hence will provide a precise probe of the neutrino mass. The redshift-dependence of the galaxy cluster abundance is expected to reduce degeneracy between neutrino and dark-energy parameters. Although clusters are complex objects with rich astrophysics complicating precise cosmological measurements, great progress has been made in mass calibration and in the mitigation of other uncertainties. Clusters represent a

physically very different probe to CMB gravitational lensing; the robustness of neutrino mass measurements will be substantially improved by having independent measurement techniques with entirely different sources of systematic errors.

1.4.2.2 CMB-S4 forecasts for M_ν

Forecasts within $\nu\Lambda$CDM: In this section we will present the results of forecasts for the constraints on neutrino mass arising from multiple probes within a minimal model of ΛCDM + neutrino mass. The forecast errors on the sum of the neutino masses from different CMB-S4 derived probes are shown in Fig. 12, plotted as a function of a prior assumed on the CMB optical depth. It can be seen that all probes perform quite similarly in the absence of an estimate of τ that is more precise than the current state of the art with *Planck* ($\sigma(\tau) = 0.007$). All probes are limited by the incomplete knowledge of the CMB optical depth; this well-known result strongly motivates improvements in external determinations of the CMB optical depth. An alternative possibility, albeit one that has not yet been demonstrated in data, is to make use of measurements of the kSZ trispectrum to constrain reionization and obtain an estimate of the optical depth. Preliminary estimates indicate that tight constraints of order $\sigma(\tau) = 0.002$ (and powerful neutrino mass measurements) might be possible with CMB-S4 kSZ, though such constraints would be less model-independent than those arising from the large-scale CMB. Small improvements in neutrino mass constraints can also be seen by adding probes with redshift resolution or the ability to probe the galaxy-spectrum shape, because these provide information that is not degenerate with τ.

We note that using only polarization lensing-reconstruction preserves nearly all the signal-to-noise ratio in a neutrino mass measurement. While we adopt the CMB lensing constraints as our conservative baseline, we find that for low $\sigma(\tau)$, CMB-S4 cluster-cosmology forecasts (with an LSST weak-lensing mass calibration) appear even more powerful than CMB lensing, motivating more research in this area.

In all cases, even for present-day optical-depth constraints, an approximately 3σ detection of the minimal mass sum is possible for CMB-S4. The fact that multiple different CMB-S4 probes should be able to achieve similar constraints will allow for cross-checks and thus increase the reliability of any claimed detection. Furthermore, unlike with prior experiments, such as Simons Observatory, we will make a near-equally significant detection using only lensing of CMB polarization; we do not need to rely on temperature-based reconstructions where extragalactic foreground systematics are a possible concern. CMB-S4 will thus provide definitive measurements of the neutrino mass sum that are more reliable than those from prior experiments. If the optimistic constraints on the optical depth of order $\sigma(\tau) \approx 0.002$ can be achieved, with either internal kSZ analyses or a large-scale cosmic variance limited, external CMB experiment, at least 5σ detections of the minimal mass sum will become possible with CMB-S4.

Forecasts with more general dark-energy assumptions: To examine the strength of the dependence of our constraints on the assumption of a particular cosmological model, we relax the assumption that the dark energy must be a cosmological constant and perform our forecasts again, this time freeing the dark-energy equation of state parameter w. The resulting constraint contours are shown in the right panel of Fig. 12. While all probes show some degeneracy between the neutrino mass and the dark-energy equation of state, this degeneracy is, to some extent, reduced in the three probes that resolve growth of structure as a function of redshift, resulting in improved neutrino mass constraints. That is because the different redshift dependences of the energy densities of dark energy and neutrinos allow the effects to be distinguished. We conclude that, especially with tomographic probes, powerful CMB-S4 measurements of neutrino mass are feasible even when allowing for somewhat more general dark-energy physics.

Before proceeding, it is useful to put a CMB-S4 detection of neutrino mass in context with anticipated constraints on M_ν from other cosmological data sets. At present, the tightest bounds on M_ν are achieved by

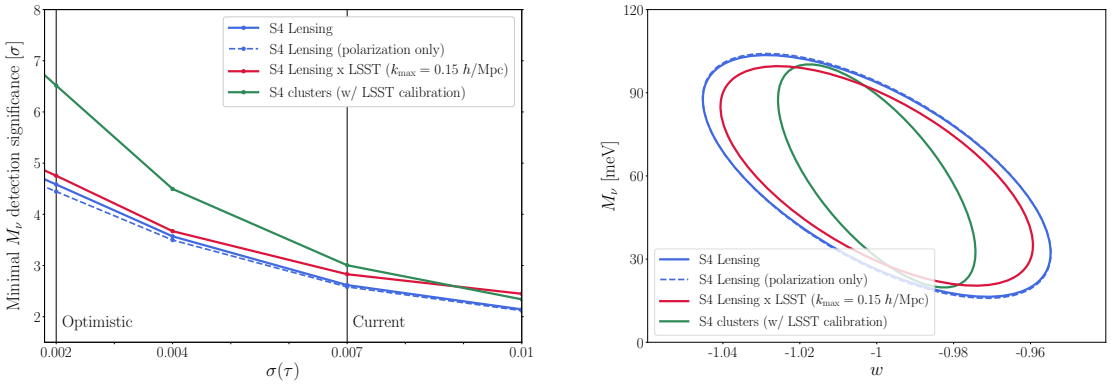

Figure 12: Left panel: Forecasted constraints on the neutrino mass sum for several different CMB-S4-derived cosmological probes, written here in terms of the significance of a detection of the minimum value consistent with oscillation data $M_\nu = 58$ meV. Neutrino mass constraints are degenerate with the optical depth to the CMB, τ. Constraints here are shown as a function of the assumed $1-\sigma$ errors on τ. All probes give similar results for the current values $\sigma(\tau) \approx 0.007$; constraints improve rapidly as the error on τ decreases. We have marked on the plot both the current τ constraint and an optimistic value derived from either kSZ analysis or an external large-scale CMB measurement. Constraints are derived from: the CMB-S4 lensing power spectrum (blue solid line); the lensing power spectrum using only polarization reconstruction (blue dashed); the CMB-S4 lensing power spectrum with the addition of LSST gold sample galaxy cross-correlations and clustering (red); CMB-S4 Sunyaev-Zel'dovich selected clusters with LSST weak lensing mass calibration (green). In all cases, DESI BAO and CMB-S4 primary CMB constraints are also assumed. Right panel: Forecast errors for joint constraints on neutrino mass and the dark energy equation of state. Probes with redshift resolution generally show somewhat less degeneracy of neutrino constraints with equation of state values, as well as smaller errors in general.

combining information in the primary CMB with a measure of the amplitude of structure at late times (in effect determining M_ν by comparing σ_8 and A_s). The amplitude of structure at late times can be determined from a variety of probes, including the CMB-S4 observables of CMB lensing and SZ cluster abundance discussed above, but also using data from galaxy surveys such as the abundance of galaxy clusters, the Lyman-α forest power spectrum, redshift-space distortions (RSDs), or weak-gravitational-lensing statistics. At present the tightest constraints on M_ν are from *Planck* CMB lensing, yielding $M_\nu < 120$ meV at 95% confidence [125]), with the latest data from the Lyman-α forest giving competitive constrains of $M_\nu < 140$ meV at 95% confidence. To date, other probes of the amplitude of structure give interesting but less stringent constraints, e.g., RSDs from the Baryon Oscillation Spectroscopic Survey (BOSS), $M_\nu < 230$ meV [226], and < 260 meV from DES lensing and galaxy clustering [227]. However, in the next decade a number of experiments are anticipated to constrain or detect M_ν at a level comparable to expectations for CMB-S4—for example, LSST, the Dark Energy Spectroscopic Instrument (DESI), *Euclid*, *WFIRST*, the Square Kilometer Array (SKA), and Simons Observatory are forecasted to reach 1σ limits on M_ν of order 10–40 meV when combined with current CMB data [134, 228, 229, 230]). In the event of no improvement in our knowledge of τ, each probe may only reach a 2–3σ detection of $M_\nu = 58$ meV. Multiple independent approaches will therefore be critical for establishing the value of the neutrino mass from cosmology. The role of CMB-S4 is therefore as a particularly robust cross-check of any data on M_ν from other experiments and, in the event of improvements to our knowledge of τ, as an experiment that provides a high-significance measure of M_ν.

Scenario	$m_{\beta\beta}$	m_β	M_ν	$\Delta N_{\rm eff}$	Conclusion
Normal hierarchy	$< 2\sigma$	$< 2\sigma$	60 meV	0	Normal neutrino physics; no evidence for BSM
Dirac neutrinos	$< 2\sigma$	...	350 meV	0	Neutrino is a Dirac particle
Sterile neutrino	$< 2\sigma$	$< 2\sigma$	350 meV	> 0	Detection of sterile neutrino consistent with short-baseline data
Diluted neutrinos	0.25 eV	0.25 eV	< 150 meV	< 0	Modified thermal history (e.g., late decay)
Exotic Neutrinos	0.25 eV	0.25 eV	< 150 meV	0	Modified thermal history; (e.g., neutrino decay to new particle)
Excluded	0.25 eV	0.25 eV	500 meV	0	Already excluded by cosmology
Dark radiation	$< 2\sigma$	$< 2\sigma$	60 meV	> 0	Evidence for new light particles; normal hierarchy for neutrinos
Late decay	$< 2\sigma$	$< 2\sigma$	60 meV	< 0	Energy injection into photons at temperature $T \lesssim 1$ MeV

Table 1-3: Relation between neutrino experiments and cosmology. We include the measurement of the Majorana mass via neutrinoless double-beta decay ($m_{\beta\beta}$) or a kinematic endpoint (m_β) compared to the cosmological measurement of the sum of the masses M_ν and the CMB measurement of $N_{\rm eff}$. Here "$< 2\sigma$" indicates an upper limit from future observations. For observations on the timescale of CMB-S4, we use $\sigma(m_{\beta\beta}) \approx 0.075$ eV and $\sigma(m_\beta) \approx 0.1$ eV. For $\Delta N_{\rm eff}$ the use of $\gtrless 0$ indicates a significant deviation from the Standard Model value.

1.4.2.3 CMB-S4 measurements of M_ν: detection scenarios and implications

CMB-S4 will make a cosmological measurement of M_ν that is complementary to terrestrial measurements of neutrino mass and other properties. In this section, we put the CMB-S4 measurement in context with laboratory neutrino experiments and present several detection scenarios and their implications.

Determining the neutrino mass scale: While CMB-S4 will determine M_ν through gravitational effects, terrestrial measurements of the neutrino mass using radioactive decay are kinematic and determine an effective electron (anti-)neutrino mass, which is an incoherent sum of mass eigenstates. Current measurements from Mainz [231] and Troitsk [232] limit this mass to < 2.0 eV. The KArlsruhe TRItium Neutrino (KATRIN) experiment [233] is expected to improve this limit by a factor of 10 and Project 8 may reach a limit of 0.04 eV[234]. Within the standard neutrino mass and cosmological paradigm, the kinematic and cosmological measurements of neutrino mass are connected through the PMNS neutrino mixing matrix. The combination of cosmological and terrestrial neutrino mass measurements can therefore test our cosmological neutrino model. A discrepancy could point to new physics, for example a modified thermal history through neutrino decay

Lepton number violation – Majorana or Dirac neutrinos: One of the most exciting connections between cosmological measurements of neutrino mass and terrestrial experiments is the complementarity between cosmological neutrino mass measurements and the search for neutrinoless double-beta decay (NLDBD). NLDBD is a hypothetical decay mode of certain nuclei, where two neutrons convert to two protons and two electrons with no emission of neutrinos. The observation of NLDBD would be transformational—it would demonstrate that neutrinos are Majorana particles and reveal a new lepton-number-violating mechanism

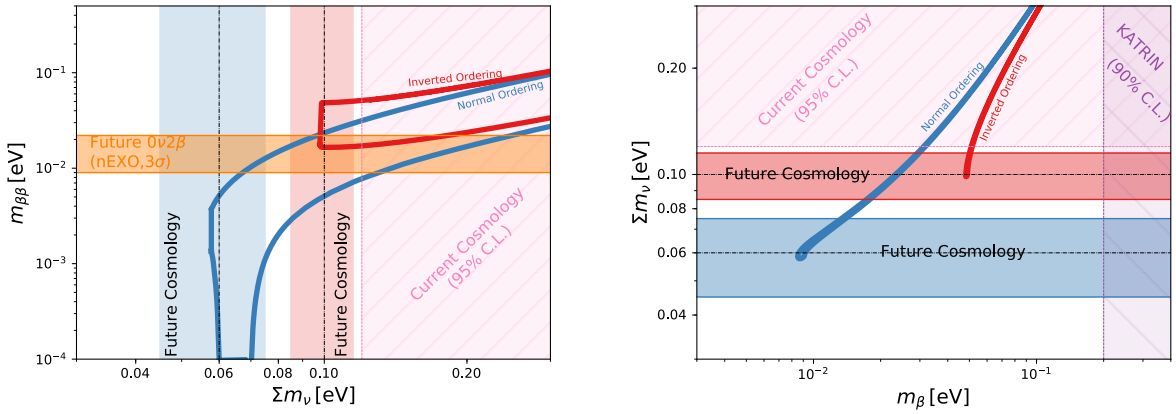

Figure 13: Left: Majorana effective neutrino mass $m_{\beta\beta}$ versus M_ν in the scenario where NLDBD is mediated by light neutrino exchange. The area enclosed by the blue and red solid lines indicate the allowed 95% ranges from neutrino oscillation experiments [235] for normal ordering (NO) and inverted ordering (IO) assuming complete ignorance of the Majorana phases. The vertical blue and red bands show the forecasted 1σ constraints on M_ν from CMB-S4 for minimal mass NO and IO. The horizontal band shows the sensitivity of future NLDBD experiments. A CMB-S4 detection of M_ν, in combination with a detection of $m_{\beta\beta}$ can constrain the Majorana phases. Right: Sum of individual the neutrino masses as a function of the electron-neutrino effective mass m_β for the NO (blue) and the IO (red). Again, the area enclosed by the blue and red solid lines indicate the allowed 95% ranges from neutrino oscillation experiments [235] for NO and IO. The horizontal bands show the future cosmological constraints around each ordering (assuming the mass of the lightest neutrino state $m_{\rm lightest} = 0\,$eV). Also shown are the anticipated limits on m_β from the KATRIN experiment in the case of no detection.

for mass generation. This new physics could potentially explain both the smallness of neutrino masses and matter-antimatter asymmetry in the Universe.

To illustrate the connection between NLDBD searches and M_ν, consider the simplest case where NLDBD is mediated by exchange of light Majorana neutrinos. Within the context of this mechanism, these experiments determine an "effective neutrino mass," $m_{\beta\beta}$, given in terms of the PMNS mixing matrix, including two unknown Majorana phases, and the individual neutrino masses. In this scenario, the absence of a signal in next generation NLDBD searches, combined with a cosmological measurement constraining $M_\nu > 100\,$meV (corresponding to either the inverted hierarchy or a minimum neutrino mass of 50 meV), would strongly point to neutrinos being Dirac particles (see Fig. 13). On the other hand, if NLDBD is observed, cosmological measurements of M_ν are then sensitive to the Majorana phases. Perhaps the most interesting scenario would be if cosmological and NLDBD measurements cannot be jointly explained by the exchange of light Majorana neutrinos and new physics is required.

Neutrino mass ordering and CP violation: In the case of normal ordering with non-degenerate neutrino mass, the CMB-S4 measurement of M_ν will provide a 2–4σ determination of the neutrino mass ordering. Fully characterizing neutrino mass ordering and CP violation are major goals of the terrestrial neutrino physics program [236]. In the scenario where the neutrino mass spectrum is normally ordered and non-degenerate, CMB-S4 would be a strong complement to terrestrial experiments by providing a measurement of neutrino ordering that is independent of oscillation parameters and $\delta_{\rm CP}$. Under all circumstances, the combination

of CMB-S4 with terrestrial determinations of neutrino ordering will provide a definitive measurement of the neutrino mass spectrum.

Sterile neutrinos: Mechanisms of introducing neutrino mass often include sterile neutrinos, with both Majorana and Dirac terms potentially contributing (e.g., Ref. [237]). A number of recent neutrino oscillation experiments have reported anomalies that are possible indications of four or more neutrino mass eigenstates with mass splittings $\mathcal{O}(1\,\mathrm{eV})$. To explain these anomalies, these neutrinos typically have relatively large mixing angles and would therefore thermalize in the early Universe, affecting primordial nucleosynthesis [238], changing $N_{\rm eff}$ by $\mathcal{O}(1)$, and M_ν by $\mathcal{O}(1\,\mathrm{eV})$. Introducing new neutrino interactions or a modified thermal history for neutrinos can accommodate additional light sterile neutrinos without violating current constraints on $N_{\rm eff}$ and M_ν. As discussed in the light relics section, CMB-S4 will provide additional constraints on neutrino-self interactions, potentially confirming or ruling out these scenarios.

Interestingly, there exist tensions in some combinations of CMB and LSS data sets that could be alleviated with the presence of massive neutrinos, extra neutrinos, or both. CMB-S4 could shed light on the sterile neutrino mass and vacuum flavor-mixing parameters invoked to explain the experimental neutrino anomalies. Telltale signatures in $N_{\rm eff}$, M_ν, and $Y_{\rm p}$ can allow CMB-S4 to probe this larger parameter space.

1.4.3 Dark energy

The discovery 20 years ago that the expansion of the Universe is accelerating presented a profound puzzle to physics, one that we have not yet solved. Our current framework can explain these observations only by invoking a new substance with unique properties (dark energy) or by changing the century-old, well-tested theory of general relativity developed by Einstein.

As the current epoch of acceleration is much later than the epoch from which the photons in the CMB originate, the behavior of dark energy or modifications of gravity do not significantly influence the properties of the primordial CMB. However, the CMB can still inform us about the properties of dark energy through two fundamental pathways. First, the projection from physical scales to the angular scales observed in a CMB map involve distance, which is affected by the expansion history along the line of sight to the last scattering surface. It is therefore sensitive to dark energy. The other pathway, involving secondary anisotropies, is even more important. These include weak gravitational lensing, as well as interactions with free electrons leading to the thermal and kinematic Sunyaev-Zeldovich effects. Therefore, as discussed in the dark-energy submission [239] to the 2020 Decadal Survey of Astronomy and Astrophysics (and endorsed by all major dark energy experimental collaborations), the CMB is a recognized probe of dark energy.

In the simplest model acceleration is driven by a cosmological constant. Although theoretically unnatural, this model does satisfy current constraints, so a clear target for CMB-S4 is to test the various predictions this model makes at late times. Using gravitational lensing of the CMB, the abundance of galaxy clusters, and cosmic velocities, CMB-S4 will measure both the expansion rate H and the amount of clustering, quantified by the parameter σ_8, as a function of time. The constraints from CMB-S4 alone will be at the 0.1% level on each and, when combined with other experiments, will reach well below this level, particularly when the power of CMB-S4 is also utilized to calibrate other probes. CMB-S4 constraints will be among the most powerful tests of the cosmological constant—more crucially, the simultaneous sensitivity to the expansion and the growth will allow us to distinguish the dark-energy paradigm from modifications to general relativity. There are many models for acceleration in the latter class, and CMB-S4 will be generically useful in constraining them.

1.4.3.1 Canonical probes: lensing-convergence power spectrum and galaxy clusters

In the basic ΛCDM cosmological model, the dark energy is assumed to be the energy of the vacuum, or equivalently an inert component with equation of state $w = p/\rho = -1$. The most common phenomenological extensions of this model are models with an expansion history deviating from the ΛCDM model in a way that is parameterized by the dark energy having a time-varying equation of state. A common parameterization is

$$w(z) = w_0 + w_a \frac{z}{1+z}. \tag{1.23}$$

Changing the energy content of the Universe has two main consequences. The first is that the expansion history changes and therefore distance measures as a function of redshift change. This is how most of the low-redshift probes, such as baryon acoustic oscillations (BAOs) and type Ia supernovae probe dark energy. For CMB-S4 this effect affects the projection of the correlations at the surface of last scattering into the anglar power spectrum. For example, changing w while keeping other parameters fixed will shift the positions of acoustic peaks in the CMB power spectrum. However, the precise measurement of the basic cosmological parameters in the presence of free w and w_a interacts in a non-trivial way with the low-redshift constraints of dark energy, which leads to improved constraints on the w–w_a plane through changing both the shape and amplitude of the observable CMB temperature and polarization power spectra, as well as breaking degeneracies with other parameters. For example, precise determination of parameters relevant for the pre-recombination era affects the precision with which the BAO ruler is known.

In Fig. 14 we show the improvement of constraints once CMB-S4 spectra (both CMB and lensing reconstruction) are added to more direct probes of dark energy. This specific forecast was made using the `GoFish` package[5] [240] and we show three representative cases. The first is the determination of expansion history from the DESI experiment based on measurements of BAOs [241], arguably the most robust probe of dark energy. In blue we show the same contour based on "3×2-point" analysis of the LSST data [242, 243], i.e., the combination of the photometric galaxy clustering, galaxy-shear cross-correlations, and shear-shear auto-correlations. This probe has a very different set of systematic errors, but a comparable total constraining power. We note that both surveys will produce further constraints. For example DESI will perform analysis of the full shape of the redshift-space power spectrum while LSST will also use other probes, such as supernovae, strong lensing and galaxy clusters. Nevertheless, this choice presents a nominal set of constraints. Upon addition of the CMB-S4 temperature, polarization, and lensing reconstruction power spectra, these constraints tighten significantly, which we show as the red ellipse in Fig. 14. We quantify this in terms of a figure of merit (FoM) that is defined to be inverse area under the ellipse ($1/\sqrt{|C|}$, where C is the 2×2 C matrix of w, w_a), which is very similar in spirit to the Dark Energy Task Force figure of merit [244]. We additionally let the neutrino mass $\sum m_\nu$ be a free parameter (see also Sect. 1.4.2), since it is known to be degenerate with dark-energy parameters [245]. We find that *Planck*+DESI BAO and LSST 3×2 analyses have comparable FoMs of approximately 70. The combined FoM of these experiments is around 200, consistent with relatively modest degeneracy breaking. However, it increases to 400 with the addition of CMB-S4 data. CMB-S4 hence contributes to a doubling of the figure of merit. We want to emphasize that part of this improvement is due to ability of CMB-S4 to break the degeneracy with the neutrino mass.

Besides the effect on the expansion history, dark energy also affects the rate at which structures form in the Universe. Most importantly, in standard general relativity, these are intrinsically linked—the given expansion history determines the growth rate. By measuring the growth over cosmic history we can in principle falsify this picture, which would be a strong indication of new physics in the gravitational sector and a truly revolutionary discovery.

CMB-S4 will measure growth using the following two main methods.

[5] `https://github.com/damonge/GoFish`

- **CMB lensing reconstruction**: Change in the growth of structures will affect the amplitude (and to a lesser extent also the shape through geometric effects) of the CMB lensing convergence power spectrum. This method is particularly powerful in combination with auto-spectra of low redshift tracers as we show in Fig. 15;
- **Galaxy clusters**: The abundance and clustering of galaxy clusters are independent probes of growth. CMB-S4 will find clusters through the tSZ effect using proven matched-filtering techniques. The tSZ is a powerful tool to find and count clusters for CMB-S4 because the detection efficiency is nearly independent of redshift for an instrument with arcminute-scale beams, and the selection function is well behaved and simple to model. The utility of cluster abundances as cosmological probes is limited by systematic uncertainties in the the observable-to-mass scaling relations. CMB-S4 will use CMB halo lensing (or optical weak lensing) to calibrate the observable-to-mass relation, aided by the well-understood selection function. The tSZ selected clusters will require optical surveys to confirm and provide redshifts for the low redshift clusters ($z \lesssim 1.5$) and near-IR follow-up observations for the remaining clusters.

We show how CMB lensing reconstruction can be converted into redshift-resolved measurements of the clustering amplitude σ_8 in the left panel of Fig. 15.

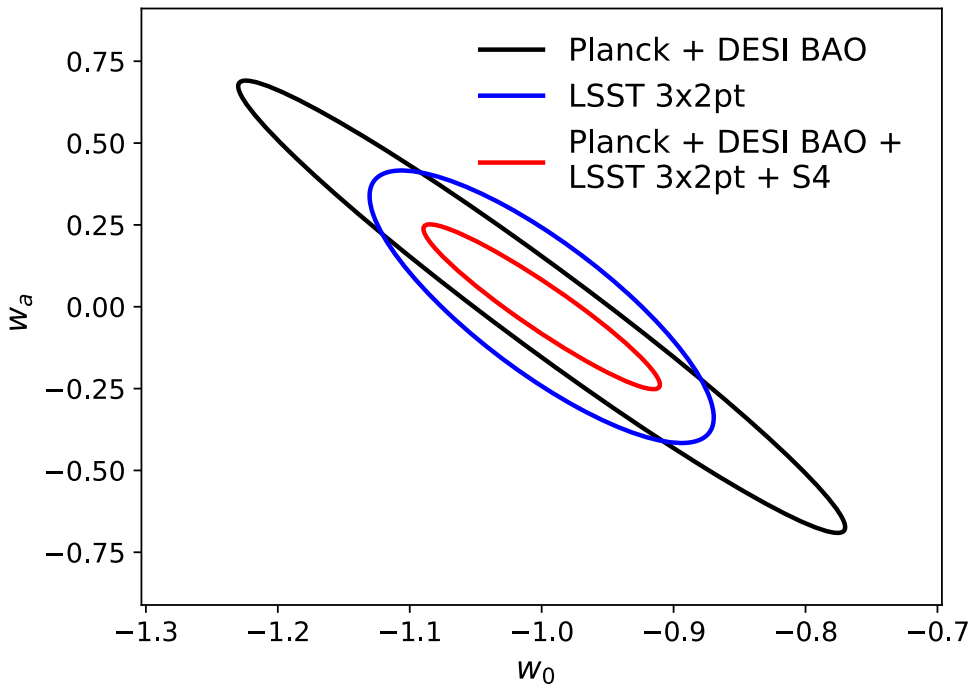

Figure 14: Improvement on the standard w_0–w_a parameters for the combination of: (i) *Planck* prior and expansion history measurements (DESI BAO) in black; (ii) LSST 3×2-point function measurements (including auto- and cross-correlation of galaxy number density and shear field fluctuations) in blue; and (iii) the combination of the first two items, with CMB-S4 power-spectrum measurements (temperature, polarization, and weak lensing reconstruction, but importantly no galaxy cluster information) in red.

1.4.3.2 Kinematic Sunyaev-Zeldovich (kSZ) effect

The kSZ effect is the Doppler shift of CMB photons caused by scattering off the plasma in late-time galaxies and clusters, which are moving with respect to the CMB. This Doppler shift causes a slight change in the measured CMB temperature, while preserving the blackbody spectrum, and therefore cannot be isolated by a multi-frequency analysis, unlike the tSZ effect. However, the broad frequency coverage of CMB-S4 is ideal for reducing other foregrounds and thus the noise on the kSZ signal.

The kSZ-induced temperature fluctuation is proportional to the galaxy *radial* peculiar velocity $v_{\rm r}$, and its optical depth to Thomson scattering $\tau_{\rm g}$ (proportional to the number of free electrons in the galaxy itself): $(\Delta T/T)_{\rm kSZ} = -\tau_{\rm g}\ v_{\rm r}$.

Thanks to its high resolution, CMB-S4 will allow unprecedented measurements of velocity fields through the kSZ effect. A measurement of the peculiar velocity can in turn constrain the amplitude of matter density fluctuations $\sigma_8(z)$ at the effective redshift of the sample, as well as the linear growth factor f, which is sensitive to dark-energy or modified-gravity models [246, 247, 248, 249]. These measurements will be able to distinguish dark energy from interesting models of modified gravity and will provide complementary constraints to redshift-space distortions and weak lensing measurements, probing larger physical scales. Figure 15 shows constraints on $f\sigma_8$ expected from CMB-S4, together with a galaxy sample from the upcoming DESI survey. We assume an overlap $f_{\rm sky}$ of 0.2, resulting in a total survey volume of 116 Gpc^3, containing 19.6 million galaxies from all DESI galaxy samples.

One caveat is that the amplitude of the signal is proportional to the optical depth of the galaxy sample used in the analysis, $\tau_{\rm g}$. This is not known a priori and is in principle degenerate with $f\sigma_8$, as can be seen in the "clustering+kSZ" curve in Fig. 15. There are several proposed ideas for breaking the optical-depth degeneracy, which range from tSZ or X-ray measurements of the galaxies/clusters themselves [250, 251] to measuring RSDs in conjunction with the kSZ effect [252]. The effect of degeneracy breaking of the optical depth can be seen in the blue solid curve in Fig. 15. Scale-dependence in growth, either caused by dark-energy perturbations (for example from a non-standard speed of sound), or by screening mechanisms in modified gravity, is not subject to the optical-depth degeneracy and can be constrained directly.

In addition, kSZ measurements can be important for dark-energy studies in a more indirect way. The high resolution of CMB-S4 allows for a direct measurement of the optical-depth profile $\tau_{\rm g}(\theta)$, since the large-scale velocity field is constant over the size of a galaxy. In turn, $\tau_{\rm g}(\theta)$ is proportional to the gas profile of the galaxy sample, allowing for calibration of baryon effects on the power spectrum, a leading systematic for weak lensing surveys aimed at measuring dark energy [253, 254].

1.4.3.3 Cosmic birefringence

In addition to probing the global dynamics of dark energy, as discussed in previous sections, CMB-S4 will also be sensitive to the imprint of new parity-violating physics within the dark-energy sector: TB and EB correlations that arise from the effect of cosmic birefringence. Detection of these parity-violating correlations would have paradigm-changing implications for cosmological scale physics, and may present a unique handle to probing microphysics of dark energy.

The simplest dynamical way to model the accelerated expansion of the Universe is to invoke a new slowly evolving scalar field that dominates its energy budget (the quintessence models for dark energy). Such a field could couple to photons through the Chern-Simons term in the electromagnetic Lagrangian, causing rotation of the linear polarization of photons propagating cosmological distances—an effect known as "cosmic birefringence" [257]. In the case of the CMB, such rotation converts some of the primordial E mode into B

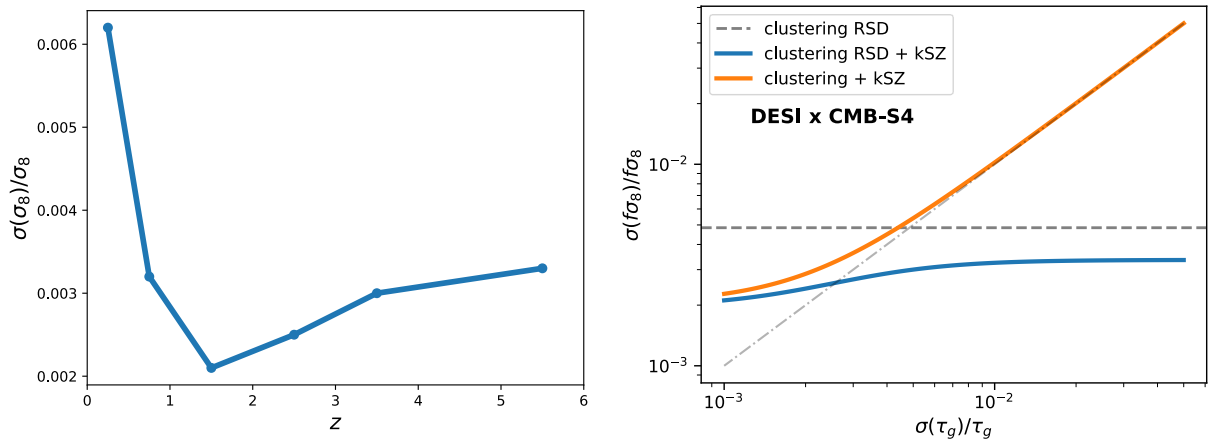

Figure 15: Constraints on the growth parameter from CMB-S4 from two independent sets of measurements. Left panel: Constraints on the matter amplitude σ_8 in tomographic redshift bins (indicated by the positions of points) from the combination of LSST galaxies and CMB-S4 lensing, assuming a fixed ΛCDM cosmology. Relaxing this assumption does not diminsh our ability to measure departures from the fiducial model. Right Panel: Constraints on $f\sigma_8$ from the kSZ effect as a function of the size of prior on $\tau_{\rm g}$ assuming a single redshift bin centered at $z = 0.75$. The straight dashed line shows results from RSDs coming from the DESI experiment. The signal from kSZ in galaxy clustering alone is plotted in orange and the combination of everything in blue. We see that even in the absence of an informative prior, the constraining power is twice that of DESI alone. For a sufficiently tight prior on $\tau_{\rm g}$, the CMB-S4 data alone can surpass DESI RSD measurements.

modes, producing characteristic TB and EB cross-correlations in the CMB maps [258, 259]. Even though there is no firm theoretical prediction for the size of this effect,[6] if observed, it would be a clear "smoking-gun" evidence for physics beyond the Standard Model, in the form of a new scalar field.

Previous studies have constrained both a uniform rotation angle α, as well as anisotropic rotation described by a power spectrum. The current tightest bound on the uniform rotation angle is $\alpha < 0.5°$ at 68% CL derived from *Planck* data [260]. The effect of a uniform cosmological polarization rotation is degenerate with systematic uncertainty on the overall instrument polarization-angle calibration. Assuming this overall angle can be calibrated to arbitrary precision, CMB-S4 would improve the constraint on uniform cosmological rotation to $\alpha < 0.2'$.

A promising way to pursue the search for cosmic birefringence is via the quadratic estimator formalism [261], which explores the off-diagonal (mode-coupling) EB correlations on small angular scales. The existing constraints were derived under the assumption of a scale-invariant rotation spectrum, for which $A \equiv L(L+1)C_L^{\alpha\alpha}/2\pi$ is independent of L. Such spectra could originate from fluctuations in a spectator scalar field present during inflation [262]. The best current bound, obtained from sub-degree scale polarization measurements with BICEP2/Keck [256], is $A < 0.11$ deg^2 (and essentially the same limit from *Planck* data [263]). More accurate measurements of polarization anisotropy at higher resolution and over a wider range of scales will significantly improve on this.

[6] One exception, for example, are the "Axiverse" models that arise in the context of string theory and feature scalar fields that produce sky-averaged rotation angles on the order of 1/137 radians (see Ref. [144]).

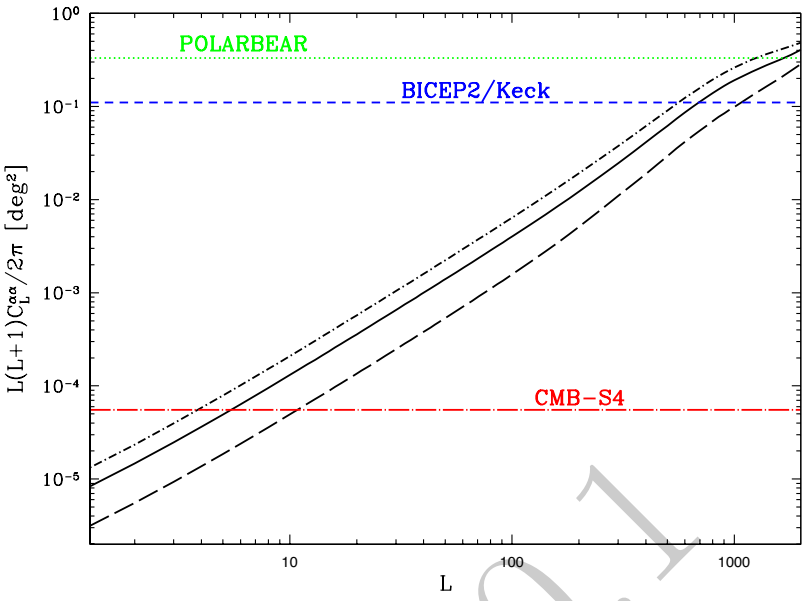

Figure 16: Black lines represent model-independent projected noise for the cosmic-birefringence rotation-angle spectrum for CMB-S4. The noise assumes no rotation signal and is calculated in three different ways: (a) assuming no delensing and using the forecasted noise in the ILC (dot-short dash line); (b) assuming 80% delensing and with forecasted noise remaining after the foreground subtraction (solid line); and (c) assuming 100% delensing and perfect foreground subtraction (long dash line). The colored lines show an example of a specific model for birefringent rotation—the scale-invariant power spectrum. The amplitude of this rotation power spectrum is set to the current 95% CL bound from POLARBEAR [255] (green dot) and BICEP2/Keck [256] (blue short dash), and to the projected bound for CMB-S4 with the noise calculated under assumption (b) (red dot-long dash line).

Figre 16 shows the forecasted noise (assuming no rotation) in the rotation-angle power spectrum $C_L^{\alpha\alpha}$ for CMB-S4 (with effective noise of 1.81 μK-arcmin, and a resolution of 1.4′), along with the predicted 95% CL bound on the amplitude A of the scale-invariant spectrum. The improvement on the current constraints is several orders of magnitude.

1.4.4 Dark matter

CMB measurements have great power in testing dark matter (DM) models and constraining parts of the parameter space that are inaccessible to laboratory experiments. In particular, the CMB directly probes the physics of cosmological DM throughout cosmic history and does not rely on assumptions about the local DM phase-space distribution within the Milky Way. Given current null results of targeted searches for well-motivated candidate models, broad scans of all possibilities are warranted; CMB-S4 will enable such an approach to the DM problem. We highlight three broad classes of DM models that are of particular interest

to searches with CMB-S4.[7] In Sect. 1.4.4.1, we discuss light DM that interacts with baryons, in Sect. 1.4.4.2, we discuss models that involve DM interactions with other new light degrees of freedom, and in Sect. 1.4.4.3, we focus on ultra-light axion-like DM particles.

1.4.4.1 Scattering with baryons

Traditional nuclear-recoil-based direct-detection experiments are only sensitive to WIMPs (weakly-interacting massive particles) with masses above about a GeV, and with such low interaction cross-sections[8] that they can penetrate the heavy shielding of detector targets [266, 264, 265]. Reducing the amount of shielding can lift the "ceiling" on the sensitivity of direct searches toward higher cross-sections [267], and new strategies are being explored to expand their sensitivity to low DM particle masses, below a GeV [194]. An entirely complementary way to probe sub-GeV DM is to search for evidence of its interactions in cosmological data. Since lower DM particle masses translate to a higher number density of scattering centers, the CMB is particularly sensitive to light particles. In addition, the CMB is sensitive to all cross-section magnitudes near and above the nuclear scale.

In the scenario in which DM scatters with protons in the early Universe, a drag force between the two cosmological fluids damps the acoustic oscillations and suppresses power in density perturbations on small scales. As a result, the CMB temperature, polarization, and lensing power spectra are suppressed at high multipoles, with respect to those in a ΛCDM universe (see the left panel of Fig. 17 for illustration). This effect has been used to search for evidence of DM-proton scattering for the case of heavy DM, using CMB and Lyman-α forest measurements [268, 269, 270].

Recently, Ref. [271] presented the first cosmological search for DM particles with any mass down to a keV (orders of magnitude below the mass thresholds of direct-detection experiments), and was followed by a number of related studies [272, 273]. In particular, Ref. [274] used *Planck* data to derive the first CMB limits on the non-relativistic effective theory of DM-proton scattering—a framework developed by the direct-detection community to characterize all available phenomenologies for scattering through a heavy mediator [275, 276, 277, 278]. Similarly, Refs. [279, 280, 273] have searched for interactions that can be parameterized by a power-law dependence of the interaction cross-section on the relative particle velocity, and reported improved limits on a wide range of models. Furthermore, Ref. [279] developed an improved treatment of non-linear effects that arise in the calculation of post-recombination scattering signals. This and related studies have enabled a robust investigation of a scenario where only a fraction of DM interacts—and tightly couples—with baryons (while the rest behaves just like the standard cold DM fluid), leading to the first robust cosmological limits on an interacting DM sub-component [279, 281]. In addition, analyses of CMB data provided essential consistency-tests of recent claims that the anomalous 21-cm signal reported by the EDGES collaboration [282] could be explained with late-time DM-baryon scattering [283]; see, for example, Refs. [284, 280].

These state-of-the-art CMB tests of DM-baryon interaction physics, which resulted in a broad exploration of new parameter space, relied primarily on moderate-resolution temperature measurements from *Planck*. Since the DM signal is increasingly prominent at higher multipoles (see Fig. 17), high-resolution measurements with CMB-S4 will thus substantially improve sensitivity to DM-baryon interactions.

In Fig. 17, we present current and projected upper limits on the cross-section for scattering on protons, as a function of DM mass, for a spin-independent velocity-independent interaction (chosen as our fiducial model).

[7] In this document, we omit discussion of DM annihilation, since the detection sensitivity is mostly saturated by current and upcoming measurements [47].

[8] For reference, one of the current largest experiments of this class, Xenon1T, is sensitive to cross-sections roughly in the range 10^{-47}–10^{-31} cm^2 [264, 265].

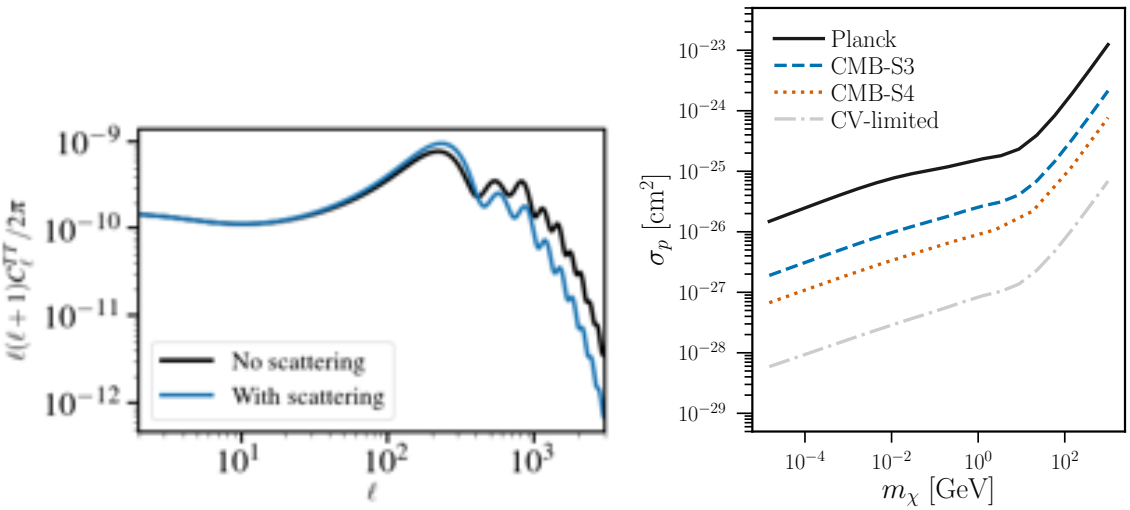

Figure 17: *Left:* Illustration of the effect of a velocity-independent spin-independent contact interaction between dark matter and baryons (with a cross-section 100 times higher than the current upper limit from *Planck*) on the CMB temperature power spectrum (blue), compared to the CDM case (black). *Right:* Upper limits on the DM-proton interaction cross-section as a function of DM mass, for spin-independent velocity-independent scattering. In case of a null detection, areas above the curves are excluded at the 95% confidence level. Shown are the current limits from *Planck* [271] and forecasts for Stage-3 experiments (CMB-S3, such as AdvACT [286]), CMB-S4, and a cosmic-variance-limited experiment (CV-limited); see also [285].

Areas above the curves are excluded at the 95% confidence level. We compare current limits obtained from *Planck* (from Ref. [271]) with forecasts for Stage-3 experiments (with a white noise level of 10μK-arcmin and resolution of 1.4′), CMB-S4, and a cosmic-variance-limited experiment (with vanishing noise levels). We note the large improvement factor that CMB-S4 delivers over the current limits, for the entire DM mass range considered.

Most of the constraining power in the case of CMB-S4 comes from the lensing anisotropy, while the temperature and polarization anisotropies contribute roughly equally to the projected constraint [285]. Furthermore, Ref. [134] has shown that an increase in sky coverage beyond about 10% (keeping all other parameters fixed) only marginally improves the projected sensitivity. Finally, Ref. [285] has also shown that DM-baryon scattering is easily distinguishable from most other new-physics effects sought by CMB experiments (the neutrino mass, new light degrees of freedom, and DM annihilation) once the lensing anisotropy is measured at the level of CMB-S4. Therefore, beyond its ability to cover vast open portions of DM parameter space, CMB-S4 also holds promise as a DM discovery tool.

Small-scale CMB anisotropy measuements enabled by CMB-S4 will probe DM-baryon interactions at the time when the Universe was much less than a thousand years old. These measurements will be sensitive to particle masses outside the detection limits of most existing direct-detection experiments; furthermore, unlike all Earth-based experiments, CMB analyses are independent on the assumptions about the local phase-space distribution of DM. Compared to the Simons Observatory forecasts [134], CMB-S4 will further improve the sensitivity to DM scattering by a factor of 4–5 (for a DM mass of 1 GeV and a velocity-independent interaction)—sufficient to enable signal confirmation and detailed subsequent studies, in the case of a marginal detection with future Simons-Observatory data. On the other hand, CMB-S4 will provide important consistency checks for small-scale-structure probes of DM microphysics, enabled by upcoming

galaxy surveys such as LSST. In particular, DM interactions can leave imprints on satellite galaxy populations [287] and other collapsed structures in the local Universe [288], many of which will be measured in detail in the coming decade of observations. However, tests of DM microphysics with small-scale-structure tracers face modeling and simulation challenges; CMB measurements that can capture the same physical effects on large scales and in the early Universe will be pivotal for robust inference of DM particle properties from observational data sets in the future.

1.4.4.2 Interactions with dark radiation

The exquisite sensitivity of the CMB to the depth and size of the DM gravitational potentials near the surface of last scattering makes it a particularly good probe of any new physics affecting the clustering of DM on large scales at early times. This sensitivity to DM density fluctuations is extended to lower redshifts via the weak gravitational lensing that CMB photons experience as they propagate to us. Similar to how tight coupling with photons inhibits the growth of baryon fluctuations until the epoch of hydrogen recombination, DM interacting with light (or massless) dark radiation (DR) at early times experiences a suppressed growth of structure due to the dark-radiation pressure opposing gravitational infall. Models where such interactions arise are diverse in their particle content (see e.g., Refs. [289, 290, 186]) and have been invoked to explain the apparent low amplitude of matter fluctuations measured by certain weak-lensing surveys [164, 187, 188]. They can also naturally arise in the context of self-interacting DM, which has been proposed to address possible anomalies on subgalactic scales [291].

The impact of DM-DR interaction on the CMB has been studied in detail in Refs. [290, 292] (see also Ref. [293] for a detailed derivation of the relevant Boltzmann equations). In short, the presence of extra DR mimics the presence of extra neutrino species (see Sect. 1.4.1) and affects the expansion history of the Universe, possibly modifying the epoch of matter-radiation equality, the CMB Silk damping tail, and the early integrated Sachs-Wolfe effect. However, unlike standard free-streaming neutrinos, the DR forms a tightly coupled fluid at early times, leading to distinct signatures on CMB fluctuations which include a phase and amplitude shift of the acoustic peaks (see Refs. [174, 217, 175]). In addition, the DR pressure prohibits the growth of interacting DM fluctuations on length scales entering the causal horizon before the epoch of DM kinematic decoupling. This weakens the depth of gravitational-potential fluctuations on these scales, affecting the source term of CMB temperature fluctuations. Finally, the modified matter clustering in the Universe due to the interaction with DR affects CMB lensing. For interacting DM models that are still allowed by the current *Planck* data, this latter effect is where CMB-S4 can significantly improve the constraints on these non-minimal DM theories.

Given the large array of possible DM theories to constrain, it is useful to pick a simple benchmark DM-DR model to assess the sensitivity of CMB-S4 to the effects described in the previous paragraph. A particularly useful model is one in which the interaction between DM and DR is mediated by a particle with mass of order a few MeV. Such theories have been put forward in the context of self-interacting DM [294, 295, 296] in order to obtain a velocity-dependent self-interaction cross-section that can fit both the observed density profiles of dwarf galaxies and of large galaxy clusters. For these models, the momentum-transfer rate between the DR and DM in the early Universe can be written as $\dot{\kappa}_{\rm DR-DM} \propto \Omega_{\rm DM} h^2 a_4 (1+z)^4$, where a_4 is a parameter that controls the strength of the DM-DR interaction that depends on the exact Lagrangian used (see Ref. [293]). Within this class of models, the most relevant parameters that can be constrained with CMB-S4 are the interaction strength a_4, the fraction of DM interacting with DR $f_{\rm int}$, and the amount of DR present in the Universe $\Omega_{\rm DR} h^2$.

In Fig. 18, we show the projected sensitivity of a CMB-S4-like experiment to the presence of DM-DR interactions in the $\Omega_{\rm DR} h^2$–a_4 plane, for two values of $f_{\rm int}$, namely 1% and 10%. For low values of the

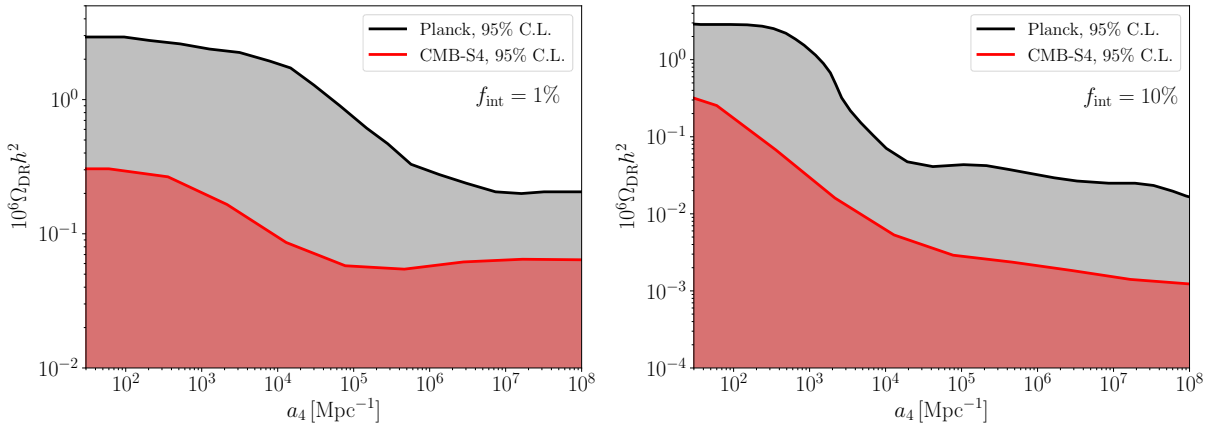

Figure 18: Dark matter-dark radiation interaction sensitivity of *Planck* (adapted from Ref. [290]) and an experiment like CMB-S4; for this plot, we assumed a configuration of CMB-S4 similar to that outlined in the CDT. The x-axis corresponds to the interaction strength, while the y-axis corresponds to the abundance of dark radiation. We show two different fractions of DM interacting with the DR, as indicated on each panel. The shaded regions are allowed at the 95% confidence-level. Note the different scales for the y-axes on each panel.

interaction strength a_4, the DR decouples very early from DM and essentially behaves like an extra free-streaming relativistic species, and the constraint on $\Omega_{\rm DR}h^2$ thus becomes equivalent to that on $\Delta N_{\rm eff}$ discussed in Sect. 1.4.1. As the DM-DR interaction strength is increased, $\Omega_{\rm DR}h^2$ becomes more severely constrained, to ensure that DM kinematic decoupling occurs before the modes probed by the CMB enter the causal horizon. In addition, the constraints become stronger as the fraction of interacting DM increases.

Looking ahead, the main difficulty in constraining theories in which DM interacts with DR using CMB-S4 will be modeling of non-linearities in the CMB lensing power spectrum, which can be important for multipoles above 500 (in the reconstructed lensing-potential power spectrum). Recent progress in this respect is already promising [297]. The CMB constraints on DM-DR interaction could be further improved by combining CMB-S4 with probes of small-scale structure, such as the Lyman-α forest or the luminosity function of Milky Way satellite galaxies (see e.g., Ref. [298]).

1.4.4.3 Axion-like particles

The QCD axion and other axion-like particles (ALPs) are well-motivated DM candidates and can contribute to the DM density (see Ref. [139] for a recent review). One example is ultralight axions (ULAs), which are non-thermally created via vacuum realignment and have a distinctive phenomenology. ULAs are predominantly non-thermal, nonrelativistic, and do not contribute to $N_{\rm eff}$.[9]

The ULAs we consider here are motivated by string theory and are associated with the geometry of the compact spatial dimensions. These axions can contribute either to the dark-matter or dark-energy budget of the Universe, depending on their particular mass, which sets the time at which the axions begin to coherently oscillate and redshift as matter. We consider axions within a range of masses $10^{-33}\,{\rm eV} \leq m_{\rm a} \leq 10^{-20}\,{\rm eV}$,

[9] Note, however, that if these axions have couplings to ordinary matter, as described in Sect. 1.4.1, then a second, relativistic population of axions is created.

with negligible couplings to the Standard Model particles. We can compare these assumptions to those used in Sect. 1.4.1; the contribution of thermal axions to $N_{\rm eff}$ applies to any mass $m_{\rm a} \lesssim 1\,{\rm eV}$, including the well known QCD axion, but depends in detail on the couplings to the Standard Model particles and on the reheat temperature. Cosmological constraints on axion dark matter are thus complementary in the space of masses and couplings to the constraints on a thermal population of axions.

At the moment, the CMB (through measurements of CMB lensing, temperature, and polarization [299], using tools developed in Refs. [300, 301]), offers the best gravitational probe of the ULA density in the regime $10^{-33}\,{\rm eV} \leq m_{\rm a} \leq 10^{-25}\,{\rm eV}$. We choose a fiducial value of the axion energy density consistent with these constraints. In this window, ULAs cannot be all of the dark matter, but can be a significant component, with density comparable to baryons and neutrinos. Given the rich spectrum of particles in the Standard Model, there is no reason to expect a trivial dark sector, and it is important to explore the power of the CMB to constrain any particle species with a potentially detectable density.

CMB-S4 will push the upper edge of the CMB ULA window to $m_{\rm a} \sim 10^{-23}\,{\rm eV}$. At higher masses still, ULAs will alter pulsar timing signatures [302, 303], suppress the clustering of neutral hydrogen at high-z (an observable probed by measurements of the Lyman-α forest flux power spectrum [304, 305, 306, 307, 308]), alter the mass spectrum of black holes through Penrose processes [144, 309, 139, 310, 311] with implications for Laser Interferometer Gravitational-Wave Observatory (LIGO) event rates, and lead to observable gravitational-wave signatures in the *Laser Interferometer Space Antenna (LISA)* band [312, 309, 310, 311] (see Ref. [313] for a recent review of ULA gravitational signatures).

1.4.4.4 Constraints on cold axion energy density

The degeneracies of ULAs with other cosmological parameters, such as $N_{\rm eff}$ or m_ν, vary depending on the axion mass [301]. Dark-energy like axions with masses around $10^{-33}\,{\rm eV}$ change the late-time expansion rate and therefore the sound horizon, changing the location of the acoustic peaks. There are thus degeneracies of the ULA density $\Omega_{\rm a}$ with the matter and curvature content. Heavier axions ($m_{\rm a} \gtrsim 10^{-26}\,{\rm eV}$) affect the expansion rate in the radiation era and reduce the angular scale of the diffusion distance, leading to a boost in the higher acoustic peaks, which has a degeneracy with $N_{\rm eff}$.

In the matter power spectrum, and thus CMB lensing power, light axions suppress clustering, suggesting a degeneracy with effects of massive neutrinos that must be broken to make an unambiguous measurement of neutrino mass using the CMB. The above-mentioned effects in the expansion rate break this degeneracy for some axion masses. There remains a significant degeneracy between $\Omega_{\rm a}$ and the sum of the neutrino masses ($\Sigma_i m_{\nu_i}$) and massive neutrinos if $m_{\rm a} \lesssim 3 \times 10^{-29}\,{\rm eV}$. Effort should be made to break these (and other) degeneracies using other data sets to establish if CMB-S4 data will show the unambiguous signature of neutrino mass, or hint at some other new physics.

We show the forecasted sensitivity to the axion energy density from CMB-S4, including lensing in the left panel of Fig. 19 (for fixed neutrino mass of $\Sigma m_\nu = 0.06\,{\rm eV}$). Adding information from the lensing reconstruction using CMB-S4 (or SO) will improve sensitivity to axion DM significantly. A percent-level measurement of the lensing deflection power at multipoles $\ell > 1000$ leads to an improvement in the error on the axion energy density of a factor of around 8 relative to the current *Planck* constraints, for an axion mass of $m_{\rm a} = 10^{-26}\,{\rm eV}$. This will allow us to test if DM has different particle components at the percent level. Furthermore, since $\Omega_{\rm a} \propto f_{\rm a}^2$, this improves the expected constraint on the axion decay constant from $10^{17}\,{\rm GeV}$ with *Planck* to $10^{16}\,{\rm GeV}$ with CMB-S4, testing the "string axiverse" scenario [144].

Using only *Planck* data, ULAs are degenerate with CDM at $m_{\rm a} = 10^{-24}\,{\rm eV}$, and constraints are still weak at $m_{\rm a} = 10^{-25}\,{\rm eV}$. CMB-S4 could make a $> 5\sigma$ detection of departures from CDM for masses as large as

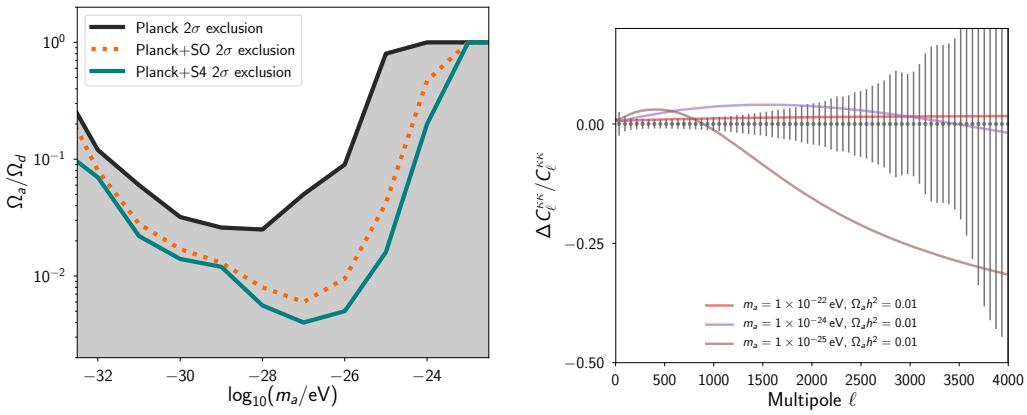

Figure 19: Constraints on ultra-light axions (ULAs). Left: Fisher-forecasted 2σ exclusion regions for the ULA mass fraction $\Omega_\mathrm{a}/\Omega_\mathrm{d}$ for the *Planck* alone, *Planck* + Simons Observatory (SO) (as discussed in Ref. [47]), and CMB-S4, where $\Omega_\mathrm{d} = \Omega_\mathrm{a} + \Omega_\mathrm{c}$. Right: Residual in lensing-convergence power spectrum $C_L^{\kappa\kappa}$ for different models including ULA DM, compared with Fisher-forecasted errors for CMB-S4.

$m_\mathrm{a} = 10^{-25}\,\mathrm{eV}$, and could improve the lower bound on DM particle mass to $m_\mathrm{a} = 10^{-23}\,\mathrm{eV}$ and fractions $\mathcal{O}(10\%)$. Realizing this sensitivity will require better modeling of the non-linear clustering of axions [314], building upon and applying the results of previous work [315, 316, 317, 318, 319, 320, 321, 322, 323, 324, 325, 326, 327, 328, 329, 330, 331].

1.4.4.5 Axion isocurvature

The axion decay-constant, f_a, specifies the scale at which the underlying $U(1)$ symmetry is broken. If $H_\mathrm{I}/2\pi < f_\mathrm{a}$, then this symmetry is broken during inflation, and the axion acquires *uncorrelated* isocurvature perturbations [332, 333, 334].[10] The uncorrelated CDM isocurvature amplitude is bounded by *Planck* to be $A_\mathrm{a}/A_\mathrm{s} < 0.038$ at 95% CL [32]. While axion isocurvature probes the same inflationary energy scale probed by primordial B modes, searches for isocurvature are independent of other constraints on the tensor-to-scalar ratio, offering a distinct test of inflationary physics, if a significant fraction of the DM is composed of axions.

The axion isocurvature amplitude is:

$$A_\mathrm{I} = \left(\frac{\Omega_\mathrm{a}}{\Omega_\mathrm{d}}\right)^2 \frac{(H_\mathrm{I}/M_\mathrm{Pl})^2}{\pi^2(\phi_\mathrm{i}/M_\mathrm{Pl})^2}\,, \tag{1.24}$$

where $\Omega_\mathrm{d} = \Omega_\mathrm{a} + \Omega_\mathrm{c}$ is the combined total primordial relic density parameter in ULAs and standard CDM. The initial axion displacement, ϕ_i, fixes the axion relic abundance such that $\Omega_\mathrm{a} = \Omega_\mathrm{a}(\phi_\mathrm{i}, m_\mathrm{a})$ [336, 337, 338, 339, 340, 341]. Thus, if the relic density and mass can be measured by independent means, such as direct detection, a measurement of the axion isocurvature amplitude can be used to measure the energy scale of inflation, H_I.

[10] We ignore the case where $H_\mathrm{I}/2\pi > f_\mathrm{a}$, since then no isocurvature fluctuations are excited. The limit $r_{0.05} \lesssim 0.1$ [125] implies that isocurvature is produced if $f_\mathrm{a} > 1.6\times10^{13}\,\mathrm{GeV}$. This accounts for the QCD axion in the "anthropic" window (roughly half of the allowed range of f_a on a logarithmic scale), axions with GUT-scale decay constants (such as string axions [335, 144]) and axions with lower f_a in models of low-scale inflation.

We forecast the errors on axion isocurvature for the baseline CMB-S4 experiment with a $1\,\mu$K-arcmin noise level and a $1'$ beam; the isocurvature limit will be improved by a factor of approximately 5 compared to *Planck*, allowing for detection of axion-type isocurvature at 2σ significance in the region $0.008 < A_{\rm I}/A_{\rm s} < 0.038$. If the QCD axion is all of the DM, axion direct-detection experiments (e.g., ADMX [342] already in operation, or CASPEr [343], in progress) and CMB-S4 could probe $H_{\rm I}$ in the range

$$2.5 \times 10^6 \lesssim H_{\rm I}/{\rm GeV} \lesssim 10^7 \quad \text{(S4+ADMX)}, \tag{1.25}$$

$$10^8 \lesssim H_{\rm I}/{\rm GeV} \lesssim 4 \times 10^9 \quad \text{(S4+CASPER)}, \tag{1.26}$$

where we have used the standard formulae relating the QCD axion mass and relic abundance to the decay constant [333]. Combining axion DM direct detection with CMB-S4 isocurvature measurements allows a unique probe of low-scale inflation, inaccessible to searches for tensor modes.

We now consider isocurvature fluctuations in ULAs, which have a number of distinctive features the CMB [344, 345, 301, 299, 300, 315]. We fix the fiducial ULA fraction to 1%, such that $\Omega_{\rm a}$ and $m_{\rm a}$ can be separately measured using the CMB-S4 lensing power, and thus using Eq. (1.24), a measurement of $A_{\rm I}$ is a measurement of $H_{\rm I}$. In contrast to the QCD axion, there are masses ($m_{\rm a} \lesssim 10^{-26}$ eV) for which tensor modes impose a stronger constraint on $H_{\rm I}$ than isocurvature. There are also regions of overlap between possible tensor and isocurvature measurements, where CMB-S4 could be used to determine isocurvature and axion parameters, yielding an independent measurement of H_I:

$$2.5 \times 10^{13} \lesssim H_{\rm I}/{\rm GeV} \lesssim 10^{14}\,\text{(ULAs, CMB-S4 alone)}\ . \tag{1.27}$$

A broader range of scenarios is considered in Ref. [17]. Already with *Planck* data, the combination of lensing reconstruction and isocurvature limits gives the posterior range for the tensor-to-scalar ratio of $r < 0.01$ for $m_{\rm a} = 10^{-24}\,{\rm eV}$ [299].

1.5 Mapping matter in the Cosmos

The third science theme relates to surveying the contents of the Universe revealed by the millimeter-wave sky.

The deep and wide CMB-S4 field will provide a unique census of a large fraction of the sky at centimeter to millimeter wavelengths. Matter in the Universe shows up in this census in multiple ways: the gravitational potential coherently shears the image of the CMB fluctuations, some CMB photons are scattered by electrons along the way, and many objects emit their own radiation. All of these help us to map out the matter in the cosmos.

The main value of CMB-S4 for non-CMB scientists will come from the deep and wide survey (although the ultra-deep survey will also be useful for these communities). In the reference design, CMB-S4 will map 70% of the sky in total intensity and linear polarization, with a cadence of around 2 days, reaching a 5σ point-source noise well below 1 mJy in the final coadded maps, along with corresponding maps of gravitational lensing and Compton-y.

The CMB-S4 survey will complement and enhance the LSST optical survey of the same region [346], the DESI spectroscopic survey [347], the *eROSITA* all-sky X-ray survey [348], and other planned and yet-to-be-imagined surveys from both ground- and space-based facilities. By going dramatically deeper than previous CMB surveys and covering a large fraction of the sky, the potential for new discoveries is high. This section provides an overview of some of the products to be derived from CMB-S4 that will be of significant utility to the broader astronomical community.

With these data, CMB-S4 will be able to probe physical processes that govern and regulate galaxy formation in various classes of objects, and probe the circumgalactic and intracluster mediums. Secondary CMB anisotropies are an excellent probe of reionization because scattering of photons by free electrons affects the observed temperature and polarization in a predictable fashion that is sensitive to its duration and morphology (or "patchiness"). CMB-S4 will leave a legacy that includes catalogs of extragalactic sources, maps of extragalactic integrated density and pressure, and multifrequency images of Galactic polarization.

These data sets will be exploited by astronomers and astrophysicists over the decades to come.

1.5.1 Extragalactic component maps

With the broad frequency coverage of CMB-S4, we can use internal-linear-combination techniques to produce maps of isolated sky signals. These products will include maps of the CMB temperature and polarization anisotropies, the reconstructed CMB gravitational-lensing potential, Compton-y maps, the cosmic infrared background, and Galactic synchrotron and dust (in both intensity and polarization). Of particular utility to the broader astronomical community will be the lensing map and the Compton-y (or tSZ) map; we detail their properties below.

Gravitational Lensing Map: One of the main goals of the CMB-S4 project is to extract cosmological information from a reconstructed map of the large-scale structures responsible for gravitationally lensing the CMB. This will constitute a map of all matter between us and the CMB, including dark matter, with a broad redshift weighting that peaks near redshift $z = 2$. The map will cover the entire footprint of the CMB-S4 survey and will represent the true mapping of matter, with map-level signal-to-noise ratio exceeding unity,

from the largest scales in the survey down to scales of approximately 12 arcminutes (representing multipole $L \simeq 1000$). Even on smaller scales, there will still be significant statistical information.

Since the contribution to CMB lensing is very broad as a function of redshift, including appreciable weight at $z < 1$ where many optical and other surveys are sensitive, this map will have significant potential for cross-correlation with data at a range of wavelengths. Thus far, CMB lensing maps have been studied in conjunction with a very diverse group of data sets, including (in order of decreasing wavelength): extragalactic radio catalogs [349, 350, 351]; maps of the Sunyaev-Zeldovich effect [352]; the cosmic infrared background [353, 354, 355, 356]; far-infrared galaxies [357]; mid-infrared galaxies [358, 359]; mid-infrared quasars [360]; optical redshift surveys [361], including filaments [362] and voids [363]; optically-selected galaxy clusters [359]; optically-selected quasars [364, 359]; optical weak lensing [365, 366]; optical photometric catalogs [367, 368]; the Lyman-α forest [369]; X-rays [370]; and γ-rays [371]. Additionally, CMB lensing has been used to measure the masses of SZ-selected [372, 373] and optically-selected [374] galaxy clusters and groups.

The lensing map from CMB-S4 will have much lower noise levels than those used in each of these earlier studies, and will additionally have very wide sky coverage. Because it is primarily based on CMB polarization data rather than temperature data, it should also be more robust against possible foreground contamination. Future analyses can thus be performed at much higher signal-to-noise ratio, with fewer concerns about contamination. Furthermore, many new data sets in many wavelength ranges will be available on the timescale of CMB-S4 that will both be deeper and have wider sky coverage than many of the studies carried out so far, including: LSST [346] for both photometric galaxy catalogs and weak lensing; DESI [375] for spectroscopic samples; and sensitive maps of ionized gas with the SZ effect from CMB-S4 itself. In addition to being used in delensing the CMB-S4 map of the primary CMB, the CMB-S4 lensing map will also provide the ability to delens the maps from future satellite CMB missions, which are unlikely to have the same internal sensitivity to lensing. The map of CMB lensing from CMB-S4 will thus represent a lasting, legacy value to the subsets of the extragalactic astronomical community working in nearly every wavelength range.

Compton-y map: Multi-frequency CMB temperature data enable the reconstruction of tSZ (Compton-y) maps by taking advantage of the known, unique tSZ spectral function. The first such maps have been produced recently using data from *Planck* [376, 352, 377, 378]. Here, we forecast the reconstruction of a Compton-y map using data from the CMB-S4 large-aperture telescopes (LATs) in combination with *Planck* (due to the large-scale atmospheric noise from the ground, *Planck* will remain useful at low ℓ). We use a harmonic-space internal-linear-combination (ILC) method to obtain post-component-separation noise curves for the tSZ signal. The sky model includes essentially all important contributions to the microwave sky (Galactic and extragalactic), and is identical to that used in Ref. [47]. The CMB-S4 LAT noise properties are described elsewhere in this document. We include *Planck* data from 30–353 GHz, assuming white noise and Gaussian beams. The ILC approach includes the option of "deprojecting" particular contaminants with a specified SED, at the cost of increased statistical noise. We specifically consider deprojecting the CMB, a fiducial cosmic infrared background (CIB) spectrum (modified blackbody with temperature of 19.6 K and spectral index of 1.2), or both.

The results of this analysis are shown in Fig. 20. The figure shows the post-component-separation noise (per mode) of the Compton-y map produced from CMB-S4 LAT and *Planck* data for various ILC-based foreground-cleaning options, in comparison to the tSZ power-spectrum signal. The CMB-S4 noise is low enough that the Compton-y field will be mapped on a mode-by-mode basis for multipoles $3000 \lesssim \ell \lesssim 5000$, even when explicitly deprojecting the CIB foreground. In fact, even with the expected level of atmospheric noise, CMB-S4 still improves enough over *Planck* to allow mapping at $\ell \approx$ few hundred. The figure also shows a similar noise curve for the baseline Simons Observatory (SO) configuration [47], demonstrating the significant gains that CMB-S4 will achieve. The total signal-to-noise ratio of the CMB-S4 tSZ power-spectrum measurement is 1570 (standard ILC), 570 (CMB deprojected), 1500 (CIB deprojected), or 130

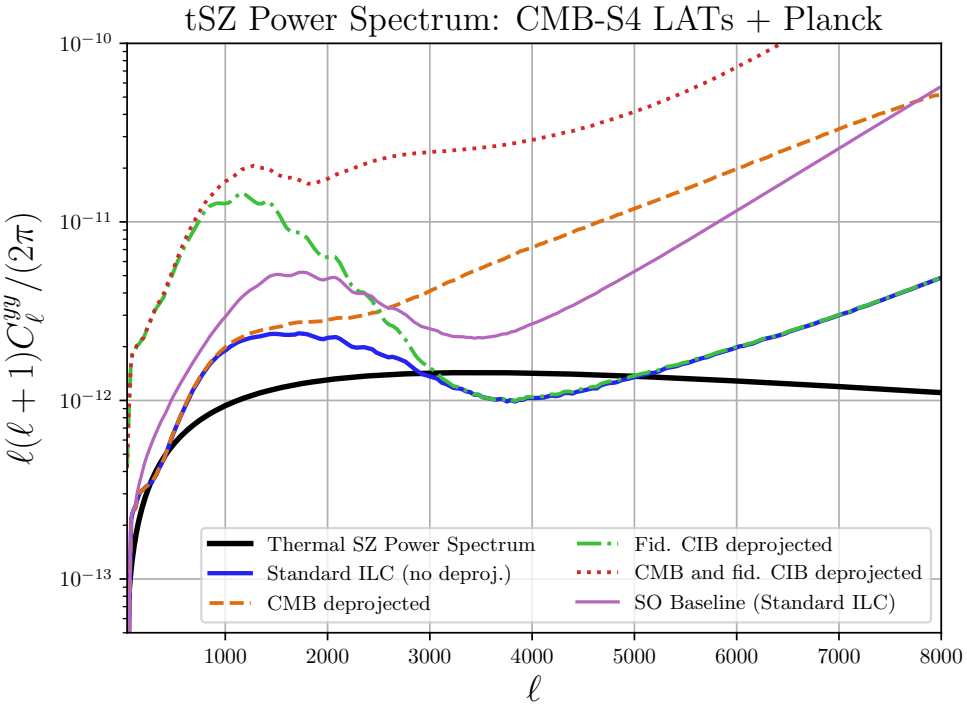

Figure 20: Post-component-separation noise for the Compton-y map reconstructed from the CMB-S4 LATs and *Planck*. The solid black curve shows the tSZ power-spectrum signal. The solid blue curve shows the ILC reconstruction noise, while the other curves show the noise levels for various foreground-deprojection options. The thin, solid magenta curve shows the ILC reconstruction noise for the Simons Observatory baseline configuration.

(CMB and CIB deprojected); for this estimate, we neglect the trispectrum contribution to the covariance matrix, considering Gaussian errors only. We also conservatively assume $f_{\rm sky} = 0.45$. For the standard ILC, this is an improvement over the current *Planck* measurement by nearly two orders of magnitude. Moreover, this estimate only captures the Gaussian contributions to the tSZ signal, which is a lower bound on the total information content in the y-map, given the significant non-Gaussianity of the tSZ field. The legacy value of this map will be immense, including cross-correlations with optical, infrared, X-ray, and intensity-mapping data sets.

1.5.2 Galaxy formation and evolution

The small fraction of CMB photons scattered during their cosmic journey create secondary anisotropies that encode the evolving spatial distribution and thermal energy of diffuse ionized gas throughout the Universe. Because the CMB is a nearly uniform back light on small scales, angular features in the scattering distortions and anisotropies generated can be used to probe *all* the ionized gas within a given region, not only that gas dense enough to emit in the X-rays or which happens to contain the particular ionic species that generate observable absorption features along the particular lines of sight to background sources in

instrument-specific redshift windows. With its unprecedented sensitivity and angular resolution, CMB-S4 will deliver transformative high signal-to-noise ratio maps of ionized gas over a wide range of scales and redshifts, from ionized bubbles during reionization to the intracluster medium of the most massive present-day halos. These maps, alone and in combination with large-scale structure probes at other wavelengths, will allow us to finally address a crucial longstanding question: *how does the energy injected by galaxies and supermassive black holes affect the surrounding baryonic reservoir of diffuse gas driving their evolution?*

In this section, we describe in detail the new physical insights and model constraints that CMB-S4 will provide by addressing this question, and present new quantitative forecasts for constraints on state-of-the-art numerical models of galaxy formation and reionization. We emphasize that due to the rich nature of this science, the forecasts presented here represent only a lower bound on the impact of CMB-S4 in this area; the range of applications is vast, and will certainly expand further by the start of the CMB-S4 survey.

1.5.2.1 Intracluster medium and circumgalactic medium

Understanding the physical processes that govern and regulate galaxy formation over cosmic time is a central goal in astrophysics. It has long been known that star formation is an inefficient process: less than 10% of the cosmic abundance of baryons has been converted into stars over the past 13.8 Gyr (e.g., [379, 380]). Yet early hydrodynamic simulations of galaxy formation predicted much larger star-formation efficiencies; over the past two decades it has become clear that this discrepancy is likely resolved by *feedback* processes that prevent the over-cooling of gas in dark matter halos (e.g., [381]). However, the exact mechanism(s) and even the basic energetics of these feedback processes remain poorly constrained. On the scale of galaxy groups and clusters, the most important source of feedback—i.e., energy and/or momentum injected into the intragroup/intracluster medium (ICM)—is expected to be that due to active galactic nuclei (AGN), supermassive black holes whose accretion disks drive powerful winds and jets of radiation into their surroundings.[11] At lower mass scales (e.g., Milky-Way-sized halos), feedback due to supernovae and stellar winds may play the dominant role in injecting feedback energy into the circumgalactic medium (CGM). This energetic feedback profoundly alters the thermodynamic structure of the ICM and CGM, heating the gas (thereby preventing star formation) and driving it to large halo-centric radii, sometimes entirely ejecting it from the halo. Such processes are likely responsible for the "missing baryons" problem, i.e., the empirical fact that low-redshift galaxies (such as the Milky Way) have a baryon deficit relative to the cosmological abundance determined from the CMB and BBN [382]. Moreover, this re-distribution of the gas leads to non-negligible changes in the dark matter distribution on scales below ≈ 10 Mpc, thus altering the matter power spectrum. The amplitude of this effect is the largest source of theoretical systematic uncertainty in cosmological constraints derived from ongoing and upcoming weak-lensing surveys (e.g., [383]). Thus, constraining the properties of AGN and supernova feedback is essential not just for understanding galaxy formation, but also for enabling next-generation constraints on dark energy and neutrino physics. Beyond feedback, the role of non-thermal pressure support sourced by gas bulk motions and turbulence in stabilizing the ICM and intragroup medium must be precisely determined in order to calibrate biases in hydrostatic-equilibrium-based estimates of cluster masses (e.g., [384, 385, 386]); however, the amplitude of this effect is currently better understood in hydrodynamical simulations than that of AGN feedback (e.g., [387, 388, 389]), and thus we focus on the latter here.

The CMB offers multiple powerful tools with which to constrain feedback processes and non-thermal pressure support in galaxies, groups, and clusters. The tSZ and kSZ effects, which are sourced by the Thomson-scattering of CMB photons off free electrons, directly probe the electron thermal pressure and momentum, respectively. Given external knowledge of the peculiar velocity field (e.g., from galaxy redshift surveys), the

[11] At high redshift ($z \gtrsim 2$), other sources of feedback (e.g., from star formation) may be of similar importance in groups and proto-clusters.

kSZ signal is a measure of the electron density. Both the tSZ and kSZ signals are redshift-independent, a unique property that is shared by few probes in observational astrophysics. The tSZ signal allows the thermal pressure of ionized gas to be measured over a wider range of halo masses, redshifts, and halo-centric radii than any other probe. The kSZ signal is essentially the only observational tool that can directly measure the ionized gas distribution with few assumptions over a wide range of halo masses, redshifts, and halo-centric radii. Moreover, the small-scale properties of both signals are strong probes of feedback. Qualitatively, AGN and supernova feedback tends to flatten the gas pressure and density profiles of halos, while decreasing the integrated pressure and density content within the virial radius of lower-mass objects (due to the ejection of gas from these shallower potential wells, in comparison to the deeper wells of larger halos). However, the details of these predictions, including their mass, redshift, and radial dependence, depend strongly on the exact feedback model and implementation. In most simulations, the relevant physics is "sub-grid"; thus, it is essential to directly measure these quantities in order to correctly calibrate the energetics of these processes.

Here, we demonstrate explicitly how CMB-S4 will achieve this goal. We focus on extracting the tSZ and kSZ signals of halos of various masses and redshifts via cross-correlations of the deep and wide CMB-S4 LAT survey with galaxy catalogs from the DESI, Baryon Oscillation Spectroscopic Survey (BOSS), and Sloan Digital Sky Survey (SDSS) spectroscopic surveys (LSST and other photometric surveys will also provide useful catalogs for such measurements) and cluster samples from the CMB-S4 tSZ-selected catalog (the *eROSITA* X-ray-selected catalog will also be useful in this context). We closely follow the methodology of Ref. [390] to forecast constraints on the stacked electron-density and pressure profiles of these halo samples. We consider four example sets of halos, with numbers drawn from DESI [347], BOSS/SDSS [391], or the CMB-S4 tSZ cluster catalog:

- low-redshift BOSS/SDSS luminous red galaxies (LRGs), $z = 0.2$, $M_{200c} = 10^{13}\,\mathrm{M}_\odot$, $N = 2.5 \times 10^5$;
- high-redshift DESI LRGs, $z = 1$, $M_{200c} = 10^{13}\,\mathrm{M}_\odot$, $N = 2.5 \times 10^5$;
- low-redshift CMB-S4 clusters, $z = 0.2$, $M_{200c} = 10^{14}\,\mathrm{M}_\odot$, $N = 1.5 \times 10^3$;
- high-redshift CMB-S4 clusters, $z = 1$, $M_{200c} = 10^{14}\,\mathrm{M}_\odot$, $N = 1.1 \times 10^3$.

In all cases, we choose narrow mass and redshift bins: $\Delta \log_{10}(M_{200c}) = 0.1$ and $\Delta z = 0.1$. The LRG samples from these optical surveys cover the entire window $0.2 < z < 1$, so stacked measurements similar to those shown here can be performed over this entire redshift range. Samples of other galaxy types (e.g., emission-line galaxies) will extend to even higher redshift, enabling similar analyses. The CMB-S4 cluster counts assumed here are drawn from Fig. 25, and will enable galaxy cluster studies from $0.1 < z < 2$. Halo masses inferred from CMB-S4 CMB lensing data (and LSST weak lensing at low-z) will be essential in this work, relating the observed baryonic profiles to the underlying matter-density field.

We apply the component-separated CMB temperature (for kSZ) and Compton-y (for tSZ) noise curves described in the forecasting methodology appendix to a stacked aperture photometry estimator to obtain error bars on the projected gas density (kSZ) and projected thermal gas pressure (tSZ) profiles of the halos. Note that we use the "velocity-reconstruction" kSZ estimator here, which uses spectroscopic redshift information to weight the CMB map in a manner that is highly robust to foreground contamination [392, 393]. Our kSZ forecasts assume that the noise in the electron-density profiles is dominated by the noise (instrumental and foreground) from the CMB data rather than noise in the velocity reconstruction; an approximate estimate indicates $\approx 10\%$ residual noise in the velocity reconstruction using DESI. Future simulation work will be necessary to precisely calibrate this effect.

The electron-pressure and density-profile error bars calculated using the methodology described above are contrasted with theoretical predictions extracted from six cosmological hydrodynamics simulations (for more

details on the simulations, see Ref. [394]): BAHAMAS (fiducial, "high-AGN," and "low-AGN" models) [395], simulations of Refs. [396, 397], EAGLE [398], and IllustrisTNG-300 [399, 400, 401]. We rescale all electron-density and pressure profiles to the same background cosmological parameter values ($\Omega_{\rm b} = 0.04898$, $\Omega_{\rm m} = 0.3111$, $h = 0.6766$ [125]), so that only the astrophysical model differences are reflected in the forecasts. These simulations all differ in significant ways (even at the level of using grid- or particle-based codes), particularly in their implementations of sub-grid models for AGN and stellar feedback. As a fiducial model, we simply take the mean of the predictions from all six simulations for each observable. We also perform a smooth extrapolation of the simulation predictions to large radii (beyond $2r_{200c}$, within which the one-halo term dominates), which is necessary for the line-of-sight projection calculations. However, the extrapolation is not significant, since we assume that the virial shock leads to a steep decline in the profiles at $2.5r_{200c}$.

The results of this analysis are shown in Figs. 21 and 22. Each figure corresponds to a different choice of halo mass and redshift, with the left panel showing the cumulative electron-density profile and the right panel showing the cumulative electron thermal-pressure profile (i.e., the cumulative thermal energy in electrons). Here, "cumulative" means "integrated within an aperture," where the angular size of the aperture in arcminutes is given on the top axis of each figure. The profiles asymptote to constant values as the full electron content or thermal energy content of the halo is enclosed. The electron-density profiles are shown in terms of τ, the Thomson scattering optical depth, while the electron pressure profiles are shown in terms of Compton-y, the line-of-sight integral of the electron pressure. The figures also show the forecast signal-to-noise ratio in each case, which range from ≈ 10 to greater than 100. All of the profile forecasts and error bars are convolved to an effective beam of FWHM = 1.4 arcmin (the CMB-S4 LAT resolution at 145 GHz). The figures also show error bars for the baseline configuration of the Simons Observatory (SO) [47], including the effect of the smaller number of clusters for the $M_{200c} = 10^{14}\,{\rm M}_\odot$ halos (6–7 times fewer clusters for these cases).

It is evident from the figures that the galaxy-formation models considered here can be distinguished at high significance with CMB-S4. Particularly important in this regard is the high angular resolution of the CMB-S4 LAT, which permits access to the inner regions of the halos at low-z and is roughly matched to the virial scale at high-z. No other astrophysical observables are sensitive to these thermodynamic properties of the gas over such large ranges in mass, redshift, and halo-centric radius. X-ray observations are limited at large cluster-centric radii, at low halo masses, and at high redshifts. However, measurements with *eROSITA* will be strongly complementary to those from CMB-S4; the combination of the two facilities will enable gas pressure and density profiles to be measured from the core to the outskirts of galaxy groups and clusters. Absorption line studies (e.g., with the Cosmic Origins Spectrograph on the *Hubble Space Telescope*) are limited to comparatively small samples of halos at low mass and low redshifts; however, they are potentially complementary to CMB-S4 measurements on stacked samples of galaxies at lower masses than considered in Figs. 21 and 22, where galaxy-formation models yield even larger differences in their predictions than seen in the figures.

The profile-based constraints shown here are only a small fraction of the total information content in the CMB-S4 dataset relevant to galaxy formation. CMB-S4 will yield tight constraints on the integrated Compton-y and τ signals as a function of halo mass and redshift ("scaling relations"). The slopes of these relations are highly sensitive to feedback models [402, 403, 404]. An optimal analysis will simultaneously incorporate constraints from the spatial distribution (profiles) and mass- and redshift-dependences of these signals. As an illustration of the constraining power of CMB-S4 in this regard, Fig. 23 shows forecasted constraints on the integrated Compton-y signal as a function of halo mass, derived from the combination of CMB-S4 data with the DESI bright galaxy sample. The plot shows the fractional constraint on the deviation of the Y-M relation from a fiducial $M^{1.79}$ power-law model. The constraints span the range of halo masses from Milky-Way-sized galaxies to massive clusters, with sub-percent constraints near a pivot halo mass of

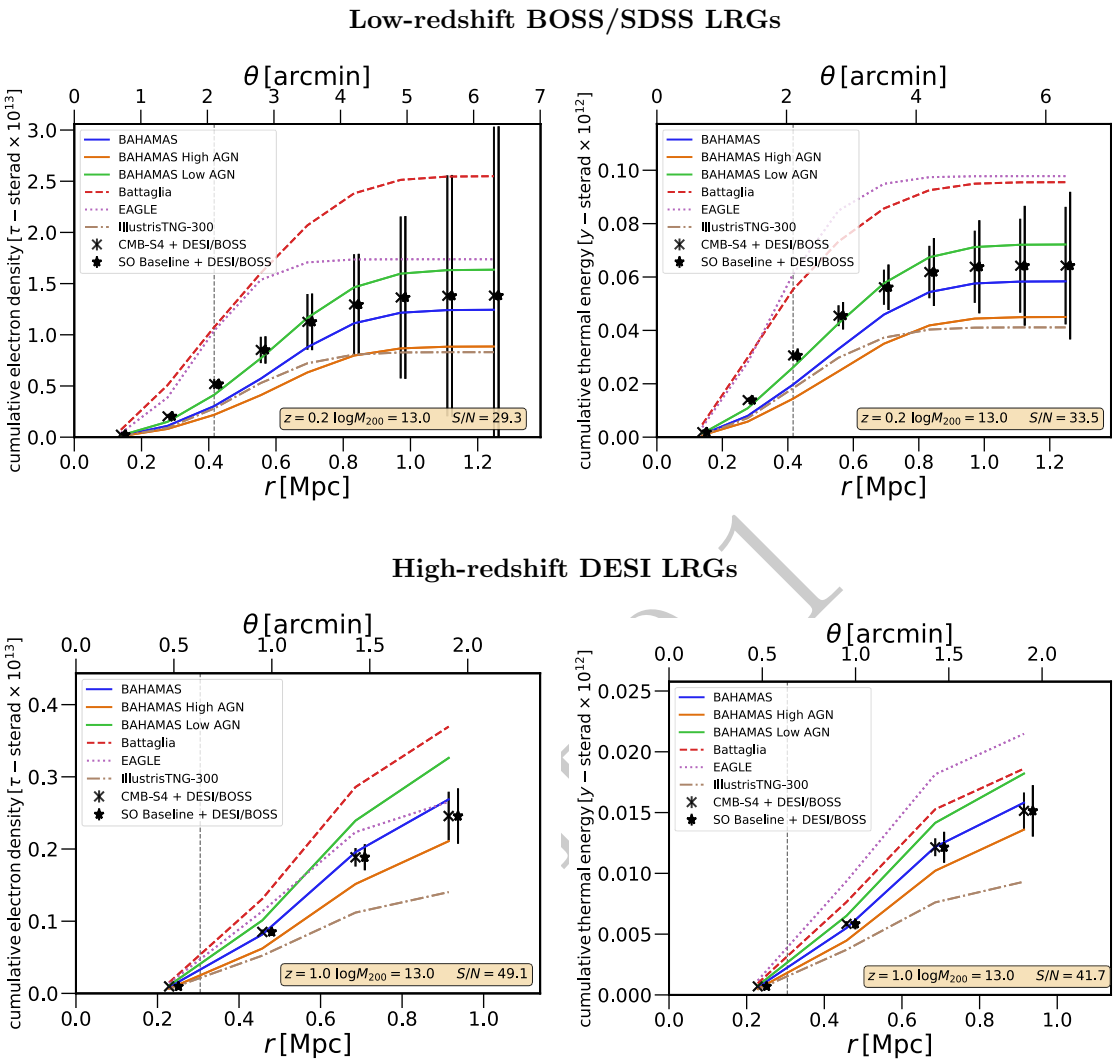

Figure 21: CMB-S4 constraints on the cumulative electron-density (left) and thermal-energy (right) profiles will distinguish between feedback models. Top row: Stacking $N = 2.5 \times 10^5$ BOSS and SDSS LRG halos of average mass $M_{200c} = 10^{13}\,\mathrm{M}_\odot$ at $z = 0.2$. The left panel is extracted from the kSZ signal and the right panel from the tSZ signal. The lines come from density and pressure profiles around such halos measured in six cosmological hydrodynamics simulations: BAHAMAS [395] (fiducial blue, "high-AGN" orange, "low-AGN" green); Battaglia et al. [396, 397] (red); EAGLE [398] (magenta); and IllustrisTNG-300 [399, 400, 401] (brown). The data points average the predictions, and show error bars determined via stacked aperture photometry applied to component-separated maps from CMB-S4 LAT and *Planck* data (or SO and *Planck* data). The dashed vertical lines denotes r_{200c}. The insets give the CMB-S4 forecast signal-to-noise ratio. The error bars are highly correlated due to the photometry method, but the models can nonetheless be distinguished at high significance. Bottom row: The same, inferred by stacking $N = 2.5 \times 10^5$ DESI LRG halos of average mass $M_{200c} = 10^{13}\,\mathrm{M}_\odot$ at $z = 1$. We emphasize that ionized gas properties in the low-mass, high-redshift regime shown in the bottom row cannot be easily measured with any other astrophysical probe.

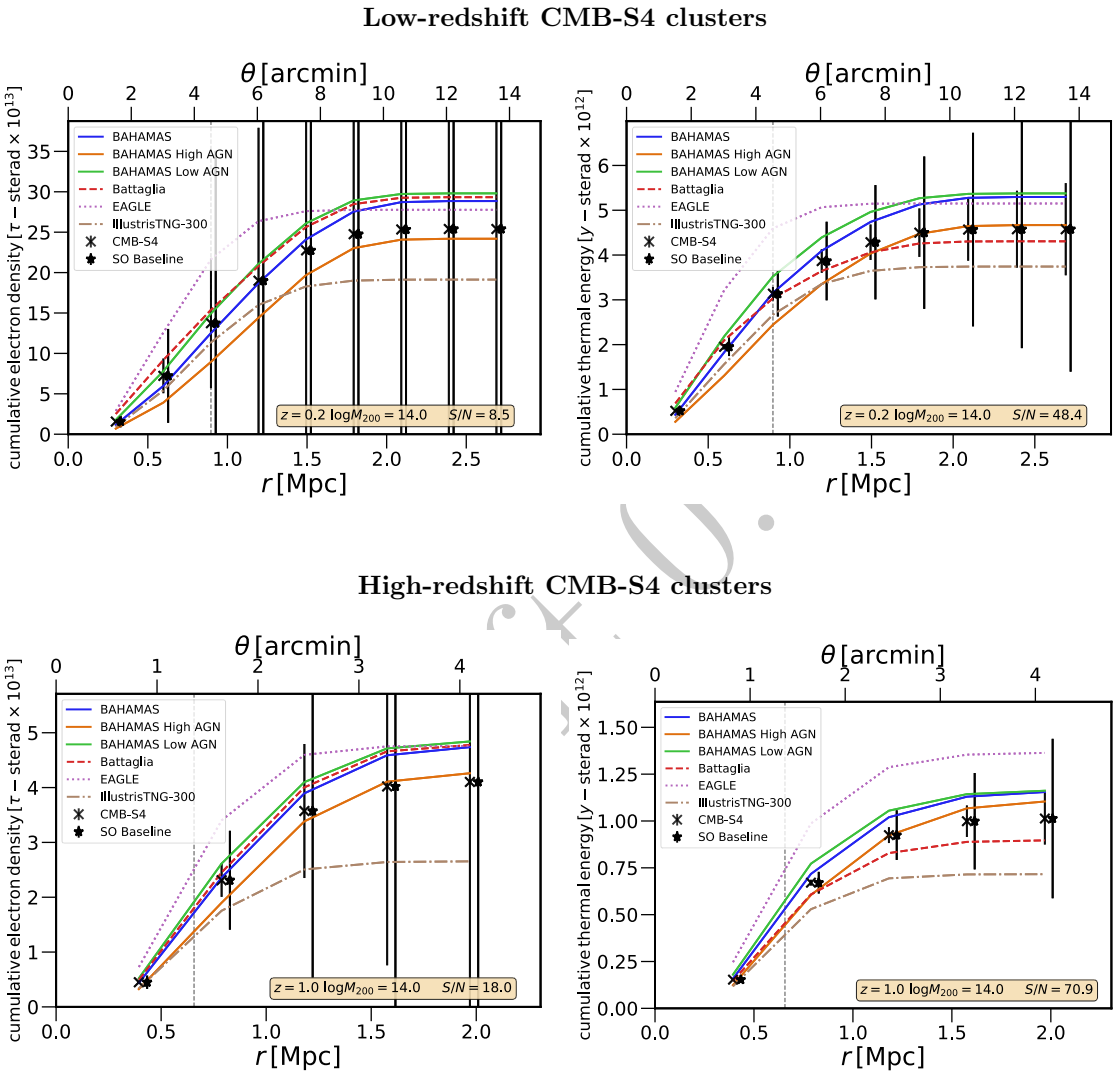

Figure 22: Top: CMB-S4 constraints on the cumulative electron-density (left) and cumulative thermal-energy (right) profiles inferred by stacking $N = 1.5 \times 10^3$ CMB-S4 clusters of average mass $M_{200c} = 10^{14}\,\mathrm{M}_\odot$ at $z = 0.2$. Bottom: The same inferred by stacking $N = 1.1 \times 10^3$ CMB-S4 clusters of average mass $M_{200c} = 10^{14}\,\mathrm{M}_\odot$ at $z = 1$. The panels, curves, and data points with error bars are analogous to those shown in Fig. 21. As in the previous figure, the signals are detected at high significance, and the galaxy-formation models can be distinguished. X-ray constraints at small radii will be complementary to those shown here.

$10^{14}\,\mathrm{M}_\odot$. These improve over current consraints by more than an order of magnitude; at Milky Way mass scales, no constraints currently exist (e.g., [404]).

Further information can be extracted by cross-correlating the CMB-S4 kSZ and tSZ data with quasars, different galaxy types (e.g., red or blue), weak-lensing maps, or filament catalogs. In the kSZ case, some of these cross-correlations will rely on a different estimator than that used here, in which the multifrequency CMB-S4 data are employed to extract the kSZ effect on small scales via component separation, filtering, and squaring of the map; forecasts indicate $S/N \approx$ few hundred for CMB-S4 in combination with LSST or *SPHEREx* using this method [405, 406]. In addition, the large-scale (two-halo) regime of the tSZ signal contains additional unique information about the evolution of the bias-weighted average thermal electron pressure of the Universe [407]. Finally, CMB-S4 will make the first detection of the polarized SZ effect [408, 409], a significant milestone in the eventual use of this signal as an astrophysical and cosmological probe. Overall, the forecasts presented here are only a first step toward exploring the rich astrophysics of galaxy formation accessible with CMB-S4.

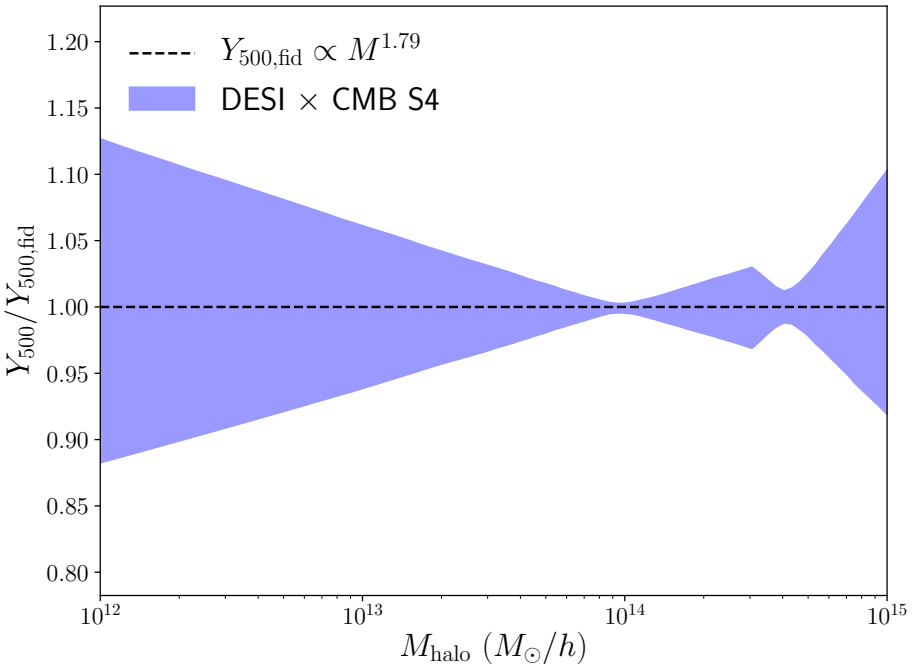

Figure 23: Fractional constraints on the integrated pressure versus halo mass relation from a joint analysis of CMB-S4 and DESI data.

1.5.2.2 Patchy reionization

The patchiness of reionization leaves its imprint on the CMB through the kSZ effect, which refers to blackbody temperature fluctuations induced by a combination of coherent bulk flows on larges scales and variations in the electron density on small scales. These "patchy kSZ" anisotropies have only recently been used to place constraints on the duration of reionization [410, 411, 412, 413]. While incremental gains in precision are expected from experiments that are underway or begin built (e.g., [414, 47]), CMB-S4 will provide definitive reionization constraints from the high-ℓ CMB, due to its much higher sensitivity. The patchy nature of

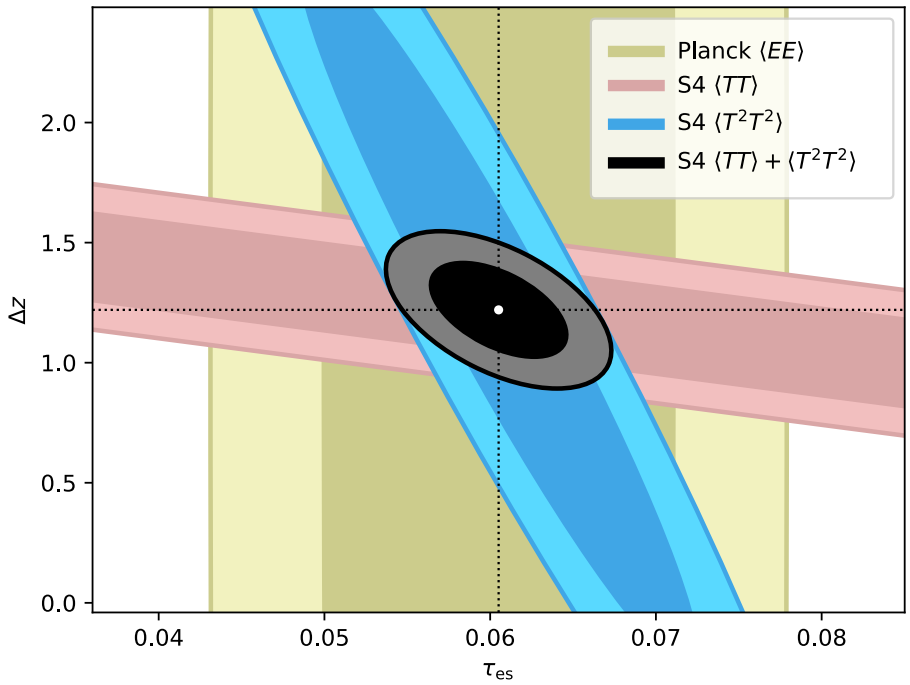

Figure 24: CMB-S4 constraints on the optical depth and duration of reionization in a joint analysis using the kSZ power spectrum and four-point function.

reionization also generates polarization fluctuations (e.g., [415, 416]). Recent work shows this signal may be detectable by CMB-S4 through the B-mode power at $\ell \approx 50$–500 or by explicit reconstruction of the optical depth at the map level [417]. Additionally, it is possible to correlate these patchy polarization anisotropies induced by patchy reionization with other tracers of large scale scale structure such as the cosmic infrared background and CMB lensing [418, 419].

Here we highlight the power of CMB-S4 through the patchy kSZ effect with forecasts based on simulations for which the predicted shape and amplitude of the kSZ power spectrum respond naturally to the variation of unknown physical parameters over their possible values. The simulation techniques are described in Refs. [420] and [421]. The spectra are simulated at discrete "step sizes" as two parameters of the underlying model are varied away from their fiducial values: the ionization efficiency (or number of atoms ionized per atom in halos above the minimum mass), ζ; and the mean free path of ionizing photons, $\lambda_{\rm mfp}$. The reionization history for each of the simulations is used to determine the Thomson scattering optical depth, $\tau_{\rm es}$, and the duration of reionization, $\Delta z \equiv z_{75} - z_{25}$, the redshift interval over which the volume filling factor of ionized regions evolved from 25 to 75 per cent. We then calculated derivatives of the power spectrum with respect to these parameters, $\tau_{\rm es}$ and Δz, by finite differencing. We impose a Gaussian prior on the late-time "homogeneous" kSZ contribution. This term is already known at the roughly 10% level, accounting for astrophysical and cosmological uncertainties [422, 423], and will be known better than this in the CMB-S4 era (e.g., by using the measurements described in the previous subsection). Additional uncertainty due to marginalization over non-kSZ foregrounds is incorporated with the "Deproj-0" (standard ILC) CMB-S4 LAT + *Planck* noise curves for the reference CMB-S4 configuration.

The results are shown in the right-hand panel of Fig. 24, where we have also included the kSZ four-point function, which provides additional information to separate early- and late-time kSZ contributions [424], by using the same excursion set simulated kSZ maps described above. The power spectrum is sensitive to the duration of reionization, but this is highly degenerate with the optical depth. However, the prior knowledge of the optical depth from *Planck* large-scale EE power spectrum measurements, which is included in our analysis via a prior $\sigma(\tau) = 7 \times 10^{-3}$, breaks this degeneracy. Thus we find $\sigma(\Delta z) \approx 0.14$ from the kSZ power spectrum. The four-point function, when combined with the *Planck* EE constraint on the optical depth, performs worse on the duration than the power spectrum, as seen in the figure. However, when combining the power spectrum and four-point constraints, we find that the τ measurement from CMB-S4 alone *improves on the current* Planck *EE-based* τ *constraint by a factor of 2–3*, with $\sigma(\tau) \approx 2,5 \times 10^{-3}$. Note that this estimate marginalizes over an unknown contribution from the low-redshift kSZ signal (albeit with a roughly 10% prior) and also assumes we have no knowledge of other foregrounds. It is thus possible that tighter constraints will result from improved measurements of low-redshift kSZ signals, as well as improved measurements of high-ℓ foregrounds.

Finally, we note that alternative scenarios, such as those in which rare quasars or very high-redshift sources play a significant role, are described by models with different parameters than we have assumed here. Thus, our forecasts by definition are uncertain and depend on the assumed model and even the fiducial parameters within that model. The high precision of the model parameter constraints we have forecasted in the standard UV-dominated scenario implies that we will be able to rule out or confirm, with high significance, other more exotic reionization scenarios such as those that include early X-ray binaries, population III sources, or rare quasars. This will especially be the case when CMB-S4 is combined with external data sets such as 21-cm and Lyman-α emitter surveys, together with independent CMB-based constraints on the optical depth from the large-scale EE power spectrum. Such discoveries are an inevitable byproduct of probing the high-precision, high-redshift frontier with CMB-S4.

1.5.2.3 Galaxy clusters

Clusters of galaxies, the largest gravitationally bound systems in the Universe, are powerful probes of both cosmology and astrophysics. The deep and wide millimeter-wave CMB-S4 sky survey will enable the identification of over 70,000 such systems at high significance ($> 5\sigma$) via measurements of the thermal Sunyaev-Zeldovich (tSZ) effect [425]. Cluster detection and characterization via the tSZ effect is highly complementary to techniques at other wavelengths (e.g., [426, 427]) because tSZ observables provide both low-scatter mass proxies and a detection method that is independent of cluster distance (since it is a spectral distortion of the CMB). As shown in Fig. 25, CMB-S4 will discover *an order of magnitude more high redshift systems* ($z > 1.5$) than ongoing and upcoming CMB experiments [428, 429, 47]. CMB-S4's deep multi-band observations will enable separation of the tSZ signal from contaminating radio and infrared emission from cluster members (Sect. 1.5.1), which will be particularly important for low-mass, high-redshift clusters.

This large and well-characterized cluster sample, in conjunction with data from LSST, will significantly improve constraints on cosmological models (Sect. 1.4.3, [430]) and, when further combined with data from the next generation ESA X-ray mission *Athena* (as well as other proposed missions, including NASA's *Lynx* and *Origins Space Telescope*), will also offer an unprecedented opportunity to understand the assembly and evolution of the massive galaxies that reside in these systems, as well as the effects of astrophysical feedback on the intracluster medium (Sect. 1.5.2).

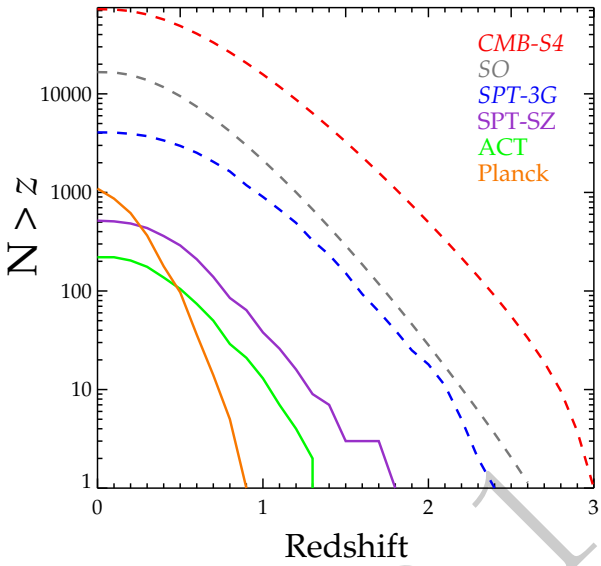

Figure 25: Cumulative number of clusters above a fixed redshift for published (solid [431, 432, 433]), and upcoming (dashed [429, 47]) CMB cluster samples. CMB-S4 will discover an order of magnitude more of the highest-redshift ($z > 1.5$) clusters than previous surveys.

1.5.2.4 Dusty star-forming galaxies

The unique combination of resolution, depth, and area covered make CMB-S4 ideal for constructing catalogs of extragalactic mm-wave sources. A remarkable and largely unanticipated result (but see, e.g., [434]) from the previous generation of CMB surveys was the discovery of large numbers of strongly lensed dusty star-forming galaxies (DSFGs, [435]), the massive galaxies that make up the high-redshift ($z > 1$) component of the cosmic infrared background. Because these objects are selected by their dust emission, which is re-radiated UV emission from intense star formation, this population of objects is complementary to samples of galaxies found from their stellar light at optical and near-IR wavelengths (rest-frame UV at high redshift) with instruments such as *Hubble* and *JWST*. The DSFG sample from the first generation South Pole Telescope (SPT) survey includes the most distant and massive halo known within the epoch of reionization (z=6.9; [436, 437]), and a galaxy cluster forming just 1.5 Gyr after the big bang [438]. Most of these sources are gravitationally lensed by intervening galaxies; this magnification enables them to be studied in detail with ALMA [439, 440], providing fast redshift determinations and increased effective spatial resolution. These first massive galaxies mark the sites of the largest overdensities in the cosmic web [437] and trace the formation of the dusty, molecular interstellar medium from the metal-poor and chemically simple raw materials present in the first galaxies. With ALMA, the lensed systems are also useful as probes of the dark-matter distribution in the foreground lensing halos [e.g., 441]. In addition to ALMA, these sources will be excellent targets to followup with *JWST*, and the catalog will also have strong synergies with surveys such as those carried out with LSST, *WFIRST*, SKA, and *eROSITA*.

The sample of DSFGs from the CMB-S4 survey is expected to contain over 100,000 sources, of which around 10,000 should be strongly lensed (see Fig. 26). Based on source counts and redshift distributions measured with SPT-SZ data [442, 440], we expect thousands of these sources to lie at $z > 7$, more than 100 to be

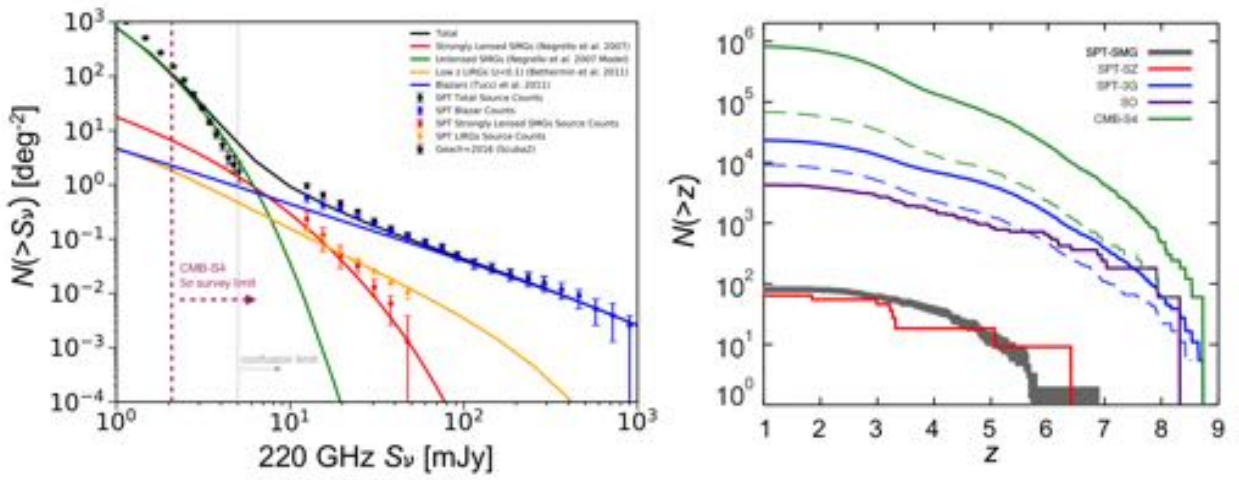

Figure 26: Left: Source density in the mm sky from SPT-SZ, SCUBA-2, and various galaxy-evolution models. With the expected 220-GHz detection threshold shown by the short-dashed line, CMB-S4 will detect over 100,000 extragalactic sources, including more than 10,000 strongly-lensed galaxies and thousands of galaxies at $z > 7$. Right: Expected number of DSFGs in the CMB-S4 survey. The *gray* line shows the measured distribution of DSFGs from the SPT-SZ survey [440], while the *red* line shown the predicted distribution from the phenomenological model of Ref. [442]. Also shown are the predicted numbers DSFGs that will be detected by the SO (*purple*), SPT-3G (*blue*), and CMB-S4 (*green*). The dashed lines show the number of sources detected above the confusion limit for a 6-m (*green dashed line*) and 10-m (*blue dashed line*) telescope.

at $z > 8$, and around 1,000 to be associated with high-redshift protoclusters (Fig. 26). The beamsize of CMB-S4 is well-matched to the expected scales of protocluster regions, building a catalogue far superior to the prelimary study of peaks in the CIB made possible using *Planck*'s all-sky survey [443]. The CMB-S4 high-redshift sources will open up a new window onto massive galaxy formation in the epoch of reionization, provide an important complement to the LSST and *WFIRST* surveys, and be prime targets for followup with ALMA and *JWST*. With the unique resource of the CMB-S4 dusty source catalog, we can directly observe the onset of dust production in the Universe, identify the first massive protoclusters of galaxies that represent the predecessors of the SZ cluster sample, and provide a well-understood target list for the high-redshift ALMA user community to explore galaxy formation.

An intriguing possibility is that CMB-S4 might be the first wide survey that can select both proto-clusters and genuine clusters of galaxies, using their different spectral signatures. Statistical samples of both kinds of source, and those intermediate between them, have never been available before.

Finally, the deep, high-resolution, multi-band data from CMB-S4 will be a rich source of "serendipitous" science, examples of which have already been demonstrated with the Atacama Cosmology Telescope (ACT), *Planck*, and SPT (e.g., strongly lensed DSFGs and mm transients).

1.5.2.5 Radio sources

The broad spectral coverage of CMB-S4 will also provide high signal-to-noise ratio intensity and polarization measurements of radio sources. Applying the model of Tucci et al. [444] with a confusion limit of 1 mJy at 90 GHz, over 100,000 AGN are expected to be detected at $> 5\sigma$ in the deep and wide survey field. An additional 5,000 sources will also be detected above 5σ in polarization [445]. This source sample, selected from the highly-uniform CMB-S4 data set covering 70% of the sky, will be an order of magnitude larger than that from upcoming CMB surveys (e.g., Ref. [47]), and will be a valuable tool for statistical studies of AGN populations ([446, 447, 448, 449, 450]). The broad spectral coverage will enable measurements of source SEDs and—for the brightest polarized sources—Faraday rotation measures. These data will also be highly complementary to higher-resolution observations at other wavelengths (e.g., VLA/VLASS, ASKAP/EMU, SKA, and *eROSITA*). In the latter case, CMB-S4 data will provide an excellent opportunity both via individual and stacked source measurements, to characterize the radio/sub-millimeter properties of over 1 million AGN to be detected in the *eROSITA* X-ray survey [451].

While the majority of radio sources detected by CMB-S4 will be flat or falling-spectrum blazars, new and rare categories of sources may emerge from the large source sample. As an example of such discovery space, Ref. [452] recently reported a small intriguing sample of low-z AGN with rising high-frequency spectra that may contain cold intrinsic dust; such AGN—which will be more easily identified with the significantly higher resolution and deeper CMB-S4 data—could provide a view of the transition stage between the star-formation and AGN phases of such galaxies. CMB-S4 will similarly provide crucial higher-frequency data for source populations detected at other wavelengths. One interesting case will be the characterization of narrow-line Seyfert 1 (NLS1) galaxies for which there is limited high-frequency data (see e.g., Ref. [453]). These galaxies are assumed to be young AGN; however, based on 37-GHz observations, their detection rate is much higher than assumed by many models [453, 454]. Observations also indicate that—contrary to expectations—relativistic jets can be generated in such sources, regardless of their radio-loudness classification based on low-frequency data. A new catalog of southern NLS1 sources has recently been released [455] for which higher-frequency data are needed. CMB-S4 will be able to provide SED determinations, as well as information on the time variability of the sources (and many other well-detected galaxies, since CMB-S4 will be a powerful time-domain survey of the mm-wave sky). By combining observations of the NLS1s with data on other types of young AGN (such as compact steep-spectrum sources, GHz-peaked spectrum sources, high-frequency peakers, and compact symmetric objects), CMB-S4 will enable studies of the launching of relativistic jets, as well as the evolutionary paths that young AGN take on their way to becoming fully-evolved, powerful radio sources.

1.5.3 The Milky Way Galaxy

Galactic polarization: One area in Galaxy-scale science for which the deep polarization data from CMB-S4 will be particularly impactful is in the characterization of the interstellar medium (ISM), the polarization of which is a particularly pernicious foreground in the search for primordial B modes (Sect. 1.3.1). The ISM is known to be highly turbulent, compressible, and magnetized and while phenomenological models provide some insight into how foreground turbulence affects the dust polarization signal, they can not yet convincingly explain a number of current observations, such as the ratio of E modes to B modes. Excitingly, synthetic polarization maps from MHD turbulence simulations coupled with CMB observations are now beginning to shed light on the properties of the turbulent ISM in our galaxy.

The E-mode and B-mode power depend on the detailed properties of the turbulent density fluctuations in the ISM and it is not possible to characterize these fluctuations without knowledge of the sonic/Alfvénic

Mach numbers in the ISM. To extract this information, CMB observations are coupled with other diffuse ISM tracers (e.g., 21 cm or H α) to obtain velocity statistics. Current results are limited by *Planck*'s sensitivity and resolution, but with future CMB-S4 polarization data and velocity information we will finally be able to place tight constraints on the parameters surrounding cosmic-ray acceleration, star formation, and diffuse ISM structure formation.

Another outstanding mystery, in the area of the star formation, is whether the magnetic fields that thread molecular clouds are strong enough to inhibit movement of gas across magnetic field lines, thereby reducing the efficiency with which stars form. By studying the linearly-polarized radiation from dust grains, which tend to align with respect to their local magnetic field [456], CMB-S4 will create highly-detailed (<1-pc resolution) maps of the magnetic field morphology for nearly a thousand molecular clouds. Using these polarization maps we will measure the disorder in the magnetic field direction [457, 458, 459, 460], the degree of polarization [461], and determine whether there is alignment between the orientation of the magnetic field and cloud structure [462]. Applying the same analysis techniques to both the clouds observed with CMB-S4 and "synthetic observations" of numerical simulations, CMB-S4 can constrain the magnetization levels within molecular clouds. We can then compare the magnetization to the star-formation efficiency measured with *Herschel*, *Spitzer*, and the *Wide-field Infrared Survey Explorer (WISE)*. The large number of molecular clouds that can be mapped by CMB-S4 is crucial, since dust polarization is only sensitive to the magnetic field component parallel to the sky and so large numbers of molecular clouds are needed to correct for this degeneracy [463]. The results from CMB-S4 will place strong constraints on the dynamical importance of magnetic fields in different stages of the star-formation process.

Galactic intensity: Deep, multi-frequency maps over about half of the sky will be a useful resource for tracing the census of star-formation, including seldom-studied regions away from the Galactic plane. There is also the potential for adding information on particluar classes of star (e.g., those with disks). Additionally, an exciting new possibility enabled by these CMB-S4 data is the search for variable Galactic sources, which we discuss in the next section.

1.6 The time-variable millimeter-wave sky

The fourth and final science theme relates to time-variable sources.

CMB-S4 will provide a unique platform to conduct a wide-field time-domain survey in the millimeter band, covering over half of the sky to few-mJy depths every two days. In this waveband, the time-variable sky is largely unexplored, with the exception of a shallow survey by *Planck*, surveys of the Galactic Plane (such as with the JCMT), targeted measurements of a few individual sources, and a single survey by SPTpol [10]; this is largely the result of limited observing time and fields of view for mm-band instruments (e.g., ALMA), which tend to focus on high-resolution observations of known objects. Despite this, a wide variety of sources are either known or believed to have particularly interesting time-variability in bands observed by CMB-S4. Expected sources include tidal disruption events, nearby supernovae, X-ray binaries, and classical novae. Particularly good candidates are γ-ray bursts and active galaxies, such as the time-variable blazar that was identified as a possible source of high energy neutrinos. The combination of high sensitivity and wide area for CMB-S4 will open a new window for time domain astronomy and multi-messenger astrophysics.

1.6.1 Gamma-ray bursts

Gamma-ray bursts (GRBs) are one of the primary time-domain science targets for CMB-S4. The spectrum of GRB afterglows is well-described by a self-absorbed synchrotron process, with a broad emission peak from approximately 100 GHz to 1 THz [464], with emission lasting on the order of one week. The existence of so-called orphan afterglows from bursts without detected prompt γ-ray emission—either because of the γ-ray instrument field of view, misalignment of the jet with Earth, or absorption of the primary γ-ray emission—is a generic prediction of GRB models, but none have ever been detected, despite a number of possible candidates (e.g., Refs. [465, 466]). The main obstacle to their detection has been that, at both short and long wavelengths, the sources are very dim and, at the frequencies where they are bright enough to be detectable (for example, in the millimeter band), either few or no blind surveys have been conducted.

CMB-S4's observing strategy and sensitivity are expected to change this picture dramatically, delivering a factor of 2000 improvement on the only previous time-domain millimeter survey [10], which had a candidate detection, and gives an expected 1700 afterglow detections from a population model of on- and off-axis bursts (PSYCHE, [467]) over a 7-year CMB-S4 survey. Other theoretical predictions find that at all times during the survey there should be an ongoing detectable GRB afterglow [468]. Detection of these objects would serve a number of scientific goals:

- confirm measurements of the beaming angle of GRBs from jet breaks and thus the total energy budget for GRBs in the Universe;
- improve modeling of off-axis emission, and connect with gravitational-wave sources;
- constrain the existence of a large population of γ-dark GRB-like objects, which are potential sources of the TeV–PeV diffuse neutrino background observed by IceCube;
- potentially detect afterglows from GRBs made by population-III stars at high-z, during and prior to reionization.

Note that uncertainties in this last item are large, but nevertheless, CMB-S4 will enter the range of required sensitivities [469]. Detection of even one of these would provide a wealth of information about the early Universe, while a non-detection would constrain models of the first generation of star formation.

1.6.2 Fast transients

Fast radio bursts (FRBs) are a striking astrophysical phenomenon of unknown origin. They have been seen serendipitously in radio-frequency observations with Areceibo, the Canadian Hydrogen Intensity Mapping Experiment (CHIME), Green Bank, and Parkes radio telescopes (e.g., Refs. [470, 471, 472]), with around 20 detected to date. Given this event rate and estimates of sky coverage, the full-sky rate of FRBs is roughly 5000 per sky per day, if they are isotropically distributed. They are remarkably bright: the known examples all have a minimum flux density ranging from 0.3 to 2 Jy at frequencies of a few GHz, plus the original "Lorimer burst" with flux of 30 Jy [473]. They also have a very short duration; many last for less than 1 ms, with durations up to 5 ms. Most have no useful polarization information, although a few (such as FRB150807 [474]) have been observed to have linear polarization at various levels.

FRBs are consistent with having random sky locations (with the exception of two repeating sources [475, 476]). They also have dispersion measures ranging from 375 to 1600 $\mathrm{pc\,cm^{-3}}$. This leads to an arrival-time dependence on frequency proportional to ν^{-2}, which is very well measured. Electrons in the Milky Way give a total dispersion measure of around 100 $\mathrm{pc\,cm^{-3}}$, supporting the idea that FRBs are at cosmological distances of order 1 Gpc. Their frequency spectrum is unknown but limited evidence in the 1–2 GHz range suggests consistency with a flat spectrum in S_ν. If these intriguing sources do have a flat spectrum, some will be potentially detectable in microwave-background experiments, with flux densities greater than a few mJy at microwave frequencies. Current TES-based detectors have a sampling time of order 2 ms, meaning that FRBs would generally be visible only in a single time sample if their microwave and radio durations are comparable. A point-source FRB signal would appear to be a single bright microwave burst at a random position in the focal plane with the spatial profile of the experiment's beam shape. If its spectrum is fairly flat, it would also appear in all channels of a multichroic detector simultaneously, and in both linear polarization channels. In the time stream, the burst itself will appear as a spike, with a subsequent decay according to the detector time-constants; this decay behavior distinguishes a sky signal from electronic glitches.

The detection of FRBs at microwave wavelengths would establish their frequency spectrum, while upper limits on their rate would significantly constrain the flux distribution. Either outcome would contribute substantially to understanding these mysterious extragalactic events.

1.6.3 Protostellar variability

Variability studies offer unique insights into the mass-accretion history of protostars. There is a fundamental disconnect between steady-state star-formation models and observed protostars—we know that at least some protostars go through explosive burst events during their evolution and that this may be important for the overall mass assembly (e.g., Ref. [477]). Circumstantial evidence suggests that most, if not all, protostars go through these stages; however, given the rarity of these large bursts, to catch one requires monitoring a huge number of protostars (thousands) over many years. CMB-S4 provides that opportunity.

A survey with the James Clerk Maxwell Telescope [478] has found that about 10% of protostars show low-level accretion variability, over timescales of a year or so [479]. This strongly suggests that we are probing

physical conditions in the inner, planet-forming, disk. In at least one case quasi-periodicity is seen over many years, suggesting a link to long-lived structure (i.e., companions or planets) within the disk. Additionally protostars are expected to be very active and a handful of extremely powerful flares have been observed in the radio [480]. Magnetic fields are believed to play an important role in funneling material from the disk onto the star (the last step for accretion). Detailed measurements of the properties of magnetic reconnection events are required to make significant progress in our understanding of this complex phenomenon. Follow-up spectroscopic studies of flares discovered with CMB-S4 could unveil the astrochemsitry of the time-varying signatures of volatile species and UV and X-ray dissociation, as well as changes in the protoplanetary disk snow-line through evaporation of ices.

Studying protostellar variability in this waveband is a new research area. The examples we give illustrate that there are important physical processes that can be discerned through measurements of variability and transient phenomena within the Milky Way. At millimeter wavelengths, so far only one modest survey (the JCMT Transient Survey) has monitored star-forming regions, and has just begun to produce results. To draw statistically significant conclusions will require a much larger survey, just like CMB-S4 will provide.

1.6.4 Accreting binary systems

Within our Galaxy, accretion in binary systems can lead to strongly time-variable emission. Observations have shown that classical novae could be easily detectable in CMB-S4, with fluxes observed to be hundreds of mJy at mm-wavelengths [481, 482], while flaring events have been observed in X-ray binaries to be tens of mJy [483].

1.6.5 Solar System

CMB-S4 will survey about 70% of the sky approximately every two days. Moving objects, such as asteroids, dwarf planets, or as yet undiscovered bodies such as Planet Nine, can be detected in difference images using their long-wavelength thermal emission. The expected mm-wave Solar System can be seen in Fig. 27. For mm-wave imaging of particular objects, an instrument like ALMA would be far more sensitive; the particular benefit of CMB-S4 will be nearly daily measurements of large numbers of bright objects over several years, along with wide sky coverage for discovery of new or unexpected objects.

Using thermal emission rather than reflected light, mm-wave measurements are less sensitive to albedo effects, and the wavelengths are long enough that molecular absorption and emission is negligible. Furthermore, the fall-off in flux as a function of distance is less severe, with the main effect being the usual $1/d^2$ dependence; optical reflected light gets an additional factor of $1/d^2$ from the distance to the Sun. The temperature of Solar-System objects in equilibrium with solar irradiance scales only as $d^{-1/2}$, while objects with substantial internal heat or radioactive heating would decrease even more slowly.

Asteroids show substantial time variability due to rotation and viewing-angle effects. Using CMB-S4, more than 1000 known asteroids will be detected, with many of these having high enough signal-to-noise ratio to chart the flux as a function of rotational phase. Comparisons with measurements in the optical band, and also the infrared (since many of these objects have been measured as part of the *NEOWISE* project [484]), will yield new insights into the surface properties and geometry of these objects (e.g., Ref. [485]).

Dwarf planets, such as Pluto, will be easily detected, with measurements possible out to roughly 100 AU. Extending further, CMB-S4 will be able to detect any possible planets of Earth radius or larger at about

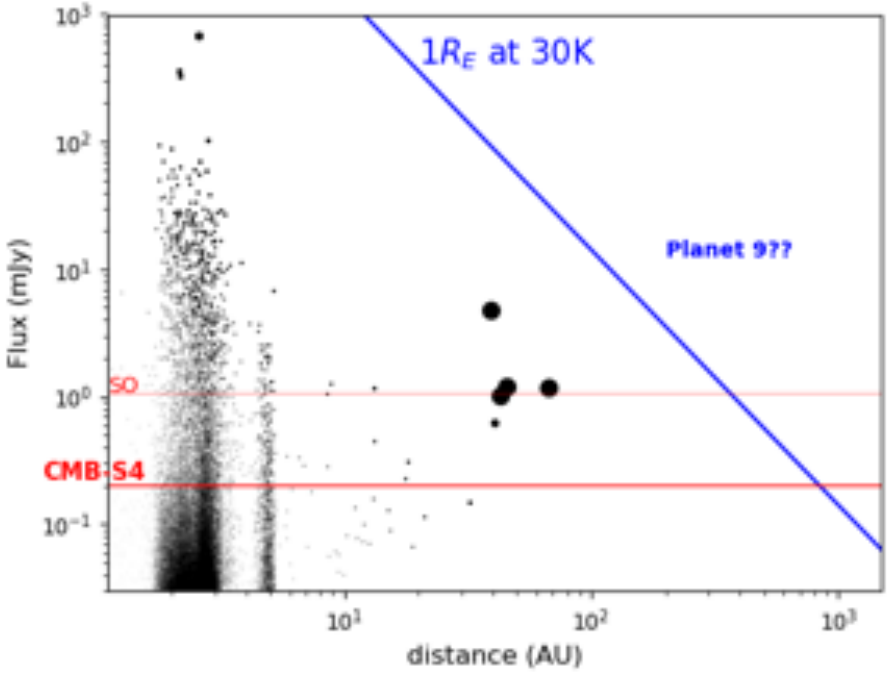

Figure 27: Millimeter-wave Solar System. Red circles show predicted asteroid flux densities at 150 GHz, crosses show estimated flux densities of known dwarf planets at 90, 150, and 220 GHz, and diagonal lines show the flux density of any possible Earth-sized planet in the outer Solar System in the CMB-S4 bands. Planet 9 is estimated to be several Earth masses at a distance of several hundred AU.

1000 AU. The recent excitement about a possible Planet Nine [486] (nominally 5–15 $M_\oplus$ at several hundred AU) has made it clear that there is substantial discovery space for new planets in the outer Solar System. Assuming an Earth-like composition, 1 $M_\oplus$ of rocky material should have an equilbrium temperature of > 30 K just from radiogenic heat. An atmosphere would further enhance the mm-wave flux. The mm-wave-sky monitoring performed by CMB-S4 offers the potential to search for a wide variety of moving objects.

1.6.6 Multi-messenger astrophysics

A wide-area sensitive mm-wave survey can play an important role in multi-messenger astrophysics, in concert with both high-energy neutrino searches and gravitational wave astronomy.

The IceCube neutrino source TXS 0506+056 appeared to be associated with a blazar [487] that is mm-bright. With CMB-S4, this source would have had nearly daily flux measurements over many years, as well as many other similar sources that could be used to characterize the statistics of variability.

The first binary neutron star merger, GW170817, was not visible at mm-wavelengths [11], most likely due to the low density of the environment for that particular event. It is expected that at least some future

events should be in denser environments that will enhance the mm-wave flux [12]. If there is no other detectable emission, CMB-S4 would provide arcminute localization as part of regular survey operations. In addition, the mm-wave light curve can be compared with emission at other wavelengths to better understand gravitational-wave events.

We do not know what fraction of future GW sources will turn out to be optically-obscured, but visible in the millimeter—so it seems wise to have an instrument that is regularly scanning the sky in this waveband. Provided that the GW source is in the southern hemisphere, then it *will* be in the CMB-S4 deep and wide survey field, and observed every few days as a matter of normal survey operations. *This same leveraging of the CMB-S4 wide survey applies to all other future examples of transient source for which astronomers would like rapid follow-up observations.*

2

Science and Measurement Requirements (*Charles Lawrence and John Ruhl*)

2.1 Introduction

The top-level science and measurement requirements for CMB-S4 are written in the Program Level Requirements document (internal project DocDB[1] document: CMBS4-doc-671). For convenience, we copy them here as Sections 2.2-2.4.

This serves as the basis for assessment of the experiment conducted by the DOE and the NSF during the development and operations periods, and it provides the baseline for the determination of the scientific success of the experiment following its operational phase.

2.2 Definition of CMB-S4: Science Goals

CMB-S4 is designed to exploit measurements of the cosmic microwave background (CMB) to dramatically push forward our understanding of the history, evolution, and contents of the Universe. The science enabled by CMB-S4 will cover a vast range of scales in length, time, and energy. CMB-S4 will allow for new insights about the Universe's earliest moments and its fundamental ingredients, the growth of cosmological structure, and the dark energy which drives the current accelerated expansion. It will also open up a new window to study transient astronomical phenomena at millimeter wavelengths and even provide new means by which to study the outer Solar System. The wide range of CMB-S4 science is enabled by an experiment designed to achieve the following four science goals.

GOAL 1: Test models of inflation by measuring or putting upper limits on r, the ratio of tensor fluctuations to scalar fluctuations.

GOAL 2: Determine the role of light relic particles in fundamental physics, and in the structure and evolution of the Universe.

GOAL 3: Measure the emergence of galaxy clusters as we know them today. Quantify the formation and evolution of the clusters and the intracluster medium during this crucial period in galaxy formation.

[1] found at https://docdb.cmb-s4.org/cgi-bin/private/ProcessDocumentAdd

GOAL 4: Explore the millimeter-wave transient sky. Measure the rate of mm-transients for the first time. Use the rate of mm-wave γ-ray bursts to contrain γ-ray-burst mechanisms. Provide mm-wave variability and polarization measurements for stars and active galactic nuclei.

2.3 Science Requirements

Reaching the science goals in §2.2 imposes the following science requirements on CMB-S4, which are numbered in alignment with the science goal, given above, which drives them.

SR1.0: CMB-S4 shall test models of inflation by putting an upper limit on r of $r \leq 0.001$ at 95% confidence if $r = 0$, or by measuring r at a 5σ level if $r > 0.003$.

SR2.0: CMB-S4 shall determine $N_{\rm eff}$ with an uncertainty ≤ 0.06 at the 95% confidence level.

SR3.1: CMB-S4 shall detect at $\geq 5\sigma$ all galaxy clusters at $z \geq 1.5$ with an integrated Compton $Y_{\rm SZ,500} \geq 10^{-12}$ over 50% of the sky.

SR3.2: CMB-S4 shall detect at $\geq 5\sigma$ all galaxy clusters at $z \geq 1.5$ with an integrated Compton $Y_{\rm SZ,500} \geq 5 \times 10^{-13}$ over 2.8% of the sky.

SR4.0: CMB-S4 shall detect γ-ray-burst afterglows brighter than 30 mJy at 93 and 145 GHz.

2.4 Measurement Requirements

In order to satisfy the science requirements in §2.3, CMB-S4 shall meet the following requirements for measurements on the sky, which are numbered in alignment with the science requirement they each support.

MR1.1: CMB-S4 shall measure Q and U over 2.8% of the sky at frequencies of 30, 40, 85, 95, 145, 155, 220 and 270 GHz, with angular resolutions of 72.8, 72.8, 25.5, 22.7, 25.5, 22.7, 13.0, and 13.0 arcminutes, respectively and Q/U-map noise levels (including all sources of noise) $\leq$ 3.5, 4.5, 0.88, 0.78, 1.2, 1.3, 3.5, and 6.0 μK-arcmin, respectively. Maximum noise levels as a function of multipole are given in Figure 28.

MR1.2: CMB-S4 shall measure Q and U over the same 2.8% of the sky at frequencies of 20, 27, 39, 93, 145, 225, and 278 GHz, with angular resolutions of 11.0, 8.4, 5.8, 2.5, 1.6, 1.1, and 1.0 arcminutes, respectively, and Q/U-map noise levels (including all sources of noise) $\leq$ 13.2, 6.5, 4.2, 0.63, 0.59, 1.9, and 4.4 μK-arcmin, respectively. Maximum noise levels as a function of multipole are given in Figure 29.

MR2.0: CMB-S4 shall measure I, Q, and U over 68% of the sky at frequencies of 27, 39, 93, 145, 225, and 278 GHz, with angular resolution of 7.4, 5.1, 2.2, 1.4, 1.0, and 0.9 arcminutes, respectively, with I-map noise levels $\leq$ 21.8, 12.4, 2.0, 2.0, 6.9 , and 16.7 μK-arcmin, respectively, and Q/U-map noise levels of $\leq$ 30.8, 17.6,

2.9, 2.8, 9.8, and 23.6 μK-arcmin, respectively. Maximum noise levels as a function of multipole are given in Figure 30.

MR3.1: CMB-S4 shall measure I over 50% of the sky at frequencies of 27, 39, 93, 145, 225, and 278 GHz, with angular resolution of 7.4, 5.1, 2.2, 1.4, 1.0, and 0.9 arcminutes, respectively, with I-map noise levels $\leq$ 21.8, 12.4, 2.0, 2.0, 6.9 , and 16.7 μK-arcmin, respectively. Maximum noise levels as a function of multipole are given in Figure 30.

MR3.2: CMB-S4 shall measure I over 2.8% of the sky at frequencies of 20, 27, 39, 93, 145, 225, and 278 GHz, with angular resolutions of 11.0, 8.4, 5.8, 2.5, 1.6, 1.1, and 1.0 arcminutes, respectively, and I-map noise levels $\leq$ 9.4, 4.6, 3.0, 0.45, 0.41, 1.3, and 3.1 μK-arcmin, respectively. Maximum noise levels as a function of multipole are given in Figure 29.

MR4.0: During normal operations CMB-S4 shall measure I, Q, and U at 93 and 145 GHz over $\geq$ 25% of the sky daily, with angular resolution $\leq$ 3 arcminutes and noise level $\leq$ 10 mJy/day, and 90% of the time the same $\geq$ 25% of the sky shall be observed for $\geq$ 5 consecutive days.

2.5 Flowdown of requirements

In Appendix A, we show that the preliminary baseline design satisfies the measurement requirements and that the measurement requirements are sufficient to meet the science requirements.

The form of the noise curves appearing in Figures 28, 29, and 30 is

$$N_\ell = \Delta^2 \exp\left(\ell(\ell+1)\frac{\theta^2_{\rm FWHM}}{8\ln 2}\right)\left(1+\left(\frac{\ell_{\rm knee}}{\ell}\right)^\alpha\right), \tag{2.1}$$

with parameters appearing in Tables 2-1, 2-2, and 2-3, with $\ell_{\rm min} = 30$ in each case.

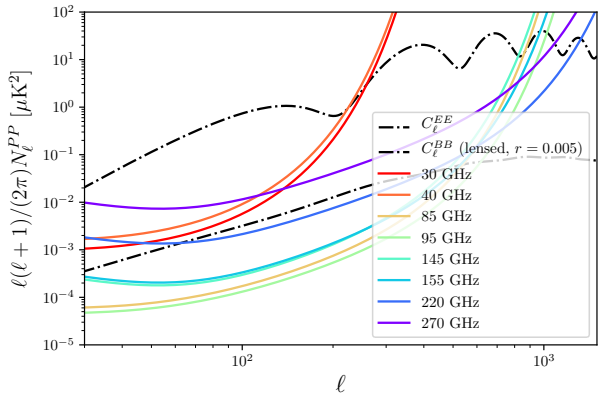

Figure 28: Required noise as a function of multipole for each frequency in polarization for the low-resolution, ultra-deep survey of 2.8% of the sky.

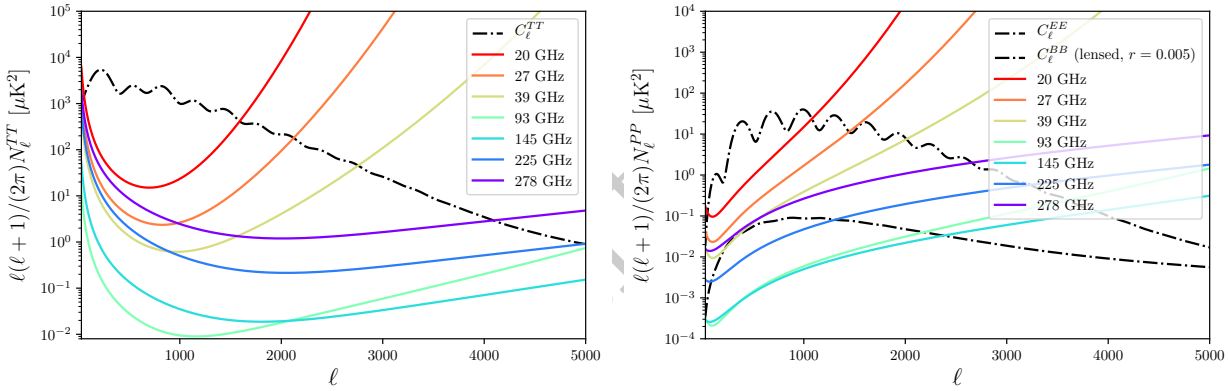

Figure 29: Required noise as a function of multipole for each frequency in intensity (left) and polarization (right) for the high-resolution, ultra-deep survey of 2.8% of the sky.

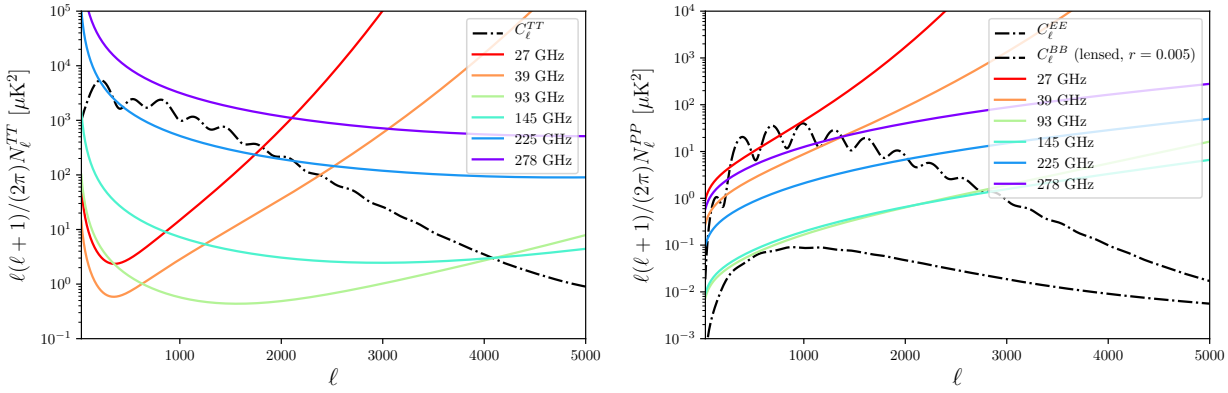

Figure 30: Required noise as a function of multipole for each frequency in intensity (left) and polarization (right) for the high-resolution, wide and deep survey of 68% of the sky.

Frequency (GHz)	**30**	**40**	**85**	**95**	**145**	**155**	**220**	**270**
$\theta_{\rm FWHM}$ (arcmin)	72.8	72.8	25.5	22.7	25.5	22.7	13.0	13.0
Δ_T (μK-arcmin)	5.64	7.14	1.41	1.24	2.71	2.9	7.5	12.85
$\ell^T_{\rm knee}$	150	150	150	150	230	230	230	230
α_T	4.4	4.4	4.4	4.4	3.8	3.8	3.8	3.8
Δ_E (μK-arcmin)	3.74	4.73	0.93	0.82	1.25	1.34	3.48	8.08
$\ell^E_{\rm knee}$	60	60	60	60	65	65	65	65
α_E	2.2	2.2	2.2	2.2	3.1	3.1	3.1	3.1
Δ_B (μK-arcmin)	3.53	4.46	0.88	0.78	1.23	1.34	3.48	5.97
$\ell^B_{\rm knee}$	60	60	60	60	60	60	60	60
α_B	1.7	1.7	1.7	1.7	3.0	3.0	3.0	3.0

Table 2-1: Parameters describing the required noise for the low-resolution, ultra-deep survey of 2.8% of the sky.

Frequency (GHz)	**20**	**27**	**39**	**93**	**145**	**225**	**278**
$\theta_{\rm FWHM}$ (arcmin)	11.0	8.4	5.8	2.5	1.6	1.1	1.0
Δ_T (μK-arcmin)	9.31	4.6	2.94	0.45	0.41	1.29	3.07
$\ell^T_{\rm knee}$	1200	1200	1200	1200	1900	2100	2100
α_T	4.2	4.2	4.2	4.2	4.1	4.1	3.9
Δ_P (μK-arcmin)	13.16	6.5	4.15	0.63	0.59	1.83	4.34
$\ell^P_{\rm knee}$	150	150	150	150	200	200	200
α_P	2.7	2.7	2.7	2.6	2.2	2.2	2.2

Table 2-2: Parameters describing the required noise for the high-resolution, ultra-deep survey of 2.8% of the sky.

Frequency (GHz)	**27**	**39**	**93**	**145**	**225**	**278**
$\theta_{\rm FWHM}$ (arcmin)	7.4	5.1	2.2	1.4	1.0	0.9
Δ_T (μK-arcmin)	21.34	11.67	1.89	2.09	6.9	16.88
$\ell^T_{\rm knee}$	415	391	1932	3917	6740	6792
α_T	3.5	3.5	3.5	3.5	3.5	3.5
Δ_P (μK-arcmin)	30.23	16.53	2.68	2.96	9.78	23.93
$\ell^P_{\rm knee}$	700	700	700	700	700	700
α_P	1.4	1.4	1.4	1.4	1.4	1.4

Table 2-3: Parameters describing the required noise for the high-resolution, wide and deep survey of 68% of the sky.

3

Preliminary Baseline Design (*Abby Vieregg and Jeff McMahon*)

3.1 Overview (*Abby Vieregg and Jeff McMahon*)

This is an overview of the preliminary baseline design. In this chapter, we present our preliminary baseline design. In the one and a half years since the CMB-S4 Decadal Science Report [**?**], all remaining critical technologies have been chosen, which significantly advances the maturity of the design.

The measurement requirements laid out in the previous chapter lead to an order of magnitude improvement in sensitivity with the corresponding control of systematics, over Stage-3 experiments. CMB-S4 must achieve sensitivity across an impressively wide range of angular resolution, from tens of arcminutes (for measuring r) to around 1.5 arcminutes (for measuring N_{eff} and clusters). Because detectors for ground-based CMB experiments are background limited, the way forward is to scale up; CMB-S4 must incorporate roughly 500k detectors to meet the ambitious sensitivity benchmarks.

The instrument must also be designed to control systematic uncertainties to the level required to actually take advantage of the unprecedented sensitivity of CMB-S4. Astrophysical foregrounds must be measured precisely with broad frequency coverage. Systematics errors, which are dominated by atmospheric fluctuations, ground pickup, and polarization errors from non-idealities in the telescopes themeselves, must be controlled.

A guiding principle in developing the design for CMB-S4 is to base the instrument design on demonstrated, scalable technologies and methodologies. The CMB-S4 design therefore has high technology readiness and is robust. We prioritize field-proven techniques where possible. The design meets the measurement requirements laid out in the previous chapter, both in terms of raw sensitivity and in terms of controlling systematic uncertainties.

3.1.1 Instrument Overview

CMB-S4 will be comprised of large and small aperture telescopes (LATs and SATs) located at two different observing sites: in Chile and at the South Pole, as shown in Figure 31. The requirement to measure large angular scales with good control of systematic uncertainties drives us toward two sizes of telescope. The SATs measure large angular scales while controlling systematic uncertainties at the level required to constrain r, while the LATs measure smaller angular scales with unprecidented precision.

The requirements also drive us to use two different observing sites with different observing strategies. Both the South Pole and Chile offer excellent observing conditions at millimeter wavelengths and well-established infrastructure that has served many CMB experiments [].

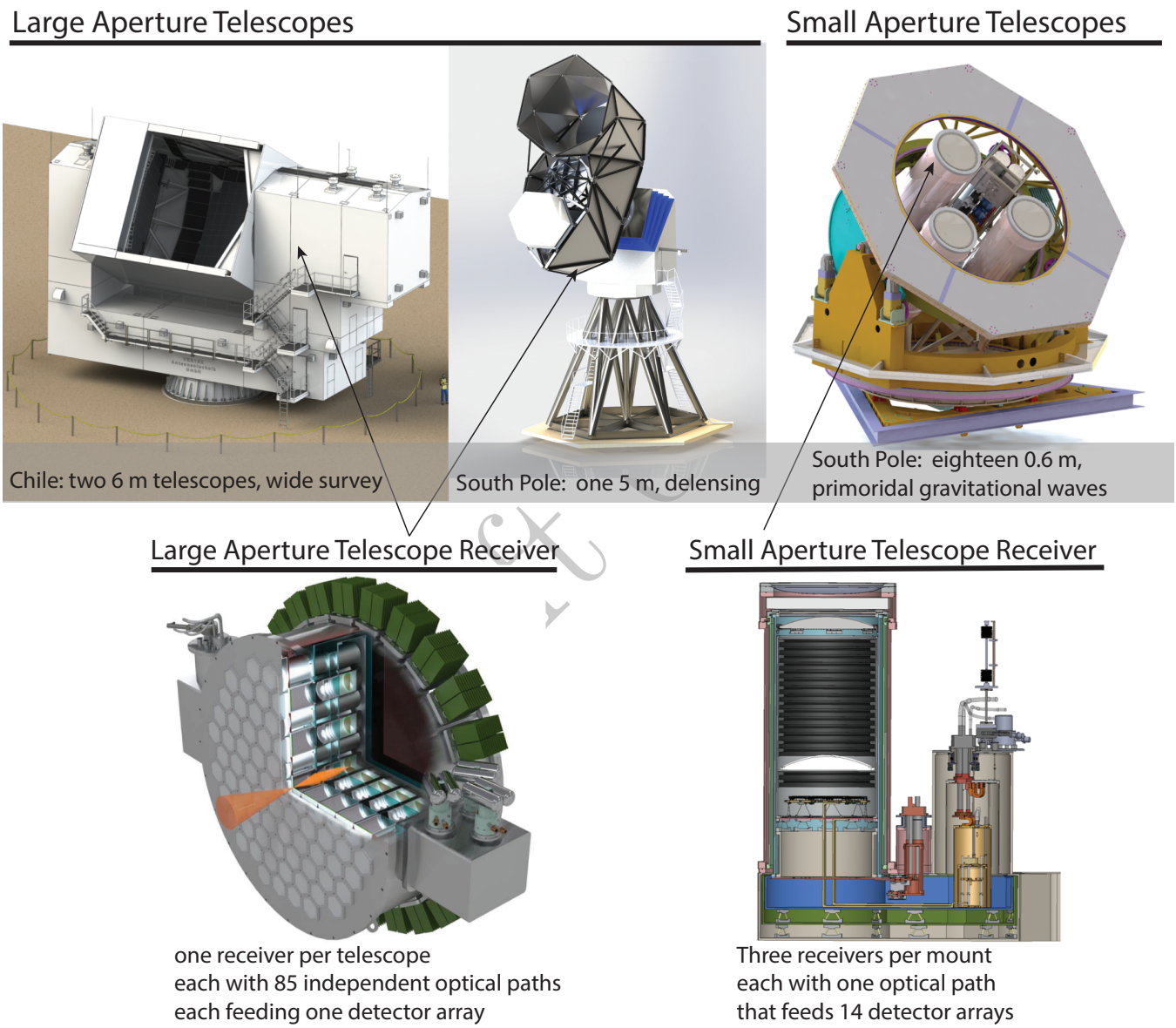

Figure 31: The telescope and receiver preliminary baseline designs. Shown are the LAT designs for South Pole and Chile, and the SAT design.

CMB-S4 achieves the sky coverage required to measure N_{eff} and clusters through a wide survey using two LATs located in Chile. This survey is located in Chile since the N_{eff} measurement requires 70% sky coverage, which is not available at South Pole. The design of the LATs in Chile is very similar to what is being implemented for Simons Observatory, but with more detectors to fully fill the telescopes' field of view.

The survey designed to measure primordial gravitational waves has two components: an ultra-deep survey using SATs at South Pole provides the sensitivity for r measurements at large angular scales, and an additional deep survey using a LAT at South Pole is specifically designed to optimize delensing for the r survey. This survey is located at South Pole to enable continuous observations on a single observing field which never rises or sets, and due to the low precipitable water vapor and more stable atmosphere with substantially lower $1/f$ noise from spacial inhomogeneities in the water vapor in the atmosphere []. The SAT design is based directly on heritage from the BICEP/Keck series of telescopes. The LAT design at South Pole is optimized to maximize throughput.

CMB-S4 will use horn-coupled transition edge sensor detectors with time domain multiplexed readout across the entire suite of telescopes. These technologies are scalable and have significant heritage in Stage-3 CMB experiments. Windows, cold optics, and thermal filters are based directly on hardware that has already been deployed on previous CMB experiments.

The CMB-S4 data acquisition and experiment control system is based directly on Stage-3 experiments, with a clear path for handling the higher data rates for CMB-S4.

3.1.2 Instrument Design Summary

Two LATs are required in Chile (CHLATs) to house the ∼200, 000 detectors required for the wide-field survey. The CHLAT design is a 6-meter crossed Dragone design, based directly on the design of the CCAT-prime and SO-LAT telescopes. The South Pole LAT (SPLAT) design is an off-axis Three-Mirror Anastigmat (TMA) on three-axis mount (elevation, azimuth, and boresight rotation), with a 5-meter primary aperture.

The SAT design is cryogenic refractor system coupled directly to a camera. Sets of three SAT optics tubes and cameras are housed in a single cryostat. There are total of 18 optics tubes and cameras, corresponding to 6 cryostats and mounts.

Tables 3-1 and 3-2 show the receiver properties for the SAT and LAT telescopes, respectively.

The detectors used across the entire array will be dichroic horn-coupled TES bolometers. Because of the sheer number of detectors, the signals require cryogenic multiplexing to manage thermal loads and reduce complexity. We accomplish this using a time-division multiplexed (TDM) readout architecture.

3.2 Detectors (*Brenna Flaugher*)

Detectors for CMB-S4 will be fabricated on silicon wafers using well tested micro-fabrication techniques built on the foundation of processes that were established for Stage-2 and Stage-3 experiments. These fabrication processes will be optimized so that $> 90\%$ of the detectors on an array are operational (i.e. can be electrically connected, optically coupled, and biased).

Property	LF		CF High		CF Low		HF	
Center frequency (GHz)	30	40	85	145	95	155	220	270
Primary lens diameter (cm)	55	55	55	55	55	55	44	44
FWHM (arcmin)	72.8	72.8	25.5	25.5	22.7	22.7	13	13
Fractional bandwidth	0.3	0.3	0.24	0.22	0.24	0.22	0.22	0.22
NET (μK$\sqrt{\text{s}}$) per detector	177	224	270	309	238	331	747	1281
N_{det} per optics tube	288	288	3524	3524	3524	3524	8438	8438
N_{tubes}	2		6		6		4	
N_{wafers}	24		72		72		36	
N_{wafers} total	204							
$N_{\text{detectors}}$	576	576	21144	21144	21144	21144	33752	33752
$N_{\text{detectors}}$ total	153232							
Data rate (18 optics tubes)	1.7 TB/day							

Table 3-1: Small-aperture telescope (SAT) receiver properties.

Detector array layout: The CMB-S4 detector arrays will be fabricated on 150-mm diameter wafers. Hexagonal tiles will be cut from the 150-mm diameter wafers such that they can be assembled in a close-packed form to make a large focal plane. Pixels are arranged on a hexagonal tile to match the instrument requirements while considering mafacturability and yield. as shown in Fig. 32.

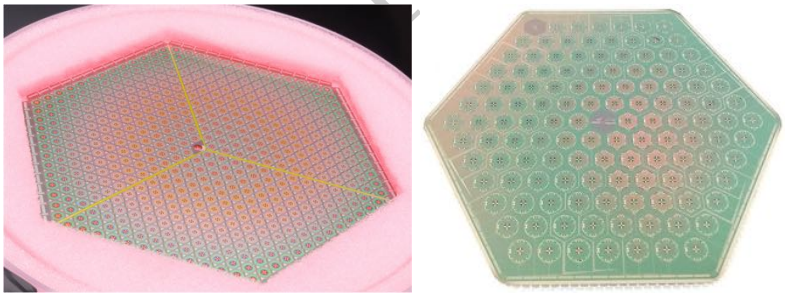

Figure 32: Pixel Layouts
(Left) Photograph of a detector array fabricated by NIST on a 150-mm diameter silicon wafer using a Rhombus layout. (Right) Photograph of a detector array fabricated by LBL/SeeQc on a 150-mm diameter silicon wafer using a Hexagonal layout.

The pixel count per hexagonal tile will range from approximately ten to five hundred, depending on the observation frequency of the detector array. Higher frequency bands will have more pixels per array. Each pixel consists of an OMT to optically couple to the pixel, radio-frequency (RF) circuits to control the RF signal (band pass filters, mode-selector and cross-under), TES bolometers to measure the incident signal, and microwave transmission lines that connect these elements as shown in Fig. 33. Each pixel on the wafer will be sensitive to two frequency bands and two orthogonal linear polarizations. Thus, each pixel will contain four TES bolometers. Each wafer will have a few percent "Dark" TES bolometers that are not connected to the optical coupling element to monitor detector sensitivity to the environment. In total, there will be approximately fifty to several thousand TES bolometers on a hexagonal tile. The electrical connection to

Property	ULF	LF		MF		HF	
Center frequency (GHz)	20	27	39	93	145	225	278
FWHM (arcmin)	10.0	7.4	5.1	2.2	1.4	1.0	0.9
Fractional bandwidth	0.25	0.22	0.46	0.38	0.28	0.27	0.16
NET (μK$\sqrt{\text{s}}$) per detector	438	383	250	302	356	737	1840
$N_{\text{detectors}}$ per tube	160	320	320	3460	3460	3744	3744
N_{wafers} per tube	4	4		4		4	

Chile (Wide Field Survey – 2 LATs

N_{tubes} per LAT	0	2	12	5
Data rate (2 LATs)	10.8 TB/day			

South Pole (Delensing Survey – 1 LAT)

N_{tubes}	1	2	12	4
Data rate (1 LAT)	5.0 TB/day			

Total (3 LATs)

$N_{\text{detectors}}$	160	1920	1920	124560	124560	52416	52416
$N_{\text{detectors}}$ total	357952						
N_{wafers}	4	24		144		56	
N_{wafers} total	228						

Table 3-2: Large-aperture telescope (LAT) receiver properties.

the detector wafer is made with rows of wire bond pads placed at the perimeter of the hexagonal detector tile.

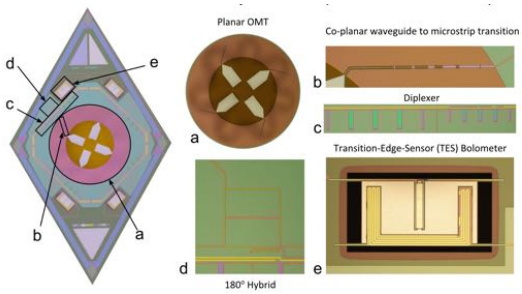

Figure 33: Components of NIST Advanced ACTPol detector pixel
Optical microscope image of an Advanced ACTPol detector pixel highlighting several of the key components. Magnified images of the major pixel components include: (a) the planar orthomode transducer; (b) the coplanar waveguide to microstrip transmission line; (c) the band-defining in-line stub filters; (d) the 180 degree hybrid tee; and (e) one of the AlMn TESs.

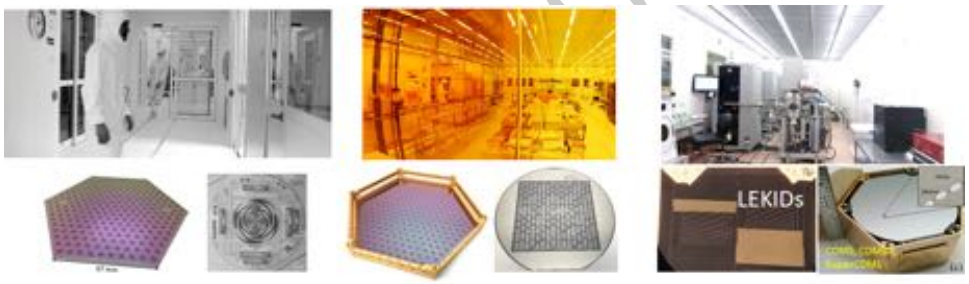

Figure 34: NANO-FAB facilities
Photographs of nanofabrication facilities and devices fabricated at: (Left) ANL (Center) LBNL/ U.C. Berkeley and (Right) SLAC

Fabrication plan: The detectors are fabricated using several cycles of material deposition, patterning, and etching to build up a complete device. Superconducting materials (niobium, aluminum and manganese-doped aluminum) and normal metals (gold and palladium) will be sputter- or e-beam evaporation deposited. Dielectric films will be deposited with plasma enhanced chemical vapor deposition. Features will be defined using stepped lithography for frontside patterning and contact-alignment lithography for backside patterning. Chemical wet etch, plasma etching and ion-milling will be used to define lithographed features. A deep reactive silicon etch will be used to release membranes for the OMT and the TES bolometer thermal isolation.

The detectors will be produced in nanofabrication facilities with extensive heritage in superconducting transition-edge sensor production, having fabricated multiple Stage-3 CMB instruments, SuperCDMS, X-ray spectrometer instruments, etc. The production plan spreads the fabrication of the roughly 700 detector wafers over five facilites to fit within each site's existing or marginally increased capacity. Photos of a few of these facilities and examples of fabricated detectors are shown in Fig. 34.

Fabrication quality control: One critical challenge for detector fabrication is to develop robust fabrication procedures that guard against process deviation. To address this, CMB fabrication facilities have been tracking processes throughout fabrication and ensure that the fabrication tools receive regular maintenance. All fabrication and metrology steps will be tracked in a computer-based logging system. The status of the fabrication tools and clean room environment, including chamber base pressure, plate temperature, clean room temperature, and humidity will be recorded each time a tool is used. The data will be continually compared to historical norms to identify deviations from process stability. This monitoring process has been implemented successfully in detector fabrication for Stage-3 experiments. While the tooling may differ between fabrication facilities, all detector arrays will be required to meet the same performance specifications, ensuring uniformity across all detector arrays.

Each detector wafer and detector pixel design includes test structures that can be used to monitor the fabrication processes and material characteristics. Sacrificial test wafers will also be carried through some process steps to monitor process steps. These methods have been proven to be useful in producing consistent detector arrays for Stage-3 fabrication. Fabrication engineers will use inspection tools including profilometers, reflectometers, ellipsometers, sheet resistance, and film stress monitors on these test structures to monitor fabrication processes attributes such as film uniformity in deposition, etch rate, surface roughness, dielectric constant of the dielectric film, sheet resistance, and film stress. Additionally, materials will be tested at cryogenic temperatures. Variable temperature four-wire resistance measurements will be used to measure the transition temperature of superconducting materials. Low-frequency ($\approx$ 2–8 GHz) diagnostic microwave resonators will be used to evaluate the loss in the dielectrics and superconducting materials.

Detector characterization: Detector characterization is an essential part of the fabrication process. Characterizing test structures, single pixels, and full arrays provides critical feedback to the fabrication process and ensures that the performance and uniformity targets are met. While finished detector arrays are tested at room temperature for connectivity, much of the detector characterization requires cryogenic temperatures to verify detector performance at operating temperatures. Here we discuss tests during the fabrication process, single pixel testing before array fabrication, and how characterized data are used to monitor detector fabrication performance. Further details on the assembly and testing of full detector modules are discussed in Sec. 3.4.

First, single pixels will be tested in a "dark" environment where there is no optical signal on the detectors. Dark tests provide the fabrication team with information about detectors such as: superconducting transition temperature of the TESs, superconducting transition shape of TESs, resistance of the TESs, saturation power of the TES bolometers, time constants of the detectors, and noise performance. These single pixel and full array testing results will be continually fed back to fabrication teams, who will make adjustments to processes to ensure that detectors achieve the specified performance. For example, if the time constant of the detectors is too fast, the thickness of the heat capacitor material (palladium) can be increased to add more heat capacity to the TES bolometers, slowing the time constant.

Single pixels will then be tested in an "optical" environment, where a blackbody signal illuminates the detectors. Optical tests will provide the fabrication team with information about the RF circuit such as optical efficiency, antenna pattern, polarization purity, and bandpass filter performance. As with dark testing, the fabrication team will make adjustments to the detector design and/or fabrication method as needed to ensure that the detectors are within specification. For example, if the frequency range of the bandpass filter is slightly high, it is possible to make a minor correction by changing the thickness of the dielectric material without changing the detector layout.

Single pixel cryogenic detector characterization is carried out using sub-Kelvin cryostats configured for specific measurements (e.g. a dark cryostat with SQUID readout for measuring the transition temperature,

resistance, and saturation power of released TES.) Each of the candidate fabrication facilities has a suite of cryostats to allow for detailed characterization of their fabrication processes and the resulting detectors.

3.3 Readout (*Zeesh Ahmed*)

3.3.1 Overview and Scope

The Readout subsystem will provide a stable and precise voltage bias to the Transition-Edge Sensor (TES) bolometers at 0.1 K, measure the current signals from them, amplify and transport the signals back to the room-temperature exterior of the receiver cryostats and then digitize and package the signals to send to the DAQ subsystem. The current is amplified by very low-noise, low-impedance amplifiers called Superconducting Quantum Interference Devices (SQUIDs). Because of the extremely large number of individual signals to measure cryogenically and report out to room temperature, the signals require cryogenic multiplexing for management of thermal loads and for ease of system integration. We accomplish this using a time-division multiplexing (TDM) architecture. In this section we first describe Readout's driving requirements and interfaces and the architecture of the CMB-S4 implementation of time-division multiplexing. Next, we describe at a high-level, the preliminary design of Readout components at 100 mK, 4 K, and at room temperature. Finally, we describe considerations for manufacturing techniques, and screening processes for quality assurance.

3.3.2 Requirements and Interfaces

The driving requirements for Readout are tabulated in Table 3-3. Broadly, they are to provide appropriate biases to the TES detectors for science and calibration modes, limit the combined readout contribution to the noise budget, limit inter-channel cross talk, and to have a sizable fraction of readout channels be operational.

Table 3-3: Readout subsystem-level requirements

Title	Requirement	Value	Origin
Readout NEI	Noise equivalent current contribution from readout shall be limited to	$<$ 5% increase in total white noise level due to readout. 1/f shape & level TBD.	Flowdown from science requirements.
Channel Operability	Working readout channels (readout-only)	$\geq$ 95%.	Flowdown from total instrument sensitivity requirements.
Detector Bias	Supply electrical bias power appropriate to the TESs	Range covering all values optimized for each observing frequency and telescope for science observation and calibration modes.	Flowdown from sensitivity requirements in each band.
Crosstalk	Limit to permissible fraction of signal level	TBD from flowdown simulations.	Systematic error budget from instrument modeling and flowdown.

3.3.3 Architecture: Time Division Multiplexing

The readout of the individual detectors will be multiplexed at the lowest temperature stage using time-division SQUID multiplexing (TDM). Figure 35a illustrates the basic TDM readout scheme. A group of TES detectors is arranged into a 2D logical array, in which each column of detectors shares a dedicated readout amplifier chain. The various rows are addressed cyclically in rapid succession to record data from the entire array. When a row of the array is actuated, a single TES bolometer in each column is read out by its associated column amplifier to record a single data sample. Each channel is revisited at a rate fast enough to capture any sky signal of interest. Each bolometer is bandwidth-limited at a frequency below the Nyquist frequency of the revisit rate, so that the signal can be reconstructed with acceptable degradation from aliasing. Time-division SQUID multiplexers have extensive on-sky heritage in the CMB community, including instruments such as the BICEP/Keck cameras and the MBAC and ACTpol cameras on ACT.

Figure 35b shows a schematic for one column of the current-generation TDM architecture. The multiplexer chip (outlined in blue) supports the first-stage SQUIDs that detect the TES signals and the superconducting switches that select among them. A detector bias/filter chip (not shown) sits between the multiplexer and the detector, contains shunt resistors that provide the TES voltage bias and inductors to limit the detector bandwidth. Both are located at 100mK within the detector module packaging. The multiplexer footprint in the focal plane is 1.8 mm^2/channel. The size of the bias/filter chip is driven by pixel bandwidth and TES sensor impedance; in practice, however, the silicon area required is roughly the same per pixel as the SQUID multiplexer chip. Superconducting wire bonds and superconducting circuit board traces pass signals between the detector wafers, filter chips, and multiplexing chips; links to the rest of the amplifier chain may be made with non-superconducting pin-socket interconnects. Loom cabling connects these module components to the SQUID Array Amplifiers (SAAs) at ≈4 K., and from there to the warm readout electronics outside the cryostat.

3.3.4 100mK Cold Electronics

CMB-S4's 100mK cold electronics perform the critical fan-out operations of the multiplexer system, sharing a limited number of amplifiers and SQUID / TES bias signals among a large array of TESs. It consists of two types of silicon chips patterned with superconducting circuitry (SQUID multiplexer chips and interface chips), as well as the associated circuit boards and cables for signal routing. The 100mK cold electronics design is tightly integrated with that of the detector module subsystem, which is described in further detail in the next section. Below we outline the current conceptual design

3.3.4.1 100mK Readout Module

The 100mK readout components consist of a SQUID multiplexer chips, "interface chips" containing the TES bias circuitry, silicon wiring chips and interface to the superconducting flex cables that route to the detector wafer. These components are all mounted to a carrier PCB with connectors that distribute the TES bias, SQUID bias, and row-select bias signals coming from the warmer stages of the readout. The PCB is mounted in a metal enclosure, which enables both modular testing of readout components before assembly into completed detector/readout modules, and also provides a magnetic shielding through a combination of superconducting and high-magnetic-permeability materials. Figure 37 shows the arrangement of components inside the box as well as the concept for how boxes stack behind the footprint of the feedhorn block in an assembled detector module. The highest-density detector wafers require six 100mK readout modules, each

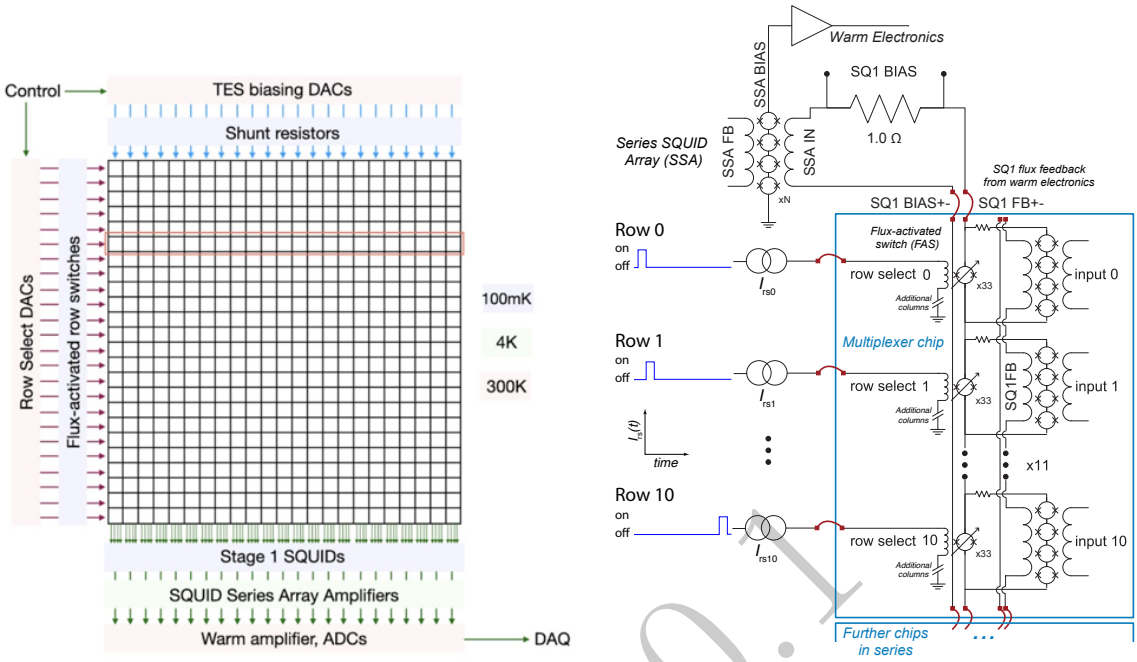

Figure 35: **Left:** Cartoon of time-division multiplexing of a TES array. The switches at left connect a single row of detectors at a time to the amplifier chain at bottom. TESs are generally biased by column, as noted at top. Colors indicate different temperature stages. **Right:** Schematic illustration of a single column of a time-division SQUID multiplexer. Each TES is coupled inductively to a first stage SQUID (SQ1). All SQ1s in a column are wired in series to the input of a SQUID array amplifier (SAA), but at any given time all but one row of SQ1s is bypassed by a flux-activated switch (FAS). The various row-select lines are biased in sequence with low-duty-cycle square waves, as shown at left.

containing 5 "columns" of multiplexer components. Lower-density detector arrays can be instrumented with a combination of fewer boxes and columns per box, depending on detector count. More details on the module design and constraints are described in Section **??**.

3.3.4.2 100mK SQUID multiplexer

The core switching functionality of TDM is implemented on a set of 100mK SQUID multiplexer chips. These are the top row of chips visible in Fig. 37, and indicated by the blue box in the schematic in Fig. 35. Each multiplexer chip is patterned with one first-stage SQUID and associated flux-activated switch for 11 TES channels, constituting 11 rows within a single readout column. Each first-stage SQUID (actually itself a small series SQUID array) amplifies the signal current from a single TES. The superconducting switches, actuated by separate "row-select" lines, short out all but one of the SQUIDs in each readout column at a time, so that only this channel is recorded by the warm amplifier chain.

The choice of 11 rows per multiplexer chip for the preliminary baseline design is driven primarily by heritage, as this matches hardware and fabrication processes currently in use. Such chips may be daisy-chained in series to allow for greater numbers of rows. Early design studies show no large benefits in wiring or fabrication cost to varying the row count. This decision is very straightforward to adjust in the chip design, and will be revisited as the instrument design matures.

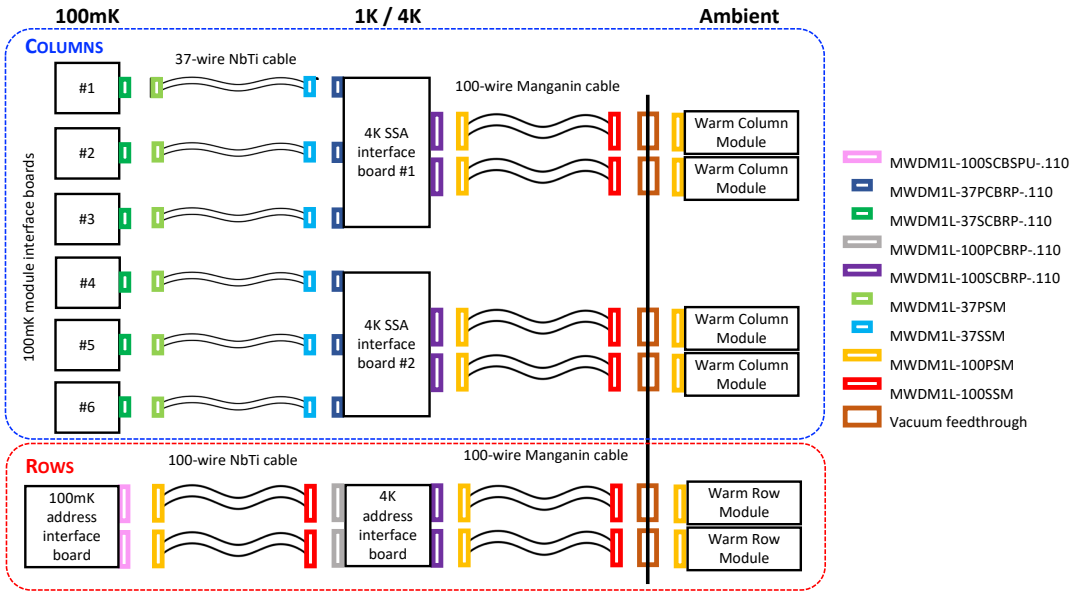

Figure 36: Cartoon of architecture for TDM readout cables and PCBs at the various key temperature stages.

3.3.4.3 100mK TES biasing

Each multiplexer chip is mated to a corresponding "interface chip", visible as the bottom row of chips in Fig. 37. These chips support two passive components of the TES bias circuit: a parallel (shunt) resistor to voltage-bias each TES, and a series inductor to define the TES bandwidth. These components ensure stable operation of the TES on its transition while avoiding TES noise aliasing at the TDM sample rate. The lines connecting the multiplexer and interface chips to the TESs must have low parasitic resistance (typically superconducting), so these chips are typically operated at the detector temperature (0.1-0.3) K.

The interface chips are much simpler to fabricate than the multiplexer chips, resulting in high yield and reproducibility. The preliminary baseline design assumes 22-channel interface chips (one per pair of multiplexer chips) to reduce cost and complexity. This choice can be easily revisited as the instrument design matures.

3.3.4.4 100mK signal routing and cables

Three types of electrical signals require distribution at the 100mK stage: TES and SQUID biases, row-addressing, and detector signals. The TES and SQUID biases and the row-address signals enter the 100mK stage at a "row address" interface board, which distributes the signals to up to six readout modules. The distribution of TES and SQUID biases is handled by six 37-pin cables, one per readout module. The carrier PCB inside the readout module distributes the TES and SQUID bias signals to the interface and SQUID multiplexer chips, connected via superconducting wirebonds. The row-address signals are distributed to one readout module, which is connected to the others via a daisy chain of standard copper flexible cables.

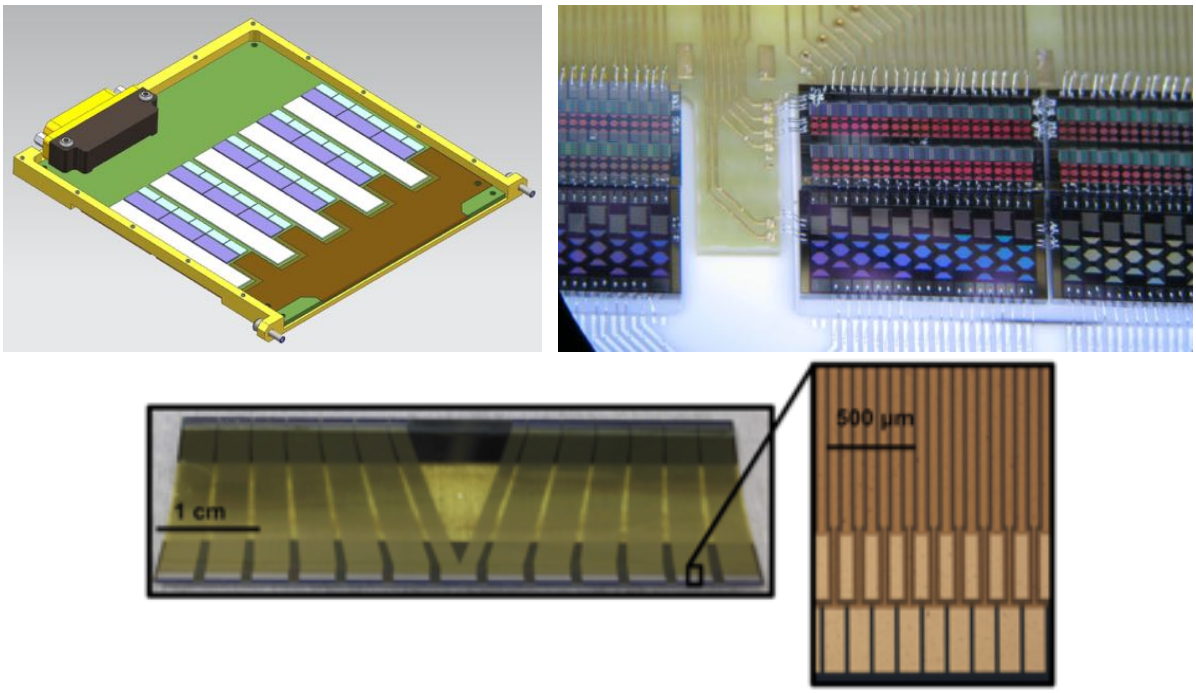

Figure 37: **Top left:** Concept design for a fully-populated 100mK readout board, assuming 11-row SQUID multiplexer chips (*light blue*) and 22-row interface chips (*violet*). A silicon routing chip (*white*) brings signals to a superconducting flexible circuit (*brown*) to the detector. Readout is via the micro-D connector at the top of the board, while rows are routed between boards via ZIF connectors on the sides (*not shown*). **Top right:** Photograph of 100mK TDM electronics, as installed in a BICEP3 detector module. The SQUID multiplexer chips (*top row*) house the first-stage SQUIDS and switches. The interface chips (*bottom row*) house the TES bias resistor and bandwidth-limiting inductor. As shown at bottom right, 11-row chips may be daisy-chained to allow for larger numbers of readout rows. All connections are by superconducting aluminum wirebonds. **Bottom:** Example of single-layer superconducting flexible cable from the the AdvACT experiment. CMB-S4 will use a similar style of cable, but with 2 layers fabricated at a larger pitch.

Signals from the detectors are handled via custom high-density flexible circuits with superconducting Aluminum traces. Use of a superconducting material such as Aluminum is critical here in order to minimize the parasitic impedance in series with the TES, which limits the range of fractional resistances at which the TES can stably operate. These superconducting circuits will be fabricated in two laminated layers on a polyimide substrate, with wirebonds on either end. One end the cable is mounted and bonded to the detector wafer, while the other end of the cable is clamped in one of the six readout modules per detector wafer, with wirebonds connecting to a silicon wiring chip, which in turn connects the TES lines to the interface chips of the readout box (see Figure 37).

3.3.5 4K Cold Electronics

The 4K Cold Electronics includes the SQUID Array Amplifiers (SAAs) which amplifies the signal for transmission to the room temperature electronics, a SQUID board which houses the SQUIDs and routes

signals to 100 mK, the associated mechanical hardware for supporting the SQUID boards, and magnetic shielding for the SQUID array amplifiers. An upper limit for the temperature of this stage is set by the SAAs, which are superconducting devices which must be cooled below approximately 5 K to sufficiently amplify signals for transmission to the warm electronics.

3.3.5.1 4K Series SQUID Array Amplifier

Each readout column has a series SQUID array amplifier (SAA) that is used to amplify the SQ1 signal.

A mature design exists that meets requirements, which is fabricated by NIST, and has significant on-sky heritage, including most recently in AdvACT and BICEP3. In previous experiments using TDM, the SAA has been located on the 4 K, 2 K or 1 K stages. The baseline plan for CMB-S4 has been to put the SSAs at the 4 K stage, but a potential upgrade would be to move the SAA to the 1 K stage. Moving the SAAs to the 1 K stage would allow them to be placed much closer to the 100 mK electronics and detectors. This would have several advantages including allowing for shorter wire runs, increased proximity of the SAAs and SQ1s, and greatly reduced risk that the SAAs do not reach sufficiently cold temperatures. Another benefit is that the resulting more compact arrangement of all sensitive devices makes it easier to enclose them in a single RF-clean volume. There may also be benefits in magnetic shielding if the SAAs can be placed within the envelope of the existing magnetic shielding for the 100 mK electronics and detectors.

The transimpedance of an SSA is known to degrade at temperatures above approximately 5 K. While the nominal temperature of the 4 K stage is sufficient to meet temperature requirements for SAA operation, excessive loading on the 4 K stage or poor thermal coupling between the SAAs and the 4 K cooler could result in the SAAs exceeding 5 K. Locating the SAAs at the 1 K stage will completely alleviate this concern because the 1 K stage will never exceed 5 K, and will never reach the low end of the operational temperature range, approximately 300 mK.

One of the primary disadvantages and uncertainties associated with locating the SAAs at the 1 K stage is the effect on SQUID screening. Requiring that the SAAs be screened at 1 K would add additional requirements on the testing infrastructure. Screening at 4 K may not provide sufficient information on potential defects from SQUID fabrication which can result in unstable operation at low temperatures. Screening a small number of devices from each fabricated wafer at 1 K may be sufficient information to determine whether the remaining devices should be screened at higher temperatures. An advantage to colder operation is that SAAs typically have improved performance at lower temperature, so operating at 1 K might result in a greater percentage of devices meeting requirements.

Power dissipation by the SAAs is negligible at 4 K or 1 K. Typical power dissipation by an SA13 is of order $0.1\mu W$, and the 1 K and 4 K stages have cooling powers of order 1 mW and 1 W, respectively. Putting the SAAs at 1 K would add power dissipation from readout to that stage, but at a very small amount. Additionally, this will be somewhat compensated for by a reduction in heat load from readout wiring. The wiring between the SAA and SQ1 needs to be superconducting, but this requirement does not exist for the wiring between the SAA and the higher temperature stages. Typical manganin wire can achieve lower thermal conductivity than CuNi clad NbTi wire between 4 K and 1 K, so this could result in a reduction in wiring heat load on the 1 K stage.

Putting the SSA at 1 K means there will be more cable length between the SSA and the warm electronics, resulting in a sharper RC rolloff at the SAA output. This will result in increased stringency on the dynamic impedance of the SSA and/or the capacitance of the 1 K to 300 K wires. The impact on the design needs to be assessed as part of an overall optimization.

3.3.5.2 4K SAA magnetically-shielded module

The SAA is extremely sensitive to magnetic field variations and gradients. Each SAA must be shielded to suppress environmental magnetic fields at the chip location. In prior designs, sets of 8 SAAs are packaged together onto a small carrier board for compact magnetic shielding. Multiple shielding materials are used including superconducting niobium metal, machineable high-permeability nickel-iron alloys, and multiple layers of thin foils of extremely high-permeability material. The resulting magnetically-shielded module has an extremely high rejection of external magnetic fields, while remaining relatively compact and modular.

3.3.6 Production Workflow for Superconducting Circuits on Silicon

The 100 mK and 4 K readout components include superconducting circuits fabricated on silicon wafers. Some of these devices, like the interface chips, are relatively simple devices that require low-loss superconducting traces. The SQUIDs including the SQUID multiplexer and SQUID array amplifer are relatively complex devices that must be carefully fabricated, and then screened at cryogenic temperature to ensure that the device meets requirements.

3.3.7 Microfabrication

Many tens of thousands of TDM SQUID channels have been fabricated and successfully deployed in astronomical instruments. Fabrication will be done at class 100 clean room facilities at the National Laboratories. The baseline fabrication plan utilizes teams of two fabrication engineers carrying batches of 150-mm TDM wafers through the fabrication process, with multiple standardized quality-control measurements.

Superconducting metals (niobium, aluminum, and niobium trilayer tunnel junctions) and normal metals (gold) will be sputter deposited. Dielectric films will be deposited with plasma enhanced chemical vapor deposition. Features will be defined using stepper lithography. Both chemical wet etch and reactive ion etching will be used to define lithographed features.

All fabrication and metrology steps will be tracked in a computer-based logging system. Status of the fabrication tools and clean-room environment, including chamber pressure, platen temperature and clean-room temperature and humidity will be recorded each time a tool is used. Data will be continually compared to historical norms to identify deviations from process stability.

Wafers include test structures that allow monitoring of fabrication processes and material characteristics. Sacrificial test wafers will also be carried through some fabrication steps for process monitoring. Fabrication engineers will use inspection tools including profilometers, reflectometers, ellipsometers, resistance sheet and film stress monitors on these test structures to monitor fabrication processes such as etch rate, surface roughness, dielectric constant of dielectric film, sheet resistance and film stress.

3.3.8 Packaging and Cryogenic Screening of Components

Electrical screening of sub-components is necessary to minimize channel loss and ensure that the integrated instruments meet sensitivity requirements. Cryogenic screening of the 100 mK and 4K readout sub-

components is necessary to ensure that they meet performance requirements, including the interface chips, SQUID multiplexer chips (SQ1), and SQUID array amplifiers (SAAs). This screening must be done below the critical temperature of the superconducting metals, and has historically been done at a temperature of 4 K, achievable by liquid helium or two-stage mechanically cooled systems. The performance of the SQUIDs, including the SQUID multiplexer and SAAs, are impacted by the environment, including magnetic shielding.

Screening of SQUID devices including SQ1 and SAA chips will include automated data-taking at cryogenic temperature to measure critical current, modulation depth, and other relevant device parameters.

The 4K electronics are assembled into a compact integrated package for cryogenic screening, with SQUID amplifiers mounted on SQUID boards and assembled into the magnetically-shielded module. This packaging also protects delicate components and connections. Any problematic devices or connections would be re-worked, and screened again, until the package has all channels operational and meeting requirements. The screened 4K electronics package is ready to be used in the integrated system.

The SQUID multiplexer chips must be packaged and screened at cryogenic temperatures to determine whether all channels meet requirements. While the SQUID multiplexer operates at 100 mK, the screening is typically done at more easily achieved 4 K temperatures. The screened chips are packaged with interface chips in assembling the 100 mK readout module.

Screening of interface chips is ideally done at cryogenic temperatures, to ensure that all traces meet requirements, but screening of a few 'witness' chips at cryogenic temperatures, combined with thorough screening of all chips at room temperature, may be sufficient to determine whether the devices are performing properly.

3.3.9 300K Warm Electronics

Fig. 38 shows the warm electronics system with custom row address control and custom column readout control modules. There is no other custom warm electronics hardware besides the two modules. The modules plug directly into the vacuum 100-pin feedthru flange connectors. The figure shows 2 row address control and 4 column readout control modules, although the two module types can be combined in any set depending on the optics tube requirements. A group of modules receives a single 48-V power feed, an Ethernet network fiber connection, and a Timing fiber for synchronization. Any of the boards can be configured as the local master via firmware. The signals are daisy-chained between the local group of modules. 48V power is supplied via a commercial bulk supply for a number of module groups. Networking is connected via an Ethernet switch to a server where a local Readout client and a DAQ client are running for control and readout. The hardware is backwards compatible with existing TDM MCE warm electronics. The modules can be plugged into the flange connectors, replacing MCE cables to MCE crates. That enables testing on existing setups with MCE to compare performance without changing the cold cables/modules in the chamber.

3.3.9.1 Warm readout modules: Hardware and Firmware

The row address control module generates the programmable voltages to select each of the 64 rows, one at a time, in the 100mK Readout Module. Row addresses are swithed at a rate of about 500 KHz, programmable. The module contains 48 channels of DACs (Digital-to-Analog Converters), limited by the available 100-pin/wire connectors/wires into the cold. For CMB-S4 with 64-channel row addresses, two modules are required for each detector wafer, with 32-channels used on each module. An on-board FPGA controls the DAC settings and rate via software/firmware. The column readout control module serves 8 channels of columns. Each channel supplies TES bias (slow DAC), SQ1 bias (fast DAC), SQ1 feedback (fast DAC),

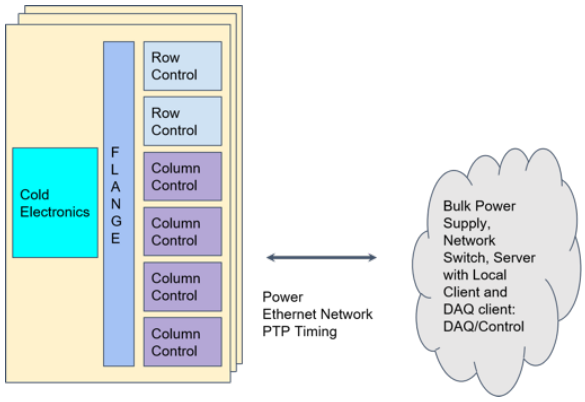

Figure 38: System diagram of warm Electronic with row address control and column readout control modules

SSA bias (slow DAC), and SSA feeback (fast DAC). Two column readout control modules are required for each 16-channel 1K/4K SSA module. Firmware on the board controls the acquisition of raw data at 125 MHz, provides a low pass digital filter, and a windowing function to average sequential samples. The result is forwarded to the server via Ethernet. For diagnostics raw data can be read out. Limited out of band monitoring can be provided which allows health monitoring during science data acquisition.

Fig. 39 shows a row address control board. Both the row and column boards will be about 5"x10". The estimate for the power dissipation is between 8W and 15W each.

Figure 39: Row address module, 5"x10" in size

3.3.9.2 Readout Software

The readout software layer runs on a separate server, connected via fiber to the telescope. This software serves as a management layer between the TDM electronics and the telescope Data Acquisition and Control

software layer, providing a clean, well defined API for control and management of the TDM electronics, while also supporting expert level debug and monitoring interfaces utilized during the development phase.

Additionally this core software supports localized configuration store and recall, a debug GUI which can be attached as needed and an interface for running local test scripts. Support for local data files storage is also provided for standalone operation or debug separate from the telescope DAQ layer.

The TDM software layer interfaces to the TDM electronics using a private Ethernet network, utilizing a reliable UDP based protocol for both register access communications and for the data path. This protocol allows for reliable communications between the software and hardware, supporting error detection and packet re-transmission while supporting lightweight implementation in a standard FPGA.

3.3.9.3 Packaging, peripherals, crates, cooling

The row address and column readout modules have the identical size and are packaged in an RF shielded enclosure. Fig. 40 shows a cartoon for a SAT with the modules in a circle around the cryostat. The module boards are conductively cooled via the enclosure to a cooling pipe routed around the circumference of the SAT (or LAT). The SAT drawing shows 72 modules, assuming 12W/module that results in less than 1kW which can easily be handled by one cooling loop. The modules do not need to be at the same temperature. There are no crates in the warm electronics since the modules are directly plugged into the flange connectors,

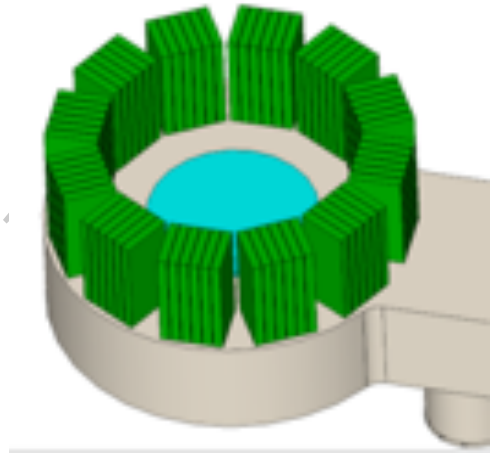

Figure 40: Cartoon of warm electronics modules mounted on a SAT

thus also eliminating flange-to-warm electronics crate cables.

The two custom module boards are commercially fabricated, board-assembled, thermal cycled without power for workman-ship screening, bench tested, assembled in the enclosure, and retested. For the electronics functionality and performance testing an emulator test board will be designed, to allow for rapid testing.

3.4 Module Assembly and Testing (*Brad Benson*)

3.4.1 Overview and Scope

The Modules and Testing sub-system is responsible for the assembly and testing of the CMB-S4 detector modules. The detector modules (see Fig. 41) are an integrated assembly consisting of feedhorns that couple microwave power to a detector array, which are readout by multiplexed readout electronics. This sub-system is responsible for the design of the module interface components (see Sec. 3.4.4), microwave coupling hardware (see Sec. 3.4.2, 3.4.3, and the assembly of these components into an integrated package (see Sec. 3.4.4) with the Detector and Readout sub-systems that can be installed and operated at 100 mK in the SAT and LAT cryostats. The Modules and Testing sub-system is also responsible for characterizing the performance of these integrated detector modules to verify that they meet CMB-S4 requirements (see Sec. 3.4.5).

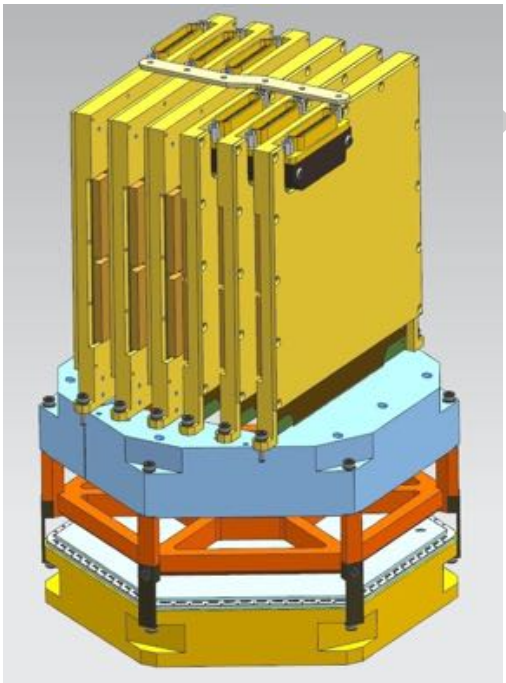

Figure 41: Concept design for the 100mK detector module. In this view, the horn array and detector wafer are at the bottom, with the readout boards at the top. The orange frame above the horn array provides heat sinking and clamping force via beryllium copper springs (not visible) on the interface wafer stack. The blue pieces provide a mounting point for the readout boxes and provide vertical clearance for routing superconducting flexible circuits (not shown).

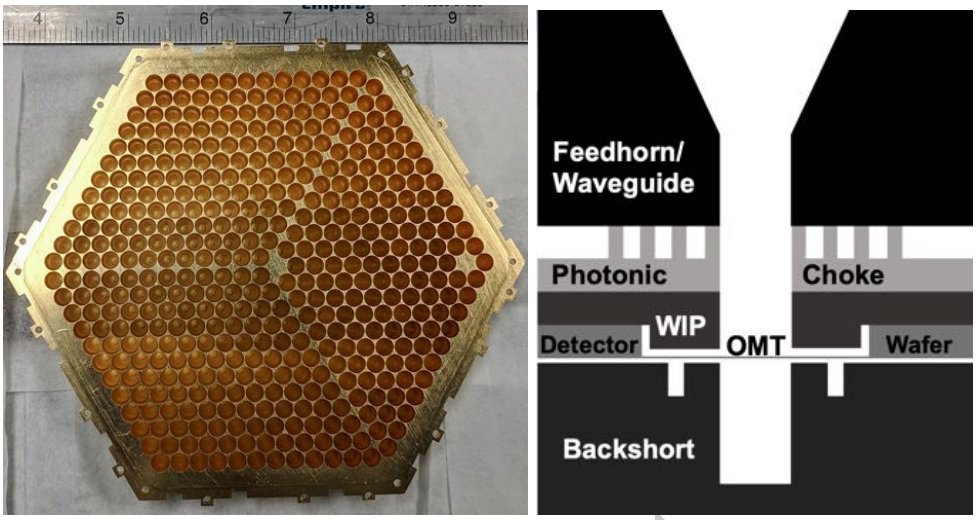

Figure 42: **Left:** An SO Al 6061 feedhorn array using spline-profiled feedhorn designs. **Right:** The feedhorn couples light onto the detector wafer. Several interface wafers improve the coupling, inlcuding a photonic choke, a waveguide interface plate, and a backshort.

3.4.2 Horn Arrays

The CMB-S4 reference design uses smooth-wall, wide-band, spline-profiled feedhorns for the detector RF coupling (see Fig 42). The feedhorn array sits above the detector wafer, and couples the light onto the orthogonal fins of the detector OMT (see Fig 33). Feedhorns are a mature technology that has been demonstrated on many CMB experiments with published CMB polarization science results across a wide range of frequencies, including ACTPol, AdvACT, SPTPol, ABS, and CLASS.

Spline-profiled feedhorns have good performance across wide bandwidths, making them ideal for multichroic pixels. Spline-profiled feedhorns maintain high coupling efficiency with small apertures, enabling denser pixel packing and thus increased sensitivity. Because their profile designs can be tuned between beam coupling efficiency and beam systematic control, spline-profiled horns allow for greater design control and balanced performance [488, 489, 490, 491].

Spline-profiled feedhorns can also be made monotonically increasing in diameter so that they can be direct-machined into metal, significantly reducing fabrication time and cost. We plan to use custom drill and reamer sets to direct-machine the feedhorn profiles into Al 6061. Al 6061 is cost-effective, low-density, and has high machinability [492]. A CMB-S4 feedhorn array at 90/150 GHz with 432 feedhorns would only take ∼15 hours to machine. The feedhorn array production can be readily performed with the tools available in most machine shops, so it can be parallelized across multiple machine shops. Because Al is superconducting at the operational temperature of the array, it requires the addition of a normal metal for heat sinking, so we will gold-plate the arrays after fabrication. This fabrication process is simple and as such has an expected yield of ∼100%.

We will use metrology on cross-sectioned feedhorns to verify that the machined profiles match the designed profiles and beam maps to check that the feedhorn performance matches simulations [492]. One significant advantage of feedhorns is that they can be tested at ambient temperature prior to integration with the

detector array. This enables rapid turnaround on array testing and reduces risk by only integrating fully vetted horn arrays with the detector arrays. Before production begins, the drill and reamer set is vetted with metrology measurements on cross-sections, and the performance of single feedhorns are measured with beam maps. During production, arrays will be produced in batches of ∼5 arrays, depending on the tool wear for the given band. The drill and reamer sets will be changed between each batch. Before production begins on a new batch, the new tooling will be vetted with metrology on single cross-sectioned horns. Witness samples of a single cross-sectioned horn will be produced between each array in a batch to track any tool wear or variation in the profiles. After the arrays are produced, we will measure several horns at several frequencies on arrays to verify performance.

3.4.3 Interface Wafers

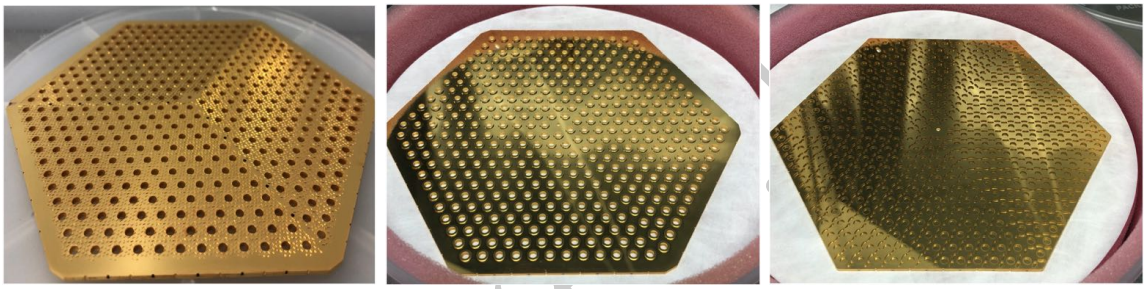

Figure 43: **Left:** A photonic choke wafer. **Center:** A waveguide interface plate. **Right:** A backshort array.

The detector stack consists of the detector wafer and a set of silicon interface wafers, that define the microwave cavity that couples power to the detectors and interface with the horn array. The interface wafers are comprised of a photonic choke to reduce leakage at the interface between the horn array and the detector stack [493], a waveguide interface plate, the detector wafer, and a ∼quarter-wave backshort (see Fig 43). Behind the backshort is a Cu heat clamp plate for heat sinking that bolts directly to the metal feedhorn array. The feed array also has additional mounting features machined directly into its design for mounting onto the focal plane. The detector module aligns the horn arrays with the detector stack by a pin and slot to account for the differential thermal contraction between the Al feedhorn array and the Si detector stack. This array package design is based on designs used for ACTPol, AdvACT, and SPTPol.

The main challenges associated with Al feedhorn arrays are achieving the necessary machining tolerances in the feedhorn profiles and the alignment of the feedhorn array with the detector stack, especially at the highest frequencies (220/280 GHz). Simulations using the scatter measured in the a 220/280 GHz feedhorn profile from non-contact metrology measurements show that the current level of variation in the profile is negligible to the feed's performance [492]. Additional simulations show that the SO 220/280 GHz array must be aligned with the detector stack to ∼10 μm. Differential thermal contraction can cause greater misalignment and add additional mechanical stress to the array, but these risks can be retired with cryogenic testing in the design phase. Additionally, the SO Al feedhorn arrays have been integrated into modules that have been cryocycled and optically tested.

3.4.4 Module Frame and Assembly

The module assembly begins by aligning and mounting the interface wafers described above to the horn array using the pin and slot as a reference guide. The superconducting flexible cables are then mounted and wirebonded to the wiring chips inside of the 100mK readout modules. One by one, the other end of the flexible cables are glued to the top of the backshort wafer (top of the detector and interface wafer stack) and wirebonded. After wirebonding each module, it is folded radially outward to accommodate the wirebonding head; a specialized jig would be used to hold each box during this process. Once all sides of the detector wafer are bonded, the horn array and interface wafers are clamped down by the copper piece with beryllium copper springs (orange in Figure 41), and one half of the readout platform (blue in Figure 41) is installed. The readout boxes and cables are then routed and bolted one-by-one to the readout platform, and then the other half of the readout platform is installed, with the remaining fasteners attached.

3.4.5 Detector Module Testing and Requirements

The performance of each detector module will be characterized as an integrated unit at the expected module operating temperature (100 mK) in dedicated test cryostats. Each detector module will undergo both dark and optical tests to ensure that the module meets CMB-S4 requirements (see Table 3-4). The full set of requirements will be specified through the development of the instrument flowdown model, taking into account sensitivity and systematic requirements. The detector module tests will be the only time that the TES properties across the entire detector wafer can be characterized, and will also characterize integrated performance of the detector wafer with the horn arrays, interface wafers, and 100 mK readout modules.

The dark tests will characterize integrated module properties such as the integrated module yield, TES properties, detector stability and time constants. The dark test cryostats will include cold-loads, blackbody sources whose temperatures can be adjusted, which can be used to estimate the detector optical efficiency from the overall response from the TES. The dark cryostats will also include IR sources that can flash the detectors with an optical signal that can measure the detectors optical time constant, and verify it matches the TES response to a voltage bias step. The overall sensitivity of the detector module, or noise equivalent temperature (NET), can be estimated from a combination in-transition noise measurements and load curves at multiple cold load temperatures.

The optical testing and characterization of the detector modules will come from a combination of tests from room temperature setups, optical sources inside the dark cryostats, and optical cryostats with a vacuum window that allow coupling to sources in the room. The horn arrays beam shapes and cross-polarization can be characterized at room temperature using a vector network analyzer test setup [488], which reliably can predict the cryogenic optical performance of these parameters for the detector module. The detector module optical efficiency and detector optical time constant can be determined by sources inside the cryostat, as described above. However, some optical measurements will require optical test cryostats, that couple power in the room through a vacuum window and onto the detectors. In particular, in this way, we plan to measure the detector frequency response using a Fourier transform spectrometer. Other optical properties will be spot-checked in optical cryostats during development, such as the beam-shape, cross-polarization, and optical efficiency. RF and magnetic pickup of the detector module and readout can be measured in an optical cryostat using sweeps of RF and magnetic sources outside the cryostat.

During prototype detector module testing development, we will make use of existing cryostats and test hardware within the collaboration. The testing and assembly plan will include redundancy to minimize delays in testing and provide timely feedback for the detector fabrication, which will rely on the testing

Table 3-4: Testing measurement requirements

Title	**Requirement**	**Origin**	**Test**
NET	Noise equivalent temperature of the detecotr module	Flowdown from sensitivity requirements in each band	In-transition noise and efficiency measurements looking into a cold-load during dark testing.
Yield	Percentage of detectors that can be readout per module	Flowdown from sensitivity requirements in each band	IV measurements of TES during dark testing
TES time constant	Time constant of the TES detector in the transition	Flowdown from sensitivity and systematic requirements in each band	TES response to voltage bias step and flashed-optical source during dark testing
TES properties	Saturation power, superconducting transition temperature, normal resistance of the TES	Flowdown from sensitivity and systematic requirements in each band	IV measurements of TES during dark testing
TES stability	Stability of the TES while in-transition	Flowdown from sensitivity and systematic requirements in each band	In-transition noise looking into a cold-load during dark testing.
RF pickup	RF response of the detectors	Flowdown from systematic requirements in each band	Sweep of RF source around cryostat during dark and optical detector testing
Magnetic pickup	Magnetic response of the detectors	Flowdown from systematic requirements in each band	Sweep of magnetic field around cryostat via Helmoltz coil during dark and optical detector testing
Bandpass	Frequency response of the detectors	Flowdown from sensitivity and systematic requirements in each band	Fourier transform spectroscopy measurements during optical testing.
Beam shape	Spatial response of the detectors	Flowdown from systematic requirements in each band	Beam-shape measurements of horns via VNA setup, with spot checks of modules during optical testing
Cross-polarization	Cross-polarization response of the horn arrays and detectors	Flowdown from systematic requirements in each band	Cross-polarization measurements of horn arrays via VNA setup, with spot checks of modules during optical testing

to assess the performance of the detector design and fabrication processes. Testing will initially aim to characterize ∼100 detectors per module, gradually increasing to full detector module readout and string testing by the end of the prototype development phase. The baseline plan calls for six prototype test cryostats, split between dark and optical detector module tests.

During detector module production testing, CMB-S4 will build new dedicated cryostats to keep pace with the required throughput. During this period, the schedule plans for the assembly and test ∼20 detector modules per month over a ∼3-year period. Given this scale, testing will be centralized in 2-3 sites in order to reduce the amount of duplication of expertise and infrastructure, with each site housing several large test cryostats capable of testing multiple detector wafers per cooldown. The baseline plan calls for the construction of eight production test cryostats, that can test seven detector modules per cooldown, split between dark and optical testing. These cryostats will be of a scale similar to what is being planned for both the LAT commissioning camera S3.5.5 and an optics tube for the SAT cryostat S3.6.3, and are expected to share common designs with one or both sets of cryostats.

3.5 Large Aperture Telescopes (*Mike Niemack*)

3.5.1 Large Aperture Telescope Overview and Scope *(Niemack and Carlstrom)*

3.5.1.1 Connecting Measurement Requirements to Specifications

The key measurement requirements for the Large Aperture Telescopes are described in Chapter 2, and an overview of the LAT specifications is presented in Table 3-2. The angular resolution and frequency range, combined with typical characteristics of the atmosphere at a good millimeter-wavelength site, and typical CMB experiment scan strategies, lead to the telescope design requirements in Tables 3-6 and 3-10. The delivered half wavefront error (HWFE), or equivalent surface error, ensures diffraction-limited performance at $\lambda = 1\,\mathrm{mm}$: the scan pointing knowledge ensures that mixing of E to B modes due to pointing errors does not limit measurements of r [494]; the scan following error is small enough to ensure uniform coverage of the target field; the scan speed is fast enough to freeze atmospheric brightness fluctuations (typically at a height of 1 km, and drifting along at $10\,\mathrm{m\,s^{-1}}$, so the speed on the sky is $0.6\,\mathrm{deg\ s^{-1}}$); the scan turn around time allows efficient observations (scans are typically a few tens of seconds, so any wasted time must be just a few seconds); and the emissivity is small enough to ensure that loading on the detectors is dominated by the CMB and atmosphere, not the telescope.

Achieving the low noise requires ≈ 250,000 detectors, but the large telescopes in Stage-3 experiments only support ≈ 10,000 detectors. Large telescopes are expensive, so a design with many more detectors per telescope is critical for controlling the overall cost. A wide-field telescope design can support ≈ 100,000 detectors; just three of these telescopes will be needed for both the deep and wide field survey and for the ultra-deep survey.

Low noise is only useful if systematic errors are also small. Systematic errors are dominated by unwanted pickup through the telescope sidelobes. Ground pickup is the main effect, but pickup from the galaxy, Sun, and Moon are also a concern. Minimizing the telescope sidelobes is therefore a key design driver. Sidelobe calculations are notoriously difficult and inaccurate, so the design has to rely heavily on practical experience from Stage-3 experiments. Small sidelobes require: (i) an unblocked (i.e., offset) optical configuration; (ii) low illumination of the mirror edges (i.e., small spillover); (iii) small scattering due to gaps between mirror panels; (iv) large clearances to avoid clipping of the beam by telescope structures; and (v) absorbing baffles

Subsystem	Loss 30/40/95/150/220/270 GHz	Temperature (K)	Notes
Camera window	0.001/0.002/0.005/0.01/0.015/0.02	300	1/2 inch UHMWPE
Filters			
Alumina	0.0002/0.0003/0.0006/0.001/0.0015/0.002	80	2 mm thick
IR blockers	0.004	300, 80, 40, 4	4 blockers
Low-pass	0.03	4, 1, 0.1	3 filters
Lenses	0.006/0.009/0.02/0.03/0.05/0.06	4, 1, 1	3 lenses
Feedhorn	0.72/0.51/0.75/0.57/0.35/0.20	1	Spillover on cold stop
Total	0.77/0.57/0.82/0.67/0.48/0.36		

Table 3-5: Update with latest calculations and for both telescope designs. Optical loss budget used for sensitivity calculations. See Table **??** for filter details.

and reflective shields to terminate unwanted sidelobes on stable surfaces, or on the cold sky. The large telescopes in Stage-3 experiments all have reflective, comoving shields that wrap around the lower part of the telescope; CMB-S4 telescopes will have more extensive shielding around the entire telescope.

Spillover onto warm surfaces increases loading on the detectors, which in turn increases the noise. Spillover is always a challenge, but the requirements for CMB-S4 are similar to those for Stage-3 experiments, so the same general approach can be used: a cold stop to limit the size of the beam on the mirrors; and oversized mirrors to direct any spillover onto the cold sky.

Polarization errors are not a strong design driver for the large-telescope mirror configuration, because those polarization errors are generally much smaller than those associated with the planar antennas or horns that feed the detectors.

If CMB-S4 is to achieve its science goals in a reasonable time, the observing efficiency must be high, so the telescopes must be reliable and easy to maintain. In practice, this means locating the drive mechanisms and electronics in protected areas, with easy access, providing lifting equipment to support the removal and installation of heavy motors, gearboxes, and brakes, and planning for on-site replacement of the axis bearings.

3.5.1.2 Introduction to Designs

The different science goals, surveys, and environments of the LATs have led to the development of different designs for the South Pole LAT (SPLAT, §3.5.2) and the Chilean LAT (CHLAT, §3.5.3).

(emphasize need to control systematics for SPLAT and the need for better resolution plus design maturity for CHLAT.)

3.5.2 South Pole Large Aperture Telescope (SPLAT) *(Emerson and Carlstrom)*

The South Pole Large Aperture Telescope (SPLAT) is an off-axis Three-Mirror Anastigmat (TMA) on an elevation over azimuth mount with an additional boresight rotation axis. The design incorporates a unique combination of features not seen before in a telescope of this size, that are key to achieving the science goals. Full bore-sight rotation allows for measurement and characterization of polarization errors. The 5m diameter primary aperture gives an angular resolution of 1.7' at $\lambda = 2$ mm. Monolithic mirrors avoid segment gaps for low scattering. The TMA layout enables high throughput with a 9.4 deg Field of View. A co-moving shield, surrounding the full telescope optics, controls pickup.

The elevation axis stands about 16m above the foundation raft, while the elevation structure has a maximum vertical sweep radius of about 16m. The total mass of the structure above the raft stands at about 414 tons.

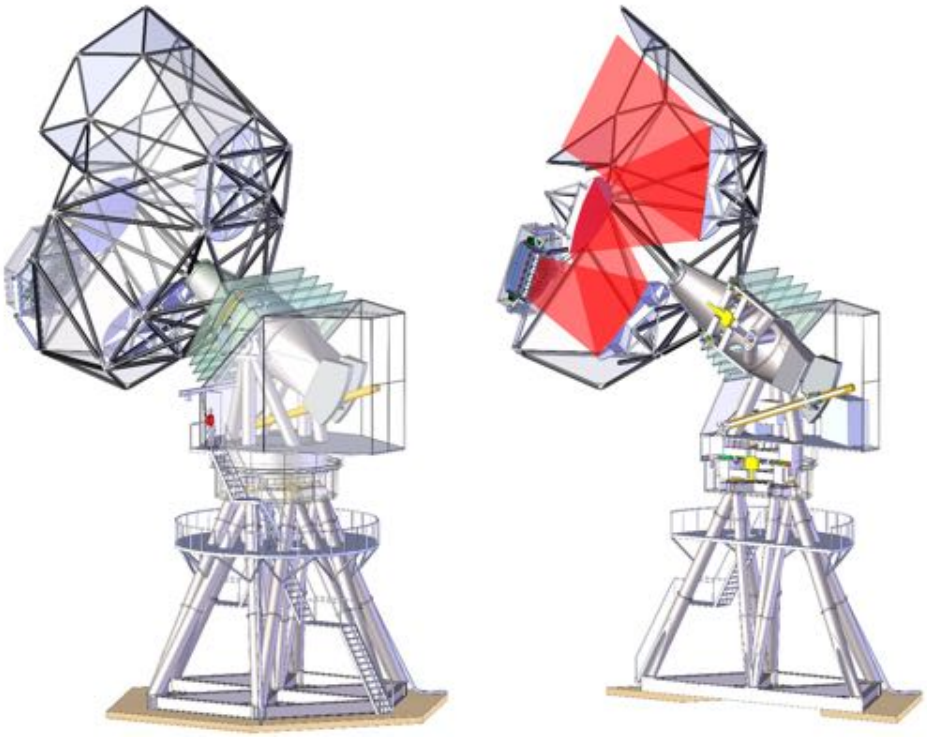

Figure 44: The receiver and three mirrors (M1, M2, and M3) are attached to the elevation tipping structure, which is completely surrounded by a co-moving baffle. The entire tipping structure rotates about the bore-sight axis. A flexible baffle extends from the bottom of the tipping structure down to the azimuth equipment cabin, which encloses all of the azimuth and elevation drive components. The elevation drive is a 7m long ball screw and nut driven by direct drive motor, while the azimuth and bore-sight axes are driven by direct drive motors built around large slew bearings. The azimuth moving structure sits atop a tall steel tower.

3.5.2.1 Requirements and Specifications

The SPLAT requirements and specifications are summarized in tables 3-6, 3-7, and 3-8.

Parameter	Value	Notes
Aperture diameter	5 m	1.7 arcmin beamwidth at 150 GHz
HWFE	$< 37\,\mu$m rms	80% Strehl ratio at $\lambda = 1$ mm
Scan pointing knowledge	< 5 arcsec rms	$< 1/10$th beamwidth at $\lambda = 1$ mm
Scan following error	< 10 arcsec rms	1/4 beamwidth at $\lambda = 1$ mm
Scan speed	3 deg s^{-1}	≈ 1 deg s^{-1} on the sky to freeze atmosphere
Scan turn around time	2 s	requires 6 deg s^{-2} acceleration
Emissivity	< 0.01	cf. a few % atmospheric loss at mm wavelengths

Table 3-6: South Pole Large Aperture Telescope (SPLAT) design requirements.

Contribution	HWFE (um RMS)	Notes
Aberrations	11.9	Uncorrected optical aberrations of TMA
Primary Mirror	26.3	Manufacturing and operational loads
Secondary Mirror	18.6	Manufacturing and operational loads
Tertiary Mirror	26.3	Manufacturing and operational loads
Tipping structure	12.2	Relative motion of mirrors
Total Telescope (RSS)	44.6	

Table 3-7: SPLAT HWFE Budget

Load case	Limit	Notes
Wind speed (ms^{-1})	35	Highest recorded 26
Seismic acceleration (g)	0	No earthquakes at the South Pole
Ambient temperature (C)	-10 to -90	Lowest recorded -83 C; highest -12
Ice (cm)	1	On all surfaces

Table 3-8: SPLAT Survival requirements.

3.5.2.2 Optical Design

The SPLAT design builds on a three mirror system concept proposed by S. Padin [2018 Applied Optics paper]. The main difference from the concept proposed in Padin 2018 is the use of freeform surfaces which enable great flexibility on the optical design and therefore allow to respect mechanical constraints. The proposed system is an f/2.6 telescope which differs from the original f/3.7. This modification yields a moderate increase in field curvature in exchange of a faster system. A TMA design offers a very large diffraction-limited FOV because its three surfaces have enough degrees of freedom to correct all the first order aberration, giving a very large field of view of about 9 deg at $\lambda \geq 1$ mm.

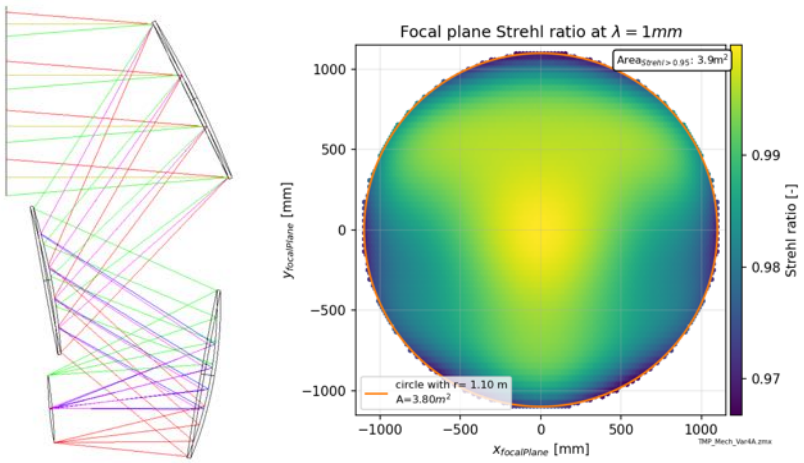

Figure 45: TMA Optical Layout - Left: raytrace of the three mirror anastigmatic system (TMA). Right: Image quality for this three mirror system quantified using the Strehl ratio, where unity corresponds to the best performance achievable.

Mirrors The primary mirror aperture is 5m, with the major diameter of about 5.7m due to the angle of incidence of the offset design. The tertiary mirror is of similar size, while the secondary mirror is only slightly smaller. The mirror sizes are summarized in Table 3-9.

The mirrors are machined aluminum. The mirror blanks are assembled from 2 or 6 solid aluminum billets, then assembled together before being machined as a single piece. This avoids unwanted pickup that would result from scattering at gaps between panels of a segmented mirror. They are supported by an aluminum space-frame cone at 6 points on the back of the mirror. The 6 points also allow the cone to be used as a warping harness to take out some low-order manufacturing errors.

The aluminum mirror support cones attach to the CFRP Tipping Structure at 2 nodes on the central strut of the aluminum cone, decoupling mirror distortions from deformations of the tipping structure.

At the South Pole, telescope mirrors generally have to be heated about 1K above ambient to prevent icing during the long polar night. The temperature rise is small, so thermal deformation is not an issue, but provision must be made to apply heat uniformly over the back of the mirror. For the machined aluminum panels on the 10-m SPT, we typically apply 50 Wm^{-2} to keep the surface clean, which adds up to about 3.1kW for the baseline design.

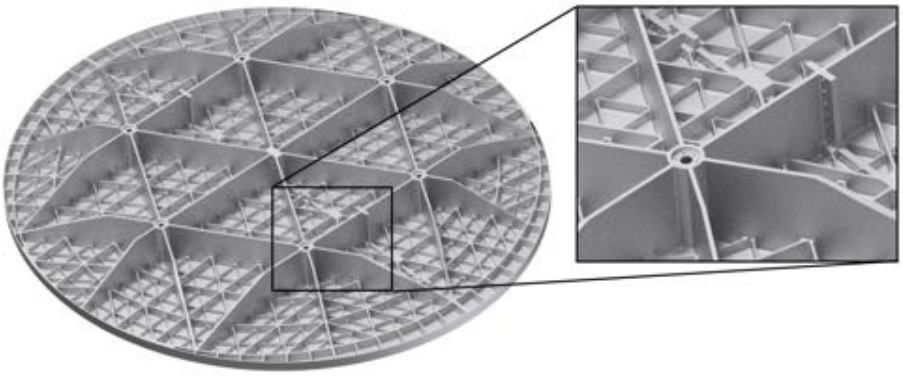

Figure 46: Rear rib structure of the primary mirror. The two halves are premachined on the rear side, and after mating faces are machined flat they are bolted and pinned together. Finally the front surface is machined to final figure.

Mirror	Major Axis	Minor Axis
M1	5.70 m	5.04 m
M2	4.86 m	3.56 m
M3	5.56 m	5.38 m

Table 3-9: SPLAT Mirror sizes

Monolithic aluminum mirrors of this size have not been built before at the surface accuracy required for CMB-S4. To mitigate the risk associated with this, a prototype mirror is being fabricated to validate manufacturing procedures and surface verification methods.

3.5.2.3 Engineering

CFRP Tipping Structure The co-moving optics and Receiver are supported by a CFRP spaceframe tipping structure. This structure must maintain the relative alignment of the mirrors, receiver, and baffle. No active mirror positioning is planned, but the receiver is mounted to a hexapod to allow refocusing.

For gravitational and thermal deformation, the main issue is image quality. Wind drives the pointing performance. To maintain a Strehl ratio degradation less than 5% at the edge of the field, the alignment of the mirrors must be maintained to the level of a few millimeters.

Thermal deformations less than 1mm require a CTE of less than 2.5ppm/K for a 10m structure with 40K soak temperature change.

CFRP is chosen as the material for the tipping structure spaceframe. This meets the thermal deformation requirements due to the low Coefficient of Thermal Expansion (CTE), while also minimizing the moving mass of the structure and maximizing specific stiffness.

Because a spaceframe structure relies almost entirely on axial stiffness of the struts, the analysis is simplified and the CFRP fiber orientations of the struts can be tailored to maximize this axial stiffness, as well as minimizing the CTE. The CTE of the layup for the baseline design is actually slightly negative, but this will be increased slightly due to the positive CTE of the stainless steel nodes.

The strut end fittings have an Invar insert to match the CTE of the CFRP tube, with a captive steel bolt that can be tightened from the outside. The length of the fitting is adjustable, so they can be set in the factory and adjusted in the field if necessary.

Each of the nodes at the many junctions of the CFRP struts will be largely unique. Fabrication is nominally by welding of steel plates followed by machining of the mating surfaces and threaded holes. 3D metal printing is also being investigated as an alternative way to fabricate these complicated metal structures efficiently.

The Tipping Structure is connected directly to an insulated rolled steel cone, which provides a stiff connection to the PA bearing and drive. At the top of the steel cone is space and access to mount a laser tracker, which will be used to verify alignment of the mirrors and receiver mounting structure. The lowest fundamental frequency of the Tipping structure, when fixed at the cone, is close to 8Hz. The entire telescope has a lowest fundamental frequency of about to 4Hz.

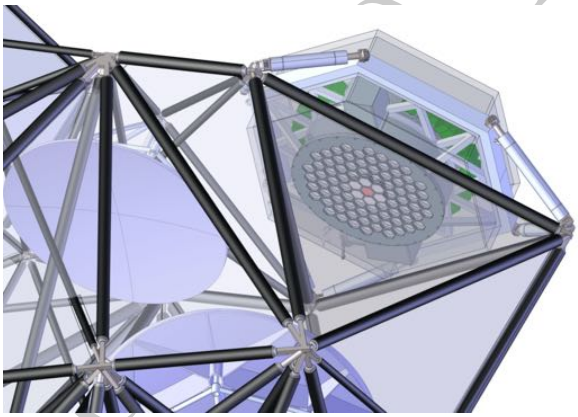

Figure 47: The LATR mounts to the top of the tipping structure via an adjustable hexapod. The entire receiver is surrounded by a lightweight insulated enclosure, with an RF-transparent foam window just in front of the receiver front plate. The hexapod actuators are individually insulated and warmed. Also shown are welded steel nodes at the intersection of CFRP struts.

Receiver Mount The SPLAT Receiver (SPLATR) is supported by a hexapod attached to a stiff, triangular frame at the top of the tipping structure truss. Focus adjustments require just a few tens of millimeters of range in the hexapod arms, but the camera is heavy (about 5t) and in an exposed location.

The camera and nearby electronics will be surrounded by a lightweight heated enclosure to protect seals, connectors, and sensitive electronics. The front of the receiver will be covered by an RF transparent foam window.

The receiver hexapod has ball screws with nuts driven by direct drive motors. Each motor has a single turn optical encoder that is used for commutation and absolute position measurements of the hexapod arms. A battery-backed electronic turns counter keeps track of motor revolutions for the arm length measurement. The ball screw has a multi-turn absolute optical encoder for a second precision measurement of arm length,

and a magnetostrictive linear sensor mounted in the tube that supports the ball nut provides a third absolute measurement of arm length to about 0.1 mm. Since there are 3 independent measures of arm length, the hexapod does not have limit switches, but the ball screws have hard mechanical stops to prevent over travel in both directions. Each arm has a spring-actuated, solenoid-released brake to hold the position of the camera when the hexapod drives are not active. The hexapod arms are enclosed in rigid, heated, insulated boxes, with flexible blankets at each end to cover the universal joint

Baffles In order to control sidelobes, the truss is completely covered with a baffle, leaving just a hole in the top for the beam to enter. The baffle is made of lightweight panels that can be covered with reflecting foil, millimeter-wavelength absorber, or a scattering surface. Baffles around the mirror and receiver support struts are attached directly to the struts. Additional struts extend up above the primary mirror to surround the incoming beam.

The panels have a foam core and thin CFRP face sheets on both sides. They attach to the inside of the CFRP truss using p-clips.

Non-sequential ray-tracing simulations have shown that reflective walls for the TMA baffles create sharp sidelobe features, with power spectra up to 100x worse than measurements and simulations of SPT. However, simulations of a scattering surface show power spectra 10x better than SPT. Studies are underway to develop realistic surface texture profiles, potentially with multi-scale structures, which could be manufactured on a large scale. Candidate profiles are being simulated with raytracing and verified using 3D printing and lab testing.

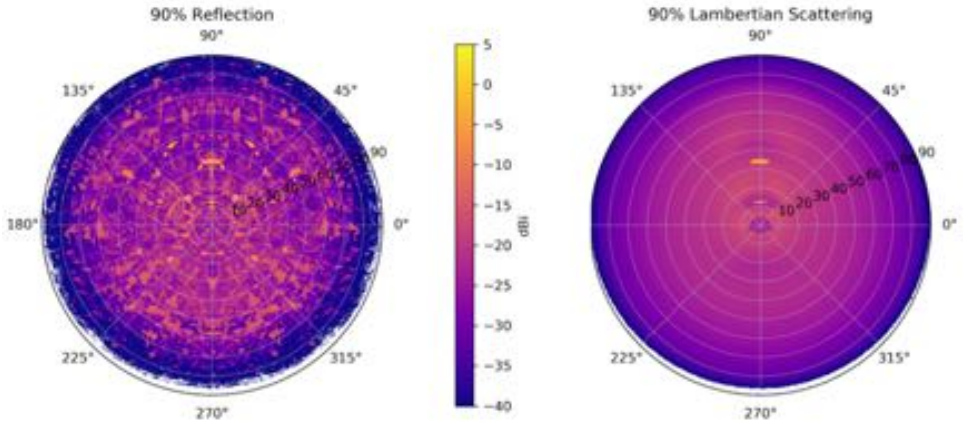

Figure 48: TMA Sidelobe Map - specular vs lambertian baffle walls

PA Axis (Boresight Rotation) Between the elevation axis and the Tipping Structure is the Boresight Rotation or Parallactic Angle (PA)slew bearing and drive. The PA axis uses direct drive motors for high stiffness, low backlash, and minimal maintenance. Motor segments are distributed around the circumference of the PA bearing.

An optical strip encoder around the PA bearing provides absolute positioning and commutation for the direct drive motor. Spring actuated, hydraulically released brakes hold the axis in high winds and when the drives are not active. A rotary joint at the center of the PA cone carries helium, power, fiber ethernet, and

nitrogen gas for the camera windows. Rotary joints have been used successfully for helium, power, and DC connections in the BICEP and Keck Array telescopes.

There are no limit switches or hard stops, since the axis can rotate continuously.

Telescope Mount The mount maintains the pointing of the telescope to within 5 arcsec rms. Wind is the main concern because it varies on short timescales. Observations typically involve scanning over the target field at 3 deg s-1, taking just a few seconds to turn around, so the acceleration during turnarounds must be 4 deg s2.

Temperatures at the South Pole can be as low as -80C (cf. -20C for Chile), so bearings, drive motors, electronics, and wiring that are appropriate for Chile may not work at the South Pole. These elements can be heated to address the lower temperatures after enclosing the bearings and isolating the instrument space from ambient temperature. Heating in general results in thermal deformations, which can affect pointing and will be addressed through a combination of modeling and measurements during commissioning.

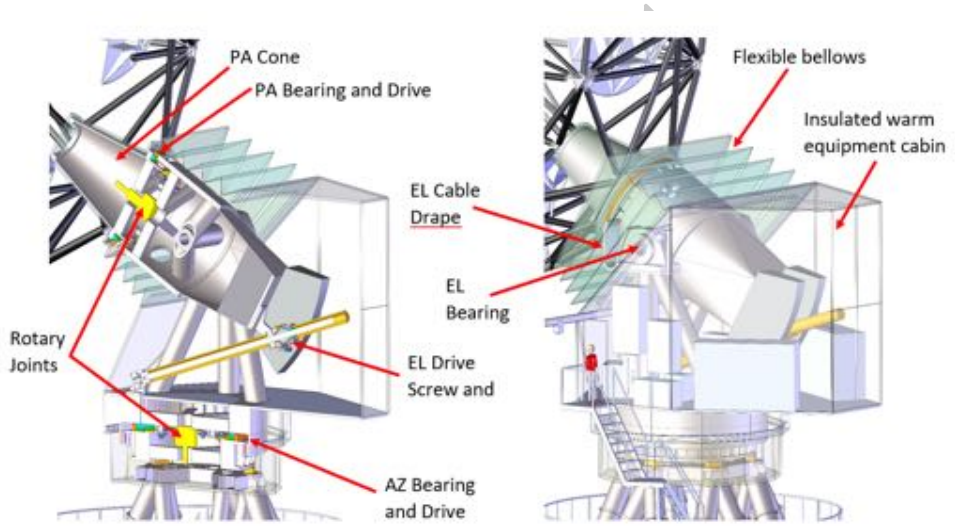

Figure 49: TMA Mount Structure. The entire elevation and azimuth mount structure is enclosed by an insulated room, kept warm by waste heat from onboard compressors and other electrical equipment. One rotary joint carry power and communication across the azimuth axis. Another rotary joint carries power, communications, and helium across the PA axis. A simple cable drape carries cabling and helium pipes across the limited-motion elevation axis.

Elevation Structure and Drive The elevation axis is a 0.6 m diameter steel shaft, supported at each end by a spherical roller bearing mounted in a standard pillow block. The pillow blocks sit on top of tripods that run directly down to the Azimuth bearing.

The elevation drive is a 7m long ball screw actuator with a non-rotating screw and a nut driven by a direct drive motor. Stiffness is the main design driver for the actuator, so it uses the largest diameter ball screw that is readily available, 160mm. The actuator has a universal joint at each end to avoid alignment problems. The actuator must accelerate the tipping structure during scan turnarounds and also support any imbalance in the tipping structure. The motor has a single-turn absolute optical encoder with a battery-backed electronic

turns counter. The encoder is used for commutation and for precision measurements of the actuator length, but the primary measurement of tipping structure elevation comes from a tape encoder on one end of the elevation shaft. A single encoder is sufficient because the elevation drive cannot twist the structure. A laser sensor mounted on the actuator universal joints provides an independent absolute measurement of actuator length to 0.5 mm, and a tiltmeter is mounted on the tipping structure to measure elevation within a few arcmin. The EL actuator has a spring-actuated, hydraulically-released brake to hold the position of the tipping structure when the drive is not active.

Azimuth Structure and Drive The azimuth (AZ) axis mechanism is a slightly larger version of the PA axis. A slew bearing connects the Support tower to the elevation tripod towers via a large ring beam structure. Direct drive motors are used for axis motion, and an optical strip encoder measures absolute position. Spring actuated, hydraulically released brakes hold the axis in high winds and when the drives are not active.

A rotary joint at the center of the azimuth bearing carries only power and fiber ethernet. The rotary joint allows continuous azimuth rotation, so hard stops and limit switches are not required.

An enclosed equipment platform surrounds the elevation structure and provides a protected space for drive cabinets, electrical cabinets, compressors, heat exchangers, and other drive components. The elevation drive ball screw mechanism is also completely enclosed within the azimuth cabin. The insulated space extends from the azimuth bearing up to the PA bearing, through a flexible bellows that accommodates motion in elevation. The compartment is warmed by waste heat from the compressors and other electronics.

A jib crane on the azimuth platform enables equipment installation and removal.

Tower Telescopes at the South Pole must be mounted on towers to give a reasonable lifetime before snow starts to bury the structure. Existing telescopes are on 5-8 m towers which sit on wood rafts. The SPLAT requires additional height to give clearance for the tipping structure, so the tower height is 10.3m. The addition of a tower reduces the stiffness of the telescope structure, resulting in worse pointing and scanning performance.

Control and Monitoring The SPLAT will have a stand-alone control system that follows a path commanded by the observatory control system, with offsets based on a generic set of scan patterns. The telescope control system works in (AZ,EL) coordinates; conversion from celestial coordinates is handled at higher level in the observatory control system using an open-source astrometry package. The telescope control system commands the motor control loops to move within safe limits, and monitors the actual positions of the telescope axes and the status of the drive systems.

Safety Telescope safety is managed by a safety-rated programmable logic controller that monitors axis limit switches and speed sensors, e-stop switches, lockouts, and access interlocks. Lights on the outside of the telescope indicate when it is safe to approach. Enclosed spaces have fire and carbon-monoxide sensors, and there are cameras for remote monitoring. The telescope design follows fire and electrical codes (NFPA 70 and similar IEC standards) and structural safety standards (DIN 18800).

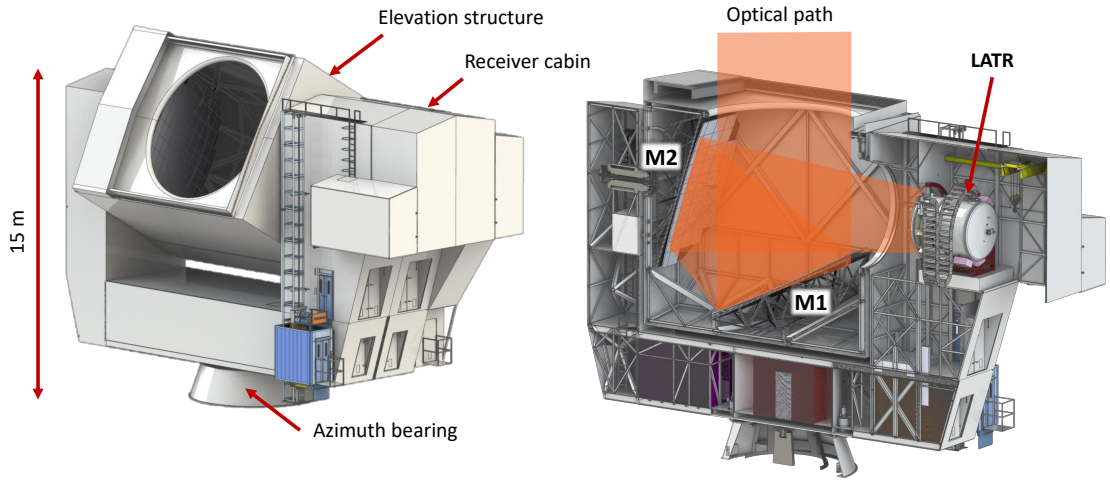

Figure 50: The Chilean Large Aperture Telescope design is based on the design of the CCAT-prime and SO-LAT telescopes [495, 496]. The mirrors (M1 and M2) are completely enclosed in the co-moving elevation structure (left), which will improve sidelobe mitigation compared to existing telescopes. The Large Aperture Telescope receiver (LATR, right) is aligned with the telescope elevation axis. This enables two new and valuable features for suppressing systematics compared to existing large telescopes: (1) the LATR can either track the elevation angle of the telescope or to be rotated independently of the telescope angle; and (2) partial boresight rotation of the telescope can be achieved because the telescope boresight can be rotated from one horizon to the other, between 0 and 180°.

3.5.3 Chile Large Aperture Telescopes (CHLATs) *(Emerson and Niemack)*

The Chilean large aperture telescopes are a 6-m crossed-Dragone design on a conventional elevation over azimuth mount, with the instrument boresight aligned with the elevation axis. This alignment facilitates instrument rotation and enables partial telescope boresight rotation, because the elevation axis can rotate a full 180°, from horizon to horizon, enabling two distinct telescope orientations at every azimuth position. The design copies the CCAT-prime and SO-LAT designs.

The reference design has two new large telescopes in Chile to support the deep and wide survey. An option is to re-use the SO-LAT and CCAT-prime, in which case no new large telescopes would be built for Chile.

Since the telescopes are copies of the SO-LAT and CCAT-prime, no prototyping is needed, and procurement contracts can be awarded early, so telescope testing can be completed before cameras are delivered.

3.5.3.1 Requirements and Specifications

The CHLAT requirements and specifications are summarized in tables 3-10, 3-11, and 3-12.

Parameter	Value	Notes
Aperture diameter[a]	5.5 m	1.5 arcmin beamwidth at 150 GHz
HWFE	$< 37\,\mu$m rms	80% Strehl ratio at $\lambda = 1$ mm
Scan pointing knowledge	< 5 arcsec rms	$< 1/10$th beamwidth at $\lambda = 1$ mm
Scan following error	< 10 arcsec rms	1/4 beamwidth at $\lambda = 1$ mm
Scan speed AZ(EL)	$3(1.5)$ deg s^{-1}	≈ 1 deg s^{-1} on the sky to freeze atmosphere
Scan turn around time	2 s	requires 6 deg s^{-2} acceleration
Emissivity	< 0.01	cf. a few % atmospheric loss at mm wavelengths

Table 3-10: Chilean large telescope design requirements. Note: (*a*) the physical aperture should be a little larger, e.g., 6 m, in order to reduce spillover and scattering.

Subsystem	HWFE (μm rms)
Primary	18
Secondary	15
Telescope alignment	21
Camera filters	10
Camera lenses	10
Camera alignment	10
Total	36

Table 3-11: CHLAT HWFE budget. Telescope errors include gravity, 15-K ambient temperature change, 1.4-K temperature gradients (in direct sunlight), 9 m s^{-1} wind (3rd quartile in Chile), and 0 scan acceleration.

Load case	
Wind speed (ms^{-1})	69
Seismic acceleration (g)	1/3
Ambient temperature (C)	-30
Ice (cm)	1
Snow[a] (cm)	120

Table 3-12: CHLAT Survival requirements. Note: (*a*) 100 kg m^{-3}.

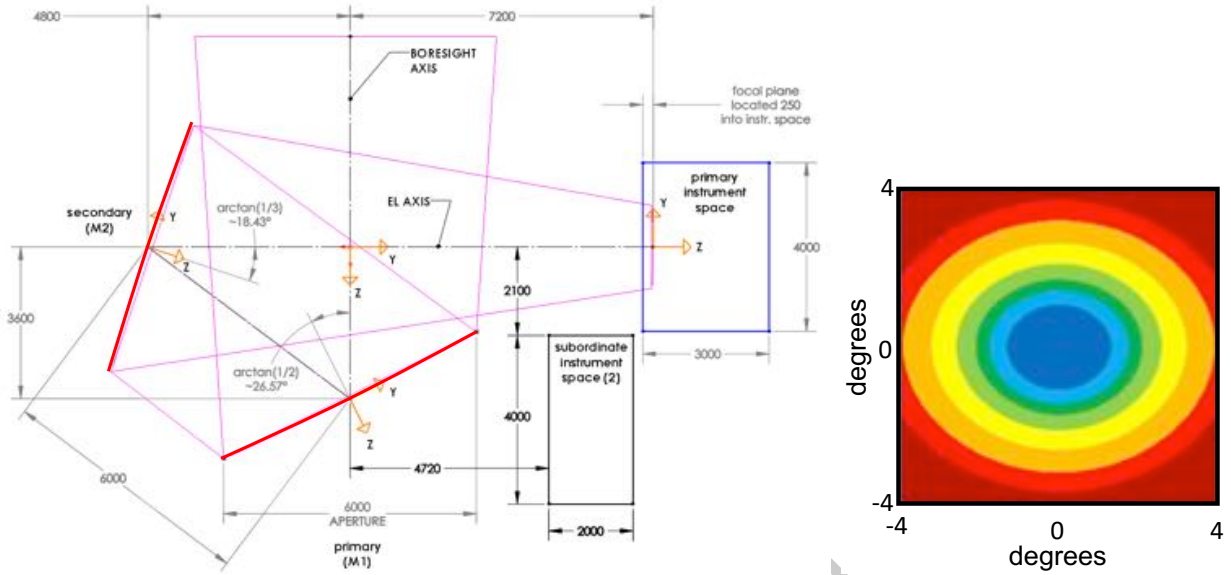

Figure 51: Mirror optics definition (left) for the CCAT-prime and SO-LAT [502]. The pink rays indicate the geometric keepout zones for a 7.8° diameter FOV illuminating the full 6-m aperture primary mirror. The primary and secondary instrument spaces are also shown. The mirrors alone provide diffraction-limited image quality across much of the usable FOV as shown by the contours (right). The contour colors (blue through red) show the regions where the Strehl ratio is > 80% at 870, 490, 345, 230, 150, 100, and 75 GHz [495]. Refractive optics can improve the optical performance beyond what is shown here within individual optics tubes.

3.5.3.2 Optical Design

The high-throughput off-axis crossed-Dragone (CD) telescope design was first proposed by Corrado Dragone [497]. This configuration has previously been used for CMB measurements by the QUIET [498] and ABS [499] projects. Larger-aperture CD designs were recently shown to be capable of achieving many times larger throughput than existing 5–10 m microwave telescopes, particularly when combined with refractive optics tubes [500]. In 2017 a 6 m CD design that includes coma corrections [501] was adopted for CCAT-prime and the Simons Observatory (Fig. 50) [502, 496, 495], and both telescopes are scheduled to begin observations in Chile in 2022.

The CD layout offers several advantages compared to other telescope designs. For CMB-S4 the most important advantages are the large diffraction-limited field of view (FOV) combined with the compactness of the two mirror configuration (Figs. 50 and 51). While modestly larger diffraction-limited FOVs have been achieved with other telescope configurations, including three mirror anastigmat designs, the alternative designs were not nearly as compact and use of a third mirror will degrade the sensitivity of the detectors due to the extra mirror emission.

The polarization properties of the CD configuration have been shown to be superior to Gregorian and Cassegrain designs, which is in part due to the smaller angles of incidence on the reflecting surfaces [503]. Systematics associated with the telescope mirrors are much smaller than systematics caused by the lenses, filters, and feedhorns inside the cameras [504, 505].

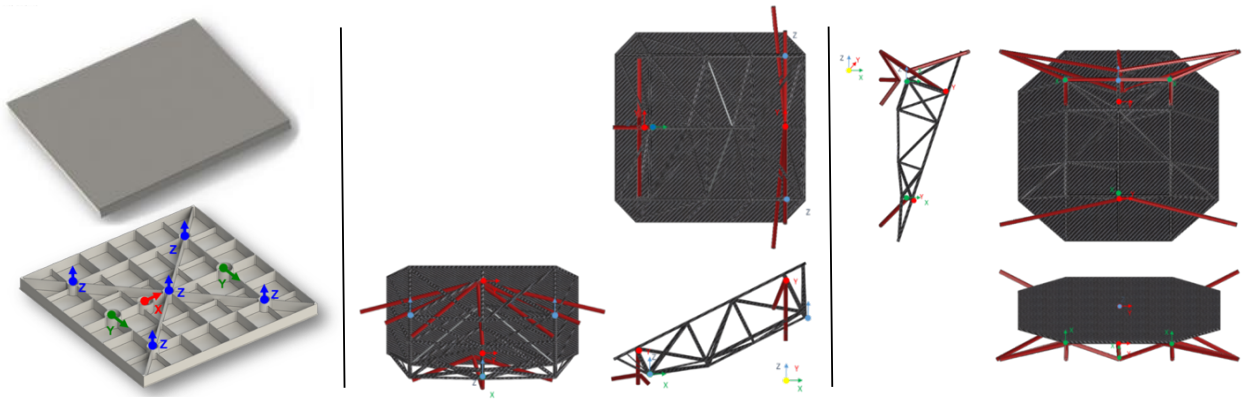

Figure 52: *Left:* Mirror panel views, reflecting surface (top), backside (bottom). The panel is 700 mm on a side and significantly light-weighted from a solid block of aluminum. Eight adjusters locate the panel. The five z-axis adjusters allow for some compensation of low order distortions. *Middle:* Three views of a preliminary carbon fiber bus structure for the primary mirror panels. The red elements are tuned CTE beams that minimize the half wavefront error and pointing error due to imperfect mirror alignment from thermal effects. *Right:* Similar views of the carbon fiber bus structure for the secondary mirror panels.

The mirrors are each approximately 6 m in diameter and will be segmented into many panels (Fig. 52) [495]. All mirrors on CMB telescopes near this diameter have been segmented thus far. The sidelobe pickup associated with the gaps between the mirrors is sufficiently small that it will not contaminate the high multipole E-mode polarization, lensing B modes, or temperature signals that will be the foci of measurements with these telescopes. The gaps between the mirrors for the CCAT-prime/SO-LAT design are required to be <0.5% per mirror at the nominal observing temperatures. This requirement both minimizes loss in the gaps and minimizes the amplitude of the sidelobes due to the panel gaps. The mirrors are supported by carbon fiber bus structures as shown in Fig. 52 to minmize variations in HWFE and pointing error due to thermal variations. Table 3-11 shows the HWFE budget.

The reference design provides a CD FOV that is >2 m diameter. An FOV this large can make coupling to arrays of detectors challenging. A natural approach to take advantage of such as large FOV is to split it into multiple independent optical paths or optics tubes [500, 506]. These optics tubes are designed to be modular and easily replaceable, which facilitates deployment of different frequencies in each optics tube. Each tube has an independent image of the primary, or Lyot stop, to control illumination of the telescope mirrors. The stop is cooled to 1 K to minimize excess background loading on the detectors. The reference Lyot stop design would geometrically illuminate 5.5 m of the 6.0-m aperture primary mirror. Thus, the mirror will provide a 0.25-m baffle in radius to control diffracted spillover [504].

Several different sizes of optics tubes have been studied for the SO-LAT/CCAT-prime telescope design, ranging from 0.2 m to 2 m diameter optics. There are a variety of practical constraints on the detector array size (detectors are typically fabricated on 150 mm wafers), availability of optics materials (e.g., the maximum single crystal silicon diameter is 450 mm), vacuum windows, filters, and mechanical structure between tubes that influence the optimal optics tube size. A few of the optics tube options that were studied and compared are discussed in [506, 507]. These and related cost versus sensitivity analyses led to the selection of optics tubes with 220 mm spacing for the preliminary baseline design. One of the appealing features of this selection is that each optics tube couples to a single detector array module, such that only one detector array and detector module design is required for each frequency.

The detector arrays within each optics tube will be feedhorn-coupled transition-edge sensor detectors. Feedhorns are one of the most mature technologies for controlling polarization systematics. They have circular beams and small polarization errors. By coupling the feedhorns through a cryogenic Lyot stop, they can be packed much more closely together, which improves the overall instrument sensitivity, but can significantly increase detector count. Roughly half of the beam from each feedhorn falls on the Lyot stop (see Table 3-5), but the sensitivity degradation is small because the stop is cold (1 K).

3.5.3.3 Engineering

Mount The mount is a fork-style elevation over azimuth design, sized to accommodate the crossed-Dragone optical layout. The mount has three main parts: a fixed support cone at the base; the yoke, which rotates in azimuth and contains all the science equipment; and the elevation housing that supports the mirrors. The design allows for elevation angles past zenith, which is useful for measuring systematic errors, and can even be driven to $-90°$ to facilitate maintenance. The chief ray between the secondary and the focal plane is along the elevation axis, so the camera can be attached to the yoke structure. Gravity acts mostly in-plane for the secondary mirror, minimizing gravitational deformation. The overall size of the structure is approximately 23 m long × 8 m wide × 16 m tall, with the elevation axis ≈ 11 m above ground for the Chile version. The total weight is 210 T (see Table 3-13).

The elevation housing contains the primary and secondary mirrors. The beam from the sky enters through a shutter that can be closed during bad weather, reflects off of the primary, over to the secondary, and then exits at a right angle to the entrance beam through the 4-m ID elevation bearing. The focal plane is ≈ 3 m beyond the bearing.

The mount is a welded steel structure, split up into transportable sections. The mirrors have machined aluminum panels, ≈ 0.7 m on a side, mounted on a CFRP back up structure (Fig. 52). Each panel has three adjusters to set the in-plane position, and five adjusters to set the height of the reflecting surface. The five height adjusters allow some correction of low-order machining errors. The back up structure is kinematically attached to the elevation housing via a 6-point connection with three vertical and three horizontal constraints.

The outside of the structure is covered with aluminum-clad insulated panels to reduce pointing errors and HWFE due to thermal gradients, which are driven mainly by solar heating. In order to provide a reasonable operating environment for equipment and personnel, the base of the yoke is temperature controlled to 15±5 C using heaters and waste heat from the science equipment with outside air for cooling. The elevation housing and yoke arms, including the camera space, are actively vented to keep the structures at outside temperature; any electronics attached directly to the camera are also at outside temperature.

Telescope servo cabinets, instrument electronics, and helium compressors are all located inside the base of the yoke, so if the camera does not have a rotator to track parallactic angle, camera connections do not have to pass through a cable wrap. The camera space has a 6-T gantry crane for loading/unloading, positioning, and assembly/disassembly work while the camera is installed.

The scanning requirements of the telescope drive the choice of bearings and drives. The drive has two motor/gearbox units for the elevation axis, and 4 motor/gearbox units for the azimuth axis. The azimuth drives are on the base of the yoke, around the support cone, and the elevation drives are in the yoke arm opposite the camera. Preliminary modal analyses of the structure suggest a first mode with a locked azimuth rotor at 2.6 Hz and a locked rotor elevation mode at 3.0 Hz [502]; both of these frequencies have increased as the design has matured.

Component	Mass (T)
Mirrors[a]	5
Camera	5
EL structure	50
Yoke	135
AZ cone	15
Total	210

Table 3-13: Chilean LAT mass. Note: (*a*) total for primary and secondary, including adjusters and back up structure.

Contribution	Pointing error (arcsec rms)
1.4-K temperature gradients[a]	2.5
$9\,\mathrm{m\,s^{-1}}$ wind[b], 15-K ambient temperature change	0.5
Random errors[c]	0.8
Radio pointing[d]	1
Total	2.9

Table 3-14: CHLAT scan pointing knowledge error budget. Notes: (*a*) In direct sunlight; (*b*) 3rd quartile in Chile; (*c*) bearing wobble, tiltmeter error, encoder coupling; (*d*) the pointing offset is measured every $\approx 1/10\,\mathrm{hr}$ using radio observations of bright point sources.

The pointing performance of the telescope (see Table 3-14) is limited mainly by deformation due to wind forces and insolation. The effects of slowly varying thermal deformation are partly corrected by continuously measuring the locations of the many point sources in each survey patch. The telescope design meets survival requirements for Chile (see Table 3-12).

Baffles and shields Errors in the shape of the beam convert temperature fluctuations on the sky to polarization, so control of systematic errors at a level appropriate for CMB-S4 requires accurate knowledge of the beam. Main-beam errors are a tractable problem for the large telescopes because the beam shape can be measured directly, using a bright source, e.g., a planet, or by filtering the CMB observations with templates that capture the effects of beam errors. In addition, CMB fluctuations on arcminute scales are small, so systematics due to beam errors are also small.

Unwanted pickup through far sidelobes is more complicated, because far sidelobes are difficult to measure or model, especially in polarization. Far sidelobes are generated by scattering from mirror panel gaps, clipping of the beam as it passes by telescope structures, and unwanted lines of sight, e.g., directly from the camera to the sky. The far sidelobes cause unwanted pickup from the ground, Sun, Moon, and galaxy. Recent work using a combination of measurements and ray-tracing has been successfully used to model far sidelobes for ACT [508], and the same techniques are being applied to CCAT-prime and the SO-LAT [504].

Scattering from panel gaps is the dominant source of far sidelobes in telescopes with segmented mirrors. The sidelobes are sharp, arc-like features, that typically account for 1% of the total response [509, 505]. If the sidelobes fall on the ground, they cause enormous pickup, so large CMB telescopes always have comoving ground shields. The shields are usually reflective to direct sidelobes to the cold sky; an absorptive shield

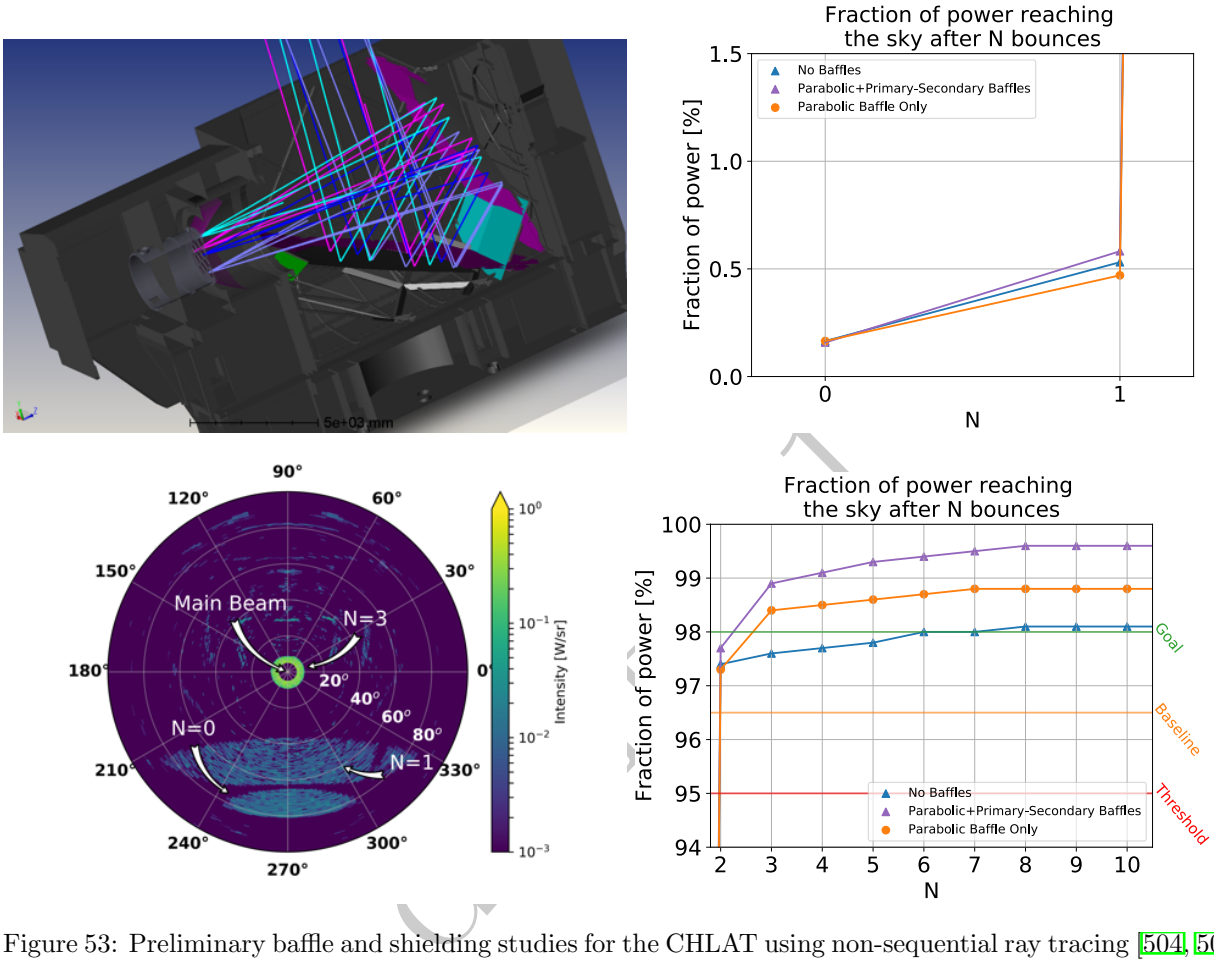

Figure 53: Preliminary baffle and shielding studies for the CHLAT using non-sequential ray tracing [504, 505]. The upper left shows a baffle configuration for the CHLAT that includes a parabolic baffle near the receiver plus large secondary and primary guard ring baffles. Current analyses suggest that having a parabolic or conical baffle (pink, left) near the receiver is important, but the large guard ring baffles (green, teal, and also pink, right) will not be needed. The position of 4 fields being launched from the focal plane of the telescope is also shown. We note that the large co-moving ground shield from the elevation structure will provide more baffling than in any previous large CMB telescope. Upper right (lower right) shows the fractional power that reaches the sky from the center field of the center camera versus number of bounces for a perfectly reflective telescope solid model for N in the interval 0–1 (2–10) bounces. Lower left shows the power density at the sky for N=3 bounces for a configuration with a parabolic baffle alone. Power density at the sky is normalized to have an injected power equal to 1 W. In this configuration, one sidelobe is expected between 60 and 80 degrees, corresponding to the direct line of sight from the receiver camera to the sky. The parabolic baffle forms a ring around the main beam at N=3, which contains most of the difference in power between the parabolic baffle and the no-baffle model. Additional analyses that build on these will inform the desired finish (generally absorbing vs. reflective) for the baffles.

would significantly suppress far sidelobes, giving a cleaner beam, but at the expense of increased loading on the detectors, which would result in lower sensitivity. The mirrors in the CCAT-prime and SO-LAT designs are completely enclosed in a metal box, which naturally acts as a comoving shield. In this respect, the design has better shielding than existing Stage-3 large telescopes.

Low spillover is critical for reducing the loading on the detectors. The part of the beam that does spill beyond the mirror edges is usually managed with reflecting baffles that direct the spillover to the sky, rather than to warm absorbers, essentially trading detector loading for sidelobes. Fig. 53 shows a spillover simulation in which rays are transmitted from the camera windows. With no baffles, the spillover on warm surfaces is $\approx 2\%$, but adding baffles around the camera, and behind the mirrors, reduces the warm spillover to $< 1\%$.

Analysis of fixed ground shields surrounding the entire telescope, as was done for ACT [510], have led to the conclusion that a realistic fixed ground shield would not significantly improve the sidelobe performance of this design. Therefore, fixed ground shields are not included in the design.

Control and monitoring The CHLATs have a stand-alone control system that follows a path commanded by the observatory control system, with offsets based on a generic set of scan patterns. The telescope control system works in (AZ, EL) coordinates; conversion from celestial coordinates is handled at higher level in the observatory control system using an open-source astrometry package. The telescope control system commands the motor control loops to move within safe limits, and monitors the actual positions of the telescope axes and the status of the drive systems.

Encoder positions, with accurate timestamps, and a summary of the drive status and faults, are reported at 200 Hz, and are available to the observatory control system within 1 s, which is fast enough to support decisions that are needed to control observations, e.g., waiting for the telescope to acquire a specific position before starting a scan. Encoder positions, and information about the status of the drive, are recorded continuously, even when observations are not running.

The telescope control system provides tools for debugging drive problems, and for acceptance testing, e.g., plots of axis position and following error vs. time, plots of following error spectral density, and measurements of the drive transfer functions.

Assembly and test The CHLATs will be assembled on-site by a contractor. The contractor could be the telescope designer, a construction company, or some combination of these.

The telescope mirrors need to be assembled and aligned before they are installed in the telescope structure. Assembly and alignment could be done at the factory, as for SO-LAT and CCAT-prime. Even if mirrors are aligned at the factory, the contractor will measure the surface profile immediately before installation using photogrammetry or a laser tracker. Photogrammetry measurements of the ALMA antennas achieved $30\,\mu$m/6 m rms error [511]; a laser tracker is a factor of a few better, with $20\,\mu$m peak error on a 6-m part. Mirror surface measurements will be made at the typical observing temperature in Chile. Following installation in the telescope, the mirror positions will be aligned, again using photogrammetry or a laser tracker.

After assembly, the drive system functions will be tested, and the following error will be measured at the axis encoders to demonstrate that the drive meets the requirements for fast scanning. The pointing stability will be demonstrated using observations of bright stars with a small optical telescope, which is fast, easy, tests many telescope and observatory systems, and quickly reveals problems that are difficult to see with slower radio measurements of the pointing. Drive system functional testing and following error testing are tasks for

the contractor, but pointing measurements will require support from CMB-S4 and use of a commissioning camera (§3.5.5).

Final alignment of the telescope optics will be based on out-of-focus holography measurements using a planet as the source. With a signal to noise ratio of 100 at $\lambda = 3\,\mathrm{mm}$, out-of-focus holography can achieve a few $\times 10\,\mu$m rms for the lowest-order modes of the wavefront error [512]. Holography measurements will be done by CMB-S4 using either a commissioning camera or the full science camera.

Safety Telescope safety is managed by a safety-rated programmable logic controller that monitors axis limit switches and speed sensors, e-stop switches, lockouts, and access interlocks. Lights on the outside of the telescope indicate when it is safe to approach. Enclosed spaces have fire and carbon-monoxide sensors, and there are cameras for remote monitoring. The telescope design follows fire and electrical codes (NFPA 70 and similar IEC standards) and structural safety standards (DIN 18800).

3.5.4 Large Aperture Telescope Receivers (LATRs) *(Benson)*

3.5.4.1 Requirements and Specifications

3.5.4.2 Optical Design *(Gallardo)*

The large aperture receiver is composed of an a array of 85 three lens cameras in an hexagonal packing. Each camera is made of three plano convex silicon lenses and a Lyot stop which reimages the primary mirror. A silica prism (with one side perpendicular to the camera axis and the other side at an angle) is placed in front of the first lens to keep the camera axes parallel. The silica prism surface tilt and clocking is defined such that the chief ray of the center field of each camera lands at the center of the detector focal plane, keeping the three lens system, Lyot stop and detector array on the same axis.

The hexagonal packaging of the optics tubes is described by the equation

$$\begin{bmatrix} x \\ y \end{bmatrix} = \frac{d_{\mathrm{center}}}{\sqrt{3}} \begin{bmatrix} \sqrt{3} & \sqrt{3}/2 \\ 0 & 3/2 \end{bmatrix} \begin{bmatrix} q \\ r \end{bmatrix}, \tag{3.1}$$

where d_{center} is the center to center distance between optics tubes (219mm) and the parameters q and r are indexing integers between -5 and 5. The field lens in the camera is a 20 cm diameter lens while the second and third lenses are limited to be 17 cm in diameter to allow for clamping clearance.

TMA For the TMA design, the surface of each lens $z(r)$ is defined as a conic surface of revolution plus 8 polynomial terms in r, with r measured from the center of the lens according to the equation

$$z(r) = \frac{cr^2}{1 + \sqrt{1 - (1+k)c^2r^2}} + \sum_{j=1}^{8} \alpha_{2j} r^{2j}, \tag{3.2}$$

where c is the curvature (defined as $c = 1/R$, with R the radius of curvature), k is the conic constant, and α_{2j} are the even coefficients of the polynomial expansion.

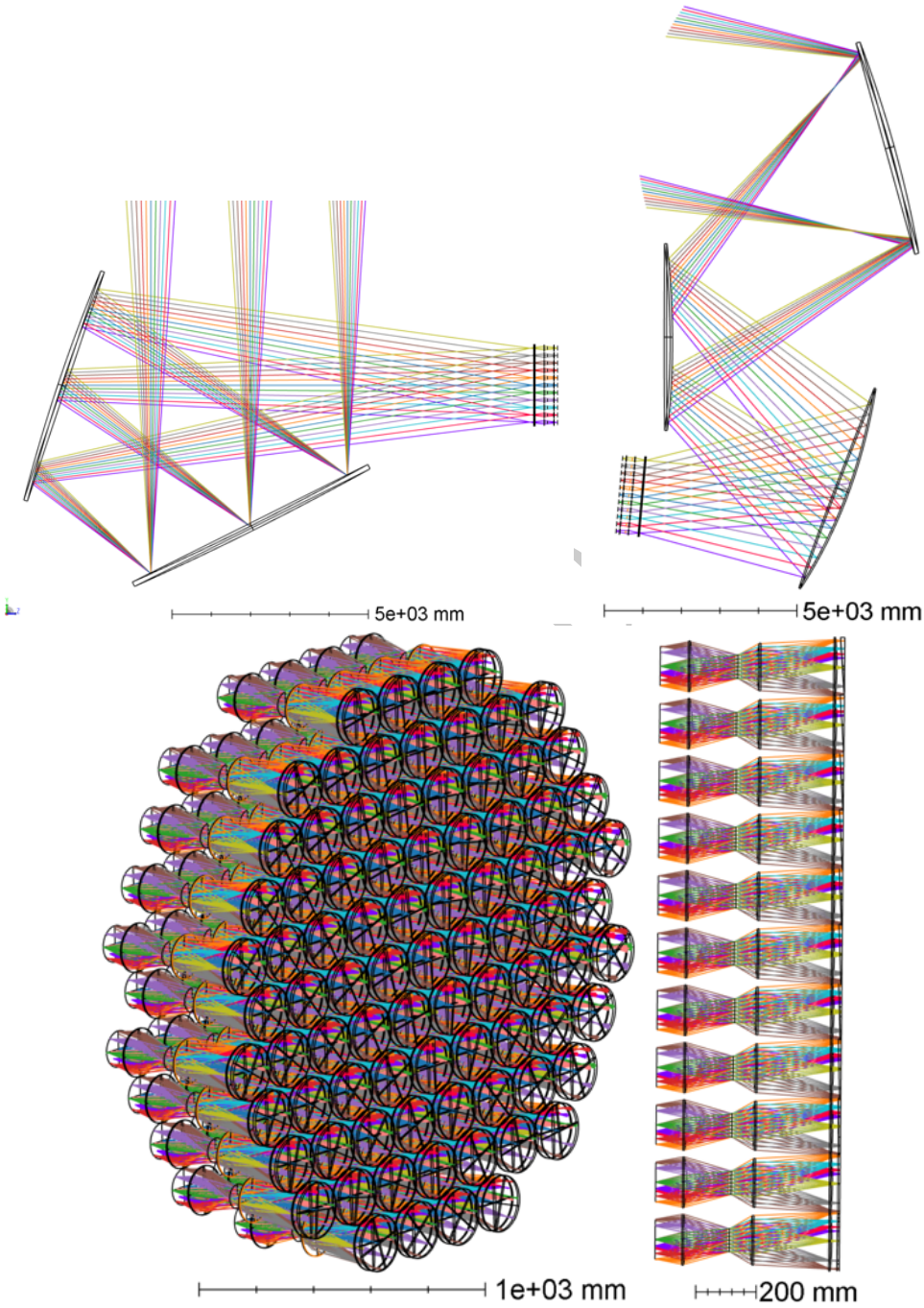

Figure 54: Raytrace of the large aperture telescope receiver configurations. Top Left: Sideview of the crossed Dragone design. Top Right: Sideview of the Three mirror anastigmat. Bottom Left: 85 tubes from the three mirror anastigmat configuration showing the three lens system and the alumina wedge. Bottom Right: three mirror anastigmat camera sideview, the two center rows are shown.

Crossed Dragone The crossed Dragone camera lenses are composed of biconic lenses whith

$$z_{\rm biconic} = \frac{c_x x^2 + c_y y^2}{1 + \sqrt{1 - (1-k_x)c_x^2 x^2 - (1+k_y)c_y^2 y^2}} + \sum_{i=1}^{16} \alpha_i x^i + \sum_{j=1}^{16} \beta_j y^j \tag{3.3}$$

with curvatures given by $c_x = \frac{1}{R_x}$ and $c_y = \frac{1}{R_y}$ and conic constants $k_{x,y}$.

The camera prescription is optimized in Zemax by minimizing the spot diameter at the focal plane, while constraining the system to keep the lens diameters within parameters specified above and the camera length to be no longer than 610 mm. An image of the primary mirror is required between lens 2 and lens 3.

3.5.4.3 Optics Components

The re-imaging cold optics are comprised of lenses, infrared (IR-)blocking, and band-defining filters and spline profiled feedhorns which couple radiation to the detector focal plane.

Silicon lenses are used due to silicon's high index of refraction ($n = 3.4$), low loss-tangent ($\tan\delta \sim 10^{-5}$) and the ability to mitigate refractive reflections with the use of machined metamaterial antireflection coatings. These antireflection coatings have demonstrated control of reflections to the 3×10^{-3} level, which minimizes sensitivity losses due to dielectric reflectance in silicon lenses [513, 514]. The LATR requires fabrication of 20 cm diameter lenses, while silicon is available in sizes up to 46cm. The fabrication of such lenses is being demonstrated concurrently by the Simons Observatory.

The IR blocking filtering scheme is largely based on recent demonstrations from other CMB experiments. The vacuum window will be 3-mm thick layer of ultra-high molecular weight (UHMW) polyethylene [515, 516]. Immediately behind the vacuum window will be a stack of 10-layers of 3-mm thick zotefoam, which acts as a multi-layer IR-filter, then followed by an alumina filter heat-sunk to 50K [517, 518]. The alumina filter will be AR coated using a laminate of plastic layers, as was demonstrated in SPT-3G [519]. The first two silicon lenses will be mounted at 4K and form an image of the telescope primary at a 1K Lyot stop. At the Lyot stop, we will also mount a metal-mesh low-pass filter, fabricated by combining a number of patterned mesh filters into a laminate stack [520], which is designed to block blue leaks in the detector pass-bands that are determined by inline microstrip filters on the detector wafer.

Finally, radiation arriving at the focal plane is coupled to the detectors through a monolithic array of spline-profiled feedhorns fabricated by machining aluminum [492]. These feeds offer tight control over beam systematic effects, ability to optimize the coupling efficiency, and ability to produce these arrays at a relatively low cost per horn. This approach has been used SPTPol, MUSTANG-2, and is being scaled up for Simons Observatory. Production at the required rate for CMB-S4 is a low risk proposition.

3.5.4.4 Cryogenics and Engineering *(Hollister and Mitchell)*

The LATR is a 3.0 m diameter, 4100 kg telescope receiver with 85 optics tubes. Each optics tube reimages the telescope optics onto a detector array that operates at 100 mK (Fig. 55). The cryostat includes four cooled stages at nominal temperatures of 40 K, 4 K, 1 K and 100 mK. The 40 K and 4 K stages are cooled by three pulse tube cryocoolers, while the 1 K and 100 mK stages are cooled by the still and mixing chamber of a modified commercial dilution refrigerator (see Table 3-15). The front plate houses the 85 hexagonal ultra high molecular weight (UHMW) polyethylene windows and, with the stainless steel plate at only 38 mm thick, has a deflection of 14.5 mm under vacuum. The design allows for the simple construction of the coldmass

Table 3-15: LAT receiver refrigerator summary.

Fridge	Type	qty	Cooling capacity per fridge			
			40 K	4 K	1 K	100 mK
PT420	Pulse tube	3	55 W	2 W		
SD400	Dilution	1			25 mW	400 μW

on an assembly platform external to the vacuum vessel. The 50 K shield assembly will be independently installed inside of the vacuum vessel. The completed coldmass will be inserted into the vessel and attached at 6 mounting points and internal to the 50 K shield assembly. The design allows for the series SQUID arrays (SSAs) and associated cabling to be easily accessible without extensive disassembly of the coldmass. To replace an optics tube, cables and thermal connections are removed from the back of the assembly allowing the optics tube to be pulled and replaced from the front. The entire structure will mount to the articulating telescope frame with an array of structural tubes - still under development. The cryogenic system is designed to operate over observing elevations between 5 to 85-degrees, and can allow for ±45 degree boresight rotation over planned survey elevations (40-70 degrees).

The 40 K and 4 K stages are nested cylindrical cans, supported by rings of G10-CR tabs that provide high axial and lateral stiffness, with low thermal conductivity. The tabs accommodate differential thermal contraction between stages by flexing inwards [521]. The 1 K and 100 mK stages are supported by carbon fiber trusses [522]. The complete assembly of cold stages and optics tubes has a total mass of $\sim$ 1 T, which is much larger than in existing CMB cameras, but the large size of the stages results in a stiff support. The cryostat windows are made of 3-mm thick UHMW polyethylene, anti-reflection coated with porous teflon sheets that are hot-pressed onto the window surfaces. The windows are clamped to the vacuum shell front plate with hexagonal metal rings. Heat loads for the complete camera are given in Table 3-16. We note that the dilution fridge has its own PT420, included in Table 3-15, that provides additional cooling power for the camera 40 K stage, but not the camera 4 K stage, which is instead used exclusively for the dilution system.

The LATR has a turbo pump attached to an ISO-150 gate valve on the back of the vacuum shell. The gate valve closes automatically in the event of a power loss. There are KF-50 ports on the front and back, for gauges and additional pumps, and pressure relief valves to protect the windows in case the vacuum shell becomes pressurized.

Cooling of large cryogenic payloads like the LATR is challenging, in particular in cryogen-free systems since 4 K cryocoolers typically have limited cooling power at high temperatures in comparison to liquid cryogens. To address this, we plan to implement a forced-flow gaseous helium system with cooling provided by high capacity external cryocoolers and gas circulation provided by a warm compressor (Fig. 56). Such systems have been used on other large cryogenic systems, such as the SuperCDMS SNOLAB [523] and CUORE [524] particle physics experiments. Helium gas flows in a circuit at a pressure of approximately 10 bar, passing through an external vessel incorporating a counterflow heat exchanger and one or more single stage Gifford-McMahon cryocoolers. The counterflow exchanger is used to cool the inflowing gas by exchange with the returning cold gas flow, the precooled gas then being cooled by the mechanical coolers. The cold gas flows in to the experiment cryostat through a tubing system with direct connection to the four cooled stages of the cryostat. Once the stages have cooled to close to 50 K, at which point the majority of the heat capacity of the metals will have been removed, the gas lines in the receiver cryostat can be isolated by removing bayonets and evacuated to avoid any heat leak resulting from residual helium gas. A system like this is expected to reduce the cooldown time for the LATR from roughly a month to approximately 10 days.

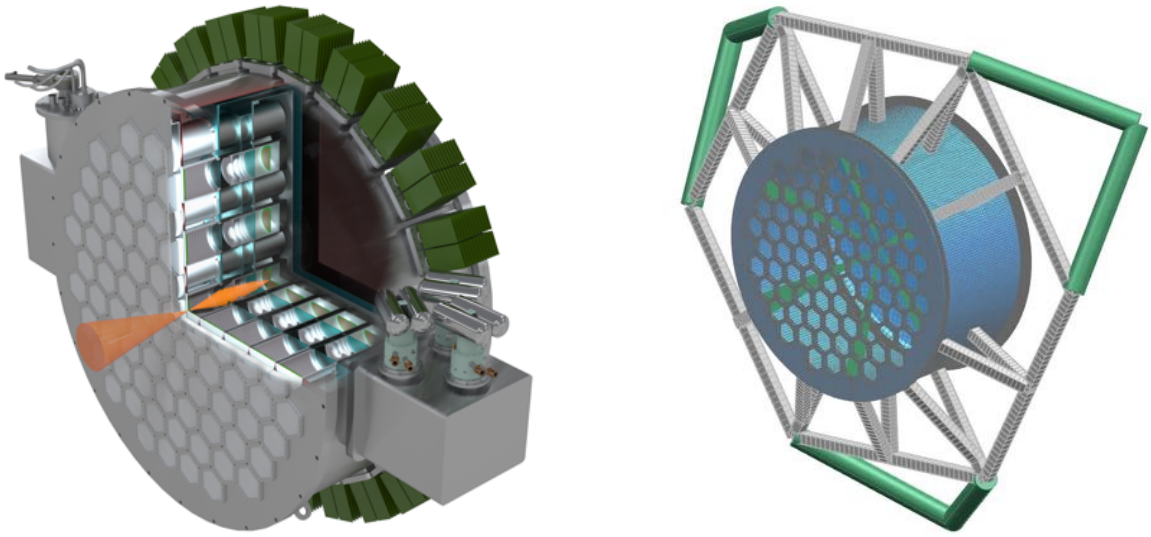

Figure 55: Overview of LATR design (left) and preliminary LATR support frame design for the SPLAT (right).

Table 3-16: Heat loads for the complete camera.

Stage	Support	Radiative	Window	Readout	Total	Cooling capacity
40 K	10.0 W	16.0 W	74.7 W	29.5 W	130 W	165 W
4 K	0.86 W	0.01 W	0.14 W	1.53 W	2.53 W	4.0 W
1 K	5.01 mW	0.01 mW	6.46 mW	0.87 mW	12.3 mW	25.0 mW
100 mK	68.6 μW	0.1 μW	0.5 μW	73.9 μW	143 μW	400 μW

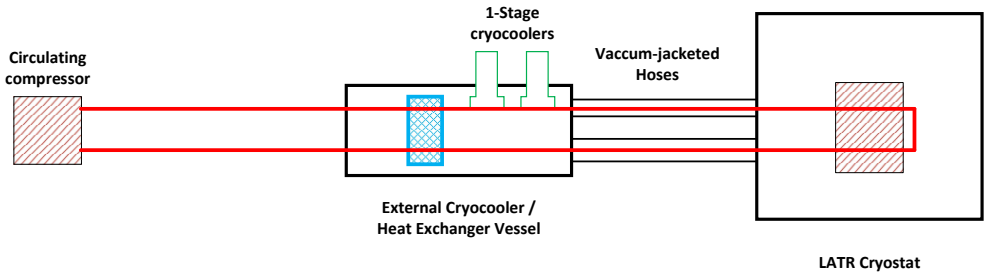

Figure 56: Schematic of the LATR rapid cooling system

3.5.5 Large Aperture Telescope Commissioning Receivers (LATCRs) *(McMahon)*

The LATCRs are a facility for critical lab tests of the receivers in North America and provide integrated end-to-end tests of optics tubes in each of the four bands (ULF, LF, MF, and UHF) on the telescope during commissioning. These verification and validation tests retire significant risks that require testing at the scale of full optics tubes.

3.5.5.1 Requirements and Specifications

The primary requirements from the LATCRs are derived from the need to do commissioning tests on each of the four bands on each of the three LATs. During the commissioning phase each receiver will enable the characterization and mitigation of a number of driving systematics on each telescope and at both sites. The beam properties and far side-lobes will be confirmed in all bands; tests will be performed to search for magnetic, optical, and other forms of scan synchronous pickup; mitigation strategies for the emerging constellations of internet satellites will be validated; key calibration systems can be verified; and the noise properties of the detectors will be verified. Each of these represent key tests for the acceptance of the system, and also provide a head start on resolving any issues efficiently. For example if problematic sidelines are discovered the telescope baffling could be adjusted— however all project planning is geared towards ensuring that this is a confirmation step rather than a fact finding mission.

To reduce the risk of any performance issues during commissioning, these receivers will be used to measure the beam performance of the LATR optics tubes. The key tests are beam shape and stray light control. These tests can be efficiently carried out with the first LAT-CR to come on line with the first optics tube of each type. This validation will confirm the optics tube design and ensure that wide angle scattering— a key driver of the ultimate system sensitivity — is well under control.

3.5.5.2 Current Examples

Two test systems similar to what is needed have been built by the CCAT and the SO collaborations. The CCAT system is a true commissioning camera while the SO system— based on a modified SAT – is a North American test facility. Both systems support only a single optics tube. The CCAT system shown in figure CCC is comprised of a dilution refrigerator mounted in a vertical vacuum shell which interfaces with a tube which holes a 40 cm diameter optics tube. This design could be adapted by adding a larger optics tube volume with support for four OTs. The SO system, while not suitable as a comissioning receiver provides an example of a north american test facility. It is designed to test end-to-end efficiency, control of stray light, band pass calibration methods, and beam measurements using cold holography. These measurement techniques will be fully demonstrated by mid 2021. The combination fo these two examples illustrates how the LATCR receiver may be designed and highlights the rapidly advancing maturity of approaches to the lab testing required for the success of CMB-S4.

3.5.6 Calibration Equipment *(Nagy and Bender)*

The LAT calibration equipment includes hardware to support both pre-deployment validation measurements in North America as well as on-site validation and calibration. The goals of the North American validation

measurements are to qualify hardware for deployment, to detect potential problems where they are easiest to fix, and to demonstrate measurement techniques that will be repeated on site. During the instrument commissioning phase of deployment, a series of validation measurements will ensure that the telescopes meet a minimum performance standard, below which components would be uninstalled at the cost of delaying science observations. More accurate calibration measurements of parameters critical for the science analysis will be interspersed with the science observations. They will be repeated at regular intervals to capture any variation with time and observing conditions.

Both the validation and calibration measurement requirements depend heavily on the science targets and instrument configuration and will continue to evolve as the project matures. Future studies will define these requirements with dedicated simulations. Though the LAT calibration requirements will not necessarily be the same at both sites, each site will have a dedicated set of calibration equipment that can be tailored to its specific needs. The list of planned measurements and corresponding calibration hardware is described below.

Bandpasses: Fourier Transform Spectrometers (FTSs) will be used to characterize and validate the observing bandpasses, which describe the relative detector response as a function of frequency. Several promising FTS designs have been demonstrated on current generation experiments e.g., [525, 526]. The bandpass measurement requirements for the LATs will likely be driven by the requirements on component separation (e.g., tSZ, CMB+kSz, and point sources), and achieving the necessary sensitivity will require precise characterization of the FTS transfer functions. These measurements will be first performed on the individual optics tubes and later during on-site calibration. While the North American and on-site FTSs may share many common design elements, they may have differences in the mounting and optical coupling as well as the required frequency resolution.

Beams: Both the main beams and wide angle sidelobe response need to be characterized in North America and on site. During the North American optics tube testing, beam maps with a thermal source will be used to determine the two-dimensional shape of the beam response and check for vignetting. Main beam measurements with the full telescope will be performed during on-site calibration with observations of planets or the Moon, which conveniently require no specialized equipment. To verify the wide angle scattering from individual optics tubes and determine the fraction of the beam that will spillover the mirrors, dedicated sidelobe measurements wll be performed during the North American optics tube validation. Similarly, while the scan strategy and baffling are designed to minimize far-sidelobe response of the full telescopes, on-site measurements are necessary confirm the observed level. In Chile, the far sidelobes can be characterized using observations of the Sun and Moon, while a tower-mounted artificial source will be required for sidelobe measurements at the South Pole.

Gain: The relative detector gain and associated temporal variation can be monitored during science observations with planets or other celestial sources. Regular electrical bias steps will also be used to track temporal variations along with elevation nods to modulate the atmospheric signal. Artificial chopped thermal sources can also be used for regular gain calibration and are being considered for laboratory and on-site measurements.

Mirrors: A tower-mounted source will be used for holographic measurements of the telescope mirrors to verify alignment after on-site assembly. Similar procedures have been successfully used by current generation LATs, and a trial run will be performed during the North American test build prior to deployment.

Additionally, the profiles of the mirror surfaces will be confirmed both pre- and post-deployment using photogrammetry or a laser tracker.

Optical Efficiency: The optical efficiency of the receivers will be verified in the North American optics tube tests using beam-filling thermal blackbody sources at known temperatures. This will ensure that the detectors can be operated under the anticipated loading conditions.

Optical Time Constants: Accurate knowledge of the detector optical time constants is critical for the LATs because the scan rate is fast relative to the beam size. The optical time constants also depend on the optical loading and will thus vary with atmospheric conditions during the science observations. Periodic measurements of a chopped thermal source, filling only a small fraction of the beam, provide a reliable way of measuring the optical time constants on the science detectors. Electrical bias steps may also be used to monitor changes in time constant without additional calibration hardware, provided that this method is demonstrated to be sufficiently accurate during North American modules testing.

Pointing: The pointing model for the high resolution LATs will be derived from point sources detected during nominal observations as well as from the CMB temperature anisotropies through comparison to existing measurements. Star cameras will provide coarse telescope pointing validation during the North American test build and on-site prior to the installation of the LAT receiver. Additional checks will be performed during on-site commissioning with short observations of planets or artificial sources.

Polarization Angle and Efficiency: During North American optics tube testing, a chopped polarized source will be used to simultaneously check both the detector polarization angles and efficiencies. The polarization angle describes the direction of a detector's linear polarization response, while the polarization efficiency quantifies its ability to reject the orthogonal polarization. On-site polarization angle measurements can be made either with observations of polarized celestial sources like Cen A and Tau A (Chile only) in the far-field or with drone- or tower-mounted sources in the mid- or near-field. Self-calibration techniques using the science data (EB and TB spectra) may be possible and would provide a valuable check on the other calibration measurements.

3.6 Small Aperture Telescopes (*John Kovac*)

3.6.1 Small Aperture Telescopes Overview and Design Drivers *(Kovac)*

3.6.1.1 Design Drivers

The ultra-deep survey, which targets the signature of primordial gravitational waves, drives the key measurement requirements for the small aperture telescopes (SATs).

The measurement challenges for this survey, outlined in Sect. 2.3, differ from those of the deep and wide survey in ways that set unique design drivers for the small aperture telescopes. To achieve the science goal of measuring r to the required precision ($\sigma(r) = 0.0005$ for a non-detection) ultimately demands measuring primordial B-mode polarization patterns with uncertainties of $< 10\,\mathrm{nK}$ at angular scales of a few degrees

on the sky. To do this requires an instrumental design that enables sufficient control of statistical noise fluctuations, galactic foregrounds, and instrumental systematics, all of which are made harder at degree scales by $1/f$ contributions to instrumental and atmospheric noise fluctuations and by the red spectrum of many foreground and systematic effects.

Small aperture telescopes offer intrinsic advantages for meeting the unique requirements of measuring r, which include:

1. **efficiency** to test, integrate, and deploy large arrays of detectors, due to their small size and large optical throughput;
2. **stability** of fully cryogenic telecopes, including their beams and internal systematics;
3. **calibrators** can be aperture-filling or easily placed in the far-field;
4. **modulators** can be aperture-filling and fully cryogenic;
5. **Mounts** can be compact and allow full boresight rotation;
6. **sidelobes** can be suppressed with unobstructed on-axis optics and superior baffling and shielding.

Additionally, small-aperture telescopes from the BICEP/Keck series at the South Pole have produced all the leading r constraints so far from ground-based B-mode measurements through Stages 1, 2, and 3. Small aperture telescopes, for example the ABS experiment, have also had the greatest success among telescopes in Chile in achieving sensitivity on degree scales, by using half-wave plate modulators to mitigate $1/f$ noise from the less stable atmosphere there. The intrinsic advantages of the small-aperture approach, combined with the experience that over the past decade, only small-aperture telescopes have demonstrated sufficient performance in degree-scale B-mode measurements to allow direct scaling that can meet the measurement requirements of CMB-S4, clearly dictate the use of small-aperture telescopes for the baseline design.

The detailed design choices for the small-aperture telescopes are driven by uniquely challenging requirements that are illustrated in Fig. 57. Many of the driving challenges require instrumental control of spurious signals and potential sources of large angular-scale noise by many orders of magnitude–for example, up to 20 orders of magnitude in the case of environmental thermal radiation variations coupling to degree-scale CMB polarization spectra. In considering changes for the baseline design compared to the small-aperture telescopes that have achieved previous deep r measurements, we have incorporated new technologies—for example dichroic detectors, dilution refrigerators, and (if small-aperture telescopes are deployed to Chile) cryogenic half-wave plate modulators—where there is a consensus that they promise improved performance while adding little technical risk. In making design choices we have distinguished between *engineering issues*, those that can be fully developed and demonstrated in the lab to retire risk, and *science issues*, those whose impact on successfully meeting the measurement and science requirements must be judged with comparison to direct experience of making deep B-mode maps. For example, most aspects of cryostat design are primarily engineering issues because we are confident our design choices can be fully validated in the lab. Examples of science issues include beam and sidelobe optical performance, polarization modulation approach, ground pickup and shielding, and other systematic effects where instrumental and environmental couplings are complex enough to require field validation. For design choices that impact these issues we have endeavored to stay close to and to build upon proven experience.

3.6.1.2 Baseline Design Summary

The baseline small-aperture design calls for six telescope mounts at the South Pole, each with a single three-tube cryostat, for a total of 18 telescope tubes. Table 3-17 summarizes the optical design features and

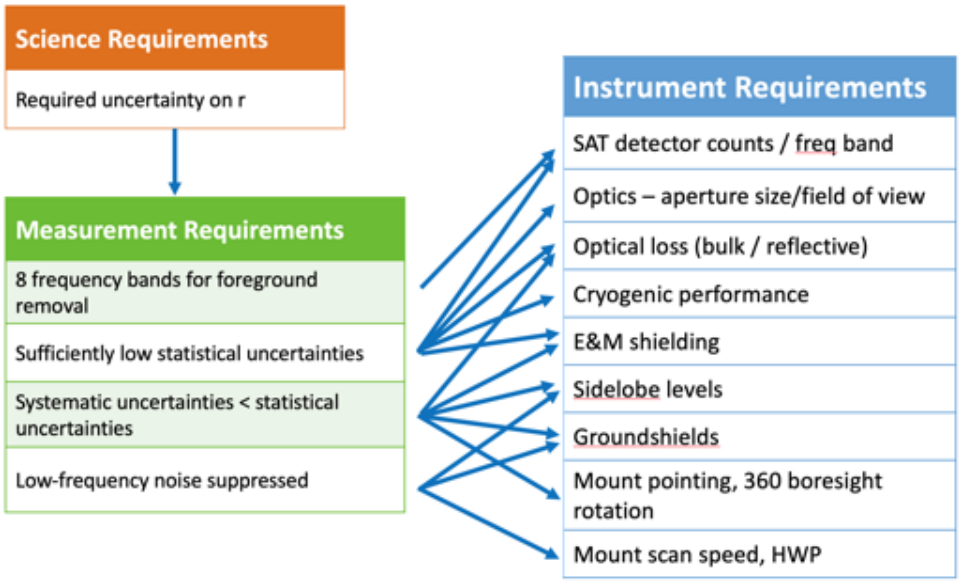

Figure 57: The small-telescopes instrument choices described in this subsection are driven by the unique measurement challenges set by measuring r to the required uncertainty using ultra-deep B-mode measurements at degree scales.

distribution of detectors between these optics tubes. The lower frequency tubes use plastic lenses, while the highest frequency tubes use silicon lenses for their known low loss.

The baseline design relies on polarization measurement by differencing pairs of orthogonal detectors, modulated by scanning the telescope in azimuth. This has been the approach successfully used by Stage 1-3 small-aperture telescopes at the South Pole, and is also the approach used by the LATs. The baseline small-aperture telescopes are compatible with the addition of continuously-rotating half-wave plates (HWPs), described in Sect. 3.6.2.3 as an additional measure to suppress atmospheric $1/f$ noise, as current experience indicates would be required if SATs will be operatated in Chile.

Details of the baseline design for each of the SAT subsystems are given in the following sections.

3.6.2 Optics *(Paine, Vieregg, Grimes)*

The unique measurement challenges of small-aperture telescopes have led to the development of simple on-axis refractors optimized for these goals. The 2-lens refractive optics of the BICEP series of experiments—BICEP1, BICEP2, Keck Array, BICEP3, and now BICEP Array—have evolved design details but used the same basic approach since 2004. The most notable upgrade has been an increase in aperture and throughput starting with BICEP3. The choice of on-axis refractive optics was re-affirmed by the SO collaboration who, after extensive comparisons between refractors with the leading alternative, crossed-Dragone reflectors, has also selected refractors for their compactness, lower cost, and easier sidelobe control.

Another key decision made for the SAT baseline design is related to the pixel density. As is well known, when the spillover illumination of the feeds was terminated at sufficiently low temperature ($< 2\,\mathrm{K}$), formal

Bands, GHz	Lenses	Field of view	Horns / Module	Modules / Tube	Detectors / Tube	Tubes
30 / 40	2× 63 cm Al	29°	12	12	576	2
85 / 145	2× 63 cm Al	29°	147	12	7056	6
95 / 155	2× 63 cm Al	29°	147	12	7056	6
220 / 270	2× 46 cm Si	29°	469	9 (up to 12)	17184	4
				total:	154,560 detectors, 18 tubes	

Table 3-17: Summary of small-aperture telescope types and numbers for the baseline design.

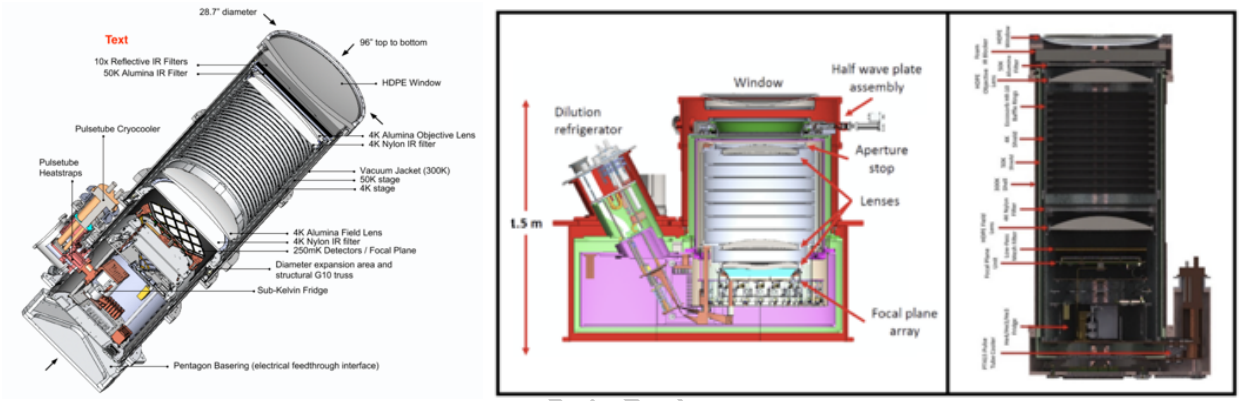

Figure 58: The CMB-S4 small-telescope receiver tubes contain simple cryogenic refractors of approximately half-meter aperture, a design based on heritage from the cryogenic refractors of the BICEP series of telescopes which have proven their performance in deep r measurements through Stages 1, 2, and 3. Shown at left is the BICEP3 telescope, which has been observing since 2015, as an example of an existing instrument that illustrates the essential optics design elements (including lenses, cold baffles, filters, and vacuum window) that all the CMB-S4 small telescopes will contain. At center and right are more recent SAT designs from the Simons Observatory and the BICEP Array, from which we have drawn proven design elements.

sensitivity optimization tends to favor feeds with diameters smaller than or comparable to the size of a diffractive spot ($f\lambda$), given a fixed optical throughput. However, the corresponding larger field strength at the edge of the aperture and the integrated spillover power terminated inside the optics tubes tend to generate near- and far-sidelobes with non-trivial polarization asymmetries through diffraction and/or small-grazing angle reflections/scattering. This corresponds to more demanding requirements for the cold aperture stop and the absorptive baffles, for illumination of the aperture by the feeds, and for the beam measurement and control of temperature to polarization leakage in analysis. For these reasons, CMB telescopes have usually chosen to under-illuminate their primary apertures. The BICEP series of experiements have used conservative edge tapers that are in the -8 to -23 dB range. For the SAT baseline design, to achieve the required detector counts we have relaxed this range slightly to allow edge tapers as high as -6 dB for the lower bands of our dichroic feed designs. There are ongoing efforts to make the cold absorbers more mechanically robust under cryogenic conditions, and better matched in polarization response. However, with this conservative choice of moderate packing density for the feeds, the SAT cold stop, baffling, and systematics contol and analysis strategies will likely not require new approaches beyond those demonstrated in Stage-3 experiments, but will certainly require careful optical prototype measurement and comparative

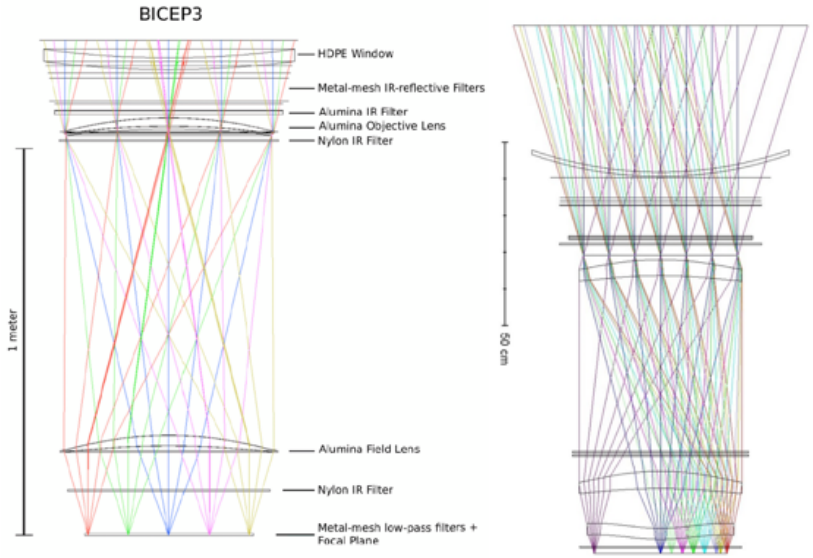

Figure 59: The detailed lens designs for CMB-S4's SATs draw heavily on heritage designs of Stage 1, 2, and 3, including realized 2-lens (BICEP, left panel), and 3-lens (SO, right panel) refractors that offer large optical throughput (etendue), symmetric main beams, and excellent polarization properties. Refractors are significantly more compact compared to crossed-Dragone telescopes with the same primary aperture, and offer advantages of symmetry and sidelobe control.

validation to ensure a sufficient improvement in end-to-end control of optical systematics has been achieved to meet CMB-S4's deeper measurement requirements.

3.6.2.1 Lenses

The lenses must be anti-reflection (AR) coated to prevent reflections at percent or better levels. The SAT baseline design baselines dichroic detectors which require similarly broadband cryogenic AR coatings on the optical elements. For the HDPE lenses, this can be done by gluing or laminating appropriate dielectric layers onto the lens surfaces. HDPE lenses with this AR coating approach have been used successfully by most of the Stage 1 and Stage 2 small-aperture telescopes, including BICEP1, BICEP2, and the telescopes of the Keck Array. For silicon lenses, subwavelength features can be cut into the lens surface with a custom three axis silicon dicing saw. These features constitute a metamaterial that behaves as a simple dielectric coating with excellent optical and mechanical properties.

The SAT baseline design will have 63-cm HDPE lenses at low frequencies and 46-cm silicon lenses at high frequencies. This distribution was driven by the resolution and throughput requirements at the lower frequencies, and the uncertainties in dielectric loss and anti-reflection coating performance of HDPE and other alternatives such as alunima at the highest frequencies. These material choices, designs, and aperture sizes are based on optics that have been fully field-demonstrated in BICEP Array and/or realized for the SO design.

An aperture size larger than $\approx 20(\lambda/2\,\mathrm{mm})\mathrm{cm}$ is required to resolve the degree-scale B modes. Beside the resolution requirements, a larger aperture offers larger optical throughput which proportionally reduces

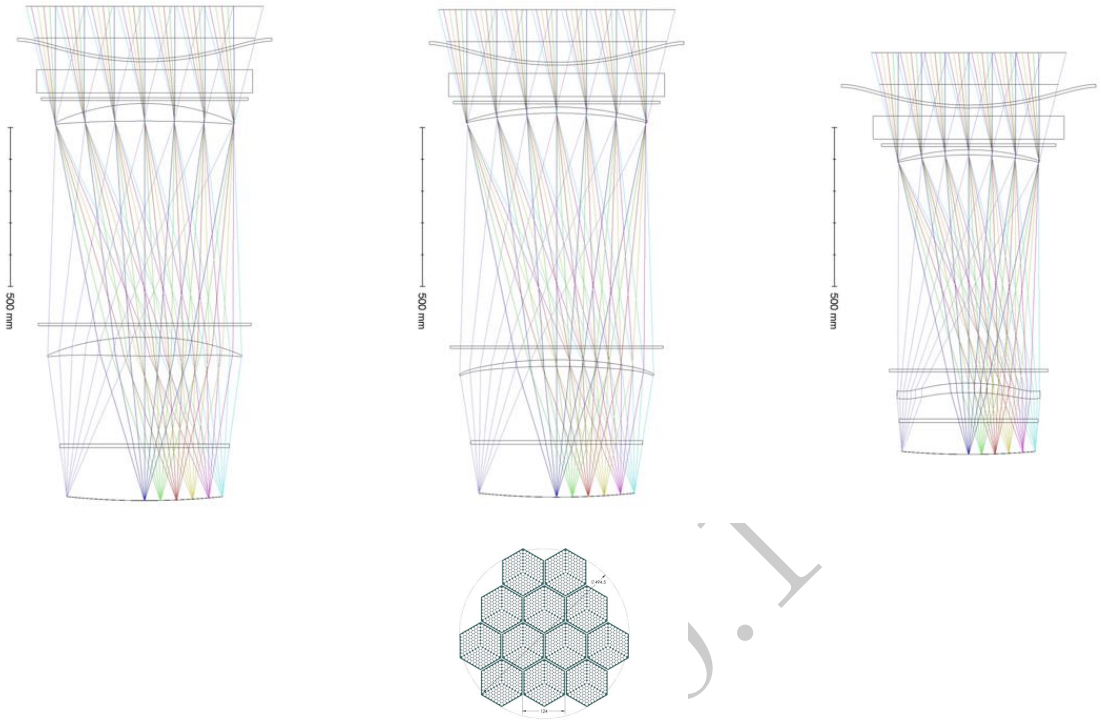

Figure 60: The SAT baseline lens and cold optics design for the 30/40, 85/145, and 95/155 GHz tubes is shown at left. It uses HDPE lenses of 630mm physical diameter, with a 560mm aperture stop. An alternative design using alumina lenses is shown at center. Both of these designs achieve excellent image quality and uniformity of aperture illumination across the full 490mm diameter of 12 detector module focal plane array, shown directly above. At right is the 220/270 GHz baseline lens design using high-purity, low-loss silicon lenses, which are limited to a 460mm physical diameter and 440mm aperture stop. It is able to couple well to detectors within a 422mm diameter on a focal plane array of the same layout, equivalent to the detector count of approximately 9 full 220/270 GHz modules.

the cost of cryogenics and telescopes given the same number of detectors. On the other hand, the size of the vacuum window that can be reliably built and the availability of the lens material present practical limitations. Low-loss HDPE and alumina lenses have been readily made for current Stage 3 SATs up to 80 cm in diameter. The Stage-3 experiment BICEP3 used alumina lenses with a 55cm aperture. BICEP Array is considering both HDPE and alumina lenses for its full range of frequencies, and has deployed HDPE lenses in its first receiver to be fielded (30/40 GHz).

For the CMB-S4 SAT baseline design, silicon lenses are chosen for high frequency bands for two main reasons. First of all, high purity-silicon is known to have very low loss. Additionally, broadband AR coating of silicon has been demonstrated and verified up to 240 GHz. However, the size restriction of the

Element	Temperature	Material	AR coat	Diameter (clear, mm)	Thickness (center, mm)	IR power (transmitted)
window	290 K	HDPE	bonded plastic	740	20	172 W
filter1 (scattering)	250-140K	foam		717	12× 3	12 W
filter2 (absorbing)	50K	alumina	bonded plastic	634	10	175 mW
filter3 (absorbing)	4K	nylon	bonded plastic	620	7.5	3.6 mW
30/40, 85/145 & 95/155 GHz baseline lens design						
lens1 (objective)	1K	HDPE	bonded plastic	570	55	549 μW
aperture stop	1K	tapered absorber		560		
lens2 (field)	1K	HDPE	bonded plastic	610	59	18 μW
220/270 GHz baseline lens design						
lens1 (objective)	1K	silicon	diced	445	16	1290 μW
aperture stop	1K	tapered absorber		440		
lens2 (field)	1K	silicon	diced	445	30	90 μW
low pass edge filter	0.1K	metal mesh		520	~ 8	

Table 3-18: Summary of small-aperture telescope optics elements for the baseline optics design. The window and filter configurations are identical for all bands. The baseline design assumes HDPE lenses for the lower three bands and silicon lenses for the highest frequency band; while HDPE or alumina lenses allow more throughput, current uncertainty in their loss and anti-reflection performance in this band drive this baseline choice.

3.6.2.2 Filters

In addition to the lenses, each of these optics tubes requires a vacuum window and several thermal filters. The vacuum window consists of HDPE anti-reflection coated with layers of expanded polytetrafluoroethylene (PTFE) or HDPE. They can now be made with 740 mm diameter and 20 mm of thickness, which contribute only a small fraction of in-band optical loading. For this size, more than 170W of thermal radiation is entering the cryostat through each of the vacuum windows. This must be significantly reduced by thermal filtering. In Stage-3 experiments such as BICEP Array, BICEP3, SPT-3G, and POLARBEAR2, adequate thermal filtering is achieved by a combination of scattering and absorptive filters. The scattering filters consist of stacks ($\approx$ 10 layers) of thinly sliced foam sheets, sometimes known as the RT-MLI (radio-transparent multi-layer insulation). The remaining infrared loading can be absorbed by IR-opaque alumina filters, whose high thermal conductivity also makes them very effective heat sinks, even in relatively thin filters. In BICEP3 and BICEP Array, a foam stack reduces the incoming thermal loading by 90% and an AR-coated alumina filter absorbs and dumps the remaining 12-18 W of power into the first stage (40K) of the pulse tube cooler.

The CMB-S4 baseline design optics stack, shown in Table 3-18), uses a similar approach for IR filtering between the vacuum window and the optics tube, with a 12-layer stack of RT-MLI followed by a 10mm thick alumina filter used for all 18 tubes and the full range of frequencies. Multi-layer plastic AR coatings for flat alumina filters have been successfully deployed on several experiments now (including BICEP Array) and are considered the lowest-risk choice for 40K stage filtering in the baseline design.

In the BICEP series of experiments, within the 4K optics tube additional nylon filters have been used to reduce loading onto the sub-Kelvin stage, and low-pass edge filters were used directly above the focal plane to reduce out-of-band direct illumination of bolometer islands. The CMB-S4 baseline design uses the larger cooling capacity of the dilution refrigerators to cool the entire optics tube, including two lenses and the microwave-absorbing aperture stop and baffling, to 1K, promising less risk of excess noise due to instrumental loading on the detectors. To allow this, the design moves the 4K nylon filter to a location just above the 1K objective lens. Given that CMB-S4's detector modules plan a feedhorn architecture that shields bolometer islands and careful design of on-wafer transmission line filters to limit blue-leaks, the low-pass edge filters may be redundant in this design. If so, this final layer of filtering can likely be demonstrated in lab testing to be unneccessary, but to keep the baseline design maximally conservative it retains these filters for now. Overall, the vacuum window and thermal filtering required by CMB-S4 SAT do not go beyond the level already demonstrated in both BICEP3 and BICEP Array and therefore present very low risks.

3.6.2.3 Half-wave Plates

In the event that SATs are deployed to Chile, those at 85 GHz and above will be equipped with continuously-rotating cryogenic half-wave plates (HWP) to help reduce the impact of the higher level of atmospheric noise fluctuations on degree-scale measurements at that site. The receiver cryostat is designed such that it is compatible with adding the HWP system. The HWP can also be used to eliminate the effects of instrumental polarization by optical elements between the HWP and the detectors. The HWP is located near the cold aperture, on the sky side of all the lenses, potentially reducing optical systematics due to the lenses and detectors. Reduction of instrumental polarization reduces temperature-to-polarization leakage, and the effects of polarized sidelobes generated by effects on the detector side of the HWP.

Our baseline HWP design is similar to that of the SO small-aperture telescopes, which is derived from the HWP implementation in the Simons Array receiver (Fig. 61). The optical element consists of three-layer stack of A-cut birefringent sapphire, with an anti-reflection coating similar to that of Alumina lenses. The SATs equipped with the HWP will have reduced aperture diameter because of the limited diameter of the sapphire material (maximum of 510 mm). The three-layer stack allows a wide-enough modulation bandwidth for the dichroic detectors. The HWP is located on the 40-K stage. Since the sapphire loss-tangent rapidly decreases as a function of temperature, the thermal emission from the HWP is negligible below 100 K. The rotation mechanism consists of superconducting mag-lev bearing and electromagnetic drive, achieving non-contact rotation. This allows smooth rotation and long-lifetime operation in the vacuum and cryogenic environment.

3.6.3 Cryostat *(Kusaka, Saba)*

3.6.3.1 Cryostat design drivers

The cryostat consists of the most-skyward lens and the aperture stop that are cooled to ≈1 K, the optics tube with cryogenic baffling and the rest of the lens(es) that are cooled to ≈1 K, and a focal plane maintained at ≈100 mK by means of a dilution refrigerator. Maintaining these temperatures rather than higher ones offers sensitivity gains, and fabrication margin for the superconducting detectors.

Our baseline design for the cryostat, which we refer to as the "3-tube" system, contains three optics tubes and focal plane assemblies, sharing a common vacuum volume, cryocoolers and a refrigerator. We chose the

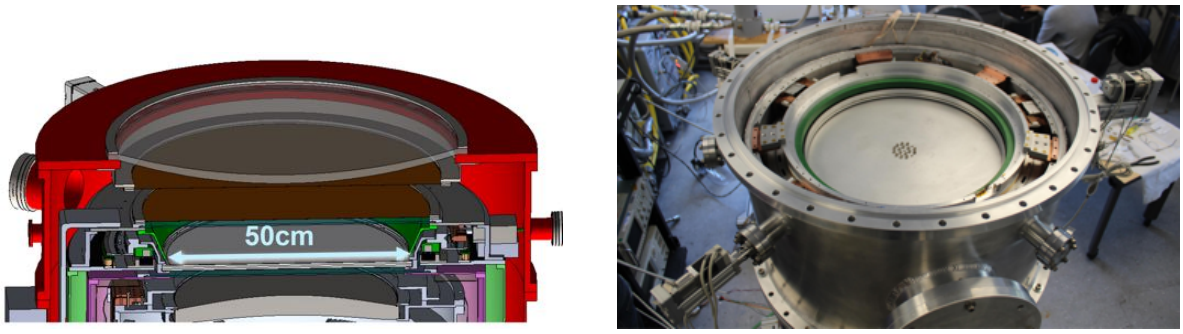

Figure 61: *Left*: drawing of the SO cryogenic half-wave plate section. The HWP system consists of the sapphire HWP and rotation mechanism adopting superconducting mag-lev bearing. The optical clear aperture is 50 cm in diameter. *Right*: a photo of the Simons Array cryogenic half-wave plate system [**?**], from which the SO system is derived.

3-tube system over the "single-tube" system, where a cryostat contains a single optics tube and focal plane assembly. Our choice was based on the following design drivers.

Electrical Power: The system of pulse-tube and dilution refrigerator coolers is the largest power consumer during operation, and supply of power is among the most expensive logistics requirements at either site. In particular, limitation in power at the South Pole may be a driving constraint. The power consumption per unit of sensitivity is among the primary figures of merit. The 3-tube cryostat allows more efficient use of power, and thus has a better power consumption figure of merit.

Modularity: The modularity of the system is a key element during the integration and testing. While a single-tube system allows more modular integration and deployment, the total number of units to deploy is smaller with the 3-tube design, and they still offer a large degree of modularity compared with the LAT cameras.

Risk: Commissioning the cryogenic systems is one of the largest schedule risks. When optimizing the system for power consumption, the 3-tube system has larger margin in cooling capacity, and thus has less risk in cryogenics. On the other hand, all the pulse-tube-cooled small-aperture systems deployed in the past (BICEP series, ABS, and CLASS) are single-tube cryostats, and this heritage translates to reduced risk. The risk reduction of the 3-tube system is an integrated part of our plan toward CD-2, where we will design, fabricate and demonstrate a prototype cryostat.

Baffling: A single-tube system must have larger separation between the three cryostats' vacuum windows (on a single telescope mount), allowing each tube to have a dedicated forebaffle centered on that tube. These centered, symmetric forebaffles are physically smaller, and thus advantageous for the single-tube system. The 3 tubes on the proposed cryostat are far enough apart to use individual forebaffles, so this advantage is maintained.

Cost: A 3-tube cryostat will be operated with a single dilution refrigerator offering cost-savings relative to the single-tube option, which requires three times more refrigerators.

Based on these design drivers, and specifically because of lower power consumption and cryogenic risk the baseline design uses the 3-tube system. Among the various multi-tube cryostat options, the *three*-tube was judged optimal because the 1-K stage and 4-K stage cooling power of the BlueFors SD400 and Cryomech

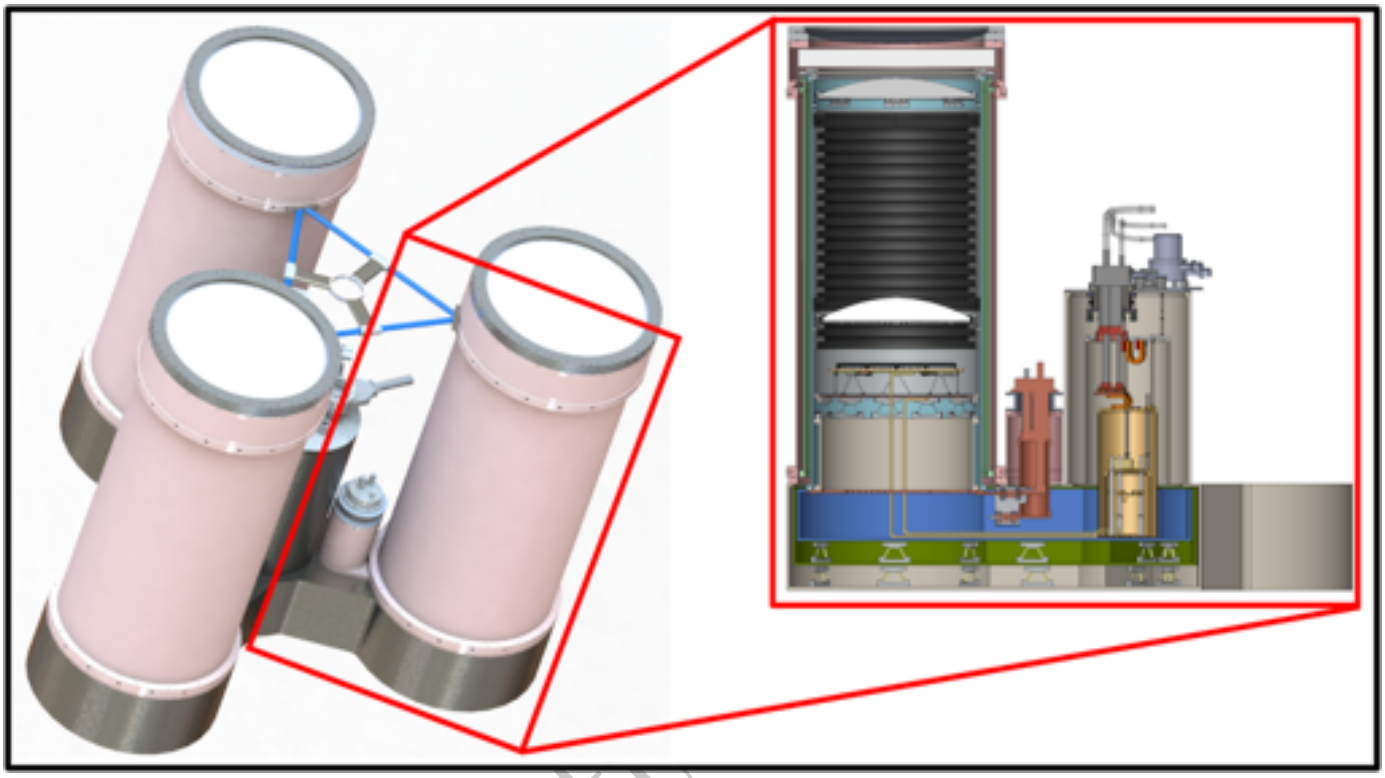

Figure 62: The baseline design "3-tube" cryostat. It accommodates three cryogenic optics tubes each fitting within a 70-cm diameter × 150-cm long envelope, cooled to 4 K by the three pulsetubes located around the lower perimeter of the cryostat and to 1 K and (for the focal planes) 100 mK by the diliution refrigerator. The optics tube shown is the low-frequency, alumina lens version, derived from the BICEP Array design. The high-frequency, silicon lens version will fit in the same volume, with bolt-on extensions between the cryostat and each vacuum window to accommodate the HWPs if deployed to Chile.

PT420 are well-matched to support three optics tubes and the focal planes. Increasing the number of optics tubes per cryostat beyond three likely requires additional cryocooling. For these reasons we limited the number of tubes per cryostat to three.

3.6.3.2 Cryogenics

The general configuration of a SAT receiver will consist of a 2-meter (TBC) cryostat with three optical tubes. As Fig. 62 shows, the cryostat will have three optics tubes maximally separated from each other, allowing the use of individual warm baffling, and connected through the "cryo-bus" at the bottom part of the cryostat. Each optics tube will have a separated top vacuum-shell section, 40 K and 4 K shields, and optics. The size of the single optical tube will be around 70 cm (TBC), comparable with the present previously deployed small-aperture instruments. This design will allow different teams to work in parallel on optics tubes that fill a single cryostat design, which would be identical for the South Pole and Chile small telescopes. A key factor of the optical tube design will be the modularity of the mechanical, optical, and readout and detector parts. That will allow a fast and straightforward replacement of parts and also the capability to reconfigure

Fridge	Type	Quantity	Power	Cooling capacity per fridge			
				45 K	4 K	1 K	100 mK
PT60	Pulse tube	1	3.3 kW	20 W			
PT420	Pulse tube	1	12.5 kW	55 W	2 W		
PT410	Pulse tube	1	8.4 kW	40 W	1 W		
SD400	Dilution	1	2.0 kW			25 mW	400 μW

Table 3-19: Refrigerators. The PT410 is only used for the dilution refregerator system.

	Loading at each stage			
	45 K	4 K	1 K	100 mK
Conductive	30 W	1.3 W	3 mW	22 μW
Radiative	20 W	$\simeq$ 0 W	3 mW	1 μW
Optical	20 W	$\simeq$ 0 W	15 mW	1 μW
Total	70 W	1.3 W	21 mW	24 μW

Table 3-20: Preliminary loading estimates. The conductive loading of the readout cables are estimated based on the current baseline readout configuration. The optical loading estimate is described in Sec. **??**. The conductive loading due to the support structure and the radiative loading are estimates based on the previous experiments such as SO SAT and BICEP Array.

the instrument observation bands to enhance multi-frequency coverage and map depth. Standardization of the parts that involve cabling, mechanical supports, and detector module interfaces has demonstrated advantages of cost savings and efficiency and is standard practice within in experiements (e.g., Keck Array, BICEP Array, SO SAT) that have deployed or are planning to deploy small-aperture telescopes at multiple frequencies.

The detectors are cooled to ≈100 mK, with intermediate stages at 1, 4, and 40 K for radiation shields, optical filters, and wiring thermal intercepts. The 40-K and 4-K stages have one PT420 pulse tube supplemented by one single-stage PT60 pulse tube for additional cooling power at the 40-K stage (see Table ??). The 40-K stage cooling capacity has relatively small margin in this system, and its validation is among the important deliverables from the prototyping activity; if deemed necessary from the prototyping, the PT60 can be replaced with a higher capacity PT90, for example, to gain larger margin while mantaining small increase of power consumption. The 100-mK stage is cooled by a BlueFors SD400 dilution refrigerator with an intermediate stage at 1 K. The dilution fridge has its own PT410, dedicated for the dilution fridge system. Flexible copper braids are used to connect the refrigerators to the cryo-bus, as well as the connection between the cryo-bus and the cryo stages of each optics-tube assembly. All the pulse-tube coolers must be kept within ≈ 45° of vertical to maintain cooling capacity.

The baseline design cryogenic architecture for a SAT receiver includes three optical tubes inside separate 40 K shield volumes, cooled by the PT60 and the first stage of the PT420 pulse tube coolers. The PT420 pulse tube second stage will cool the three tubes down to 4 K. The PT410 will provide the base temperature to run the dilution refrigerator, which in turn provides the cooling to 1 K and 100 mK stages. The 1-K stage provides thermal intercepts for the wiring and mechanical structure, as well as the cooling for part of the optics tubes including cryogenic baffling and (some of) the lenses. The focal plane operates on the 100-mK stage. The required cooling power for the SAT can be extrapolated considering the design of SO

SAT, which has similar configuration using dilution refrigerator, and the BICEP Array receiver. Table ?? shows preliminary thermal loading estimates. The 40-K and 1-K stages have relatively small margin, and thus one of the main focus in the prototyping activity.

In order to mitigate input thermal loads, the 40-K and 4-K radiative shields have to be wrapped with Multi-Layer Insulation aluminized mylar. Moreover, the mechanical supports between the stages have stringent requirements in terms of their thermal conductivity. The current generation of cryogenic instruments for CMB uses G10 fiberglass supports (sometimes supplemented by titanium tension members) above 40 K or 4 K, and the composite carbon fiber ones at lower temperatures. These solutions will be implemented in the SAT design. The choice of materials for the shields and the thermal straps is crucial. Based on past experience, we will largely use high-conductivity 1100 Aluminum for the radiative shields and 101 Oxygen-free Copper for cold plates. For the design of the heat straps, depending on the temperature stage, we will use copper braids or foil shims 101 Oxygen-free Copper, or annealed 6-N aluminum strips. Their design maximizes the thermal conductivity allowing the differential thermal contraction due to the cooling process to take place without damaging the cryogenic system.

Superconducting devices such as TES bolometers and KIDs are sensitive to the presence of external magnetic fields. Also, the readout architecture for TES bolometers is based on the use of Superconducting Quantum Interference Devices (SQUIDs), which are very sensitive magnetometers. These millimeter-wave sensors and the cold readout electronics are therefore quite sensitive to electromagnetic pickup induced by even very weak magnetic fields. The Earth's magnetic field (modulated by the telescope scan), as well as fields produced by the instrumentation surrounding the experiment, are potential sources. This pickup can result in the production of artifacts in the CMB temperature and polarization maps that can be challenging to disentangle and remove. A common strategy for mitigating these effects is to implement magnetic shields in the cryostat mechanical design, a technique that is currently adopted in all the Stage-3 CMB experiments such as BICEP Array, SPT-3G, and Advanced ACT. The shielding strategy varies from experiment to experiment but it is based on the interleaving of high permeability and superconductive material layers. The baseline design for the SAT magnetic shield is assumed to copy that of BICEP Array, which uses a high-permeability (Amuneal A4K) cylinder around the 40-K tube combined with a Niobium superconductive cup at 300 mK (or at 1 K for S4), to reduce magnetic fields by a factor of about 200 at the focal plane. Additional shielding layers are usually added locally in the detectors/SQUID areas. Looking again at the BICEP Array architecture, its FPU detector module design provides an additional factor of 500 shielding with the use of an A4K planar sheet and a Niobium enclosure; a similar shielding factor at the detector modules is assumed to be achievable for the S4 baseline design. The use of finite-element model simulation software (e.g., COMSOL Multiphysics) can help optimize the shielding configuration.

3.6.3.3 Mechanics

Survival requirements on the vacuum jacket and vacuum window include: safe storage to temperatures of −90 C and maintenance of vacuum to temperatures of −40 C. In past experiments the latter has been straightforward to achieve with silicone elastomeric o-rings. In operation the cryostats will be contained in an environmental enclosure which surrounds the telescope mount, with heated airflow directed around the vacuum window to eliminate frost/snow accumulation, so exposure of cryostat components to colder ambient temperatures while in operation is not expected.

Within the cryostat, pointing rigidity of the optical tubes is maintained by arranging for kinematic constraint of the thermal standoffs, with rigid triangulated G10/carbon fiber truss elements supporting bottom end of the 50-K, 4-K, and 1-K stages and Ti-Al-4V tensile members providing radial constraint at the top (open) end of each tube [527]. Lenses are supported from optics tubes using tangential-blade standoffs which

provide thermal conductance while maintaining concentricity and relieving radial strain from differential thermal contraction. Based on pointing performance of Keck Array and BICEP3, we expect pointing effects from gravitational deflections of the optical elements within the cryostat to be easily limited to < 15 arcsec with such a mechanical support system, and to be repeatable. The cryostats themselves are supported in the telescope mount with rigid triangulated space frame members which connect hard points near the top and bottom vacuum flanges to mounting points on the inner diameter of the boresight rotation stage that surround the cryostat's center of gravity.

The total cryostat mass is estimated to be 1800 kg (approximately three times that of a BICEP Array cryostat). SAT cryostat assembly (both in North America and in the field) will take place on dedicated wheeled lab stands designed to distribute their mass over a 2×2 m footprint, minimizing requirements for specially-reinforced lab floors. Assembly of the cryostats requires a well-controlled 2-ton hoist with a hook height of ≥ 12.5 feet.

3.6.3.4 Cryostat Readout and Control

The small-aperture telescope cryostats share the same control and monitoring interface as the LAT cameras (described briefly in Sect. 3.5.3.3). We monitor temperature sensors, vacuum gauge and valve, and the status of the refrigerator and compressor. Control interfaces are used for heaters, the vacuum valve, refrigerator, and compressor.

Control and monitoring for each SAT integrates into the overall observatory control software in the form of one or more subsystems, as outline in Sect. **??**. The requirements for timing synchronization are modest and the monitoring data rate is insignificant in comparison to the bolometer data.

3.6.4 Mount *(Pryke)*

The CMB-S4 baseline design mount for the small-aperture telescopes is a 3-axis fast-scanning mount, based on the existing design of the (Stage 3) BICEP Array mount (see Fig. 63 and Ref. [527]).

The CMB-S4 mount must be capable of carrying the SAT receiver and their associated electronics and cryogenic equipment and of scanning them on the sky rapidly enough to make differential degree-scale measurements in the presence of $1/f$ instrumental noise and changing atmosphere and ground signals. It must achieve an accuracy of pointing knowledge while scanning that ensures sufficient control of systematic uncertainties, both in mixing of E to B modes due to pointing reconstruction errors [494] and in cross-referencing maps across SAT frequencies and with the LAT data for accurate galactic foreground and lensing separation. It must provide 3-axis rotation, including full rotation around the boresight axis to allow both for suppression of instrumental systematics in polarization measurement and for consistency checks offered by a full set of null tests [528]. It must provide an environmental enclosure to protect the cryostats, electonics, and other elements from extremes of temperature or snow exposure and to offer a stable operating environment with reliable interior access to all critical components. The design requirements are summarized in Table 3-21.

The baseline design mount illustrated in Fig. 63 meets the design requirements using the existing BICEP Array mount design. Although this mount was originally designed for four individual small-aperture telescope cryostats, each with a single pulsetube, its size is well-suited to mount the single 3-tube cryostat with three pulsetubes and dilution refrigerator. This mount includes two separate rotary unions which allow continuous rotation about the azimuth axis and the array boresight axis without the need for cable wraps. These rotary unions each contain 10 helium channels. Eight of these connect the pulse tubes and their compressors, while

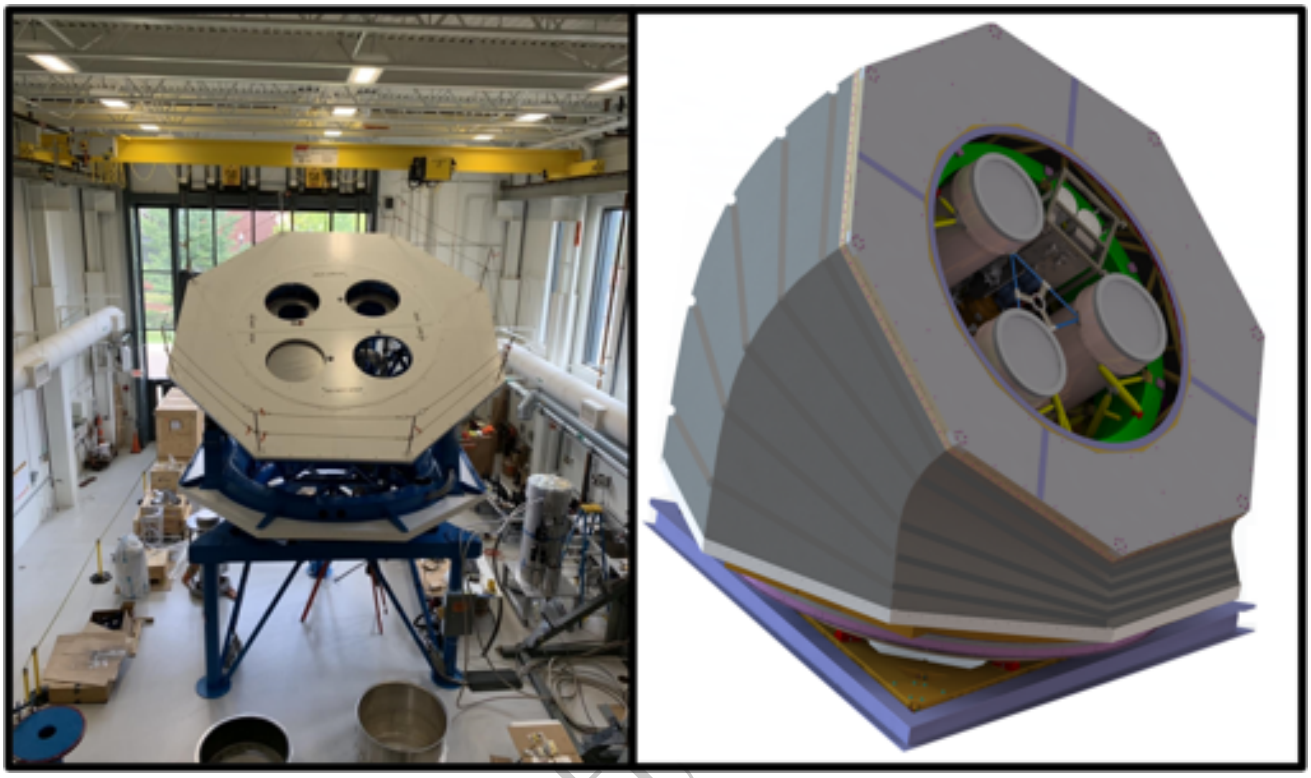

Figure 63: The CMB-S4 small-aperture telescope baseline design telescope mount is based on the existing BICEP Array mount design (left). Although originally designed for four individual small-aperture telescope cryostats (each with a single pulsetube), its size is well-suited to mount the single 3-tube cryostat with three pulsetubes and dilution refrigerator (right). It allows three axis motion with infinite rotation (using rotary feedthroughs) on the azimuth and boresight axes, and a design that allows for full environmental enclosure with space for interior access to all critical components.

Parameter	Value	Notes
Mass of instrument	up to 4500 kg	includes cryostat, DR system, electronics, forebaffle
Motion	3 axis	full boresight rotation of instrument and forebaffle
Scan pointing knowledge	< 15 arcsec rms	$< 1/20$th beamwidth at $\lambda = 1$ mm
Scan speed AZ/EL/TH	$5/1/1$ deg s^{-1}	≈ 3 deg s^{-1} on the sky for fast diff. measurements
Scan accel. AZ/EL/TH	$3/1/1$ deg s^{-2}	turnaround efficiency
Range AZ/EL/TH	$\infty/45\ldots110/\infty$	continuous AZ desirable
Shipping envelope	standard double pallet	deployment via C-130 / standard vehicles
Mount mass	< 25 tons	includes instrument, comoving forebaffle and scoop
Survival: wind	70 m s^{-1}	Chile dominates
Survival: seismic	0.3 g	Chile dominates
Survival: temperature	-90 C	Pole dominates

Table 3-21: Small-telescope mount design requirements.

two channels serve as pressure guards. An additional nitrogen channel provides a pressurized environment on front end of the cryostats which prevents water absorption into the window material. Slip rings at the ends of the unions additionally provide data and power connections to electronics across separately rotating stages of the mount. These rotary unions allow the helium compressors required to operate the pulse tube coolers to sit below the mount structure in the stationary equipment room. Helium lines route upwards into the lower (ground fixed) half of the first rotary union and then out through the upper half which rotates in azimuth along with the receivers. The hoses from the upper half are then routed through a short cable chain that provides flexure when rotating in elevation. The second rotary union is then similarly connected between the elevation and boresight stages. Modifications to the current mount design will be required mount the dilution refrigerator gas handling system inside the envelope of the instrument package which co-rotates on the boresight stage, and engineering work will be required to ensure this system can operate while tilting up to 45° from vertical.

The mount provides a flexible environmental seal that fully encloses the components seen in Fig. 63, while exposing only the vacuum window, forebaffle, and co-rotating shields (see Fig. 64). Access to the telescope for service is from an equipment room below which houses helium compressors and control computers, similar to existing BICEP and Keck Array facilities currently in use at the South Pole. The access passage through the azimuth bearing is large in diameter, and is designed to accommodate installation of cryostats and other components as well as personnel access, all within the interior environmental space of the observatory complex. Alternatively, cryostats may be lifted into the mount from above using a crane.

3.6.4.1 Control and monitoring

The large and small telescopes share a common control and monitoring interface (see Sect. **??**). Drive amplifiers, brushless servo motors, reducers and drives, encoders, emergency stop and safety interlock systems are specific to each telescope design. Based on the systems developed for the Keck Array and BICEP Array mounts, we expect these drives to consume 10 kW peak power.

3.6.5 Ground Shields and Exterior Baffles *(Schmitt)*

Extended beam response can couple to the warm ground or the Galaxy/Sun/Moon during CMB scans, potentially adding structure at the degree scales relevant for the r measurement. A key advantage of the small-aperture telescope approach is that the entire telescope can be enclosed in multiple levels of shielding, significantly reducing the effect of sidelobes. Indeed, all of the leading r constraints to date have used similar shielding strategies to absorb sidelobes and/or reflect them to the cold sky.

The first level of baffling is a co-moving absorptive cylinder which extends around each SAT receiver tube window aperture. Sidelobes—usually at $\gtrsim 10°$ scales—that terminate on this surface see a constant-temperature load, and therefore do not contribute to degree-scale structure in the map (although the extra loading slightly decreases sensitivity). Like in the BICEP experiments, we will also use an additional fixed, reflective ground shield that surrounds the entire telescope mount. While no rays from the aperture couple directly to the ground shield, those that diffract over the lip of the co-moving forebaffle tubes do; the ground shield ensures that rays must diffract twice before terminating on the warm ground. A ray that couples to the ground shield can add azimuth-fixed structure to the map, which must then be filtered from the timestreams. Figure 64 illustrates the levels of shielding around the 3-tube cryostat.

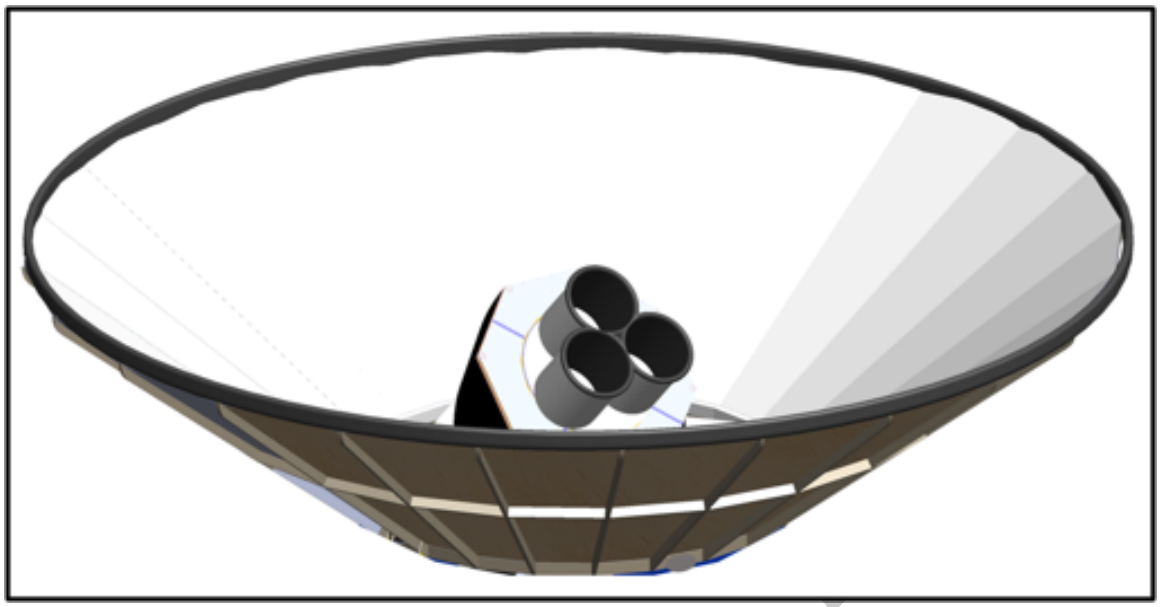

Figure 64: Exterior view of the small-telescope mount and shielding. Each SAT receiver tube is surrounded by a co-moving absorptive forebaffle. The mount sits within a large reflective ground shield. A flexible environmental seal surrounds the mount structure.

The dominant sources of sidelobes in small-aperture telescopes will be different from those in the large-aperture case. Instead of mirror scattering and panel gaps, the most important effects for the SATs will be: diffraction at the cold stop and primary aperture; scattering from the window, filters, and other optical elements near the aperture; and non-sequential reflections between optical elements. We expect to model the beams using Zemax and GRASP simulations to demonstrate that we can meet the stringent systematics requirements. These models will then be confronted with *in situ* measurements, both of the sidelobes themselves and of the amplitude and temporal stability of the ground pickup signals on the relevant angular scales, taken with and without various levels of shielding.

Small-aperture CMB experiments have often used a so-called double-diffraction criterion to minimize far-sidelobe coupling to the ground or Galaxy during scanning. This can be enforced using a co-moving forebaffle and fixed ground shield. We enforce the double-diffraction criterion (that ground radiation needs to diffract over the ground shield, and again over the forebaffle, before entering the window) with several key rays, including prescriptions that: (1) no ray within the field-of-view may couple directly with the forebaffle or ground shield at any observing elevation; (2) no ray originating from any optics tube window may couple directly with the ground shield; and (3) no portion of the forebaffle (or any moving shield) may protrude above the height of the ground shield at any observing elevation (including an additional safety margin, in degrees). At 50 degrees minimum elevation, we find that the SAT receiver can be shielded with a 1.75 m tall, 0.8 m radius forebaffle and a 5.9 m tall, 12.4 m radius ground shield, which is the smallest achievable ground shield size for a 2-shield scenario (given the maximum forebaffle size allowed by the SAT receiver design). Results of this study can be found in Figure 65. While a tertiary shield (between forebaffle and ground shield) could in principle reduce the dimensions of the ground shield, the systematics of such a design are currently less well-understood. Note that a tertiary shield has not yet been fielded in any existing SAT and thus lacks heritage in the CMB field.

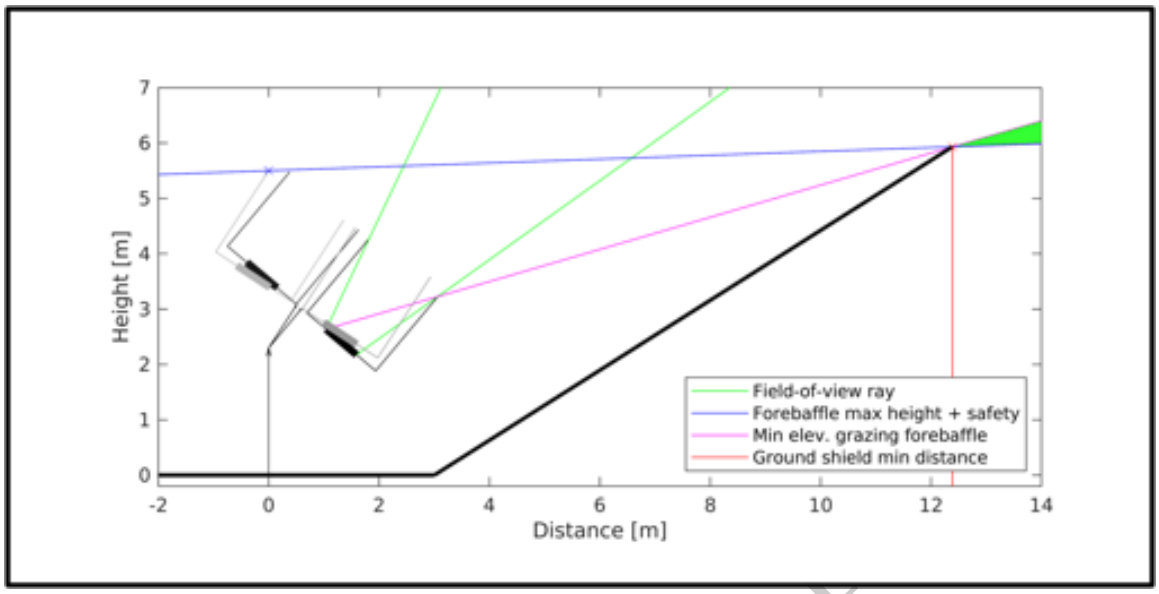

Figure 65: Using a double-diffraction criterion, at 50 degrees minimum elevation, we find that the SAT receiver can be shielded with a 1.75 m tall, 0.8 m radius forebaffle and a 5.9 m tall, 12.4 m radius ground shield, which is the smallest achievable ground shield size for a 2-shield scenario (given the maximum forebaffle size allowed by the SAT receiver design).

3.6.6 Calibration *(Karkare)*

SAT calibration measurements serve several purposes. First, calibration can verify that the SATs meet baseline requirements during integration and on-site commissioning. Second, science analyses require certain instrument properties to be known to a pre-defined precision. Finally, calibration measurements are used to test for various classes of instrumental systematics. The calibration strategy and required equipment outlined here are largely based on experience with multiple generations of small-aperture telescopes across collaborations [529, 498, 499, 530]. Several of the SAT instrument characteristics that need to be measured are in common with the LATs, and in these cases the equipment will be designed to be interchangeable wherever possible. However, the unique requirements of the inflation survey—exquisite control of additive systematics at degree angular scales [528]—necessitate *in situ* measurements that can only be done with specialized equipment, identified below and illustrated in Fig. 66.

Main beam shapes: Mismatches between the beam shapes of co-located, orthogonally-polarized detectors can leak the ~ 100 μK temperature anisotropies into polarization. While the lowest-order beam difference modes can be modeled and filtered out, higher-order, unmodeled residual leakage is a potential additive systematic at the angular scales relevant for the r measurement [531]. Measuring the main beam shapes to high precision allows us to constrain this systematic and account for it in analysis. The measurement is facilitated by the relatively short SAT far-field distance (∼hundreds of meters, depending on frequency): the South Pole observatory buildings are located a comparable distance apart, so that a telescope can observe a source on a separate building (Fig. 66 a).

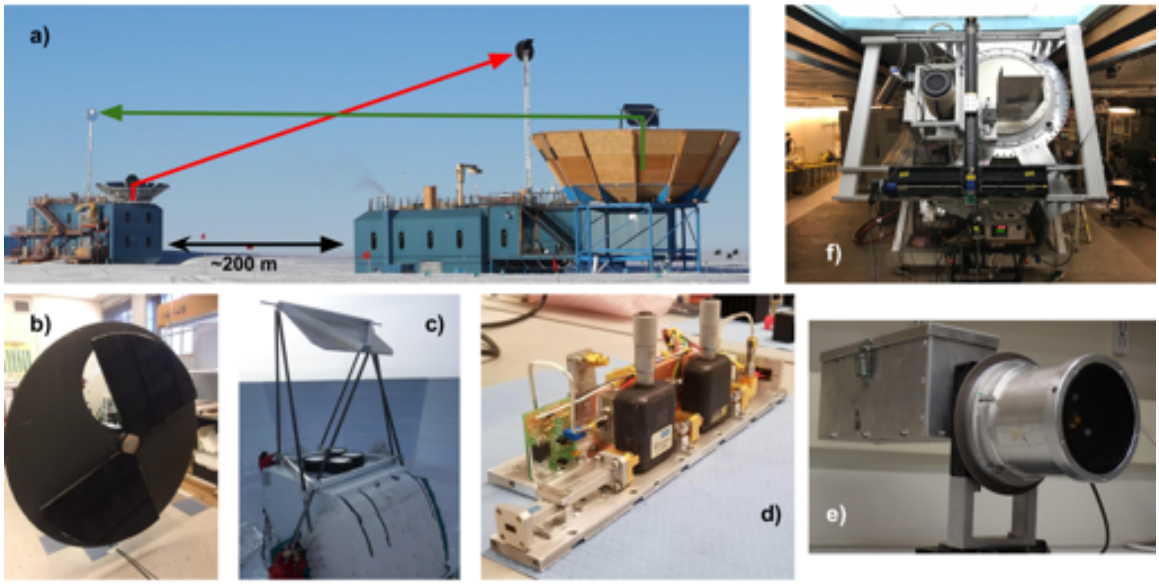

Figure 66: a) The South Pole observatory buildings allow beam measurements in the far field using redirecting mirrors and sources mounted on masts. b) The BICEP thermal chopper in lab with the protective enclosure removed. The carbon fiber blade, coated in Eccosorb HR-10, spins at 14 Hz. c) The flat redirecting mirror mounted above the Keck Array. d) An amplified microwave source, with two variable attenuators and the waveguide output visible. e) A rotating polarized stage for the amplified source. A horn is visible behind a polarizing grid. For use in the field, the stage is placed in a heated enclosure and mounted on a mast. f) Fourier Transform Spectrometer measurements on SPT-3G at the South Pole, illustrating coupling to the cryostat and the use of several degrees of freedom to optimally couple to the optics.

- *Chopped Thermal Source*: A thermal source that chops between an ambient-temperature thermal load and the sky will be used to map the main beams in the far field. A large aperture size and fast chop rate are needed for acceptable signal-to-noise and demodulation performance; the current BICEP chopper features a 24" aperture and 14 Hz chop rate (Fig. 66 b; [532]). The enclosure must also be light enough to be raised on a mast, and stiff enough to withstand chop-induced vibrations.
- *Mast*: A mast on each building will be used to hold sources at a sufficient height such that they can be observed above the horizon from a separate building with a redirecting flat mirror, and from the same building to probe wide angles. It must be easily raised when loaded and hold the source steady in windy conditions.
- *Far-field Flat Mirror*: A large, flat mirror will be mounted above the SATs to redirect their beams over the lip of the ground shield and towards a calibration source (Fig. 66 c). The mirror should be large enough to intercept all of the beams from at least one receiver and flat enough so that the beams are not distorted. Integrating the design of the mirror with that of the mount will facilitate installation.

Far Sidelobes: Off-axis response that is not absorbed by the forebaffle can add structure to the maps by coupling to features on the ground or the Galaxy during CMB scans. Measuring this region of the beam requires access to a wide range of angles from the boresight and an artificial source with large dynamic range to probe dim features far from the main beam [533].

- *Amplified Microwave Source*: Broad spectrum microwave noise sources will be used for far sidelobe and polarized beam measurements (see below). Similar to those used by BICEP, they will amplify room-temperature thermal noise and multiply/filter the signal to ranges appropriate for the various detector bandpasses (Fig. 66 d). Variable attenuators allow for control of output power over a large dynamic range and the signal is chopped with a microwave switch. For the sidelobe measurement, the source is mounted on a mast close to the receiver so that it can be viewed without the far-field flat mirror.

Polarized Beams: Detector polarization angles, cross-polar response, and the full polarized beams ($T/Q/U$ beams) will all be measured using a polarized source in the far field [534]. Large systematic uncertainty in the polarization angles with respect to the sky would leak E to B. While self-calibration with TB and EB can be used to estimate the overall rotation angle, polarization calibration can also determine the absolute angles and enable constraints on parity-violating physics.

- *Rotating Polarized Source*: The amplified microwave source (see above) will be mounted on a rotating stage so that the source polarization angle can be varied (Fig. 66 e). The angle is referenced to gravity to measure the absolute angle. For this measurement, the source is placed in the far field and observed using the far-field flat mirror.

Bandpasses: Precise knowledge of the detectors' spectral response is required to separate Galactic foregrounds from the CMB; unmodeled differential bandpasses between detector pairs could also leak temperature into polarization.

- *Fourier Transform Spectrometer*: FTSs have been used by numerous experiments for bandpass measurements, and the basic design could be in common with that used for the LATs (Fig. 66 f; [525, 526, 535]). We anticipate making FTS measurements when the receiver is on the mount. To minimize optical systematics the FTS will need to optimally couple to each detector's beam, requiring multi-axis motion.

In addition to these key calibrations driven by requirements on degree-scale systematics, numerous other measurements will be made throughout the commissioning process and *in situ*, which feed into validation of receiver performance and science observations. In all cases the required hardware will be designed to couple securely and repeatably to the SATs to facilitate ease of use at the various sites:

- Optical efficiency using *aperture-filling thermal loads*. There is scope for significant improvement over heritage calibrators, e.g. in temperature control, optical geometry, andr secure coupling to the cryostat. Such a device could also be used to probe forebaffle loading by intercepting varying angles exiting the window.
- Beam shapes in the aperture plane using a *small thermal chopper and 2-axis motion stage*.
- Polarization angles in the aperture plane using *wire grids and dielectric sheet calibrators* [536, 537].
- Magnetic sensitivity using *Helmholtz coils*.
- RFI sensitivity (e.g., handheld radio and satellite communication) using *RF test sources and antennas*.
- Vibration sensitivity using *accelerometers*.
- Pointing model using *star cameras* attached to the mounts.

3.7 Data Acquisition & Control (*Laura Newburgh*)

The reference data acquisition and experiment control subsystem is closely based on that used in existing Stage-3 CMB experiments, with a clear technical path to handling the higher data rates from CMB-S4. This subsystem encompasses *(a)* the acquisition of high-rate data (∼400 Hz, 32 bits per detector) from the detector arrays and the acquisition of low-rate data from "housekeeping" sources on each telescope (eg. cryogenic thermometry, telescope position encoders and motion metrics, pressure gauges, calibrators, networking statistics), and at the site if requested (eg. networking, disk space, power and water cooling data); *(b)* control of these subsystems including an observation sequencer to command the subsystems in series for each telescope; *(c)* real-time monitoring of housekeeping and data quality statistics; *(d)* non-critical alarms for out-of-range data; and *(e)* the provision of timing and frequency reference signals. The scope of DAQ and the purview of the Observatory Control System (OCS) including control, data aggregation, and monitoring connections to the telescopes and data management is shown in Figure 67.

In the following, each CMB-S4 site is considered a completely independent entity; the logistical differences between a polar and a Chilean site impose different scan strategies and requirements and DAQ has not received a requirement that we control the two sites with co-dependencies. Thus, the DAQ framework at both sites will be identical, but are not planned to be connected.

The total expected data rate to disk from CMB-S4, summed across both sites, is approximately 8 Gbit/s, dominated by bolometer data.

3.7.1 Observatory Control System

The Observatory Control System (OCS) is a distributed control system designed to coordinate data acquisition across each observatory site. The OCS will facilitate both automated and user-interactive control of

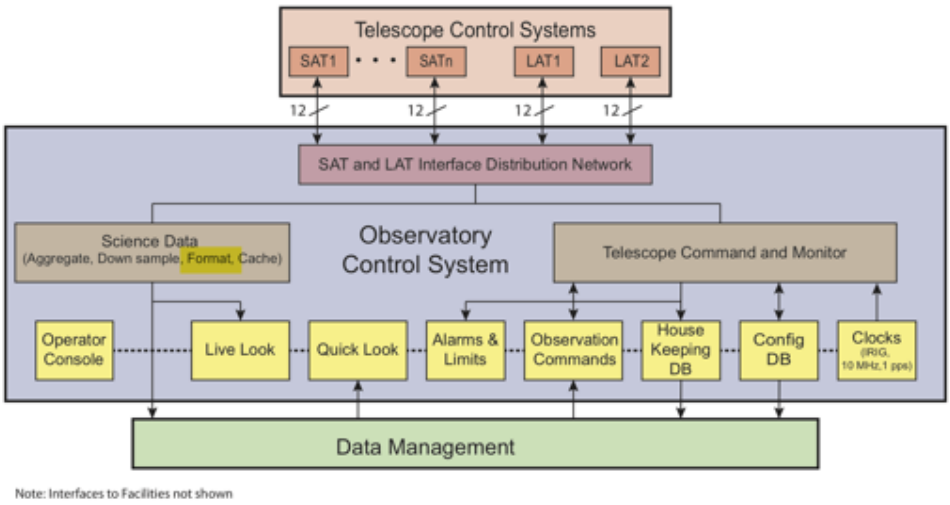

Figure 67: An overview of the observatory control system, including the alarms, data acquisition control, and monitoring, including the interface to all telescope platforms.

site systems including multiple telescope platforms, warm readout, telescope encoders, half-wave plates, etc. The full set of subsystems are likely to include a combination of commercial devices alongside specialized hardware designed for CMB-S4 or adapted from existing CMB projects.

3.7.1.1 Control Framework

The control system framework will be based upon a collection of software servers for each associated piece of hardware. Each of these long running software servers (or daemons) interface with a hardware or software component to coordinate data acquisition. Command of these servers and data exchange from them will be implemented on top of mature remote procedure-call and publish-subscribe systems supplied by existing open-source, community-maintained software libraries such as crossbar.io. This structure describes the Observatory Control System being built by the Simons Observatory collaboration, which forms a baseline for consideration of control systems for use on CMB-S4 [**?**]. A simple example of two software servers and a commanding client are shown in Figure 68.

All devices will produce status information, such as the success or failure of requested operations, in a standard OCS-defined format, facilitating the logging and monitoring of disparate systems. Control software will operate by translating high-level requests (such as a request to observe a certain sky field for a certain amount of time) into a sequence of lower-level tasks, and then initiating and monitoring the execution of those tasks on the relevant subsystems. Any on-going device operations that are unrelated to specific observing requests will be initiated and monitored through the same system, but by different, persistent high-level control daemons within OCS.

For non-commercial, ad-hoc devices, such a server can be written as the primary means of control for the device. In the case of commercial devices, the associated server might consist of a simple translation of OCS requests into requests on the device's native high-level interface. Suitable libraries, example code, and ample documentation will be provided by OCS maintainers for use in the development of subsystem servers.

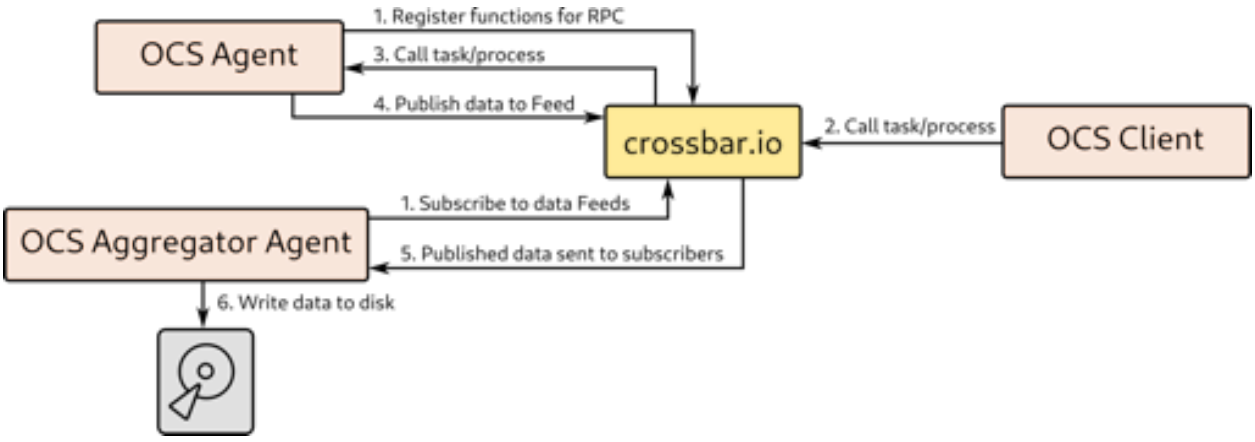

Figure 68: The interaction of two OCS Agents and a single OCS Client in the SO OCS system. A generic Agent registers its functions for remote procedure call with the central crossbar.io server. The OCS Client calls these functions, and the generic OCS Agent publishes data in the publish-subscribe model, while the OCS Aggregator Agent subscribes, getting a copy of the data and writing it to disk. Figure from [**?**].

The OCS maintainers place a strong emphasis on facilitating contributions from subsystem experts without requiring deep knowledge of OCS implementation details or extensive computing experience. Python and C++ will both be supported as implementation languages, but it is anticipated that Python will be the most common choice. So that subsystem maintainers can more easily test their implementations locally, the OCS software stack will support a variety of commonly-deployed systems as well as virtualized and containerized operation.

An example of a lab tested, multi-node, OCS network from the Simons Observatory is shown in Figure 69. This is the network for a single small aperture telescope (SAT), and contains several software servers (pressure gauges, Lakeshore thermometry devices, labjacks, power supply) written by subsystem experts working on the hardware, demonstrating the flexibility available when thorough documentation and support is available. The network contains a dedicated readout electronics computer, a main housekeeping systems computer, and three smaller computers for special interfaces to hardware, one of which happens to host the crossbar server that provides RPC and Pub/Sub. CMB-S4 may make different hardware choices, each of which would have a new hardware-specific software server associated with it. The most important anticipated difference between this SAT example and CMB-S4 is the detector readout: here is it a Smurf based readout system, but a new detector readout interface would need to be written for CMB-S4.

While individual telescope subsystems within the observatory may produce large volumes of data, or may need to operate in hard real-time to meet performance requirements, there are no interactions between subsystems that require exchange or analysis of large amounts of data in order to maintain instrument performance. Furthermore, the synchronization requirements, when coordinating operations of various systems, need not exceed several milliseconds. This precision is easily achieved simply using clocks synchronized using Network Time Protocol over local Ethernet networks, which generally provides timing precision better than a millisecond.

As a result of this loose coupling, we are free to adopt a simple OCS architecture wherein all devices accept commands and exchange low-speed data on the observatory network using a simple interface schema defined by the OCS.

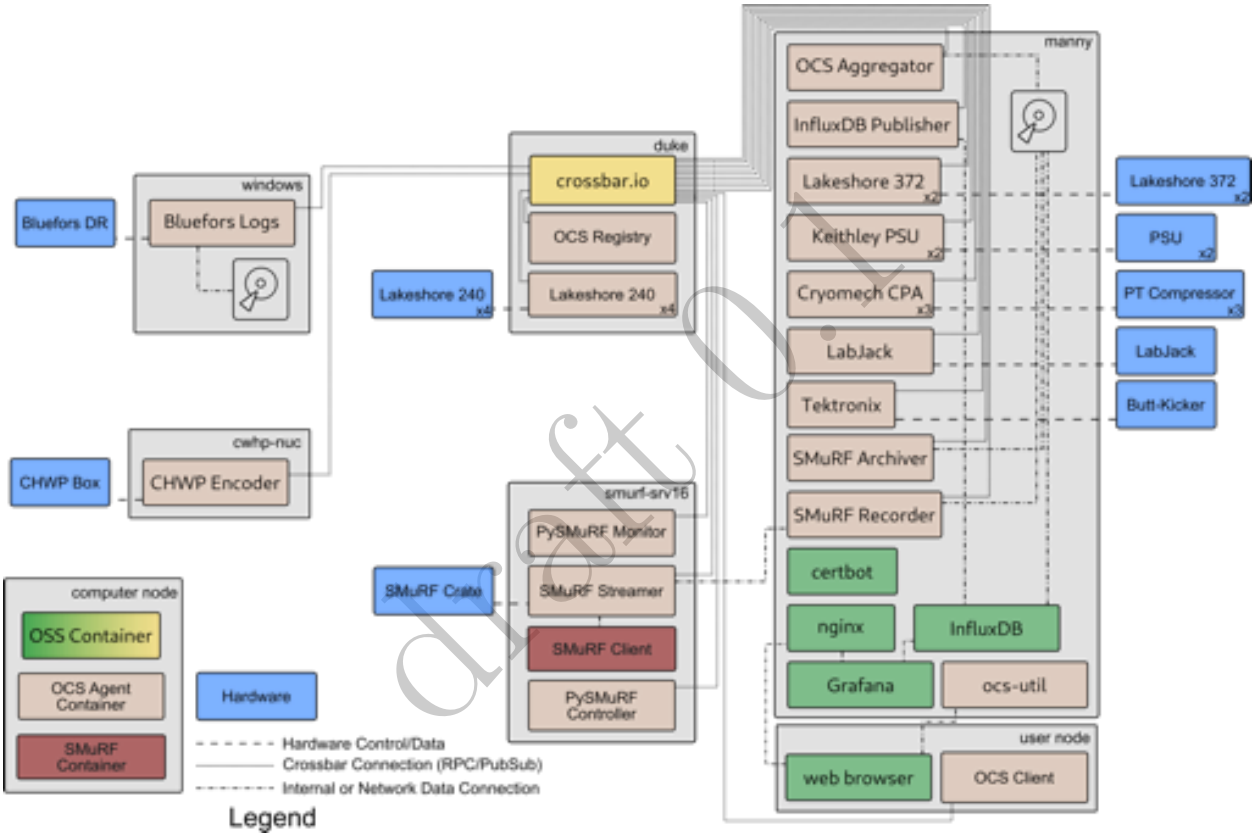

Figure 69: The OCS environment for the first small aperture telescope (SAT) during testing at the University of California San Diego. Figure from [**?**].

3.7.1.2 Observation Scheduling

While the OCS will support direct control of observations by an operator, it is anticipated that most observations will be scheduled ahead of time. In most cases, this can be done by a secure, user-friendly web interface. Examples of high-level commands include moving the telescope in a specified direction, sky scans, and detector tuning. The interface would contain rudimentary validation of the observing plan, then convert the high-level plan to the equivalent sequence of low-level commands that will be run at the appropriate time, via the OCS. It will also be possible to manually enter the low-level commands, if necessary. All commands will be logged to facilitate monitoring and auditing.

3.7.1.3 Bolometer Readout Control

Bolometer readout is managed by specialized readout crates, capable of acquiring the data at the required data throughput (up to 4 Gbps / site). Each readout crate will be managed at a high-level by the OCS. It will be possible to initiate calibrations and tuning, modify the cadence, and start and stop readout from the OCS.

3.7.1.4 Telescope Platform Control

The telescope control system is comprised of an isolated computing environment that communicates directly with the telescope on-board computer (provided by the telescope manufacturer). This system receives pointing data and diagnostics from the telescope at a fixed rate, and schedules observations by providing a sequence of scan profiles to control the telescope position and velocity. Commanding to the telescope is asynchronous with data acquisition to avoid reliance on strict real-time processing, while allowing the on-board control loop to run at a fast enough rate (typically ~ 100 Hz) for smooth telescope operation. The control system interfaces with the OCS to receive high-level scheduling commands, send status messages, and process alarms.

3.7.1.5 Cryogenic Control

Safety is a key priority when operating the cryogenic control system. As such, commanding of the cryogenic system will be developed in cooperation with the vendor and relevant members of the collaboration to ensure that the cryogenic system cannot be put into an unsafe state via the OCS. We require the OCS interface remain high level, such that direct control over valves, etc will not be included in the OCS scope.

3.7.1.6 Housekeeping Control

During normal operations the housekeeping OCS software servers will be configured to collect data from their associated subsystems. Control of these systems, such as the configuration of readout channels, updating of parameters or similar, will be handled by the same software servers and controlled via the exposed remote procedure calls provided by the server.

3.7.2 Data Acquisition

3.7.2.1 Bolometer readout

Following the designs in existing projects, the warm readout electronics (Sec. **??**) will be connected to Ethernet through several intermediate control computers (L1 aggregators) implementing the interface to the warm electronics (either Ethernet or a custom format implemented through a PCI-E card, depending on the modernization discussed in the previous section). These convert the data to a generic format and collate the responses from multiple boards, then forward them to another system (L2 aggregator) by Ethernet, which in turn assembles final data frames from an entire focal plane. As we do not record phase information, there is no clear benefit to taking data jointly from multiple telescopes and we plan to treat each telescope as an independent entity for the purposes of data acquisition.

The intermediate format used by the L1 and L2 aggregators is baselined as the common format currently used by SPT-3G, POLARBEAR2, and Simons Observatory, but may be adapted to S4 pursuant to the needs of the instrument. This format will, to the extent possible and to the extent to which the L2 aggregator and later data acquisition steps depend on it, be independent of the employed readout technology, limiting the impact of changes in readout design (Sec. **??**) to hardware and software changes on the L1 aggregator points.

The L2 aggregator forms the only serial chokepoint in the data flow and needs to be able to aggregate at minimum one focal plane's worth of data in one place. This architecture has been demonstrated on SPT-3G with 16,000 channels. The highest-burdened serial stage of this data collation uses CPU time linearly with channel count and is a factor of three from the limit of a 2017-era CPU, allowing scaling to single receivers of 50,000 detectors, comparable to that planned for CMB-S4 (Table **??**), without any further engineering effort.

Similarly, we are currently baselining the data acquisition code written for SPT-3G and POLARBEAR2 and planned in use by Simons Observatory, which appears capable of handling the high data rates expected for CMB-S4 in limited testing. Extensive software research and development work for bolometer data acquisition is not expected to be required to meet the data loss requirement of $<0.001\%$.

After the L2 aggregator, data is forwarded to a first-level disk cache for later non-real-time unification with housekeeping data, compression, and archival. This follows the succesful strategy employed by all stage-3 instruments and is a highly parallel process that can scale to CMB-S4 data rates in sythetic tests.

3.7.2.2 Telescope Platform Readout

Telescope platform readout is a unique housekeeping system. It differs from most other housekeeping systems by the inclusion of several high data rate outputs ($\sim$ 100 Hz). These data feeds are included in the normal housekeeping system when writing to disk. When being forwarded to the live monitoring system, a downsampled feed of data will be provided that will allow both live and historical monitoring of platform housekeeping fields.

3.7.2.3 Housekeeping Readout

In addition to bolometer data, we will record data from a variety of housekeeping systems, which include telescope mount encoders and tilt meters, cryostat thermometry, pressure gauges, power supplies, calibration

equipment, dilution refrigerator data (helium flows, pressures, temperatures, compressor data), a weather station, status variables, and other monitors of the observatory status. Although the housekeeping data in principle can be high rate (up to $\sim$ 1kHz), we expect most data streams to be slow ($\sim$1Hz), and when higher cadences are required (for example the telescope mount data above) a downsampled stream would be sent to the monitor to keep the live monitoring efficient. A computer running acquisition for subsystems will be responsible for packing its own data into timestamped containers that are sent via Ethernet to the first-level disk cache. The container data structure supports time-ordered data with different sample rates; most of the housekeeping systems will be sampled much slower ($\sim$1 Hz) than bolometer data. All subsystems will be synchronized via IRIG-B002, as discussed in **??**, so timestamps can be used to identify and aggregate simultaneous data. It is not necessary for this process to occur in real time (although it will be nearly real time in practice), so it is mostly insensitive to lags in delivery from particular subsystems. The bolometers dominate the overall data rate, so the additional housekeeping subsystems will not be a substantial burden on the network or the first-level disk cache.

After the first-level disk cache, we plan a third data aggregation step (L3) that happens asynchronously using an on-site computing cluster. At L3, the auxiliary data streams are merged into the same files as the high-rate bolometer data so that all the data at a particular time are co-located for correlation analyses during processing. A second copy of the auxiliary data will be stored to a database for retrieval by tasks that do not also require the bolometer data and can benefit from a more lightweight interface, such as site monitoring.

3.7.2.4 DAQ network design

The DAQ components will be connected by a 10 Gbps (or better) Ethernet network, which will support the data rates envisioned. All Ethernet communications will use standard TCP/IP framing, which simplifies implementation and debugging and will meet data integrity goals. While it is anticipated that a standard operating system TCP/IP stack will be performant enough to meet requirements, userspace direct processing of TCP packets (via, e.g., DPDK) is an option that would allow higher throughput if necessary. No specialized custom networking equipment or custom kernel drivers are envisioned. To reduce congestion, the high-speed and low-speed components of the DAQ may be on different networks.

3.7.2.5 Observatory Timing

Synchronization for each observatory will be accomplished with either PTP network timing (with optional IRIG-B002 timestamps if required) distributed to the bolometer readout, telescope encoders, and other housekeeping subsystems. A timing card specified for use by most Stage-3 experiments will provide absolute GPS timestamps and can free-run without a GPS lock with minimal drift (5 parts in 10^{11}) over 24 hour time scales. It is highly configurable, including outputs of PTP, IRIG-B timestamps, a 10 MHz oscillator, and a pulse-per-second (PPS). With an Allen variance on the 10 MHz oscillator of $< 10^{-11}$ s, these achieve the stringent requirements necessary for frequency-based readout as well as the 1μs absolute timing accuracy sufficient for all readout and subsystems baselined in this white paper. In particular, we are not baselining a synchronization pulse or word to be distributed across the site, however individual subsystems (e.g. synchronization between readout crates on a platform) may be required and specified by the subsystem, and that synchronization signal could be timestamped and recorded as well.

3.7.2.6 File format specification

The baseline SPT3G file format is a (potentially-compressed) binary stream of "frames." Each frame contains one or more "frame objects" which are automatically serialized from its code implementation using the C++11 `cereal` library as well as some metadata.

The binary stream is platform-independent and introspectable. Due to the streaming format, it is possible to concatenate files in order to merge them. As an optimization, the file reader supports lazy deserialization of the binary representations ("blobs") and transparent decompression of the input stream.

3.7.3 Monitoring and Alarms

Monitoring and alarms are an integral part of the OCS design.

3.7.3.1 Remote Monitoring of Telescope and Housekeeping Subsystems

The data monitoring subsystem is a server/client system that aggregates data from each of the subsystems that communicates with the OCS, and presents it over an authenticated web interface for monitoring of data quality and site status. The server provides a common API for each connected client to supply and receive monitoring information from other subsystems, and to issue alarms. Each telescope site maintains one monitoring server, and clients can connect from anywhere to request data, often from multiple sites. This system is separate from the main data management system described in 3.8, as it largely handles data provided in near-real-time (< 5 s latency), although it should also be able to retrieve archived data should a client request it.

For example, one such client would be a housekeeping consumer that monitors the state of each cryogenic system. This client provides a web interface to view housekeeping data retrieved from the server, and issues alarms if temperatures are out of scope. An alarm may be issued as an email to the operations team, a text message or a telephone call to the site, or a simple warning on the web interface.

The design of the monitoring system will be flexible and scalable, allowing monitoring of anything from a single lab with one device to an entire site. The monitoring system will have the capability to handle at least an update rate of 100,000 fields/second. To facilitate viewing of large amounts of historical data, the monitoring system will support decimated views of archived data. All web browser clients, including those on mobile phones and tablets, will be supported.

3.7.3.2 Remote monitoring of real-time statistics and detector time streams

A separate monitor/viewer is maintained for bolometer data at each telescope site, either streaming in near-real-time, or as snapshots of specific statistics (e.g. average current noise in a particular frequency range, depth into TES transition). These data can be used during calibration runs, and for monitoring data quality during normal observing periods. For example, one might issue an alarm if too many channels are outside of the normal operating range on the TES transition. Subsets of the data aggregated by this monitor are also sent to the central monitoring server.

3.7.3.3 Non-safety Alarms and notification systems

The Alarms system actively monitors the data feeds from the OCS and checks those values against some configurable threshold to determine how to elevate the alarm state to the notification system. All alarm states can be viewed via a web interface. Non-severe warnings will trigger low priority alerts, such as email and Slack messages. More severe warnings can be elevated higher priority alerts, triggering notifications such as phone calls and SMS messages. The system will also support integration of any existing site-specific notification methods.

3.7.3.4 Propagation of safety alarms to notification systems

Hardware and personnel safety is the responsibility of the hardware subsystem and safety management, and the DAQ scope does not include critical hardware or personal safety alarms, nor support software-based critical safety protocols. However, any networked alarms, faults, flags, or status (eg e-stop pressed) can be integrated into the DAQ monitor to allow monitoring of those alarms along with the rest of the observatory monitoring. Propagation of safety alarms follows the same path through the system as non-safety alarms to higher priority alert systems.

3.8 Data Management (*Julian Borrill*)

3.8.1 Overview

3.8.1.1 Scope

The Data Management (DM) subsystem receives the raw instrument data from the Data Acquisition subsystem at each observing site and delivers a range of intermediate data products to the scientific collaboration, and all intermediate and final data products, together with the software used to generate them, to the scientific community. Specifically the DM scope includes

- the registration of all data on receipt from Data Acquisition
- the movement of all data, from each site to the primary US data center, between data centers, and from the primary data center to the collaboration and community;
- the secure archival storage of the full raw dataset and all derived data products;
- the production of daily single-frequency maps from all telescopes;
- the identification of spatial and temporal transients in the daily large aperture telescope maps, and the issuing of alerts to the community;
- the monitoring of daily data quality for all telescopes, and the issuing of alerts to operations contol;
- the characterization of each instrument and its observations from all design, testing, and field data;
- the production of single-frequency maps from the full data and a variety of data subsets, including time-domain systematics mitigation;

- the generation of corresponding mock datasets to support uncertainty quantification and debiasing;
- the delivery of validated and documented science-grade intermediate data products (well-characterized single-frequency maps and the corresponding experiment model) to the collaboration for all science analyses;
- the receipt of feedback from the collaboration on the quality and sufficiency of the intermediate data products, and the adaptation of the data processing pipelines accordingly;
- the delivery of validated and documented science-grade intermediate and final data products, and all software used to generate them, to the scientific community.

In addition, during the construction project the DM subsystem is regularly exercised to validate the experiment design, the DM subsystem design and its implementation, and the various science analysis pipelines.

3.8.1.2 Design Drivers & Assumptions

The design of the DM subsystem is driven by the data rates at each site, the daily and total data volumes, the computational complexity of the data processing, and the schedule for delivery of each type of data product. Table 3-22 shows the data rates for each type of telescope in the Preliminary Baseline Design.

Telescopes	Detectors (KDet)	Sampling Rate (Hz)	Raw Data Rate (Samples/Second)	Compressed Data Rate (Gbps)
CHLAT	270	400	9.7×10^7	1.09
SPLAT	126	400	4.6×10^7	0.51
SAT	155	100	1.5×10^7	0.17

Table 3-22: Data rates of each telescope type, assuming a 35% compression factor.

The Chilean data are assumed to be transferred over fiber-optic networks to the US, with on-site storage for up to 1 month of data (390 TB) in case of network outage. The South Pole data are asumed to be transferred by disk annually, with on-site storage for up to 2 years of data (5.8 PB) to provide failsafe margin. The entire dataset (54 PB) is archived at two distinct US data centers to provide protection against catastrophic failure.

Table 3-23 shows the computational requirements for the daily map-making for each type of telescope in the Preliminary Baseline Design.

Daily maps of the Chilean data are assumed to be produced on allocated computational resources in the US, while daily maps of the South Pole data are assumed to be produced on dedicated on-site computational resources with the maps and any alerts generated from them transferred daily over the network to the US.

The largest single data processing would involve the simulation and reduction of mock data for the full science-quality data volume from the largest single frequency (CHLAT 90/150 GHz). Assuming 20% observing efficiency for 7 years, O(2000) FLOP to simulate and O(1000) FLOP to reduce each sample, and two full copies of the data in memory at once to enable destructive processing and reprocessing, this would require 24 EFLOP of cycles and 13 PB of memory; single-season simulation and reduction, by comparison, would require 3.4 EFLOP and 2 PB, and single-season reduction of field data 1.1 EFLOP and 2 PB. Since resources

Telescopes	Cycles (TFLOP)	Peak Memory (TB)	Daily Map Data Volume (GB)	Total Map Data Volume (TB)
CHLAT	0.93	13	54	139
SPLAT	0.44	6.5	4.5	12
SAT	0.13	1.2	0.02	0.05

Table 3-23: Computational requirements for daily map-making asuming filter-and-bin map-making with O(10) FLOP/sample and all of the data at one frequency in memory at once.

at such scale are beyond the budget of the project, and their peak use will only be occasional, we assume that they will be obtained by allocation from national High Performance Computing (HPC) and High Throughput Computing (HTC) facilities run by DOE and NSF.

3.8.1.3 Subsystem Design

Figure 70 shows a schematic view of the Preliminary Baseline Design of the DM subsystem, including on-site resources, data-transport systems, archival storage, computing systems, the overall software stack, and data distribution within and outside of the project. This design is based on the assumption that there will be sufficient bandwidth to transfer the Chilean data to the US in real time, but that this will not be the case for South Pole data. Should the bandwidth from the South Pole become sufficient the design will be adjusted accordingly.

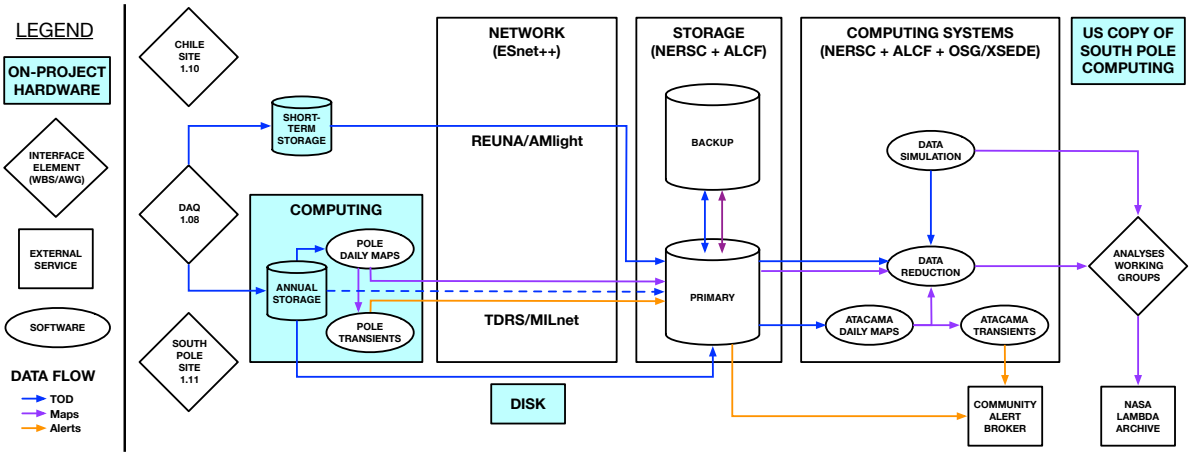

Figure 70: Schematic view of the DM infrastructure, spanning the range from Data Acquisition to Science Analyses, with on-project hardware highlighted in cyan. Note that the named allocated networking, storage and compute resources are indicative and anticipated, not yet confirmed.

Figure 71 shows a schematic view of the DM pipeline, including internal interfaces betwen different elements within the DM subsystem and external interfaces to other project subsystems, the scentific collaboration's Analysis Working Groups, and the wider scientific community.

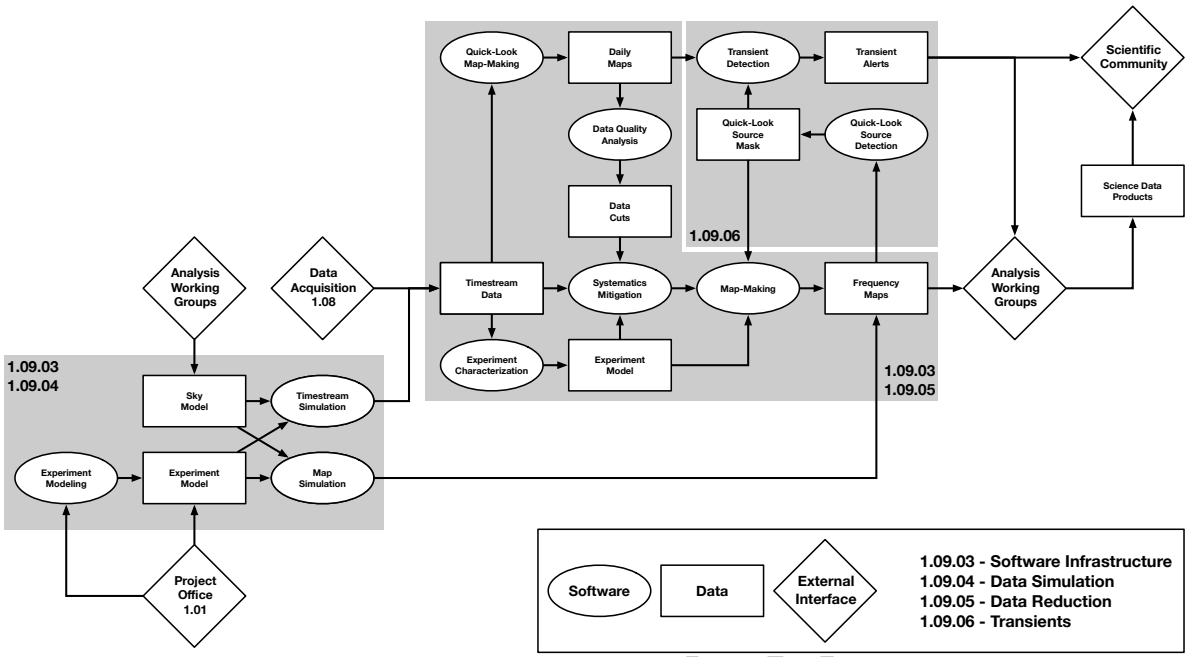

Figure 71: Schematic view of the DM pipeline, spanning software infrastructure, data simulation, data reduction, and transient detection, and including internal and external interfaces.

The following sections provide a more detailed view of the Preliminary Baseline Design, broken down by the Level 3 elements within the DM subsystem, which cover Data Movement, Software Infrastructure, Data Simulation, Data Reduction, Transients, and Site Hardware respectively.

3.8.2 Data Movement

3.8.2.1 Registration and Archiving

The backbone of the data movement subsystem is a registry of data products, with an associated API for archiving products for long term storage, transporting products between data centers, and extracting products for use by CMB-S4 team members and the public.

Here we define data products as any simulated or real piece of data, and may include raw or processed detector timestreams, maps, instrument models, or any other auxiliary data products. Each item is added to the registry with associated metadata such as data type, author, a timestamp, and the location(s) in which the item is stored. Each data center, including those at each observing site, maintains a local copy of the registry that is synchronized with the Primary Data Center. The registry is updated any time an item is created, transmitted between data centers, or archived for long term storage.

The registration software and interface should be sufficiently flexible and robust to support a variety of use cases, including asynchronous data transfer from the South Pole, continuously streaming data transfer from the Chilean site, and interactive requests from users. Software currently under consideration includes Librar-

ian[1], which was developed by the HERA collaboration and is baselined for use by the Simons Observatory; and Rucio[2], developed by CERN for managing large scientific datasets.

A preliminary version of the registry with a basic feature set will be made available for initial data challenges, while the development of the complete system is underway. Each data challenge will provide a testing platform for the data movement software, with the goal of providing a fully operational system prior to telescope commissioning.

3.8.2.2 Transmission

Data will be transferred from observation sites to the primary data center. From the primary U.S. data center the data will be transferred over ESnet to the secondary center to provide a secure backup. The various reference design paths are illustrated in Fig. 72. Practical considerations lead to different data transfer workflows for the Chilean site and for the South Pole site, which are described below.

For the Chilean site, a fiber-optic network connection will be made to the nearby ALMA Array Operations Site as part of site development. From there, the data will traverse REUNA, the Chilean science network, then AmLight, which provides transport from Chile to the US, then ESnet, the DOE high-performance networking facility, and then arrive at the data centers. To provide resilience in the event of network outages, an on-site disk buffer with one month of capacity will be deployed. The network bandwidth will be sufficient to allow for catch-up after outages, i.e. the transfer of the backlog in the disk buffer while current data operations continue after the outage. The data transfer infrastructure at the Chilean site will employ a Data Transfer Node (DTN - as described in the Science DMZ [538] model) which will interface with the data centers for file transfers. The DTN will be able to transfer data to the secondary data center if the primary data center is offline (e.g. due to maintenance or outage). The network path will be tested and characterized using perfSONAR [539] to ensure that data transfers are reliable and performant.

From the South Pole, daily transfers of reduced data products will use the TDRS satellite link and MILnet. These transfer capabilities are controlled by the limited number of satellites in orbits visible from the South Pole and the limited fraction of the day during which they are above the horizon. As noted above, current network data-transfer capabilities (about 100 GB/day) are not sufficient for the full CMB-S4 data rate. For the reference design we will therefore plan to store each year's data on site and transfer them to the U.S. at the start of each Austral summer, however we will also continue to work with NSF and DOE to investigate possibilities for implementing a connection to the US data center with sufficient bandwidth to stream the data.

3.8.2.3 Internal Distribution

All CMB-S4 collaboration members will have access to the raw data and to intermediate data products up to and including the well-characterized single-frequency maps. The main mode for the distribution of data to the collaboration will be via the primary data center, where all collaboration members will also be eligible to have user accounts and have access to significant compute resources. Given its volume, typically we expect users to bring their code to the time-domain data, and only to transfer map-domain data to their local computing resources (though these can obviously be processed at NERSC too). Although they lie outside of the remit of the data-management subsystem, we anticipate that additional derived data products

[1] https://github.com/HERA-Team/librarian
[2] https://rucio.cern.ch

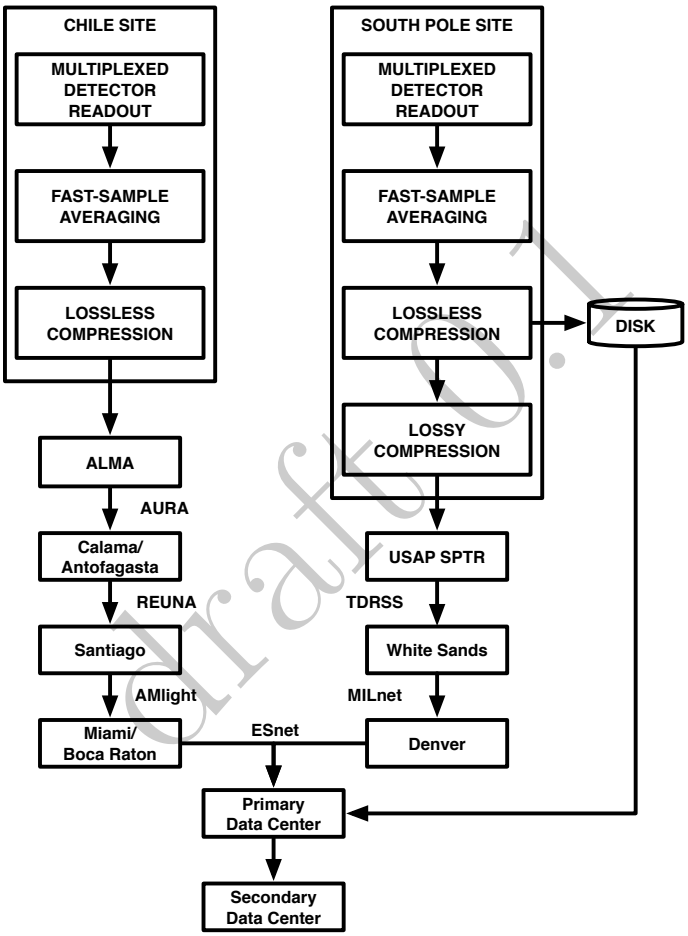

Figure 72: Schematic view of data-transport paths from acquisition to the U.S. data centers for the Chile and South Pole sites.

(e.g., component-separated maps, maps of the lensing potential, power spectra and likelihood codes) will be similarly distributed.

3.8.2.4 External Distribution

Public releases of CMB-S4 data products will occur at regular intervals through well-established CMB data archives. Maps of all flavors (single-frequency, foreground-cleaned CMB, lensing potential, etc), catalogs of galaxies and galaxy clusters, the CMB power spectra, and cosmological parameter likelihood codes will be archived at NASA's Legacy Archive for Microwave Background Data (LAMBDA), including both the real data and subsets of the supporting suites of Monte Carlo map realizations. Time-domain data and the full Monte Carlo suites, together with the code used to process them, will be made available through public directories at NERSC, where users will also have access to the computational resources needed to make practical use of such large data sets. We will also make the data-management software stack (complete with full documentation) public wherever possible both through a public repository on a version control system such as github and as a standard installation at NERSC.

3.8.3 Software Infrastructure

The Software Infrastructure component of Data Management (DM) is responsible for defining several key interfaces between other components, for managing the deployment and execution of software developed by other DM components, and for tracking generated data products and their provenance. The goal of software infrastructure is to enable the simulation and reduction of data on our computing platforms in a reasonably automated fashion while recording the details of what was done to enable reproducibility and future data exploration.

For fast data quality checks and transient detection, realtime streaming and HTC data processing will occur on a variety of platforms. These include "on-site" computing (both at the South Pole cluster and smaller systems in Chile), OSG / grid resources, and possibly novel computing in transit on the network (FABRIC). This rapid computing does not use algorithms requiring simultaneous access to large amounts of data. Less frequent bulk reprocessing of data will occur at several HPC centers in the US (NERSC, ALCF, perhaps others). These computing resources will enable simulation and reduction algorithms that can benefit from larger data volumes in memory.

Across all computing resources we must deploy our software stack in the way that is most appropriate for a given platform. Each computing platform has its own mechanisms for scheduling and running jobs and different constraints on I/O. Regardless of the system, we must track the processing history of data products.

3.8.3.1 Data Model

The "Data Model" describes how real and simulated data and metadata is stored in memory and on disk. It includes the software interfaces to access data / metadata and mechanisms to index the raw and processed data. These interfaces are used by simulation and reduction codes.

The initial raw data format on disk is defined by our interface to the DAQ L2 subsystem. This is currently baselined to use the SPT3G serialized frame format. This raw data is delivered to accessible storage locations (either on-site or in the US) by the *Data Movement* L3 component. Rapid processing of the raw data for

quality checks and transients will happen on HTC compute systems. Because of the nature of these systems (smaller, more isolated compute units, high network connectivity, etc), we intend to stream the raw SPT3G data directly to the compute resources. This in-memory and over-the-wire data format has worked well for existing stage 3 experiments on HTC computing systems.

In addition to being streamed directly to the fast-turnaround HTC processing, the raw data will also be transferred by *Data Movement* to longer-term storage and archival locations (likely associated with the US HPC computing centers). At this point, the raw data may be deserialized and repacked into an archival format suitable for both parallel I/O and long-term legacy access. This is an area of investigation and evaluation during the design phase of the project.

Bulk reprocessing and simulation of data on HPC systems will use the TOAST software framework, which has a ten year history of CMB simulation and analysis at scale on HPC computing resources. With suitable plugins, TOAST workflows can read / write data to any on-disk format. The in-memory data format consists of simple containers of arrays and leverages MPI shared memory to reduce the aggregate footprint in large jobs. To the extent possible, we will strive to make the in-memory data interface for HPC and HTC workflows similar. This will ease the writing of simulation and reduction software that is intended to run on both types of computing platforms.

Indexing of raw and derived data products is essential for nearly every step of the processing. Data selection using such an index is needed for building workflows that target specific parts of the instrument, observing fields, site conditions, etc. The basic metadata needed to build such an index is received by DM as part of the data interface to DAQ. Further metadata may be generated by later steps of the processing. Existing and past experiments have used a variety of ad-hoc solutions including relational databases, simple text files, and clever directory structures to find data files based on selection criteria. The data indexing system must work across a variety of use cases. For example, on-site computing must be able to access selections of recent metadata for local processing without using the network. Building jobs at an HPC center may involve querying hundreds of different data properties to select files to stage from archival storage. The details of this indexing system will be established during the project design phase.

3.8.3.2 Processing Model

The "Processing Model" describes the interfaces that simulation and reduction code must conform to in order to function within a larger workflow on our computing platforms. In also includes tools for building those workflows, as well as any optimizations needed to enable those workflows to perform well enough to meet our requirements.

On HTC computing resources, workflows will be represented as G3Pipeline objects consisting of G3Modules. This implies that the code running on these platforms will need to exist as or be wrapped into a G3Module / G3Pipeline. On HPC computing resources, workflows will be represented as TOAST Pipeline objects consisting of Operators and other Pipelines. The simulation and analysis code running on these platforms will exist as or be wrapped into an Operator / Pipeline. We will provide tools to enable such encapsulation and / or abstraction to ease running of some simulation and reduction operators in both types of workflows.

On all computing resources, our processing model must include tools to construct needed workflows from specified data selections. We will be creating workflows for data quality checks using both on-site and US computing resources, building workflows to do larger scale null tests and bulk reprocessing, and workflows that conduct Monte Carlo simulations to establish processing transfer functions and estimate statistical errors. The generation of all these types of workflows are within the scope of this L4 area.

Current and future HPC systems (and perhaps some portion of HTC resources) increasingly include a large fraction of manycore (GPU-like) resources in their available time allocations. We will enable the use of these resources for some of our workflows where it makes sense in terms of performance required to meet our goals.

3.8.3.3 Workflow Execution

"Workflow execution" includes the tools for constructing jobs from our workflows that can run on our computing resources, the submission and tracking of those jobs, and also tracking the provenance of generated data products. Even with substantial automation, we will require personnel resources for managing and orchestrating these tools, and that effort is included here as well.

The types of jobs we will be building and running span the range of small serial workflows using on-site resources dealing with recently acquired data up to large parallel workflows that reprocess a large quantity of archival data. Jobs will need to be built for running locally, running on HTC resources (e.g. using HTCondor), and running on HPC centers (e.g. using Slurm or other interfaces). We will focus specifically on the two large use cases that we need: a system for running daily quality checks and transient detection, and a system for coordinating large scale processing for simulations, data releases, etc.

Workflow execution will benefit from the advances being made to support the Superfacility initiative. This is a model for supporting high performance networking and computing for experimental science, spearheaded by LBNL. It integrates tools and technologies to enable automated, reslient workflows, including tools for data movement, management and sharing; real-time computing and network support; workflow automation via an API (for access to both NERSC and ESnet), and federated identity across DOE facilities. A recent focus of this effort is in cross-facility workflows, an emerging need across the DOE Office of Science. This work (including tools for data management and containerization) will facilitate data analysis pipelines that need to operate across diverse computing facilities, including clusters at DOE labs, the ASCR user facilities, and cloud computing. This work will be of particular benefit to CMB-S4, which will need to coordinate computing across several locations.

All data simulation and processing steps that modify data will record information about what was done. This would include (for example) the software versions used, all configuration options, etc. For a given output data product, it will be possible to track what processing was done to that data. This is true regardless of the computing platform used. A draft system for this provenance tracking will be developed during the design phase of the project.

3.8.3.4 Software Deployment

The software stacks used for simulation and reduction of data include specific CMB-S4 code as well as a wide range of off-the-shelf software packages in a variety of languages. Deployment of these software stacks will vary based on the specific computing platform, but we plan to use established techniques.

Software dependencies can have a large impact on the ease of deployment for our software stack. We will establish policies for inclusion of software dependencies that prioritize packages with long-term support and broad use (not just within astrophysics). For specialized packages we need for our software stack we will establish a long term support plan with contingencies for future deprecation by the upstream developers.

Current deployment techniques used in the field include container solutions (e.g. docker, singularity) that can bundle the complete software stack and transmit it at run time to HPC compute nodes or HTC processes. These containers are built automatically as part of the continuous integration process of testing the software.

Another common deployment technique for HTC jobs is the CVMFS distributed filesystem. On local systems and some specialized HPC environments, a combination of Python packages and manual compilation is used.

A goal of this L4 area is to simplify and automate the deployment process as much as possible. CMB-S4 is not the only science team that needs to operate computing across multiple sites, and we can leverage work already underway to support this model across DOE sites. For example, data management tools (eg DataFed) or portable containerization technologies deployed by DOE ASCR user facilities could be used by CMB-S4 with little additional effort. API interfaces are already being developed at several HPC centers in the USA (e.g. NERSC, TACC), and we expect a coordinated set of API end points to emerge in the next 2 years for all HPC centers. This would enable us to build truly automated analysis pipelines.

3.8.4 Data Simulation

Simulated data play key roles in CMB studies, including in the design and development of experiments and requirements; the validation and verification of their reduction and analysis pipelines; and the quantification of uncertainties in and removal of biases from their science results using Monte Carlo methods. Data simulation includes modeling both the experiment and the sky it will observe, along with generating simulated data sets both in the map- and the time-domains.

While the development of detailed models of individual sky components is outside of the realm of the DM subsystem, it does include the assembly of such models into total skies to be as inputs for simulated data sets. The total sky includes the temperature and polarization components of the scalar, tensor and non-Gaussian CMB; the extragalactic foregrounds (and their associated lensing of the CMB); and the galactic foregrounds. Realistic sky models will be particularly important for optimizing the frequency coverage of the various telescopes, and for the validation and verification of key science analysis algorithms and implementations including foreground cleaning and delensing. We will seek to support joint analyses of CMB-S4 with large-scale structure observations by adopting common extragalactic skies with experiments such as LSST, *WFIRST*, and *Euclid*.

The data simulation step applies the experiment model to the sky model to generate the data that would be gathered by the instrument making its observation of that sky. This includes signals from the sky, the atmosphere, and the ground, possibly modulated by a half-wave plate, convolved with each detector's beam and bandpass, converted to a signal by the detector, and fed through the readout system, and incorporating all of the detector-detector correlations, for example from multichroic pixels or highly multiplexed readout. The complexity of the processing and scale of the data necessarily introduce a trade-off between computational cost and realism, reflected in the prioritization of both map- and time-domain simulations (with time-domain syntheses also requiring reduction to maps before analysis). The development and deployment of these two paths will be coupled to take advantage of the strengths of each approach and the ability to cross-check them against one another. Specifically, we will ensure that each approach is able to synthesize data from the same combinations of experiment and sky model.

3.8.4.1 Experiment Modeling

Experiment modeling provides a parametric model of the entire experiment, comprising the instrument optics and electronics, the observation environment, and survey strategy. The parameterization should be rich enough to support the most detailed (and therefore computationally expensive) time-domain syntheses, while also providing standard reduced representations sufficient for approximate (but computationally cheaper)

map-domain and Fisher forecasting approaches. Developing this model necessitates participating in the project-wide activity to document a complete, sufficient, and unique characterization of the instrument and observation, and generate interfaces suitable for simulation, reduction, and analysis software.

3.8.4.2 Map Domain Simulation

Map domain simulation includes the design, deployment, testing, and documentation of systems to simulate map-domain data based on the application of the experiment model to a given sky model, incorporating all key map-domain systematic effects either fully or as residuals and possibly including maps generated from the reduction of simulated time-domain data.

3.8.4.3 Time Domain Simulation

Time domain simulation includes the design, deployment, testing, and documentation of systems to simulate time-domain data based on the application of the experiment model to a given sky model. The primary inputs for the time domain simulations include the experimental model, the sky model, instrumental and atmospheric noise models, and the scan strategy for each instrument. Another essential function of the time domain simulations is to include key time-domain systematic effects either fully or as residuals, including ground pickup, polarization leakage, beam systematics, polarization angle systematics, pointing systematics, readout crosstalk, bandpass systematics, gain variation, and non-linearities in the detector responses.

3.8.5 Data Reduction

The following text is from the reference design.

The data reduction pipelines form the core of the DM subsystem. Comprising experiment characterization, live monitoring, and map-making, they must produce all of the data products required to monitor the performance of the instruments and to support all of the various science analyses, and be able to do so with the required cadence. Note that both the characterization and monitoring pipelines must run near-autonomously and, for the South Pole data, they must be able to be executed on site.

3.8.5.1 Data Quality

The Data Quality subsystem is responsible for quicklook monitoring and analysis of data, typically lagging real time by less than 24 hours. This view of CMB-S4 data is essential to catch instrumental problems that are too subtle to be noticed by on-site operators but which must be swiftly corrected to ensure proper science operations. The 24 hour cadence of Data Quality also fulfills the needs of the Transients subsystem (§3.8.6), which will further process the daily sky maps produced by Data Quality to identify time-variable sources. Finally, the statistics compiled by Data Quality will provide a summary of the full CMB-S4 dataset that can be used for data selection in the mapmaking process and as a resource for in-depth studies.

The monitoring provided by the Data Quality subsystem is distinct from real time on-site monitoring and alarms that are part of the Data Acquisition system (add cross-ref). The real time monitoring is primarily concerned with detecting problems that could affect the safety of the instrument or its operators, but it will not attempt to process the large volume of bolometer data generated by CMB-S4. The daily data reduction

will include evaluation of responsivity and noise for all detectors to determine that the instrument as a whole is operating with the expected sensitivity. Daily sky maps will be derived using a simplified map-making pipeline with high-pass filtering to enable transient source detection; the responsivity and noise of these daily maps will be another important data quality monitor.

With nearly real time transfer of all Chile site data to North America, the Data Quality activities for those telescopes can be performed using North American computing resources (NERSC). However, because we don't anticipate being able to transfer the full South Pole dataset via satellite, Data Quality processing of South Pole data will use on-site computing hardware (§3.8.7.2).

The data quality statistics obtained from detector timestreams and daily maps will be stored in a database that can be accessed by collaboration members and used to locate interesting data for follow-up studies.

3.8.5.2 Experiment Characterization

While CMB-S4 will spend the vast majority of its time on surveying the deep and wide regions (cross-ref?), a variety of other observation types will be necessary to fully characterize the instrument. These include using astronomical or hardware calibration sources to determine beam shapes and pointing, tests of detector function and noise optimization, and efforts to characterize sources of systematic error. Experiment characterization activities will be especially important during the deployment and early stages of operations.

The Experiment Characterization subsystem will develop data analysis software needed to extract the desired parameters from these calibration activities. To be useful, these analysis will have to run rapidly; for operations at the South Pole, this means using only on-site computing hardware.

The wide range of characterization activities implies a wide range of analysis needs. The Experiment Characterization subsystem will address this challenge by developing flexible tools for timestream analysis and mapmaking, which will overlap substantially with the Data Quality subsystem. Since calibration and characterization of the instruments often includes hardware and site activites, we will collaborate with other areas of the CMB-S4 project or university groups who are engaged in this effort.

3.8.5.3 TOD to Maps

Reducing time-ordered data into maps involves the following steps:

1. Data selection based on data quality flags and chosen data split scheme
2. Noise-weighting and calibration based on experiment characterization
3. Filtering out modes that are compromised by systematics and/or unresolved by the data
4. Solving for a sky map that is consistent with the data model
5. Deriving a statistical description of the signal and noise content of the sky map

Data selection employs the data quality database to reject data that are not science quality. Cuts are applied at observation, detector and time sample level. Data are also split into disjoint subsets that have independent noise and systematics to facilitate unbiased science analysis.

Noise-weighting and calibration translates digitized detector time samples into thermodynamical units. Each detector sample is assigned a statistical weight reflecting the statistical uncertainty associated with it. The weight is derived from measured detector noise.

Filtering includes pure time-domain filters such as polynomials and spatial filters such as ground-synchronous templates and detector mismatch templates. The singular focus on B-mode polarization for the small aperture telescopes and the supporting delensing survey benefit from filtering out all potential sources of temperature-to-polarization and E-to-B-mode leakage. In contrast, the Chilean large aperture survey will require a filter stack with minimal mode loss to support analysis of intensity and polarization at a large range of angular scales.

Solving for a map means taking the time-ordered data and the associated noise covariance model and finding the sky signal that minimizes the residual in the signal model. The CMB-S4 filter stack will be optimized to reject a majority of systematics and low frequency noise fluctuations, allowing for fast and simple mapmaking that treats the remaining noise as uniform and uncorrelated. This approach is referred to as *filter-and-bin*. In an effort to limit mode loss from filtering in the wide field maps, CMB-S4 will study the applicability of minimally biased mapmaking methods in place of filter-and-bin.

Deriving a statistical description of signal and noise is a critical part of the mapmaking process. For signal, this means measuring the pipeline transfer function resulting from filtering. The low resolution SAT maps allow us to evaluate a full observation matrix, a linear transformation that maps input signal to output signal. The observation matrix can be used to rapidly map a large volume of signal realizations to characterize the transfer function. LAT maps cannot be described with a similar matrix due to resource requirements so a large volume of TOD-to-map simulations is required.

The maps must also be characterized for their optical and frequency response. This is particularly relevant for cluster science via SZ effect where the measurement is performed right at the beam scale and the effective beam and bandpass may vary across the map. TOD-to-maps subsystem must provide estimates and uncertainties of effective beam and bandpass associated with each delivered map. The spatial variation may either be captured in the estimates (preferred but costly) or overall uncertainty. These data products are derived from outputs of Experiment Characterization.

If map pixel noise is uncorrelated, statistical description of the noise and systematics is a map of achieved noise depth at each sky pixel for Stokes I, Q and U. Unfortunately filtering, residual noise fluctuations and systematics will introduce small correlations between sky pixels. A full statistical description would be a voluminous pixel-pixel noise covariance matrix that is unwieldy for subsequent science analysis. In place of such a matrix, we will provide large numbers of Monte Carlo noise maps that capture noise and systematic residual correlations and allow analysis pipelines to measure the uncertainty and potential bias in their estimators. The Monte Carlo simulations must include TOD-to-map processing to capture relevant effects but the synthesis of timelines may either involve simulation modules or sign-flipping real timelines to cancel the sky signal.

3.8.6 Transients

Recent studies predict a few thousand transient phenomina will be detectable by CMB-S4. The actual rate of alerts issued by CMB-S4 will also depends on a policy about issuing subsequent alerts on the same phenomina, e.g. for every significant detected change in flux.

All detected alerts will be Public, once confidence in the detections are established.

3.8.6.1 Common Tools

The transient WBS will derive a common toolkit providing software for configuration into the specific transient piplelines and supporting pipelines that will process data from the Pole and Atacama LATs.

The tools will use framework software, services, file format/ data model tools and standards from the Data Movement and Software Infrastucutre WBS elements. Common Tools and will use the overall build/test and software engineering methods provided by the DM sub-system.

The primary input to the Transient Pipelines are the Pole and Atacama Quality Assurance Frequency Maps. During development, Transients will rely on Data Reduction WBS element to provide these products derived from simulated data. The Transients sub-system may also obtain observational data from the other surveys, and process that data into an acceptable input product.

Because transient detection in mm surveys is a newly developing field, transient pipeline development starts late in the overall CMB-S4 project plan. This allows the project to take take advantange of emerging developments in transient detection techniques. Estimation of the effort needed is based on the work needed to translate and adapt software from code bases from other surveys as they would exist in in the final two yeras before commissioning..

Analogous concepts apply to the development of Supplimental Pipelines.

3.8.6.2 Atacama Detections

Operations Concept: Observations from the two Atacama LATs are forwarded promptly to the US Rapid Processing Facility and processed daily into the Atacama Quality Assurance Frequency Maps product. Soon after, in the same facility, the Atacama Transient Pipeline Processing reads these maps, producing undecorated alerts. The effect of this is that transients are produced in batch. In the baseline, this batch processing occurs once/day. Since there are two LATs at the Atacama Site, and it is possible that each LAT will have its own, independent transient pipeline run.

The Undecorated Alerts are sent to the Decorate and Record Process described below. The Quick Look Source Masks, and detection maps synthesized by the transient piplines, housekeeping and provenance data are placed into the Atacama Transient Dataset Cache.

The Supporting Transient Pipelines would run on the regular bulk computing in the CMB-S4 Superfaclity, and deposit their output into the US Archive. These supporting datasets will be drawn from the US Archive to support Atacama Transient Pipeline Processing.

Housekeeping procedures manage the Atacama Detection Dataset Cache. These procedures ingest products produced by the Supporting Transient Pipelines into the cache, ingest data produced by the Atacama Transient Pipeline into the CMB-S4 Transient Dataset in the US Archive, and purge the Atacama Transient Dataset Cache as needed.

By the final year of the construction project, the Atacama Transient Pipline will be integrated using the Rapid Processing System.

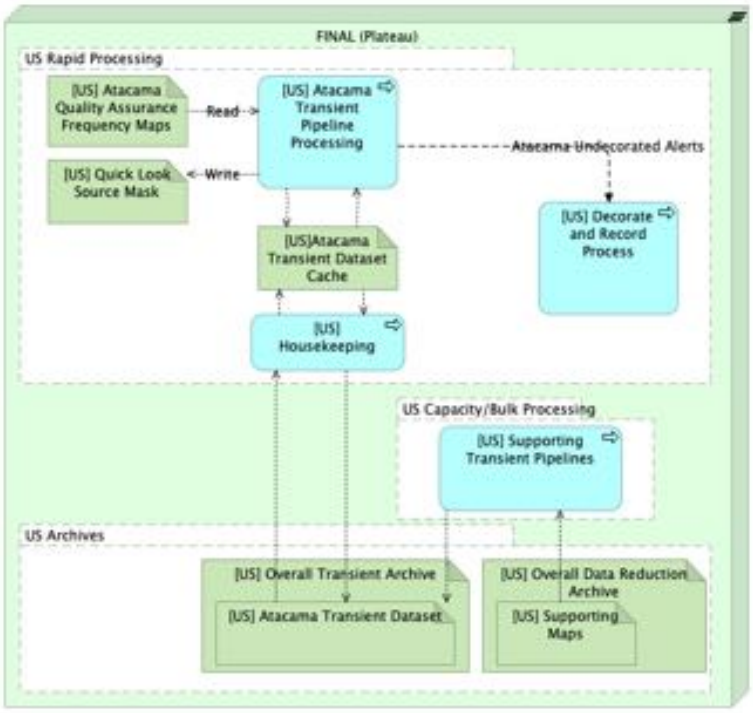

Figure 73: Drawing showing data flow for the Atacama instance of the Transient pipeline, along with its Supporting Transient Pipelines

3.8.6.3 Pole Detections

Operations concept: The data flow for transients at the Pole is driven by the the baseline assumption that networking from the Pole will have low bandwidth. Because of this constraint, the Pole Transient Pipline will run at the Pole. Since The rate of transient phenomina detectipns rate is small, alert traffic can be accomidated by the baseline network.

In the baseline, The Pole Quality Assurance Maps are produced on a daily cadence. The Pole Transient Pipeline Processing runs promptly once this pre-requisite product becomes available.

Similar to the processing for the Atacama Transients, outputs of the Pole Transients Pipeline are undecorated alerts, which are transmitted to the Decorate and Record process (described below) in the Rapid Processing Facility.

Other products emitted by the transient pipline are placed into Pole Transient Dataset Cache. One such Product is the Quick Look Source Mask, which is made available for quick look operations at the Pole.

Like the Atacama Transient Piplines, the Pole Transient Pipline depends on a number of input data products which are produced by Supporting Transient Pipelines. The Supporting Piplines, must also run at the Pole whenever their inputs reside solely at the Pole. These pipelines place their outputs, into the Pole Detection Dataset Cache. Otherwise these piplines could run in the US Superfacilty.

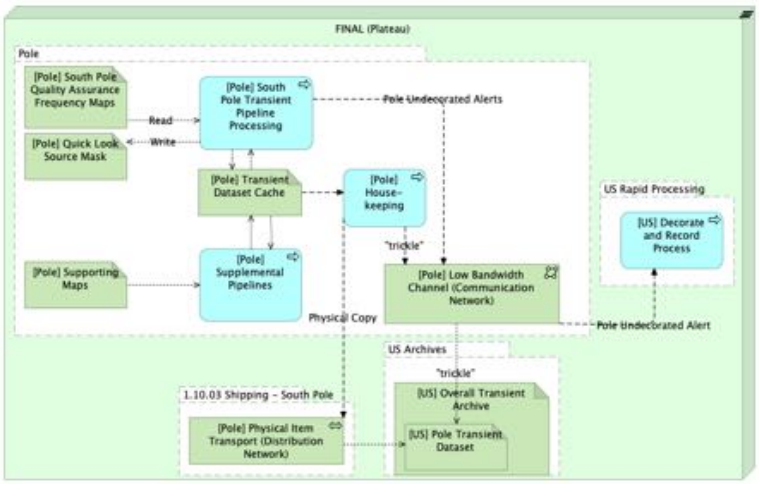

Figure 74: Drawing showing data flow for the Pole instance of the Transient pipeline, along with its Supporting Transient Pipelines

Even with baseline level networking, sufficient background data transfer capacity exists to support downloads for activies such as debugging, software maintenance, and other housekeeping functions. However, network availablity and reliablity complicate the maintenace of the coherency of of the Pole Transient Dataset Cache with the Transient Dataset in the US Archive. Baseline bandwidth supports a housekeeping process trickling this data back to to the US using background data transfers, or returning the data via physical transport to the US Archive in the Austral spring.

Unlike the Transient Cache supporting Atacama transient processing, the Pole Transient Cache requires backup and disaster recovery support.

In the final year of the project, the Pole Transient syteme will be integrated using the Pole Test Stand, which is located in the US.

3.8.6.4 Distribution

The Distribution WBS area is responsible for direct distribution of alerts to the community via community-provided event brokers. Recall that distribution of other products is the responsibility of the Internal Distribution and External Distribution WBS elements of the project.

The Decorate and Record process recieves undecorated transient alerts from both the Pole Transient Pipleline and the Atacama Transient Pipeline. Its function is to provide alerts to one or more brokers in the community-provided transient ecosystem. Sub-Functions include naming, including resolving any naming conflicts due to independent detection the same transient in the south pole and Atacama pipelines, managing broker connections, and rendering alerts into supported message formats for each of (possibly) multiple brokers which might make up the community-provided ecosysystem.

The Decorate and Record process could also function as a “firewall” for transient production errors, for example preventing a cascade of alerts due to a software flaw.

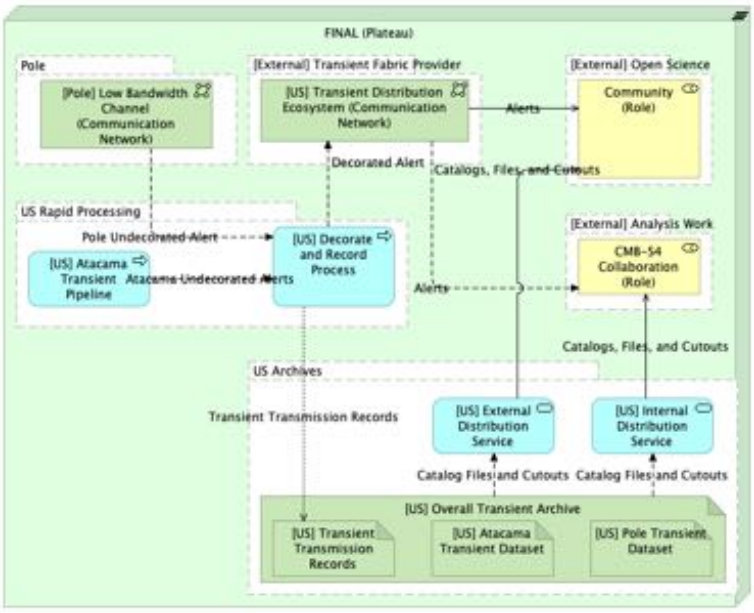

Figure 75: Drawing showing mechanisms for distribution of Transient Alerts and the larger Transient Dataset to the Science Analysis working groups and to the greater community.

Additional annotations beyond alert messages originating in the Transient Detection Piplelines are the responsiblity of the sources science work group, and are out of scope of the construction and follow on operations projects. The science working groups may provide value-added annotationions to alerts, for example, additional classification and validation information. The science working groups will have ablity to monitor the alert stream via community brokers a to monitor the transient-related data in the the CMB-S4 archive.

3.8.7 Site Hardware

The baseline design assumes sufficient network bandwidth from Chile to return the data to the primary U.S. data center essentially in real time, following the models of both the Simons Observatory and LSST. As such, we only need to provide a sufficient local storage to hold a few days data in the event of a temporary network outage. However this is not assumed to be the case from the South Pole, and instead we follow the model of the South Pole Telescope and BICEP/Keck experiments, with a small subset of the raw data, together with some reduced data products, transferred over the network to the US each day, and the entire data set stored on site and shipped once a year. [WHAT ABOUT NEW "REQUIREMENT" FOR FULL-BANDWIDTH DATA TO BE TRANSFERRED FROM POLE REAL TIME?] This means that the South Pole site must be provided with not only sufficient disk to store and transport a year's data, but also with sufficient computing resources to perform all time-critical data reductions—primarily to generate the data products that will be sent over the network each day, including live monitoring for data quality and transient studies. This piece of the data-management system requires close coordination with the site infrastructure systems to ensure that sufficient space and power are available for the on-site computing resources, especially at the South Pole. Specific design parameters for computing resources at the Chile and South Pole sites are detailed below.

3.8.7.1 Chile

As discussed in Section 3.8.1.2, the Chilean data are assumed to be transferred quasi-real-time over fiber-optic networks to the US, with on-site storage for up to 1 month of data in case of network outage. The primary computing hardware at the Chilean site will be to support the roughly 390 TB of storage required for 1 month of data.

3.8.7.2 South Pole

As discussed in Section 3.8.1.2, the Chilean data are assumed to be transferred quasi-real-time over fiber-optic networks to the US, the South Pole data are asumed to be transferred by disk annually, with on-site storage for up to 2 years of data to provide failsafe margin. A large part of the South Pole site hardware will be to support this 5.8 PB of storage. The other major piece is a data analysis cluster used to process raw time-ordered data into fast-turnaround maps to be used for data quality checks and (crucially) the transient search described in Section 3.8.6.

3.9 Sites (*Kam Arnold & Amy Bender*)

3.9.1 Site Requirements & Considerations

The CMB-S4 scientific requirements necessitate a site with access to wide area sky coverage and a site that allows for the small area ultra-deep survey. Chile and the South Pole are the only mature CMB sites that can meet these two needs. The science requirements flow through the instrument design into requirements on the site infrastructure required to support the instruments themselves, the instruments required to commission and calibrate them, and the logistics to support the entire project through commissioning and into operations.

3.9.1.1 Site locations: design drivers and overview

State-of-the-art CMB observations require the highest and driest sites on Earth to achieve high atmospheric transmittance and low atmospheric emission within the spectral bands required. The two best sites developed for CMB observations are South Pole in Antarctica and Cerro Toco in the Chilean Andes. The atmospheric transmittance at the relevent frequencies has been studied extensively (e.g., Refs. [540, 541]). Both of these sites have been in use for several decades and have hosted many CMB telescopes (see, for example, [542, 543, 544, 545, 546]). Known information about the atmospheric conditions at these sites was used in the sensitivity forecasts described in [**?**].

The Chilean Atacama site, at a latitude of 23° South, has access to more than 80% of the sky, enabling observations of the 70% of the sky required by many of the science goals discussed above. The South Pole site, on the other hand, is better suited to deep integration on a small portion of the sky. This makes the South Pole site particularly well-suited to making observations on the ultra-deep field. The Preliminary Baseline Design (PBD) presented here achieves the CMB-S4 science goals with the configuration of telescopes shown in Table 3-24. If r is measured during the early phases of the project, it would trigger a re-evaluation of this SAT allocation decision based on optimizing the scientific return given this new knowledge. The Chile site will be designed to be expandable to support SATs, but the infrastructure design presented in this document only supports the two LATs planned in the PBD.

Site	Number of LATs	Number of SAT cryostats	Number of individual SATs
Chile	2	0	0
South Pole	1	6	18

Table 3-24: Number of LATs and SATs at each site.

The long history of CMB observations from these sites has led to significant infrastructure buildup at each, and a solid understanding of the additional infrastructure required to enable CMB-S4. Large-aperture and small-aperture telescopes of similar size to those required for CMB-S4 have already been deployed to each site; the primary new features of CMB-S4 which drive project and site requirements are the number of detectors per telescope, and the number of small-aperture telescopes that will be deployed. These demand a larger-scale integration effort, higher power requirements, and higher data bandwidths than previously fielded experiments at each site. We assume here that we will not re-use any existing CMB instrumentation infrastructure at the site, and cost the site development appropriately. The infrastructure required at each site is described below.

3.9.1.2 Site Infrastructure Requirements

To achieve the measurement requirements of CMB-S4, the instruments need to operate at their specified performance at the site, with at least the required observing efficiency. This can be expressed as a few general categories of requirements on the sites, enumerated below.

1. Logistics: Each site must facilitate the logistics necessary to install, commission, and operate the instruments, including personnel support, transportation, and site access for personnel and equipment, and facilitation of all instrument operation modes. The logistical support must be robust to ensure timely deployment and high observing efficiency.
2. Instrument Facilities: Each site must provide the facilities necessary to commission and install the instruments
3. Utility Services: Each site must provide the utility services necessary to commission, install, and operate the instruments
4. Safety & Regulatory Compliance: Each site must accomplish these requirements safely and within all applicable agency, national, local, and other applicable regulations.

This PBD primarily focuses on the design aspects of (2) and (3), reserving discussions of logistics and regulatory compliance for other documents. Some general comments are made here. The infrasturcure design that satisfies these requirements is very site-specific, so it is described in sections 3.9.2 and 3.9.3 below. **Instrument Facilities**: The facilities required to support the commissioning, installation, and operation of the instrument include include the mechanical mounts for the telescopes themselves, the labs or other space required to assemble the instruments, and all the civil infrastructure necessary to access those facilities with personnel and the utility services. **Utility Services**: The instrument requirements for services that are most important in site design are the need for electrical power, communication, and computing. The electrical power required at each site, detailed by major electrical consumption category, is given in Table 3-25. The communication requirements include the transfer of data, communication to support the logistics of instrument operations, and communications to support the safety and security of personnel and equipment on the site. The raw bandwidth of data being generated is given in Tables 3-1 and 3-2.

	Average power	
Equipment	Chile Total [kW]	SP Total [kW]
LATs (including receiver and readout but not DAQ)	210	105
SATs (including receiver and readout but not DAQ)	0	264
Cooling system	30	14
DAQ, compute, and office	44	34
Data management	10	50
Site power	30	20
Total	304	487

Table 3-25: Power budget for each site. Note that requirements will be re-evaluated in the context of any redistribution of SATs.

3.9.2 Chilean Site, Integration and Commissioning (*Kam Arnold*)

BaselineDesign/CHSITE.tex: this is is the input tex file for the Chilean Site, Integration and Commissioning section of the PBDR.

The preliminary baseline layout of the Chilean site is shown in Fig. **??**. This layout uses the area that has been studied by existing CMB instruments, and satisfies the facilities requirements for the instrument and operation. The maximum horizon blockage seen within this area (presented by Cerro Toco) is 15°. Rock in this area is generally appropriate for construction of the necessary foundations, and the instruments will not present significant new horizon blockage to existing instruments.

3.9.2.1 Some general requirements considerations

The logistics requirements discussed above flow into some important design considerations for the site. The site is designed to support remote science operations at all time, and require only minimal on-site maintenance to maintain instrument performance and observatory operations. The observatory is required to stay operational, including power, communication, and the ability to remotely start observations, even if access is prevented by weather for up to 14 days. Personnel stay at a low-elevation facility (at approximately 3,000 m.a.s.l.) in or near San Pedro. They have the ability to fully monitor and controal the site from that facility. Transportation to the site is over public road, highway up to 4000 m.a.s.l, and dirt road above 5000 m.a.s.l.

3.9.2.2 Instrument Facilities

All facility buildings are shown on Figure **??**. The inset describes each component of this layout. A table of the instrument facilities, and their driving requirements, is shown in table **??**. The remaining items shown in **??** are the roads that provide access to the instrument facilities, and the infrastructure that supports the distribution of the site utility services.

The low-elevation facility is not shown here. This facility will not be built by the CMB-S4 project, but an existing facility will be contracted. Several possibilities for this facility exist, the selection will be made based on the experience of previous observatories in the area.

3.9.2.3 Utility Services

- Power, including PVA. Motivate PVA from robustness, cost point of view
- communication, including high-bandwidth and redundant control
- Computing and LAN on-site
- Cooling

3.9.3 South Pole Site, Integration and Commissioning (*Amy Bender*)

3.9.3.1 South Pole Overview & Site Layout

Telescopes for CMB-S4 will be sited in the dark sector at the South Pole, a designated radio-quiet zone. Fig. 76 shows an aerial view of the dark sector and the existing scientific installations. The cold temperatures at the South Pole necessitate buildings along with the telescopes to support assembly of the receivers and general maitenance throughout operations. Three of the SAT telescopes will be adjacent to the MAPO building (including one in the existing BICEP Array position). A second laboratory building will support and connect with the other three SAT telescopes in a separate installation. The SPLAT will be supported with a dedicated high bay. The placement of the buildings within the dark sector has three general first requirements. First, the view around the SATs is required to be clear 2° above the lip of the ground shields. Second, the prevailing wind direction and snow drift should be accounted for in the relative placement of the buildings and telescopes. Finally, the locations should not conflict with the existing scientific installations (i.e, IceCube Neutrino Observatory, South Pole Telescope) and other zones where construction is not allowed.

3.9.3.2 Site Management

South Pole Station is a National Science Foundation supported research facility. In addition to the scientific installations shown above, the main station and operations outbuildings provides housing and other support for on-site personnel and activities. On-site logistics will be coordinated with the Antarctic Support Contract (ASC). Outdoor construction is performed in the austral summer (November–February), while interior work can be done in the austral winter (February– November). Cargo arrives at the Pole in the austral summer, either by LC-130 airplane or via a month-long overland traverse from McMurdo station. Cargo gets to McMurdo either via air (C-17 or LC-130) throughout the season, or by ship late in the austral summer. We currently baseline a mixture of air transport and traverse for CMB-S4.

3.9.3.3 Site Utilities

General site utilities include the generation and distribution of electrical power and distribution of optical fiber to enable communications and data transfer between the different facilities on-site. The breakdown

Figure 76: Photograph of existing scientific facilities in the dark sector at the South Pole. Photo credit: XX?

of power requirements for CMB-S4 at the South Pole is shown in Table **??**, with a total average power of 487kW. Accounting for the maximum power usage possible brings the total up to 561 kW. Adding $\sim 25\%$ margin brings the total required power to 700kW. Generators supplying the power will have built-in redundancy. Uninterruptible power supplies (UPS) located in each of the telescope facilities will provide additional redundancy to maintain computers, readout electronics, and SAT drive motors in case of short duration outages. The total power required above will likely require new power generation equipment at the South Pole. We are working with NSF to better understand the currently available power limit, and to ensure CMB-S4's power requirements can be met.

Optical fiber will connect all three telescope facilities to the science laboratory in the main station, which will be used both as a centralized control room and the site of the data management system. As described in Sec. 3.8.1.2, data will be stored on-site with the physical drives shipped from the South Pole to North America on a yearly basis. Additionally, a fraction of the data (∼100 GB/day) will be transmitted North on a daily basis as part of the existing satellite transfer of scientific data.

3.9.3.4 SPLAT Facility

Infrastructure specific to the SPLAT will include the ice pad that serves as the telescope foundation, connections to power and data utilities, and finally a heated maintenance high bay. The high bay will support assembly of the LATCR and LATR and their installation onto the SPLAT. Fig. 77 shows a preliminary design of the high bay and how the telescope would dock with it. The high bay design includes a drive system to move the building away from the telescope, providing the clearance for full boresight rotation of the SPLAT. Front and rear doors along with an interior gantry crane will enable the camera to be loaded into and moved through the high bay. Finally, the high bay also contains a cooling loop that circulates a glycol mix through

the PTC compressors and radiates the thermal energy out to ambient. This will allow the receivers to cool and operate in the the high bay as needed.

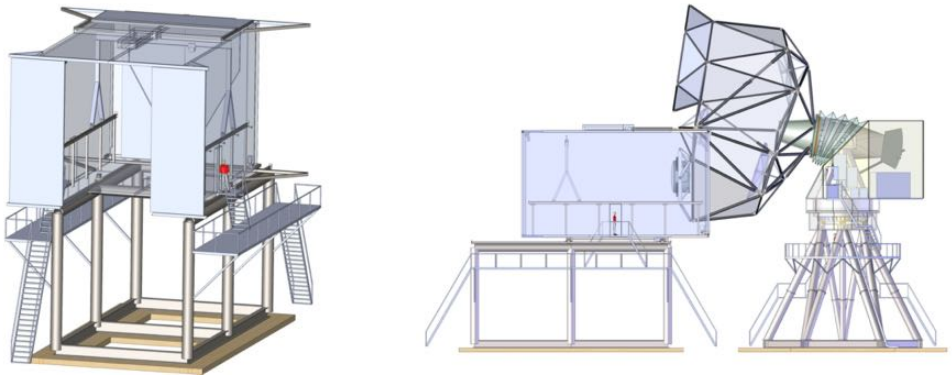

Figure 77: A heated maintenance high bay will support assembly of the LATCRand LATRand their installation on the telescope. The high bay includes rear access to load cargo and front access to dock the SPLAT.

3.9.3.5 SAT Facilities

Each SAT will be installed on top of a standalone tower and control room. An ice pad of compacted snow topped with a wooden raft footer will serve as the foundation for these towers. Tower height is determined based on known snow accumulation rates as well as the ability to connect to the adjacent building via a walkway. Mounted on top of the tower is a control room that will serve as environmentally controlled space for helium compressors and electronics. The control room will have a standalone glycol loop that removes heat from the three compressors and radiates it away outside.

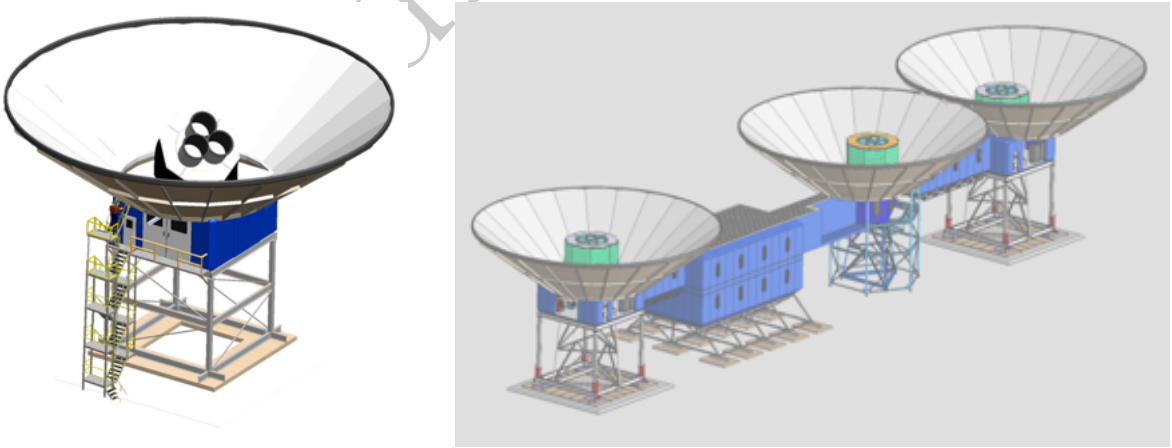

Figure 78: Each SAT will sit on top of a dedicated control room and tower. Three SATs will link to a single maintenance and support building via walkways as shown in this rendering.

A service and maintenance building will connect with three SATs via walkways as shown in Figure 78. Two such installations are planned for CMB-S4. The existing Martin A. Pomerantz Observatory building

(MAPO), which currently connects to the BICEP Array tower, will be one of these buildings. A duplicate blue building will be constructed to support the second set of SAT telescopes. On-site assembly of the SAT receivers will occur in the laboratory space of these buildings.

3.9.3.6 On-site Construction, Integration, and Commissioning

Construction of the facilities described above will span approximately six years. Exterior construction will occur during the austral summers, with interiors completed throughout the austral winter. Initial SPLAT commissioning will take place using the commissioning receiver (see Sec. 3.5.5). The LATCR will be used to verify the optical properties of the fully integrated telescope, such as pointing, beam shape, and optical efficiency. Additionally, it will provide an important first opportunity to exercise the fully integrated observatory control with all components, data acquisition, and data management systems. The following year, the LATR will be integrated at the south pole and installed onto to the telescope for commissioning. The SATs will be assembled and commissioned in parallel with that of the SPLAT receivers, with three SATs installed each year. Commissioning of the fully integrated telescopes will be similar between the SPLATand the SATs, although each system will use optimized equipment as described in Sec. 3.5.6 and Sec. 3.6.6. Early commissioning will focus on operation of the detector and readout systems and achieving the desired noise equivalent temperature. Sensitivity to microphonic vibrations and radio-frequency interference will be characterized. Following this, the telescope pointing, beam (including far sidelobes), and polarization response will be measured. Finally, test survey observations will be conducted. Following the completion of these commissioning tasks, the telescopes will transition to calibration (source scans, bandpass measurements) and subsequently survey operations.

4

Science Analysis (*Huffenberger & Meyers*)

4.1 Introduction

For the purposes of this document, the analysis of CMB-S4 data is divided into two stages: (1) the synthesis of raw detector, pointing, and housekeeping data into single-frequency maps of the sky; and (2) further processing of those maps into data products such as CMB lensing maps, temperature, polarization, and lensing power spectra, and catalogs of galaxy clusters and emissive sources, and using these downstream data products to derive scientific results. In this document, the first stage of analysis is part of the Preliminary Baseline Design under the Data Management subsystem (Sect. 3.8), while the second stage of analysis is referred to as "Science Analysis" and is treated in this chapter (see Fig. 79 for a graphical illustration of this division).

The vast array of CMB-S4 science goals discussed in Chapter 1 will correspondingly necessitate many different types of post-map analyses, and a full accounting of all these types of analyses and the different options for carrying them out would fill a 200-page document by itself. Here we limit ourselves to short discussions of the analyses involved in some of the key CMB-S4 science goals, including the pursuit of a background of primordial gravitational waves, the search for light relics in the early Universe, measuring the mass of the neutrinos, constraining the nature of dark energy, learning about galaxy formation and evolution, and producing legacy catalogs of galaxy clusters and emissive sources. In the following sections, we describe the major analysis steps involved in post-map CMB data analysis and how they relate to these primary science goals, and we discuss major outstanding algorithm choices for certain of the analysis steps. For much more detail on all of these steps, and on the synthesis of raw data to maps, see Chapter 8 of the CMB-S4 Science Book [17].

4.2 Design-driving Science Analyses

4.2.1 Tensor-to-scalar ratio r (*Bischoff & Wu*)

To go from frequency maps to parameter constraints on r, we need to remove two sources of astrophysical contamination, ascertain that residuals from instrumental systematics effects are small compared to the statistical uncertainty, and extract pure B modes from the maps. This is because the degree-scale B-mode polarization signature expected from PGWs is known to be significantly smaller than these other sources of contaminations, if unmitigated.

The first source of astrophysical contamination comes from within the Galaxy—polarized dust emission and synchrotron radiation both generate B modes in the mm-wave band. To separate the CMB signal from the contaminating foregrounds, data from multiple bands will be combined, either in a cross-spectrum analysis or

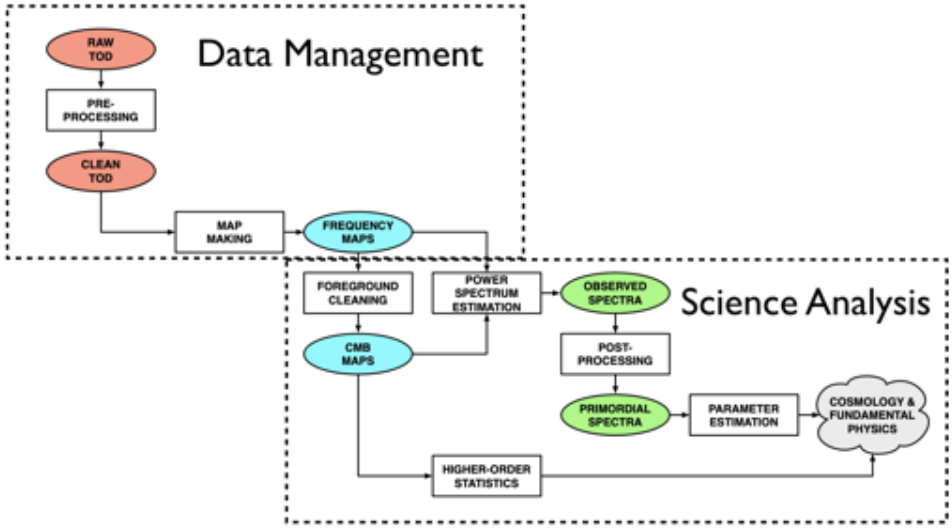

Figure 79: Schematic view of the CMB-S4 data analysis pipeline (from figure 88 of the CMB-S4 Science Book), with boxes illustrating which elements are grouped under Data Management (Sect. 3.8) and which elements are grouped under Science Analyses (this chapter).

by making linear combinations of maps in different bands to produce a "pure-CMB" map for power spectrum estimation. In either case, an underlying model of foreground behavior is assumed—even if that model is simply an assumption regarding the level to which the spectral behavior of foregrounds varies over the sky. There are two challenges related to uncertainties in foreground modeling: one statistical and one systematic. The statistical issue is simply how to propagate the statistical uncertainty on the foreground model to uncertainties on cosmological parameters. In explicitly parameterized foreground models, this happens automatically through the covariance resulting from the fit. For non-parametric models, this covariance can be assessed through Monte-Carlo methods, but making many independent realizations of large-scale Galactic foregrounds is problematic because of the strongly non-Gaussian behavior of these foregrounds. The other aspect comes from systematic residuals that are not modeled either at the likelihood level or for making map linear combinations. This requires iteration in the analysis through assessment in the goodness-of-fit, to evolve the foreground models such that the residuals are small.

The second source of astrophysical contamination is the B modes from gravitational lensing of the CMB E modes. Delensing is a term that encompasses techniques that remove the impact of lensing from parameter estimation—in this case, the degradation of the r constraint due to the extra sample variance from the lensing B modes. To delens for r, we make an estimate of lensing B modes given the measured E modes and an optimal estimate of the lensing potential ϕ. Techniques for estimating optimal ϕ is under development and is described in more detail in Sect. 4.3.3. With a lensing B template at hand, we can then either subtract the resultant lensing B template from the frequency maps or use it as a pseudo-frequency map in a cross-spectrum analysis.

Known instrumental systematic effects that generate spurious B modes include residual beam mismatch, gain variation, detector cross-talk, polarization angle error, and many others. Mitigation techniques for each effects have to be developed for the specific instrument configuration and this will be one of the major focus of on-going CMB-S4 design discussions.

Additional sources of contamination to B-mode searches are intrinsic to observing a finite patch of sky and to pseudo-C_ℓ methods, including ambiguous (not clearly E or B) modes around the edges of the sky patch and spurious B modes introduced in analysis. Spurious/ambiguous B modes can be dealt with either by estimating the statistical bias to the final B-mode spectrum or by constructing a matrix representing the effect of any analysis steps on the true sky [547]. The latter approach involves constructing an $\mathcal{N}_{\rm pixel}$-by-$\mathcal{N}_{\rm pixel}$ matrix, equal in size to the full pixel-pixel covariance, and will not be feasible for high-resolution CMB-S4 data but could be used in analyzing lower-resolution data.

Perhaps the most important aspect of any contamination mitigation is the estimate of the residual contamination after cleaning. If this estimate is inaccurate, it will lead directly to biases in the final determination of the amplitude of the cleaned power spectrum. In the case of PGW searches, this leads directly to a bias in the tensor-to-scalar ratio r. To avoid this bias, all of the contamination-mitigation methods discussed above will need to effectively marginalize over uncertainties in our knowledge of the contamination sources and mechanisms.

4.2.2 Light relics (*Loverde & Reichardt*)

The light relic constraints from CMB-S4 will be based on measurements of the CMB temperature and polarization (TT, TE and EE) power spectra. The three conceptual steps are to produce minimum-variance, foreground-suppressed maps, to measure the power spectra of these maps, and then to compare the measured power spectra to models to establish light relic and other constraints.

Maps and Power spectra. As in the tensor-to-scalar ratio analysis, the first step will be constructing a minimum-variance, foreground-suppressed map. This step can be done by combining the frequency maps into a constrained minimum variance map, or equivalently at the power spectrum level by combining the cross-frequency spectra; there are existing pipelines for either approach. Note that while there are similarities to the tensor-to-scalar ratio analysis, the TT, TE and EE power spectra are much brighter than the foreground signals and the required level of foreground rejection is lower as a result. With the maps in hand, we plan to estimate the power spectra using the Monte-Carlo-based cross-spectrum approaches advocated in Ref. [548**?**]. These Monte-Carlo based approaches avoid the computational botteneck of the maximum-likelihood methods which scale as $\mathcal{O}(\mathcal{N}_{\rm map\,pixels}{}^3)$ that were used by early CMB experiments (e.g., Refs. [549], [550]). In the Monte-Carlo approaches, a biased estimate of the angular power spectrum of the data is obtained by simply binning and averaging the product of the spherical harmonic transforms of many independent pairs of observed maps of the sky. Recall that CMB-S4 will make a complete map of the survey region every two days. While this simple estimate (known as the "pseudo-C_ℓ spectrum") is biased by sky windowing and any filtering applied to the data before or after mapmaking (including the effects of instrument beam and pixelization), the bias can be measured and removed using a suite of Monte-Carlo simulations. In these simulations, one "observes" and analyzes simulated maps of the sky, and use the results to construct a matrix describing the net effect of the map-making and pseudo-C_ℓ spectrum estimate on the simulated data. The matrix is then inverted, and the inverse matrix is applied to the measured pseudo-C_ℓs to provide an unbiased estimate of the true power spectra on the sky. Some version of this Monte-Carlo treatment is expected to be implemented for CMB-S4.

Parameter estimation. The final step in the light relic analysis is the estimation of cosmological parameters from the CMB power spectrum. The final step in the analysis of a CMB data set is the estimation of cosmological parameters from This involves estimating the likelihood of the observed power spectra given

a model parameterized by the standard six ΛCDM parameters, possible extensions of the cosmological model, and any nuisance parameters involving the instrument, foregrounds, and other sources of systematic uncertainty. The current industry standard for this part of the analysis is to use Markov-chain Monte-Carlo (MCMC) methods, in particular the implementation in CosmoMC [551]. It is expected that CMB-S4 will use similar MCMC methods.

4.2.3 Galaxy clusters (*Battaglia & Vieira*)

An additional post-map product of interest for CMB-S4 is the location and properties of compact sources, in particular clusters of galaxies identified through the thermal SZ effect. The standard practice for extracting SZ clusters from multifrequency millimeter-wave maps is through the application of a Fourier-domain spatial-spectral filter [552]. The computational effort involved in this step is small compared to the estimation of power spectra and higher-order correlations, and the algorithms are well-developed and fully implemented for multi-frequency data sets (e.g., Ref. [553, 432])—however, the cluster density could be high enough in CMB-S4 data that approaches more sophisticated than the simple matched filter (e.g., Ref. [554]) could be required to maximize cluster yield.

4.2.4 Gamma-ray Bursts (*Battaglia & Vieira*)

One class of analyses that is not represented in Fig. 79 and does not strictly come under the heading of post-single-frequency-map analysis is the area of time-domain and transient astronomy. As discussed in Sects. 1.6.5 and 1.6, CMB-S4 will be a rich data set for detecting mm-wave GRB afterglows, monitoring the light curves of AGN, and discovering new planets. These science goals will require analyses of the time-ordered detector data that are very different from the standard pipeline that will create single-frequency maps of full-depth data. In particular for GRB afterglows, science yield will be maximized by a quasi-real-time alert system linked to the transient alert mechanisms in the wider community. At least at the South Pole, this will require on-site computing and analysis software that runs autonomously.

4.3 Complementary Science Analyses

4.3.1 Cosmic Inflation (*Alvarez & Sherwin*)

A promising path towards probing alternatives to simple single field slow roll inflation is via searches for primordial non-Gaussianity [555, 556], primarily through measurements of the bispectrum [557]. Techniques to measure the amplitudes of the most relevant shapes of the bispectrum (e.g. the KSW estimator, or the shape-independent Modal estimator) have been successfully implemented in the Planck and WMAP analyses[558]; these can also be directly applied to CMB-S4. CMB-S4 will gain more information by probing new modes in polarization and at small scales over approximately half the sky. Constraining non-Gaussianity from smaller scales also implies that foreground bispectra from SZ, CIB and ISW (as well as galactic foregrounds) are expected to be a more significant contaminant than for Planck and WMAP; these foreground bispectra can be mitigated with multifrequency component seperation, estimator modification, and direct simulation approaches. In addition, a new challenge that is expected to arise on small angular

scales is that gravitational lensing correlates different scales; delensing approaches, as developed for both T/E power spectra and B-modes, will thus be required for the bispectrum constraints to reach their full constraining power on primordial non-Gaussianity.

Further constraints on inflation models can be obtained from the power spectrum [559]. The ability of CMB-S4 to make small-scale polarization measurements of the CMB power spectra will allow for improved constraints on the spectral index and its running, as well as on more general deviations of the primordial curvature power spectrum from simple scale-invariance [560, 561]. The analysis methods and challenges here are generally similar to those required to constrain light relics.

Additional information on new physics – in particular on new physics that violates parity – can be obtained from constraints on the cosmic birefringence, the rotation of the CMB polarization direction as the photons propagate from emission to our telescopes [562]. For CMB-S4, there will be two primary channels to obtain constraints on cosmic birefringence. The measurement of isotropic birefringence (where all polarization is rotated by a single angle) can be obtained from a measurement of the E-B cross-polarization power spectrum [255]; degeneracies with instrumental angle errors can potentially be broken by noting that instrumental angle errors should also affect the foreground polarization direction, whereas true cosmic birefringence should not affect the foreground polarization. Anisotropic birefringence (whereby the polarization is rotated by an angle that varies across the sky) [261, 263, 563] can be measured in a manner similar to CMB lensing reconstruction by estimating the breaking of statistical anisotropy induced by this effect; current estimators generally rely on quadratic estimator methods, and CMB-S4 can expect strong constraints from the EB quadratic estimator. However, more optimal methods could likely be developed, e.g. estimators that make use of the reduction of noise by delensing.

4.3.2 The Dark Universe (*Loverde & Reichardt*)

Measurements of the CMB power spectrum constrain a wide range of cosmological models in addition to $N_{\rm eff}$. The power spectrum measurement and MCMC parameter estimation pipelines outlined in §4.2.2 will be also be used to constrain models of dark energy, dark matter, etc.

4.3.3 Mapping Matter (*Alvarez & Sherwin*)

CMB lensing. (*Alvarez & Sherwin*) The current state of the art in lensing reconstruction from CMB data is the quadratic estimator method [564], [565]. These quadratic estimators are the first step in an iterative estimation of the true likelihood, and in the weak-lensing limit they are nearly optimal. To harness the full power of CMB-S4 lensing information, however, it will likely be necessary to develop lensing estimators that more closely approximate the maximum likelihood solution. Development of maximum-likelihood algorithms or their equivalent is underway [566, 567] and first demonstrations on ground-based CMB data sets have recently been reported.

Another outstanding question, particularly for delensing, is what information to include in the ϕ estimate. The baseline assumption in the CMB-S4 Science Book and in many other publications is that the ϕ reconstruction for CMB-S4 will come entirely from the combination of CMB E-mode and B-mode polarization, from the so-called EB estimator. This is partially because at CMB-S4 noise levels the EB estimator has the lowest noise, but it is also because any estimators involving temperature are potentially contaminated by foregrounds, particularly at high multipoles. But there is still significant information to be gained from the

temperature field, even at CMB-S4 noise levels (cf. figure 43 in Ref. [17]), and recent work has hinted at ways to mitigate foreground contamination in temperature-based lensing estimators [568]. As shown in Ref. [569], information from tracers of ϕ other than the CMB can also improve delensing results, even at CMB-S4 noise levels. One analysis challenge will be to build the optimal combination of all these ϕ estimators that is also robust to foreground contamination.

Component maps and cross-correlation with other surveys. (*Battaglia & Vieira*) (*Alvarez & Sherwin*) It has become increasingly clear, even since the publication of v1 of the CMB-S4 Science Book, that a wealth of exciting science will come from the combination of CMB-S4 data with survey data from other instruments at other wavelengths. These contributions will come both in the area of constraints on cosmological parameters and in increased knowledge of processes on smaller scales and in our local Universe. As shown in Chapter 1, cross-correlations with optical data in particular can lead to improved constraints on the growth of structure, the sum of the neutrino masses, the nature of dark energy, and the primordial power spectrum, as well as informing our understanding of galaxy formation and evolution. Fully exploiting this area of science will require building analysis pipelines jointly with experts in data from other surveys.

Among the challenges and questions in this area of analysis will be whether to perform the analyses in real or harmonic space, how to estimate the covariance of the cross-correlations, and, as in CMB power spectrum analyses, how to deal with contaminating signals and estimate the residual contamination after cleaning. This last point will be key to obtaining precise and accurate determinations of cosmological parameters and constraints on galaxy feedback models through correlations of optical observables with maps of CMB lensing and the tSZ and kSZ effects. In particular, contamination from the tSZ is currently the limiting factor in correlation analyses of optical data and CMB lensing [570, 571], so the foreground mitigation schemes discussed above for lensing reconstruction are also critical to cross-correlation. In general, foreground treatment will be a key aspect of the production of component maps such as the Compton-y map and the CMB blackbody map (see Sect. 1.5.1). As with power spectrum estimation, it will be crucial not only to minimize the contamination in the component maps but also to have accurate estimates of the residual contamination and to propagate these estimates through any cross-correlation analysis involving component maps.

Sources (*Battaglia & Vieira*)

4.3.4 Other Transient Phenomena (*Battaglia & Vieira*)

4.4 Sky simulations

Simulations will be a key aspect of the entire CMB-S4 analysis pipeline, both in the stages handled by the data management subsystem and in post-map analyses. As discussed in Sect. 3.8, we assume here that the software for synthesizing mock skies into simulated time-ordered detector data and maps is part of the data management subsystem, but that the creation of the simulated skies themselves will occur outside of the data management sub-system. Sky simulations that will be useful for CMB-S4 fall into two main categories: (1) simulations of the polarized mm-wave emission from our own galaxy; and (2) simulations of the (mostly) unpolarized emission from extragalactic sources. These present different challenges and will likely come from independent sources.

Comprehensive, accurate, and flexible simulations of Galactic emission will be critical for reaching the CMB-S4 goals in the search for primordial gravitational waves. Key challenges in the generation of simulations of Galactic emission include:

- the level of coherence of diffuse emission across observing frequencies, as any decoherence will limit the efficacy of cleaning a foreground from one observing band using the measurement in a different band;
- the existence or not of a simple parametric emission law for each component emission, such as power laws (for synchrotron) or modified blackbody emission (for dust components);
- the absolute level of foreground emission (in particular for those components that do not scale simply as a function of frequency, such as the superposition of many individual sources with a specific emission law each);
- whether or not emissions for which the level of polarization is unknown or unclear must be modeled and treated for CMB-S4 or can be safely neglected;
- The level at which foregrounds can be treated as Gaussian random fields, which is an assumption of certain foreground cleaning approaches.
- the reliability of models based on observations at angular resolution lower than that of CMB-S4, integrated in broad frequency bands, and with a sensitivity limit at least an order of magnitude worse than what will be achieved with CMB-S4.

Simulations of extragalactic emission will be important for estimating contamination to small-scale power spectra and lensing maps, and they will play a crucial role in validating analysis methods and verifying results in the area of cross-correlation with surveys at other wavelengths. This requires simulated maps at many wavelengths with the same underlying initial conditions and large-scale structure fluctuations, and with the proper correlations between observables such as CMB lensing potential, tSZ and kSZ, galaxy positions, and galaxy weak-lensing shear. A key challenge in the area of extragalactic simulations will be the competing needs of high accuracy at small angular scales—which can only be achieved with full hydrodynamical simulations—and the ability to create quickly many realizations with different cosmologies and galaxy-formation parameters.

4.5 Implementation

As described in Sect. 3.8, the volume of raw, time-ordered data in CMB-S4 will necessitate both the provisioning of unprecedented computing resources and innovation in CMB data processing algorithms. Once the raw data have been reduced to single-frequency maps, however, the data volume for CMB-S4 will no longer be significantly large than that of *Planck*. Implementation of the standard methods in the field for post-map processing is not expected to overly tax the computing resources of the field. If minimum-variance methods are used for certain post-map analysis steps—for instance the simultaneous estimation of the CMB lensing potential, the unlensed fields, and cosmological parameters as described in [566]—or if full pixel-pixel matrix methods are used for spurious/ambiguous B-mode cleaning, the requirement for computing resources could be higher.

4.6 Validation and verification

The importance of the key CMB-S4 science goals and the challenge of not only achieving the necessary sensitivity but also demonstrating that the final signal is not significantly affected by contamination or bias, compels us to set up a framework in which we can validate any software used for the key science analyses and verify that the algorithms and implementation thereof produce unbiased results with the expected precision on simulated data. This process is already happening in the PGW forecasting working group through a series of data challenges, and we expect to extend the data challenge framework to key results from the large-area, large-aperture surveys in the near future.

5

Project Overview (*John Corlett*)

5.1 Introduction

The CMB-S4 Collaboration and a pre-Project Development Group of experienced project professionals jointly contributed to the development of a Work Breakdown Structure (WBS), Organization, Cost Book, Resource Loaded Schedule, and Risk Registry. The reference design and project baseline prepared for this document is the basis for subsequent design and project development work to be completed by the Interim Project Office and the Collaboration during 2019–2020. A permanent Integrated Project Office will be established in 2020 to manage the construction phase which starts in 2021.

The CMB-S4 project total estimated cost is currently $591.6M (fully loaded and escalated to the year of expenditure) including a 35% contingency budget. In-kind contributions delivered by Private and International partners are expected and would reduce the total cost to NSF and DOE. Critical R&D is in progress, funded by DOE. There is a pending proposal to NSF for Design and Development support under the NSF MSRI-R1 program. An eight-year construction project is anticipated (2021–2029) with a transition to operations starting with completion of commissioning of the 1st telescope in 2026. Long lead procurements for the construction project will start in 2021.

5.2 Scope, work breakdown structure, and cost

The CMB-S4 Work Breakdown Structure (WBS) includes twelve major categories as shown in Table 6.1. The distribution of WBS elements by funding agency will be discussed with the Joint Coordination Group established by the funding agencies. As these plans mature there will be a general understanding of the proposed responsibilities of each funding agency and partners providing in-kind contributions. The scope distribution will leverage the capabilities of universities, national laboratories, and industry.

The cost estimate shown in Table 5-1 includes all Materials & Services (M&S) and Salaries, Wages and Fringe Benefit (SWF) costs for the project. The M&S costs and labor resources are estimated at the lowest (task) level in the Project Schedule. The costs in the schedule are given in FY19 dollars. Appropriate overhead and escalation are done external to Primavera, within the Cobra Project cost management and reporting software that will eventually be used to compute earned value. It is foreseen that all Project tracking and reporting will be done using Cobra and Primavera software for the duration of the Project. The cost estimate is the full cost, i.e., does not take credit for contributions from collaborating institutions supported by private and international partners, e.g., Large Aperture Telescopes currently under construction in Chile as part of the Simons Observatory, and Large and Small Aperture Telescopes proposed by international collaborators. The value of in-kind contributions could reduce the total cost of the CMB-S4 project by 20–25%.

Scientific labor resources not in project management roles, i.e., scientific and technical development work, are provided to the Project through research program support outside of the Project. This is the traditional funding model used for DOE and NSF joint projects including LSST, ATLAS, and CMS. The approach

equalizes the treatment of the collaboration's experimental physicists with respect to their cost to Projects, regardless of their funding source.

The cost contingency estimate was constructed using input from subject matter experts with previous experience in previous CMB experiments and similar NSF MREFC projects and DOE MIE projects. The current estimate of contingency budget or reserve is 35% of the base cost estimate. As the design, cost estimates, and schedules mature the contingency as a percentage of the base cost estimate is expected to decrease to 30% or less. The target range for the start of the CMB-S4 construction project is 25–30%.

The contingency estimate was compared to similar large research infrastructure projects sponsored by the DOE and NSF and is reasonably consistent with other projects at this early stage of project development.

WBS Level 2 Element	Total Cost ($M)
Total Estimated Cost (TEC)	
1.01 – Project Management	19.6
1.03 – Detectors	39.5
1.04 – Readout	59.9
1.05 – Module Assembly & Testing	31.8
1.06 – Large Aperture Telescopes	86.5
1.07 – Small Aperture Telescopes	52.3
1.08 – Observation Control & Data Acquisition	13.9
1.09 – Data Management	26.9
1.10 – Chile Infrastructure	38.1
1.11 – South Pole Infrastructure	37.0
1.12 – Integration & Commissioning	7.7
Direct TEC	413.2
TEC Contingency (35%)	144.6
Total TEC	557.9
Other Project Cost (OPC)	
1.01 – Project Management	7.0
1.02 – Research & Development	24.2
Direct OPC	31.2
OPC Contingency (35%) – excludes R&D	2.5
Total OPC	33.7
Total Project Cost (TPC)	
TEC + OPC with contingency	591.6

Table 5-1: CMB-S4 WBS structure and cost.

The resource-loaded schedule determines the annual funding profile. The schedule is technically driven starting in 2022, i.e., the technically efficient schedule unconstrained by funding in any year. The resulting funding profile is provided in the following table.

	FY19	FY20	FY21	FY22	FY23	FY24	FY25	FY26	FY27	FY28	Total
OPC	4.3	11.4	17.9	0.0	0.0	0.0	0.0	0.0	0.0	0.0	33.6
TEC	0.0	0.0	7.1	80.8	127.7	184.0	93.5	50.6	13.5	0.5	557.9
TPC	4.3	11.4	25.0	80.8	127.7	184.0	93.5	50.6	13.5	0.5	557.9
Operations	...	...	...	...	...	...	...	1.0	5.0	10.0	16.0

Table 5-2: CMB-S4 funding profile.

5.2.0.1 WBS dictionary

The WBS Dictionary defines scope of each CMB-S4 WBS element as described in Table 5-3.

5.2.0.2 Scope management plan

The scope of the CMB-S4 project is defined to meet the scientific and technical requirements. The reference design and emerging conceptual design meets these requirements as demonstrated by the flow down of science requirements to the proposed project scope. The delivery of the project scope will be time phased and elements of the project scope will be added and deleted as necessary and in accordance with the configuration management plans. Changes to the project scope will be subject to formal change control procedures and approved at the appropriate level of authority. For example, minor changes can be approved by the Level 2 or Level 3 managers, major changes by the Project Director and/or Project Manager, and finally changes affecting the overall scientific performance or key performance parameters will need to be approved by the funding agencies and partners.

Scope contingency options will be identified and managed including the timing of decision points, both for scope reductions and scope restoration or scope additions. A scope management plan will be developed describing this process.

5.2.1 Organization

CMB-S4 is both a scientific collaboration and a nascent DOE/NSF project. While these are certainly tightly-coupled, they do have different roles and responsibilities; the overall organization of CMB-S4 therefore decouples into the organization of the collaboration and the project.

5.2.1.1 Collaboration organization

During the 2013 Snowmass particle physics project planning exercise, the US CMB community came together and recognized:

1. that realizing the extraordinary scientific potential of the CMB would require an increase in the sensitivity of our instruments corresponding to moving from tens to hundreds of thouands of detectors;

WBS Element	Description
1.01 – Project Management	Labor, travel, and materials necessary to plan, track, organize, manage, maintain communications, conduct reviews, and perform necessary safety, risk, and QA tasks during all phases of the project. Overall project Systems Engineering is a subsection of this wbs element. However, subsystem-related management and support activities for planning, estimating, tracking, and reporting as well as their specific EH&S and QA tasks are included in each of the subsystems.
1.02 – Research & Development	Labor, travel and materials necessary to support development of a Conceptual Design (pre CD-1 for DOE). Activities include design of detector wafers and the readout systems, data management, optical design, and aspects of the cryostat design for both large and small telescopes.
1.03 – Detectors	Labor, materials, and equipment associated with the design, fabrication and testing of the detector wafers.
1.04 – Readout	Labor, materials, and equipment associated with the design, fabrication and testing of the detector readout system.
1.05 – Module Assembly & Testing	Labor, materials, and equipment associated with the design, parts fabrication, assembly and testing of the detector modules.
1.06 – Large Aperture Telescopes	Labor, materials, and equipment associated with the design, prototyping, materials selection, construction and certification for the Large Aperture Telescope (LAT) System.
1.07 – Small Aperture Telescopes	Labor, materials, and equipment associated with the design, prototyping, materials selection, construction and certification for the Small Aperture Telescope (SAT) System.
1.08 – Observation Control & Data Acquisition	Labor, materials, and equipment associated with the design, construction, certification, and delivery of the control systems for the observatories and data acquisition.
1.09 – Data Management	Labor, materials, and equipment associated with the design, construction, certification, and delivery of the data management system.
1.10 – Chile Infrastructure	Labor, travel, and materials necessary to plan, track, manage, maintain communications, conduct reviews, and perform necessary safety monitoring on site including management of all shipping of CMB-S4 components to Chile and oversite of construction activities on site.
1.11 – South Pole Infrastructure	Labor, travel, and materials necessary to plan, track, manage, maintain communications, conduct reviews, and perform necessary safety monitoring on site including management of all shipping of CMB-S4 components to the South Pole and oversite of construction activities on site.
1.12 – Integration & Commissioning	On Site Integration and Commissioning of the CMB-S4 telescopes and infrastructure in Chile and the South Pole.

Table 5-3: WBS dictionary.

2. that the cost of an experiment of this scale would limit us to a single instance, in contrast to the long history of having multiple completing experiments at any epoch;

3. that the challenges of fielding such an experiment would primarily be associated with scaling existing technologies (in hardware and data management) to unprecedented levels; and

4. that meeting these scaling challenges would require adding the unique capabilities of DOE laboratories to the long-standing NSF program.

The community therefore proposed CMB-S4 to the 2014 Particle Physics Project Prioritization Process (P5) as single, community-wide, experiment, jointly supported by DOE and NSF. After P5 recommended CMB-S4 under all budget scenarios, in 2015 the CMB community started holding biannual workshops—open to CMB scientists from around the world—to develop and refine the concept. At the request of DOE and NSF, in late 2016 the Astronomy and Astrophysics Advisory Committee (AAAC) convened a Concept Definintion Taskforce (CDT) to conduct a CMB-S4 concept study, and the resulting report was unanimously accepted in late 2017.

One recommendation of the CDT report was that the community should organize itself into a formal collaboration, and an Interim Collaboration Coordination Committee was elected to coordinated this process. The resulting draft bylaws were refined at the Spring 2018 community workshop, and overwhelmingly ratified on March 19th 2018, bringing the CMB-S4 collaboration into being, and the first elections for the various officers of the collaboration were completed by the end of April 2018.

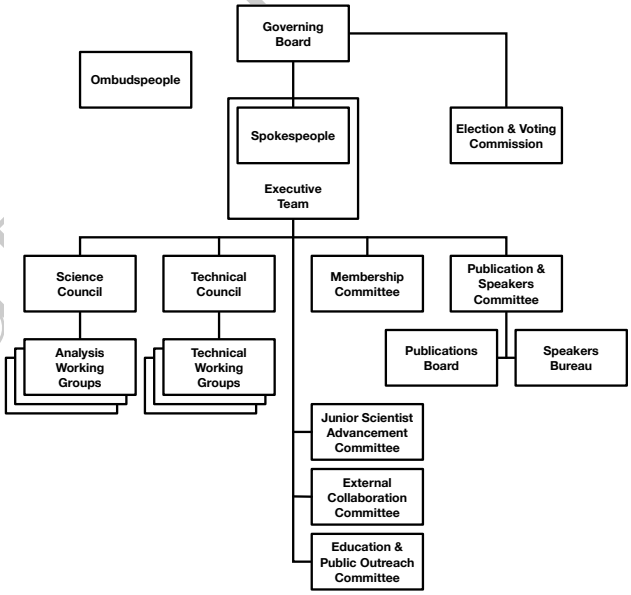

Figure 80: Organizational chart of the CMB-S4 collaboration.

Figure 80 shows the organizational structure of the CMB-S4 collaboration. The Governing Board sets policy and provides oversight to an Executive Team led by two equal co-Spokespersons which is responsible for the day-to-day management of the collaboration. A number of Councils, Committees, and Working Groups then carry out the necessary work to enable the overall scientific goals of the collaboration. As of summer 2019 the collaboration has 198 members, 71 of whom hold positions within the organizational structure. These members represent 11 countries on 4 continents, and 76 institutions comprising 16 national laboratories and 60 universities. It should be noted that collaboration members from both national laboratories and universities are engaged in the entire scope of work, and that US institutional affiliation does not automatically map to specifically DOE or NSF scope.

5.2.1.2 Project organization

The CMB-S4 project organization including lines of authority, communication, oversight and advisory committees will be consistent with the expectations for large research infrastructure projects sponsored by the NSF and DOE. This includes a core project office reporting to institutions directly accountable to NSF and DOE for the successful delivery of the CMB-S4 project. The lead institutions will establish oversight committees and will work with the project office to ensure the necessary advisory committees are effective.

The general approach is to develop and deliver the CMB-S4 project with an Integrated Project Office and project organization established by the institutions leading the NSF CMB-S4 MREFC project and the DOE CMB-S4 Major Item of Equipment (MIE) project. The lead NSF institution will be the NSF partner for the MREFC Cooperative Agreement, and the lead DOE institution will be a DOE M&O contractor (National Laboratory) identified by DOE as the lead integrator for the MIE project.

The organization and management approach will adhere to the following principles:

1. one experiment undertaken by a single collaboration and run as one project;
2. joint NSF and DOE oversight and management, currently a Joint Coordination Group (JCG), with a lead agency to be defined prior to approval of the integrated project baseline;
3. lead institutions accountable to NSF and DOE for the MREFC and MIE projects, respectively;
4. lead institutions establish a project governance agreement that engages all major institutional partners, e.g., an Integrated Project Steering Committee (IPSC) comprised of the major institutions delivering project scope including universities, DOE labs, and private and international partners;
5. a single Integrated Project Office established by the lead institutions and their oversight council, e.g., the IPSC, with clear reporting lines to NSF and DOE;
6. clarity in the NSF and DOE scope of work to ensure direct lines of accountability to each agency and clearly defined management interfaces;
7. integrated Project Office prepared agreements for contributions by private and international partners; and,
8. common management systems that meet the needs of both funding agencies, e.g., project cost and schedule tools, systems engineering processes, etc.

Prior to the establishment of the lead institutions, an Interim Project Office (see Fig. 81) will coordinate the development of management plans that adhere to the principles described above and prepare for the project execution phase. The Interim Project Office will report monthly progress on project development efforts and R&D activities to the Joint Coordination Group established by NSF and DOE. The Interim Project Office is led by the Interim Project Director. The transition to the construction phase will include the appointment of a permanent management structure.

The Interim Project Office, with the support of the Collaboration, will continue to mature the experiment design and project execution plans during 2019–2020. The Interim Project Office will transition into a permanent Integrated Project Office in 2020 to prepare for the construction phase which starts in 2021. A key feature of the organization is the role of collaboration members in the Project Office, primarily as leaders of the Level 2 systems. The Level 2 managers are supported by engineering and project management professionals. The NSF/DOE scope distribution will promote the engagement and participation of universities

and national laboratories. Graduate students, postdocs, professional technicians and engineers are expected to be involved in all aspects of the project.

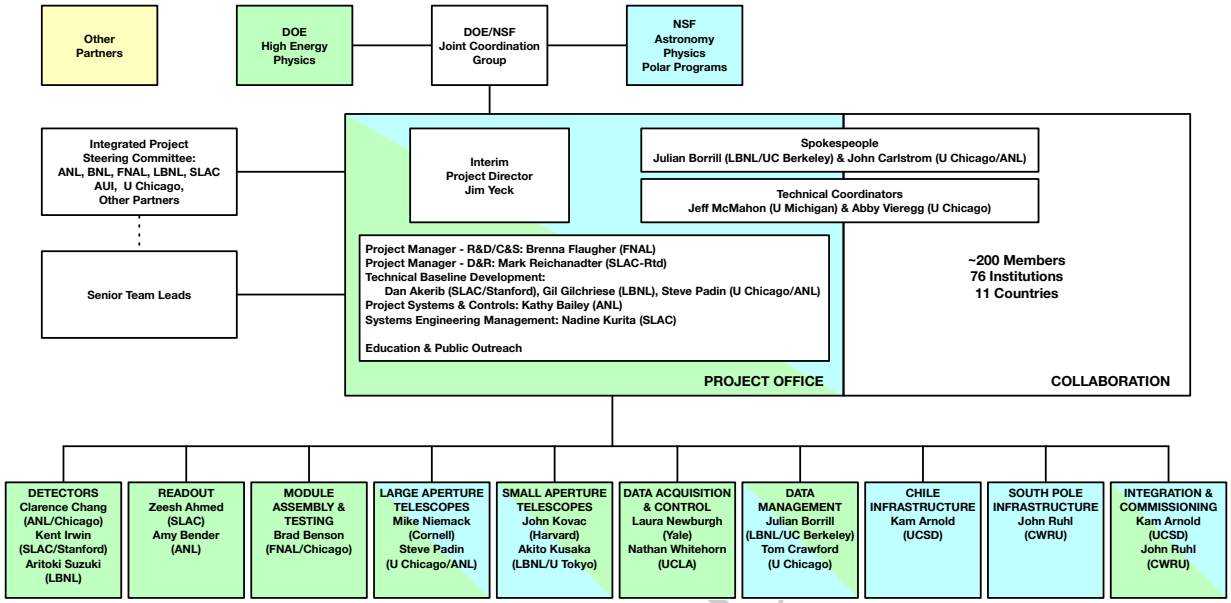

Figure 81: Organizational chart of the interim project office. The figure includes a notional distribution of project scope by funding agency (NSF = blue, DOE = green, Other = yellow). We are actively pursuing partners who could make significant scope contributions in areas aligned with their expertise.

5.2.1.3 Private and international partners

The CMB-S4 Project is a collaborative project, with the scientific Collaboration members serving in technical leadership roles in the project. This is similar to many successful projects including IceCube, ATLAS, and CMS. The lines of accountability for project delivery are clearly defined within the project organization. The project office is responsible for forming partnerships with key stakeholder institutions including DOE National Laboratories, universities, and potential collaborating observatories/projects such as the Simons Observatory, South Pole Observatory, and the CCAT-prime project. Partnerships are also expected to include foreign institutions participating in the CMB-S4 Science Collaboration and contributing to the CMB-S4 Project.

5.2.1.4 In-kind contributions

The CMB-S4 project is expected to include significant contributions from collaborating institutions supported by funding agencies other than NSF and DOE. These "in-kind" contributions will be defined as deliverables to the project. The collaborating institutions agree to deliver items, e.g., instrumentation and effort, required for the success of the CMB-S4 project. The actual cost of each item is the responsibility of the collaborating institution providing the In-kind deliverable. The current best estimate of the value of in-kind contributions is 20–25% or the total cost of the project. This includes both existing infrastructure, telescopes currently under construction, and telescopes and instrumentation proposed by international collaborators.

The CMB-S4 Project Director (PD) is responsible for ensuring the successful delivery of all in-kind contributions required for the CMB-S4 project. The PD is supported in this role by the NSF, DOE, international funding agencies, private foundations, the collaboration and their elected spokesperson, the host institutions, and the Project Office and Level 2 and Level 3 managers. The management approach engages all of these parties in the process of defining and ensuring the delivery of in-kind contributions from partners.

In-kind contributions will be defined in Memoranda of Understanding (MoU) and/or Statements of Work (SoW) executed between the Project Office and the contributing institutions. The MoUs or SoWs define the in-kind contributions for each collaborating institution including the schedule milestones for the institution's deliverables. The Project Director is responsible for sign off on the in-kind deliverables.

Milestones for the in-kind deliverables will be defined in the CMB-S4 project schedule. Progress against these milestones is evaluated during monthly schedule reviews by the Project Office and Level 2 managers. Large deliverables are the terminal milestone for a sequence of lower level milestones. This procedure includes determining the completion forecast for each milestone and taking corrective action when needed.

The project management approach is the same for the entire project: in-kind scope delivered by partners or scope supported by NSF or DOE. The only difference is in the tracking of actual costs, in-kind actual costs are tracked by the collaborating institution providing the in-kind deliverable and are not tracked by the Project Office.

5.3 Cost, schedule, and risk

The project has developed a task based detailed resource loaded schedule which was reviewed by an external panel of experts in December 2018. The estimate follows the guidance in the NSF Large Facilities Manual, NSF 17-066 and the Project Management for the Acquisition of Capital Assets, DOE 413.3b.

For the task-based estimate, tasks were defined at the lowest level elements of the WBS. The entire ensemble of tasks represents all the required resources, activities, and components of the entire project. Each of the tasks are scheduled and estimated by the teams using accepted techniques. The estimates are documented with a Basis of Estimate (BOE) developed by the subsystems leads and stored in a set of google documents which can be ingested into the PrimaveraTM scheduling program. To facilitate proper integration into the CMB-S4 project control system, standard PrimaveraTM layouts are used to enter the information into the database. The schedule has 1110 activities, 1928 relationships, 5 Level 1, 20 Level 2 and 299 Level 3 Milestones for the CMB-S4 project.

5.3.1 Cost

Each detailed task-based cost estimate corresponds to a task in the project schedule. For that specific task, resources and their quantities are assigned from a standardized list of resources. The list includes multiple resource classes in each of the categories: labor, materials/non-labor, or travel. A task estimate consists of the number of hours of each labor resource class, the base-year dollar cost of each materials/non-labor resource class, the number of trips for each travel resource class, and the basis for each estimate.

5.3.2 Schedule

Table 5-4 shows the proposed the NSF Level 1 Milestones along with the corresponding DOE Critical Decision Milestones and Fig. 82 shows a summary of the schedule and high level milestones. The Interim Project Office, jointly supported by NSF and DOE, will further define the schedule for NSF and DOE reviews and approvals with two guiding objectives, a technically driven schedule and coordinated agency reviews and approvals. This approach is necessary for a single integrated project and the clear delineation of scope and responsibilities for each funding agency and partner. The critical path is driven by fabrication of detector wafers and delivery of assembled and tested detector modules to the large aperture telescopes.

The schedule development strategy is to define a schedule that is consistent with the funding potentially available during FY2019-FY2021, and subsequently technically driven. The project is working towards an early completion milestone that contains limited schedule float and a year of schedule float following this early project complete milestone is included in the overall project complete milestone (CD-4). The Interim Project Office will continue to optimize the schedule and include explicit float for activities that are not on the critical path. The best opportunity to improve on the schedule is to reduce the time required to deliver the full quantity of the Detectors and Readout (D&R) components. This is a major focus of the R&D program supported by the DOE. The Interim Project Office formed a D&R Task Force in early 2019 to evaluate existing fabrication and testing capabilities and to provide recommendations on production plans A formal review of the resulting detector fabrication plan will be completed in mid-2019.

NSF Level 1 Milestone (DOE Critical Decision)	Schedule (FY)
Pre-Conceptual Design (CD-0, Mission Need)	Q3 2019
Preliminary Baseline (CD-1/3a, Cost Range/Long-Lead Procurement)	Q3 2021
Preliminary Design Review (CD-2, Performance Baseline)	Q2 2022
Final Deign Review (CD-3, Start of Construction)	Q4 2023
Completion of 1st Telescope (CD-4a, Initial Operations)	Q2 2026
Project Completion(CD-4, Operations)	Q1 2029

Table 5-4: Funding agency milestones.

5.3.3 Reporting and contingency management

The Project will provide reports on a regular basis to NSF and DOE management. The objective of the reporting is to compile essential technical, cost, schedule and performance data into reports to aid in the monitoring and management of the Project.

All cost account managers (CAMs) will submit monthly written narrative reports to the Project Office detailing specific progress on the pertinent subsystems. These reports summarize the activities of the previous month, describe the activities planned for the upcoming month, and include comments and concerns. In addition, performance reporting, including cost and schedule variance reporting, are submitted by the CAMs. These are collected and summarized in a corresponding monthly report prepared by the CMB-S4 management team. This report outlines progress, problems, and budget and schedule status, including comparisons of projected status versus actual status.

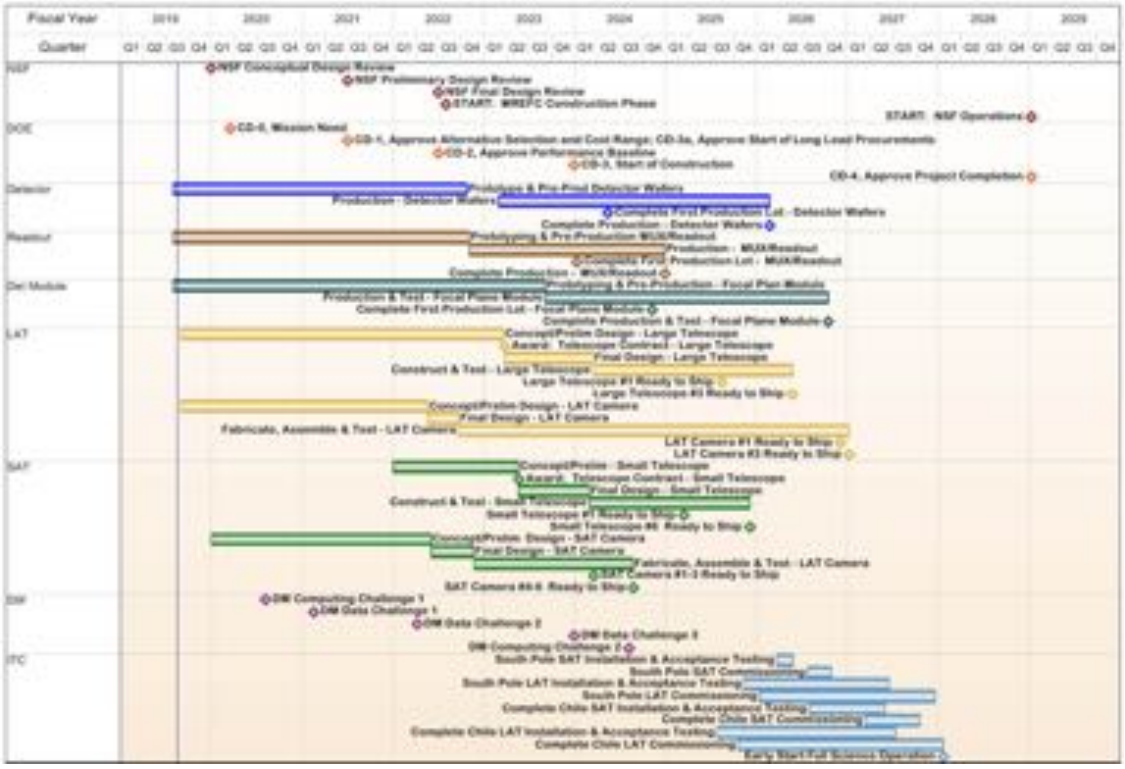

Figure 82: CMB-S4 schedule and milestone summary.

Requests for cost and/or schedule contingency usage will be included in the monthly reports and will generate a change request which must be approved by (depending on the amount requested) the project change control board, project management, laboratory and agency program officers prior to allocation of funds.

5.4 Risks and opportunities

5.4.1 Risk and opportunity management plan

The CMB-S4 Risk and Opportunity Management Plan, describes the continuous risk and opportunity management (RM) process implemented by the project. RM is a disciplined approach to managing project risks throughout the life cycle of the project. This plan is consistent with DOE O413.3B, "Project Management for the Acquisition of Capital Assets," and the NSF 17-066, "NSF Large Facilities Manual." The plan establishes the methods of assessing CMB-S4 project risk and opportunities for all subsystems as well as the system as a whole. Project risk and opportunity are managed throughout the life of the project, from development through construction and commissioning phases.

The primary goal is to manage the risks and opportunities associated with the development and construction of CMB-S4 and focus on understanding, reducing, or eliminating identified risks. Project risks and opportunities are centrally managed, but are the result of project-wide integrated and quantitative assessment which supports management decision-making. The statistical analysis of the residual risk after the planned mitigations informs the project contingency analysis for both cost and schedule.

Current and comprehensive risk updates provide management with additional information in preparing for and reacting to contingent events and adverse outcomes to planned events. The process also provides a uniform language for tracking risk elements and communicating that information. The Risk Registry documents the risk assessment, mitigation strategy, and the residual risk after mitigation. It also includes information about all identified risks within the project. The registry has incorporated lessons learned in several recent projects. Risk Review Board meetings with the project leads will be held on a regular basis to review critical project risks, updates to the registry and status on mitigations. The Risk Register is maintained by the Systems Engineering and the risk management execution is owned by the project management.

The current risk registry for CMB-S4 is being used to define the R&D programs to mitigate risks and to develop the baseline plan for the overall project. A series of risk management meetings were held with each WBS Level 2 system leads and their designated technical experts. The primary purpose of these meetings were to discuss "why" risk management is an essential tool for all levels of project management, as it helps the team communicate and work together to reduce the negative impacts and increase positive impacts. The other goal was the "how" of risk management which included identifying risks, developing informative risk statement, accessing the current probability and impacts of the risks and their possible mitigations. Risk review board meetings will be held regularly to discuss the top risks of the program and update status and changes to the risk registry, as well as action tracking.

5.4.2 Risk/opportunity register

The CMB-S4 risk registry has 140 risks identified and assessed. There are four (4) risks that are currently assessed at critical and 38 risks at high. Table 5-5 provides the current assessment summary for the identified risks and Table 5-6 summarizes the top risks of this program. The project is working on mitigations to ensure that these risks are lowered to reasonable levels that are consistent with our overall project timeline and performance.

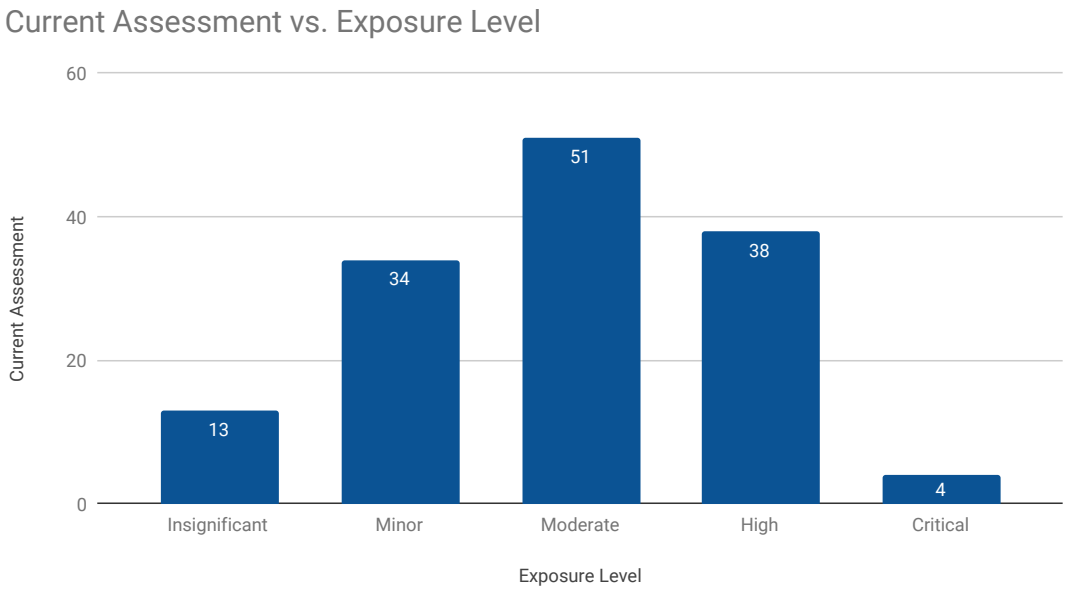

Table 5-5: CMB-S4 risk registry current assessment exposure level. This table shows the current assessment exposure level of the risks that have been identified.

In summary, CMB-S4 will require a large increase in the number of detectors and associated readout components and camera optical elements as compared to Stage-3 experiments. Improving reliability and throughput is important. Technology development is being targeted to mitigate cost, schedule, and performance risk, as well as to exploit opportunities to reduce cost.

5.5 Value management—alternative analysis and selection

The work proposed here will be evaluated through a well-established value engineering process. The first of three phases in this process is the Functional Analysis to define the technical scope, including current design decisions in the context of the full project, as well as known requirements (performance, operational, environment, etc.). Each of the functions will be classified as basic or secondary through their connection to the flow down requirements. The second phase is the Alternative Analysis, which establishes which among the space of solutions could best meet project objectives relative to a reference design. For each of these options weighted criteria are defined (i.e. requirements, cost, schedule, production, operations, risks, complexity,

Risk Description	Current Assessment	Mitigation	Post Mitigated Assessment
IF decrease in fab or performance yield over production period (define criterion) THEN reduces experiment sensitivity and/or increases cost/schedule	Critical	1) Multiple fab houses with duplicate capabilities hedges risk of any single point failure of affecting sustained yield. 2) Demonstrate sustained yield early, and start fabrication of science-grade wafers after CD-3A. 3) At least 6 m of schedule float to critical path.	Moderate
IF the minimum required foundries can't produce detectors that meet performance at the end of pre-production, then impact to cost, schedule and/or performance.	Critical	Investigating two Detector foundries in the DOE complex, other agency foundries and commerical foundries. Holding a review of foundries and supporting prototypes to establish processes.	Moderate
IF detector requirements are not established before the technology downselect, THEN science performance could be impacted	Critical	Determine flowdown of science to survey to detector/readout requirements. Perform required simulations to support flowdown.	Minor
IF end-to-end noise floor in science band exceeds (e.g. >20% of in-band background limit) in yielded packages THEN reduces experiment sensitivity and/or increases cost/schedule	Critical	Early development and testing of at least two MUX technologies with orthogonal risks across noise, integration complexity and TRL AND integration testing with sensors End-to-end testing and validation by CD-2	Minor
IF 1-2 (TBD) fully characterized test beds doesn't exist THEN throughput reduction and/or increase cost/schedule	High	Support costruction of testbeds by CD-1	Minor
IF pipeline is inefficient on next-generation energy-constrained architectures THEN analysis is resource-limited	High	1) Demonstrate range of required performance parameters by CD1. 2) Fund continued fab effort during pre-CD0 to characterize proceses.	Moderate
IF insufficient quality hires available THEN schedule delay with consequences for experiment design simulations and production pipeline development	High	Start DM recruiting pre-CD-1	Moderate
IF wafer fabrication yield <67% (yield = Tc, dielectric, island release, electrical connections meet spec for wafer) THEN reduces experiment sensitivity and/or increases cost/schedule	High	1) Demonstrate reliability of fab steps and with prototype wafer, 2) Multiple fab houses demonstrate yield statistics on 5-10% of targeted science-grade wafer count, 3) If single step is responsible, explore altnerate processes or dedicated machines.	Moderate
IF the interface to Det/Readout are not well understood and documented, then communication protocols may not work well and other technical problems could occur	High	Identify and documenet interfaces early and perform end-t-end testing early to validate these interfaces.	Moderate
IF the hardware is late, then they could miss cargo delivery times for pole	High	1. Phase of deliverables to use more seasons for things that could be done early 2. Have major hardware ready 3 months early. 3. Early verification testing 4. Need to identify the big deliverables and how to mitigate (Decision dates in schedule, LAT not ready by x date, install over 2 seasons or winter) 5. Delay start of pole operations	Moderate
IF integrated detector module noise performance doesn't meet specification THEN we don't achieve map depth in observing time	High	1. Flowdown of requirements 2. Alternative analysis for technology choices 3. Early end-to-end testing to validate performance	Moderate

Table 5-6: CMB-S4 Risk Registry. This table is a summary of the major risks that have been analyzed by the collaboration. A description of the risk and its impact are presented in the first two columns. The 'current assessment' is derived from the product of a probability factor and an impact factor. The planned mitigation action is listed in the third column, followed by a projected post-mitigated risk assessment in the fourth column.

flexibility, maintainability, safety, development cost/schedule) that will be used to evaluate the approaches. These considerations inform the weaknesses/risks that will be studied in a prioritized way through the above scenarios, subject to cost and schedule constraints. Through this phase, implications on cost, schedule, risks, and opportunities are evaluated and updated. Finally, the third phase is the Implementation in which the results of the Alternative Analysis with regard to scoring against the weighted criteria will be presented to the Project Office and/or a designated review team to arrive at a decision to either select or reject a design, or to do further work. Through this process, we will manage risk, maximize opportunity, and promote discussion and support for the final decisions.

5.6 Operations plan

5.6.1 Transition to operations

Completion of commissioning of the first telescope marks the start of CMB-S4 operations and completion of commissioning of the last telescope is the completion of the construction project. The transition from commissioning to operations will occur over a 2–3 year period and will involve a significant change in staffing at the sites, data centers, and partner institutions. A successful operations phase will require transitioning key personnel from Integration & Commissioning to operations and hiring new staff with skills that are appropriate for operations. A transition plan will be developed to cover this period.

5.6.2 Operations

The basic operations model for CMB-S4 will be observations with multiple telescopes and cameras distributed across two sites, with observing priorities and specifications optimized for the CMB-S4 science goals, and data from all instruments shared throughout the entire CMB-S4 collaboration. Scientists working at laboratories and universities will coordinate the observations, monitor the data, design and implement the data pipeline, and carry out science analyses. Instruments at both sites will collect data nearly continuously. These data will include calibrations as well as CMB observations. Nearly all observations will be automated, so that local operators on the sites will not be needed during routine observations. The two CMB-S4 sites though remote, are both sufficiently well-established that fielding the CMB-S4 instrumentation does not represent a large risk, and costs and schedule estimates can be predicted from past experience. Site-specific planning and management are required because there are many site-specific issues such as power generation, safety monitoring, data storage and transfer. The Chile site is at very high altitude (5200 m, barometric pressure about half sea-level) and must deal with snow removal, but is accessible year round. Staff and visitors are housed in San Pedro de Atacama (2400 m, population 2500) and make the one hour drive up to the site as needed. The South Pole gets very cold (−80 C), is not accessible mid February through late October, and suffers shipping restrictions on the size and weight of parts, but the small winterover staff is housed within 1 km from the telescopes, and is always available. At both sites, major maintenance is generally in summer when the weather is worst for observing.

The operations cost is based on a preliminary bottom-up estimate that includes management, site staff, utilities, instrument maintenance, data transmission, data products, pipeline upgrades, collaboration management, and science analysis. The effort is roughly 30 FTE/year for data products and pipeline upgrades, 15 FTE/year for science analysis, and 25 FTE/year for management and site support. The annual operations cost is $32M in 2019 dollars, excluding 20 FTE/year of scientist effort supported by DOE research funds. If

the DOE-supported scientist effort is included, annual operations are 10% of the construction cost, which is typical for an observatory.

5.7 R&D and pre-conceptual design

The CMB-S4 Collaboration is preparing for CD-1/PDR on the timescale of April 2021. R&D and pre-Conceptual design work is aimed at reducing risk and firming up cost and schedule estimates.

Funding to support these efforts has been provided by DOE and funding has been requested from NSF through a MSRI-R1 proposal.

R&D is focused on Detectors and Readout while the pre-Conceptual Design studies are aimed at 5 distinct areas: Cold Optics, Ground Pickup Sidelobes and Beam systematics, LAT Cryostat Design, SAT Cryocooler test and Data Management.

The interim project office includes an R&D and pre-Conceptual Design manager that works with the collaboration Technical Coordinators (see Fig. 81). Progress on R&D and pre-Conceptual Design work is reported to the manager and to the interim project office on a monthly basis.

A short summary of the R&D and pre-Conceptual Design efforts is given below.

Detectors and Readout: The highest technical risk to the CMB-S4 project was identified by the CDT and the December 2018 review as detector fabrication and testing capacity. ANL and LBNL/HYPRES have already demonstrated the capability to fabricate sinuous antenna detectors that are compatible with fmux readout. The near term R&D will focus on bringing these fabrication facilities up to speed to fabricate another possible combination, OMT horn-coupled detectors that are compatible with umux (and dfMUX) readout, optimized to operate at the planned 100mK focal plane temperature. The long term goal is to have the performance of a CMB-S4 wafer and detector module fully characterized and understood by October 2020.

Cold Optics: CMB-S4 requires more cold optical elements that any previous CMB experiment. These include lenses, filters, half-wave plates (HWP), and baffling materials. The lenses, half-wave plates, and absorbing filters require high quality anti-reflection (AR) coatings. The goal of this effort is to demonstrate implementations of these technologies to enable performance forecasting and technology selection by CD-1.

Ground Pickup & Sidelobes (SATs and LATs): Systematic errors due to ground pickup, and pickup from the Sun, Moon, and galaxy are a critical issue for CMB-S4 and have been identified as one of the most significant project risks. Pickup adds noise and biases in measurements of r and $N_{\rm eff}$, and must be carefully controlled if CMB-S4 is to meet its ambitious science goals. This effort is focused on modeling pickup for the CMB-S4 large and small telescopes, using a mix of physical optics and ray tracing tools, with inputs and techniques verified by sidelobe measurements from Stage-3 telescopes and laboratory measurements.

LAT Cryostat Design: The key design driver for the large telescope cameras is accommodating enough detectors to achieve the required mapping speed. Existing large camera designs, e.g., the Simons Observatory LAT cryostat, are too small. This effort is aimed at developing a new concept for CMB-S4, including consideration of the optimum pixel spacing, optics tube diameter and spacing, and detector wafer configuration and will develop a preliminary solid model of the new camera concept that will provide a basis for detailed design.

SAT Cryocooler Test: The cooling capacity of 4-K and 40-K stages are the driver for the cryostat design of CMB-S4 SAT. The cryocooling system is the dominant contributor to the power budget at the site. This activity covers a quick test of the cooling capacity for currently available dilution refrigerators and pulse tube systems and will enable an early start to the SAT cryostat design effort.

Data Management: CMB-S4 faces the twin challenges of controlling systematic effects to unprecedented precision and the extraordinary volume of the data to be processed. This effort addresses activities associated with these challenges that are on the critical path to CD-1 either because they are required to inform the baseline design (systematics simulations) or because they have critical milestones on that timescale (data processing at scale and on new computing architectures).

Appendices

A

Design Validation

A.1 Technical Design to Measurement Requirements (*Borrill*)

A.2 Measurement Requirements to Science Requirements

(*Huffenberger & Meyers*)

Appendix A.2 documents how well the project measurement requirements (Section 2.4) satisfy the project science requirements (Section 2.3). The four science requirements are the most important and technically challenging parts of the science case: tensor-to-scalar ratio, light relics, galaxy clusters, and gamma ray burst transients. Thus any experiment with measurement capabilities that exceed our measurement requirements should be able to achieve our science requirements, and therefore support the entire science case for the project (Chapter 1).

The measurement requirements are presented as a set of noise curves for temperature and polariztion in Figures 28–30. For these noise curves, equation (2.1) provides the functional form and Tables 2-1–2-3 provide the parameters.

A.2.1 Tensor-to-scalar ratio r (Science Requirement 1.0) (*Bischoff & Wu*)

To validate that the instrument configuration set for the PBDR has sufficient sensitivity to reach the r science goal, we generate and analyze map-based simulations that matches the expected output from timestream-based simulations to obtain the expected $\sigma(r)$. In this section, we first describe the procedures through which we obtain the map-based simulations that calibrate against both the Data Management simulations and the performance of current experiments. We then describe the analysis methods and results. We find that for the PBDR instrument configuration, ...

A.2.1.1 Noise realizations

We generate noise realizations using different approaches for the SATs and for the LAT. For the SATs, we rescale the input per-band noise levels from the Data Management simulation output given BICEP/Keck performance. For the LAT, we take the noise levels from the Data Management simulations, as stated in Sect. **??**. To produce map-level simulations, we.... *details of the BK/CMB-S4 ratio.*

Taking these map noise levels for the SATs and the LAT, we then generate Gaussian noise realizations at each band and divide by the square-root of the coverage pattern generated by the Data Management simulations such that the noise "blows up around the edge" as it does in real maps. The generation of the coverage pattern is described in Sect. **??**.

A.2.1.2 Signal simulations

To make simulated sky maps we add realizations of lensed CMB both without and with an r component to models of the Galactic foregrounds. We used the following seven foreground models. These are identical to the foreground models used for validation in the DSR.

0. Simple Gaussian realizations of synchrotron and dust with power-law angular power spectra at amplitudes set to match the observations in the BICEP/Keck field, and simple uniform SEDs (power law for synchrotron, modified blackbody for dust).
1. The PySM[1] model `a1d1f1s1`, where the letters refer to anomalous microwave emission, dust, free-free and synchrotron respectively, and the numbers are the base models described in Ref. [572].
2. The PySM model `a2d4f1s3`, where the models have been updated to variants that are also described in Ref. [572]. Note that these include 2% polarized AME, a curvature of the synchrotron SED, and a two-temperature model for dust.
3. The PySM model `a2d7f1s3`, where the dust model has been updated to a sophisticated physical model of dust grains as described in Ref. [573]. This model is interesting in that it does not necessarily conform to the modified blackbody SED.
4. The dust in model 3 is replaced by a model of polarized dust emission that incorporates HI column density maps as tracers of the dust intensity structures, and a phenomenological description of the Galactic magnetic field as described in Ref. [574]. The model is expanded beyond that described in the paper to produce a modest amount of decorrelation of the dust emission pattern as a function of frequency motivated by the analysis of *Planck* data in Ref. [575].
5. A toy model where the dust decorrelation suggested in figure 3 of Ref. [575] is taken at face value ($\mathcal{R}_{80}^{217\times353} = 0.85$). While such a model is not ruled out by current data it appears to be very hard to produce such strong decorrelation in physics-based models. We also note that Ref. [576] have reanalyzed the same *Planck* data and, while they find that the high level of decorrelation in this model is consistent with the data, their best fit to that same data has no decorrelation.
6. A model based on MHD simulations [577] of the Galactic magnetic field, which naturally produces non-Gaussian correlated dust and synchrotron emission.

Models 1 to 4 use the actual large-scale modes of the real sky as measured above the noise in the *Planck* data. This means that these models are intrinsically "single-realization," and this must be borne in mind when interpreting the results. Models 4 and 6 are not based on *Planck*, but still contain a fixed signal realization. Models 0 and 5 have different seeds for each signal map and include the (Gaussian) sample variance. The PySM models fill in the small-scale structure with power-law Gaussian extrapolations, while models 4 and 6 naturally produce non-Gaussian small-scale structure. However, all of these models are consistent with current data, and we should be careful not to necessarily associate nominal sophistication with greater probability to more closely reflect reality.

A.2.1.3 Analysis & Results

To make simulated maps the noise realizations described in Sect. A.2.1.1 are added to the sky models described in Sect. A.2.1.2, and potentially also the systematics realizations described in Sect. **??**. For each

[1] `https://github.com/bthorne93/PySM_public`

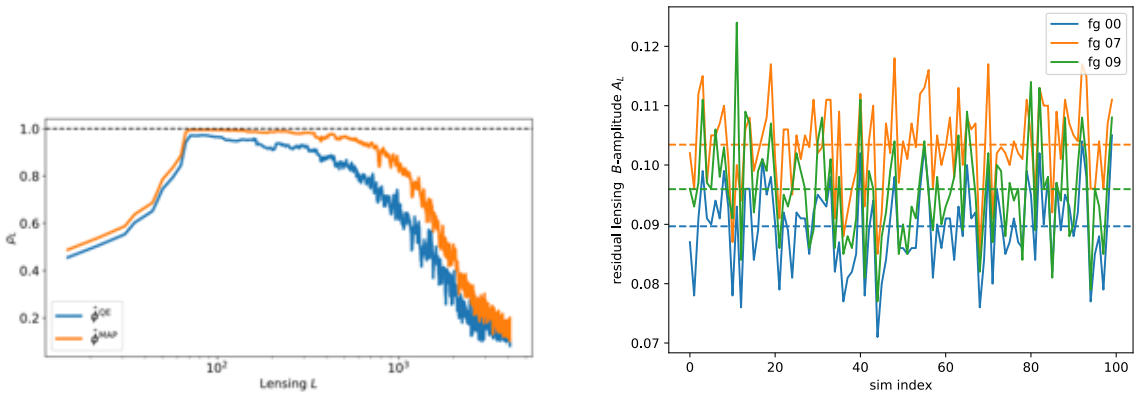

Figure 83: *Left panel:* Cross-correlation of the lensing quadratic and iterated tracer to the input lensing simulation. Lensing multipoles L most relevant to degree-scale delensing are centred on $L \simeq 500$ *Right panel:* Residual lensing B-amplitudes expected from the lensing templates built from the ILC maps for the 100 simulations for each of the foreground model 00, 07 and 09 (solid), together with their mean value (dashed). These were calculated as the spectrum of the template minus input lensing $B-$power across the central region of the mapped area. (95GHz no fg on left panel, placeholders for better plot)

realization one then has a stack of multi-frequency $I/Q/U$ maps containing non-uniform noise, foregrounds and signal, and the challenge is to re-analyze them to recover the parameter of interest (in this case r). This can be done by different teams using different methods, and could be done in a blind manner, although we have not done this yet.

In this validation, we apply one of the methods used in the DSR, which is an evolution of the parametric multi-component fit to the ensemble of auto- and cross-spectra as used for the BICEP/Keck analysis to date [578, 579]. This method fits the observed bandpowers to a model composed of the lensing expectation plus dust and synchrotron contributions and a possible r component. Dust and synchrotron each have an amplitude ($A_{\rm d}$ and $A_{\rm s}$), a spatial spectral parameter ($\alpha_{\rm d}$ and $\alpha_{\rm s}$), and a frequency spectral parameter ($\beta_{\rm d}$ and $\beta_{\rm s}$). We also allow dust/synchrotron correlation (ϵ), and decorrelation of the dust patterns over frequency ($\Delta_{\rm d}$).

A new addition to this validation is the incorporation of a lensing template as a pseudo-band to the ensemble of auto- and cross-spectra. In the DSR, we artificially scaled down the ΛCDM lensing signal to $A_{\rm L}$ of 0.1, expected by analytic predictions. We describe in detail the generation of the lensing template in Sect. A.2.1.4 and report results in Sect. A.2.1.5.

A.2.1.4 Delensing

(Carron)Building of the lensing B-mode templates follows a curved-sky version of iterative algorithm exposed in Ref. [**?**]. At each step, gradients of the lensing map likelihood are calculated and used to progress towards the maximum a posteriori lensing map reconstruction. This procedure corresponds to estimating a delensed E-mode map at each step, and obtaning from it it a novel quadratic estimator with modified weights to capture additional lensing signal. Throughout, only polarization data is used, since temperature carry little additional information at these noise levels. Inclusion of the temperature also would also lead to a less

robust iterative search owing to the stronger lensing 'mean-field' and the larger expected relevance of high-ℓ foregrounds in temperature.

The statistical dependence of the lensing map reconstruction noise to the CMB to delens can induce strong spurious signatures. To avoid this, all B-modes multipoles lower than 200 are projected out in the CMB likelihood, assigning them infinite noise, for a negligible cost in reconstruction noise. This ensures none of the degree scale B LAT polarization data is actually present in the lensing tracer and spuriously introduced in this way in the SAT signal. This deprojection is performed with the help of a precomputed large dense matrix, which increases the memory footprint of the lensing template building, but does not affect the pipeline performance.

The computational cost of the template building is further kept under control by approximating the mean-field gradient (that captures the response to anisotropies unrelated to lensing, such as masking, beam assymetries or inhomogeneous noise) constant through iterations. Generally, the polarization mean-field is small on the scales most relevant for degree-scale delensing, centred on lensing multipoles $L \simeq 500$. Under inspection, artefacts of this approximation can be seen as large scales features most prominent close to the edges of the mapped area, but this does not affect the delensing capabilities of the tracer.

We performed a total of 12 iterations on the ILC cleaned maps. For delensing purposes, the main effect of the ILC combination is the inverse-variance weighting of the noise at high multipole where large parts of the lensing signal comes from. The last couple of iterations were performed with higher accuracy parameters to ensure proper convergence. For this reason they use a fair fraction of the total cost, even if the actual gain is small if visible. The results are shown on Fig. 83. In the scenario with largest foreground amplitude (07), the templates are able to remove very close to 90% of the lensing power, in great agreement with analytical forecasts. These forecasts indicates that an additional percentage points could be further achieved by extending the CMB multipoles used in building the templates from 3000 to higher $\ell_{\rm max}$ but this has not been tested so far. In other respect, the templates are expected to achieve optimality, in a statistical sense. No relevant adverse effect of the foregrounds (except the decreases delensing efficiency owing to the higher power) has been seen so far on these maps.

A.2.1.5 Results

A.2.1.6 Instrumental systematics

A.2.2 Light relics (Science Requirement 2.0) (*Loverde & Reichardt*)

The second key science requirement of CMB-S4 is to probe for the existence of new light relics by measuring $N_{\rm eff}$, with a 2-σ uncertainty ≤ 0.06. Changes to the light relic density $N_{\rm eff}$ lead to the most significant shifts in the damping tail (small angular scales) of the CMB power spectra. Thus the sensitivity of a CMB survey to $N_{\rm eff}$ depends critically on its ability to map small scale fluctuations. Measuring the relevant modes at high signal-to-noise requires a low-noise, relatively high-resolution, and wide-area-coverage survey of temperature and polarization anisotropy. Extragalactic foregrounds limit the constraining power of the temperature auto spectrum on small angular scales, and so the improvements in constraints on $N_{\rm eff}$ expected from CMB-S4 are driven by the improved measurements of the TE and EE power spectra.

The CMB-S4 Science Book [17] and Science Case and Reference Design [394] explored constraints on $N_{\rm eff}$ over a wide range of experimental configurations. The qualitative lessons on how $N_{\rm eff}$ constraints are affected by changes to the noise level, beam size, and sky fraction that were presented in those studies remain unchanged, and are illustrated in Fig. 84. As can be seen from the figure, reduction of the noise level, either through

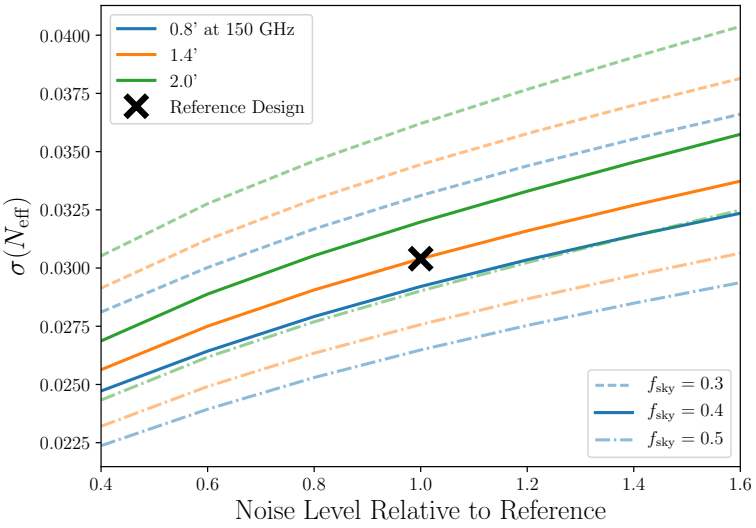

Figure 84: Impact of changes to the noise level, beam size, and sky fraction on forecasted 1σ constraints on $N_{\rm eff}$ with $Y_{\rm p}$ fixed by BBN consistency. Changes to $f_{\rm sky}$ are taken here at fixed map depth. The forecasts shown in this figure have less detailed modeling of atmospheric effects and foreground cleaning than those shown elsewhere. The results should therefore be taken as a guide to how various experimental design choices impact the constraining power for light relics, but the specific values of the constraints should be taken to be accurate only at the level of about 10%.

increased detector count or extended observing time, leads to improved constraints on $N_{\rm eff}$, though significant improvements require fairly large improvements to the map depth of the survey. This is due to the rapid drop in CMB power in the damping tail on small angular scales and to the impact of residual foregrounds, which act as additional noise. Compared to the reference design, increasing the size of the telescope dish leads to a modest improvement in constraints on light relics, while reducing the dish size produces a slightly sharper drop in the constraining power. Observing a larger fraction of the sky (at a fixed map noise level) allows access to more independent small-scale modes, and results in tighter constraints on $N_{\rm eff}$. For fixed total observing time, the exponential suppression of the primary CMB temperature and polarization on small angular scales favors observations of as much sky as possible. Since those works, we have further developed the treatment of galactic and extragalactic foregrounds and the extent to which foregrounds limit the accessible sky area. We have also worked to estimate the levels of potential bias on the measured $N_{\rm eff}$ due to foregrounds and instrumental effects.

Throughout this section, we assume the baseline survey and predicted map noise levels described in §**??**. As described in that section, the forecasted map noise levels are based on the achieved detector noise properties in current experiments and include effects such elevation-dependent atmospheric emission and correlated noise. We assume that the existing Planck observations will be used over sky outside the galactic mask that is not observed by CMB-S4.

A.2.2.1 Foregrounds and point-source removal

For the deep and wide field forecast, the sky model consists of a set of auto- and cross- power spectra for the set of instrument bands (similar to Ref. [580]). It is built from power spectrum templates and source count models. In addition to the CMB, the foreground signals include tSZ, kSZ, Galactic cirrus, radio point sources, and dusty point sources. We scale these with a single frequency dependence per component to translate the power spectra between the frequency bands of CMB-S4, which we treat as delta functions at the central frequencies.

The tSZ and kSZ power spectral templates come from the hydrodynamic simulations of [397]. The tSZ frequency dependence uses the non-relativistic formula, and the kSZ effect has the same frequency dependence at the CMB. The Galactic cirrus template comes from the treatment of [580]. It is a power law $\propto \ell^{-0.7}$, using the amplitude they found for the clean portions of the sky. The frequency dependence is $\propto \nu^{3.8}$ in flux density units.

Radio point-source counts come from [444] at 148 GHz (their model C2Ex). We scale them to other bands as a power law with index -0.5 in flux density units. Dusty point-source counts come from [581] at 217 GHz, but we adjusted them on the faint end to match the SPT 220-GHz source counts [447]. The dusty sources are scaled from 217 GHz with a graybody spectrum with $\beta^{\rm CIB} = 2.1$ and $T^{\rm CIB} = 9.7\,{\rm K}$. The power spectral templates for the point sources are flat with an amplitude that depends on the integrated, squared flux density, weighted by the source counts. We model the correlation between dusty sources and the tSZ using a halo model as in Ref. [582, 125].

We estimate the residual point-source power after masking while accounting for the instrument noise and beam. In each band, and based on the total power spectrum of the sky model and the noise model, we compute the variance after applying a filter optimized for point-source detection. The variance is a function of the prospective flux cut, which sets the power of the point-source component. We compare the filtered variance to the amplitude of a filtered point source to determine the signal-to-noise ratio of sources (as a function of the flux cut). We choose the flux cut so that it self-consistently excludes sources with signal-to-noise ratio greater than 5.

For each source population, we identify the best band for excluding sources by scaling the per-band flux cuts back to the reference frequency and comparing them. For radio sources, 90 GHz finds the intrinsically faintest sources due to a combination of the band's noise, beam, and SED. For dusty sources, 270 GHz is the best. Assuming these deepest source cuts determine the source mask, we finally compute the overall level of unmasked residual source power from each population and add it to the total sky model.

A.2.2.2 Fisher forecasts

For the forecasts, we begin with the multi-frequency model described in section A.2.2.1 and noise spectra based on the depth maps **??**. A harmonic space ILC algorithm [583] is used to derive foreground reduced temperature and polarization spectra and noise spectra. The component separated noise curves and extragalactic foreground residuals computed from the procedure above were then used in a Fisher forecast to determine the expected constraints on $N_{\rm eff}$. The CMB-S4 noise was combined with a model for the noise from the *Planck* satellite, in an inverse variance sum. Doing so reduces the noise on the large scale temperature modes which would be contaminated by the atmosphere for CMB-S4 alone. Contamination from extragalactic residuals was then added, which acts much like an additional source of noise. We imposed a cut at $\ell_{\rm min} = 30$, and we took $\ell_{\rm max} = 5000$ for all spectra. A model for *Planck* temperature data was included for $\ell < 30$ on $f_{\rm sky} = 0.8$.

We assumed a cosmology described by ΛCDM+$N_{\rm eff}+\sum m_\nu$, assuming BBN consistency to fix the primordial helium density $Y_{\rm p}$. The TT, TE, EE, and $\phi\phi$ spectra were included, with the lensing reconstruction noise calculated using the minimum variance combination of quadratic estimators [564, 565], including the improvement from iterative EB reconstruction [584, 585]. The small improvements which come from delensing T and E spectra [586] were also included.

The resulting noise curves were then used in a Fisher forecast to compute the errors on $N_{\rm eff}$. The sky fractions for CMB-S4 observations were calculated for each choice of minimum elevation, galactic cut, and scan strategy as shown in Table **??**. *Planck* observations were assumed to cover the rest of the sky which is not observed by CMB-S4 and also lies outside the galactic mask. As can be seen in Table **??**, the elevation penalty reduces the usable effective sky fraction which leads to the slightly weaker constraints compared to the nominal scan strategy without elevation penalty. The results for the forecasts for the nominal schedule are shown in Fig. **??**.

A.2.3 Galaxy clusters (Science Requirements 3.1, 3.2) (*Battaglia & Vieira*)

A.2.4 Gamma-ray-burst transients (Science Requirement 4.0) (*Battaglia & Vieira*)

References

[1] **BICEP2, Keck Array** Collaboration, P. A. R. Ade *et al.*, "Improved Constraints on Cosmology and Foregrounds from BICEP2 and Keck Array Cosmic Microwave Background Data with Inclusion of 95 GHz Band," *Phys. Rev. Lett.* **116** (2016) 031302, arXiv:1510.09217 [astro-ph.CO].

[2] R. Kallosh and A. Linde, "Universality Class in Conformal Inflation," *JCAP* **1307** (2013) 002, arXiv:1306.5220 [hep-th].

[3] A. A. Starobinsky, "A New Type of Isotropic Cosmological Models Without Singularity," *Phys.Lett.* **B91** (1980) 99–102.

[4] F. L. Bezrukov and M. Shaposhnikov, "The Standard Model Higgs boson as the inflaton," *Phys. Lett.* **B659** (2008) 703–706, arXiv:0710.3755 [hep-th].

[5] M. Cicoli, C. P. Burgess, and F. Quevedo, "Fibre Inflation: Observable Gravity Waves from IIB String Compactifications," *JCAP* **0903** (2009) 013, arXiv:0808.0691 [hep-th].

[6] K. N. Abazajian *et al.*, "Light Sterile Neutrinos: A White Paper," arXiv:1204.5379 [hep-ph].

[7] R. Essig *et al.*, "Working Group Report: New Light Weakly Coupled Particles," in *Community Summer Study 2013: Snowmass on the Mississippi (CSS2013), Minneapolis, MN, USA, July 29-August 6, 2013*. 2013. arXiv:1311.0029 [hep-ph].

[8] J. Alexander *et al.*, "Dark Sectors 2016 Workshop: Community Report," arXiv:1608.08632 [hep-ph].

[9] D. Green *et al.*, "Messengers from the Early Universe: Cosmic Neutrinos and Other Light Relics," *Bull. Am. Astron. Soc.* **51** no. 7, (2019) 159, arXiv:1903.04763 [astro-ph.CO].

[10] N. Whitehorn, T. Natoli, P. A. R. Ade, J. E. Austermann, J. A. Beall, A. N. Bender, B. A. Benson, L. E. Bleem, J. E. Carlstrom, C. L. Chang, H. C. Chiang, H.-M. Cho, R. Citron, T. M. Crawford, A. T. Crites, T. de Haan, M. A. Dobbs, W. Everett, J. Gallicchio, E. M. George, A. Gilbert, N. W. Halverson, N. Harrington, J. W. Henning, G. C. Hilton, G. P. Holder, W. L. Holzapfel, S. Hoover, Z. Hou, J. D. Hrubes, N. Huang, J. Hubmayr, K. D. Irwin, R. Keisler, L. Knox, A. T. Lee, E. M. Leitch, D. Li, J. J. McMahon, S. S. Meyer, L. Mocanu, J. P. Nibarger, V. Novosad, S. Padin, C. Pryke, C. L. Reichardt, J. E. Ruhl, B. R. Saliwanchik, J. T. Sayre, K. K. Schaffer, G. Smecher, A. A. Stark, K. T. Story, C. Tucker, K. Vanderlinde, J. D. Vieira, G. Wang, and V. Yefremenko, "Millimeter Transient Point Sources in the SPTpol 100 Square Degree Survey," *Ap. J.* **830** (Oct., 2016) 143, arXiv:1604.03507 [astro-ph.HE].

[11] K. D. Alexander, E. Berger, W. Fong, P. K. G. Williams, C. Guidorzi, R. Margutti, B. D. Metzger, J. Annis, P. K. Blanchard, D. Brout, D. A. Brown, H.-Y. Chen, R. Chornock, P. S. Cowperthwaite, M. Drout, T. Eftekhari, J. Frieman, D. E. Holz, M. Nicholl, A. Rest, M. Sako, M. Soares-Santos, and V. A. Villar, "The Electromagnetic Counterpart of the Binary Neutron Star Merger LIGO/Virgo GW170817. VI. Radio Constraints on a Relativistic Jet and Predictions for Late-time Emission from the Kilonova Ejecta," *Ap. J. Lett.* **848** (Oct., 2017) L21, arXiv:1710.05457 [astro-ph.HE].

[12] E. Berger, "Short-Duration Gamma-Ray Bursts," *Ann. Rev. Astron. Astroph.* **52** (Aug., 2014) 43–105, arXiv:1311.2603 [astro-ph.HE].

[13] **Planck** Collaboration, Planck Collaboration XXIV, "Planck 2013 Results. XXIV. Constraints on primordial non-Gaussianity," *Astron. Astrophys.* **571** (2014) A24, arXiv:1303.5084 [astro-ph.CO].

[14] Planck Collaboration XVII, "Planck 2015 results. XVII. Constraints on primordial non-Gaussianity," arXiv:1502.01592 [astro-ph.CO].

[15] R. L. Arnowitt, S. Deser, and C. W. Misner, "The Dynamics of general relativity," *Gen. Rel. Grav.* **40** (2008) 1997–2027, arXiv:gr-qc/0405109 [gr-qc].

[16] R. Namba, M. Peloso, M. Shiraishi, L. Sorbo, and C. Unal, "Scale-dependent gravitational waves from a rolling axion," *JCAP* **1601** no. 01, (2016) 041, arXiv:1509.07521 [astro-ph.CO].

[17] **CMB-S4** Collaboration, K. N. Abazajian *et al.*, "CMB-S4 Science Book, First Edition," arXiv:1610.02743 [astro-ph.CO].

[18] A. Linde, "Gravitational waves and large field inflation," *JCAP* **1702** no. 02, (2017) 006, arXiv:1612.00020 [astro-ph.CO].

[19] D. Babich, P. Creminelli, and M. Zaldarriaga, "The Shape of Non-Gaussianities," *JCAP* **0408** (2004) 009, arXiv:astro-ph/0405356 [astro-ph].

[20] E. Komatsu *et al.*, "Non-Gaussianity as a Probe of the Physics of the Primordial Universe and the Astrophysics of the Low Redshift Universe," arXiv:0902.4759 [astro-ph.CO].

[21] P. D. Meerburg, J. Meyers, A. van Engelen, and Y. Ali-Haïmoud, "CMB B -mode non-Gaussianity," *Phys. Rev.* **D93** no. 12, (2016) 123511, arXiv:1603.02243 [astro-ph.CO].

[22] J. M. Maldacena and G. L. Pimentel, "On graviton non-Gaussianities during inflation," *JHEP* **09** (2011) 045, arXiv:1104.2846 [hep-th].

[23] L. Bordin, P. Creminelli, M. Mirbabayi, and J. Noreña, "Tensor Squeezed Limits and the Higuchi Bound," *JCAP* **1609** no. 09, (2016) 041, arXiv:1605.08424 [astro-ph.CO].

[24] A. Agrawal, T. Fujita, and E. Komatsu, "Large tensor non-Gaussianity from axion-gauge field dynamics," *PRD* **97** no. 10, (2018) 103526, arXiv:1707.03023 [astro-ph.CO].

[25] G. Domènech, T. Hiramatsu, C. Lin, M. Sasaki, M. Shiraishi, and Y. Wang, "CMB Scale Dependent Non-Gaussianity from Massive Gravity during Inflation," *JCAP* **1705** no. 05, (2017) 034, arXiv:1701.05554 [astro-ph.CO].

[26] H. Lee, D. Baumann, and G. L. Pimentel, "High-Scale Inflation and the Tensor Tilt," arXiv:1607.03735 [hep-th].

[27] H. Lee, D. Baumann, and G. L. Pimentel, "Non-Gaussianity as a Particle Detector," *JHEP* **12** (2016) 040, arXiv:1607.03735 [hep-th].

[28] D. Baumann, G. Goon, H. Lee, and G. L. Pimentel, "Partially Massless Fields During Inflation," *JHEP* **04** (2018) 140, arXiv:1712.06624 [hep-th].

[29] **Planck** Collaboration, Planck Collaboration X, "Planck 2018 results. X. Constraints on inflation," arXiv:1807.06211 [astro-ph.CO].

[30] C. L. Bennett *et al.*, "First Year Wilkinson Microwave Anisotropy Probe (WMAP) Observations: Preliminary Maps and Basic Results," *Astrophys. J. Suppl.* **148** (2003) 1, arXiv:astro-ph/0302207.

[31] D. N. Spergel *et al.*, "First Year Wilkinson Microwave Anisotropy Probe (WMAP) Observations: Determination of Cosmological Parameters," *Astrophys. J. Suppl.* **148** (2003) 175, arXiv:astro-ph/0302209.

[32] Planck Collaboration XX, "Planck 2015 results. XX. Constraints on inflation," arXiv:1502.02114 [astro-ph.CO].

[33] A. Slosar *et al.*, "Scratches from the Past: Inflationary Archaeology through Features in the Power Spectrum of Primordial Fluctuations," arXiv:1903.09883 [astro-ph.CO].

[34] S. L. Bridle, A. M. Lewis, J. Weller, and G. Efstathiou, "Reconstructing the primordial power spectrum," *Mon. Not. Roy. Astron. Soc.* **342** (July, 2003) L72–L78, arXiv:astro-ph/0302306 [astro-ph].

[35] Z.-K. Guo, D. J. Schwarz, and Y.-Z. Zhang, "Reconstruction of the primordial power spectrum from CMB data," *Journal of Cosmology and Astro-Particle Physics* **2011** (Aug., 2011) 031, arXiv:1105.5916 [astro-ph.CO].

[36] R. Hlozek, J. Dunkley, G. Addison, J. W. Appel, J. R. Bond, C. Sofia Carvalho, S. Das, M. J. Devlin, R. Dünner, T. Essinger-Hileman, J. W. Fowler, P. Gallardo, A. Hajian, M. Halpern, M. Hasselfield, M. Hilton, A. D. Hincks, J. P. Hughes, K. D. Irwin, J. Klein, A. Kosowsky, T. A. Marriage, D. Marsden, F. Menanteau, K. Moodley, M. D. Niemack, M. R. Nolta, L. A. Page, L. Parker, B. Partridge, F. Rojas, N. Sehgal, B. Sherwin, J. Sievers, D. N. Spergel, S. T. Staggs, D. S. Swetz, E. R. Switzer, R. Thornton, and E. Wollack, "The Atacama Cosmology Telescope: A Measurement of the Primordial Power Spectrum," *Ap. J.* **749** (Apr., 2012) 90, arXiv:1105.4887 [astro-ph.CO].

[37] M. Aich, D. K. Hazra, L. Sriramkumar, and T. Souradeep, "Oscillations in the inflaton potential: Complete numerical treatment and comparison with the recent and forthcoming CMB datasets," *Phys. Rev.* **D 87** (Apr., 2013) 083526, arXiv:1106.2798 [astro-ph.CO].

[38] P. Hunt and S. Sarkar, "Reconstruction of the primordial power spectrum of curvature perturbations using multiple data sets," *Journal of Cosmology and Astro-Particle Physics* **2014** (Jan., 2014) 025, arXiv:1308.2317 [astro-ph.CO].

[39] R. de Putter, E. V. Linder, and A. Mishra, "Inflationary freedom and cosmological neutrino constraints," *Phys. Rev.* **D 89** (May, 2014) 103502, arXiv:1401.7022 [astro-ph.CO].

[40] V. Miranda, W. Hu, C. He, and H. Motohashi, "Nonlinear excitations in inflationary power spectra," *Phys. Rev.* **D 93** (Jan., 2016) 023504.

[41] D. K. Hazra, A. Shafieloo, G. F. Smoot, and A. A. Starobinsky, "Primordial features and Planck polarization," *Journal of Cosmology and Astro-Particle Physics* **2016** (Sept., 2016) 009.

[42] C. Dvorkin and W. Hu, "Generalized Slow Roll for Large Power Spectrum Features," *Phys. Rev.* **D81** (2010) 023518, arXiv:0910.2237 [astro-ph.CO].

[43] C. Dvorkin and W. Hu, "CMB Constraints on Principal Components of the Inflaton Potential," *Phys. Rev.* **D82** (2010) 043513, arXiv:1007.0215 [astro-ph.CO].

[44] C. Dvorkin and W. Hu, "Complete WMAP Constraints on Bandlimited Inflationary Features," *Phys. Rev.* **D84** (2011) 063515, arXiv:1106.4016 [astro-ph.CO].

[45] G. Obied, C. Dvorkin, C. Heinrich, W. Hu, and V. Miranda, "Inflationary Features and Shifts in Cosmological Parameters from Planck 2015 Data," *Phys. Rev.* **D96** no. 8, (2017) 083526, arXiv:1706.09412 [astro-ph.CO].

[46] G. Obied, C. Dvorkin, C. Heinrich, W. Hu, and V. Miranda, "Inflationary versus reionization features from *Planck* 2015 data," *Phys. Rev.* **D98** no. 4, (2018) 043518, arXiv:1803.01858 [astro-ph.CO].

[47] The Simons Observatory Collaboration, P. Ade, J. Aguirre, Z. Ahmed, S. Aiola, A. Ali, D. Alonso, M. A. Alvarez, K. Arnold, P. Ashton, and et al., "The Simons Observatory: Science goals and forecasts," *ArXiv e-prints* (Aug., 2018) , arXiv:1808.07445.

[48] J. R. Bond and G. Efstathiou, "Cosmic background radiation anisotropies in universes dominated by nonbaryonic dark matter," *Astrophys. J.* **285** (1984) L45–L48.

[49] H. Kodama and M. Sasaki, "Evolution of Isocurvature Perturbations. 1. Photon - Baryon Universe," *Int. J. Mod. Phys.* **A1** (1986) 265.

[50] H. Kodama and M. Sasaki, "Evolution of Isocurvature Perturbations. 2. Radiation Dust Universe," *Int. J. Mod. Phys.* **A2** (1987) 491.

[51] W. Hu and N. Sugiyama, "Toward understanding CMB anisotropies and their implications," *Phys. Rev.* **D51** (1995) 2599–2630, astro-ph/9411008.

[52] K. Moodley, M. Bucher, J. Dunkley, P. G. Ferreira, and C. Skordis, "Constraints on isocurvature models from the WMAP first-year data," *Phys. Rev.* **D70** (2004) 103520, arXiv:astro-ph/0407304 [astro-ph].

[53] R. Bean, J. Dunkley, and E. Pierpaoli, "Constraining Isocurvature Initial Conditions with WMAP 3-year data," *Phys. Rev.* **D74** (2006) 063503, astro-ph/0606685.

[54] K. Enqvist, H. Kurki-Suonio, and J. Valiviita, "Limits on isocurvature fluctuations from boomerang and MAXIMA," *Phys. Rev.* **D62** (2000) 103003, arXiv:astro-ph/0006429 [astro-ph].

[55] C. J. MacTavish *et al.*, "Cosmological parameters from the 2003 flight of BOOMERANG," *Astrophys. J.* **647** (2006) 799–812, arXiv:astro-ph/0507503 [astro-ph].

[56] **WMAP** Collaboration, J. Dunkley *et al.*, "Five-Year Wilkinson Microwave Anisotropy Probe (WMAP) Observations: Likelihoods and Parameters from the WMAP data," *Astrophys. J. Suppl.* **180** (2009) 306–329, arXiv:0803.0586 [astro-ph].

[57] **Planck** Collaboration, Planck Collaboration XXII, "Planck 2013 results. XXII. Constraints on inflation," *Astron. Astrophys.* **571** (2014) A22, arXiv:1303.5082 [astro-ph.CO].

[58] S. Mollerach, "Isocurvature Baryon Perturbations and Inflation," *Phys.Rev.* **D42** (1990) 313–325.

[59] V. F. Mukhanov, H. Feldman, and R. H. Brandenberger, "Theory of cosmological perturbations. Part 1. Classical perturbations. Part 2. Quantum theory of perturbations. Part 3. Extensions," *Phys.Rept.* **215** (1992) 203–333.

[60] T. Moroi and T. Takahashi, "Effects of cosmological moduli fields on cosmic microwave background," *Phys.Lett.* **B522** (2001) 215–221, hep-ph/0110096.

[61] D. H. Lyth and D. Wands, "Generating the curvature perturbation without an inflaton," *Phys. Lett.* **B524** (2002) 5–14, arXiv:hep-ph/0110002 [hep-ph].

[62] D. H. Lyth, C. Ungarelli, and D. Wands, "The Primordial density perturbation in the curvaton scenario," *Phys.Rev.* **D67** (2003) 023503, astro-ph/0208055.

[63] M. Postma, "The Curvaton scenario in supersymmetric theories," *Phys. Rev.* **D67** (2003) 063518, hep-ph/0212005.

[64] S. Kasuya, M. Kawasaki, and F. Takahashi, "MSSM curvaton in the gauge mediated SUSY breaking," *Phys. Lett.* **B578** (2004) 259–268, hep-ph/0305134.

[65] M. Ikegami and T. Moroi, "Curvaton scenario with Affleck-Dine baryogenesis," *Phys. Rev.* **D70** (2004) 083515, hep-ph/0404253.

[66] A. Mazumdar and A. Perez-Lorenzana, "Sneutrino condensate as a candidate for the hot big bang cosmology," *Phys. Rev.* **D70** (2004) 083526, hep-ph/0406154.

[67] R. Allahverdi, K. Enqvist, A. Jokinen, and A. Mazumdar, "Identifying the curvaton within MSSM," *JCAP* **0610** (2006) 007, hep-ph/0603255.

[68] E. Papantonopoulos and V. Zamarias, "Curvaton Dynamics in Brane-worlds," *JCAP* **0611** (2006) 005, gr-qc/0608026.

[69] A. Mazumdar and J. Rocher, "Particle physics models of inflation and curvaton scenarios," *Phys. Rept.* **497** (2011) 85–215, arXiv:1001.0993.

[70] A. Mazumdar and S. Nadathur, "The curvaton scenario in the MSSM and predictions for non-Gaussianity," *Phys. Rev. Lett.* **108** (2012) 111302, arXiv:1107.4078.

[71] C. Gordon and A. Lewis, "Observational constraints on the curvaton model of inflation," *Phys.Rev.* **D67** (2003) 123513, astro-ph/0212248.

[72] C. Gordon and K. A. Malik, "WMAP, neutrino degeneracy and non-Gaussianity constraints on isocurvature perturbations in the curvaton model of inflation," *Phys. Rev.* **D69** (2004) 063508, arXiv:astro-ph/0311102 [astro-ph].

[73] E. Di Valentino, M. Lattanzi, G. Mangano, A. Melchiorri, and P. Serpico, "Future constraints on neutrino isocurvature perturbations in the curvaton scenario," *Phys.Rev.* **D85** (2012) 043511, arXiv:1111.3810.

[74] T. L. Smith and D. Grin, "Probing A Panoply of Curvaton-Decay Scenarios Using CMB Data," arXiv:1511.07431 [astro-ph.CO].

[75] D. Grin, O. Doré, and M. Kamionkowski, "Do baryons trace dark matter in the early universe?," *Phys. Rev. Lett.* **107** (2011) 261301, arXiv:1107.1716 [astro-ph.CO].

[76] D. Grin, O. Doré, and M. Kamionkowski, "Compensated Isocurvature Perturbations and the Cosmic Microwave Background," *Phys. Rev.* **D84** (2011) 123003, arXiv:1107.5047 [astro-ph.CO].

[77] D. Grin, D. Hanson, G. P. Holder, O. Doré, and M. Kamionkowski, "Baryons do trace dark matter 380,000 years after the big bang: Search for compensated isocurvature perturbations with WMAP 9-year data," *Phys. Rev.* **D89** no. 2, (2014) 023006, arXiv:1306.4319 [astro-ph.CO].

[78] C. He, D. Grin, and W. Hu, "Compensated isocurvature perturbations in the curvaton model," *Phys. Rev.* **D92** no. 6, (2015) 063018, arXiv:1505.00639 [astro-ph.CO].

[79] T. L. Smith, J. B. Mu'ñoz, R. Smith, K. Yee, and D. Grin, "Baryons still trace dark matter: probing CMB lensing maps for hidden isocurvature," *Phys. Rev.* **D96** no. 8, (2017) 083508, arXiv:1704.03461 [astro-ph.CO].

[80] P. D. Meerburg *et al.*, "Primordial Non-Gaussianity," arXiv:1903.04409 [astro-ph.CO].

[81] L. Senatore, K. M. Smith, and M. Zaldarriaga, "Non-Gaussianities in Single Field Inflation and their Optimal Limits from the WMAP 5-year Data," *JCAP* **1001** (2010) 028, arXiv:0905.3746 [astro-ph.CO].

[82] C. Bennett, D. Larson, J. Weiland, N. Jarosik, G. Hinshaw, *et al.*, "Nine-Year Wilkinson Microwave Anisotropy Probe (WMAP) Observations: Final Maps and Results," arXiv:1212.5225 [astro-ph.CO].

[83] N. Arkani-Hamed and J. Maldacena, "Cosmological Collider Physics," arXiv:1503.08043 [hep-th].

[84] X. Chen, M. H. Namjoo, and Y. Wang, "Quantum Primordial Standard Clocks," *JCAP* **1602** no. 02, (2016) 013, arXiv:1509.03930 [astro-ph.CO].

[85] N. Arkani-Hamed, D. Baumann, H. Lee, and G. L. Pimentel, "The Cosmological Bootstrap: Inflationary Correlators from Symmetries and Singularities," arXiv:1811.00024 [hep-th].

[86] N. Barnaby and M. Peloso, "Large Nongaussianity in Axion Inflation," *Phys. Rev. Lett.* **106** (2011) 181301, arXiv:1011.1500 [hep-ph].

[87] N. Barnaby and S. Shandera, "Feeding your Inflaton: Non-Gaussian Signatures of Interaction Structure," *JCAP* **1201** (2012) 034, arXiv:1109.2985 [astro-ph.CO].

[88] N. Barnaby, J. Moxon, R. Namba, M. Peloso, G. Shiu, and P. Zhou, "Gravity waves and non-Gaussian features from particle production in a sector gravitationally coupled to the inflaton," *Phys. Rev.* **D86** (2012) 103508, arXiv:1206.6117 [astro-ph.CO].

[89] R. Namba, E. Dimastrogiovanni, and M. Peloso, "Gauge-flation confronted with Planck," *JCAP* **1311** (2013) 045, arXiv:1308.1366 [astro-ph.CO].

[90] E. Silverstein and D. Tong, "Scalar speed limits and cosmology: Acceleration from D-cceleration," *Phys. Rev.* **D70** (2004) 103505, arXiv:hep-th/0310221 [hep-th].

[91] N. Arkani-Hamed, P. Creminelli, S. Mukohyama, and M. Zaldarriaga, "Ghost inflation," *JCAP* **0404** (2004) 001, arXiv:hep-th/0312100 [hep-th].

[92] M. Alishahiha, E. Silverstein, and D. Tong, "DBI in the sky," *Phys. Rev.* **D70** (2004) 123505, arXiv:hep-th/0404084 [hep-th].

[93] X. Chen, M.-x. Huang, S. Kachru, and G. Shiu, "Observational signatures and non-Gaussianities of general single field inflation," *JCAP* **0701** (2007) 002, arXiv:hep-th/0605045 [hep-th].

[94] C. Cheung, P. Creminelli, A. L. Fitzpatrick, J. Kaplan, and L. Senatore, "The Effective Field Theory of Inflation," *JHEP* **03** (2008) 014, arXiv:0709.0293 [hep-th].

[95] X. Chen and Y. Wang, "Quasi-Single Field Inflation and Non-Gaussianities," *JCAP* **1004** (2010) 027, arXiv:0911.3380 [hep-th].

[96] A. J. Tolley and M. Wyman, "The Gelaton Scenario: Equilateral non-Gaussianity from multi-field dynamics," *Phys. Rev.* **D81** (2010) 043502, arXiv:0910.1853 [hep-th].

[97] S. Cremonini, Z. Lalak, and K. Turzynski, "Strongly Coupled Perturbations in Two-Field Inflationary Models," *JCAP* **1103** (2011) 016, arXiv:1010.3021 [hep-th].

[98] A. Achucarro, J.-O. Gong, S. Hardeman, G. A. Palma, and S. P. Patil, "Features of heavy physics in the CMB power spectrum," *JCAP* **1101** (2011) 030, arXiv:1010.3693 [hep-ph].

[99] D. Baumann and D. Green, "Signatures of Supersymmetry from the Early Universe," *Phys. Rev.* **D85** (2012) 103520, arXiv:1109.0292 [hep-th].

[100] P. Creminelli, "On non-Gaussianities in single-field inflation," *JCAP* **0310** (2003) 003, arXiv:astro-ph/0306122 [astro-ph].

[101] D. Baumann, D. Green, and R. A. Porto, "B-modes and the Nature of Inflation," *JCAP* **1501** no. 01, (2015) 016, arXiv:1407.2621 [hep-th].

[102] M. Alvarez *et al.*, "Testing Inflation with Large Scale Structure: Connecting Hopes with Reality," arXiv:1412.4671 [astro-ph.CO].

[103] D. Baumann, D. Green, H. Lee, and R. A. Porto, "Signs of Analyticity in Single-Field Inflation," *Phys. Rev.* **D93** no. 2, (2016) 023523, arXiv:1502.07304 [hep-th].

[104] D. Baumann and D. Green, "Equilateral Non-Gaussianity and New Physics on the Horizon," *JCAP* **1109** (2011) 014, arXiv:1102.5343 [hep-th].

[105] D. Green, M. Lewandowski, L. Senatore, E. Silverstein, and M. Zaldarriaga, "Anomalous Dimensions and Non-Gaussianity," *JHEP* **10** (2013) 171, arXiv:1301.2630 [hep-th].

[106] V. Assassi, D. Baumann, D. Green, and L. McAllister, "Planck-Suppressed Operators," *JCAP* **1401** (2014) 033, arXiv:1304.5226 [hep-th].

[107] P. Creminelli and M. Zaldarriaga, "Single-Field Consistency Relation for the 3-Point Function," *JCAP* **0410** (2004) 006, arXiv:astro-ph/0407059 [astro-ph].

[108] E. Nelson and S. Shandera, "Statistical Naturalness and non-Gaussianity in a Finite Universe," *Phys. Rev. Lett.* **110** no. 13, (2013) 131301, arXiv:1212.4550 [astro-ph.CO].

[109] M. LoVerde, E. Nelson, and S. Shandera, "Non-Gaussian Mode Coupling and the Statistical Cosmological Principle," *JCAP* **1306** (2013) 024, arXiv:1303.3549 [astro-ph.CO].

[110] S. Nurmi, C. T. Byrnes, and G. Tasinato, "A non-Gaussian landscape," *JCAP* **1306** (2013) 004, arXiv:1301.3128 [astro-ph.CO].

[111] B. Bonga, S. Brahma, A.-S. Deutsch, and S. Shandera, "Cosmic variance in inflation with two light scalars," *JCAP* **1605** no. 05, (2016) 018, arXiv:1512.05365 [astro-ph.CO].

[112] M. Zaldarriaga, "Non-Gaussianities in models with a varying inflaton decay rate," *Phys. Rev.* **D69** (2004) 043508, arXiv:astro-ph/0306006 [astro-ph].

[113] J.-L. Lehners and S. Renaux-Petel, "Multifield Cosmological Perturbations at Third Order and the Ekpyrotic Trispectrum," *Phys. Rev.* **D80** (2009) 063503, arXiv:0906.0530 [hep-th].

[114] J. C. Hill, "Foreground Biases on Primordial Non-Gaussianity Measurements from the CMB Temperature Bispectrum: Implications for Planck and Beyond," arXiv:1807.07324 [astro-ph.CO].

[115] D. Babich and M. Zaldarriaga, "Primordial bispectrum information from cmb polarization," *Phys. Rev. D* **70** (Oct, 2004) 083005, https://link.aps.org/doi/10.1103/PhysRevD.70.083005.

[116] E. Silverstein and A. Westphal, "Monodromy in the CMB: Gravity Waves and String Inflation," *Phys.Rev.* **D78** (2008) 106003, arXiv:0803.3085 [hep-th].

[117] L. McAllister, E. Silverstein, and A. Westphal, "Gravity Waves and Linear Inflation from Axion Monodromy," *Phys.Rev.* **D82** (2010) 046003, arXiv:0808.0706 [hep-th].

[118] R. Flauger, L. McAllister, E. Pajer, A. Westphal, and G. Xu, "Oscillations in the CMB from Axion Monodromy Inflation," *JCAP* **1006** (2010) 009, arXiv:0907.2916 [hep-th].

[119] S. R. Behbahani, A. Dymarsky, M. Mirbabayi, and L. Senatore, "(Small) Resonant non-Gaussianities: Signatures of a Discrete Shift Symmetry in the Effective Field Theory of Inflation," *JCAP* **1212** (2012) 036, arXiv:1111.3373 [hep-th].

[120] S. R. Behbahani and D. Green, "Collective Symmetry Breaking and Resonant Non-Gaussianity," *JCAP* **1211** (2012) 056, arXiv:1207.2779 [hep-th].

[121] E. Dimastrogiovanni, M. Fasiello, and M. Kamionkowski, "Imprints of Massive Primordial Fields on Large-Scale Structure," *JCAP* **1602** (2016) 017, arXiv:1504.05993 [astro-ph.CO].

[122] S. Endlich, A. Nicolis, and J. Wang, "Solid Inflation," *JCAP* **1310** (2013) 011, arXiv:1210.0569 [hep-th].

[123] A. Maleknejad and M. M. Sheikh-Jabbari, "Gauge-flation: Inflation From Non-Abelian Gauge Fields," *Phys. Lett.* **B723** (2013) 224–228, arXiv:1102.1513 [hep-ph].

[124] P. Adshead, D. Blas, C. P. Burgess, P. Hayman, and S. P. Patil, "Magnon Inflation: Slow Roll with Steep Potentials," arXiv:1604.06048 [hep-th].

[125] **Planck** Collaboration, Planck Collaboration VI, "Planck 2018 results. VI. Cosmological parameters," arXiv:1807.06209 [astro-ph.CO].

[126] A. Lewis, A. Challinor, and D. Hanson, "The shape of the CMB lensing bispectrum," *JCAP* **1103** (2011) 018, arXiv:1101.2234 [astro-ph.CO].

[127] LSST Science Collaboration, P. A. Abell, J. Allison, S. F. Anderson, J. R. Andrew, J. R. P. Angel, L. Armus, D. Arnett, S. J. Asztalos, T. S. Axelrod, S. Bailey, D. R. Ballantyne, J. R. Bankert, W. A. Barkhouse, J. D. Barr, L. F. Barrientos, A. J. Barth, J. G. Bartlett, A. C. Becker, J. Becla, T. C. Beers, J. P. Bernstein, R. Biswas, M. R. Blanton, J. S. Bloom, J. J. Bochanski, P. Boeshaar, K. D. Borne, M. Bradac, W. N. Brandt, C. R. Bridge, M. E. Brown, R. J. Brunner, J. S. Bullock, A. J. Burgasser, J. H. Burge, D. L. Burke, P. A. Cargile, S. Chandrasekharan, G. Chartas, S. R. Chesley, Y.-H. Chu, D. Cinabro, M. W. Claire, C. F. Claver, D. Clowe, A. J. Connolly, K. H. Cook, J. Cooke, A. Cooray, K. R. Covey, C. S. Culliton, R. de Jong, W. H. de Vries, V. P. Debattista, F. Delgado, I. P. Dell'Antonio, S. Dhital, R. Di Stefano, M. Dickinson, B. Dilday, S. G. Djorgovski, G. Dobler, C. Donalek, G. Dubois-Felsmann, J. Durech, A. Eliasdottir, M. Eracleous, L. Eyer, E. E. Falco, X. Fan, C. D. Fassnacht, H. C. Ferguson, Y. R. Fernandez, B. D. Fields, D. Finkbeiner, E. E. Figueroa, D. B. Fox, H. Francke, J. S. Frank, J. Frieman, S. Fromenteau, M. Furqan, G. Galaz, A. Gal-Yam, P. Garnavich, E. Gawiser, J. Geary, P. Gee, R. R. Gibson, K. Gilmore, E. A. Grace, R. F. Green, W. J. Gressler, C. J. Grillmair, S. Habib, J. S. Haggerty, M. Hamuy, A. W. Harris, S. L. Hawley, A. F. Heavens, L. Hebb, T. J. Henry, E. Hileman, E. J. Hilton, K. Hoadley, J. B. Holberg, M. J. Holman, S. B. Howell, L. Infante, Z. Ivezic, S. H. Jacoby, B. Jain, R, Jedicke, M. J. Jee, J. G. Jernigan, S. W. Jha, K. V. Johnston, R. L. Jones, M. Juric, M. Kaasalainen, Styliani, Kafka, S. M. Kahn, N. A. Kaib, J. Kalirai, J. Kantor, M. M. Kasliwal, C. R. Keeton, R. Kessler, Z. Knezevic, A. Kowalski, V. L. Krabbendam, K. S. Krughoff, S. Kulkarni, S. Kuhlman, M. Lacy,

S. Lepine, M. Liang, A. Lien, P. Lira, K. S. Long, S. Lorenz, J. M. Lotz, R. H. Lupton, J. Lutz, L. M. Macri, A. A. Mahabal, R. Mandelbaum, P. Marshall, M. May, P. M. McGehee, B. T. Meadows, A. Meert, A. Milani, C. J. Miller, M. Miller, D. Mills, D. Minniti, D. Monet, A. S. Mukadam, E. Nakar, D. R. Neill, J. A. Newman, S. Nikolaev, M. Nordby, P. O'Connor, M. Oguri, J. Oliver, S. S. Olivier, J. K. Olsen, K. Olsen, E. W. Olszewski, H. Oluseyi, N. D. Padilla, A. Parker, J. Pepper, J. R. Peterson, C. Petry, P. A. Pinto, J. L. Pizagno, B. Popescu, A. Prsa, V. Radcka, M. J. Raddick, A. Rasmussen, A. Rau, J. Rho, J. E. Rhoads, G. T. Richards, S. T. Ridgway, B. E. Robertson, R. Roskar, A. Saha, A. Sarajedini, E. Scannapieco, T. Schalk, R. Schindler, S. Schmidt, S. Schmidt, D. P. Schneider, G. Schumacher, R. Scranton, J. Sebag, L. G. Seppala, O. Shemmer, J. D. Simon, M. Sivertz, H. A. Smith, J. A. Smith, N. Smith, A. H. Spitz, A. Stanford, K. G. Stassun, J. Strader, M. A. Strauss, C. W. Stubbs, D. W. Sweeney, A. Szalay, P. Szkody, M. Takada, P. Thorman, D. E. Trilling, V. Trimble, A. Tyson, R. Van Berg, D. V. Berk, J. VanderPlas, L. Verde, B. Vrsnak, L. M. Walkowicz, B. D. Wandelt, S. Wang, Y. Wang, M. Warner, R. H. Wechsler, A. A. West, O. Wiecha, B. F. Williams, B. Willman, D. Wittman, S. C. Wolff, W. M. Wood-Vasey, P. Wozniak, P. Young, A. Zentner, and H. Zhan, "LSST Science Book, Version 2.0," *Science* no. November, (Dec, 2009) 596, arXiv:0912.0201.

[128] N. Dalal, O. Dore, D. Huterer, and A. Shirokov, "The imprints of primordial non-gaussianities on large-scale structure: scale dependent bias and abundance of virialized objects," *Phys.Rev.* **D77** (2008) 123514, arXiv:0710.4560 [astro-ph].

[129] U. Seljak, "Extracting primordial non-gaussianity without cosmic variance," *Phys.Rev.Lett.* **102** (2009) 021302, arXiv:0807.1770 [astro-ph].

[130] M. Schmittfull and U. Seljak, "Parameter constraints from cross-correlation of CMB lensing with galaxy clustering," *Phys. Rev.* **D 97** no. 12, (June, 2018) 123540, arXiv:1710.09465.

[131] M. Münchmeyer, M. S. Madhavacheril, S. Ferraro, M. C. Johnson, and K. M. Smith, "Constraining local non-Gaussianities with kSZ tomography," arXiv:1810.13424 [astro-ph.CO].

[132] A.-S. Deutsch, E. Dimastrogiovanni, M. C. Johnson, M. Munchmeyer, and A. Terrana, "Reconstruction of the remote dipole and quadrupole fields from the kinetic Sunyaev Zel'dovich and polarized Sunyaev Zel'dovich effects," arXiv:1707.08129 [astro-ph.CO].

[133] K. M. Smith, M. S. Madhavacheril, M. Münchmeyer, S. Ferraro, U. Giri, and M. C. Johnson, "KSZ tomography and the bispectrum," arXiv:1810.13423 [astro-ph.CO].

[134] J. Aguirre *et al.* (Simons Observatory Collaboration), "The Simons Observatory: Science Goals and Forecasts," *JCAP* **02** (2019) 056, arXiv:1808.07445 [astro-ph.CO].

[135] D. Jeong, E. Komatsu, and B. Jain, "Galaxy-CMB and galaxy-galaxy lensing on large scales: Sensitivity to primordial non-Gaussianity," *Phys. Rev.* **D 80** no. 12, (Dec., 2009) 123527, arXiv:0910.1361.

[136] Y. Ono, M. Ouchi, Y. Harikane, J. Toshikawa, M. Rauch, S. Yuma, M. Sawicki, T. Shibuya, K. Shimasaku, M. Oguri, C. Willott, M. Akhlaghi, M. Akiyama, J. Coupon, N. Kashikawa, Y. Komiyama, A. Konno, L. Lin, Y. Matsuoka, S. Miyazaki, T. Nagao, K. Nakajima, J. Silverman, M. Tanaka, Y. Taniguchi, and S.-Y. Wang, "Great Optically Luminous Dropout Research Using Subaru HSC (GOLDRUSH). I. UV luminosity functions at z $\sim$ 4-7 derived with the half-million dropouts on the 100 deg^2 sky," *PASJ* **70** (Jan., 2018) S10, arXiv:1704.06004.

[137] Y. Harikane, M. Ouchi, Y. Ono, S. Saito, P. Behroozi, S. More, K. Shimasaku, J. Toshikawa, Y.-T. Lin, M. Akiyama, J. Coupon, Y. Komiyama, A. Konno, S.-C. Lin, S. Miyazaki, A. J. Nishizawa,

T. Shibuya, and J. Silverman, "GOLDRUSH. II. Clustering of galaxies at z $\sim$ 4-6 revealed with the half-million dropouts over the 100 deg^2 area corresponding to 1 Gpc^3," *PASJ* **70** (Jan., 2018) S11, arXiv:1704.06535.

[138] J. S. Dunlop, "Observing the First Galaxies," *ArXiv e-prints* **396** (2013) 223, arXiv:1205.1543.

[139] D. J. E. Marsh, "Axion Cosmology," *Phys. Rept.* **643** (2016) 1–79, arXiv:1510.07633 [astro-ph.CO].

[140] K. Abazajian, G. M. Fuller, and M. Patel, "Sterile neutrino hot, warm, and cold dark matter," *Phys. Rev.* **D64** (2001) 023501, arXiv:astro-ph/0101524 [astro-ph].

[141] A. Strumia and F. Vissani, "Neutrino masses and mixings and...," arXiv:hep-ph/0606054 [hep-ph].

[142] L. Ackerman, M. R. Buckley, S. M. Carroll, and M. Kamionkowski, "Dark Matter and Dark Radiation," *Phys. Rev. D* **79** (2009) 023519, arXiv:0810.5126 [hep-ph].

[143] A. Boyarsky, O. Ruchayskiy, and M. Shaposhnikov, "The Role of sterile neutrinos in cosmology and astrophysics," *Ann. Rev. Nucl. Part. Sci.* **59** (2009) 191–214, arXiv:0901.0011 [hep-ph].

[144] A. Arvanitaki, S. Dimopoulos, S. Dubovsky, N. Kaloper, and J. March-Russell, "String Axiverse," *Phys. Rev.* **D81** (2010) 123530, arXiv:0905.4720 [hep-th].

[145] D. Cadamuro, S. Hannestad, G. Raffelt, and J. Redondo, "Cosmological bounds on sub-MeV mass axions," *JCAP* **1102** (2011) 003, arXiv:1011.3694 [hep-ph].

[146] D. E. Kaplan, G. Z. Krnjaic, K. R. Rehermann, and C. M. Wells, "Dark Atoms: Asymmetry and Direct Detection," *JCAP* **1110** (2011) 011, arXiv:1105.2073 [hep-ph].

[147] F.-Y. Cyr-Racine and K. Sigurdson, "Cosmology of atomic dark matter," *Phys. Rev.* **D87** no. 10, (2013) 103515, arXiv:1209.5752 [astro-ph.CO].

[148] C. Brust, D. E. Kaplan, and M. T. Walters, "New Light Species and the CMB," *JHEP* **12** (2013) 058, arXiv:1303.5379 [hep-ph].

[149] S. Weinberg, "Goldstone Bosons as Fractional Cosmic Neutrinos," *Phys.Rev.Lett.* **110** (2013) 241301, arXiv:1305.1971 [astro-ph.CO].

[150] A. Salvio, A. Strumia, and W. Xue, "Thermal axion production," *JCAP* **1401** (2014) 011, arXiv:1310.6982 [hep-ph].

[151] M. Kawasaki, M. Yamada, and T. T. Yanagida, "Observable dark radiation from a cosmologically safe QCD axion," *Phys. Rev.* **D91** no. 12, (2015) 125018, arXiv:1504.04126 [hep-ph].

[152] P. W. Graham, D. E. Kaplan, and S. Rajendran, "Cosmological Relaxation of the Electroweak Scale," *Phys. Rev. Lett.* **115** no. 22, (2015) 221801, arXiv:1504.07551 [hep-ph].

[153] D. Baumann, D. Green, and B. Wallisch, "A New Target for Cosmic Axion Searches," arXiv:1604.08614 [astro-ph.CO].

[154] N. Arkani-Hamed, T. Cohen, R. T. D'Agnolo, A. Hook, H. D. Kim, and D. Pinner, "Nnaturalness," arXiv:1607.06821 [hep-ph].

[155] Z. Chacko, N. Craig, P. Fox, and R. Harnik, "Cosmology in Mirror Twin Higgs and Neutrino Masses," *JHEP* **07** (2017) 023, arXiv:1611.07975 [hep-ph].

[156] N. Craig, S. Koren, and T. Trott, "Cosmological Signals of a Mirror Twin Higgs," *JHEP* **05** (2017) 038, arXiv:1611.07977 [hep-ph].

[157] Z. Chacko, D. Curtin, M. Geller, and Y. Tsai, "Cosmological Signatures of a Mirror Twin Higgs," *JHEP* **09** (2018) 163, arXiv:1803.03263 [hep-ph].

[158] M. Archidiacono, E. Giusarma, S. Hannestad, and O. Mena, "Cosmic Dark Radiation and Neutrinos," *Adv. High Energy Phys.* **2013** (2013) 191047, arXiv:1307.0637 [astro-ph.CO].

[159] J. Bernal, L. Verde, and A. Riess, "The Trouble with H_0," *JCAP* **10** (2016) 019, arXiv:1607.05617 [astro-ph.CO].

[160] B. Zhang, M. Childress, T. Davis, N. Karpenka, C. Lidman, B. Schmidt, and M. Smith, "A Blinded Determination of H_0 from Low-Redshift Type Ia Supernovae, Calibrated by Cepheid Variables," *Mon. Not. Roy. Astron. Soc.* **471** (2017) 2254, arXiv:1706.07573 [astro-ph.CO].

[161] G. Addison, D. Watts, C. Bennett, M. Halpern, G. Hinshaw, and J. Weiland, "Elucidating ΛCDM: Impact of Baryon Acoustic Oscillation Measurements on the Hubble Constant Discrepancy," *Astrophys. J.* **853** (2018) 119, arXiv:1707.06547 [astro-ph.CO].

[162] K. Aylor, M. Joy, L. Knox, M. Millea, S. Raghunathan, and K. Wu, "Sounds Discordant: Classical Distance Ladder & ΛCDM-Based Determinations of the Cosmological Sound Horizon," arXiv:1811.00537 [astro-ph.CO].

[163] N. MacCrann, J. Zuntz, S. Bridle, B. Jain, and M. Becker, "Cosmic Discordance: Are Planck CMB and CFHTLenS Weak Lensing Measurements Out of Tune?," *Mon. Not. Roy. Astron. Soc.* **451** (2015) 2877, arXiv:1408.4742 [astro-ph.CO].

[164] J. Lesgourgues, G. Marques-Tavares, and M. Schmaltz, "Evidence for dark matter interactions in cosmological precision data?," *JCAP* **1602** no. 02, (2016) 037, arXiv:1507.04351 [astro-ph.CO].

[165] F. Köhlinger *et al.*, "KiDS-450: The Tomographic Weak Lensing Power Spectrum and Constraints on Cosmological Parameters," *Mon. Not. Roy. Astron. Soc.* **471** (2017) 4412, arXiv:1706.02892 [astro-ph.CO].

[166] S. Joudaki *et al.*, "KiDS-450 + 2dFLenS: Cosmological Parameter Constraints from Weak Gravitational Lensing Tomography and Overlapping Redshift-Space Galaxy Clustering," *Mon. Not. Roy. Astron. Soc.* **474** (2018) 4894, arXiv:1707.06627 [astro-ph.CO].

[167] D. Weinberg, J. Bullock, F. Governato, R. Kuzio de Naray, and A. Peter, "Cold Dark Matter: Controversies on Small Scales," *Proc. Nat. Acad. Sci.* **112** (2015) 12249, arXiv:1306.0913 [astro-ph.CO].

[168] G. Mangano, G. Miele, S. Pastor, T. Pinto, O. Pisanti, *et al.*, "Relic neutrino decoupling including flavor oscillations," *Nucl.Phys.* **B729** (2005) 221–234, arXiv:hep-ph/0506164 [hep-ph].

[169] E. Grohs, G. M. Fuller, C. T. Kishimoto, M. W. Paris, and A. Vlasenko, "Neutrino energy transport in weak decoupling and big bang nucleosynthesis," *Phys. Rev.* **D93** no. 8, (2016) 083522, arXiv:1512.02205 [astro-ph.CO].

[170] P. F. de Salas and S. Pastor, "Relic neutrino decoupling with flavour oscillations revisited," *JCAP* **1607** no. 07, (2016) 051, arXiv:1606.06986 [hep-ph].

[171] P. J. E. Peebles, "Primordial Helium Abundance and the Primordial Fireball. II," *Astrophys. J.* **146** (1966) 542.

[172] D. Dicus, E. Kolb, Gleeson, Sudarshan, V. Teplitz, and M. Turner, "Primordial Nucleosynthesis Including Radiative, Coulomb, and Finite-Temperature Corrections to Weak Rates," *Phys. Rev. D* **26** (1982) 2694.

[173] Z. Hou, R. Keisler, L. Knox, M. Millea, and C. Reichardt, "How Massless Neutrinos Affect the Cosmic Microwave Background Damping Tail," *Phys. Rev.* **D87** (2013) 083008, arXiv:1104.2333 [astro-ph.CO].

[174] S. Bashinsky and U. Seljak, "Neutrino perturbations in CMB anisotropy and matter clustering," *Phys. Rev.* **D69** (2004) 083002, arXiv:astro-ph/0310198 [astro-ph].

[175] D. Baumann, D. Green, J. Meyers, and B. Wallisch, "Phases of New Physics in the CMB," *JCAP* **1601** (2016) 007, arXiv:1508.06342 [astro-ph.CO].

[176] D. Baumann, D. Green, and M. Zaldarriaga, "Phases of New Physics in the BAO Spectrum," *JCAP* **11** (2017) 007, arXiv:1703.00894 [astro-ph.CO].

[177] N. Bell, E. Pierpaoli, and K. Sigurdson, "Cosmological Signatures of Interacting Neutrinos," *Phys. Rev. D* **73** (2006) 063523, arXiv:astro-ph/0511410 [astro-ph].

[178] A. Friedland, K. Zurek, and S. Bashinsky, "Constraining Models of Neutrino Mass and Neutrino Interactions with the Planck Satellite," arXiv:0704.3271 [astro-ph].

[179] F.-Y. Cyr-Racine and K. Sigurdson, "Limits on Neutrino-Neutrino Scattering in the Early Universe," *Phys. Rev.* **D90** no. 12, (2014) 123533, arXiv:1306.1536 [astro-ph.CO].

[180] I. M. Oldengott, C. Rampf, and Y. Y. Y. Wong, "Boltzmann hierarchy for interacting neutrinos I: formalism," *JCAP* **1504** no. 04, (2015) 016, arXiv:1409.1577 [astro-ph.CO].

[181] L. Lancaster, F.-Y. Cyr-Racine, L. Knox, and Z. Pan, "A Tale of Two Modes: Neutrino Free-Streaming in the Early Universe," *JCAP* **07** (2017) 033, arXiv:1704.06657 [astro-ph.CO].

[182] I. M. Oldengott, T. Tram, C. Rampf, and Y. Y. Y. Wong, "Interacting neutrinos in cosmology: exact description and constraints," *JCAP* **11** (Nov., 2017) 027, arXiv:1706.02123.

[183] C. D. Kreisch, F.-Y. Cyr-Racine, and O. Doré, "The Neutrino Puzzle: Anomalies, Interactions, and Cosmological Tensions," arXiv:1902.00534 [astro-ph.CO].

[184] R. J. Wilkinson, C. Boehm, and J. Lesgourgues, "Constraining Dark Matter-Neutrino Interactions using the CMB and Large-Scale Structure," *JCAP* **1405** (2014) 011, arXiv:1401.7597 [astro-ph.CO].

[185] M. Escudero, O. Mena, A. C. Vincent, R. J. Wilkinson, and C. Boehm, "Exploring dark matter microphysics with galaxy surveys," *jcap* **1509** no. 09, (2015) 034, arXiv:1505.06735 [astro-ph.CO].

[186] M. A. Buen-Abad, G. Marques-Tavares, and M. Schmaltz, "Non-Abelian dark matter and dark radiation," *Phys. Rev.* **D92** no. 2, (2015) 023531, arXiv:1505.03542 [hep-ph].

[187] Z. Chacko, Y. Cui, S. Hong, T. Okui, and Y. Tsai, "Partially Acoustic Dark Matter, Interacting Dark Radiation, and Large Scale Structure," *JHEP* **12** (2016) 108, arXiv:1609.03569 [astro-ph.CO].

[188] M. A. Buen-Abad, M. Schmaltz, J. Lesgourgues, and T. Brinckmann, "Interacting Dark Sector and Precision Cosmology," *JCAP* **1801** no. 01, (2018) 008, arXiv:1708.09406 [astro-ph.CO].

[189] C. Brust, Y. Cui, and K. Sigurdson, "Cosmological Constraints on Interacting Light Particles," *JCAP* **08** (2017) 020, arXiv:1703.10732 [astro-ph.CO].

[190] G. Choi, C.-T. Chiang, and M. LoVerde, "Probing Decoupling in Dark Sectors with the Cosmic Microwave Background," *JCAP* **1806** no. 06, (2018) 044, arXiv:1804.10180 [astro-ph.CO].

[191] S. Dodelson, K. Heitmann, C. Hirata, K. Honscheid, A. Roodman, U. Seljak, A. Slosar, and M. Trodden, "Cosmic Visions Dark Energy: Science," arXiv:1604.07626 [astro-ph.CO].

[192] K. N. Abazajian *et al.*, "Neutrino Physics from the Cosmic Microwave Background and Large Scale Structure," *Astropart. Phys.* **63** (2015) 66–80, arXiv:1309.5383 [astro-ph.CO].

[193] Z. Chacko, Y. Cui, S. Hong, and T. Okui, "Hidden dark matter sector, dark radiation, and the CMB," *Phys. Rev.* **D92** (2015) 055033, arXiv:1505.04192 [hep-ph].

[194] M. Battaglieri *et al.*, "US Cosmic Visions: New Ideas in Dark Matter 2017: Community Report," in *U.S. Cosmic Visions: New Ideas in Dark Matter College Park, MD, USA, March 23-25, 2017*. 2017. arXiv:1707.04591 [hep-ph]. http://lss.fnal.gov/archive/2017/conf/fermilab-conf-17-282-ae-ppd-t.pdf.

[195] D. Green and S. Rajendran, "The Cosmology of Sub-MeV Dark Matter," *JHEP* **10** (2017) 013, arXiv:1701.08750 [hep-ph].

[196] S. Knapen, T. Lin, and K. Zurek, "Light Dark Matter: Models and Constraints," *Phys. Rev. D* **96** (2017) 115021, arXiv:1709.07882 [hep-ph].

[197] V. Gluscevic and K. Boddy, "Constraints on Scattering of keV–TeV Dark Matter with Protons in the Early Universe," *Phys. Rev. Lett.* **121** (2018) 081301, arXiv:1712.07133 [astro-ph.CO].

[198] M. Markevitch, A. H. Gonzalez, D. Clowe, A. Vikhlinin, L. David, W. Forman, C. Jones, S. Murray, and W. Tucker, "Direct constraints on the dark matter self-interaction cross-section from the merging galaxy cluster 1E0657-56," *Astrophys. J.* **606** (2004) 819–824, arXiv:astro-ph/0309303 [astro-ph].

[199] R. Essig, R. Harnik, J. Kaplan, and N. Toro, "Discovering New Light States at Neutrino Experiments," *Phys. Rev. D* **82** (2010) 113008, arXiv:1008.0636 [hep-ph].

[200] B. Wallisch, "Cosmological Probes of Light Relics," arXiv:1810.02800 [astro-ph.CO].

[201] P. Adshead, Y. Cui, and J. Shelton, "Chilly Dark Sectors and Asymmetric Reheating," *JHEP* **06** (2016) 016, arXiv:1604.02458 [hep-ph].

[202] L. A. Boyle and A. Buonanno, "Relating gravitational wave constraints from primordial nucleosynthesis, pulsar timing, laser interferometers, and the CMB: Implications for the early Universe," *Phys. Rev.* **D78** (2008) 043531, arXiv:0708.2279 [astro-ph].

[203] A. Stewart and R. Brandenberger, "Observational Constraints on Theories with a Blue Spectrum of Tensor Modes," *JCAP* **0808** (2008) 012, arXiv:0711.4602 [astro-ph].

[204] P. D. Meerburg, R. Hložek, B. Hadzhiyska, and J. Meyers, "Multiwavelength constraints on the inflationary consistency relation," *Phys. Rev.* **D91** no. 10, (2015) 103505, arXiv:1502.00302 [astro-ph.CO].

[205] M. Maggiore, "Gravitational Wave Experiments and Early Universe Cosmology," *Phys. Rept.* **331** (2000) 283, arXiv:gr-qc/9909001 [gr-qc].

[206] R. Easther and E. Lim, "Stochastic Gravitational Wave Production After Inflation," *JCAP* **04** (2006) 010, arXiv:astro-ph/0601617 [astro-ph].

[207] J. Dufaux, A. Bergman, G. Felder, L. Kofman, and J.-P. Uzan, "Theory and Numerics of Gravitational Waves from Preheating after Inflation," *Phys. Rev. D* **76** (2007) 123517, arXiv:0707.0875 [astro-ph].

[208] M. Amin, M. Hertzberg, D. Kaiser, and J. Karouby, "Nonperturbative Dynamics of Reheating After Inflation: A Review," *Int. J. Mod. Phys. D* **24** (2014) 1530003, arXiv:1410.3808 [hep-ph].

[209] C. Caprini and D. Figueroa, "Cosmological Backgrounds of Gravitational Waves," *Class. Quant. Grav.* **35** (2018) 163001, arXiv:1801.04268 [astro-ph.CO].

[210] P. Adshead, J. Giblin, and Z. Weiner, "Gravitational Waves from Gauge Preheating," *Phys. Rev. D* **98** (2018) 043525, arXiv:1805.04550 [astro-ph.CO].

[211] M. Amin, J. Fan, K. Lozanov, and M. Reece, "Cosmological Dynamics of Higgs Potential Fine Tuning," *Phys. Rev. D* **99** (2019) 035008, arXiv:1802.00444 [hep-ph].

[212] W. Fischler and J. Meyers, "Dark Radiation Emerging After Big Bang Nucleosynthesis?," *Phys. Rev.* **D83** (2011) 063520, arXiv:1011.3501 [astro-ph.CO].

[213] J. Hasenkamp, "Dark Radiation from the Axino Solution of the Gravitino Problem," *Phys. Lett. B* **707** (2012) 121, arXiv:1107.4319 [hep-ph].

[214] D. Hooper, F. S. Queiroz, and N. Y. Gnedin, "Non-Thermal Dark Matter Mimicking An Additional Neutrino Species In The Early Universe," *Phys. Rev.* **D85** (2012) 063513, arXiv:1111.6599 [astro-ph.CO].

[215] J. Hasenkamp and J. Kersten, "Dark Radiation from Particle Decay: Cosmological Constraints and Opportunities," *JCAP* **08** (2013) 024, arXiv:1212.4160 [hep-ph].

[216] M. Zaldarriaga and D. D. Harari, "Analytic approach to the polarization of the cosmic microwave background in flat and open universes," *Phys. Rev.* **D52** (1995) 3276–3287, arXiv:astro-ph/9504085 [astro-ph].

[217] B. Follin, L. Knox, M. Millea, and Z. Pan, "First Detection of the Acoustic Oscillation Phase Shift Expected from the Cosmic Neutrino Background," *Phys. Rev. Lett.* **115** no. 9, (2015) 091301, arXiv:1503.07863 [astro-ph.CO].

[218] E. Aver, K. A. Olive, and E. D. Skillman, "The effects of He I λ10830 on helium abundance determinations," *JCAP* **1507** no. 07, (2015) 011, arXiv:1503.08146 [astro-ph.CO].

[219] K. Saikawa and S. Shirai, "Primordial gravitational waves, precisely: The role of thermodynamics in the Standard Model," *JCAP* **1805** no. 05, (2018) 035, arXiv:1803.01038 [hep-ph].

[220] **Particle Data Group** Collaboration, K. A. Olive *et al.*, "Review of Particle Physics," *Chin. Phys.* **C38** (2014) 090001.

[221] J. R. Bond and A. S. Szalay, "The Collisionless Damping of Density Fluctuations in an Expanding Universe," *Astrophys. J.* **274** (1983) 443–468.

[222] J. Lesgourgues and S. Pastor, "Massive neutrinos and cosmology," *Phys.Rept.* **429** (2006) 307–379, arXiv:astro-ph/0603494 [astro-ph].

[223] C.-P. Ma, "Linear power spectra in cold + hot dark matter models: Analytical approximations and applications," *Astrophys. J.* **471** (1996) 13–23, arXiv:astro-ph/9605198 [astro-ph].

[224] W. Hu and D. J. Eisenstein, "Small scale perturbations in a general MDM cosmology," *Astrophys.J.* **498** (1998) 497, arXiv:astro-ph/9710216 [astro-ph].

[225] W. Hu, D. J. Eisenstein, and M. Tegmark, "Weighing neutrinos with galaxy surveys," *Phys.Rev.Lett.* **80** (1998) 5255–5258, arXiv:astro-ph/9712057 [astro-ph].

[226] **BOSS** Collaboration, S. Alam *et al.*, "The clustering of galaxies in the completed SDSS-III Baryon Oscillation Spectroscopic Survey: cosmological analysis of the DR12 galaxy sample," *Mon. Not. Roy. Astron. Soc.* **470** no. 3, (2017) 2617–2652, arXiv:1607.03155 [astro-ph.CO].

[227] **DES** Collaboration, T. M. C. Abbott *et al.*, "Dark Energy Survey year 1 results: Cosmological constraints from galaxy clustering and weak lensing," *Phys. Rev.* **D98** no. 4, (2018) 043526, arXiv:1708.01530 [astro-ph.CO].

[228] **DESI** Collaboration, A. Aghamousa *et al.*, "The DESI Experiment Part I: Science,Targeting, and Survey Design," arXiv:1611.00036 [astro-ph.IM].

[229] L. Amendola *et al.*, "Cosmology and fundamental physics with the Euclid satellite," *Living Rev. Rel.* **21** no. 1, (2018) 2, arXiv:1606.00180 [astro-ph.CO].

[230] T. Brinckmann, D. C. Hooper, M. Archidiacono, J. Lesgourgues, and T. Sprenger, "The promising future of a robust cosmological neutrino mass measurement," *JCAP* **1901** (2019) 059, arXiv:1808.05955 [astro-ph.CO].

[231] C. Kraus *et al.*, "Final results from phase II of the Mainz neutrino mass search in tritium beta decay," *Eur. Phys. J.* **C40** (2005) 447–468, arXiv:hep-ex/0412056 [hep-ex].

[232] **Troitsk** Collaboration, V. N. Aseev *et al.*, "An upper limit on electron antineutrino mass from Troitsk experiment," *Phys. Rev.* **D84** (2011) 112003, arXiv:1108.5034 [hep-ex].

[233] **KATRIN** Collaboration, J. Angrik *et al.*, "KATRIN design report 2004,".

[234] **Project 8** Collaboration, A. Ashtari Esfahani *et al.*, "Determining the neutrino mass with cyclotron radiation emission spectroscopy?Project 8," *J. Phys.* **G44** no. 5, (2017) 054004, arXiv:1703.02037 [physics.ins-det].

[235] "http://www.nu-fit.org/.".

[236] R. B. Patterson, "Prospects for Measurement of the Neutrino Mass Hierarchy," *Ann. Rev. Nucl. Part. Sci.* **65** (2015) 177–192, arXiv:1506.07917 [hep-ex].

[237] P. Langacker, "Neutrino Masses from the Top Down," *Ann. Rev. Nucl. Part. Sci.* **62** (2012) 215–235, arXiv:1112.5992 [hep-ph].

[238] K. N. Abazajian, "Telling three from four neutrinos with cosmology," *Astropart. Phys.* **19** (2003) 303–312, arXiv:astro-ph/0205238 [astro-ph].

[239] A. Slosar, T. Davis, D. Eisenstein, R. Hložek, M. Ishak-Boushaki, R. Mand elbaum, P. Marshall, J. Sakstein, and M. White, "Dark Energy and Modified Gravity," *arXiv e-prints* (Mar, 2019) arXiv:1903.12016, arXiv:1903.12016 [astro-ph.CO].

[240] S. Mishra-Sharma, D. Alonso, and J. Dunkley, "Neutrino masses and beyond-Λ CDM cosmology with LSST and future CMB experiments," *Phys. Rev.* **D 97** no. 12, (Jun, 2018) 123544, arXiv:1803.07561 [astro-ph.CO].

[241] DESI Collaboration, A. Aghamousa, J. Aguilar, S. Ahlen, S. Alam, L. E. Allen, C. Allende Prieto, J. Annis, S. Bailey, C. Balland, O. Ballester, C. Baltay, L. Beaufore, C. Bebek, T. C. Beers, E. F. Bell, J. L. Bernal, R. Besuner, F. Beutler, C. Blake, H. Bleuler, M. Blomqvist, R. Blum, A. S. Bolton, C. Briceno, D. Brooks, J. R. Brownstein, E. Buckley-Geer, A. Burden, E. Burtin, N. G. Busca, R. N. Cahn, Y.-C. Cai, L. Cardiel-Sas, R. G. Carlberg, P.-H. Carton, R. Casas, F. J. Castand er, J. L. Cervantes-Cota, T. M. Claybaugh, M. Close, C. T. Coker, S. Cole, J. Comparat, A. P. Cooper, M. C. Cousinou, M. Crocce, J.-G. Cuby, D. P. Cunningham, T. M. Davis, K. S. Dawson, A. de la Macorra, J. De Vicente, T. Delubac, M. Derwent, A. Dey, G. Dhungana, Z. Ding, P. Doel, Y. T. Duan, A. Ealet, J. Edelstein, S. Eftekharzadeh, D. J. Eisenstein, A. Elliott, S. Escoffier, M. Evatt, P. Fagrelius, X. Fan, K. Fanning, A. Farahi, J. Farihi, G. Favole, Y. Feng, E. Fernandez, J. R. Findlay, D. P. Finkbeiner, M. J. Fitzpatrick, B. Flaugher, S. Flender, A. Font-Ribera, J. E. Forero-Romero, P. Fosalba, C. S. Frenk, M. Fumagalli, B. T. Gaensicke, G. Gallo, J. Garcia-Bellido, E. Gaztanaga, N. Pietro Gentile Fusillo, T. Gerard, I. Gershkovich, T. Giannantonio, D. Gillet, G. Gonzalez-de-Rivera, V. Gonzalez-Perez, S. Gott, O. Graur, G. Gutierrez, J. Guy, S. Habib, H. Heetderks, I. Heetderks, K. Heitmann, W. A. Hellwing, D. A. Herrera, S. Ho, S. Holland, K. Honscheid, E. Huff, T. A. Hutchinson, D. Huterer, H. S. Hwang, J. M. Illa Laguna, Y. Ishikawa, D. Jacobs, N. Jeffrey, P. Jelinsky, E. Jennings, L. Jiang, J. Jimenez, J. Johnson, R. Joyce, E. Jullo, S. Juneau, S. Kama, A. Karcher, S. Karkar, R. Kehoe, N. Kennamer, S. Kent, M. Kilbinger, A. G. Kim, D. Kirkby, T. Kisner, E. Kitanidis, J.-P. Kneib, S. Koposov, E. Kovacs, K. Koyama, A. Kremin, R. Kron, L. Kronig, A. Kueter-Young, C. G. Lacey, R. Lafever, O. Lahav, A. Lambert, M. Lampton, M. Land riau, D. Lang, T. R. Lauer, J.-M. Le Goff, L. Le Guillou, A. Le Van Suu, J. H. Lee, S.-J. Lee, D. Leitner, M. Lesser, M. E. Levi, B. L'Huillier, B. Li, M. Liang, H. Lin, E. Linder, S. R. Loebman, Z. Lukić, J. Ma, N. MacCrann, C. Magneville, L. Makarem, M. Manera, C. J. Manser, R. Marshall, P. Martini, R. Massey, T. Matheson, J. McCauley, P. McDonald, I. D. McGreer, A. Meisner, N. Metcalfe, T. N. Miller, R. Miquel, J. Moustakas, A. Myers, M. Naik, J. A. Newman, R. C. Nichol, A. Nicola, L. Nicolati da Costa, J. Nie, G. Niz, P. Norberg, B. Nord, D. Norman, P. Nugent, T. O'Brien, M. Oh, K. A. G. Olsen, C. Padilla, H. Padmanabhan, N. Padmanabhan, N. Palanque-Delabrouille, A. Palmese, D. Pappalardo, I. Pâris, C. Park, A. Patej, J. A. Peacock, H. V. Peiris, X. Peng, W. J. Percival, S. Perruchot, M. M. Pieri, R. Pogge, J. E. Pollack, C. Poppett, F. Prada, A. Prakash, R. G. Probst, D. Rabinowitz, A. Raichoor, C. H. Ree, A. Refregier, X. Regal, B. Reid, K. Reil, M. Rezaie, C. M. Rockosi, N. Roe, S. Ronayette, A. Roodman, A. J. Ross, N. P. Ross, G. Rossi, E. Rozo, V. Ruhlmann-Kleider, E. S. Rykoff, C. Sabiu, L. Samushia, E. Sanchez, J. Sanchez, D. J. Schlegel, M. Schneider, M. Schubnell, A. Secroun, U. Seljak, H.-J. Seo, S. Serrano, A. Shafieloo, H. Shan, R. Sharples, M. J. Sholl, W. V. Shourt, J. H. Silber, D. R. Silva, M. M. Sirk, A. Slosar, A. Smith, G. F. Smoot, D. Som, Y.-S. Song, D. Sprayberry, R. Staten, A. Stefanik, G. Tarle, S. Sien Tie, J. L. Tinker, R. Tojeiro, F. Valdes, O. Valenzuela, M. Valluri, M. Vargas-Magana, L. Verde, A. R. Walker, J. Wang, Y. Wang, B. A. Weaver, C. Weaverdyck, R. H. Wechsler, D. H. Weinberg, M. White, Q. Yang, C. Yeche, T. Zhang, G.-B. Zhao, Y. Zheng, X. Zhou, Z. Zhou, Y. Zhu, H. Zou, and Y. Zu, "The DESI Experiment Part I: Science,Targeting, and Survey Design," *arXiv e-prints* (Oct, 2016) arXiv:1611.00036, arXiv:1611.00036 [astro-ph.IM].

[242] LSST Science Collaboration, P. A. Abell, J. Allison, S. F. Anderson, J. R. Andrew, J. R. P. Angel, L. Armus, D. Arnett, S. J. Asztalos, T. S. Axelrod, S. Bailey, D. R. Ballantyne, J. R. Bankert, W. A. Barkhouse, J. D. Barr, L. F. Barrientos, A. J. Barth, J. G. Bartlett, A. C. Becker, J. Becla, T. C. Beers, J. P. Bernstein, R. Biswas, M. R. Blanton, J. S. Bloom, J. J. Bochanski, P. Boeshaar, K. D. Borne, M. Bradac, W. N. Brandt, C. R. Bridge, M. E. Brown, R. J. Brunner, J. S. Bullock, A. J. Burgasser, J. H. Burge, D. L. Burke, P. A. Cargile, S. Chand rasekharan, G. Chartas, S. R. Chesley, Y.-H. Chu, D. Cinabro, M. W. Claire, C. F. Claver, D. Clowe, A. J. Connolly, K. H. Cook, J. Cooke, A. Cooray, K. R. Covey, C. S. Culliton, R. de Jong, W. H. de Vries, V. P. Debattista, F. Delgado, I. P. Dell'Antonio, S. Dhital, R. Di Stefano, M. Dickinson, B. Dilday, S. G. Djorgovski, G. Dobler, C. Donalek, G. Dubois-Felsmann, J. Durech, A. Eliasdottir, M. Eracleous, L. Eyer, E. E.

Falco, X. Fan, C. D. Fassnacht, H. C. Ferguson, Y. R. Fernandez, B. D. Fields, D. Finkbeiner, E. E. Figueroa, D. B. Fox, H. Francke, J. S. Frank, J. Frieman, S. Fromenteau, M. Furqan, G. Galaz, A. Gal-Yam, P. Garnavich, E. Gawiser, J. Geary, P. Gee, R. R. Gibson, K. Gilmore, E. A. Grace, R. F. Green, W. J. Gressler, C. J. Grillmair, S. Habib, J. S. Haggerty, M. Hamuy, A. W. Harris, S. L. Hawley, A. F. Heavens, L. Hebb, T. J. Henry, E. Hileman, E. J. Hilton, K. Hoadley, J. B. Holberg, M. J. Holman, S. B. Howell, L. Infante, Z. Ivezic, S. H. Jacoby, B. Jain, R, Jedicke, M. J. Jee, J. Garrett Jernigan, S. W. Jha, K. V. Johnston, R. L. Jones, M. Juric, M. Kaasalainen, Styliani, Kafka, S. M. Kahn, N. A. Kaib, J. Kalirai, J. Kantor, M. M. Kasliwal, C. R. Keeton, R. Kessler, Z. Knezevic, A. Kowalski, V. L. Krabbendam, K. S. Krughoff, S. Kulkarni, S. Kuhlman, M. Lacy, S. Lepine, M. Liang, A. Lien, P. Lira, K. S. Long, S. Lorenz, J. M. Lotz, R. H. Lupton, J. Lutz, L. M. Macri, A. A. Mahabal, R. Mandelbaum, P. Marshall, M. May, P. M. McGehee, B. T. Meadows, A. Meert, A. Milani, C. J. Miller, M. Miller, D. Mills, D. Minniti, D. Monet, A. S. Mukadam, E. Nakar, D. R. Neill, J. A. Newman, S. Nikolaev, M. Nordby, P. O'Connor, M. Oguri, J. Oliver, S. S. Olivier, J. K. Olsen, K. Olsen, E. W. Olszewski, H. Oluseyi, N. D. Padilla, A. Parker, J. Pepper, J. R. Peterson, C. Petry, P. A. Pinto, J. L. Pizagno, B. Popescu, A. Prsa, V. Radcka, M. J. Raddick, A. Rasmussen, A. Rau, J. Rho, J. E. Rhoads, G. T. Richards, S. T. Ridgway, B. E. Robertson, R. Roskar, A. Saha, A. Sarajedini, E. Scannapieco, T. Schalk, R. Schindler, S. Schmidt, S. Schmidt, D. P. Schneider, G. Schumacher, R. Scranton, J. Sebag, L. G. Seppala, O. Shemmer, J. D. Simon, M. Sivertz, H. A. Smith, J. Allyn Smith, N. Smith, A. H. Spitz, A. Stanford, K. G. Stassun, J. Strader, M. A. Strauss, C. W. Stubbs, D. W. Sweeney, A. Szalay, P. Szkody, M. Takada, P. Thorman, D. E. Trilling, V. Trimble, A. Tyson, R. Van Berg, D. Vand en Berk, J. VanderPlas, L. Verde, B. Vrsnak, L. M. Walkowicz, B. D. Wand elt, S. Wang, Y. Wang, M. Warner, R. H. Wechsler, A. A. West, O. Wiecha, B. F. Williams, B. Willman, D. Wittman, S. C. Wolff, W. M. Wood-Vasey, P. Wozniak, P. Young, A. Zentner, and H. Zhan, "LSST Science Book, Version 2.0," *arXiv e-prints* (Dec, 2009) arXiv:0912.0201, arXiv:0912.0201 [astro-ph.IM].

[243] The LSST Dark Energy Science Collaboration, R. Mandelbaum, T. Eifler, R. Hložek, T. Collett, E. Gawiser, D. Scolnic, D. Alonso, H. Awan, R. Biswas, J. Blazek, P. Burchat, N. E. Chisari, I. Dell'Antonio, S. Digel, J. Frieman, D. A. Goldstein, I. Hook, Ž. Ivezić, S. M. Kahn, S. Kamath, D. Kirkby, T. Kitching, E. Krause, P.-F. Leget, P. J. Marshall, J. Meyers, H. Miyatake, J. A. Newman, R. Nichol, E. Rykoff, F. J. Sanchez, A. Slosar, M. Sullivan, and M. A. Troxel, "The LSST Dark Energy Science Collaboration (DESC) Science Requirements Document," *arXiv e-prints* (Sep, 2018) arXiv:1809.01669, arXiv:1809.01669 [astro-ph.CO].

[244] A. Albrecht, G. Bernstein, R. Cahn, W. L. Freedman, J. Hewitt, W. Hu, J. Huth, M. Kamionkowski, E. W. Kolb, L. Knox, J. C. Mather, S. Staggs, and N. B. Suntzeff, "Report of the Dark Energy Task Force," *arXiv e-prints* (Sep, 2006) astro–ph/0609591, arXiv:astro-ph/0609591 [astro-ph].

[245] S. Hannestad, "Neutrino Masses and the Dark Energy Equation of State:Relaxing the Cosmological Neutrino Mass Bound," *Phys. Rev.* **L 95** no. 22, (Nov, 2005) 221301, arXiv:astro-ph/0505551 [astro-ph].

[246] S. Bhattacharya and A. Kosowsky, "Dark Energy Constraints from Galaxy Cluster Peculiar Velocities," *Phys. Rev.* **D77** (2008) 083004, arXiv:0712.0034 [astro-ph].

[247] A. Kosowsky and S. Bhattacharya, "A Future Test of Gravitation Using Galaxy Cluster Velocities," *Phys. Rev.* **D80** (2009) 062003, arXiv:0907.4202 [astro-ph.CO].

[248] E.-M. Mueller, F. de Bernardis, R. Bean, and M. D. Niemack, "Constraints on gravity and dark energy from the pairwise kinematic Sunyaev-Zeldovich effect," *Astrophys. J.* **808** no. 1, (2015) 47, arXiv:1408.6248 [astro-ph.CO].

[249] E.-M. Mueller, F. de Bernardis, R. Bean, and M. D. Niemack, "Constraints on massive neutrinos from the pairwise kinematic Sunyaev-Zel'dovich effect," *Phys. Rev.* **D92** no. 6, (2015) 063501, arXiv:1412.0592 [astro-ph.CO].

[250] D. Alonso, J. C. Hill, R. Hložek, and D. N. Spergel, "Measurement of the thermal Sunyaev-Zel'dovich effect around cosmic voids," *Phys. Rev.* **D 97** no. 6, (Mar., 2018) 063514, arXiv:1709.01489.

[251] S. Flender, D. Nagai, and M. McDonald, "Constraints on the optical depth of galaxy groups and clusters," *Astrophys. J.* **837** no. 2, (2017) 124, arXiv:1610.08029 [astro-ph.CO].

[252] N. S. Sugiyama, T. Okumura, and D. N. Spergel, "Will kinematic Sunyaev-Zel'dovich measurements enhance the science return from galaxy redshift surveys?," *JCAP* **1** (Jan., 2017) 057, arXiv:1606.06367.

[253] M. P. van Daalen, J. Schaye, C. M. Booth, and C. D. Vecchia, "The effects of galaxy formation on the matter power spectrum: A challenge for precision cosmology," *Mon. Not. Roy. Astron. Soc.* **415** (2011) 3649–3665, arXiv:1104.1174 [astro-ph.CO].

[254] I. Mohammed, D. Martizzi, R. Teyssier, and A. Amara, "Baryonic effects on weak-lensing two-point statistics and its cosmological implications," arXiv:1410.6826 [astro-ph.CO].

[255] **POLARBEAR** Collaboration, P. A. R. Ade *et al.*, "POLARBEAR Constraints on Cosmic Birefringence and Primordial Magnetic Fields," *Phys. Rev.* **D92** (2015) 123509, arXiv:1509.02461 [astro-ph.CO].

[256] **Keck Arrary, BICEP2** Collaboration, P. A. R. Ade *et al.*, "BICEP2 / Keck Array IX: New bounds on anisotropies of CMB polarization rotation and implications for axionlike particles and primordial magnetic fields," *Phys. Rev.* **D96** no. 10, (2017) 102003, arXiv:1705.02523 [astro-ph.CO].

[257] S. M. Carroll, "Quintessence and the rest of the world," *Phys. Rev. Lett.* **81** (1998) 3067–3070, arXiv:astro-ph/9806099 [astro-ph].

[258] M. Kamionkowski, "How to De-Rotate the Cosmic Microwave Background Polarization," *Phys. Rev. Lett.* **102** (2009) 111302, arXiv:0810.1286 [astro-ph].

[259] V. Gluscevic, M. Kamionkowski, and A. Cooray, "De-Rotation of the Cosmic Microwave Background Polarization: Full-Sky Formalism," *Phys. Rev.* **D80** (2009) 023510, arXiv:0905.1687 [astro-ph.CO].

[260] **Planck** Collaboration, Planck Collaboration Int. XLIX, "Planck intermediate results. XLIX. Parity-violation constraints from polarization data," *Astron. Astrophys.* **596** (2016) A110, arXiv:1605.08633 [astro-ph.CO].

[261] V. Gluscevic, D. Hanson, M. Kamionkowski, and C. M. Hirata, "First CMB Constraints on Direction-Dependent Cosmological Birefringence from WMAP-7," *Phys. Rev.* **D86** (2012) 103529, arXiv:1206.5546 [astro-ph.CO].

[262] M. Pospelov, A. Ritz, C. Skordis, A. Ritz, and C. Skordis, "Pseudoscalar perturbations and polarization of the cosmic microwave background," *Phys. Rev. Lett.* **103** (2009) 051302, arXiv:0808.0673 [astro-ph].

[263] D. Contreras, P. Boubel, and D. Scott, "Constraints on direction-dependent cosmic birefringence from Planck polarization data," *JCAP* **12** (Dec., 2017) 046, arXiv:1705.06387.

[264] T. Emken and C. Kouvaris, "How blind are underground and surface detectors to strongly interacting dark matter?," *Phys. Rev.* **D 97** no. 11, (June, 2018) 115047, arXiv:1802.04764 [hep-ph].

[265] B. J. Kavanagh, "Earth scattering of superheavy dark matter: Updated constraints from detectors old and new," *Phys. Rev.* **D 97** no. 12, (June, 2018) 123013, arXiv:1712.04901 [hep-ph].

[266] P. Cushman, C. Galbiati, D. N. McKinsey, H. Robertson, T. M. P. Tait, D. Bauer, A. Borgland, B. Cabrera, F. Calaprice, J. Cooley, T. Empl, R. Essig, E. Figueroa-Feliciano, R. Gaitskell, S. Golwala, J. Hall, R. Hill, A. Hime, E. Hoppe, L. Hsu, E. Hungerford, R. Jacobsen, M. Kelsey, R. F. Lang, W. H. Lippincott, B. Loer, S. Luitz, V. Mandic, J. Mardon, J. Maricic, R. Maruyama, R. Mahapatra, H. Nelson, J. Orrell, K. Palladino, E. Pantic, R. Partridge, A. Ryd, T. Saab, B. Sadoulet, R. Schnee, W. Shepherd, A. Sonnenschein, P. Sorensen, M. Szydagis, T. Volansky, M. Witherell, D. Wright, and K. Zurek, "Snowmass CF1 Summary: WIMP Dark Matter Direct Detection," *ArXiv e-prints* (Oct., 2013) , arXiv:1310.8327 [hep-ex].

[267] D. Hooper and S. D. McDermott, "Robust Constraints and Novel Gamma-Ray Signatures of Dark Matter That Interacts Strongly With Nucleons," *Phys. Rev.* **D97** no. 11, (2018) 115006, arXiv:1802.03025 [hep-ph].

[268] X. Chen, S. Hannestad, and R. J. Scherrer, "Cosmic microwave background and large scale structure limits on the interaction between dark matter and baryons," *ArXiv Astrophysics e-prints* (Feb., 2002) , astro-ph/0202496.

[269] K. Sigurdson, M. Doran, A. Kurylov, R. R. Caldwell, and M. Kamionkowski, "Dark-matter electric and magnetic dipole moments," *Phys. Rev.* **D 70** no. 8, (Oct., 2004) 083501, astro-ph/0406355.

[270] C. Dvorkin, K. Blum, and M. Kamionkowski, "Constraining Dark Matter-Baryon Scattering with Linear Cosmology," *Phys. Rev. D* **89** no. 2, (2014) 023519, arXiv:1311.2937 [astro-ph.CO].

[271] V. Gluscevic and K. K. Boddy, "Constraints on Scattering of keV-TeV Dark Matter with Protons in the Early Universe," *Physical Review Letters* **121** no. 8, (Aug., 2018) 081301, arXiv:1712.07133.

[272] K. K. Boddy and V. Gluscevic, "First cosmological constraint on the effective theory of dark matter-proton interactions," *Phys. Rev.* **D 98** no. 8, (Oct, 2018) 083510, arXiv:1801.08609 [astro-ph.CO].

[273] W. L. Xu, C. Dvorkin, and A. Chael, "Probing sub-GeV dark matter-baryon scattering with cosmological observables," *Phys. Rev.* **D 97** no. 10, (May, 2018) 103530, arXiv:1802.06788.

[274] K. K. Boddy and V. Gluscevic, "First Cosmological Constraint on the Effective Theory of Dark Matter-Proton Interactions," *ArXiv e-prints* (Jan., 2018) , arXiv:1801.08609.

[275] J. Fan, M. Reece, and L.-T. Wang, "Non-relativistic effective theory of dark matter direct detection," *JCAP* **1011** (2010) 042, arXiv:1008.1591 [hep-ph].

[276] A. L. Fitzpatrick, W. Haxton, E. Katz, N. Lubbers, and Y. Xu, "The Effective Field Theory of Dark Matter Direct Detection," *JCAP* **1302** (2013) 004, arXiv:1203.3542 [hep-ph].

[277] N. Anand, A. L. Fitzpatrick, and W. C. Haxton, "Weakly interacting massive particle-nucleus elastic scattering response," *Phys. Rev.* **C89** no. 6, (2014) 065501, arXiv:1308.6288 [hep-ph].

[278] J. B. Dent, L. M. Krauss, J. L. Newstead, and S. Sabharwal, "General analysis of direct dark matter detection: From microphysics to observational signatures," *Phys. Rev.* **D92** no. 6, (2015) 063515, arXiv:1505.03117 [hep-ph].

[279] K. K. Boddy, V. Gluscevic, V. Poulin, E. D. Kovetz, M. Kamionkowski, and R. Barkana, "Critical assessment of CMB limits on dark matter-baryon scattering: New treatment of the relative bulk velocity," *Phys. Rev.* **D 98** no. 12, (Dec, 2018) 123506, arXiv:1808.00001 [astro-ph.CO].

[280] T. R. Slatyer and C.-L. Wu, "Early-Universe constraints on dark matter-baryon scattering and their implications for a global 21 cm signal," *Phys. Rev.* **D 98** no. 2, (July, 2018) 023013, arXiv:1803.09734.

[281] R. de Putter, O. Doré, J. Gleyzes, D. Green, and J. Meyers, "Dark Matter Interactions, Helium, and the CMB," *ArXiv e-prints* (May, 2018) , arXiv:1805.11616.

[282] J. D. Bowman, A. E. E. Rogers, R. A. Monsalve, T. J. Mozdzen, and N. Mahesh, "An absorption profile centred at 78 megahertz in the sky-averaged spectrum," *Nature* **555** (Mar., 2018) 67–70, arXiv:1810.05912.

[283] R. Barkana, "Possible interaction between baryons and dark-matter particles revealed by the first stars," *Nature* **555** (Mar., 2018) 71–74, arXiv:1803.06698.

[284] E. D. Kovetz, V. Poulin, V. Gluscevic, K. K. Boddy, R. Barkana, and M. Kamionkowski, "Tighter limits on dark matter explanations of the anomalous EDGES 21 cm signal," *Phys. Rev.* **D 98** no. 10, (Nov, 2018) 103529, arXiv:1807.11482 [astro-ph.CO].

[285] Z. Li, V. Gluscevic, K. K. Boddy, and M. S. Madhavacheril, "Disentangling dark physics with cosmic microwave background experiments," *Phys. Rev.* **D 98** no. 12, (Dec, 2018) 123524, arXiv:1806.10165 [astro-ph.CO].

[286] R. J. Thornton, P. A. R. Ade, S. Aiola, F. E. Angilè, M. Amiri, J. A. Beall, D. T. Becker, H. M. Cho, S. K. Choi, P. Corlies, K. P. Coughlin, R. Datta, M. J. Devlin, S. R. Dicker, R. Dünner, J. W. Fowler, A. E. Fox, P. A. Gallardo, J. Gao, E. Grace, M. Halpern, M. Hasselfield, S. W. Henderson, G. C. Hilton, A. D. Hincks, S. P. Ho, J. Hubmayr, K. D. Irwin, J. Klein, B. Koopman, D. Li, T. Louis, M. Lungu, L. Maurin, J. McMahon, C. D. Munson, S. Naess, F. Nati, L. Newburgh, J. Nibarger, M. D. Niemack, P. Niraula, M. R. Nolta, L. A. Page, C. G. Pappas, A. Schillaci, B. L. Schmitt, N. Sehgal, J. L. Sievers, S. M. Simon, S. T. Staggs, C. Tucker, M. Uehara, J. van Lanen, J. T. Ward, and E. J. Wollack, "The Atacama Cosmology Telescope: The Polarization-sensitive ACTPol Instrument," *The Astrophysical Journal Supplement Series* **227** no. 2, (Dec, 2016) 21, arXiv:1605.06569 [astro-ph.IM].

[287] E. O. Nadler, V. Gluscevic, K. K. Boddy, and R. H. Wechsler, "Constraints on Dark Matter Microphysics from the Milky Way Satellite Population," *arXiv e-prints* (Apr, 2019) arXiv:1904.10000, arXiv:1904.10000 [astro-ph.CO].

[288] A. Drlica-Wagner, Y.-Y. Mao, S. Adhikari, R. Armstrong, A. Banerjee, N. Banik, K. Bechtol, S. Bird, K. K. Boddy, A. Bonaca, J. Bovy, M. R. Buckley, E. Bulbul, C. Chang, G. Chapline, J. Cohen-Tanugi, A. Cuoco, F.-Y. Cyr-Racine, W. A. Dawson, A. Díaz Rivero, C. Dvorkin, D. Erkal, C. D. Fassnacht, J. García-Bellido, M. Giannotti, V. Gluscevic, N. Golovich, D. Hendel, Y. D. Hezaveh, S. Horiuchi, M. J. Jee, M. Kaplinghat, C. R. Keeton, S. E. Koposov, T. S. Li, R. Mandelbaum, S. D. McDermott, M. McNanna, M. Medford, M. Meyer, M. Marc, S. Murgia, E. O. Nadler, L. Necib, E. Nuss, A. B. Pace, A. H. G. Peter, D. A. Polin, C. Prescod-Weinstein, J. I. Read, R. Rosenfeld, N. Shipp, J. D. Simon, T. R. Slatyer, O. Straniero, L. E. Strigari, E. Tollerud, J. A. Tyson, M.-Y. Wang, R. H. Wechsler, D. Wittman, H.-B. Yu, G. Zaharijas, Y. Ali-Haïmoud, J. Annis, S. Birrer, R. Biswas, J. Blazek, A. M. Brooks, E. Buckley-Geer, R. Caputo, E. Charles, S. Digel, S. Dodelson, B. Flaugher, J. Frieman, E. Gawiser, A. P. Hearin, R. Hložek, B. Jain, T. E. Jeltema, S. M. Koushiappas, M. Lisanti, M. LoVerde, S. Mishra-Sharma, J. A. Newman, B. Nord, E. Nourbakhsh, S. Ritz, B. E. Robertson, M. A. Sánchez-Conde, A. Slosar, T. M. P. Tait, A. Verma, R. Vilalta, C. W. Walter, B. Yanny, and A. R. Zentner, "Probing the Fundamental Nature of Dark Matter with the Large Synoptic Survey Telescope," *arXiv e-prints* (Feb, 2019) arXiv:1902.01055, arXiv:1902.01055 [astro-ph.CO].

[289] L. G. van den Aarssen, T. Bringmann, and C. Pfrommer, "Is dark matter with long-range interactions a solution to all small-scale problems of Λ CDM cosmology?," *Phys. Rev. Lett.* **109** (2012) 231301, arXiv:1205.5809 [astro-ph.CO].

[290] F.-Y. Cyr-Racine, R. de Putter, A. Raccanelli, and K. Sigurdson, "Constraints on Large-Scale Dark Acoustic Oscillations from Cosmology," *Phys. Rev. D* **89** no. 6, (2014) 063517, arXiv:1310.3278 [astro-ph.CO].

[291] J. S. Bullock and M. Boylan-Kolchin, "Small-Scale Challenges to the ΛCDM Paradigm," *Ann. Rev. Astron. Astrophys.* **55** (2017) 343–387, arXiv:1707.04256 [astro-ph.CO].

[292] R. Krall, F.-Y. Cyr-Racine, and C. Dvorkin, "Wandering in the Lyman-alpha Forest: A Study of Dark Matter-Dark Radiation Interactions," *JCAP* **1709** no. 09, (2017) 003, arXiv:1705.08894 [astro-ph.CO].

[293] F.-Y. Cyr-Racine, K. Sigurdson, J. Zavala, T. Bringmann, M. Vogelsberger, and C. Pfrommer, "ETHOS – an effective theory of structure formation: From dark particle physics to the matter distribution of the Universe," *Phys. Rev.* **D93** no. 12, (2016) 123527, arXiv:1512.05344 [astro-ph.CO].

[294] S. Tulin, H.-B. Yu, and K. M. Zurek, "Resonant Dark Forces and Small Scale Structure," *Phys. Rev. Lett.* **110** (2013) 111301, arXiv:1210.0900 [hep-ph].

[295] S. Tulin, H.-B. Yu, and K. M. Zurek, "Beyond Collisionless Dark Matter: Particle Physics Dynamics for Dark Matter Halo Structure," *Phys. Rev. D* **87** (2013) 115007, arXiv:1302.3898 [hep-ph].

[296] M. Kaplinghat, S. Tulin, and H.-B. Yu, "Dark Matter Halos as Particle Colliders: A Unified Solution to Small-Scale Structure Puzzles from Dwarfs to Clusters," arXiv:1508.03339 [astro-ph.CO].

[297] M. Vogelsberger, J. Zavala, F.-Y. Cyr-Racine, C. Pfrommer, T. Bringmann, and K. Sigurdson, "ETHOS - An Effective Theory of Structure Formation: Dark matter physics as a possible explanation of the small-scale CDM problems," *Mon. Not. Roy. Astron. Soc.* **460** (2016) 1399, arXiv:1512.05349 [astro-ph.CO].

[298] A. Schneider, "Astrophysical constraints on resonantly produced sterile neutrino dark matter," *JCAP* **1604** no. 04, (2016) 059, arXiv:1601.07553 [astro-ph.CO].

[299] R. Hložek, D. J. E. Marsh, and D. Grin, "Using the Full Power of the Cosmic Microwave Background to Probe Axion Dark Matter," *Mon. Not. Roy. Astron. Soc.* **476** no. 3, (2018) 3063–3085, arXiv:1708.05681 [astro-ph.CO].

[300] R. Hložek, D. Grin, D. J. Marsh, and P. G. Ferreira, "A search for ultralight axions using precision cosmological data," *Phys. Rev.* **D91** no. 10, (2015) 103512, arXiv:1410.2896 [astro-ph.CO].

[301] R. Hložek, D. J. E. Marsh, D. Grin, R. Allison, J. Dunkley, and E. Calabrese, "Future CMB tests of dark matter: ultra-light axions and massive neutrinos," arXiv:1607.08208 [astro-ph.CO].

[302] I. De Martino, T. Broadhurst, S. H. Henry Tye, T. Chiueh, H.-Y. Schive, and R. Lazkoz, "Recognizing Axionic Dark Matter by Compton and de Broglie Scale Modulation of Pulsar Timing," *Phys. Rev. Lett.* **119** no. 22, (2017) 221103, arXiv:1705.04367 [astro-ph.CO].

[303] N. K. Porayko *et al.*, "Parkes Pulsar Timing Array constraints on ultralight scalar-field dark matter," arXiv:1810.03227 [astro-ph.CO].

[304] V. Iršič, M. Viel, M. G. Haehnelt, J. S. Bolton, and G. D. Becker, "First constraints on fuzzy dark matter from Lyman-α forest data and hydrodynamical simulations," *Phys. Rev. Lett.* **119** no. 3, (2017) 031302, arXiv:1703.04683 [astro-ph.CO].

[305] T. Kobayashi, R. Murgia, A. De Simone, V. Iršič, and M. Viel, "Lyman-α constraints on ultralight scalar dark matter: Implications for the early and late universe," *Phys. Rev.* **D96** no. 12, (2017) 123514, arXiv:1708.00015 [astro-ph.CO].

[306] E. Armengaud, N. Palanque-Delabrouille, C. Yèche, D. J. E. Marsh, and J. Baur, "Constraining the mass of light bosonic dark matter using SDSS Lyman-α forest," *Mon. Not. Roy. Astron. Soc.* **471** no. 4, (2017) 4606–4614, arXiv:1703.09126 [astro-ph.CO].

[307] K.-H. Leong, H.-Y. Schive, U.-H. Zhang, and T. Chiueh, "Testing extreme-axion wave dark matter using the BOSS Lyman-Alpha forest data," arXiv:1810.05930 [astro-ph.CO].

[308] M. Nori, R. Murgia, V. Iršič, M. Baldi, and M. Viel, "Lyman-α forest and non-linear structure characterization in Fuzzy Dark Matter cosmologies," arXiv:1809.09619 [astro-ph.CO].

[309] A. Arvanitaki and S. Dubovsky, "Exploring the String Axiverse with Precision Black Hole Physics," *Phys. Rev.* **D83** (2011) 044026, arXiv:1004.3558 [hep-th].

[310] M. J. Stott and D. J. E. Marsh, "Black hole spin constraints on the mass spectrum and number of axionlike fields," *Phys. Rev.* **D98** no. 8, (2018) 083006, arXiv:1805.02016 [hep-ph].

[311] N. Kitajima, J. Soda, and Y. Urakawa, "Gravitational wave forest from string axiverse," *JCAP* **1810** no. 10, (2018) 008, arXiv:1807.07037 [astro-ph.CO].

[312] D. Baumann, H. S. Chia, and R. A. Porto, "Probing Ultralight Bosons with Binary Black Holes," *Phys. Rev.* **D99** no. 4, (2019) 044001, arXiv:1804.03208 [gr-qc].

[313] D. Grin, M. A. Amin, V. Gluscevic, R. Hl?zek, D. J. E. Marsh, V. Poulin, C. Prescod-Weinstein, and T. L. Smith, "Gravitational probes of ultra-light axions," arXiv:1904.09003 [astro-ph.CO].

[314] D. J. E. Marsh, "WarmAndFuzzy: the halo model beyond CDM," arXiv:1605.05973 [astro-ph.CO].

[315] D. J. E. Marsh and J. Silk, "A Model For Halo Formation With Axion Mixed Dark Matter," *Mon. Not. Roy. Astron. Soc.* **437** no. 3, (2014) 2652–2663, arXiv:1307.1705 [astro-ph.CO].

[316] H.-Y. Schive, M.-H. Liao, T.-P. Woo, S.-K. Wong, T. Chiueh, T. Broadhurst, and W. Y. P. Hwang, "Understanding the Core-Halo Relation of Quantum Wave Dark Matter from 3D Simulations," *Phys. Rev. Lett.* **113** no. 26, (2014) 261302, arXiv:1407.7762 [astro-ph.GA].

[317] H.-Y. Schive, T. Chiueh, and T. Broadhurst, "Cosmic Structure as the Quantum Interference of a Coherent Dark Wave," *Nature Phys.* **10** (2014) 496–499, arXiv:1406.6586 [astro-ph.GA].

[318] H.-Y. Schive, T. Chiueh, T. Broadhurst, and K.-W. Huang, "Contrasting Galaxy Formation from Quantum Wave Dark Matter, ψDM, with ΛCDM, using Planck and Hubble Data," *Astrophys. J.* **818** no. 1, (2016) 89, arXiv:1508.04621 [astro-ph.GA].

[319] V. H. Robles, V. Lora, T. Matos, and F. J. Sánchez-Salcedo, "Evolution of a dwarf satellite galaxy embedded in a scalar field dark matter halo," *Astrophys. J.* **810** no. 2, (2015) 99, arXiv:1404.3424 [astro-ph.GA].

[320] J. Veltmaat and J. C. Niemeyer, "Cosmological particle-in-cell simulations with ultralight axion dark matter," *Phys. Rev.* **D94** no. 12, (2016) 123523, arXiv:1608.00802 [astro-ph.CO].

[321] X. Du, C. Behrens, J. C. Niemeyer, and B. Schwabe, "Core-halo mass relation of ultralight axion dark matter from merger history," *Phys. Rev.* **D95** no. 4, (2017) 043519, arXiv:1609.09414 [astro-ph.GA].

[322] J. Zhang, Y.-L. S. Tsai, J.-L. Kuo, K. Cheung, and M.-C. Chu, "Ultralight Axion Dark Matter and Its Impact on Dark Halo Structure in N-body Simulations," *Astrophys. J.* **853** no. 1, (2018) 51, arXiv:1611.00892 [astro-ph.CO].

[323] S.-R. Chen, H.-Y. Schive, and T. Chiueh, "Jeans Analysis for Dwarf Spheroidal Galaxies in Wave Dark Matter," *Mon. Not. Roy. Astron. Soc.* **468** no. 2, (2017) 1338–1348, arXiv:1606.09030 [astro-ph.GA].

[324] H.-Y. Schive and T. Chiueh, "Halo abundance and assembly history with extreme-axion wave dark matter at $z \geq 4$," *Mon. Not. Roy. Astron. Soc.* **473** no. 1, (2018) L36–L40, arXiv:1706.03723 [astro-ph.CO].

[325] F. X. Linares Cedeño, A. X. González-Morales, and L. Arturo Ureña López, "Towards a calculation of the halo mass function of a scalar field dark matter," *J. Phys. Conf. Ser.* **1030** no. 1, (2018) 012006.

[326] X. Du, B. Schwabe, J. C. Niemeyer, and D. Büurger, "Tidal disruption of fuzzy dark matter subhalo cores," *Phys. Rev.* **D97** no. 6, (2018) 063507, arXiv:1801.04864 [astro-ph.GA].

[327] I. De Martino, T. Broadhurst, S. H. H. Tye, T. Chiueh, and H.-Y. Schive, "Dynamical Evidence of a Solitonic Core of $10^9 M_\odot$ in the Milky Way," arXiv:1807.08153 [astro-ph.GA].

[328] S.-C. Lin, H.-Y. Schive, S.-K. Wong, and T. Chiueh, "Self-consistent construction of virialized wave dark matter halos," *Phys. Rev.* **D97** no. 10, (2018) 103523, arXiv:1801.02320 [astro-ph.CO].

[329] V. H. Robles, J. S. Bullock, and M. Boylan-Kolchin, "Scalar Field Dark Matter: Helping or Hurting Small-Scale Problems in Cosmology?," arXiv:1807.06018 [astro-ph.CO].

[330] J. Veltmaat, J. C. Niemeyer, and B. Schwabe, "Formation and structure of ultralight bosonic dark matter halos," *Phys. Rev.* **D98** no. 4, (2018) 043509, arXiv:1804.09647 [astro-ph.CO].

[331] M. Nori and M. Baldi, "AX-GADGET: a new code for cosmological simulations of Fuzzy Dark Matter and Axion models," *Mon. Not. Roy. Astron. Soc.* **478** no. 3, (2018) 3935–3951, arXiv:1801.08144 [astro-ph.CO].

[332] M. Axenides, R. H. Brandenberger, and M. S. Turner, "Development of Axion Perturbations in an Axion Dominated Universe," *Phys. Lett.* **B126** (1983) 178.

[333] P. Fox, A. Pierce, and S. D. Thomas, "Probing a QCD string axion with precision cosmological measurements," arXiv:hep-th/0409059 [hep-th].

[334] M. P. Hertzberg, M. Tegmark, and F. Wilczek, "Axion Cosmology and the Energy Scale of Inflation," *Phys.Rev.* **D78** (2008) 083507, arXiv:0807.1726 [astro-ph].

[335] P. Svrcek and E. Witten, "Axions In String Theory," *JHEP* **06** (2006) 051, arXiv:hep-th/0605206 [hep-th].

[336] J. Preskill, M. B. Wise, and F. Wilczek, "Cosmology of the Invisible Axion," *Phys. Lett.* **B120** (1983) 127–132.

[337] L. F. Abbott and P. Sikivie, "A Cosmological Bound on the Invisible Axion," *Phys. Lett.* **B120** (1983) 133–136.

[338] M. Dine and W. Fischler, "The Not So Harmless Axion," *Phys. Lett.* **B120** (1983) 137–141.

[339] M. S. Turner, "Coherent Scalar Field Oscillations in an Expanding Universe," *Phys. Rev.* **D28** (1983) 1243.

[340] P. J. Steinhardt and M. S. Turner, "Saving the Invisible Axion," *Phys. Lett.* **B129** (1983) 51.

[341] D. J. E. Marsh and P. G. Ferreira, "Ultra-Light Scalar Fields and the Growth of Structure in the Universe," *Phys. Rev.* **D82** (2010) 103528, arXiv:1009.3501 [hep-ph].

[342] **ADMX** Collaboration, S. J. Asztalos *et al.*, "A SQUID-based microwave cavity search for dark-matter axions," *Phys. Rev. Lett.* **104** (2010) 041301, arXiv:0910.5914 [astro-ph.CO].

[343] D. Budker, P. W. Graham, M. Ledbetter, S. Rajendran, and A. Sushkov, "Proposal for a Cosmic Axion Spin Precession Experiment (CASPEr)," *Phys. Rev.* **X4** no. 2, (2014) 021030, arXiv:1306.6089 [hep-ph].

[344] D. J. E. Marsh, D. Grin, R. Hlozek, and P. G. Ferreira, "Axiverse cosmology and the energy scale of inflation," *Phys. Rev.* **D87** (2013) 121701, arXiv:1303.3008 [astro-ph.CO].

[345] D. J. E. Marsh, D. Grin, R. Hlozek, and P. G. Ferreira, "Tensor Interpretation of BICEP2 Results Severely Constrains Axion Dark Matter," *Phys. Rev. Lett.* **113** no. 1, (2014) 011801, arXiv:1403.4216 [astro-ph.CO].

[346] **LSST Collaboration** Collaboration, Z. Ivezic, J. Tyson, R. Allsman, J. Andrew, and R. Angel, "LSST: from Science Drivers to Reference Design and Anticipated Data Products," arXiv:0805.2366 [astro-ph].

[347] DESI Collaboration, A. Aghamousa, J. Aguilar, S. Ahlen, S. Alam, L. E. Allen, C. Allende Prieto, J. Annis, S. Bailey, C. Balland, and et al., "The DESI Experiment Part I: Science,Targeting, and Survey Design," *ArXiv e-prints* (Oct., 2016) , arXiv:1611.00036 [astro-ph.IM].

[348] A. Merloni, P. Predehl, W. Becker, H. Böhringer, T. Boller, H. Brunner, M. Brusa, K. Dennerl, M. Freyberg, P. Friedrich, A. Georgakakis, F. Haberl, G. Hasinger, N. Meidinger, J. Mohr, K. Nandra, A. Rau, T. H. Reiprich, J. Robrade, M. Salvato, A. Santangelo, M. Sasaki, A. Schwope, J. Wilms, and t. German eROSITA Consortium, "eROSITA Science Book: Mapping the Structure of the Energetic Universe," *ArXiv e-prints* (Sept., 2012) , arXiv:1209.3114 [astro-ph.HE].

[349] K. M. Smith, O. Zahn, and O. Dore, "Detection of Gravitational Lensing in the Cosmic Microwave Background," *Phys. Rev.* **D76** (2007) 043510, arXiv:0705.3980 [astro-ph].

[350] C. M. Hirata, S. Ho, N. Padmanabhan, U. Seljak, and N. A. Bahcall, "Correlation of CMB with large-scale structure: II. Weak lensing," *Phys. Rev.* **D78** (2008) 043520, arXiv:0801.0644 [astro-ph].

[351] **ACT** Collaboration, R. Allison *et al.*, "The Atacama Cosmology Telescope: measuring radio galaxy bias through cross-correlation with lensing," *Mon. Not. Roy. Astron. Soc.* **451** no. 1, (2015) 849–858, arXiv:1502.06456 [astro-ph.CO].

[352] J. C. Hill and D. N. Spergel, "Detection of thermal SZ-CMB lensing cross-correlation in Planck nominal mission data," *JCAP* **1402** (2014) 030, arXiv:1312.4525 [astro-ph.CO].

[353] G. Holder, M. Viero, O. Zahn, K. Aird, B. Benson, *et al.*, "A Cosmic Microwave Background Lensing Mass Map and Its Correlation with the Cosmic Infrared Background," *Astrophys.J.* **771** (2013) L16, arXiv:1303.5048 [astro-ph.CO].

[354] **Planck** Collaboration, Planck Collaboration XVIII, "Planck 2013 results. XVIII. The gravitational lensing-infrared background correlation," *Astron. Astrophys.* **571** (2014) A18, arXiv:1303.5078 [astro-ph.CO].

[355] **POLARBEAR** Collaboration, P. A. R. Ade *et al.*, "Evidence for Gravitational Lensing of the Cosmic Microwave Background Polarization from Cross-correlation with the Cosmic Infrared Background," *Phys. Rev. Lett.* **112** (2014) 131302, arXiv:1312.6645 [astro-ph.CO].

[356] **ACT** Collaboration, A. van Engelen *et al.*, "The Atacama Cosmology Telescope: Lensing of CMB Temperature and Polarization Derived from Cosmic Infrared Background Cross-Correlation," *Astrophys. J.* **808** no. 1, (2015) 7, arXiv:1412.0626 [astro-ph.CO].

[357] F. Bianchini *et al.*, "Cross-correlation between the CMB lensing potential measured by Planck and high-z sub-mm galaxies detected by the Herschel-ATLAS survey," *Astrophys. J.* **802** no. 1, (2015) 64, arXiv:1410.4502 [astro-ph.CO].

[358] L. E. Bleem *et al.*, "A Measurement of the Correlation of Galaxy Surveys with CMB Lensing Convergence Maps from the South Pole Telescope," *Astrophys. J.* **753** (2012) L9, arXiv:1203.4808 [astro-ph.CO].

[359] **Planck** Collaboration, Planck Collaboration XVII, "Planck 2013 results. XVII. Gravitational lensing by large-scale structure," *Astron. Astrophys.* **571** (2014) A17, arXiv:1303.5077 [astro-ph.CO].

[360] J. E. Geach *et al.*, "A Direct Measurement of the Linear Bias of Mid-infrared-selected Quasars at $z \approx 1$ Using Cosmic Microwave Background Lensing," *Astrophys. J.* **776** (2013) L41, arXiv:1307.1706 [astro-ph.CO].

[361] A. R. Pullen, S. Alam, S. He, and S. Ho, "Constraining Gravity at the Largest Scales through CMB Lensing and Galaxy Velocities," *Mon. Not. Roy. Astron. Soc.* **460** no. 4, (2016) 4098–4108, arXiv:1511.04457 [astro-ph.CO].

[362] S. He, S. Alam, S. Ferraro, Y.-C. Chen, and S. Ho, "The detection of the imprint of filaments on cosmic microwave background lensing," *Nat. Astron.* **2** no. 5, (2018) 401–406, arXiv:1709.02543 [astro-ph.CO].

[363] Y.-C. Cai, M. Neyrinck, Q. Mao, J. A. Peacock, I. Szapudi, and A. A. Berlind, "The lensing and temperature imprints of voids on the Cosmic Microwave Background," *Mon. Not. Roy. Astron. Soc.* **466** no. 3, (2017) 3364–3375, arXiv:1609.00301 [astro-ph.CO].

[364] B. D. Sherwin *et al.*, "The Atacama Cosmology Telescope: Cross-Correlation of CMB Lensing and Quasars," *Phys. Rev.* **D86** (2012) 083006, arXiv:1207.4543 [astro-ph.CO].

[365] N. Hand *et al.*, "First Measurement of the Cross-Correlation of CMB Lensing and Galaxy Lensing," *Phys. Rev.* **D91** no. 6, (2015) 062001, arXiv:1311.6200 [astro-ph.CO].

[366] J. Liu and J. C. Hill, "Cross-correlation of Planck CMB Lensing and CFHTLenS Galaxy Weak Lensing Maps," *Phys. Rev.* **D92** no. 6, (2015) 063517, arXiv:1504.05598 [astro-ph.CO].

[367] **DES, SPT** Collaboration, E. J. Baxter *et al.*, "Joint Measurement of Lensing-Galaxy Correlations Using SPT and DES SV Data," *Mon. Not. Roy. Astron. Soc.* **461** (Oct., 2016) 4099–4114, arXiv:1602.07384 [astro-ph.CO].

[368] **DES** Collaboration, T. Giannantonio *et al.*, "CMB lensing tomography with the DES Science Verification galaxies," *Mon. Not. Roy. Astron. Soc.* **456** no. 3, (2016) 3213–3244, arXiv:1507.05551 [astro-ph.CO].

[369] C. Doux, E. Schaan, E. Aubourg, K. Ganga, K.-G. Lee, D. N. Spergel, and J. Tréguer, "First detection of cosmic microwave background lensing and Lyman- α forest bispectrum," *Phys. Rev.* **D94** no. 10, (2016) 103506, arXiv:1607.03625 [astro-ph.CO].

[370] G. Hurier, P. Singh, and C. Hernández-Monteagudo, "First measurement of the cross-correlation between CMB weak lensing and X-ray emission," arXiv:1711.10774 [astro-ph.CO].

[371] N. Fornengo, L. Perotto, M. Regis, and S. Camera, "Evidence of Cross-correlation between the CMB Lensing and the Γ-ray sky," *Astrophys. J.* **802** no. 1, (2015) L1, arXiv:1410.4997 [astro-ph.CO].

[372] E. J. Baxter *et al.*, "A Measurement of Gravitational Lensing of the Cosmic Microwave Background by Galaxy Clusters Using Data from the South Pole Telescope," *Astrophys. J.* **806** no. 2, (2015) 247, arXiv:1412.7521 [astro-ph.CO].

[373] **Planck** Collaboration, Planck Collaboration XXIV, "Planck 2015 results. XXIV. Cosmology from Sunyaev-Zeldovich cluster counts," *Astron. Astrophys.* **594** (2016) A24, arXiv:1502.01597 [astro-ph.CO].

[374] **ACT** Collaboration, M. Madhavacheril *et al.*, "Evidence of Lensing of the Cosmic Microwave Background by Dark Matter Halos," *Phys. Rev. Lett.* **114** no. 15, (2015) 151302, arXiv:1411.7999 [astro-ph.CO]. [Addendum: Phys. Rev. Lett.114,no.18,189901(2015)].

[375] **DESI** Collaboration, M. Levi *et al.*, "The DESI Experiment, a whitepaper for Snowmass 2013," arXiv:1308.0847 [astro-ph.CO].

[376] Planck Collaboration XXI, "Planck 2013 results. XXI. Power spectrum and high-order statistics of the Planck all-sky Compton parameter map," *A & A* **571** (Nov., 2014) A21, arXiv:1303.5081.

[377] Planck Collaboration XXII, "Planck 2015 results. XXII. A map of the thermal Sunyaev-Zeldovich effect," *A & A* **594** (Sept., 2016) A22, arXiv:1502.01596.

[378] R. Khatri, "An alternative validation strategy for the Planck cluster catalogue and y-distortion maps," *A & A* **592** (July, 2016) A48, arXiv:1505.00778.

[379] M. Fukugita and P. J. E. Peebles, "The Cosmic Energy Inventory," *Ap. J.* **616** (Dec., 2004) 643–668, astro-ph/0406095.

[380] A. Gallazzi, J. Brinchmann, S. Charlot, and S. D. M. White, "A census of metals and baryons in stars in the local Universe," *Mon. Not. Roy. Astron. Soc.* **383** (Feb., 2008) 1439–1458, arXiv:0708.0533.

[381] K. Schawinski, D. Thomas, M. Sarzi, C. Maraston, S. Kaviraj, S.-J. Joo, S. K. Yi, and J. Silk, "Observational evidence for AGN feedback in early-type galaxies," *Mon. Not. Roy. Astron. Soc.* **382** (Dec., 2007) 1415–1431, arXiv:0709.3015.

[382] J. N. Bregman, "The Search for the Missing Baryons at Low Redshift," *Ann. Rev. Astron. Astroph.* **45** (Sept., 2007) 221–259, arXiv:0706.1787.

[383] T. Eifler, E. Krause, S. Dodelson, A. R. Zentner, A. P. Hearin, and N. Y. Gnedin, "Accounting for baryonic effects in cosmic shear tomography: determining a minimal set of nuisance parameters using PCA," *Mon. Not. Roy. Astron. Soc.* **454** (Dec., 2015) 2451–2471, arXiv:1405.7423.

[384] D. Nagai, A. V. Kravtsov, and A. Vikhlinin, "Effects of Galaxy Formation on Thermodynamics of the Intracluster Medium," *Astrophys. J.* **668** (2007) 1–14, arXiv:astro-ph/0703661 [astro-ph].

[385] E. T. Lau, D. Nagai, and K. Nelson, "Weighing Galaxy Clusters with Gas. I. On the Methods of Computing Hydrostatic Mass Bias," *Ap. J.* **777** no. 2, (Nov, 2013) 151, arXiv:1306.3993 [astro-ph.CO].

[386] X. Shi, E. Komatsu, D. Nagai, and E. T. Lau, "Analytical model for non-thermal pressure in galaxy clusters - III. Removing the hydrostatic mass bias," *Mon. Not. Roy. Astron. Soc.* **455** no. 3, (Jan, 2016) 2936–2944, arXiv:1507.04338 [astro-ph.CO].

[387] E. T. Lau, A. V. Kravtsov, and D. Nagai, "Residual Gas Motions in the Intracluster Medium and Bias in Hydrostatic Measurements of Mass Profiles of Clusters," *Ap. J.* **705** (Nov., 2009) 1129–1138, arXiv:0903.4895 [astro-ph.CO].

[388] K. Nelson, E. T. Lau, and D. Nagai, "Hydrodynamic Simulation of Non-thermal Pressure Profiles of Galaxy Clusters," *Ap. J.* **792** (Sept., 2014) 25, arXiv:1404.4636.

[389] J. D. Emberson, N. Frontiere, S. Habib, K. Heitmann, P. Larsen, H. Finkel, and A. Pope, "The Borg Cube Simulation: Cosmological Hydrodynamics with CRK-SPH," *ArXiv e-prints* (Nov., 2018) , arXiv:1811.03593.

[390] N. Battaglia, S. Ferraro, E. Schaan, and D. N. Spergel, "Future constraints on halo thermodynamics from combined Sunyaev-Zel'dovich measurements," *JCAP* **11** (Nov., 2017) 040, arXiv:1705.05881.

[391] K. S. Dawson *et al.*, "The Baryon Oscillation Spectroscopic Survey of SDSS-III," *Astronomical Journal* **145** (2013) 10, arXiv:1208.0022 [astro-ph.CO].

[392] S. Ho, S. Dedeo, and D. Spergel, "Finding the Missing Baryons Using CMB as a Backlight," arXiv:0903.2845 [astro-ph.CO].

[393] **ACTPol** Collaboration, E. Schaan *et al.*, "Evidence for the kinematic Sunyaev-Zel'dovich effect with the Atacama Cosmology Telescope and velocity reconstruction from the Baryon Oscillation Spectroscopic Survey," *Phys. Rev.* **D93** no. 8, (2016) 082002, arXiv:1510.06442 [astro-ph.CO].

[394] K. Abazajian *et al.*, "CMB-S4 Science Case, Reference Design, and Project Plan," arXiv:1907.04473 [astro-ph.IM].

[395] I. G. McCarthy, J. Schaye, S. Bird, and A. M. C. Le Brun, "The BAHAMAS project: calibrated hydrodynamical simulations for large-scale structure cosmology," *Mon. Not. Roy. Astron. Soc.* **465** (Mar., 2017) 2936–2965, arXiv:1603.02702.

[396] N. Battaglia, J. R. Bond, C. Pfrommer, J. L. Sievers, and D. Sijacki, "Simulations of the Sunyaev-Zel'dovich Power Spectrum with Active Galactic Nucleus Feedback," *Ap. J.* **725** (Dec., 2010) 91–99, arXiv:1003.4256.

[397] N. Battaglia, J. R. Bond, C. Pfrommer, and J. L. Sievers, "On the Cluster Physics of Sunyaev-Zel'dovich and X-Ray Surveys. II. Deconstructing the Thermal SZ Power Spectrum," *Ap. J.* **758** (Oct., 2012) 75, arXiv:1109.3711.

[398] J. Schaye, R. A. Crain, R. G. Bower, M. Furlong, M. Schaller, T. Theuns, C. Dalla Vecchia, C. S. Frenk, I. G. McCarthy, J. C. Helly, A. Jenkins, Y. M. Rosas-Guevara, S. D. M. White, M. Baes, C. M. Booth, P. Camps, J. F. Navarro, Y. Qu, A. Rahmati, T. Sawala, P. A. Thomas, and J. Trayford, "The EAGLE project: simulating the evolution and assembly of galaxies and their environments," *Mon. Not. Roy. Astron. Soc.* **446** (Jan., 2015) 521–554, arXiv:1407.7040.

[399] R. Weinberger, V. Springel, L. Hernquist, A. Pillepich, F. Marinacci, R. Pakmor, D. Nelson, S. Genel, M. Vogelsberger, J. Naiman, and P. Torrey, "Simulating galaxy formation with black hole driven thermal and kinetic feedback," *Mon. Not. Roy. Astron. Soc.* **465** (Mar., 2017) 3291–3308, arXiv:1607.03486.

[400] D. J. Barnes, M. Vogelsberger, R. Kannan, F. Marinacci, R. Weinberger, V. Springel, P. Torrey, A. Pillepich, D. Nelson, R. Pakmor, J. Naiman, L. Hernquist, and M. McDonald, "A census of cool-core galaxy clusters in IllustrisTNG," *Mon. Not. Roy. Astron. Soc.* **481** (Dec., 2018) 1809–1831, arXiv:1710.08420.

[401] V. Springel, R. Pakmor, A. Pillepich, R. Weinberger, D. Nelson, L. Hernquist, M. Vogelsberger, S. Genel, P. Torrey, F. Marinacci, and J. Naiman, "First results from the IllustrisTNG simulations: matter and galaxy clustering," *Mon. Not. Roy. Astron. Soc.* **475** (Mar., 2018) 676–698, arXiv:1707.03397.

[402] Planck Collaboration Int. XI, "Planck intermediate results. XI. The gas content of dark matter halos: the Sunyaev-Zeldovich-stellar mass relation for locally brightest galaxies," *A & A* **557** (Sept., 2013) A52, arXiv:1212.4131.

[403] A. M. C. Le Brun, I. G. McCarthy, and J.-B. Melin, "Testing Sunyaev-Zel'dovich measurements of the hot gas content of dark matter haloes using synthetic skies," *Mon. Not. Roy. Astron. Soc.* **451** (Aug., 2015) 3868–3881, arXiv:1501.05666.

[404] J. C. Hill, E. J. Baxter, A. Lidz, J. P. Greco, and B. Jain, "Two-halo term in stacked thermal Sunyaev-Zel'dovich measurements: Implications for self-similarity," *Phys. Rev.* **D 97** no. 8, (Apr., 2018) 083501, arXiv:1706.03753.

[405] J. C. Hill, S. Ferraro, N. Battaglia, J. Liu, and D. N. Spergel, "Kinematic Sunyaev-Zeldovich Effect with Projected Fields: A Novel Probe of the Baryon Distribution with Planck, WMAP, and WISE Data," *Phys. Rev. Lett.* **117** no. 5, (2016) 051301, arXiv:1603.01608 [astro-ph.CO].

[406] S. Ferraro, J. C. Hill, N. Battaglia, J. Liu, and D. N. Spergel, "The Kinematic Sunyaev-Zel'dovich Effect with Projected Fields II: prospects, challenges, and comparison with simulations," arXiv:1605.02722 [astro-ph.CO].

[407] V. Vikram, A. Lidz, and B. Jain, "A Measurement of the Galaxy Group-Thermal Sunyaev-Zel'dovich Effect Cross-Correlation Function," *Mon. Not. Roy. Astron. Soc.* **467** (May, 2017) 2315–2330, arXiv:1608.04160.

[408] A. Hall and A. Challinor, "Detecting the polarization induced by scattering of the microwave background quadrupole in galaxy clusters," *Phys. Rev.* **D 90** no. 6, (Sept., 2014) 063518, arXiv:1407.5135.

[409] A.-S. Deutsch, M. C. Johnson, M. Münchmeyer, and A. Terrana, "Polarized Sunyaev Zel'dovich tomography," *JCAP* **4** (Apr., 2018) 034, arXiv:1705.08907.

[410] C. L. Reichardt, L. Shaw, O. Zahn, K. A. Aird, B. A. Benson, L. E. Bleem, J. E. Carlstrom, C. L. Chang, H. M. Cho, T. M. Crawford, A. T. Crites, T. de Haan, M. A. Dobbs, J. Dudley, E. M. George, N. W. Halverson, G. P. Holder, W. L. Holzapfel, S. Hoover, Z. Hou, J. D. Hrubes, M. Joy, R. Keisler, L. Knox, A. T. Lee, E. M. Leitch, M. Lueker, D. Luong-Van, J. J. McMahon, J. Mehl, S. S. Meyer, M. Millea, J. J. Mohr, T. E. Montroy, T. Natoli, S. Padin, T. Plagge, C. Pryke, J. E. Ruhl, K. K. Schaffer, E. Shirokoff, H. G. Spieler, Z. Staniszewski, A. A. Stark, K. Story, A. van Engelen, K. Vanderlinde, J. D. Vieira, and R. Williamson, "A Measurement of Secondary Cosmic Microwave

Background Anisotropies with Two Years of South Pole Telescope Observations," *Ap. J.* **755** (Aug., 2012) 70, arXiv:1111.0932 [astro-ph.CO].

[411] O. Zahn, C. L. Reichardt, L. Shaw, A. Lidz, K. A. Aird, B. A. Benson, L. E. Bleem, J. E. Carlstrom, C. L. Chang, H. M. Cho, T. M. Crawford, A. T. Crites, T. de Haan, M. A. Dobbs, O. Doré, J. Dudley, E. M. George, N. W. Halverson, G. P. Holder, W. L. Holzapfel, S. Hoover, Z. Hou, J. D. Hrubes, M. Joy, R. Keisler, L. Knox, A. T. Lee, E. M. Leitch, M. Lueker, D. Luong-Van, J. J. McMahon, J. Mehl, S. S. Meyer, M. Millea, J. J. Mohr, T. E. Montroy, T. Natoli, S. Padin, T. Plagge, C. Pryke, J. E. Ruhl, K. K. Schaffer, E. Shirokoff, H. G. Spieler, Z. Staniszewski, A. A. Stark, K. Story, A. van Engelen, K. Vanderlinde, J. D. Vieira, and R. Williamson, "Cosmic Microwave Background Constraints on the Duration and Timing of Reionization from the South Pole Telescope," *Ap. J.* **756** (Sept., 2012) 65, arXiv:1111.6386.

[412] E. M. George, C. L. Reichardt, K. A. Aird, B. A. Benson, L. E. Bleem, J. E. Carlstrom, C. L. Chang, H.-M. Cho, T. M. Crawford, A. T. Crites, T. de Haan, M. A. Dobbs, J. Dudley, N. W. Halverson, N. L. Harrington, G. P. Holder, W. L. Holzapfel, Z. Hou, J. D. Hrubes, R. Keisler, L. Knox, A. T. Lee, E. M. Leitch, M. Lueker, D. Luong-Van, J. J. McMahon, J. Mehl, S. S. Meyer, M. Millea, L. M. Mocanu, J. J. Mohr, T. E. Montroy, S. Padin, T. Plagge, C. Pryke, J. E. Ruhl, K. K. Schaffer, L. Shaw, E. Shirokoff, H. G. Spieler, Z. Staniszewski, A. A. Stark, K. T. Story, A. van Engelen, K. Vanderlinde, J. D. Vieira, R. Williamson, and O. Zahn, "A Measurement of Secondary Cosmic Microwave Background Anisotropies from the 2500 Square-degree SPT-SZ Survey," *Ap. J.* **799** (Feb., 2015) 177, arXiv:1408.3161.

[413] **Planck** Collaboration, Planck Collaboration Int. XLVII, "Planck intermediate results. XLVII. Planck constraints on reionization history," arXiv:1605.03507 [astro-ph.CO].

[414] E. Calabrese *et al.*, "Precision Epoch of Reionization studies with next-generation CMB experiments," *JCAP* **1408** (2014) 010, arXiv:1406.4794 [astro-ph.CO].

[415] C. Dvorkin and K. M. Smith, "Reconstructing Patchy Reionization from the Cosmic Microwave Background," *Phys. Rev.* **D79** (2009) 043003, arXiv:0812.1566 [astro-ph].

[416] C. Dvorkin, W. Hu, and K. M. Smith, "B-mode CMB polarization from patchy screening during reionization," *Phys. Rev.* **D 79** no. 10, (May, 2009) 107302, arXiv:0902.4413 [astro-ph.CO].

[417] A. Roy, A. Lapi, D. Spergel, and C. Baccigalupi, "Observing patchy reionization with future CMB polarization experiments," *JCAP* **5** (May, 2018) 014, arXiv:1801.02393.

[418] C. Feng and G. Holder, "Detecting electron density fluctuations from cosmic microwave background polarization using a bispectrum approach," *Phys. Rev.* **D 97** no. 12, (June, 2018) 123523, arXiv:1801.05396.

[419] C. Feng and G. Holder, "Searching for patchy reionization from cosmic microwave background with hybrid quadratic estimators," *ArXiv e-prints* (Aug., 2018) , arXiv:1808.01592.

[420] M. A. Alvarez and T. Abel, "The Effect of Absorption Systems on Cosmic Reionization," *Ap. J.* **747** (Mar., 2012) 126, arXiv:1003.6132 [astro-ph.CO].

[421] M. A. Alvarez, "The Kinetic Sunyaev-Zel'dovich Effect from Reionization: Simulated Full-sky Maps at Arcminute Resolution," *Ap. J.* **824** (June, 2016) 118, arXiv:1511.02846.

[422] L. D. Shaw, D. H. Rudd, and D. Nagai, "Deconstructing the Kinetic SZ Power Spectrum," *Ap. J.* **756** (Sept., 2012) 15, arXiv:1109.0553 [astro-ph.CO].

[423] H. Park, M. A. Alvarez, and J. R. Bond, "The Impact of Baryonic Physics on the Kinetic Sunyaev-Zel'dovich Effect," *Ap. J.* **853** (Feb., 2018) 121, arXiv:1710.02792.

[424] K. M. Smith and S. Ferraro, "Detecting Patchy Reionization in the Cosmic Microwave Background," *Physical Review Letters* **119** no. 2, (July, 2017) 021301.

[425] R. A. Sunyaev and Ya. B. Zeldovich, "The Observations of relic radiation as a test of the nature of X-Ray radiation from the clusters of galaxies," *Comments Astrophys. Space Phys.* **4** (1972) 173–178.

[426] J. E. Carlstrom, G. P. Holder, and E. D. Reese, "Cosmology with the Sunyaev-Zel'dovich Effect," *Ann. Rev. Astron. Astroph.* **40** (2002) 643–680.

[427] D. H. Weinberg, M. J. Mortonson, D. J. Eisenstein, C. Hirata, A. G. Riess, and E. Rozo, "Observational Probes of Cosmic Acceleration," *Phys. Rept.* **530** (2013) 87–255, arXiv:1201.2434 [astro-ph.CO].

[428] M. Niemack, P. Ade, J. Aguirre, F. Barrientos, J. Beall, *et al.*, "ACTPol: A polarization-sensitive receiver for the Atacama Cosmology Telescope," *Proc.SPIE Int.Soc.Opt.Eng.* **7741** (2010) 77411S, arXiv:1006.5049 [astro-ph.IM].

[429] **SPT-3G** Collaboration, B. A. Benson *et al.*, "SPT-3G: A Next-Generation Cosmic Microwave Background Polarization Experiment on the South Pole Telescope," *Proc. SPIE Int. Soc. Opt. Eng.* **9153** (2014) 91531P, arXiv:1407.2973 [astro-ph.IM].

[430] M. S. Madhavacheril, N. Battaglia, and H. Miyatake, "Fundamental physics from future weak-lensing calibrated Sunyaev-Zel'dovich galaxy cluster counts," *Phys. Rev.* **D 96** no. 10, (Nov., 2017) 103525, arXiv:1708.07502.

[431] Planck Collaboration, P. A. R. Ade, N. Aghanim, M. Arnaud, M. Ashdown, J. Aumont, C. Baccigalupi, A. J. Banday, R. B. Barreiro, R. Barrena, and et al., "Planck 2015 results. XXVII. The second Planck catalogue of Sunyaev-Zeldovich sources," *A & A* **594** (Sept., 2016) A27, arXiv:1502.01598.

[432] **SPT** Collaboration, L. E. Bleem *et al.*, "Galaxy Clusters Discovered via the Sunyaev-Zel'dovich Effect in the 2500-square-degree SPT-SZ survey," *Astrophys. J. Suppl.* **216** no. 2, (2015) 27, arXiv:1409.0850 [astro-ph.CO].

[433] M. Hilton, M. Hasselfield, C. Sifón, N. Battaglia, S. Aiola, V. Bharadwaj, J. R. Bond, S. K. Choi, D. Crichton, R. Datta, M. J. Devlin, J. Dunkley, R. Dünner, P. A. Gallardo, M. Gralla, A. D. Hincks, S.-P. P. Ho, J. Hubmayr, K. M. Huffenberger, J. P. Hughes, B. J. Koopman, A. Kosowsky, T. Louis, M. S. Madhavacheril, T. A. Marriage, L. Maurin, J. McMahon, H. Miyatake, K. Moodley, S. Næss, F. Nati, L. Newburgh, M. D. Niemack, M. Oguri, L. A. Page, B. Partridge, B. L. Schmitt, J. Sievers, D. N. Spergel, S. T. Staggs, H. Trac, A. van Engelen, E. M. Vavagiakis, and E. J. Wollack, "The Atacama Cosmology Telescope: The Two-season ACTPol Sunyaev-Zeldovich Effect Selected Cluster Catalog," *Ap. J. Suppl.* **235** (Mar., 2018) 20, arXiv:1709.05600.

[434] M. Negrello, F. Perrotta, J. González-Nuevo, L. Silva, G. de Zotti, G. L. Granato, C. Baccigalupi, and L. Danese, "Astrophysical and cosmological information from large-scale submillimetre surveys of extragalactic sources," *Mon. Not. Roy. Astron. Soc.* **377** (June, 2007) 1557–1568, astro-ph/0703210.

[435] J. Vieira, T. Crawford, E. Switzer, P. Ade, K. Aird, *et al.*, "Extragalactic millimeter-wave sources in South Pole Telescope survey data: source counts, catalog, and statistics for an 87 square-degree field," *Astrophys.J.* **719** (2010) 763–783, arXiv:0912.2338 [astro-ph.CO].

[436] M. L. Strandet, A. Weiss, C. De Breuck, D. P. Marrone, J. D. Vieira, M. Aravena, M. L. N. Ashby, M. Béthermin, M. S. Bothwell, C. M. Bradford, J. E. Carlstrom, S. C. Chapman, D. J. M. Cunningham, C.-C. Chen, C. D. Fassnacht, A. H. Gonzalez, T. R. Greve, B. Gullberg, C. C. Hayward, Y. Hezaveh, K. Litke, J. Ma, M. Malkan, K. M. Menten, T. Miller, E. J. Murphy, D. Narayanan, K. A. Phadke, K. M. Rotermund, J. S. Spilker, and J. Sreevani, "ISM Properties of a Massive Dusty Star-forming Galaxy Discovered at $z \sim 7$," *Ap. J. Lett.* **842** (June, 2017) L15, arXiv:1705.07912.

[437] D. P. Marrone, J. S. Spilker, C. C. Hayward, J. D. Vieira, M. Aravena, M. L. N. Ashby, M. B. Bayliss, M. Béthermin, M. Brodwin, M. S. Bothwell, J. E. Carlstrom, S. C. Chapman, C.-C. Chen, T. M. Crawford, D. J. M. Cunningham, C. De Breuck, C. D. Fassnacht, A. H. Gonzalez, T. R. Greve, Y. D. Hezaveh, K. Lacaille, K. C. Litke, S. Lower, J. Ma, M. Malkan, T. B. Miller, W. R. Morningstar, E. J. Murphy, D. Narayanan, K. A. Phadke, K. M. Rotermund, J. Sreevani, B. Stalder, A. A. Stark, M. L. Strandet, M. Tang, and A. Weiß, "Galaxy growth in a massive halo in the first billion years of cosmic history," *Nature* **553** (Jan., 2018) 51–54, arXiv:1712.03020.

[438] T. B. Miller, S. C. Chapman, M. Aravena, M. L. N. Ashby, C. C. Hayward, J. D. Vieira, A. Weiß, A. Babul, M. Béthermin, C. M. Bradford, M. Brodwin, J. E. Carlstrom, C.-C. Chen, D. J. M. Cunningham, C. De Breuck, A. H. Gonzalez, T. R. Greve, J. Harnett, Y. Hezaveh, K. Lacaille, K. C. Litke, J. Ma, M. Malkan, D. P. Marrone, W. Morningstar, E. J. Murphy, D. Narayanan, E. Pass, R. Perry, K. A. Phadke, D. Rennehan, K. M. Rotermund, J. Simpson, J. S. Spilker, J. Sreevani, A. A. Stark, M. L. Strandet, and A. L. Strom, "A massive core for a cluster of galaxies at a redshift of 4.3," *Nature* **556** (Apr., 2018) 469–472, arXiv:1804.09231.

[439] A. Weiß, C. De Breuck, D. P. Marrone, J. D. Vieira, J. E. Aguirre, K. A. Aird, M. Aravena, M. L. N. Ashby, M. Bayliss, B. A. Benson, M. Béthermin, A. D. Biggs, L. E. Bleem, J. J. Bock, M. Bothwell, C. M. Bradford, M. Brodwin, J. E. Carlstrom, C. L. Chang, S. C. Chapman, T. M. Crawford, A. T. Crites, T. de Haan, M. A. Dobbs, T. P. Downes, C. D. Fassnacht, E. M. George, M. D. Gladders, A. H. Gonzalez, T. R. Greve, N. W. Halverson, Y. D. Hezaveh, F. W. High, G. P. Holder, W. L. Holzapfel, S. Hoover, J. D. Hrubes, K. Husband, R. Keisler, A. T. Lee, E. M. Leitch, M. Lueker, D. Luong-Van, M. Malkan, V. McIntyre, J. J. McMahon, J. Mehl, K. M. Menten, S. S. Meyer, E. J. Murphy, S. Padin, T. Plagge, C. L. Reichardt, A. Rest, M. Rosenman, J. Ruel, J. E. Ruhl, K. K. Schaffer, E. Shirokoff, J. S. Spilker, B. Stalder, Z. Staniszewski, A. A. Stark, K. Story, K. Vanderlinde, N. Welikala, and R. Williamson, "ALMA Redshifts of Millimeter-selected Galaxies from the SPT Survey: The Redshift Distribution of Dusty Star-forming Galaxies," *Ap. J.* **767** (Apr., 2013) 88, arXiv:1303.2726 [astro-ph.CO].

[440] M. L. Strandet, A. Weiss, J. D. Vieira, C. de Breuck, J. E. Aguirre, M. Aravena, M. L. N. Ashby, M. Béthermin, C. M. Bradford, J. E. Carlstrom, S. C. Chapman, T. M. Crawford, W. Everett, C. D. Fassnacht, R. M. Furstenau, A. H. Gonzalez, T. R. Greve, B. Gullberg, Y. Hezaveh, J. R. Kamenetzky, K. Litke, J. Ma, M. Malkan, D. P. Marrone, K. M. Menten, E. J. Murphy, A. Nadolski, K. M. Rotermund, J. S. Spilker, A. A. Stark, and N. Welikala, "The Redshift Distribution of Dusty Star-forming Galaxies from the SPT Survey," *Ap. J.* **822** (May, 2016) 80, arXiv:1603.05094.

[441] Y. D. Hezaveh, N. Dalal, D. P. Marrone, Y.-Y. Mao, W. Morningstar, D. Wen, R. D. Blandford, J. E. Carlstrom, C. D. Fassnacht, G. P. Holder, A. Kemball, P. J. Marshall, N. Murray, L. Perreault Levasseur, J. D. Vieira, and R. H. Wechsler, "Detection of Lensing Substructure Using ALMA Observations of the Dusty Galaxy SDP.81," *Ap. J.* **823** (May, 2016) 37, arXiv:1601.01388.

[442] M. Béthermin, C. De Breuck, M. Sargent, and E. Daddi, "The influence of wavelength, flux, and lensing selection effects on the redshift distribution of dusty, star-forming galaxies," *A & A* **576** (Apr., 2015) L9, arXiv:1502.04710.

[443] Planck Collaboration Int. XXXIX, "Planck intermediate results. XXXIX. The Planck list of high-redshift source candidates," *A & A* **596** (Dec., 2016) A100, arXiv:1508.04171.

[444] M. Tucci, L. Toffolatti, G. de Zotti, and E. Martínez-González, "High-frequency predictions for number counts and spectral properties of extragalactic radio sources. New evidence of a break at mm wavelengths in spectra of bright blazar sources," *A & A* **533** (Sept., 2011) A57, arXiv:1103.5707.

[445] G. Puglisi, V. Galluzzi, L. Bonavera, J. Gonzalez-Nuevo, A. Lapi, M. Massardi, F. Perrotta, C. Baccigalupi, A. Celotti, and L. Danese, "Forecasting Polarized Radio Sources for CMB observations," *ArXiv e-prints* (Dec., 2017) , arXiv:1712.09639.

[446] T. Murphy, E. M. Sadler, R. D. Ekers, M. Massardi, P. J. Hancock, E. Mahony, R. Ricci, S. Burke-Spolaor, M. Calabretta, R. Chhetri, G. de Zotti, P. G. Edwards, J. A. Ekers, C. A. Jackson, M. J. Kesteven, E. Lindley, K. Newton-McGee, C. Phillips, P. Roberts, R. J. Sault, L. Staveley-Smith, R. Subrahmanyan, M. A. Walker, and W. E. Wilson, "The Australia Telescope 20 GHz Survey: the source catalogue," *Mon. Not. Roy. Astron. Soc.* **402** (Mar., 2010) 2403–2423, arXiv:0911.0002.

[447] L. M. Mocanu, T. M. Crawford, J. D. Vieira, K. A. Aird, M. Aravena, J. E. Austermann, B. A. Benson, M. Béthermin, L. E. Bleem, M. Bothwell, J. E. Carlstrom, C. L. Chang, S. Chapman, H.-M. Cho, A. T. Crites, T. de Haan, M. A. Dobbs, W. B. Everett, E. M. George, N. W. Halverson, N. Harrington, Y. Hezaveh, G. P. Holder, W. L. Holzapfel, S. Hoover, J. D. Hrubes, R. Keisler, L. Knox, A. T. Lee, E. M. Leitch, M. Lueker, D. Luong-Van, D. P. Marrone, J. J. McMahon, J. Mehl, S. S. Meyer, J. J. Mohr, T. E. Montroy, T. Natoli, S. Padin, T. Plagge, C. Pryke, A. Rest, C. L. Reichardt, J. E. Ruhl, J. T. Sayre, K. K. Schaffer, E. Shirokoff, H. G. Spieler, J. S. Spilker, B. Stalder, Z. Staniszewski, A. A. Stark, K. T. Story, E. R. Switzer, K. Vanderlinde, and R. Williamson, "Extragalactic Millimeter-wave Point-source Catalog, Number Counts and Statistics from 771 deg^2 of the SPT-SZ Survey," *Ap. J.* **779** (Dec., 2013) 61, arXiv:1306.3470.

[448] D. Marsden, M. Gralla, T. A. Marriage, E. R. Switzer, B. Partridge, M. Massardi, G. Morales, G. Addison, J. R. Bond, D. Crichton, S. Das, M. Devlin, R. Dünner, A. Hajian, M. Hilton, A. Hincks, J. P. Hughes, K. Irwin, A. Kosowsky, F. Menanteau, K. Moodley, M. Niemack, L. Page, E. D. Reese, B. Schmitt, N. Sehgal, J. Sievers, S. Staggs, D. Swetz, R. Thornton, and E. Wollack, "The Atacama Cosmology Telescope: dusty star-forming galaxies and active galactic nuclei in the Southern survey," *Mon. Not. Roy. Astron. Soc.* **439** (Apr., 2014) 1556–1574, arXiv:1306.2288 [astro-ph.CO].

[449] Planck Collaboration XXVI, "Planck 2015 results. XXVI. The Second Planck Catalogue of Compact Sources," *A & A* **594** (Sept., 2016) A26, arXiv:1507.02058.

[450] B. Partridge, L. Bonavera, M. López-Caniego, R. Datta, J. Gonzalez-Nuevo, M. Gralla, D. Herranz, A. Lähteenmäki, L. Mocanu, H. Prince, J. Vieira, N. Whitehorn, and L. Zhang, "Can CMB Surveys Help the AGN Community?," *Galaxies* **5** (Aug., 2017) 47.

[451] A. Kolodzig, M. Gilfanov, R. Sunyaev, S. Sazonov, and M. Brusa, "AGN and QSOs in the eROSITA All-Sky Survey. I. Statistical properties," *A & A* **558** (Oct., 2013) A89, arXiv:1212.2151 [astro-ph.CO].

[452] Planck Collab. Int. XLV, "Planck intermediate results. XLV. Radio spectra of northern extragalactic radio sources," *A & A* **596** (Dec., 2016) A106, arXiv:1606.05120.

[453] A. Lähteenmäki, E. Järvelä, T. Hovatta, M. Tornikoski, D. L. Harrison, M. López-Caniego, W. Max-Moerbeck, M. Mingaliev, T. J. Pearson, V. Ramakrishnan, A. C. S. Readhead, R. A. Reeves, J. L. Richards, Y. Sotnikova, and J. Tammi, "37 GHz observations of narrow-line Seyfert 1 galaxies," *A & A* **603** (July, 2017) A100, arXiv:1703.10365.

[454] A. Lähteenmäki, E. Järvelä, V. Ramakrishnan, M. Tornikoski, J. Tammi, R. J. C. Vera, and W. Chamani, "Radio jets and gamma-ray emission in radio-silent narrow-line Seyfert 1 galaxies," *A & A* **614** (June, 2018) L1, arXiv:1806.02058.

[455] S. Chen, M. Berton, G. La Mura, E. Congiu, V. Cracco, L. Foschini, J. H. Fan, S. Ciroi, P. Rafanelli, and D. Bastieri, "Probing narrow-line Seyfert 1 galaxies in the southern hemisphere," *A & A* **615** (Aug., 2018) A167, arXiv:1801.07234.

[456] B.-G. Andersson, A. Lazarian, and J. E. Vaillancourt, "Interstellar Dust Grain Alignment," *Ann. Rev. Astron. Astroph.* **53** (Aug., 2015) 501–539.

[457] L. Davis, Jr. and J. L. Greenstein, "The Polarization of Starlight by Aligned Dust Grains.," *Ap. J.* **114** (Sept., 1951) 206.

[458] S. Chandrasekhar and E. Fermi, "Magnetic Fields in Spiral Arms.," *Ap. J.* **118** (July, 1953) 113.

[459] R. H. Hildebrand, L. Kirby, J. L. Dotson, M. Houde, and J. E. Vaillancourt, "Dispersion of Magnetic Fields in Molecular Clouds. I," *Ap. J.* **696** (May, 2009) 567–573.

[460] M. Houde, J. E. Vaillancourt, R. H. Hildebrand, S. Chitsazzadeh, and L. Kirby, "Dispersion of Magnetic Fields in Molecular Clouds. II.," *Ap. J.* **706** (Dec., 2009) 1504–1516.

[461] L. M. Fissel, P. A. R. Ade, F. E. Angilè, P. Ashton, S. J. Benton, M. J. Devlin, B. Dober, Y. Fukui, N. Galitzki, N. N. Gandilo, J. Klein, A. L. Korotkov, Z.-Y. Li, P. G. Martin, T. G. Matthews, L. Moncelsi, F. Nakamura, C. B. Netterfield, G. Novak, E. Pascale, F. Poidevin, F. P. Santos, G. Savini, D. Scott, J. A. Shariff, J. Diego Soler, N. E. Thomas, C. E. Tucker, G. S. Tucker, and D. Ward-Thompson, "Balloon-Borne Submillimeter Polarimetry of the Vela C Molecular Cloud: Systematic Dependence of Polarization Fraction on Column Density and Local Polarization-Angle Dispersion," *Ap. J.* **824** (June, 2016) 134, arXiv:1509.05298.

[462] Planck Collaboration Int. XXXV, "*Planck* intermediate results. XXXV. Probing the role of the magnetic field in the formation of structure in molecular clouds," *A & A* **586** (2016) A138, arXiv:1502.04123.

[463] P. K. King, L. M. Fissel, C.-Y. Chen, and Z.-Y. Li, "Modelling dust polarization observations of molecular clouds through MHD simulations," *Mon. Not. Roy. Astron. Soc.* **474** (Mar., 2018) 5122–5142, arXiv:1709.08641.

[464] G. Vedrenne and J.-L. Atteia, *Gamma-Ray Bursts*. 2009.

[465] G. Ghirlanda, D. Burlon, G. Ghisellini, R. Salvaterra, M. G. Bernardini, S. Campana, S. Covino, P. D'Avanzo, V. D'Elia, A. Melandri, T. Murphy, L. Nava, S. D. Vergani, and G. Tagliaferri, "GRB Orphan Afterglows in Present and Future Radio Transient Surveys," *PASA* **31** (May, 2014) e022, arXiv:1402.6338 [astro-ph.HE].

[466] G. P. Lamb, M. Tanaka, and S. Kobayashi, "Transient survey rates for orphan afterglows from compact merger jets," *Mon. Not. Roy. Astron. Soc.* **476** (June, 2018) 4435–4441, arXiv:1712.00418 [astro-ph.HE].

[467] G. Ghirlanda, G. Ghisellini, R. Salvaterra, L. Nava, D. Burlon, G. Tagliaferri, S. Campana, P. D'Avanzo, and A. Melandri, "The faster the narrower: characteristic bulk velocities and jet opening angles of gamma-ray bursts," *Mon. Not. Roy. Astron. Soc.* **428** (Jan., 2013) 1410–1423, arXiv:1210.1215 [astro-ph.HE].

[468] B. D. Metzger, P. K. G. Williams, and E. Berger, "Extragalactic Synchrotron Transients in the Era of Wide-field Radio Surveys. I. Detection Rates and Light Curve Characteristics," *Ap. J.* **806** (June, 2015) 224, arXiv:1502.01350 [astro-ph.HE].

[469] D. Macpherson and D. Coward, "Multiwavelength detectability of Pop III GRBs from afterglow simulations," *Mon. Not. Roy. Astron. Soc.* **467** (May, 2017) 2476–2493.

[470] E. F. Keane and E. Petroff, "Fast radio bursts: search sensitivities and completeness," *Mon. Not. Roy. Astron. Soc.* **447** (Mar., 2015) 2852–2856, arXiv:1409.6125 [astro-ph.HE].

[471] P. C. Boyle and Chime/Frb Collaboration, "First detection of fast radio bursts between 400 and 800 MHz by CHIME/FRB," *The Astronomer's Telegram* **11901** (Aug., 2018) .

[472] V. Ravi, "The observed properties of fast radio bursts," *Mon. Not. Roy. Astron. Soc.* **482** (Jan., 2019) 1966–1978, arXiv:1710.08026 [astro-ph.HE].

[473] D. R. Lorimer, M. Bailes, M. A. McLaughlin, D. J. Narkevic, and F. Crawford, "A Bright Millisecond Radio Burst of Extragalactic Origin," *Science* **318** (Nov., 2007) 777, arXiv:0709.4301.

[474] V. Ravi, R. M. Shannon, M. Bailes, K. Bannister, S. Bhandari, N. D. R. Bhat, S. Burke-Spolaor, M. Caleb, C. Flynn, A. Jameson, S. Johnston, E. F. Keane, M. Kerr, C. Tiburzi, A. V. Tuntsov, and H. K. Vedantham, "The magnetic field and turbulence of the cosmic web measured using a brilliant fast radio burst," *Science* **354** (Dec., 2016) 1249–1252, arXiv:1611.05758 [astro-ph.HE].

[475] L. G. Spitler, P. Scholz, J. W. T. Hessels, S. Bogdanov, A. Brazier, F. Camilo, S. Chatterjee, J. M. Cordes, F. Crawford, J. Deneva, R. D. Ferdman, P. C. C. Freire, V. M. Kaspi, P. Lazarus, R. Lynch, E. C. Madsen, M. A. McLaughlin, C. Patel, S. M. Ransom, A. Seymour, I. H. Stairs, B. W. Stappers, J. van Leeuwen, and W. W. Zhu, "A repeating fast radio burst," *Nat.* **531** (Mar., 2016) 202–205, arXiv:1603.00581 [astro-ph.HE].

[476] CHIME/FRB Collaboration, "A second source of repeating fast radio bursts," *Nat.* **566** (Jan., 2019) 235–238, arXiv:1901.04525 [astro-ph.HE].

[477] P. J. Armitage, "Physical processes in protoplanetary disks," *ArXiv e-prints* (Sept., 2015) , arXiv:1509.06382 [astro-ph.SR].

[478] D. Johnstone, G. J. Herczeg, S. Mairs, J. Hatchell, G. C. Bower, H. Kirk, J. Lane, G. S. Bell, S. Graves, Y. Aikawa, H.-R. V. Chen, W.-P. Chen, M. Kang, S.-J. Kang, J.-E. Lee, O. Morata, A. Pon, P. Scicluna, A. Scholz, S. Takahashi, H. Yoo, and The JCMT Transient Team, "The JCMT Transient Survey: Stochastic and Secular Variability of Protostars and Disks In the Submillimeter Region Observed over 18 Months," *Ap. J.* **854** (Feb., 2018) 31, arXiv:1801.03537 [astro-ph.SR].

[479] S. Mairs, D. Johnstone, H. Kirk, J. Lane, G. S. Bell, S. Graves, G. J. Herczeg, P. Scicluna, G. C. Bower, H.-R. V. Chen, J. Hatchell, Y. Aikawa, W.-P. Chen, M. Kang, S.-J. Kang, J.-E. Lee, O. Morata, A. Pon, A. Scholz, S. Takahashi, H. Yoo, and The JCMT Transient Team, "The JCMT Transient Survey: Identifying Submillimeter Continuum Variability over Several Year Timescales Using Archival JCMT Gould Belt Survey Observations," *Ap. J.* **849** (Nov., 2017) 107, arXiv:1710.03761 [astro-ph.SR].

[480] J. Forbrich, M. J. Reid, K. M. Menten, V. M. Rivilla, S. J. Wolk, U. Rau, and C. J. Chandler, "Extreme Radio Flares and Associated X-Ray Variability from Young Stellar Objects in the Orion Nebula Cluster," *Ap. J.* **844** (Aug., 2017) 109, arXiv:1706.05562 [astro-ph.HE].

[481] R. J. Ivison, D. H. Hughes, H. M. Lloyd, M. K. Bang, and M. F. Bode, "Millimetre and Submillimetre Continuum Observations of Nova Cygni 1992 - a New Test of Mass Ejection Models," *Mon. Not. Roy. Astron. Soc.* **263** (Aug., 1993) L43.

[482] L. Chomiuk, J. D. Linford, J. Yang, T. J. O'Brien, Z. Paragi, A. J. Mioduszewski, R. J. Beswick, C. C. Cheung, K. Mukai, T. Nelson, V. A. R. M. Ribeiro, M. P. Rupen, J. L. Sokoloski, J. Weston, Y. Zheng, M. F. Bode, S. Eyres, N. Roy, and G. B. Taylor, "Binary orbits as the driver of γ-ray emission and mass ejection in classical novae," *Nat.* **514** (Oct., 2014) 339–342, arXiv:1410.3473 [astro-ph.HE].

[483] J. M. Paredes, J. Martí, M. Peracaula, G. Pooley, and I. F. Mirabel, "Exploring the high frequency emission of radio loud X-ray binaries," *A & A* **357** (May, 2000) 507–514, arXiv:astro-ph/0005517 [astro-ph].

[484] J. R. Masiero, E. Redwing, A. K. Mainzer, J. M. Bauer, R. M. Cutri, T. Grav, E. Kramer, C. R. Nugent, S. Sonnett, and E. L. Wright, "Small and Nearby NEOs Observed by NEOWISE During the First Three Years of Survey: Physical Properties," *Astron. J.* **156** (Aug., 2018) 60, arXiv:1806.04759 [astro-ph.EP].

[485] T. Müller, A. Marciniak, C. Kiss, R. Duffard, V. Ali-Lagoa, P. Bartczak, M. Butkiewicz-Bak, G. Dudzinski, E. Fernandez-Valenzuela, G. Marton, N. Morales, J.-L. Ortiz, D. Oszkiewicz, T. Santana-Ros, P. Santos-Sanz, R. Szakats, A. Takacsne Farkas, and E. Varga-Verebelyi, "Small Bodies Near and Far (SBNAF): Characterization of asteroids and TNOs," *European Planetary Science Congress* **11** (Sept., 2017) EPSC2017–474.

[486] K. Batygin and M. E. Brown, "Evidence for a Distant Giant Planet in the Solar System," *Astron. J.* **151** (Feb., 2016) 22, arXiv:1601.05438 [astro-ph.EP].

[487] IceCube Collaboration, M. G. Aartsen, M. Ackermann, J. Adams, J. A. Aguilar, M. Ahlers, M. Ahrens, I. Al Samarai, D. Altmann, K. Andeen, and et al., "Multimessenger observations of a flaring blazar coincident with high-energy neutrino IceCube-170922A," *Science* **361** (July, 2018) eaat1378, arXiv:1807.08816 [astro-ph.HE].

[488] S. M. Simon, J. Austermann, J. A. Beall, S. K. Choi, K. P. Coughlin, S. M. Duff, P. A. Gallardo, S. W. Henderson, F. B. Hills, S.-P. P. Ho, J. Hubmayr, A. Josaitis, B. J. Koopman, J. J. McMahon, F. Nati, L. Newburgh, M. D. Niemack, M. Salatino, A. Schillaci, B. L. Schmitt, S. T. Staggs, E. M. Vavagiakis, J. Ward, and E. J. Wollack, "The design and characterization of wideband spline-profiled feedhorns for Advanced ACTPol," in *Millimeter, Submillimeter, and Far-Infrared Detectors and Instrumentation for Astronomy VIII*, vol. 9914 of *Proc. SPIE*, p. 991416. July, 2016.

[489] G. Yassin, P. Kittara, A. Jiralucksanawong, S. Wangsuya, J. Leech, and M. Jones, "A High Performance Horn for Large Format Focal Plane Arrays," in *Eighteenth International Symposium on Space Terahertz Technology*, A. Karpov, ed., p. 199. 2007.

[490] L. Zeng, C. L. Bennett, D. T. Chuss, and E. J. Wollack, "A Low Cross-Polarization Smooth-Walled Horn With Improved Bandwidth," *IEEE Transactions on Antennas and Propagation* **58** (Apr., 2010) 1383–1387.

[491] C. Granet, G. L. James, R. Bolton, and G. Moorey, "A Smooth-Walled Spline-Profile Horn as an Alternative to the Corrugated Horn for Wide Band Millimeter-Wave Applications," *IEEE Transactions on Antennas and Propagation* **52** (Mar., 2004) 848–854.

[492] S. M. Simon, J. E. Golec, A. Ali, J. Austermann, J. A. Beall, S. M. M. Bruno, S. K. Choi, K. T. Crowley, S. Dicker, B. Dober, S. M. Duff, E. Healy, C. A. Hill, S.-P. P. Ho, J. Hubmayr, Y. Li, M. Lungu, J. M. an dJohn Orlowski-Scherer, M. Salatino, S. Staggs, , E. J. Wollack, Z. Xu, and N. Zhu, "Feedhorn development and scalability for simons observatory and beyond," in *Millimeter, Submillimeter, and Far-Infrared Detectors and Instrumentation for Astronomy VIII*, vol. 10708 of *Proc. SPIE*, pp. 10708 – 10708 – 12. 2018. https://doi.org/10.1117/12.2313405.

[493] E. J. Wollack, K. U-yen, and D. T. Chuss, "Photonic choke-joints for dual-polarization waveguides,".

[494] W. Hu, M. M. Hedman, and M. Zaldarriaga, "Benchmark parameters for CMB polarization experiments," *Phys.Rev.* **D67** (2003) 043004, arXiv:astro-ph/0210096 [astro-ph].

[495] S. C. Parshley, M. Niemack, R. Hills, *et al.*, "The optical design of the six-meter CCAT-prime and Simons Observatory telescopes," in *Society of Photo-Optical Instrumentation Engineers (SPIE) Conference Series*, vol. 10700 of *Society of Photo-Optical Instrumentation Engineers (SPIE) Conference Series*, p. 1070041. July, 2018. arXiv:1807.06678 [astro-ph.IM].

[496] N. Galitzki *et al.*, "The Simons Observatory: Instrument Overview," *Proc. SPIE Int. Soc. Opt. Eng.* **10708** (2018) 1070804, arXiv:1808.04493 [astro-ph.IM].

[497] C. Dragone, "Offset multireflector antennas with perfect pattern symmetry and polarization discrimination," *AT T Technical Journal* **57** (Sept., 1978) 2663–2684.

[498] C. Bischoff, A. Brizius, I. Buder, Y. Chinone, K. Cleary, R. N. Dumoulin, A. Kusaka, R. Monsalve, S. K. Næss, L. B. Newburgh, G. Nixon, R. Reeves, K. M. Smith, K. Vanderlinde, I. K. Wehus, M. Bogdan, R. Bustos, S. E. Church, R. Davis, C. Dickinson, H. K. Eriksen, T. Gaier, J. O. Gundersen, M. Hasegawa, M. Hazumi, C. Holler, K. M. Huffenberger, W. A. Imbriale, K. Ishidoshiro, M. E. Jones, P. Kangaslahti, D. J. Kapner, C. R. Lawrence, E. M. Leitch, M. Limon, J. J. McMahon, A. D. Miller, M. Nagai, H. Nguyen, T. J. Pearson, L. Piccirillo, S. J. E. Radford, A. C. S. Readhead, J. L. Richards, D. Samtleben, M. Seiffert, M. C. Shepherd, S. T. Staggs, O. Tajima, K. L. Thompson, R. Williamson, B. Winstein, E. J. Wollack, and J. T. L. Zwart, "The Q/U Imaging ExperimenT Instrument," *Ap. J.* **768** (May, 2013) 9, arXiv:1207.5562 [astro-ph.IM].

[499] A. Kusaka, J. Appel, T. Essinger-Hileman, J. A. Beall, L. E. Campusano, H.-M. Cho, S. K. Choi, K. Crowley, J. W. Fowler, P. Gallardo, M. Hasselfield, G. Hilton, S.-P. P. Ho, K. Irwin, N. Jarosik, M. D. Niemack, G. W. Nixon, M. Nolta, J. Page, Lyman A., G. A. Palma, L. Parker, S. Raghunathan, C. D. Reintsema, J. Sievers, S. M. Simon, S. T. Staggs, K. Visnjic, and K.-W. Yoon, "Results from the Atacama B-mode Search (ABS) experiment," *Journal of Cosmology and Astro-Particle Physics* **2018** (Sept., 2018) 005.

[500] M. D. Niemack, "Designs for a large-aperture telescope to map the CMB 10X faster," *Appl. Opt.* **55** (2016) 1688–96, arXiv:1511.04506 [astro-ph.IM].

[501] C. Dragone, "First-order correction of aberrations in Cassegrainian and Gregorian antennas," *IEEE Transactions on Antennas and Propagation* **31** (Sept., 1983) 764–775.

[502] S. C. Parshley, J. Kronshage, *et al.*, "CCAT-prime: a novel telescope for sub-millimeter astronomy," in *Society of Photo-Optical Instrumentation Engineers (SPIE) Conference Series*, vol. 10700 of *Society of Photo-Optical Instrumentation Engineers (SPIE) Conference Series*, p. 107005X. July, 2018. arXiv:1807.06675 [astro-ph.IM].

[503] H. Tran, A. Lee, S. Hanany, M. Milligan, and T. Renbarger, "Comparison of the crossed and the Gregorian Mizuguchi-Dragone for wide- field millimeter-wave astronomy," *Applied Optics* **47** (Jan., 2008) 103–109.

[504] P. A. Gallardo *et al.*, "Studies of Systematic Uncertainties for Simons Observatory: Optical Effects and Sensitivity Considerations," *Proc. SPIE Int. Soc. Opt. Eng.* **10708** (2018) 107083Y, arXiv:1808.05152 [astro-ph.IM].

[505] J. E. Gudmundsson, P. A. Gallardo, R. Puddu, S. R. Dicker, A. E. Adler, A. M. Ali, A. Bazarko, G. E. Chesmore, G. Coppi, N. F. Cothard, N. Dachlythra, M. Devlin, R. Dünner, G. Fabbian, N. Galitzki, J. E. Golec, S.-P. Patty Ho, P. C. Hargrave, A. M. Kofman, A. T. Lee, M. Limon, F. T. Matsuda, P. D. Mauskopf, K. Moodley, F. Nati, M. D. Niemack, J. Orlowski-Scherer, L. A. Page, B. Partridge, G. Puglisi, C. L. Reichardt, C. E. Sierra, S. M. Simon, G. P. Teply, C. Tucker, E. J. Wollack, Z. Xu, and N. Zhu, "The Simons Observatory: modeling optical systematics in the Large Aperture Telescope," *Applied Optics* **60** no. 4, (Feb., 2021) 823, arXiv:2009.10138 [astro-ph.IM].

[506] S. R. Dicker *et al.*, "Cold optical design for the large aperture Simons' Observatory telescope," *Proc. SPIE Int. Soc. Opt. Eng.* **10700** (2018) 107003E, arXiv:1808.05058 [astro-ph.IM].

[507] C. A. Hill *et al.*, "BoloCalc: a sensitivity calculator for the design of Simons Observatory," *Proc. SPIE Int. Soc. Opt. Eng.* **10708** (2018) 1070842, arXiv:1806.04316 [astro-ph.IM]. [Astronomy9,1070842(2018)].

[508] P. A. Gallardo, N. F. Cothard, R. Puddu, R. Dunner, B. J. Koopman, M. D. Niemack, S. M. Simon, and E. J. Wollack, "Far Sidelobes from Baffles and Telescope Support Structures in the Atacama Cosmology Telescope," 2018. arXiv:1808.05101 [astro-ph.IM].

[509] P. A. F. Rojas *et al.*, "Far sidelobe effects from panel gaps of the Atacama Cosmology Telescope," *Proc. SPIE Int. Soc. Opt. Eng.* **9914** (2016) 99142Q.

[510] J. M. Fowler *et al.*, "Optical Design of the Atacama Cosmology Telescope and the Millimeter Bolometric Array Camera," *Appl. Opt.* **46** (2007) 3444–3454, arXiv:astro-ph/0701020 [astro-ph].

[511] J. G. Mangum, J. W. M. Baars, A. Greve, R. Lucas, R. C. Snel, P. Wallace, and M. Holdaway, "Evaluation of the ALMA Prototype Antennas," *Publ. Astron. Soc. Pac.* **118** (2006) 1257, arXiv:astro-ph/0609329 [astro-ph].

[512] B. Nikolic, R. E. Hills, and J. S. Richer, "Measurement of antenna surfaces from in- and out-of-focus beam maps using astronomical sources," *A & A* **465** (Apr., 2007) 679–683, astro-ph/0612241.

[513] R. Datta, C. D. Munson, M. D. Niemack, J. J. McMahon, J. Britton, E. J. Wollack, J. Beall, M. J. Devlin, J. Fowler, P. Gallardo, J. Hubmayr, K. Irwin, L. Newburgh, J. P. Nibarger, L. Page, M. A. Quijada, B. L. Schmitt, S. T. Staggs, R. Thornton, and L. Zhang, "Large-aperture wide-bandwidth antireflection-coated silicon lenses for millimeter wavelengths," *Applied Optics* **52** no. 36, (Dec., 2013) 8747, arXiv:1307.4715 [astro-ph.IM].

[514] G. E. Chesmore, T. Mroczkowski, J. McMahon, S. Sutariya, A. Josaitis, and L. Jensen, "Reflectometry Measurements of the Loss Tangent in Silicon at Millimeter Wavelengths," *arXiv e-prints* (Dec., 2018) arXiv:1812.03785, arXiv:1812.03785 [astro-ph.IM].

[515] E. C. Shaw, P. A. R. Ade, S. Akers, M. Amiri, J. Austermann, J. Beall, D. T. Becker, S. J. Benton, A. S. Bergman, J. J. Bock, J. R. Bond, S. A. Bryan, H. C. Chiang, C. R. Contaldi, R. S. Domagalski, O. Doré, S. M. Duff, A. J. Duivenvoorden, H. K. Eriksen, M. Farhang, J. P. Filippini, L. M. Fissel, A. A. Fraisse, K. Freese, M. Galloway, A. E. Gambrel, N. N. Gandilo, K. Ganga, A. Grigorian, R. Gualtieri, J. E. Gudmundsson, M. Halpern, J. Hartley, M. Hasselfield, G. Hilton, W. Holmes, V. V. Hristov, Z. Huang, J. Hubmayr, K. D. Irwin, W. C. Jones, A. Kahn, C. L. Kuo, Z. D. Kermish, A. Lennox, J. S. Y. Leung, S. Li, P. V. Mason, K. Megerian, L. M. Mocanu, L. Moncelsi, T. A. Morford, J. M. Nagy, R. Nie, C. B. Netterfield, M. Nolta, B. Osherson, I. L. Padilla, A. S. Rahlin, S. Redmond, C. Reintsema, L. J. Romualdez, J. E. Ruhl, M. C. Runyan, J. A. Shariff, C. Shiu, J. D. Soler, X. Song, H. Thommesen, A. Trangsrud, C. Tucker, R. S. Tucker, A. D. Turner, J. Ullom, J. F. van der List, J. Van Lanen, M. R. Vissers, A. C. Weber, S. Wen, I. K. Wehus, D. V. Wiebe, and E. Y.

Young, "Design and pre-flight performance of SPIDER 280 GHz receivers," *arXiv e-prints* (Dec., 2020) arXiv:2012.12407, arXiv:2012.12407 [astro-ph.IM].

[516] Z. Xu, T. Bhandarkar, G. Coppi, A. M. Kofman, J. L. Orlowski-Scherer, N. Zhu, A. M. Ali, K. Arnold, J. E. Austermann, S. K. Choi, J. Connors, N. F. Cothard, M. Devlin, S. Dicker, B. Dober, S. M. Duff, G. Fabbian, N. Galitzki, S. K. Haridas, K. Harrington, E. Healy, S.-P. P. Ho, J. Hubmayr, J. Iuliano, J. Lashner, Y. Li, M. Limon, B. J. Koopman, H. McCarrick, J. Moore, F. Nati, M. D. Niemack, C. L. Reichardt, K. Perez Sarmiento, J. Seibert, M. Silva-Feaver, R. F. Sonka, S. Staggs, R. J. Thornton, E. M. Vavagiakis, M. R. Vissers, S. Walker, Y. Wang, E. J. Wollack, and K. Zheng, "The Simons Observatory: the Large Aperture Telescope Receiver (LATR) Integration and Validation Results," *arXiv e-prints* (Dec., 2020) arXiv:2012.07862, arXiv:2012.07862 [astro-ph.IM].

[517] J. H. Kang, P. A. R. Ade, Z. Ahmed, R. W. Aikin, K. D. Alexander, D. Barkats, S. J. Benton, C. A. Bischoff, J. J. Bock, H. Boenish, R. Bowens-Rubin, J. A. Brevik, I. Buder, E. Bullock, V. Buza, J. Connors, J. Cornelison, B. P. Crill, M. Crumrine, M. Dierickx, L. Duband, C. Dvorkin, J. P. Filippini, S. Fliescher, J. A. Grayson, G. Hall, M. Halpern, S. Harrison, S. R. Hildebrandt, G. C. Hilton, H. Hui, K. D. Irwin, K. S. Karkare, E. Karpel, J. P. Kaufman, B. G. Keating, S. Kefeli, S. A. Kernasovskiy, J. M. Kovac, C. L. Kuo, N. A. Larsen, K. Lau, E. M. Leitch, M. Lueker, K. G. Megerian, L. Moncelsi, T. Namikawa, B. Netterfield, H. T. Nguyen, R. O'Brient, R. W. Ogburn, S. Palladino, C. Pryke, B. Racine, S. Richter, A. Schillaci, R. Schwarz, C. D. Sheehy, A. Soliman, T. St. Germaine, Z. K. Staniszewski, B. Steinbach, R. V. Sudiwala, G. P. Teply, K. L. Thompson, J. E. Tolan, C. Tucker, A. D. Turner, C. Umiltà, A. G. Vieregg, A. Wandui, A. C. Weber, D. V. Wiebe, J. Willmert, C. L. Wong, W. L. K. Wu, H. Yang, W. Yoon, K., and C. Zhang, "2017 upgrade and performance of BICEP3: a 95GHz refracting telescope for degree-scale CMB polarization," in *Millimeter, Submillimeter, and Far-Infrared Detectors and Instrumentation for Astronomy IX*, J. Zmuidzinas and J.-R. Gao, eds., vol. 10708 of *Society of Photo-Optical Instrumentation Engineers (SPIE) Conference Series*, p. 107082N. July, 2018. arXiv:1808.00567 [astro-ph.IM].

[518] J. A. Sobrin, P. A. R. Ade, Z. Ahmed, A. J. Anderson, J. S. Avva, R. Basu Thakur, A. N. Bender, B. A. Benson, J. E. Carlstrom, F. W. Carter, T. W. Cecil, C. L. Chang, J. F. Cliche, A. Cukierman, T. de Haan, J. Ding, M. A. Dobbs, D. Dutcher, W. Everett, A. Foster, J. Gallichio, A. Gilbert, J. C. Groh, S. T. Guns, N. W. Halverson, A. H. Harke-Hosemann, N. L. Harrington, J. W. Henning, W. L. Holzapfel, N. Huang, K. D. Irwin, O. B. Jeong, M. Jonas, T. S. Khaire, A. M. Kofman, M. Korman, D. L. Kubik, S. Kuhlmann, C. L. Kuo, A. T. Lee, A. E. Lowitz, S. S. Meyer, D. Michalik, J. Montgomery, A. Nadolski, T. Natoli, H. Nguyen, G. I. Noble, V. Novosad, S. Padin, Z. Pan, J. Pearson, C. M. Posada, W. Quan, A. Rahlin, J. E. Ruhl, J. T. Sayre, E. Shirokoff, G. Smecher, A. A. Stark, K. T. Story, A. Suzuki, K. L. Thompson, C. Tucker, K. Vanderlinde, J. D. Vieira, G. Wang, N. Whitehorn, V. Yefremenko, K. W. Yoon, and M. Young, "Design and characterization of the SPT-3G receiver," in *Millimeter, Submillimeter, and Far-Infrared Detectors and Instrumentation for Astronomy IX*, J. Zmuidzinas and J.-R. Gao, eds., vol. 10708 of *Society of Photo-Optical Instrumentation Engineers (SPIE) Conference Series*, p. 107081H. July, 2018. arXiv:1809.00032 [astro-ph.IM].

[519] A. Nadolski, J. D. Vieira, J. A. Sobrin, A. M. Kofman, P. A. R. Ade, Z. Ahmed, A. J. Anderson, J. S. Avva, R. Basu Thakur, A. N. Bender, B. A. Benson, L. Bryant, J. E. Carlstrom, F. W. Carter, T. W. Cecil, C. L. Chang, J. R. Cheshire, G. E. Chesmore, J. F. Cliche, A. Cukierman, T. de Haan, M. Dierickx, J. Ding, D. Dutcher, W. Everett, J. Farwick, K. R. Ferguson, L. Florez, A. Foster, J. Fu, J. Gallicchio, A. E. Gambrel, R. W. Gardner, J. C. Groh, S. Guns, R. Guyser, N. W. Halverson, A. H. Harke-Hosemann, N. L. Harrington, R. J. Harris, J. W. Henning, W. L. Holzapfel, D. Howe, N. Huang, K. D. Irwin, O. Jeong, M. Jonas, A. Jones, M. Korman, J. Kovac, D. L. Kubik, S. Kuhlmann, C. L. Kuo, A. T. Lee, A. E. Lowitz, J. McMahon, J. Meier, S. S. Meyer, D. Michalik, J. Montgomery,

T. Natoli, H. Nguyen, G. I. Noble, V. Novosad, S. Padin, Z. Pan, P. Paschos, J. Pearson, C. M. Posada, W. Quan, A. Rahlin, D. Riebel, J. E. Ruhl, J. T. Sayre, E. Shirokoff, G. Smecher, A. A. Stark, J. Stephen, K. T. Story, A. Suzuki, C. Tandoi, K. L. Thompson, C. Tucker, K. Vanderlinde, G. Wang, N. Whitehorn, V. Yefremenko, K. W. Yoon, and M. R. Young, "Broadband, millimeter-wave antireflection coatings for large-format, cryogenic aluminum oxide optics," *Applied Optics* **59** no. 10, (Apr., 2020) 3285, arXiv:1912.04272 [physics.ins-det].

[520] P. A. R. Ade, G. Pisano, C. Tucker, and S. Weaver, "A review of metal mesh filters," in *Society of Photo-Optical Instrumentation Engineers (SPIE) Conference Series*, J. Zmuidzinas, W. S. Holland, S. Withington, and W. D. Duncan, eds., vol. 6275 of *Society of Photo-Optical Instrumentation Engineers (SPIE) Conference Series*, p. 62750U. June, 2006.

[521] J. L. Orlowski-Scherer, N. Zhu, Z. Xu, A. Ali, K. S. Arnold, P. C. Ashton, G. Coppi, M. Devlin, S. Dicker, N. Galitzki, P. A. Gallardo, B. Keating, A. T. Lee, M. Limon, M. Lungu, A. May, J. McMahon, M. D. Niemack, L. Piccirillo, G. Puglisi, M. Salatino, M. Silva-Feaver, S. M. Simon, R. Thornton, and E. M. Vavagiakis, "Simons Observatory large aperture receiver simulation overview," in *Society of Photo-Optical Instrumentation Engineers (SPIE) Conference Series*, vol. 10708 of *Society of Photo-Optical Instrumentation Engineers (SPIE) Conference Series*, p. 107083X. July, 2018. arXiv:1808.06648 [astro-ph.IM].

[522] N. Zhu, J. L. Orlowski-Scherer, Z. Xu, A. Ali, K. S. Arnold, P. C. Ashton, G. Coppi, M. J. Devlin, S. Dicker, N. Galitzki, P. A. Gallardo, S. W. Henderson, S.-P. P. Ho, J. Hubmayr, B. Keating, A. T. Lee, M. Limon, M. Lungu, P. D. Mauskopf, A. J. May, J. McMahon, M. D. Niemack, L. Piccirillo, G. Puglisi, M. Sathyanarayana Rao, M. Salatino, M. Silva-Feaver, S. M. Simon, S. Staggs, R. Thornton, J. N. Ullom, E. M. Vavagiakis, B. Westbrook, and E. J. Wollack, "Simons Observatory large aperture telescope receiver design overview," in *Society of Photo-Optical Instrumentation Engineers (SPIE) Conference Series*, vol. 10708 of *Society of Photo-Optical Instrumentation Engineers (SPIE) Conference Series*, p. 1070829. July, 2018. arXiv:1808.10037 [astro-ph.IM].

[523] M. I. Hollister, D. A. Bauer, R. C. Dhuley, P. Lukens, L. D. Martin, M. K. Ruschman, R. L. Schmitt, and G. L. Tatkowski, "The cryogenics design of the SuperCDMS SNOLAB experiment," in *Materials Science and Engineering Conference Series*, vol. 278 of *Materials Science and Engineering Conference Series*, p. 012118. Dec., 2017.

[524] C. Alduino, F. Alessandria, M. Balata, D. Biare, M. Biassoni, C. Bucci, A. Caminata, L. Canonica, L. Cappelli, G. Ceruti, A. Chiarini, N. Chott, M. Clemenza, S. Copello, A. Corsi, O. Cremonesi, A. D'Addabbo, S. Dell'Oro, L. Di Paolo, M. L. Di Vacri, A. Drobizhev, M. Faverzani, E. Ferri, M. A. Franceschi, R. Gaigher, L. Gladstone, P. Gorla, M. Guetti, L. Ioannucci, Y. G. Kolomensky, C. Ligi, L. Marini, T. Napolitano, S. Nisi, A. Nucciotti, I. Nutini, T. O'Donnell, D. Orlandi, J. L. Ouellet, C. E. Pagliarone, L. Pattavina, A. Pelosi, M. Perego, E. Previtali, B. Romualdi, A. Rotilio, C. Rusconi, D. Santone, V. Singh, M. Sisti, L. Taffarello, E. Tatananni, F. Terranova, S. L. Wagaarachchi, J. Wallig, and C. Zarra, "The CUORE cryostat: An infrastructure for rare event searches at millikelvin temperatures," *Cryogenics* **102** (Sept., 2019) 9–21, arXiv:1904.05745 [physics.ins-det].

[525] K. Karkare, P. A. Ade, Z. Ahmed, R. Aikin, K. Alexander, M. Amiri, D. Barkats, S. Benton, C. Bischoff, J. Bock, *et al.*, "Keck array and bicep3: spectral characterization of 5000+ detectors," in *Millimeter, Submillimeter, and Far-Infrared Detectors and Instrumentation for Astronomy VII*, vol. 9153, p. 91533B, International Society for Optics and Photonics. 2014.

[526] Z. Pan, M. Liu, R. B. Thakur, B. A. Benson, D. J. Fixsen, H. Goksu, E. Rath, and S. S. Meyer, "Compact millimeter-wavelength fourier-transform spectrometer," *Applied optics* **58** no. 23, (2019) 6257–6267.

[527] M. Crumrine, P. A. R. Ade, Z. Ahmed, R. W. Aikin, K. D. Alexander, D. Barkats, S. J. Benton, C. A. Bischoff, J. J. Bock, R. Bowens-Rubin, J. A. Brevik, I. Buder, E. Bullock, V. Buza, J. Connors, J. Cornelison, B. P. Crill, M. Dierickx, L. Duband, C. Dvorkin, J. P. Filippini, S. Fliescher, J. A. Grayson, G. Hall, M. Halpern, S. A. Harrison, S. R. Hildebrandt, G. C. Hilton, H. Hui, K. D. Irwin, J. H. Kang, K. S. Karkare, E. Karpel, J. P. Kaufman, B. G. Keating, S. Kefeli, S. A. Kernasovskiy, J. M. Kovac, C. L. Kuo, N. A. Larsen, K. Lau, E. M. Leitch, M. V. Lueker, K. G. Megerian, L. Moncelsi, T. Namikawa, C. B. Netterfield, H. T. Nguyen, R. O'Brient, R. W. Ogburn, S. Palladino, C. Pryke, B. Racine, S. Richter, R. Schwarz, A. Schillaci, C. D. Sheehy, A. Soliman, T. St. Germaine, Z. K. Staniszewski, B. Steinbach, R. V. Sudiwala, G. P. Teply, K. L. Thompson, J. E. Tolan, C. E. Tucker, A. D. Turner, C. Umiltà, A. G. Vieregg, A. Wandui, A. C. Weber, D. V. Wiebe, J. Willmert, C. L. Wong, W. L. K. Wu, E. Yang, K. W. Yoon, and C. Zhang, "BICEP Array cryostat and mount design," in *Millimeter, Submillimeter, and Far-Infrared Detectors and Instrumentation for Astronomy IX*, vol. 10708 of *Society of Photo-Optical Instrumentation Engineers (SPIE) Conference Series*, p. 107082D. July, 2018. arXiv:1808.00569 [astro-ph.IM].

[528] **BICEP2** Collaboration, P. A. R. Ade *et al.*, "BICEP2 III: Instrumental Systematics," *Astrophys. J.* **814** no. 2, (2015) 110, arXiv:1502.00608 [astro-ph.IM].

[529] Y. Takahashi, P. Ade, D. Barkats, J. Battle, E. Bierman, *et al.*, "Characterization of the BICEP Telescope for High-Precision Cosmic Microwave Background Polarimetry," *Astrophys.J.* **711** (2010) 1141–1156, arXiv:0906.4069 [astro-ph.CO].

[530] S. A. Bryan, S. M. Simon, M. Gerbino, G. Teply, A. Ali, Y. Chinone, K. Crowley, G. Fabbian, P. A. Gallardo, N. Goeckner-Wald, B. Keating, B. Koopman, A. Kusaka, F. Matsuda, P. Mauskopf, J. McMahon, F. Nati, G. Puglisi, C. L. Reichardt, M. Salatino, Z. Xu, and N. Zhu, "Development of calibration strategies for the Simons Observatory," in *Millimeter, Submillimeter, and Far-Infrared Detectors and Instrumentation for Astronomy IX*, J. Zmuidzinas and J.-R. Gao, eds., vol. 10708 of *Society of Photo-Optical Instrumentation Engineers (SPIE) Conference Series*, p. 1070840. July, 2018. arXiv:1810.04633 [astro-ph.IM].

[531] BICEP2 Collaboration, Keck Array Collaboration, P. A. R. Ade, Z. Ahmed, R. W. Aikin, D. Barkats, S. J. Benton, C. A. Bischoff, J. J. Bock, R. Bowens-Rubin, J. A. Brevik, I. Buder, E. Bullock, V. Buza, J. Connors, J. Cornelison, B. P. Crill, M. Crumrine, M. Dierickx, L. Duband, J. P. Filippini, S. Fliescher, J. Grayson, G. Hall, M. Halpern, S. Harrison, S. R. Hildebrandt, G. C. Hilton, H. Hui, K. D. Irwin, J. Kang, K. S. Karkare, E. Karpel, J. P. Kaufman, B. G. Keating, S. Kefeli, S. A. Kernasovskiy, J. M. Kovac, C. L. Kuo, N. A. Larsen, K. Lau, E. M. Leitch, M. Lueker, K. G. Megerian, L. Moncelsi, T. Namikawa, C. B. Netterfield, H. T. Nguyen, R. O'Brient, I. Ogburn, R. W., S. Palladino, C. Pryke, B. Racine, S. Richter, A. Schillaci, R. Schwarz, C. D. Sheehy, A. Soliman, T. St. Germaine, Z. K. Staniszewski, B. Steinbach, R. V. Sudiwala, G. P. Teply, K. L. Thompson, J. E. Tolan, C. Tucker, A. D. Turner, C. Umilta, A. G. Vieregg, A. Wandui, A. C. Weber, D. V. Wiebe, J. Willmert, C. L. Wong, W. L. K. Wu, H. Yang, K. W. Yoon, and C. Zhang, "BICEP2/Keck Array XI: Beam Characterization and Temperature-to-Polarization Leakage in the BK15 Data Set," *Ap. J.* **884** no. 2, (Oct., 2019) 114, arXiv:1904.01640 [astro-ph.IM].

[532] K. S. Karkare, P. A. R. Ade, Z. Ahmed, K. D. Alexander, M. Amiri, D. Barkats, S. J. Benton, C. A. Bischoff, J. J. Bock, H. Boenish, R. Bowens-Rubin, I. Buder, E. Bullock, V. Buza, J. Connors, J. P. Filippini, S. T. Fliescher, J. A. Grayson, M. Halpern, S. A. Harrison, G. C. Hilton, V. V. Hristov, H. Hui, K. D. Irwin, J. H. Kang, E. Karpel, S. Kefeli, S. A. Kernasovskiy, J. M. Kovac, C. L. Kuo, E. M. Leitch, M. Lueker, K. G. Megerian, V. Monticue, T. Namikawa, C. B. Netterfield, H. T. Nguyen, R. O'Brient, R. W. Ogburn, C. L. Pryke, C. D. Reintsema, S. Richter, M. T. St. Germaine, R. Schwarz, C. D. Sheehy, Z. K. Staniszewski, B. Steinbach, G. P. Teply, K. L. Thompson, J. E. Tolan,

C. Tucker, A. D. Turner, A. G. Vieregg, A. Wandui, A. Weber, J. Willmert, C. L. Wong, W. L. K. Wu, and K. W. Yoon, "Optical characterization of the BICEP3 CMB polarimeter at the South Pole," in *Millimeter, Submillimeter, and Far-Infrared Detectors and Instrumentation for Astronomy VIII*, W. S. Holland and J. Zmuidzinas, eds., vol. 9914 of *Society of Photo-Optical Instrumentation Engineers (SPIE) Conference Series*, p. 991430. July, 2016. arXiv:1607.04567 [astro-ph.IM].

[533] BICEP2 and Keck Array Collaborations, P. A. R. Ade, R. W. Aikin, D. Barkats, S. J. Benton, C. A. Bischoff, J. J. Bock, K. J. Bradford, J. A. Brevik, I. Buder, E. Bullock, C. D. Dowell, L. Duband, J. P. Filippini, S. Fliescher, S. R. Golwala, M. Halpern, M. Hasselfield, S. R. Hildebrandt, G. C. Hilton, H. Hui, K. D. Irwin, J. H. Kang, K. S. Karkare, J. P. Kaufman, B. G. Keating, S. Kefeli, S. A. Kernasovskiy, J. M. Kovac, C. L. Kuo, E. M. Leitch, M. Lueker, K. G. Megerian, C. B. Netterfield, H. T. Nguyen, R. O'Brient, I. Ogburn, R. W., A. Orlando, C. Pryke, S. Richter, R. Schwarz, C. D. Sheehy, Z. K. Staniszewski, R. V. Sudiwala, G. P. Teply, K. Thompson, J. E. Tolan, A. D. Turner, A. G. Vieregg, A. C. Weber, C. L. Wong, and K. W. Yoon, "BICEP2/Keck Array. IV. Optical Characterization and Performance of the BICEP2 and Keck Array Experiments," *Ap. J.* **806** no. 2, (June, 2015) 206, arXiv:1502.00596 [astro-ph.IM].

[534] J. Cornelison, P. A. R. Ade, Z. Ahmed, M. Amiri, D. Barkats, R. Basu Thakur, C. Bischoff, J. J. Bock, H. Boenish, E. Bullock, V. Buza, J. R. Cheshire, J. Connors, M. Crumrine, A. J. Cukierman, E. V. Denison, M. Dierickx, L. Duband, M. Eiben, S. Fatigoni, J. P. Filippini, S. Fliescher, N. Goeckner-Wald, D. C. Goldfinger, J. A. Grayson, P. Grimes, G. Hall, G. Halal, M. Halpern, S. A. Harrison, S. Henderson, S. Hildebrandt, G. C. Hilton, J. Hubmayr, H. Hui, K. D. Irwin, J. Kang, K. Karkare, E. Karpel, S. Kefeli, S. A. Kernasovkiy, J. M. Kovac, C. L. Kuo, K. Lau, E. Leitch, K. G. Megerian, L. Minutolo, L. Moncelsi, Y. Nakato, T. Namikawa, H. T. Nguyen, R. O'Brient, R. W. Ogburn, S. Palladino, N. Precup, T. Prouve, C. Pryke, B. Racine, C. D. Reintsema, S. Richter, A. Schillaci, B. Schmitt, R. Schwarz, C. D. Sheehy, A. Soliman, T. St. Germaine, B. Steinbach, R. V. Sudiwala, G. P. Teply, K. L. Thompson, J. E. Tolan, C. Tucker, A. D. Turner, C. Umilta, A. G. Vieregg, A. Wandui, A. C. Weber, D. V. Wiebe, J. Willmert, C. L. Wong, W. L. K. Wu, E. Yang, K. W. Yoon, E. Young, C. Yu, L. Zeng, C. Zhang, and S. Zhang, "Polarization calibration of the BICEP3 CMB polarimeter at the South Pole," in *Society of Photo-Optical Instrumentation Engineers (SPIE) Conference Series*, vol. 11453 of *Society of Photo-Optical Instrumentation Engineers (SPIE) Conference Series*, p. 1145327. Dec., 2020. arXiv:2012.05934 [astro-ph.IM].

[535] F. Matsuda, L. Lowry, A. Suzuki, M. Aguilar Fáundez, K. Arnold, D. Barron, F. Bianchini, K. Cheung, Y. Chinone, T. Elleflot, G. Fabbian, N. Goeckner-Wald, M. Hasegawa, D. Kaneko, N. Katayama, B. Keating, A. T. Lee, M. Navaroli, H. Nishino, H. Paar, G. Puglisi, P. L. Richards, J. Seibert, P. Siritanasak, O. Tajima, S. Takatori, C. Tsai, and B. Westbrook, "The POLARBEAR Fourier transform spectrometer calibrator and spectroscopic characterization of the POLARBEAR instrument," *Review of Scientific Instruments* **90** no. 11, (Nov., 2019) 115115, arXiv:1904.02901 [astro-ph.IM].

[536] C. W. O'Dell, D. S. Swetz, and P. T. Timbie, "Calibration of millimeter-wave polarimeters using a thin dielectric sheet," *IEEE Transactions on Microwave Theory and Techniques* **50** no. 9, (Sep., 2002) 2135–2141.

[537] O. Tajima, H. Nguyen, C. Bischoff, A. Brizius, I. Buder, and A. Kusaka, "Novel Calibration System with Sparse Wires for CMB Polarization Receivers," *Journal of Low Temperature Physics* **167** no. 5-6, (June, 2012) 936–942.

[538] E. Dart, L. Rotman, B. Tierney, M. Hester, and J. Zurawski, "The science dmz: A network design pattern for data-intensive science," in *SC '13: Proceedings of the International Conference on High Performance Computing, Networking, Storage and Analysis*, pp. 1–10. 2013.

[539] A. Hanemann, J. W. Boote, E. L. Boyd, J. Durand, L. Kudarimoti, R. Lapacz, D. M. Swany, S. Trocha, and J. Zurawski, "Perfsonar: A service oriented architecture for multi-domain network monitoring," in *Proceedings of the Third International Conference on Service-Oriented Computing*, ICSOC'05, pp. 241–254. Springer-Verlag, Berlin, Heidelberg, 2005. http://dx.doi.org/10.1007/11596141_19.

[540] A. P. Lane, "Submillimeter Transmission at South Pole," in *Astrophysics From Antarctica*, G. Novak and R. Landsberg, eds., vol. 141 of *Astronomical Society of the Pacific Conference Series*, pp. 289–295. 1998.

[541] D. A. Erasmus, "An Analysis of CLoud Cover and Water Valor for the ALMA Project," *A Report to European Southern Observatories* (Dec, 2002) . https://www.eso.org/gen-fac/pubs/astclim/espas/radioseeing/pdf/ALMAFnlRep_Erasmus_Dec2002.pdf.

[542] R. W. Ogburn, P. A. R. Ade, R. W. Aikin, M. Amiri, S. J. Benton, C. A. Bischoff, J. J. Bock, J. A. Bonetti, J. A. Brevik, E. Bullock, B. Burger, G. Davis, C. D. Dowell, L. Duband, J. P. Filippini, S. Fliescher, S. R. Golwala, M. Gordon, M. Halpern, M. Hasselfield, G. Hilton, V. V. Hristov, H. Hui, K. Irwin, J. P. Kaufman, B. G. Keating, S. A. Kernasovskiy, J. M. Kovac, C. L. Kuo, E. M. Leitch, M. Lueker, T. Montroy, C. B. Netterfield, H. T. Nguyen, R. O'Brient, A. Orlando, C. L. Pryke, C. Reintsema, S. Richter, J. E. Ruhl, M. C. Runyan, R. Schwarz, C. D. Sheehy, Z. K. Staniszewski, R. V. Sudiwala, G. P. Teply, K. Thompson, J. E. Tolan, A. D. Turner, A. G. Vieregg, D. V. Wiebe, P. Wilson, and C. L. Wong, "BICEP2 and Keck array operational overview and status of observations," in *Millimeter, Submillimeter, and Far-Infrared Detectors and Instrumentation for Astronomy VI*, vol. 8452 of *Proc. SPIE* , p. 84521A. Sept., 2012. arXiv:1208.0638 [astro-ph.IM].

[543] J. E. Carlstrom, P. A. R. Ade, K. A. Aird, B. A. Benson, L. E. Bleem, S. Busetti, C. L. Chang, E. Chauvin, H.-M. Cho, T. M. Crawford, A. T. Crites, M. A. Dobbs, N. W. Halverson, S. Heimsath, W. L. Holzapfel, J. D. Hrubes, M. Joy, R. Keisler, T. M. Lanting, A. T. Lee, E. M. Leitch, J. Leong, W. Lu, M. Lueker, D. Luong-Van, J. J. McMahon, J. Mehl, S. S. Meyer, J. J. Mohr, T. E. Montroy, S. Padin, T. Plagge, C. Pryke, J. E. Ruhl, K. K. Schaffer, D. Schwan, E. Shirokoff, H. G. Spieler, Z. Staniszewski, A. A. Stark, C. Tucker, K. Vanderlinde, J. D. Vieira, and R. Williamson, "The 10 Meter South Pole Telescope," *PASP* **123** (May, 2011) 568, arXiv:0907.4445 [astro-ph.IM].

[544] J. W. Fowler, M. D. Niemack, S. R. Dicker, A. M. Aboobaker, P. A. R. Ade, E. S. Battistelli, M. J. Devlin, R. P. Fisher, M. Halpern, P. C. Hargrave, A. D. Hincks, M. Kaul, J. Klein, J. M. Lau, M. Limon, T. A. Marriage, P. D. Mauskopf, L. Page, S. T. Staggs, D. S. Swetz, E. R. Switzer, R. J. Thornton, and C. E. Tucker, "Optical design of the atacama cosmology telescope and the millimeter bolometric array camera," *Appl. Opt.* **46** no. 17, (Jun, 2007) 3444–3454. http://ao.osa.org/abstract.cfm?URI=ao-46-17-3444.

[545] K. Arnold, N. Stebor, P. A. R. Ade, Y. Akiba, A. E. Anthony, M. Atlas, D. Barron, A. Bender, D. Boettger, J. Borrill, S. Chapman, Y. Chinone, A. Cukierman, M. Dobbs, T. Elleflot, J. Errard, G. Fabbian, C. Feng, A. Gilbert, N. Goeckner-Wald, N. W. Halverson, M. Hasegawa, K. Hattori, M. Hazumi, W. L. Holzapfel, Y. Hori, Y. Inoue, G. C. Jaehnig, A. H. Jaffe, N. Katayama, B. Keating, Z. Kermish, R. Keskitalo, T. Kisner, M. L. Jeune, A. T. Lee, E. M. Leitch, E. Linder, F. Matsuda, T. Matsumura, X. Meng, N. J. Miller, H. Morii, M. J. Myers, M. Navaroli, H. Nishino, T. Okamura, H. Paar, J. Peloton, D. Poletti, C. Raum, G. Rebeiz, C. L. Reichardt, P. L. Richards, C. Ross, K. M. Rotermund, D. E. Schenck, B. D. Sherwin, I. Shirley, M. Sholl, P. Siritanasak, G. Smecher, B. Steinbach, R. Stompor, A. Suzuki, J. Suzuki, S. Takada, S. Takakura, T. Tomaru, B. Wilson, A. Yadav, and O. Zahn, "The simons array: expanding polarbear to three multi-chroic telescopes," vol. 9153, p. 91531F. Aug., 2014. https://doi.org/10.1117/12.2057332.

[546] K. Harington, T. Marriage, A. Ali, C. L. Appel, John W.and Bennett, F. Boone, M. Brewer, M. Chan, D. T. Chuss, F. Colazo, S. Dahal, K. Denis, R. Dunner, J. Eimer, T. Essinger-Hileman, P. Fluxa, M. Halpern, G. Hilton, G. F. Hinshaw, J. Hubmayr, J. Iuliano, J. Karakla, J. McMahon, N. T. Miller, S. H. Miseley, G. Palma, L. Parker, M. Petroff, B. Pradenas, K. Rostern, M. Sagliocca, D. Valle, D. Watts, E. Wollack, Z. Xu, and L. Zeng, "The Cosmology Large Angular Scale Surveyor," vol. 9914. 2016. https://doi.org/10.1117/12.2233125.

[547] **BICEP2** Collaboration, P. A. R. Ade *et al.*, "Detection of B-Mode Polarization at Degree Angular Scales by BICEP2," *Phys. Rev. Lett.* **112** no. 24, (2014) 241101, arXiv:1403.3985 [astro-ph.CO].

[548] E. Hivon, K. M. Gorski, C. B. Netterfield, B. P. Crill, S. Prunet, and F. Hansen, "Master of the cosmic microwave background anisotropy power spectrum: a fast method for statistical analysis of large and complex cosmic microwave background data sets," *Astrophys. J.* **567** (2002) 2, arXiv:astro-ph/0105302 [astro-ph].

[549] E. L. Wright, "Scanning and mapping strategies for CMB experiments," arXiv:astro-ph/9612006 [astro-ph].

[550] J. R. Bond, A. H. Jaffe, and L. Knox, "Estimating the power spectrum of the cosmic microwave background," *Phys. Rev.* **D57** (1998) 2117–2137, arXiv:astro-ph/9708203 [astro-ph].

[551] A. Lewis and S. Bridle, "Cosmological parameters from CMB and other data: a Monte- Carlo approach," *Phys. Rev.* **D66** (2002) 103511, astro-ph/0205436.

[552] J.-B. Melin, J. G. Bartlett, and J. Delabrouille, "Catalog extraction in SZ cluster surveys: a matched filter approach," *A & A* **459** (Nov., 2006) 341–352, astro-ph/0602424.

[553] Planck Collaboration XXIX, "Planck 2013 results. XXIX. The Planck catalogue of Sunyaev-Zeldovich sources," *Astron. Astrophys.* **571** (2014) A29, arXiv:1303.5089 [astro-ph.CO].

[554] E. Pierpaoli, S. Anthoine, K. M. Huffenberger, and I. Daubechies, "Reconstructing Sunyaev-Zeldovich clusters in future CMB experiments," *Mon. Not. Roy. Astron. Soc.* **359** (2005) 261–271, arXiv:astro-ph/0412197 [astro-ph].

[555] J. Maldacena, "Non-gaussian features of primordial fluctuations in single field inflationary models," *Journal of High Energy Physics* **2003** no. 5, (May, 2003) 013, arXiv:astro-ph/0210603 [astro-ph].

[556] K. N. Abazajian *et al.*, "Inflation Physics from the Cosmic Microwave Background and Large Scale Structure," *Astropart. Phys.* **63** (2015) 55–65, arXiv:1309.5381 [astro-ph.CO].

[557] N. Bartolo, E. Komatsu, S. Matarrese, and A. Riotto, "Non-Gaussianity from inflation: theory and observations," *Phys. Rept.* **402** no. 3-4, (Nov., 2004) 103–266, arXiv:astro-ph/0406398 [astro-ph].

[558] Planck Collaboration XXII, "Planck 2013 results. XXII. Constraints on inflation," arXiv:1303.5082 [astro-ph.CO].

[559] Planck Collaboration, Y. Akrami, F. Arroja, M. Ashdown, J. Aumont, C. Baccigalupi, M. Ballardini, A. J. Banday, R. B. Barreiro, N. Bartolo, S. Basak, K. Benabed, J. P. Bernard, M. Bersanelli, P. Bielewicz, J. J. Bock, J. R. Bond, J. Borrill, F. R. Bouchet, F. Boulanger, M. Bucher, C. Burigana, R. C. Butler, E. Calabrese, J. F. Cardoso, J. Carron, A. Challinor, H. C. Chiang, L. P. L. Colombo, C. Combet, D. Contreras, B. P. Crill, F. Cuttaia, P. de Bernardis, G. de Zotti, J. Delabrouille, J. M. Delouis, E. Di Valentino, J. M. Diego, S. Donzelli, O. Doré, M. Douspis, A. Ducout, X. Dupac, S. Dusini, G. Efstathiou, F. Elsner, T. A. Enßlin, H. K. Eriksen, Y. Fantaye, J. Fergusson, R. Fernandez-Cobos, F. Finelli, F. Forastieri, M. Frailis, E. Franceschi, A. Frolov, S. Galeotta, S. Galli, K. Ganga,

C. Gauthier, R. T. Génova-Santos, M. Gerbino, T. Ghosh, J. González-Nuevo, K. M. Górski, S. Gratton, A. Gruppuso, J. E. Gudmundsson, J. Hamann, W. Handley, F. K. Hansen, D. Herranz, E. Hivon, D. C. Hooper, Z. Huang, A. H. Jaffe, W. C. Jones, E. Keihänen, R. Keskitalo, K. Kiiveri, J. Kim, T. S. Kisner, N. Krachmalnicoff, M. Kunz, H. Kurki-Suonio, G. Lagache, J. M. Lamarre, A. Lasenby, M. Lattanzi, C. R. Lawrence, M. Le Jeune, J. Lesgourgues, F. Levrier, A. Lewis, M. Liguori, P. B. Lilje, V. Lindholm, M. López-Caniego, P. M. Lubin, Y. Z. Ma, J. F. Macías-Pérez, G. Maggio, D. Maino, N. Mandolesi, A. Mangilli, A. Marcos-Caballero, M. Maris, P. G. Martin, E. Martínez-González, S. Matarrese, N. Mauri, J. D. McEwen, P. D. Meerburg, P. R. Meinhold, A. Melchiorri, A. Mennella, M. Migliaccio, S. Mitra, M. A. Miville-Deschênes, D. Molinari, A. Moneti, L. Montier, G. Morgante, A. Moss, M. Münchmeyer, P. Natoli, H. U. Nørgaard-Nielsen, L. Pagano, D. Paoletti, B. Partridge, G. Patanchon, H. V. Peiris, F. Perrotta, V. Pettorino, F. Piacentini, L. Polastri, G. Polenta, J. L. Puget, J. P. Rachen, M. Reinecke, M. Remazeilles, A. Renzi, G. Rocha, C. Rosset, G. Roudier, J. A. Rubiño-Martín, B. Ruiz-Granados, L. Salvati, M. Sandri, M. Savelainen, D. Scott, E. P. S. Shellard, M. Shiraishi, C. Sirignano, G. Sirri, L. D. Spencer, R. Sunyaev, A. S. Suur-Uski, J. A. Tauber, D. Tavagnacco, M. Tenti, L. Toffolatti, M. Tomasi, T. Trombetti, J. Valiviita, B. Van Tent, P. Vielva, F. Villa, N. Vittorio, B. D. Wandelt, I. K. Wehus, S. D. M. White, A. Zacchei, J. P. Zibin, and A. Zonca, "Planck 2018 results. X. Constraints on inflation," *A & A* **641** (Sept., 2020) A10, arXiv:1807.06211 [astro-ph.CO].

[560] X. Chen, "Primordial Features as Evidence for Inflation," *JCAP* **1201** (2012) 038, arXiv:1104.1323 [hep-th].

[561] P. Adshead, C. Dvorkin, W. Hu, and E. A. Lim, "Non-Gaussianity from step features in the inflationary potential," *Phys. Rev.* **D 85** no. 2, (Jan., 2012) 023531, arXiv:1110.3050 [astro-ph.CO].

[562] L. Pogosian, M. Shimon, M. Mewes, and B. Keating, "Future CMB constraints on cosmic birefringence and implications for fundamental physics," *Phys. Rev.* **D 100** no. 2, (July, 2019) 023507, arXiv:1904.07855 [astro-ph.CO].

[563] T. Namikawa, Y. Guan, O. Darwish, B. D. Sherwin, S. Aiola, N. Battaglia, J. A. Beall, D. T. Becker, J. R. Bond, E. Calabrese, G. E. Chesmore, S. K. Choi, M. J. Devlin, J. Dunkley, R. Dünner, A. E. Fox, P. A. Gallardo, V. Gluscevic, D. Han, M. Hasselfield, G. C. Hilton, A. D. Hincks, R. Hložek, J. Hubmayr, K. Huffenberger, J. P. Hughes, B. J. Koopman, A. Kosowsky, T. Louis, M. Lungu, A. MacInnis, M. S. Madhavacheril, M. Mallaby-Kay, L. Maurin, J. McMahon, K. Moodley, S. Naess, F. Nati, L. B. Newburgh, J. P. Nibarger, M. D. Niemack, L. A. Page, F. J. Qu, N. Robertson, A. Schillaci, N. Sehgal, C. Sifón, S. M. Simon, D. N. Spergel, S. T. Staggs, E. R. Storer, A. van Engelen, J. van Lanen, and E. J. Wollack, "Atacama Cosmology Telescope: Constraints on cosmic birefringence," *Phys. Rev.* **D 101** no. 8, (Apr., 2020) 083527, arXiv:2001.10465 [astro-ph.CO].

[564] W. Hu and T. Okamoto, "Mass reconstruction with cmb polarization," *Astrophys.J.* **574** (2002) 566–574, arXiv:astro-ph/0111606 [astro-ph].

[565] T. Okamoto and W. Hu, "CMB lensing reconstruction on the full sky," *Phys. Rev.* **D67** (2003) 083002, arXiv:astro-ph/0301031 [astro-ph].

[566] M. Millea, E. Anderes, B. D. Wandelt, and M. Millea, "Bayesian delensing of CMB temperature and polarization," arXiv:1708.06753 [astro-ph.CO].

[567] J. Caldeira, W. L. K. Wu, B. Nord, C. Avestruz, S. Trivedi, and K. T. Story, "DeepCMB: Lensing Reconstruction of the Cosmic Microwave Background with Deep Neural Networks," arXiv:1810.01483 [astro-ph.CO].

[568] M. S. Madhavacheril and J. C. Hill, "Mitigating Foreground Biases in CMB Lensing Reconstruction Using Cleaned Gradients," *Phys. Rev.* **D98** no. 2, (2018) 023534, arXiv:1802.08230 [astro-ph.CO].

[569] A. Manzotti, "Future cosmic microwave background delensing with galaxy surveys," *Phys. Rev.* **D97** no. 4, (2018) 043527, arXiv:1710.11038 [astro-ph.CO].

[570] **DES, SPT** Collaboration, T. M. C. Abbott *et al.*, "Dark Energy Survey Year 1 Results: Joint Analysis of Galaxy Clustering, Galaxy Lensing, and CMB Lensing Two-point Functions," arXiv:1810.02322 [astro-ph.CO].

[571] **DES** Collaboration, E. J. Baxter *et al.*, "Dark Energy Survey Year 1 Results: Methodology and Projections for Joint Analysis of Galaxy Clustering, Galaxy Lensing, and CMB Lensing Two-point Functions," arXiv:1802.05257 [astro-ph.CO].

[572] B. Thorne, J. Dunkley, D. Alonso, and S. Naess, "The Python Sky Model: software for simulating the Galactic microwave sky," arXiv:1608.02841 [astro-ph.CO].

[573] B. Hensley, *On the nature of interstellar grains*. PhD thesis, Princeton University, 2015.

[574] T. Ghosh, F. Boulanger, P. G. Martin, A. Bracco, F. Vansyngel, J. Aumont, J. J. Bock, O. Doré, U. Haud, P. M. W. Kalberla, and P. Serra, "Modelling and simulation of large-scale polarized dust emission over the southern Galactic cap using the GASS Hi data," *A & A* **601** (May, 2017) A71, arXiv:1611.02418.

[575] Planck Collaboration, "Planck intermediate results. L. Evidence of spatial variation of the polarized thermal dust spectral energy distribution and implications for CMB B-mode analysis," *A & A* **599** (Mar., 2017) A51, arXiv:1606.07335.

[576] C. Sheehy and A. Slosar, "No evidence for dust B-mode decorrelation in Planck data," *ArXiv e-prints* (Sept., 2017) , arXiv:1709.09729.

[577] A. G. Kritsuk, S. D. Ustyugov, and M. L. Norman, "The structure and statistics of interstellar turbulence," *New Journal of Physics* **19** no. 6, (June, 2017) 065003, arXiv:1705.01912.

[578] BICEP 2, Keck Array and Planck Collaborations, "Joint Analysis of BICEP2/Keck Array and Planck Data," *Phys. Rev. Lett.* **114** (2015) 101301, arXiv:1502.00612 [astro-ph.CO].

[579] **BICEP2, Keck Array** Collaboration, P. A. R. Ade *et al.*, "BICEP2 / Keck Array X: Constraints on Primordial Gravitational Waves using Planck, WMAP, and New BICEP2/Keck Observations through the 2015 Season," *Submitted to: Phys. Rev. Lett.* (2018) , arXiv:1810.05216 [astro-ph.CO].

[580] J. Dunkley, E. Calabrese, J. Sievers, G. E. Addison, N. Battaglia, E. S. Battistelli, J. R. Bond, S. Das, M. J. Devlin, R. Dünner, J. W. Fowler, M. Gralla, A. Hajian, M. Halpern, M. Hasselfield, A. D. Hincks, R. Hlozek, J. P. Hughes, K. D. Irwin, A. Kosowsky, T. Louis, T. A. Marriage, D. Marsden, F. Menanteau, K. Moodley, M. Niemack, M. R. Nolta, L. A. Page, B. Partridge, N. Sehgal, D. N. Spergel, S. T. Staggs, E. R. Switzer, H. Trac, and E. Wollack, "The Atacama Cosmology Telescope: likelihood for small-scale CMB data," *JCAP* **7** (July, 2013) 025, arXiv:1301.0776.

[581] M. Béthermin, E. Daddi, G. Magdis, M. T. Sargent, Y. Hezaveh, D. Elbaz, D. Le Borgne, J. Mullaney, M. Pannella, V. Buat, V. Charmandaris, G. Lagache, and D. Scott, "A Unified Empirical Model for Infrared Galaxy Counts Based on the Observed Physical Evolution of Distant Galaxies," *Ap. J.* **757** no. 2, (Oct, 2012) L23, arXiv:1208.6512 [astro-ph.CO].

[582] Planck Collaboration, P. A. R. Ade, N. Aghanim, C. Armitage-Caplan, M. Arnaud, M. Ashdown, F. Atrio-Barand ela, J. Aumont, C. Baccigalupi, A. J. Banday, R. B. Barreiro, J. G. Bartlett, E. Battaner, K. Benabed, A. Benoît, A. Benoit-Lévy, J. P. Bernard, M. Bersanelli, M. Bethermin, P. Bielewicz, K. Blagrave, J. Bobin, J. J. Bock, A. Bonaldi, J. R. Bond, J. Borrill, F. R. Bouchet, F. Boulanger, M. Bridges, M. Bucher, C. Burigana, R. C. Butler, J. F. Cardoso, A. Catalano, A. Challinor, A. Chamballu, X. Chen, H. C. Chiang, L. Y. Chiang, P. R. Christensen, S. Church, D. L. Clements, S. Colombi, L. P. L. Colombo, F. Couchot, A. Coulais, B. P. Crill, A. Curto, F. Cuttaia, L. Danese, R. D. Davies, R. J. Davis, P. de Bernardis, A. de Rosa, G. de Zotti, J. Delabrouille, J. M. Delouis, F. X. Désert, C. Dickinson, J. M. Diego, H. Dole, S. Donzelli, O. Doré, M. Douspis, X. Dupac, G. Efstathiou, T. A. Enßlin, H. K. Eriksen, F. Finelli, O. Forni, M. Frailis, E. Franceschi, S. Galeotta, K. Ganga, T. Ghosh, M. Giard, Y. Giraud-Héraud, J. González-Nuevo, K. M. Górski, S. Gratton, A. Gregorio, A. Gruppuso, F. K. Hansen, D. Hanson, D. Harrison, G. Helou, S. Henrot-Versillé, C. Hernández-Monteagudo, D. Herranz, S. R. Hildebrand t, E. Hivon, M. Hobson, W. A. Holmes, A. Hornstrup, W. Hovest, K. M. Huffenberger, A. H. Jaffe, T. R. Jaffe, W. C. Jones, M. Juvela, P. Kalberla, E. Keihänen, J. Kerp, R. Keskitalo, T. S. Kisner, R. Kneissl, J. Knoche, L. Knox, M. Kunz, H. Kurki-Suonio, F. Lacasa, G. Lagache, A. Lähteenmäki, J. M. Lamarre, M. Langer, A. Lasenby, R. J. Laureijs, C. R. Lawrence, R. Leonardi, J. León-Tavares, J. Lesgourgues, M. Liguori, P. B. Lilje, M. Linden-Vørnle, M. López-Caniego, P. M. Lubin, J. F. Macías-Pérez, B. Maffei, D. Maino, N. Mand olesi, M. Maris, D. J. Marshall, P. G. Martin, E. Martínez-González, S. Masi, M. Massardi, S. Matarrese, F. Matthai, P. Mazzotta, A. Melchiorri, L. Mendes, A. Mennella, M. Migliaccio, S. Mitra, M. A. Miville-Deschênes, A. Moneti, L. Montier, G. Morgante, D. Mortlock, D. Munshi, J. A. Murphy, P. Naselsky, F. Nati, P. Natoli, C. B. Netterfield, H. U. Nørgaard-Nielsen, F. Noviello, D. Novikov, I. Novikov, S. Osborne, C. A. Oxborrow, F. Paci, L. Pagano, F. Pajot, R. Paladini, D. Paoletti, B. Partridge, F. Pasian, G. Patanchon, O. Perdereau, L. Perotto, F. Perrotta, F. Piacentini, M. Piat, E. Pierpaoli, D. Pietrobon, S. Plaszczynski, E. Pointecouteau, G. Polenta, N. Ponthieu, L. Popa, T. Poutanen, G. W. Pratt, G. Prézeau, S. Prunet, J. L. Puget, J. P. Rachen, W. T. Reach, R. Rebolo, M. Reinecke, M. Remazeilles, C. Renault, S. Ricciardi, T. Riller, I. Ristorcelli, G. Rocha, C. Rosset, G. Roudier, M. Rowan-Robinson, J. A. Rubiño-Martín, B. Rusholme, M. Sandri, D. Santos, G. Savini, D. Scott, M. D. Seiffert, P. Serra, E. P. S. Shellard, L. D. Spencer, J. L. Starck, V. Stolyarov, R. Stompor, R. Sudiwala, R. Sunyaev, F. Sureau, D. Sutton, A. S. Suur-Uski, J. F. Sygnet, J. A. Tauber, D. Tavagnacco, L. Terenzi, L. Toffolatti, M. Tomasi, M. Tristram, M. Tucci, J. Tuovinen, M. Türler, L. Valenziano, J. Valiviita, B. Van Tent, P. Vielva, F. Villa, N. Vittorio, L. A. Wade, B. D. Wandelt, N. Welikala, M. White, S. D. M. White, B. Winkel, D. Yvon, A. Zacchei, and A. Zonca, "Planck 2013 results. XXX. Cosmic infrared background measurements and implications for star formation," *A & A* **571** (Nov, 2014) A30, arXiv:1309.0382 [astro-ph.CO].

[583] M. Tegmark and G. Efstathiou, "A method for subtracting foregrounds from multi-frequency cmb sky maps," *Mon. Not. Roy. Astron. Soc.* **281** (1996) 1297, arXiv:astro-ph/9507009 [astro-ph].

[584] C. M. Hirata and U. Seljak, "Reconstruction of lensing from the cosmic microwave background polarization," *Phys. Rev.* **D68** (2003) 083002, arXiv:astro-ph/0306354 [astro-ph].

[585] K. M. Smith, D. Hanson, M. LoVerde, C. M. Hirata, and O. Zahn, "Delensing CMB Polarization with External Datasets," *JCAP* **1206** (2012) 014, arXiv:1010.0048 [astro-ph.CO].

[586] D. Green, J. Meyers, and A. van Engelen, "CMB Delensing Beyond the B Modes," arXiv:1609.08143 [astro-ph.CO].